How open is the asteroid-mass primordial black hole window?

Matthew Gorton* and Anne M. Green†

School of Physics and Astronomy, University of Nottingham, Nottingham, NG7 2RD, United Kingdom

* matthew.gorton@nottingham.ac.uk, †anne.green@nottingham.ac.uk

March 7, 2024

arXiv:2403.03839v1 [astro-ph.CO] 6 Mar 2024

Abstract

Primordial black holes (PBHs) can make up all of the dark matter (DM) if their mass, m, is in the so-called 'asteroid-mass window', $10^{17}\,\mathrm{g} \lesssim m \lesssim 10^{22}\,\mathrm{g}$. Observational constraints on the abundance of PBHs are usually calculated assuming they all have the same mass, however this is unlikely to be a good approximation. PBHs formed from the collapse of large density perturbations during radiation domination are expected to have an extended mass function (MF), due to the effects of critical collapse. The PBH MF is often assumed to be lognormal, however it has recently been shown that other functions are a better fit to numerically calculated MFs. We recalculate both current and potential future constraints for these improved fitting functions. We find that for current constraints the asteroid-mass window narrows, but remains open (i.e. all of the DM can be in the form of PBHs) unless the PBH MF is wider than expected. Future evaporation and microlensing constraints may together exclude all of the DM being in PBHs, depending on the width of the PBH MF and also the shape of its low and high mass tails.

Contents

1 Introduction **1**

2 Method **2**

3 Results **7**

4 Conclusions **9**

References **11**

A Comparison with previous constraints for lognormal mass function **14**

1 Introduction

Primordial black holes (PBHs) may have formed in the early Universe [1–3] and are a potential dark matter (DM) candidate. The most commonly-studied PBH formation mechanism is the collapse of large density fluctuations generated by inflation. The abundance of PBHs is constrained by

observations over a wide range of PBH masses (see Refs. [4–7] for recent reviews). PBHs can only account for all the DM if their mass m lies in the range $10^{17}\,\mathrm{g} \lesssim m \lesssim 10^{22}\,\mathrm{g}$, often referred to as the 'asteroid-mass window'. Lighter PBHs making up all of the DM is excluded by limits on the products of their evaporation, while planetary and Solar mass PBHs are excluded by microlensing and other observations.

Typically observational constraints are calculated assuming that PBHs have a delta-function mass function (MF). However, PBHs formed from the collapse of large density perturbations are expected to have an extended mass function. Due to critical collapse, the mass of a PBH depends on both the horizon mass and the amplitude of the density fluctuation from which it forms. Consequently even if PBHs all form at the same time, from a narrow peak in the primordial power spectrum, they have a range of masses [8–10]. Furthermore, the peaks in the primordial power spectrum that are produced by concrete inflation models, for instance hybrid inflation with a mild waterfall transition [11], can be broad.

With an extended PBH MF the constraints are 'smeared out'; for each constraint the tightest limit on the fraction of DM in the form of PBHs, f_{PBH}, is weakened, however the range of peak masses [1] for which $f_{\mathrm{PBH}} = 1$ is excluded is wider [12–14]. Refs. [12–14] calculated constraints on PBHs with a lognormal MF, which provides a reasonable fit to the MFs found for PBHs produced by various inflation models [12, 15]. However, Gow et al. [16] found that the MFs they calculate are better fit by other functions, specifically a skew-lognormal distribution and a form motivated by critical collapse. As Gow et al. [16] mention, the shape of the low mass tail is important when considering evaporation constraints on PBHs with MFs which peak in the asteroid-mass window. It is important to ascertain how the extent to which the asteroid-mass window remains open (i.e. for what range of peak masses $f_{\mathrm{PBH}} = 1$ is allowed) depends on the shape of the PBH MF.

We recalculate the constraints on f_{PBH} in the asteroid-mass window for the MF fitting functions presented in Ref. [16]. Sec. 2 presents the constraints we consider, the fits to the PBH MF that we use and their time evolution, and the method for applying the constraints to extended mass functions. We present the current and prospective future constraints on PBHs with extended MFs in Sec. 3 and conclude with discussion in Sec. 4.

2 Method

In Sec. 2.1 we overview the (current and proposed future) evaporation and stellar microlensing constraints that we use. In Sec. 2.2 we overview the best-performing MF fitting functions from Ref. [16] and the evolution of the MF due to evaporation, and in Sec. 2.3 we outline how the constraints are applied to extended mass functions.

2.1 Constraints on PBHs around the asteroid-mass window

The constraints on PBHs with masses $m \lesssim 10^{17}\,\mathrm{g}$ and $m \gtrsim 10^{22}\,\mathrm{g}$ arise from PBH evaporation via Hawking radiation (Sec. 2.1.1) and stellar microlensing (Sec. 2.1.2) respectively. The constraints that we consider (both existing and prospective) are shown in Fig. 1 for a delta-function PBH MF.

2.1.1 PBH evaporation

PBHs formed from the collapse of large density perturbations rapidly lose angular momentum and charge [17, 18]. Hawking [19, 20] showed that a non-rotating, uncharged black hole (BH) of mass

[1] Here and throughout peak mass refers to the mass at which the mass function is maximal.

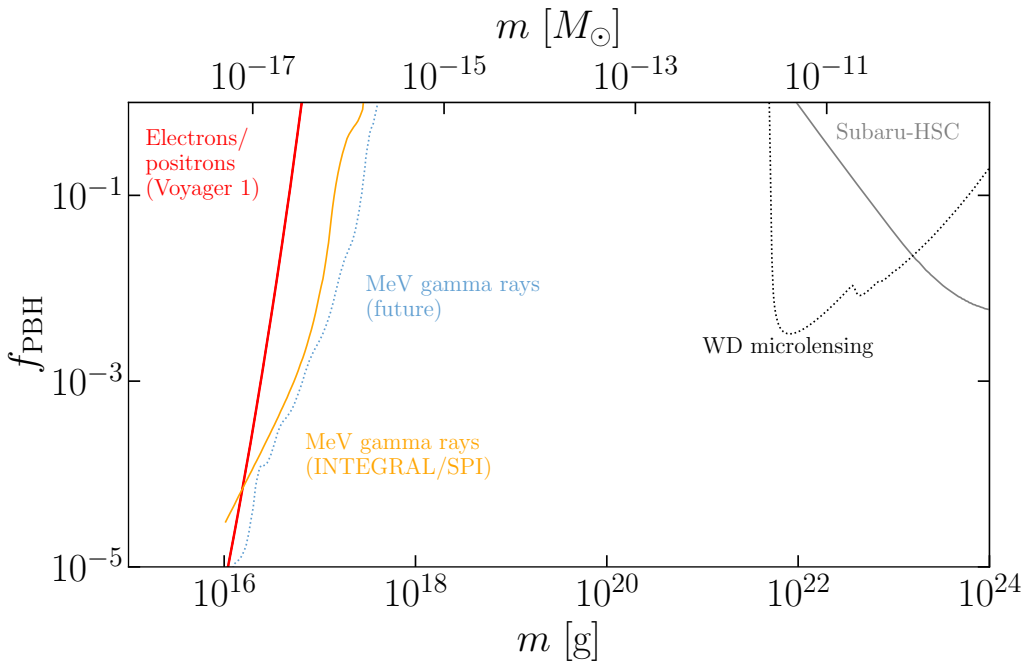

Figure 1: The constraints we use on the fraction of dark matter in PBHs, $f_{\rm PBH}$, as a function of the PBH mass, m, assuming a delta-function PBH MF. Current constraints are shown as solid lines and prospective future constraints as dotted lines. The current evaporation constraints are from Voyager 1 measurements of the local flux of electrons and positrons [22] (red) and INTEGRAL/SPI observations of MeV gamma rays [23] (orange). The current stellar microlensing constraints in this mass range are from Subaru-HSC [24], as calculated in Ref. [25] (grey). The prospective future evaporation constraints are from a MeV gamma-ray telescope [26] (light blue) while the microlensing constraints are for a LMC white dwarf survey [27] (black).

m radiates with a temperature

$$k_{\rm B}T_{\rm BH} = \frac{\hbar c^3}{8\pi G m} = 1.06 \left(\frac{m}{10^{16}\,{\rm g}}\right)^{-1} {\rm MeV}, \tag{1}$$

where c is the speed of light, G is the gravitational constant, $\hbar$ is the reduced Planck constant and $k_{\rm B}$ is the Boltzmann constant.

As a result of Hawking radiation, in the absence of accretion or mergers, the mass of a BH decreases at a rate [18, 20]

$$\frac{{\rm d}m}{{\rm d}t} = -\frac{\hbar c^4}{G^2}\frac{\alpha(m)}{m^2}, \tag{2}$$

where $\alpha(m)$ parameterizes the number of particle species which can be emitted at a significant rate from a BH of mass m. BHs with mass $m \gg 10^{17}\,{\rm g}$ can only emit photons and neutrinos, while those with smaller masses (and higher temperatures) can emit other particle species, such as electrons and positrons [18, 21]. Unstable particles emitted by PBHs decay to stable secondary particles, such as photons and electrons. The total emission of a given species from a PBH is the combination of the primary (i.e. directly emitted) and secondary components. As a result of Hawking evaporation, the PBH mass changes with time and PBHs have a finite lifetime. Since the PBH mass is time-dependent, the PBH mass function (MF) also evolves with time (see Sec. 2.2.2).

Constraints on the fraction of dark matter consisting of PBHs, $f_{\rm PBH}$, can be obtained by comparing the flux of Hawking-emitted particles from PBHs with observations (see Ref. [28] for a recent review of PBH evaporation constraints). For a delta-function MF, existing constraints exclude $f_{\rm PBH} = 1$ for PBHs with mass $m \lesssim 10^{17}\,{\rm g}$. There are various evaporation constraints, from

different particle species and observations, calculated using different assumptions, with different uncertainties (see Ref. [28]). We consider two illustrative constraints, from INTEGRAL/SPI observations of MeV gamma rays [23] and Voyager 1 measurements of the flux of electrons and positrons [22]. The INTEGRAL/SPI MeV gamma-ray limit places tight constraints on $f_{\rm PBH}$ (for a delta-function MF) for $10^{16}\,{\rm g} \lesssim m \lesssim 10^{17}\,{\rm g}$, while the Voyager 1 $e^{\pm}$ observations place tight constraints on $f_{\rm PBH}$ for $m \lesssim 10^{16}\,{\rm g}$. As we will see in Sec. 3, the constraint that rules out $f_{\rm PBH} = 1$ for the largest value of m doesn't necessarily exclude $f_{\rm PBH} = 1$ for the largest peak mass for broad, extended MFs.

Ref. [23] calculates constraints from gamma rays produced by positrons from PBH evaporation annihilating with electrons in the interstellar medium, including the contribution from positrons that first form a positronium bound state. We use the constraint (shown with a dashed purple line in Fig. 1 of Ref. [23]) obtained using the INTEGRAL/SPI limit on the flux of MeV gamma rays from a component with a Navarro-Frenk-White (NFW) density profile from Ref. [29]. We use the Voyager 1 $e^{\pm}$ constraint in the left panel of Fig. 2 of Ref. [22] with astrophysical background subtraction for their propagation model A, which has strong diffusive reacceleration.

Proposed future MeV gamma-ray telescopes have the potential to place tighter constraints on evaporating PBHs, extending the range of masses where $f_{\rm PBH} = 1$ is excluded to larger m. As an illustrative case we consider the projected constraints from observations towards the Galactic Centre (assuming a NFW profile) by the proposed GECCO telescope from Fig. 9 of Ref. [26].

2.1.2 Microlensing

Stellar microlensing is the temporary amplification of a background star that occurs when a compact object passes close to the line of sight to the star [30]. Observations of stars in M31 by Subaru-HSC [24] have been used to constrain $f_{\rm PBH}$ in the mass range $10^{22}\,{\rm g} \lesssim m \lesssim 10^{28}\,{\rm g}$ [24, 25].

Accounting for the finite size of the source stars weakens the constraints significantly from those calculated assuming a point-like source [31, 32]. Additionally, for PBHs with masses $m \lesssim 10^{-11} M_{\odot} \sim 10^{22}\,{\rm g}$, the Schwarzschild radius of the PBHs is comparable to the wavelength of the light used to observe the stars, resulting in diffraction and interference effects. Due to these 'wave optics' effects, it is not possible to constrain PBHs with $m \lesssim 10^{-11} M_{\odot} \sim 10^{22}\,{\rm g}$ using microlensing surveys of main-sequence stars [27, 32]. We use the point-like lens constraint from Fig. 4 of Ref. [25].

To minimise the finite source and wave optics effects, Ref. [27] suggests a survey of white dwarfs in the Large Magellanic Cloud (LMC) using shorter wavelength observations. They find such a survey could place significantly tighter constraints on PBHs with mass $m \sim 10^{(22-23)}\,{\rm g}$. We use the constraint from Fig. 8 of Ref. [27] that accounts for both finite source and wave optics effects.

2.2 PBH mass functions and evolution

2.2.1 Initial mass functions

The initial PBH mass function (MF) can be defined as

$$\psi(m_{\rm i}, t_{\rm i}) \equiv \frac{1}{\rho_{\rm i}} \frac{{\rm d}\rho(m_{\rm i}, t_{\rm i})}{{\rm d}m_{\rm i}}\,, \tag{3}$$

where $\rho(m_{\rm i}, t_{\rm i})$ is the comoving mass density in PBHs of initial mass $m_{\rm i}$ at the time they form, $t_{\rm i}$, and $\rho_{\rm i}$ is the initial total comoving mass density of PBHs. Due to near critical gravitational collapse [33], the mass of a PBH formed depends on the amplitude, δ, of the perturbation from which it forms as well as the horizon mass, $M_{\rm H}$: $m_{\rm i} = k M_{\rm H} (\delta - \delta_{\rm c})^{\gamma}$, where $\delta_{\rm c}$ is the threshold

for PBH formation, and k and $\gamma \simeq 0.36$ are constants [8] [2]. Consequently even if all PBHs form at the same time, i.e. from a delta-function peak in the primordial power spectrum, they will have a range of masses [8–10]. In this case the critical collapse (CC) initial MF is well approximated, assuming the probability distribution of the amplitude of the fluctuations is gaussian, by

$$\psi_{\rm CC}(m_{\rm i}, t_{\rm i}) = \frac{1}{\gamma m_{\rm p} \Gamma(\gamma+1)} \left(\frac{m_{\rm i}}{m_{\rm p}}\right)^{1/\gamma} \exp\left[-\left(\frac{m_{\rm i}}{m_{\rm p}}\right)^{1/\gamma}\right], \tag{4}$$

where $m_{\rm p}$ is the mass at which the MF peaks and Γ is the gamma function.

In reality the primordial power spectrum will have finite width, and PBHs will form on a range of scales. For various inflation models the MFs calculated, taking critical collapse into account, can be roughly approximated by a lognormal (LN) distribution [12, 15]:

$$\psi_{\rm LN}(m_{\rm i}, t_{\rm i}) = \frac{1}{\sqrt{2\pi}\sigma m_{\rm i}} \exp\left(-\frac{\ln^2(m_{\rm i}/m_{\rm c})}{2\sigma^2}\right), \tag{5}$$

where σ is the width and $m_{\rm c}$ is the mean of $m_{\rm i}\psi_{\rm LN}(m_{\rm i}, t_{\rm i})$. The LN MF has been widely adopted as the canonical extended PBH MF (for instance when applying observational constraints to extended mass functions [13, 14]).

Gow et al. [16] investigated more accurate fitting functions for the initial MF of PBHs formed from a symmetric peak in the primordial power spectrum. They parameterise the peak in the power spectrum of the curvature perturbation, $\mathcal{P}_\zeta(k)$, as lognormal,

$$\mathcal{P}_\zeta(k) = A\frac{1}{\sqrt{2\pi}\Delta} \exp\left(-\frac{\ln^2(k/k_{\rm p})}{2\Delta^2}\right), \tag{6}$$

where A and Δ are the amplitude and width of the peak and $k_{\rm p}$ is the comoving wavenumber at which it occurs. We have found that the broad peak in the primordial power spectrum produced by hybrid inflation with a mild waterfall transition [11] is fairly well-approximated by a lognormal with $\Delta \sim 5$. Ref. [16] calculates the PBH MF numerically as in Ref. [35], using the traditional (BBKS) peaks theory method [36] with a modified gaussian window function [3].

Gow et al. [16, 35] find that for narrow peaks in the power spectrum, $\Delta \lesssim 0.3$, critical collapse dominates the PBH MF; the MF is independent of the width of the power spectrum and skewed towards low masses. For $\Delta \gtrsim 0.5$ the width of the peak becomes important. As Δ is increased the width of the MF increases and the skew towards low masses decreases, and for large Δ (the transition occurs between $\Delta = 2$ and 5) their MFs are skewed towards large masses [16]. Of the fitting functions they consider, the two that best reproduce this behaviour are the skew-lognormal and generalised critical collapse functions. The skew-lognormal (SLN) MF is a generalisation of the lognormal with non-zero skewness:

$$\psi_{\rm SLN}(m_{\rm i}, t_{\rm i}) = \frac{1}{\sqrt{2\pi}\sigma m_{\rm i}} \exp\left(-\frac{\ln^2(m_{\rm i}/m_{\rm c})}{2\sigma^2}\right)\left[1 + {\rm erf}\left(\alpha\frac{\ln(m_{\rm i}/m_{\rm c})}{\sqrt{2}\sigma}\right)\right], \tag{7}$$

where α controls the skewness of the MF; for negative (postive) α the MF is skewed to low (high)

[2] The criterion for PBH formation is traditionally specified in terms of the density contrast $\delta = (\rho - \bar{\rho})/\bar{\rho}$. More recently it has been realised that the criterion is best specified in terms of the compaction function [34], and the dependence of the PBH mass on the compaction function has the same power law scaling.

[3] More recently Germani and Sheth [37] have formulated a procedure for calculating the abundance and MF of PBHs, using the statistics of the compaction function. They find (assuming a gaussian distribution for the perturbations) that the low mass tail of the MF is generically (i.e. for any primordial power spectrum) a power law, $\psi(m_{\rm i}, t_{\rm i}) \propto m_{\rm i}^{1/\gamma}$, while at large masses there is a cut off, which depends on the shape and amplitude of the power spectrum.

masses [4]. The generalised critical collapse (GCC) MF [5] is given by

$$\psi_{\rm GCC}(m_{\rm i}, t_{\rm i}) = \frac{\beta}{m_{\rm p}} \left[\Gamma\left(\frac{\alpha+1}{\beta}\right)\right]^{-1} \left(\frac{\alpha}{\beta}\right)^{\frac{\alpha+1}{\beta}} \left(\frac{m_{\rm i}}{m_{\rm p}}\right)^{\alpha} \exp\left[-\frac{\alpha}{\beta}\left(\frac{m_{\rm i}}{m_{\rm p}}\right)^{\beta}\right], \tag{8}$$

where $m_{\rm p}$ is the mass at which the GCC MF peaks, and α and β are parameters that control its behaviour in the low and high-mass tails respectively (for $m_{\rm i} \ll m_{\rm p}$, $\psi_{\rm GCC}(m_{\rm i}, t_{\rm i}) \propto m_{\rm i}^{\alpha}$). The GCC MF is a generalisation of the critical collapse MF obtained assuming all PBHs form at the same time, Eq. (4), which corresponds to Eq. (8) with $\alpha = \beta = 1/\gamma$ [9]. Gow et al. [16] find that the GCC MF is a better fit to their calculated MFs than the SLN for narrow peaks ($\Delta \lesssim 0.5$) where critical collapse dominates the PBH MF and it has negative skew, while for broad peaks ($\Delta \gtrsim 5$) the SLN is a better fit.

Ref. [16] focuses on stellar-mass PBHs. For the three fitting functions we consider (LN, SLN and GCC), we choose values for the mass parameters ($m_{\rm c}$ or $m_{\rm p}$) in the asteroid-mass window. For the parameters which govern the shape of the MF (α, β and σ), we adopt the best-fit parameter values in Table II of Ref. [16] [6] i.e. for simplicity we assume that these parameters do not depend on the PBH mass, or equivalently the position of the peak in the primordial power spectrum, $k_{\rm p}$. To facilitate comparison between the constraints obtained with different fitting functions, we present the constraints for the LN and SLN MF in terms of the peak mass, i.e. the mass at which the MF is maximal, $m_{\rm p}$. For the LN, $m_{\rm p} = m_{\rm c}\exp(-\sigma^2)$, while for the SLN there is no analytic expression for $m_{\rm p}$.

2.2.2 Time evolution of the mass function

The MFs presented in Sec. 2.2.1 are fits to the initial MFs calculated in Ref. [16]. For PBHs with initial mass $m_{\rm i} \lesssim 1 \times 10^{15}\,{\rm g}$, Hawking evaporation leads to significant ($> 10\%$) mass loss by the present day, and hence the MF varies with time [38–41]. Therefore for extended MFs that are peaked at sufficiently small $m_{\rm p}$ and/or are sufficiently broad that there is a significant abundance of PBHs with initial masses $m_{\rm i} \lesssim 1 \times 10^{15}\,{\rm g}$, the time evolution of the MF should be taken into account.

To evaluate the PBH mass today at time $t = t_0$, we follow Ref. [41] and approximate $\alpha(m)$ as depending only on the initial mass, $\alpha(m) \approx \alpha_{\rm eff}(m_{\rm i})$. Integrating Eq. (2), the PBH mass today, $m(t_0)$, can be expressed as

$$m(t_0) \approx \left(m_{\rm i}^3 - 3\frac{\hbar c^4}{G^2}\alpha_{\rm eff}(m_{\rm i})t_0\right)^{1/3}, \tag{9}$$

where the formation time, $t_{\rm i}$, has been set to zero since $t_0 \gg t_{\rm i}$. Here, $\alpha_{\rm eff}(m_{\rm i})$ is defined as

$$\alpha_{\rm eff}(m_{\rm i}) \equiv \frac{G^2}{\hbar c^4}\frac{m_{\rm i}^3}{3\tau}, \tag{10}$$

where τ is the PBH lifetime (which can be calculated numerically e.g. using `BlackHawk` [42,43]). This definition ensures that the PBH lifetime is calculated accurately for all initial masses $m_{\rm i}$.

Using the conservation of the number of PBHs, the PBH MF today, $\psi(m, t_0)$, defined as

$$\psi(m, t_0) \equiv \frac{1}{\rho_{\rm i}}\frac{{\rm d}\rho(m, t_0)}{{\rm d}m}, \tag{11}$$

[4] For consistency we use the same notation for the parameters of the fitting functions as Gow et al. [16], however the α parameters in the SLN and generalised critical collapse fitting functions affect their shapes in different ways.

[5] In Ref. [16], this is referred to as the 'CC3' model.

[6] Table II of Ref. [16] contains the best-fit parameter values for the SLN and GCC MFs, we are grateful to Andrew Gow for providing those for the LN MF via email.

where $\rho(m, t_0)$ is the comoving mass density in PBHs with present day mass m, can be expressed in terms of the initial PBH MF, $\psi(m_{\rm i}, t_{\rm i})$, defined in Eq. (3), as [41, 44]

$$\psi(m, t_0) = \left(\frac{m}{m_{\rm i}}\right)^3 \psi(m_{\rm i}, t_{\rm i}). \tag{12}$$

The equivalent expression in Ref. [41] contains a factor that can be written as $(m/m_{\rm i})$ squared, rather than cubed, since they are considering number, rather than mass, densities.

2.3 Calculating constraints for extended MFs

We use the method introduced in Ref. [13] to apply constraints to extended MFs (a similar method is presented in Ref. [45]). The constraint on the fraction of dark matter in PBHs can be expressed as [13]

$$f_{\rm PBH} \leq \left[\int {\rm d}m \frac{\psi_{\rm N}(m, t_0)}{f_{\rm max}(m)}\right]^{-1}, \tag{13}$$

where $f_{\rm max}(m)$ is the maximum fraction of dark matter in PBHs allowed for a delta-function MF, and $\psi_{\rm N}(m, t_0)$ is defined as

$$\psi_{\rm N}(m, t_0) \equiv \frac{1}{\rho(t_0)} \frac{{\rm d}\rho(m, t_0)}{{\rm d}m}, \tag{14}$$

where $\rho(t_0)$ is the total comoving mass density in PBHs today. This definition of the MF is normalised to unity today $\int {\rm d}m \psi_{\rm N}(m, t_0) = 1$, while the MF $\psi(m, t_0)$ defined in Eq. (11) in Sec. 2.2.2 is not, since the total mass in PBHs decreases with time due to evaporation. As discussed in Sec. 2.2.2 PBHs with initial mass $m_{\rm i} \lesssim 1 \times 10^{15}$ g lose a non-negligible fraction of their mass by the present day. Therefore for the evaporation constraints the MF should be evolved to the present day using Eq. (12) before calculating $\psi_{\rm N}(m, t_0)$ by renormalizing to the present day PBH mass density.

For the evaporation constraints $f_{\rm max}(m)$ decreases rapidly with decreasing m, as the Hawking temperature is inversely proportional to the mass, Eq. (1). Consequently, for sufficiently wide MFs peaked at the lower end of the asteroid-mass range, the contribution to Eq. (13) from $f_{\rm max}(m)$ at smaller masses than the constraints are publicly available for ($m \lesssim 10^{15}$ g for the Voyager 1 constraints [22] and $m < 10^{16}$ g for the INTEGRAL/SPI MeV gamma-ray constraints [23]) may be important. At the smallest masses where constraints are publicly available, $f_{\rm max}(m) \propto m^q$ with $q \approx 2 - 3$ to a good approximation, and we assume that the power-law form, $f_{\rm max}(m) \propto m^q$, continues to smaller masses. We have checked that the resulting extended MF constraints do not change significantly (by no more than a factor of a few at peak masses where $f_{\rm PBH} \sim 1$) if instead $f_{\rm max}(m)$ becomes constant at small masses.

3 Results

In this section we calculate the constraints on the time-evolved LN, SLN, and GCC PBH mass functions presented in Sec. 2.2.1, for the constraints reviewed in Sec. 2.1 using the method presented in Sec. 2.3. We do this first for the existing limits in Sec. 3.1, and then for the future prospective limits in Sec. 3.2.

3.1 Existing constraints

Fig. 2 shows current constraints on the fraction of DM in PBHs, $f_{\rm PBH}$, for the fitting functions presented in Sec. 2.2.1 for PBHs arising from a log-normal peak in the power spectrum, Eq. (6), with width $\Delta = 0, 2$ and 5 ($\Delta = 0$ corresponds to a delta-function peak). These values span the

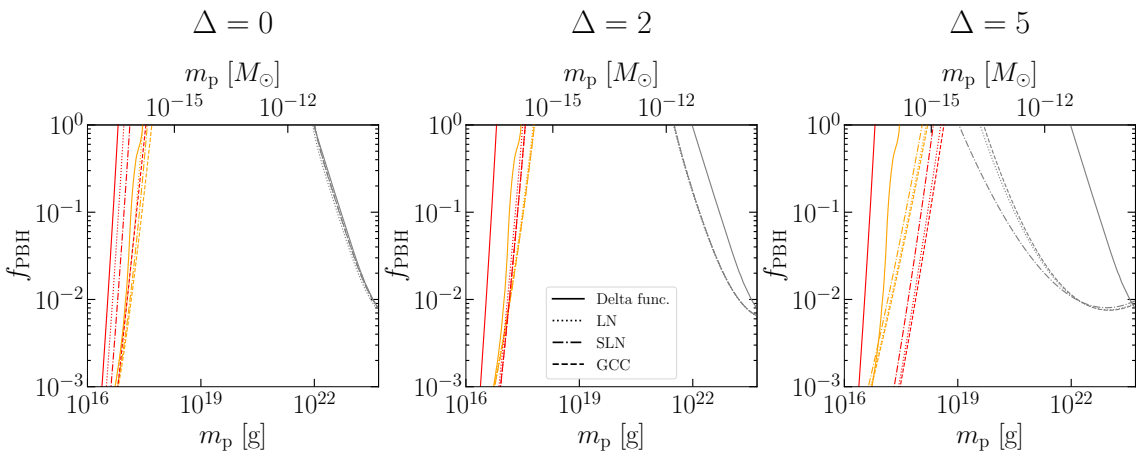

Figure 2: Current constraints on the fraction of dark matter in PBHs, $f_{\rm PBH}$, as a function of the mass at which the PBH MF peaks, $m_{\rm p}$, for PBHs formed from a lognormal peak in the primordial power spectrum, Eq. (6), with width $\Delta = 0, 2$ and 5 (from left to right). Constraints for the lognormal (LN), skew-lognormal (SLN) and generalised critical collapse (GCC) MFs are shown with dotted, dot-dashed, and dashed lines respectively, while the original constraints, calculated assuming a delta-function MF are shown with solid lines. The constraints shown are from Voyager 1 measurements of the local flux of electrons and positrons [22] (red), INTEGRAL/SPI observations of MeV gamma rays [23] (orange), and the Subaru-HSC microlensing survey [24] as calculated in Ref. [25] (grey). In the $\Delta = 2$ case, the constraints for the SLN and GCC MFs are indistinguishable.

range of values considered by Ref. [16]. As discussed in Sec. 2.1, the constraints we consider are from INTEGRAL/SPI observations of MeV gamma rays [23], Voyager 1 measurements of the local flux of electrons and positrons [22], and the Subaru-HSC microlensing survey [24] as calculated in Ref. [25].

As previously seen in e.g. Refs. [6, 13], compared to the delta-function MF constraints, the tightest extended MF constraint is weakened, while $f_{\rm PBH} = 1$ is excluded over a wider range of peak masses $m_{\rm p}$. As anticipated in Ref. [16], the constraints depend on the shape of the low and high mass tails of the MF. Nevertheless, even for the widest power spectrum considered, $\Delta = 5$, there remains a range of peak masses for which $f_{\rm PBH} = 1$ is allowed for all three extended mass functions. Our evaporation constraints for extended MFs appear closer to the delta-function MF constraints than previously found for the LN MF (see e.g. Fig. 20 of Ref. [6]). As we discuss in App. A, this is largely an artefact of the LN MF constraints previously being plotted in terms of the parameter $m_{\rm c}$ which appears in the definition of the lognormal MF (see Eq. (5)) rather than the peak mass, $m_{\rm p}$.

For small Δ the MFs calculated in Ref. [16] are skewed towards low masses and the best-fit LN underestimates the low-mass tail and overestimates the high-mass tail. At a given $m_{\rm p}$, the evaporation and microlensing constraints for a LN MF are therefore less and slightly more stringent, respectively, than those for the better fitting SLN and GCC MFs. For $\Delta = 0$, the Voyager 1 constraint for the GCC MF (the best-performing function for $\Delta \lesssim 0.5$ [16]) at a given $m_{\rm p}$ is more stringent than the constraints for the LN and SLN MFs by an order of magnitude or more. This is because the power-law tail of the GCC MF at low masses is much larger than the low-mass tails of the LN and SLN MFs, and the constraint from Voyager 1 is especially tight at low m. The INTEGRAL/SPI MeV gamma-ray constraints for the different extended MFs are more similar, as this constraint is relatively weak for the range of m where the differences between the MFs are large. Since the microlensing constraints for each MF agree closely, and the extended MF constraints from INTEGRAL/SPI observations of MeV gamma rays are more stringent than those

from Voyager 1, the range of $m_{\rm p}$ where $f_{\rm PBH} = 1$ is allowed is fairly similar for each MF. For $\Delta = 0$, for the best fitting GCC MF, $f_{\rm PBH} = 1$ is allowed for $5 \times 10^{17}\,{\rm g} \lesssim m_{\rm p} \lesssim 1 \times 10^{22}\,{\rm g}$, a slightly narrower mass range than for the LN MF.

For $\Delta = 2$, the MF calculated in Ref. [16] is close to symmetric, and all three MFs provide a very good fit [16]. Therefore the constraints for the extended MFs are very similar, with $f_{\rm PBH} = 1$ being allowed for $6 \times 10^{17}\,{\rm g} \lesssim m_{\rm p} \lesssim 3 \times 10^{21}\,{\rm g}$. For $\Delta = 5$, the MF calculated in Ref. [16] is skewed towards large masses and the SLN MF provides a significantly better fit than the LN and GCC MFs. For the SLN MF $f_{\rm PBH} = 1$ is allowed for $2 \times 10^{18}\,{\rm g} \lesssim m_{\rm p} \lesssim 1 \times 10^{19}\,{\rm g}$. The LN and GCC MFs over (under) estimate the MF at low (high) masses, resulting in overly stringent evaporation (overly weak microlensing) constraints. The range of $m_{\rm p}$ where $f_{\rm PBH} = 1$ is allowed is therefore wider and shifted to larger $m_{\rm p}$ (compared to the better-fitting SLN MF). For $\Delta = 5$ the strongest evaporation constraints come from Voyager 1, even though for a delta-function MF the INTEGRAL/SPI MeV gamma-ray constraint excludes $f_{\rm PBH} = 1$ at larger masses than the Voyager 1 constraint (see Fig. 1). This is because for $\Delta = 5$ the MF is sufficiently wide that it is non-negligible in the mass range $m \lesssim 10^{16}\,{\rm g}$ where the Voyager 1 constraint is more stringent than the INTEGRAL/SPI MeV gamma-ray constraint, and for the Voyager 1 constraint the integral in Eq. (13) is dominated by this mass range. This highlights that for a broad MF the tightest constraint (i.e. the constraint that rules out $f_{\rm PBH} = 1$ at the largest peak mass) might not be the constraint which is tightest for a delta-function MF.

For $\Delta \lesssim 2$, the difference between the evaporation constraints calculated using the time-evolved MF $\psi_{\rm N}(m, t_0)$ and the initial MF $\psi(m_{\rm i}, t_{\rm i})$ is no more than 10%, for $m_{\rm p} \gtrsim 10^{17}\,{\rm g}$. For $\Delta = 5$, the constraints obtained using $\psi_{\rm N}(m, t_0)$ and $\psi(m_{\rm i}, t_{\rm i})$ differ by no more than a factor of two at $m_{\rm p} = 10^{17}\,{\rm g}$ and less than $\approx 20\%$ at peak masses where $f_{\rm PBH} \sim 1$. For broader mass functions (or for MFs peaked at smaller masses [41]) the effect on the constraints on $f_{\rm PBH}$ would be larger.

3.2 Prospective future constraints

Fig. 3 shows prospective future constraints obtained from MeV gamma-ray telescopes [26] and a proposed microlensing survey of white dwarfs in the LMC [27], as discussed in Sec. 2.1. Due to the improved sensitivity compared to existing observations, $f_{\rm PBH} = 1$ is excluded over a wider peak mass range than for existing constraints. In particular for the broadest peak in the primordial power spectrum, $\Delta = 5$, $f_{\rm PBH} = 1$ is excluded across the whole asteroid-mass window for all three MFs, and the maximum allowed PBH dark matter fraction is $f_{\rm PBH} \sim 0.2 - 0.4$. For $\Delta = 5$ the current Voyager 1 constraint [22] rules out $f_{\rm PBH} = 1$ at larger $m_{\rm p}$ than the projected future MeV gamma-ray constraint that we consider, even though the largest mass for which $f_{\rm PBH} = 1$ is excluded for a delta-function MF is smaller for the Voyager 1 $e^{\pm}$ constraint. As for the current MeV gamma-ray constraint, this is because the low-mass tails of the widest MFs are large at $m \lesssim 10^{16}\,{\rm g}$, where the delta-function MF constraint from Voyager 1 [22] is tighter.

4 Conclusions

If the PBH mass function is a delta-function then PBHs with mass in the asteroid-mass window, $10^{17}\,{\rm g} \lesssim m_{\rm p} \lesssim 10^{22}\,{\rm g}$, can make up all of the DM, i.e. $f_{\rm PBH} = 1$. However, due to critical collapse, PBHs formed from the collapse of large density perturbations are expected to have an extended MF, even if they form from a narrow peak in the power spectrum. Refs. [6, 13] found that the range of masses for which $f_{\rm PBH} = 1$ is allowed is much smaller for the commonly used lognormal MF than for a delta-function MF. We have explored how the constraints on $f_{\rm PBH}$ in the asteroid-mass window depend on the shape of the PBH MF. In addition to a lognormal MF, we use

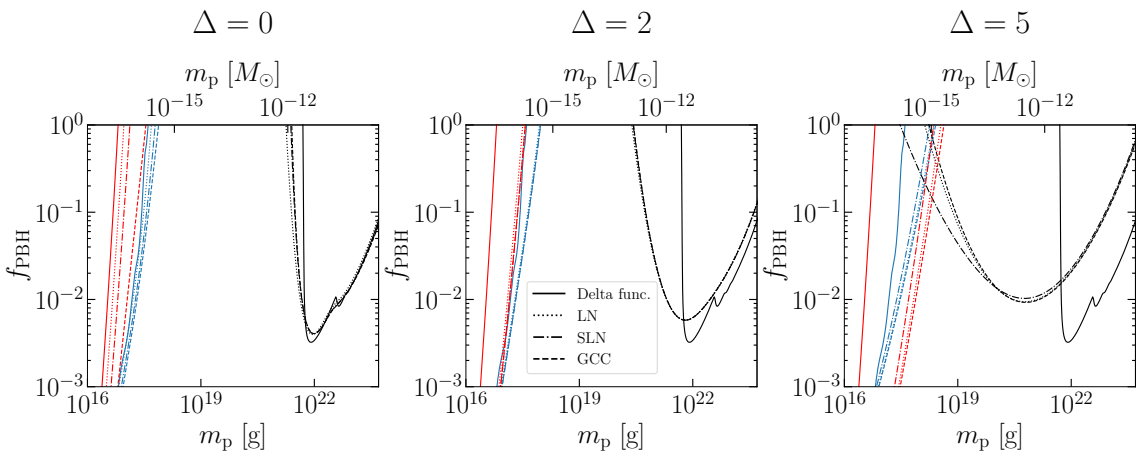

Figure 3: Prospective future constraints on the fraction of dark matter in PBHs, $f_{\rm PBH}$, as a function of the mass at which the PBH MF peaks, $m_{\rm p}$, for PBHs formed from a lognormal peak in the primordial power spectrum with width $\Delta = 0, 2$ and 5 (from left to right). The line styles for the MFs are the same as in Fig. 2. The future constraints shown are from future MeV gamma-ray telescopes (assuming a NFW profile for the Galactic DM halo) [26] (light blue) and stellar microlensing of white dwarfs in the LMC [27] (black). For comparison we also show the current constraints from Voyager 1 measurements of the $e^{\pm}$ flux (red) from Fig. 2.

the skew-lognormal and generalised critical collapse MFs, which Gow et al. [16] found provided a better fit to the MFs they calculated than the lognormal.

We find, using the constraints from Voyager 1 measurements of the local $e^{\pm}$ flux [22], INTEGRAL/SPI observations of MeV gamma rays [23], and microlensing constraints from Subaru-HSC [24, 25], that the asteroid-mass window is typically narrower (i.e. $f_{\rm PBH} = 1$ is allowed for a smaller range of peak masses, $m_{\rm p}$) for the better fitting MFs than for the lognormal MF. Nevertheless, for the widest primordial power spectrum considered by Gow et al. [16], there is still a range of $m_{\rm p}$ values ($2 \times 10^{18}\ {\rm g} \lesssim m_{\rm p} \lesssim 1 \times 10^{19}\ {\rm g}$) where $f_{\rm PBH} = 1$ is allowed for the skew-lognormal mass function, which is the best-fitting mass function in this case.

The constraint that excludes $f_{\rm PBH} = 1$ over the widest range of PBH masses for a delta-function MF does not always exclude $f_{\rm PBH} = 1$ for the widest range of peak masses for extended mass functions. For instance the largest mass for which $f_{\rm PBH} = 1$ is excluded for a delta-function MF is smaller for the Voyager 1 $e^{\pm}$ constraint than for the MeV gamma-ray constraints (see Fig. 1). However for the widest MFs we consider, the Voyager 1 constraint rules out $f_{\rm PBH} = 1$ at larger $m_{\rm p}$ than the current INTEGRAL/SPI MeV gamma-ray constraint and also the projected future MeV gamma-ray constraint that we consider. This shows that tighter constraints on PBHs with $m \lesssim 10^{16}\ {\rm g}$ would be beneficial for constraining PBHs with broad MFs.

Future gamma-ray observations will improve limits on the abundance of PBHs with masses $m \lesssim 5 \times 10^{17}\ {\rm g}$, while a proposed LMC white dwarf microlensing survey could provide tighter constraints for $5 \times 10^{21}\ {\rm g} \lesssim m \lesssim 2 \times 10^{23}\ {\rm g}$. Together, these constraints could potentially exclude asteroid-mass PBHs with a broad MF making up all of the DM. However the evaporation and microlensing constraints are sensitive to the shape of the low and high mass tails of the MF respectively. An accurate calculation of the shape of the tails of the MF will therefore be essential in future for assessing whether evaporation and microlensing constraints allow asteroid-mass PBHs to make up all of the DM. This also demonstrates the importance of developing new observational probes of PBHs with mass $10^{18}\ {\rm g} \lesssim m \lesssim 10^{22}\ {\rm g}$, such as femtolensing of gamma-ray bursts (GRBs) [46, 47], GRB lensing parallax [48, 49], microlensing of X-ray pulsars [50], their effects on stars, e.g. Refs. [32, 51, 52], or on the orbits of planets [53] and satellites [54].

Acknowledgements

We are grateful to Jérémy Auffinger, Andrew Gow and Sunao Sugiyama for useful discussions, and to Andrew Gow for providing the best-fit parameter values for the lognormal mass function. MG is supported by a United Kingdom Science and Technologies Facilities Council (STFC) studentship. AMG is supported by STFC grant ST/P000703/1. For the purpose of open access, the authors have applied a CC BY public copyright licence to any Author Accepted Manuscript version arising.

Data Availability Statement
No new data were created during this study.

References

[1] Y. B. Zel'dovich and I. D. Novikov, *The Hypothesis of Cores Retarded during Expansion and the Hot Cosmological Model*, Soviet Astron. AJ (Engl. Transl.), **10**, 602 (1967).

[2] B. J. Carr and S. W. Hawking, *Black holes in the early Universe*, Mon. Not. Roy. Astron. Soc. **168**, 399 (1974), doi:10.1093/mnras/168.2.399.

[3] B. J. Carr, *The Primordial black hole mass spectrum*, Astrophys. J. **201**, 1 (1975), doi:10.1086/153853.

[4] A. M. Green and B. J. Kavanagh, *Primordial Black Holes as a dark matter candidate*, J. Phys. G **48**(4), 043001 (2021), doi:10.1088/1361-6471/abc534, 2007.10722.

[5] B. Carr and F. Kuhnel, *Primordial Black Holes as Dark Matter: Recent Developments*, Ann. Rev. Nucl. Part. Sci. **70**, 355 (2020), doi:10.1146/annurev-nucl-050520-125911, 2006.02838.

[6] B. Carr, K. Kohri, Y. Sendouda and J. Yokoyama, *Constraints on primordial black holes*, Rept. Prog. Phys. **84**(11), 116902 (2021), doi:10.1088/1361-6633/ac1e31, 2002.12778.

[7] P. Villanueva-Domingo, O. Mena and S. Palomares-Ruiz, *A brief review on primordial black holes as dark matter*, Front. Astron. Space Sci. **8**, 87 (2021), doi:10.3389/fspas.2021.681084, 2103.12087.

[8] J. C. Niemeyer and K. Jedamzik, *Near-critical gravitational collapse and the initial mass function of primordial black holes*, Phys. Rev. Lett. **80**, 5481 (1998), doi:10.1103/PhysRevLett.80.5481, astro-ph/9709072.

[9] J. Yokoyama, *Cosmological constraints on primordial black holes produced in the near critical gravitational collapse*, Phys. Rev. D **58**, 107502 (1998), doi:10.1103/PhysRevD.58.107502, gr-qc/9804041.

[10] J. C. Niemeyer and K. Jedamzik, *Dynamics of primordial black hole formation*, Phys. Rev. D **59**, 124013 (1999), doi:10.1103/PhysRevD.59.124013, astro-ph/9901292.

[11] S. Clesse and J. García-Bellido, *Massive Primordial Black Holes from Hybrid Inflation as Dark Matter and the seeds of Galaxies*, Phys. Rev. D **92**(2), 023524 (2015), doi:10.1103/PhysRevD.92.023524, 1501.07565.

[12] A. M. Green, *Microlensing and dynamical constraints on primordial black hole dark matter with an extended mass function*, Phys. Rev. D **94**(6), 063530 (2016), doi:10.1103/PhysRevD.94.063530, 1609.01143.

[13] B. Carr, M. Raidal, T. Tenkanen, V. Vaskonen and H. Veermäe, *Primordial black hole constraints for extended mass functions*, Phys. Rev. D **96**(2), 023514 (2017), doi:10.1103/PhysRevD.96.023514, 1705.05567.

[14] F. Kühnel and K. Freese, *Constraints on Primordial Black Holes with Extended Mass Functions*, Phys. Rev. D **95**(8), 083508 (2017), doi:10.1103/PhysRevD.95.083508, 1701.07223.

[15] K. Kannike, L. Marzola, M. Raidal and H. Veermäe, *Single Field Double Inflation and Primordial Black Holes*, JCAP **09**, 020 (2017), doi:10.1088/1475-7516/2017/09/020, 1705.06225.

[16] A. D. Gow, C. T. Byrnes and A. Hall, *Accurate model for the primordial black hole mass distribution from a peak in the power spectrum*, Phys. Rev. D **105**(2), 023503 (2022), doi:10.1103/PhysRevD.105.023503, 2009.03204.

[17] B. Carter, *Charge and particle conservation in black hole decay*, Phys. Rev. Lett. **33**, 558 (1974), doi:10.1103/PhysRevLett.33.558.

[18] D. N. Page, *Particle Emission Rates from a Black Hole: Massless Particles from an Uncharged, Nonrotating Hole*, Phys. Rev. D **13**, 198 (1976), doi:10.1103/PhysRevD.13.198.

[19] S. W. Hawking, *Black hole explosions*, Nature **248**, 30 (1974), doi:10.1038/248030a0.

[20] S. W. Hawking, *Particle Creation by Black Holes*, Commun. Math. Phys. **43**, 199 (1975), doi:10.1007/BF02345020, [Erratum: Commun.Math.Phys. 46, 206 (1976)].

[21] D. N. Page, *Particle Emission Rates from a Black Hole. 3. Charged Leptons from a Nonrotating Hole*, Phys. Rev. D **16**, 2402 (1977), doi:10.1103/PhysRevD.16.2402.

[22] M. Boudaud and M. Cirelli, *Voyager 1 $e^{\pm}$ Further Constrain Primordial Black Holes as Dark Matter*, Phys. Rev. Lett. **122**(4), 041104 (2019), doi:10.1103/PhysRevLett.122.041104, 1807.03075.

[23] M. Korwar and S. Profumo, *Updated constraints on primordial black hole evaporation*, JCAP **05**, 054 (2023), doi:10.1088/1475-7516/2023/05/054, 2302.04408.

[24] H. Niikura *et al.*, *Microlensing constraints on primordial black holes with Subaru/HSC Andromeda observations*, Nature Astron. **3**(6), 524 (2019), doi:10.1038/s41550-019-0723-1, 1701.02151.

[25] D. Croon, D. McKeen, N. Raj and Z. Wang, *Subaru-HSC through a different lens: Microlensing by extended dark matter structures*, Phys. Rev. D **102**(8), 083021 (2020), doi:10.1103/PhysRevD.102.083021, 2007.12697.

[26] A. Coogan *et al.*, *Hunting for dark matter and new physics with GECCO*, Phys. Rev. D **107**(2), 023022 (2023), doi:10.1103/PhysRevD.107.023022, 2101.10370.

[27] S. Sugiyama, T. Kurita and M. Takada, *On the wave optics effect on primordial black hole constraints from optical microlensing search*, Mon. Not. Roy. Astron. Soc. **493**(3), 3632 (2020), doi:10.1093/mnras/staa407, 1905.06066.

[28] J. Auffinger, *Primordial black hole constraints with Hawking radiation—A review*, Prog. Part. Nucl. Phys. **131**, 104040 (2023), doi:10.1016/j.ppnp.2023.104040, 2206.02672.

[29] J. Berteaud, F. Calore, J. Iguaz, P. D. Serpico and T. Siegert, *Strong constraints on primordial black hole dark matter from 16 years of INTEGRAL/SPI observations*, Phys. Rev. D **106**(2), 023030 (2022), doi:10.1103/PhysRevD.106.023030, 2202.07483.

[30] B. Paczynski, *Gravitational microlensing by the galactic halo*, Astrophys. J. **304**, 1 (1986), doi:10.1086/164140.

[31] N. Smyth, S. Profumo, S. English, T. Jeltema, K. McKinnon and P. Guhathakurta, *Updated Constraints on Asteroid-Mass Primordial Black Holes as Dark Matter*, Phys. Rev. D **101**(6), 063005 (2020), doi:10.1103/PhysRevD.101.063005, 1910.01285.

[32] P. Montero-Camacho, X. Fang, G. Vasquez, M. Silva and C. M. Hirata, *Revisiting constraints on asteroid-mass primordial black holes as dark matter candidates*, JCAP **08**, 031 (2019), doi:10.1088/1475-7516/2019/08/031, 1906.05950.

[33] M. W. Choptuik, *Universality and scaling in gravitational collapse of a massless scalar field*, Phys. Rev. Lett. **70**, 9 (1993), doi:10.1103/PhysRevLett.70.9.

[34] A. Escrivà, C. Germani and R. K. Sheth, *Universal threshold for primordial black hole formation*, Phys. Rev. D **101**(4), 044022 (2020), doi:10.1103/PhysRevD.101.044022, 1907.13311.

[35] A. D. Gow, C. T. Byrnes, P. S. Cole and S. Young, *The power spectrum on small scales: Robust constraints and comparing PBH methodologies*, JCAP **02**, 002 (2021), doi:10.1088/1475-7516/2021/02/002, 2008.03289.

[36] J. M. Bardeen, J. R. Bond, N. Kaiser and A. S. Szalay, *The Statistics of Peaks of Gaussian Random Fields*, Astrophys. J. **304**, 15 (1986), doi:10.1086/164143.

[37] C. Germani and R. K. Sheth, *The Statistics of Primordial Black Holes in a Radiation-Dominated Universe: Recent and New Results*, Universe **9**(9), 421 (2023), doi:10.3390/universe9090421, 2308.02971.

[38] B. J. Carr, K. Kohri, Y. Sendouda and J. Yokoyama, *New cosmological constraints on primordial black holes*, Phys. Rev. D **81**, 104019 (2010), doi:10.1103/PhysRevD.81.104019, 0912.5297.

[39] B. J. Carr, K. Kohri, Y. Sendouda and J. Yokoyama, *Constraints on primordial black holes from the Galactic gamma-ray background*, Phys. Rev. D **94**(4), 044029 (2016), doi:10.1103/PhysRevD.94.044029, 1604.05349.

[40] Y.-F. Cai, C. Chen, Q. Ding and Y. Wang, *Cosmological standard timers from unstable primordial relics*, Eur. Phys. J. C **83**(10), 913 (2023), doi:10.1140/epjc/s10052-023-12046-0, 2112.10422.

[41] M. R. Mosbech and Z. S. C. Picker, *Effects of Hawking evaporation on PBH distributions*, SciPost Phys. **13**(4), 100 (2022), doi:10.21468/SciPostPhys.13.4.100, 2203.05743.

[42] A. Arbey and J. Auffinger, *BlackHawk: A public code for calculating the Hawking evaporation spectra of any black hole distribution*, Eur. Phys. J. C **79**(8), 693 (2019), doi:10.1140/epjc/s10052-019-7161-1, 1905.04268.

[43] A. Arbey and J. Auffinger, *Physics Beyond the Standard Model with BlackHawk v2.0*, Eur. Phys. J. C **81**, 910 (2021), doi:10.1140/epjc/s10052-021-09702-8, 2108.02737.

[44] J. Cang, Y. Gao and Y.-Z. Ma, *21-cm constraints on spinning primordial black holes*, JCAP **03**(03), 012 (2022), doi:10.1088/1475-7516/2022/03/012, 2108.13256.

[45] N. Bellomo, J. L. Bernal, A. Raccanelli and L. Verde, *Primordial Black Holes as Dark Matter: Converting Constraints from Monochromatic to Extended Mass Distributions*, JCAP **01**, 004 (2018), doi:10.1088/1475-7516/2018/01/004, 1709.07467.

[46] A. Gould, *Femtolensing of Gamma-Ray Bursters*, Astrophysical Journal, Letters **386**, L5 (1992), doi:10.1086/186279.

[47] A. Katz, J. Kopp, S. Sibiryakov and W. Xue, *Femtolensing by Dark Matter Revisited*, JCAP **12**, 005 (2018), doi:10.1088/1475-7516/2018/12/005, 1807.11495.

[48] R. J. Nemiroff and A. Gould, *Probing for MACHOs of mass* 10^{-15}*-solar-mass - * 10^{-7}*-solar-mass with gamma-ray burst parallax spacecraft*, Astrophys. J. Lett. **452**, L111 (1995), doi:10.1086/309722, astro-ph/9505019.

[49] S. Jung and T. Kim, *Gamma-ray burst lensing parallax: Closing the primordial black hole dark matter mass window*, Phys. Rev. Res. **2**(1), 013113 (2020), doi:10.1103/PhysRevResearch.2.013113, 1908.00078.

[50] Y. Bai and N. Orlofsky, *Microlensing of X-ray Pulsars: a Method to Detect Primordial Black Hole Dark Matter*, Phys. Rev. D **99**(12), 123019 (2019), doi:10.1103/PhysRevD.99.123019, 1812.01427.

[51] J. Smirnov, A. Goobar, T. Linden and E. Mörtsell, *White Dwarfs in Dwarf Spheroidal Galaxies: A New Class of Compact-Dark-Matter Detectors* (2022), 2211.00013.

[52] N. Esser and P. Tinyakov, *Constraints on primordial black holes from observation of stars in dwarf galaxies*, Phys. Rev. D **107**(10), 103052 (2023), doi:10.1103/PhysRevD.107.103052, 2207.07412.

[53] T. X. Tran, S. R. Geller, B. V. Lehmann and D. I. Kaiser, *Close encounters of the primordial kind: a new observable for primordial black holes as dark matter* (2023), 2312.17217.

[54] B. Bertrand, M. Cuadrat-Grzybowski, P. Defraigne, M. Van Camp and S. Clesse, *Observing dark matter clumps and asteroid-mass primordial black holes in the solar system with gravimeters and GNSS networks* (2023), 2312.14520.

A Comparison with previous constraints for lognormal mass function

Carr and collaborators [6, 13] have previously calculated constraints on $f_{\rm PBH}$ for a lognormal (LN) MF with width $\sigma = 2$ (see e.g. Fig. 20 of Ref. [6]). Their constraints differ significantly more from the delta-function MF constraints than is the case for the widest LN MF we consider, which has $\sigma = 1.8$ [16]. In this appendix we outline the reasons for this apparent difference.

Fig. 4 shows the most stringent constraints on $f_{\rm PBH}$, from Voyager 1 [22], for a LN MF with $\sigma = 1.8$ and $\sigma = 2$ plotted as a function of both $m_{\rm c}$ and $m_{\rm p}$. The main reason for the apparent difference between our results in Fig. 2 and those in Fig. 20 of Ref. [6] is that the constraints appear significantly different when plotted in terms of the peak mass, $m_{\rm p}$, than when plotted in terms of the parameter $m_{\rm c}$, which appears in the definition of the LN MF (Eq. (5)). This mass parameter, $m_{\rm c}$, is the mean of $m_{\rm i}\psi(m_{\rm i}, t_{\rm i})$ for the LN MF and is related to the peak mass by $m_{\rm c} = m_{\rm p}\exp(\sigma^2)$, so that for $\sigma \approx 2$, $m_{\rm c} \approx 50 m_{\rm p}$. The peak mass better reflects the typical mass of the PBHs, and plotting constraints in terms of the peak mass also allows comparison with other mass functions

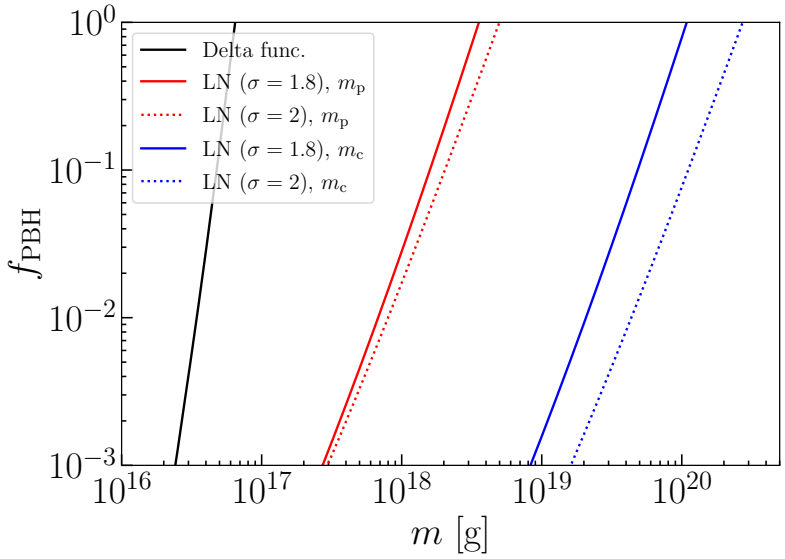

Figure 4: The constraints on the fraction of dark matter in PBHs, $f_{\rm PBH}$, from Voyager 1 measurements of the local flux of electrons and positrons [22] for a delta-function MF and a lognormal (LN) MF. The constraint for a delta-function MF is shown with a black solid line as a function of the PBH mass m. The constraint for the LN MF, Eq. (5), is shown as a function of both $m_{\rm p}$ (red) and $m_{\rm c}$ (blue) for $\sigma = 1.8$ and 2 (solid and dotted lines respectively).

with a single peak. Furthermore the value for the width of the LN used in Refs. [6, 13], $\sigma = 2$, is larger than that of the best fit LN to the widest power spectrum considered by Gow et al. [16], $\sigma = 1.8$, and this relatively small difference in σ leads to a significant shift in the evaporation constraint when it is plotted as a function of $m_{\rm c}$.

KCL-PH-TH/2024-14

Multimessenger signals from compact axion star mergers

Liina Chung-Jukko[a],* Eugene A. Lim[a], and David J. E. Marsh[a]
[a] *Theoretical Particle Physics and Cosmology Group, Physics Department, King's College London, Strand, London WC2R 2LS, United Kingdom*

Axion dark matter can form stable, self-gravitating, and coherent configurations known as axion stars, which are rendered unstable above a critical mass by the Chern-Simons coupling to electromagnetism. We study, using numerical relativity, the merger and subsequent decay of compact axion stars. We show that two sub-critical stars can merge, and form a more massive, excited and critical star, which survives for a finite period before rapidly decaying via electromagnetic radiation. We find a rich multimessenger signal, composed of gravitational waves, electromagnetic radiation, and axion radiation. The gravitational wave signal is broken into two parts: a weak and broad signal from the merger, followed by a much stronger signal of almost fixed frequency from the decay. The electromagnetic radiation follows only the gravitational waves from the decay, while the axion signal is continuous throughout the process. We briefly discuss the detectability of such a signal.

arXiv:2403.03774v1 [astro-ph.CO] 6 Mar 2024

I. INTRODUCTION

Axion stars are self-gravitating compact objects formed of the QCD axion [1–11] or axion-like particles [12–17]. If the axion forms part or all of dark matter (DM), these stars would be expected to be abundant inside DM halos (for initial formation mechanisms, see Refs. [18–22]). As a time-periodic solution of the Einstein-Klein-Gordon equations, axion stars belong to the solitonic class of oscillatons [23, 24]. In the regime of strong gravity, these stars are compact, relativistic objects, where the mass of the compact star goes as $M_s \sim m_{\rm Pl}^2/m$. Throughout this work, units of the axion mass, m, are absorbed by choice of length and time units, and we furthermore use geometrized units with $G = c = 1$ [1].

Axions are coupled to electromagnetism (EM) through a Chern-Simons term with coupling constant $g_{a\gamma}$. In Ref. [25] we studied the instability of compact stars induced by $g_{a\gamma}$. Compact axion stars decay into a less massive and less compact remnant for masses M_s larger than a critical value, which is set by the coupling constant, $g_{a\gamma}^{\rm crit} \propto M_s^{-1.35}$. We demonstrated how this decay process is due to parametric resonance between the axion star and the EM field, which causes the star to lose energy by emitting EM radiation at its characteristic frequency. More specifically, when the characteristic frequency of the oscillating axion star lies within the parametric resonance band of the underlying scalar field, ϕ, the oscillations of the star drive photons out of the electromagnetic field, causing a strong burst of EM radiation. We discuss the shutting down of the parametric resonance process in more detail in Appendix A. The instability of compact axion stars in the strong gravity regime studied in Ref. [25] is in agreement with previous studies of the instability of non-compact axion stars in the weak field regime [26, 27], and other related work (e.g. Refs. [8, 9, 28–30]).

Hence, the existence of compact axion stars is restricted by their coupling to electromagnetism, which naturally raises the possibility of mergers as a formation mechanism for compact axion stars, as any "pristine" super-critical stars created in the early universe e.g. following Ref. [20], would rapidly decay. Therefore in the following we investigate the EM interaction of an axion star created by a head-on collision of two less compact but gravitationally stable stars. The original stars belong to the sub-critical compactness [2] region found in Ref. [31] where the merger leads to the formation of another excited but stable star (for more compact stars the merger leads to the prompt formation of a black hole). Compact axion stars are gravitational objects, and thus one expects their merger [32] and subsequent decay to produce gravitational waves, in addition to the EM and axion (scalar) radiation seen already in Ref. [25]. We extract, for the first time, the full multimessenger signal in GW, EM and axions caused by axion star collisions and decays. An example signal extracted from the clean decay of an isolated compact axion star [25] is shown in Fig. 1 (the more complex signal from mergers will be shown later in the paper).

Our calculations are performed in the strong gravity regime, using the 3+1 numerical relativity code GRChombo [34–36], hence capturing all backreactions and other gravitational effects. We show that two stars originally in the stable region of the plane given by the two

* liina.jukko@kcl.ac.uk

[1] To convert from our simulation units, as displayed on the figures, to physical units, the unit of m has to be multiplied by $m_{\rm Pl}^{-2}$ before doing the usual conversion from geometrized units with factors of G and c.

[2] In this paper, we use the same definition for the compactness parameter C as in [31]. For an axion star mass M_s, $C = GM_s/R$, where R is the effective radius of the star (includes 95% of its mass).

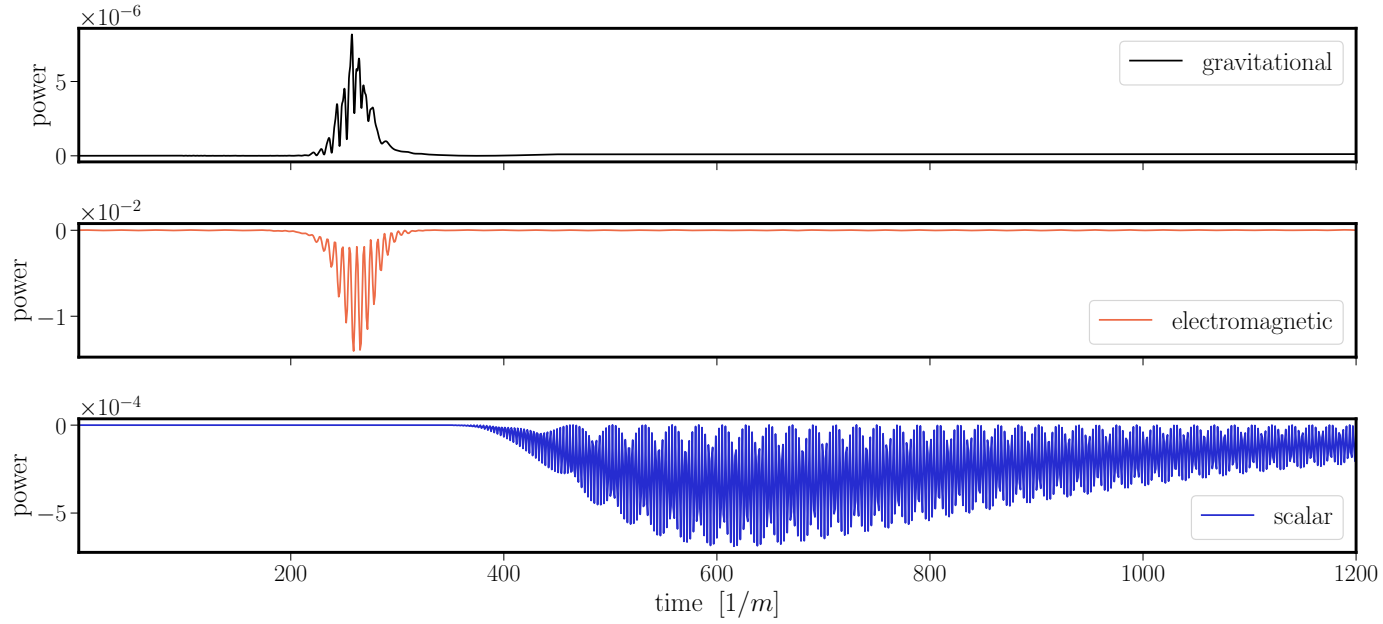

FIG. 1. Multimessenger signal of axion star decay by electromagnetic instability, for an isolated super-critical star: gravitational power (luminosity) (*top*), total flux of electromagnetic energy (*middle*), and corresponding total flux of the scalar energy (*bottom*). Note that power is dimensionless in geometrized units. Signals are extracted over a sphere of radius $r = 80m^{-1}$, and the power in electromagnetic and scalar radiation is obtained by integrating the corresponding flux. We note that the electromagnetic and GW signal reach the observer at the same time, as both travel at the speed of light, whereas the scalar emission is delayed as it is massive. The different frequency wave modes in the scalar emission are responsible for the long tail in the total scalar flux, as lower frequency modes travel more slowly away from the decaying star. The EM and scalar fluxes are calculated according to the method from Eq. 11 in Ref. [33], and the gravitational power with the usual gravitational luminosity formula (see Appendix C1).

dimensionful parameters $(M_s, g_{a\gamma})$ (i.e. below the critical line $g_{a\gamma}^{\rm crit}(M_s)$) can merge and form a highly excited, more compact star that correspondingly has a lower critical coupling, and is thus unstable electromagnetically. This merged star then decays through parametric resonance just as the single stars studied in [25], emitting a strong EM burst. [3] The GW signal of the decay in Fig. 1 does not exhibit any ringdown hierarchy as no black hole is formed. Instead, its frequency matches the axion mass, implying that it is primarily sourced by the quadrupole moment during the decay process. The GW signal from the merger is largely unaffected by the EM coupling, and agrees with the results of Ref. [31] (which included axion self-interactions but no EM coupling). Thus, the multimessenger signal of compact axion star mergers has a distinct portrait: an initial weak GW signal from the merger, followed by a louder GW burst and accompanying EM signal, and finally a delayed and prolonged axion signal.

This paper is organised as follows: Section II introduces our oscillaton model and the initial set up of our simulations. Section III outlines the story of two axion star colliding head-on, merging, and the merged star decaying through the electromagnetic instability demonstrated in [25]. Section IV shows the gravitational wave signal from the electromagnetic decay of axion stars, and the combined signal from the merger and decay process, followed by the full multimessenger signal in Section V. Finally, we discuss the observational consequences of our findings in Section VI.

II. THEORY

Our work in this paper uses the same oscillaton model as in our previous study [25]. The total action is

$$S = \int d^4x\sqrt{-g}\left[\frac{m_{\rm Pl}^2}{16\pi}R - \frac{1}{2}\partial_\mu\phi\partial^\mu\phi - \frac{1}{2}m^2\phi^2 - \frac{1}{4}F_{\mu\nu}F^{\mu\nu} - \frac{g_{a\gamma}}{4}\phi F_{\mu\nu}\tilde{F}^{\mu\nu}\right], \tag{1}$$

where ϕ denotes the axion field, and R the Ricci scalar. The electromagnetic field strength tensor and its dual are defined as

$$F_{\mu\nu} = \partial_\mu A_\nu - \partial_\nu A_\mu, \quad \widetilde{F}^{\mu\nu} = \frac{1}{2\sqrt{-g}}\varepsilon^{\mu\nu\rho\sigma}F_{\rho\sigma}, \tag{2}$$

[3] As in Ref. [25], an EM seed is required to trigger the resonance: in our simulations such a seed is given by a weak propagating EM wave, modelling ambient radiation in the galaxy.

with the totally antisymmetric Levi-Civita symbol $\varepsilon^{\mu\nu\rho\sigma}$, defined through $\varepsilon^{0123} = +1$.

The axion pseudoscalar field is coupled to the field strength tensor through the Chern-Simons term (last term in Eq. 1), where the coupling constant $g_{a\gamma}$ sets the strength of the interaction. Moreover, the stress-energy tensor can be calculated from the action in Eq. (1) to solve Einstein's equations $G_{\mu\nu} = 8\pi m_{\rm Pl}^{-2} T_{\mu\nu}$ (see e.g. Ref. [37]), where we note that the Chern-Simons topological term does not enter the stress-energy tensor.

The parametric resonance process, as described in Section I, is driven by the sourced Maxwell's equation for the evolution of the field strength tensor, Eq. (4),

$$\nabla^\mu \nabla_\mu \phi - m^2 \phi = \frac{g_{a\gamma}}{4} F_{\mu\nu} \tilde{F}^{\mu\nu}, \tag{3}$$

$$\nabla_\mu F^{\mu\nu} = -g_{a\gamma} J^\nu, \tag{4}$$

where the current J^ν is given by $J^\nu = \partial_\mu \phi \tilde{F}^{\mu\nu}$. In general, resonance can happen provided that the photon frequency lies within the parametric resonance band. As we discussed in [25], the axion mass implies that the oscillations of the star go as $\omega \sim m \sim R_s^{-1}$, hence setting a bandwidth for the photon frequencies that can drive the parametric resonance process.

Our system of coupled axion star, electromagnetism and the metric is solved using GRChombo [34–36]. We follow the same procedure to find initial conditions for the axion star and the electromagnetic field as in our previous work [25]. The axion star initial set up is built following Refs. [23, 31, 38–42], while the implementation of the electromagnetic field follows the methodology introduced in Refs. [43–47]. Specifically, for the superposition of two axion stars as initial conditions, we use the profiles introduced in Ref. [31, 48, 49] where the spatial metric is renormalized to reduced gauge artifacts. The EM initial conditions were set up as outlined in Ref. [25], with the initial EM amplitude kept the same for all stars ($C_x = 0.001 m_{\rm Pl}$), but a frequency of $k^{(x)} \equiv 2\pi/\lambda \sim 0.10m$ for the single, more massive star and $k^{(x)} \sim 0.12m$ for the colliding stars.

As we solve the fully non-linear evolution equations numerically, our simulations include all backreactions. We implement periodic boundary conditions in the propagation direction of our electromagnetic plane wave seed to keep the radiation in the simulation box, and Sommerfeld boundary conditions in the remaining two directions. The Sommerfeld boundary conditions absorb outgoing radiation at the boundary of our simulation box which improves the accuracy of gravitational wave signal extraction from the simulation. The evolution of the scalar field is not affected by the choice of boundary conditions, as the main effect of implementing Sommerfeld boundary conditions is to absorb outgoing gravitational and electromagnetic radiation. The convergence of our simulation, along with the convergence of the extracted gravitational waves, is discussed in Appendix B.

III. MERGERS AND ELECTROMAGNETIC INSTABILITY

Our story of two axion stars colliding head-on and merging, is captured in Fig. 2, which demonstrates the evolution of the energy density in the scalar and EM fields over time in a slice through our simulation box. We start with two gravitationally and electromagnetically stable stars that collide and form a highly excited merged star that is stable gravitationally, but which after some time decays electromagnetically through parametric resonance. From now on, we will call the star resulting from the collision and merger of the two original axion stars "merged star", as opposed to the "single star" which is directly set up by the initial conditions.

More specifically, we start with compact axion stars in the sub-critical region demonstrated in [31], where the head-on merger of these stars leads to a highly excited, more compact star. Our stars are initially separated by a distance of $40m^{-1}$, and have a mass of $M_s = 0.36 m_{\rm Pl}^2/m$. Using the scaling relation between the critical coupling of a compact star and its mass $g_{a\gamma}^{\rm crit} \propto M_s^{-1.35}$, which we demonstrated in Ref. [25], this gives our initial stars a critical coupling of $g_{a\gamma}^{\rm crit} \sim 24.6 m_{\rm Pl}^{-1}$.

Hence, we collide these stars with a coupling value of $g_{a\gamma} = 20 m_{\rm Pl}^{-1}$, which ensures that the interaction between the stars and the electromagnetic field is negligible before the merger, since the coupling value lies in the stable region of the $(M_s, g_{a\gamma})$ plane (under the critical line $g_{a\gamma}^{\rm crit}(M_s)$), as demonstrated in Ref. [25]. In other words, the decay of the original stars through the parametric resonance process, as outlined in Section I, is forbidden.

However, the stars collide and merge to form a single highly excited star, as shown in [31]. This merged star potentially possesses a critical coupling below the coupling set in the simulation ($g_{a\gamma} = 20 m_{\rm Pl}^{-1}$). We note that evaluating the critical coupling of this merged star analytically is not straightforward, as the star is highly excited with some "breathing mode" oscillation patterns and gravitational cooling by axion emission [24], and hence does not map directly to the simple compact stars with critical line found in Ref. [25]. Nonetheless, approximating the merged star's effective radius by the location where the scalar energy density has dropped to 5% of its central value, we compute the ADM mass of the merged star, which gives us an estimate of its critical coupling from the critical line in [25]. We find $g_{a\gamma}^{\rm crit} \sim 16 m_{\rm Pl}^{-1}$, which is below the simulated value. Hence, we expect parametric resonance to kick in after the merger and cause the merged star to decay.

This is indeed what we observe in our simulations, with the merging of the original stars shown in the upper set of panels of Fig. 2, corresponding to $t = 0m^{-1}$ to $t = 340m^{-1}$, and the parametric decay of the merged star at later times $t = 630m^{-1}$ to $t = 700m^{-1}$ in the lower set of panels. The electromagnetic decay leaves behind a less compact remnant, and we discuss the corresponding shutting down of the resonance process in Appendix A.

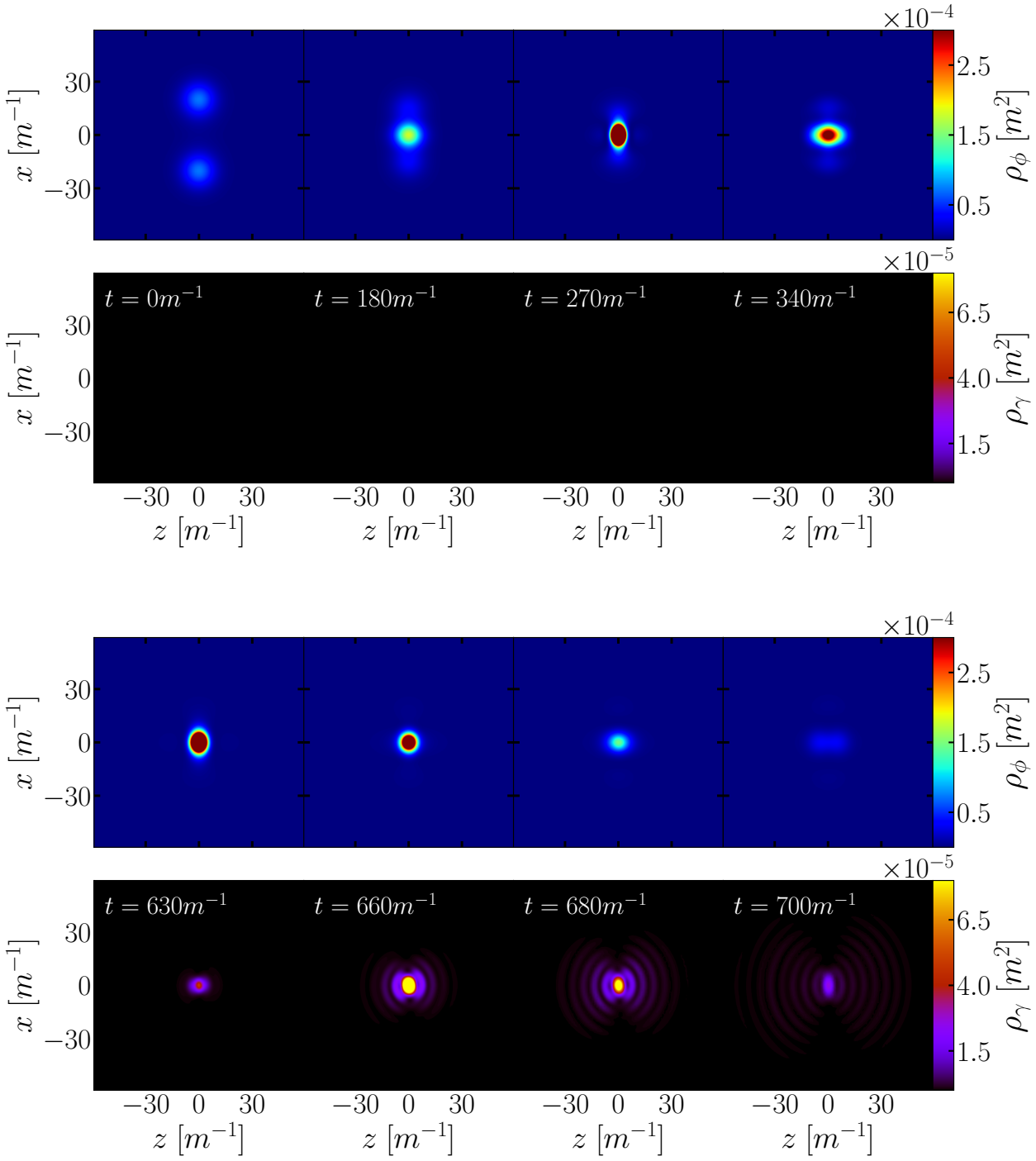

FIG. 2. Evolution of the energy density in the scalar (*blue panels*) and EM field (*black panels*) as a slice through the center of our simulation box. We start with two stable stars of mass $M_s = 0.36 m_{\rm Pl}^2/m$ at $t = 0m^{-1}$, which merge to form a highly excited, but stable star (around $t \sim 180m^{-1}$). Our coupling value is $g_{a\gamma} = 20 m_{\rm Pl}^{-1}$, implying that the final merger star is super-critical according to Ref. [25], resulting in the decay of the merged star through parametric resonance (see the lower set of panels). This happens because, due to the higher mass, the critical coupling of the merged star is lower than the critical coupling of the original stars, allowing the parametric resonance process after the merger. The initial seed electromagnetic field (not visible on this scale) is polarised in the x-direction and propagating from the right to the left. A movie of our simulations can be found through this link.

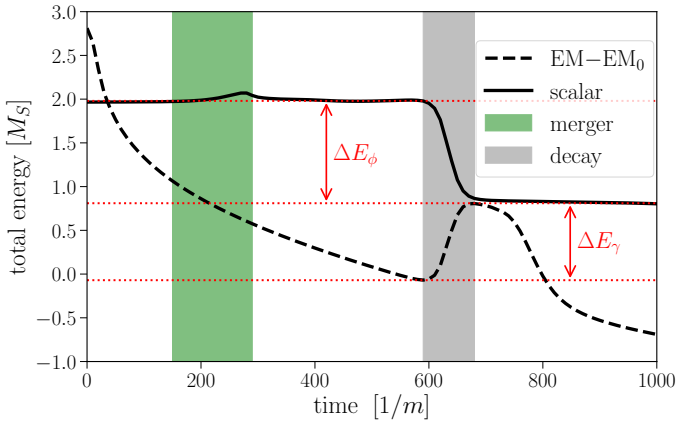

FIG. 3. Total simulation box energy in the scalar (*solid line*) and electromagnetic field (*dashed line*) for the merger and electromagnetic decay process. The merger timescale is shown in green, and the decay through parametric resonance of the resulting highly excited merged star in grey. The energy is in units of the original colliding stars' mass. The electromagnetic energy EM_0 immediately before the decay has been subtracted from the total; the decrease in the EM energy is due to the absorbing boundary conditions. Strong amplification of the EM field during the decay of the excited merged star is clearly visible (ΔE_γ). The unphysical bump in the total scalar energy corresponds to the lapse being driven to its minimum value due to the large curvatures present at merger.

The same merger and decay process is shown in terms of the total energy in the scalar and electromagnetic field in Fig. 3. The green area corresponds to the merging process, while the grey area shows the time span of the parametric resonance decay of the merged star. We have scaled the energies to the mass of the original star (M_s), and hence the solid line representing the scalar energy starts at $2M_s$. The total scalar energy in the simulation box stays roughly constant before and after the merger of the stars, but decays through the parametric resonance process after $t \sim 600m^{-1}$, as expected. Accordingly, the electromagnetic energy in the box is strongly amplified during parametric resonance. The decay process pictured in Fig. 3 is in perfect agreement with the decay of single compact stars that we studied in [25].

We use Sommerfeld boundary conditions for our simulation box and hence the electromagnetic radiation is constantly being absorbed at the boundaries of our box, which explains its decrease until the parametric resonance kicks in. Furthermore, note the *total* EM energy of the box is larger than that of the scalar – this is due to the large box size we used in our simulations since the EM seed wave fills the entire domain. The key physical effect is the EM energy "bump" occuring at $t = 600m^{-1}$, i.e. $\Delta E_\gamma \sim \Delta E_\phi$ where scalar energy is converted into EM energy via parameteric resonance.

The power spectrum of the electromagnetic field at the start of the simulation and right after the decay of the merged star has happened is shown in Fig. 4. The dashed black line demonstrates the original seed (polarised in the x-direction), while the coloured lines corresponding

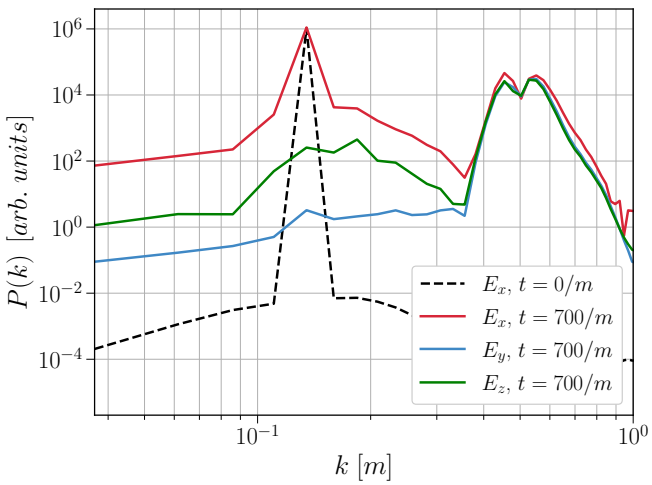

FIG. 4. The power spectrum of the electromagnetic field at the start of the simulation ($t = 0m^{-1}$) and after the decay of the merged star ($t = 700m^{-1}$). A clear excitation in all the EM components around the characteristic frequency of the star, $k \sim 0.5m$, is visible. The E_y component of the emission does not acquire energy at the seed frequency due to our Sommerfeld boundary conditions.

to $t = 700m^{-1}$ show all the components of the EM field (E_x, E_y, E_z), with a clear excitation around $k \sim 0.5m$, which corresponds to the characteristic frequency of the star, and demonstrates parametric resonance. Similar to the power of a single star decay discussed in [25], the EM power is approximately isotropic. Interestingly, there is a small double peak around $k \sim 0.5m$, which is likely due to a slight difference in excitation frequency of the oscillations around the collision axis and that perpendicular to it.

IV. GRAVITATIONAL WAVES

In Fig. 5 we show the gravitational wave signal corresponding to the electromagnetic decay of a single compact star with mass $M_s = 0.60m_{\mathrm{Pl}}^2/m$, using $g_{a\gamma} = 16m_{\mathrm{Pl}}^{-1}$. The two polarisation modes of GWs are captured through the real and imaginary parts of the Newton-Penrose Weyl scalars Ψ_4 (see, e.g. Ref.[50]). Fig. 5 shows the real and imaginary part of the $l = 2, m = 0$ mode, although the $l = 2, m = \pm 2$ modes were observed to be of similar amplitudes. The signal is extracted at $r = 80m^{-1}$.

As the decay of the star is not symmetric (for example, our electromagnetic seed is polarised in one direction and propagating in another), both gravitational polarisation modes are excited, corresponding to the real and imaginary parts of the Weyl scalar. In contrast, the merger signal is axisymmetric, and hence only a single polarisation mode is excited. We also notice that this decay signal does not have a ringdown hierarchy like black hole mergers, creating a distinct signature.

Moreover, in Fig. 6 we map the whole gravitational

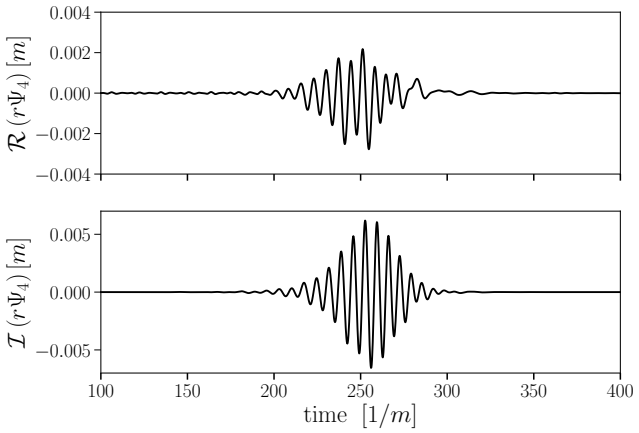

FIG. 5. Gravitational wave waveform of the $l = 2, m = 0$ mode for the electromagnetic decay of a single star. The waveform is extracted at $r = 80m^{-1}$ at refinement level 2. This gravitational wave, corresponding to a burst of electromagnetic energy, does not exhibit a ringdown. We note that the $l = 2, m = \pm 2$ modes were of similar order of magnitude.

wave waveform for the merger of two stars and the subsequent parametric decay process, outlined in Section III. The gravitational wave signal from the merger at around $t \sim 350m^{-1}$ has already been studied in [31]. We note that the GW signal from the decay of the merged star into photons around $t \sim 750m^{-1}$ closely matches the signal from the decay of a single star shown in Fig. 5.

The frequency of the oscillations in the GW signal were computed by taking a Fourier transform, and found to be around $\omega \sim m$ for the decay, which matches the frequency of the EM flux through the same surface (see Section V), and moreover the mass of the scalar field. The frequency match $\omega \sim m$ can be understood from linearising the axion-GW interaction. The frequency of the merger signal, on the other hand, is around one order of magnitude lower, $\omega \sim 0.1m$. For an axion mass of $m = 10^{-12}$ eV, the decay frequency corresponds to $f \sim 10^3$Hz, implying that both the decay and the merger frequencies lie close to the current peak sensitivity of the LIGO band.

Finally, we study the gravitational wave energy resulting from the electromagnetic decay of the star. Fig. 7 shows the cumulative energy in the gravitational wave signal from the decay of the merged star for the dominant l modes, extracted from the signal between $t = 600m^{-1}$ to $t = 900m^{-1}$. This spans the decay process of the merged star. As expected from other compact objects, the dominant mode is the quadrupole, $l = 2$. Comparing these modes to the modes excited by the decay of the single star (maximum energy in each mode shown as dashed lines), we note that the spectrum of the merged star has more power in higher multipoles as the merger excites asymmetric spatially oscillating modes in the star (the single star, on the other hand, is spherically symmetric before the decay process). Concretely, less than 1% of the GW energy from the decay of a single star is found in modes $l > 2$, whereas the merged star has around 10% of the energy in the $l = 3$ and $l = 4$ modes.

The total gravitational energy (E_{GW}) from the decay is $\sim 0.03\%$ of the total energy of the original stars ($2M_s$), comparable to the ratio in black hole head-on mergers. We expect this efficiency to be similar for non-head on mergers as it is driven by the decay process. On the other hand, the electromagnetic decay of the merged axion star carries around ten times more energy in gravitational waves than the merger of axion stars.

Our simulations also demonstrate that the total gravitational energy emitted by the single star decay scales roughly linearly with compactness, with an increase of over 90% in the energy emitted from $C = 0.10$ to $C = 0.14$, keeping the coupling constant fixed at $g_{a\gamma} = 16m_{\rm Pl}^{-1}$. However, as the value of the axion-photon coupling affects the decay process significantly, a multiparameter study would be required for a full understanding of the energy scaling.

V. MULTIMESSENGER SIGNAL

As the previous sections have explored in detail, the electromagnetic instability of the axion star results in a multimessenger signal, with both an electromagnetic and a gravitational component. The gravitational wavefront and the electromagnetic energy ejected are expected to reach an observer away from the source at the same time, travelling at the speed of light. This is represented in Fig. 1, where the upper two panels represent the gravitational power (in black) from the decay of a single star (corresponding to the wavefront in Fig. 5), and the corresponding total flux of electromagnetic energy (in orange), integrated over a sphere at the same radius ($r = 80m^{-1}$).

The bottom panel (in blue) represents the scalar (axion) waves ejected by the star, captured by the total scalar flux over the same sphere. These total energy fluxes are calculated by integrating over the flux in Eq. 11 of Ref. [33]. Firstly, we observe that the scalar energy is around two orders of magnitude lower than its electromagnetic counterpart (the power units are the same in both panels), hence being a subdominant effect. Secondly, the total scalar flux is delayed compared to the EM and GW signals, as massive modes travel slower than light [4]. In addition, in the decay process, different wave modes of the scalar field are excited as the star transitions from one state to another. These scalar waves of different wavelengths travel at different speeds, resulting in a long tail of total scalar flux as shown in Fig. 1, as longer

[4] To confirm the delay of the massive modes compared to the EM and GW signal, we computed the expected time delay for the single star decay using the relativistic dispersion relation and $k \sim 0.5m$, which corresponds to the characteristic frequency of the star, assuming it matches the maximum group velocity. This gives us $\Delta t \sim 100m^{-1}$, which matches the time delay in Fig.1.

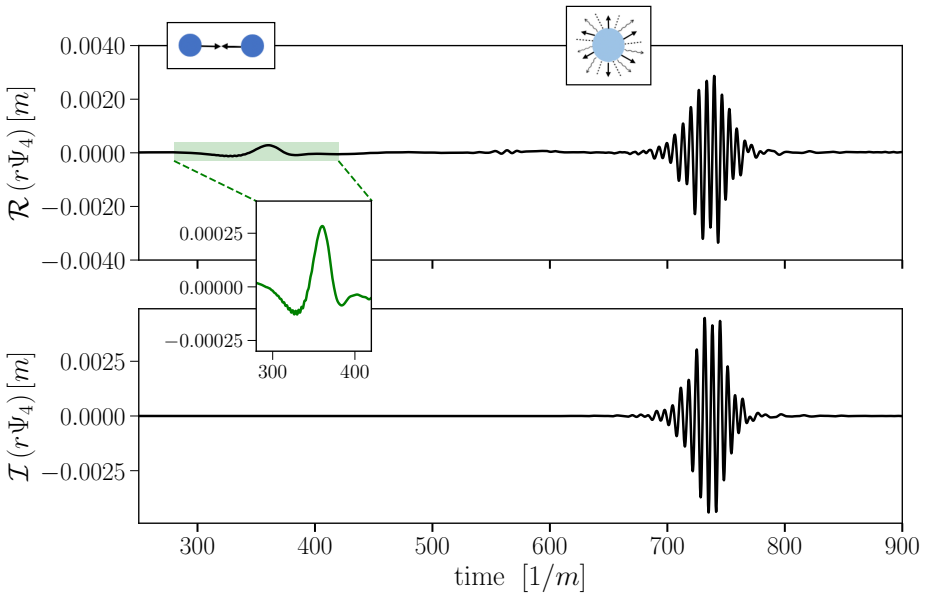

FIG. 6. Gravitational wave waveforms for the merger and subsequent decay process, showing the dominant quadrupole mode $l = 2, m = 0$. We note that the $l = 2, m = \pm 2$ modes were of the same order of magnitude than the mode shown. The wavefronts were extracted at radius $r = 80m^{-1}$, refinement level 2. The first excitation around $t = 350m^{-1}$ in the real part corresponds to the merger signal, and the second excitation around $t = 750m^{-1}$ is the signal from the electromagnetic decay of the star. In the case of the decay, both the real and imaginary parts are excited, meaning that both gravitational polarisation modes are present. A zoomed in picture of the signal from the merger of the stars is depicted as a green wavefront, corresponding to the shaded green region in the main plot.

wavelength modes travel slower (recall that $\omega^2 = k^2 + m^2$ for a free scalar wave) resulting in the characteristic "dispersion" of the wave packet.

In Fig. 8 we show the corresponding GW, EM and scalar signals for the merger simulations. The GW and EM signals from the decay phase are strikingly similar to the single star case, with a relatively small GW bump from the merger. On the other hand, the merged star emits scalar waves immediately following the merger at $t \sim 300m^{-1}$, due to being in an excited state [24] ending in a burst during the electromagnetic decay phase.

Finally, we comment on the energy scales of the system: the largest source of emitted energy in the parametric, electromagnetic decay of an axion star is the electromagnetic emission from the star, which is around two orders of magnitude larger than the scalar emission. The gravitational energy emitted is a further two orders of magnitude smaller than the scalar emission, hence creating a clear hierarchy in the magnitude of the signals emitted. For a scalar field mass of $m = 10^{-12}$ eV, the total electromagnetic energy ejected by the parametric decay of the merged star is around 10^{49}J, which compares to the energy scale of a supernova.

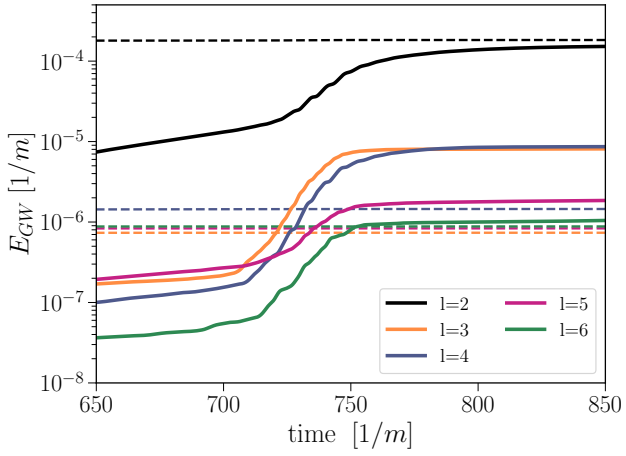

FIG. 7. Cumulative gravitational energy in each l mode for the decay of the merged star (corresponding to the signal at $t \sim 750m^{-1}$ in Fig. 6). The dashed lines indicate the maximum energy of the corresponding mode for the single star decay. We note that the $l = 2$ mode dominates, as expected, and that the spectrum of the merged star is more varied than the single one, where most of the energy is in the dominant $l = 2$ mode.

VI. DISCUSSION AND CONCLUSIONS

In this work we have studied, in fully non-linear simulations, the multimessenger signal produced by the collision of two compact axion stars close to the critical mass defined by the axion-photon coupling. The initial merger produces a GW signal consistent with that expected for real scalar boson stars [31, 32]. This signal is relatively small in amplitude, due to the low compactness of $C < 0.14$. The merger forms an excited, more massive axion star that crosses the threshold of electromagnetic stability. This star subsequently decays

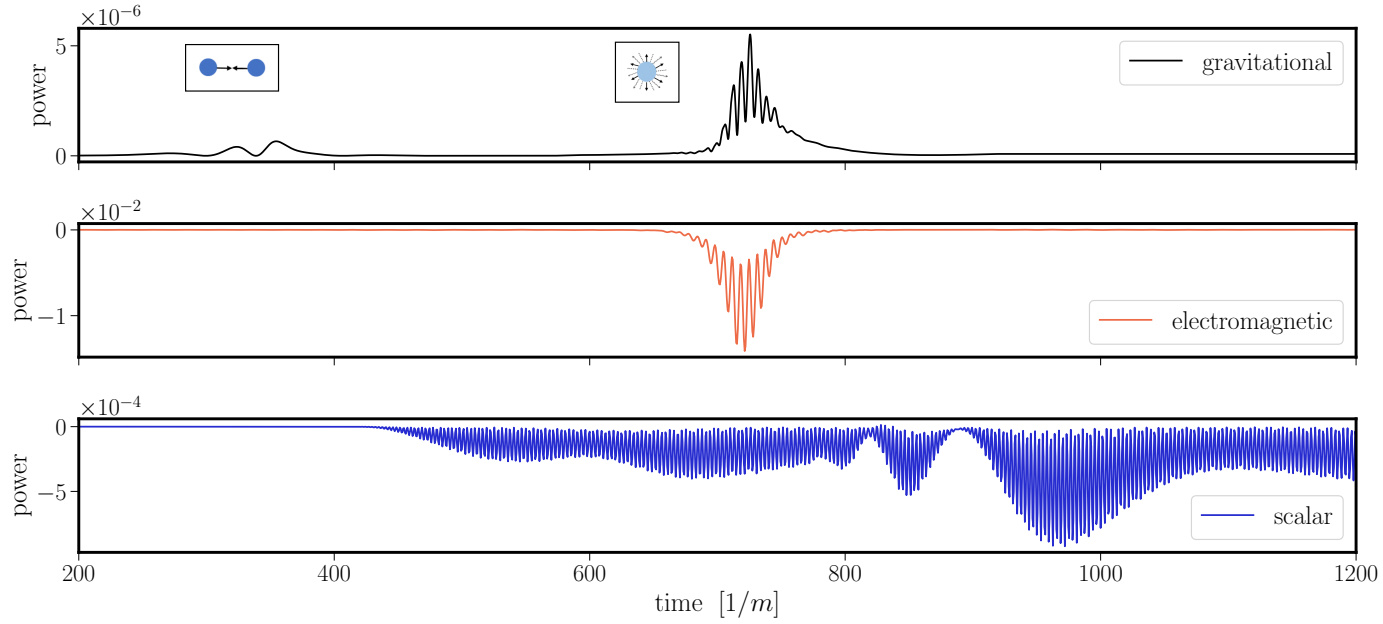

FIG. 8. Multimessenger signal from the merger of two axion stars and subsequent decay of the merged star, caused by an electromagnetic instability: the gravitational power (*top*), total flux of electromagnetic energy extracted over a sphere at the same radius as the GW signal, $r = 80m^{-1}$ (*middle*), and corresponding total flux of the scalar energy (*bottom*), where the power in electromagnetic and scalar radiation is obtained by integrating the corresponding flux. The different frequency wave modes in the scalar emission are responsible for the long tail in the scalar flux, as lower frequency modes travel slower away from the decaying star. The system starts shedding scalar waves already due to the merger which happens around $t \sim 300m^{-1}$, resulting in a complex pattern of scalar radiation after the electromagnetic decay (around $t \sim 750m^{-1}$).

into electromagnetic radiation via parametric resonance, triggered by ambient photons. The excited super-critical star first cools by emission of axions, and then explodes, emitting axions, GWs, and photons. The GWs from the decay are almost monochromatic, at a frequency one order of magnitude larger than the GWs from collision, and do not follow a ringdown hierarchy. GWs from the decay carry over one order of magnitude more energy than those from the merger.

The length of time of the delay between merger and decay is fixed by the coupling $g_{a\gamma}$, the mass of the merged star (which defines its critical coupling), as well as the amplitude of the EM seed through a logarithmic dependence, as we confirmed in [25]. The dominant energy in the decay is carried by photons, since criticality is governed by parametric resonance of the Chern-Simons interaction between axions and photons. The energy in photons is two orders of magnitude larger than the energy in axions, which itself is two orders of magnitude more than the energy in GWs.

This paper has been concerned with the theory and simulation of axion star mergers and explosions, computing for the first time the decay channels. We discuss briefly here the observational consequences, but leave full study to a future work. By colliding two axion stars of mass $M_s = 0.36m_{\rm Pl}^2/m$, $C = 0.03$ each, with axion parameters $m = 10^{-12}$ eV, $g_{a\gamma} = 20m_{\rm Pl}^{-1}$, selected to give rise to GWs from merger and decay in the LIGO frequency band, we determined that the GWs would be visible up to distances of ~ 110 Mpc and 270 Mpc, for merger and decay respectively. The calculations follow Eq. 13 in [44], assuming a detected strain $h = 10^{-22}$, which is the current LIGO peak sensitivity for the decay frequency range. If GW emission and photon emission from the decay could both be observed, then with the right waveform model and timing data this may allow the weaker merger GW signal to be extracted from noise in post-processing.

An axion star explosion from higher mass axions produces high frequency GWs, for example $m \approx 10^{-6}$ eV gives GWs in the GHz band, although the luminosity would be smaller as the axion star mass scales inversely to m. Such high frequency GWs can be detected using microwave cavities [51] (such as the ones commonly used in axion dark matter haloscopes) or phononic materials [52] . We have not considered this possibility in detail for GWs from axion star explosions, as the signal is likely too weak to give sensitivity to large astronomical distances, but this may warrant further investigation.

For GWs in the LIGO band, the EM radiation is emitted in the kHz band with total energy comparable to a supernova. Some consequences of the EM radiation emitted by an axion star explosion in this band are discussed in Refs. [53, 54]. However, for a multimessenger signal including GWs, there are several important differences to consider for the photon emission compared to

Refs. [53, 54]. Compact stars giving a GW signal require a different formation mechanism: the core halo-mass relation [18] for axion stars in dark matter halos predicts that compact axion stars are extremely rare, if present at all. One possible mechanism to form compact axion stars is outlined in Ref. [20], which involves a spike in the axion primordial power spectrum, which could emerge due to phase transitions and string network decay after inflation (e.g. as axiton formation in Ref. [55]), or blue inflationary isocurvature [56]. In such mechanisms, compact axion stars can form at rare density peaks, much like primordial black holes. Another possibility involves an extended matter dominated epoch [57]. The physics of an individual explosion will be the same as studied in Refs. [53, 54], but the population level effects will be absent. Furthermore, a multimessenger signal involving GWs will probe only the local Universe at $D \lesssim 300$Mpc, rather than the early universe $z > 10$ considered in Refs. [53, 54].

The EM emission from the explosion of an axion star in the kHz band is efficiently absorbed by neutral hydrogen, causing it to ionize [58]. Thus, we would observe the EM emission indirectly from the heating of the surrounding gas. Following Ref. [53, 54] we find that in the Milky Way, taking values for the free electron density and baryon temperature in virial equilibrium, the absorption length for photons in the kHz band is short, on the order of parsecs. Thus the photons from an exploding axion star in the local Universe heat the surrounding gas and rapidly ionize and shock it; the resulting emission in optical frequencies from the hot expanding gas may resemble a supernova with no associated production of heavy elements.

It may also be possible to detect the semi-relativistic axions produced. Axion dark matter haloscope data is normally analysed assuming a search for the cold galactic axions of the standard halo model [59]. However, the physics of axion-photon conversion can happen also for relativistic axions, such as those of the "cosmic axion background" [60]. In particular, the broadband DMRadio proposal [61] covers the correct frequency range for axions that are part of a multimessenger signal of an axion star explosion with accompanying GWs in the LIGO band.

ACKNOWLEDGEMENTS

We would like to thank Lewis Croney, Miguel Escudero, Tamara Evstafyeva and Thomas Helfer for useful discussions. We also thank members of the GRTL Collaboration for technical support and help. LCJ is supported by a studentship funded by the Science and Technologies Facilities Council (UK). DJEM is supported by an Ernest Rutherford Fellowship from the Science and Technologies Facilities Council (ST/T004037/1). This work used the DiRAC@Durham Cosma facility managed by the Institute for Computational Cosmology on behalf of the STFC DiRAC HPC Facility (www.dirac.ac.uk), under DiRAC grant ACTP238. The equipment was funded by BEIS capital funding via STFC capital grants ST/P002293/1, ST/R002371/1 and ST/S002502/1, Durham University and STFC operations grant ST/R000832/1.

[1] R. D. Peccei and H. R. Quinn, CP Conservation in the Presence of Instantons, Phys. Rev. Lett. **38**, 1440 (1977).
[2] S. Weinberg, A New Light Boson?, Phys. Rev. Lett. **40**, 223 (1978).
[3] F. Wilczek, Problem of Strong p and t Invariance in the Presence of Instantons, Phys. Rev. Lett. **40**, 279 (1978).
[4] J. E. Kim, Weak Interaction Singlet and Strong CP Invariance, Phys. Rev. Lett. **43**, 103 (1979).
[5] M. A. Shifman, A. I. Vainshtein, and V. I. Zakharov, Can Confinement Ensure Natural CP Invariance of Strong Interactions?, Nucl. Phys. B **166**, 493 (1980).
[6] M. Dine, W. Fischler, and M. Srednicki, A Simple Solution to the Strong CP Problem with a Harmless Axion, Phys. Lett. B **104**, 199 (1981).
[7] A. R. Zhitnitsky, On Possible Suppression of the Axion Hadron Interactions. (In Russian), Sov. J. Nucl. Phys. **31**, 260 (1980).
[8] J. Preskill, M. B. Wise, and F. Wilczek, Cosmology of the Invisible Axion, Phys. Lett. B **120**, 127 (1983).
[9] L. F. Abbott and P. Sikivie, A Cosmological Bound on the Invisible Axion, Phys. Lett. B **120**, 133 (1983).
[10] M. Dine and W. Fischler, The Not So Harmless Axion, Phys. Lett. B **120**, 137 (1983).
[11] L. Di Luzio, M. Giannotti, E. Nardi, and L. Visinelli, The landscape of QCD axion models, Phys. Rept. **870**, 1 (2020), arXiv:2003.01100 [hep-ph].
[12] M. S. Turner, Coherent Scalar Field Oscillations in an Expanding Universe, Phys. Rev. D **28**, 1243 (1983).
[13] E. Witten, Some Properties of O(32) Superstrings, Phys. Lett. B **149**, 351 (1984).
[14] M. Khlopov, B. A. Malomed, and I. B. Zeldovich, Gravitational instability of scalar fields and formation of primordial black holes, Mon. Not. Roy. Astron. Soc. **215**, 575 (1985).
[15] P. Svrcek and E. Witten, Axions In String Theory, JHEP **06**, 051, arXiv:hep-th/0605206.
[16] P. Arias, D. Cadamuro, M. Goodsell, J. Jaeckel, J. Redondo, and A. Ringwald, WISPy Cold Dark Matter, JCAP **06**, 013, arXiv:1201.5902 [hep-ph].
[17] D. J. E. Marsh, Axion Cosmology, Phys. Rept. **643**, 1 (2016), arXiv:1510.07633 [astro-ph.CO].
[18] H.-Y. Schive, T. Chiueh, and T. Broadhurst, Cosmic Structure as the Quantum Interference of a Coherent Dark Wave, Nature Phys. **10**, 496 (2014), arXiv:1406.6586 [astro-ph.GA].
[19] D. G. Levkov, A. G. Panin, and I. I. Tkachev, Gravitational Bose-Einstein condensation in the kinetic regime, Phys. Rev. Lett. **121**, 151301 (2018), arXiv:1804.05857 [astro-ph.CO].

[20] J. Y. Widdicombe, T. Helfer, D. J. E. Marsh, and E. A. Lim, Formation of Relativistic Axion Stars, JCAP **10**, 005, arXiv:1806.09367 [astro-ph.CO].

[21] B. Eggemeier and J. C. Niemeyer, Formation and mass growth of axion stars in axion miniclusters, Phys. Rev. D **100**, 063528 (2019), arXiv:1906.01348 [astro-ph.CO].

[22] J. Chen, X. Du, E. W. Lentz, D. J. E. Marsh, and J. C. Niemeyer, New insights into the formation and growth of boson stars in dark matter halos, Phys. Rev. D **104**, 083022 (2021), arXiv:2011.01333 [astro-ph.CO].

[23] E. Seidel and W. M. Suen, Oscillating soliton stars, Phys. Rev. Lett. **66**, 1659 (1991).

[24] E. Seidel and W.-M. Suen, Formation of solitonic stars through gravitational cooling, Phys. Rev. Lett. **72**, 2516 (1994), arXiv:gr-qc/9309015.

[25] L. M. Chung-Jukko, E. A. Lim, D. J. E. Marsh, J. C. Aurrekoetxea, E. de Jong, and B.-X. Ge, Electromagnetic instability of compact axion stars, Phys. Rev. D **108**, L061302 (2023), arXiv:2302.10100 [hep-ph].

[26] M. P. Hertzberg and E. D. Schiappacasse, Dark Matter Axion Clump Resonance of Photons, JCAP **11**, 004, arXiv:1805.00430 [hep-ph].

[27] D. G. Levkov, A. G. Panin, and I. I. Tkachev, Radioemission of axion stars, Phys. Rev. D **102**, 023501 (2020), arXiv:2004.05179 [astro-ph.CO].

[28] T. W. Kephart and T. J. Weiler, LUMINOUS AXION CLUSTERS, Phys. Rev. Lett. **58**, 171 (1987).

[29] M. Boskovic, R. Brito, V. Cardoso, T. Ikeda, and H. Witek, Axionic instabilities and new black hole solutions, Phys. Rev. D **99**, 035006 (2019), arXiv:1811.04945 [gr-qc].

[30] T. Ikeda, R. Brito, and V. Cardoso, Blasts of Light from Axions, Phys. Rev. Lett. **122**, 081101 (2019), arXiv:1811.04950 [gr-qc].

[31] T. Helfer, E. A. Lim, M. A. G. Garcia, and M. A. Amin, Gravitational Wave Emission from Collisions of Compact Scalar Solitons, Phys. Rev. D **99**, 044046 (2019), arXiv:1802.06733 [gr-qc].

[32] G. F. Giudice, M. McCullough, and A. Urbano, Hunting for Dark Particles with Gravitational Waves, JCAP **10**, 001, arXiv:1605.01209 [hep-ph].

[33] K. Clough, Continuity equations for general matter: applications in numerical relativity, Class. Quant. Grav. **38**, 167001 (2021), arXiv:2104.13420 [gr-qc].

[34] K. Clough, P. Figueras, H. Finkel, M. Kunesch, E. A. Lim, and S. Tunyasuvunakool, GRChombo : Numerical Relativity with Adaptive Mesh Refinement, Class. Quant. Grav. **32**, 245011 (2015), arXiv:1503.03436 [gr-qc].

[35] T. Andrade *et al.*, GRChombo: An adaptable numerical relativity code for fundamental physics, J. Open Source Softw. **6**, 3703 (2021), arXiv:2201.03458 [gr-qc].

[36] M. Radia, U. Sperhake, A. Drew, K. Clough, P. Figueras, E. A. Lim, J. L. Ripley, J. C. Aurrekoetxea, T. França, and T. Helfer, Lessons for adaptive mesh refinement in numerical relativity, Class. Quant. Grav. **39**, 135006 (2022), arXiv:2112.10567 [gr-qc].

[37] E. V. Gorbar, K. Schmitz, O. O. Sobol, and S. I. Vilchinskii, Gauge-field production during axion inflation in the gradient expansion formalism, Phys. Rev. D **104**, 123504 (2021), arXiv:2109.01651 [hep-ph].

[38] T. Helfer, D. J. E. Marsh, K. Clough, M. Fairbairn, E. A. Lim, and R. Becerril, Black hole formation from axion stars, JCAP **03**, 055, arXiv:1609.04724 [astro-ph.CO].

[39] M. Alcubierre, R. Becerril, S. F. Guzman, T. Matos, D. Nunez, and L. A. Urena-Lopez, Numerical studies of Phi**2 oscillatons, Class. Quant. Grav. **20**, 2883 (2003), arXiv:gr-qc/0301105.

[40] F. Michel and I. G. Moss, Relativistic collapse of axion stars, Phys. Lett. B **785**, 9 (2018), arXiv:1802.10085 [gr-qc].

[41] L. A. Urena-Lopez, T. Matos, and R. Becerril, Inside oscillatons, Class. Quant. Grav. **19**, 6259 (2002).

[42] L. A. Urena-Lopez, Oscillatons revisited, Class. Quant. Grav. **19**, 2617 (2002), arXiv:gr-qc/0104093.

[43] M. Zilhão, H. Witek, and V. Cardoso, Nonlinear interactions between black holes and Proca fields, Class. Quant. Grav. **32**, 234003 (2015), arXiv:1505.00797 [gr-qc].

[44] T. Helfer, J. C. Aurrekoetxea, and E. A. Lim, Cosmic String Loop Collapse in Full General Relativity, Phys. Rev. D **99**, 104028 (2019), arXiv:1808.06678 [gr-qc].

[45] C. Gundlach, J. M. Martin-Garcia, G. Calabrese, and I. Hinder, Constraint damping in the Z4 formulation and harmonic gauge, Class. Quant. Grav. **22**, 3767 (2005), arXiv:gr-qc/0504114.

[46] C. Palenzuela, L. Lehner, and S. Yoshida, Understanding possible electromagnetic counterparts to loud gravitational wave events: Binary black hole effects on electromagnetic fields, Phys. Rev. D **81**, 084007 (2010), arXiv:0911.3889 [gr-qc].

[47] D. Hilditch, An Introduction to Well-posedness and Free-evolution, Int. J. Mod. Phys. A **28**, 1340015 (2013), arXiv:1309.2012 [gr-qc].

[48] T. Helfer, U. Sperhake, R. Croft, M. Radia, B.-X. Ge, and E. A. Lim, Malaise and remedy of binary boson-star initial data, Class. Quant. Grav. **39**, 074001 (2022), arXiv:2108.11995 [gr-qc].

[49] T. Evstafyeva, U. Sperhake, T. Helfer, R. Croft, M. Radia, B.-X. Ge, and E. A. Lim, Unequal-mass boson-star binaries: initial data and merger dynamics, Class. Quant. Grav. **40**, 085009 (2023), arXiv:2212.08023 [gr-qc].

[50] T. W. Baumgarte and S. L. Shapiro, *Numerical relativity : solving Einstein's equations on the computer* (Cambridge University Press, Cambridge, 2010).

[51] A. Berlin, D. Blas, R. Tito D'Agnolo, S. A. R. Ellis, R. Harnik, Y. Kahn, and J. Schütte-Engel, Detecting high-frequency gravitational waves with microwave cavities, Phys. Rev. D **105**, 116011 (2022), arXiv:2112.11465 [hep-ph].

[52] Y. Kahn, J. Schütte-Engel, and T. Trickle, Searching for High Frequency Gravitational Waves with Phonons, (2023), arXiv:2311.17147 [hep-ph].

[53] M. Escudero, C. K. Pooni, M. Fairbairn, D. Blas, X. Du, and D. J. E. Marsh, Axion Star Explosions: A New Source for Axion Indirect Detection, (2023), arXiv:2302.10206 [hep-ph].

[54] X. Du, D. J. E. Marsh, M. Escudero, A. Benson, D. Blas, C. K. Pooni, and M. Fairbairn, Soliton Merger Rates and Enhanced Axion Dark Matter Decay, (2023), arXiv:2301.09769 [astro-ph.CO].

[55] A. Vaquero, J. Redondo, and J. Stadler, Early seeds of axion miniclusters, JCAP **04**, 012, arXiv:1809.09241 [astro-ph.CO].

[56] S. Kasuya and M. Kawasaki, Axion isocurvature fluctuations with extremely blue spectrum, Phys. Rev. D **80**, 023516 (2009), arXiv:0904.3800 [astro-ph.CO].

[57] A. L. Erickcek and K. Sigurdson, Reheating Effects in the Matter Power Spectrum and Implications for Substruc-

ture, Phys. Rev. D **84**, 083503 (2011), arXiv:1106.0536 [astro-ph.CO].
[58] B. Bolliet, J. Chluba, and R. Battye, Spectral distortion constraints on photon injection from low-mass decaying particles, Mon. Not. Roy. Astron. Soc. **507**, 3148 (2021), arXiv:2012.07292 [astro-ph.CO].
[59] B. M. Brubaker, L. Zhong, S. K. Lamoreaux, K. W. Lehnert, and K. A. van Bibber, HAYSTAC axion search analysis procedure, Phys. Rev. D **96**, 123008 (2017), arXiv:1706.08388 [astro-ph.IM].
[60] J. A. Dror, H. Murayama, and N. L. Rodd, Cosmic axion background, Phys. Rev. D **103**, 115004 (2021), [Erratum: Phys.Rev.D 106, 119902 (2022)], arXiv:2101.09287 [hep-ph].
[61] L. Brouwer *et al.* (DMRadio), Proposal for a definitive search for GUT-scale QCD axions, Phys. Rev. D **106**, 112003 (2022), arXiv:2203.11246 [hep-ex].
[62] R. Croft, T. Helfer, B.-X. Ge, M. Radia, T. Evstafyeva, E. A. Lim, U. Sperhake, and K. Clough, The gravitational afterglow of boson stars, Class. Quant. Grav. **40**, 065001 (2023), arXiv:2207.05690 [gr-qc].

Appendix A: Shutting down of resonance

Axion stars can experience an electromagnetic instability if their characteristic frequency lies within the electromagnetic resonance band, as we first demonstrated in [25], and further in this work for the case of a merged star. In Fig. 9, we show how the parametric resonance process responsible for the decay of the star into electromagnetic radiation does not dissipate the whole star, but shuts down due to the dilution of the star.

As the star enters parametric resonance, its shedding of energy causes the star to dilute, increasing its size. Since the characteristic frequency of the star is linked to its size, the change in frequency means that the star slides off the resonance frequency band and hence the process stops, leaving behind a less compact, dilute remnant. This is seen in the upper plot of Fig. 9 for the single star, where the original star represented by the black line has decayed into a significantly less energetic, less compact star, shown in green. The magnification of the energy density of the remnant star, shown with a dashed green line, demonstrates its broader energy distribution. This indicates a larger radius, and hence different characteristic frequency to the original star.

Similarly, in the bottom plot the original two stars are shown in black, the merged star created by their collision in orange, and the remnant after the electromagnetic decay in green, with the magnification of the remnant energy with a dashed green line. The corresponding times, shown in the legend, can be mapped to the process represented as a whole in Fig. 3. As the merged star is created by the collision of the single stars, its energy distribution has some additional features compared to the single star, which are discussed in Section III. These features are also present in the remnant, which exhibits a broader energy distribution and hence a larger radius than the original stars, as expected.

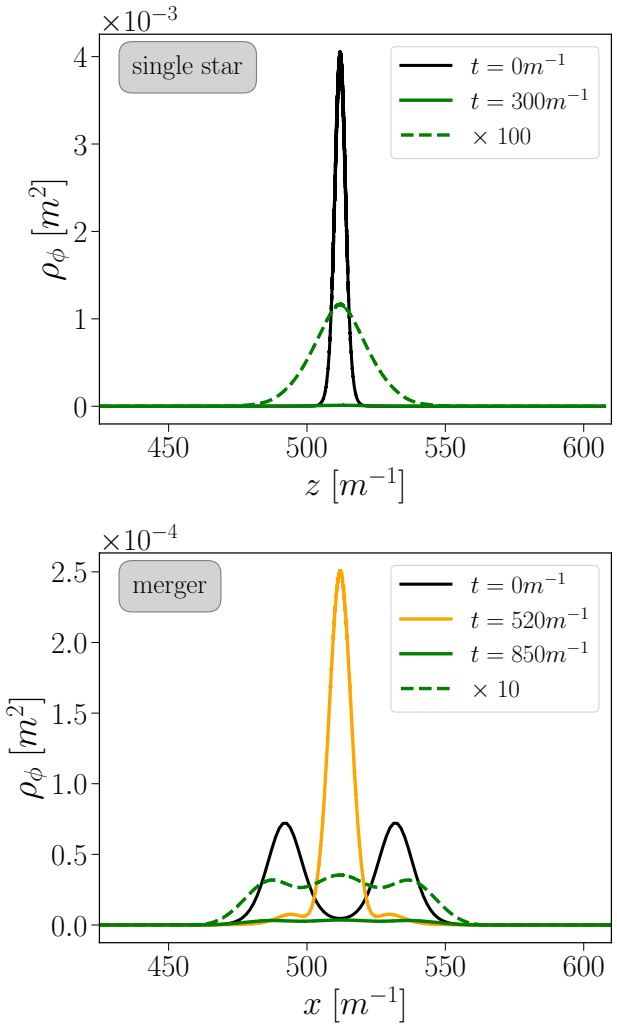

FIG. 9. Radial profiles of the scalar energy density ρ_ϕ of a single star decay (*top*) and the merger process (*bottom*). The original set up is shown in black (single star on the top and two stars on the bottom plot), and the remnant after the electromagnetic decay has happened, in green. The dashed green line is a magnification of the remnant energy density, to demonstrate its energy distribution, which indeed has a larger radius and broader shape than the corresponding original star, as the star has diluted in the parametric resonance process. The magnification factors are 100 and 10, for the single and merged stars, respectively. The merged star created trough the collision of the two sigle stars in the bottom plot, which subsequently decays through parametric resonance, is shown in orange. We note that these radial profiles have been taken through the center of the simulation box, with the other two coordinates at $512m^{-1}$, and we have chosen the x-axis for the merger process, as the stars are originally aligned along x.

Appendix B: Convergence testing

1. General convergence

We demonstrate the convergence of our simulation by monitoring the ratio of the difference in the scalar field ϕ value between the high and medium, and the medium and low resolution runs, summing over a stencil of 7 points, centered at the middle of our simulation box. The box had a size $L = 1024m^{-1}$ and a maximum of 7 refinement levels. The number of coarse grid points used for each resolution was $N^3 = 256^3$, $N^3 = 384^3$, and $N^3 = 512^3$ (from lower to higher resolution). The region of convergence, defined by the ratio being below 1, is demonstrated by the grey area in Fig. 10, alongside the ratio values (shown with the black solid line), as a function of time.

We note that there is a peak at around $t \sim 400m^{-1}$ which does not fall in the region of convergence. This is due to the regridding forced on the simulation by the gravitational wave extraction tool. Our numerical relativity code GRChombo includes an adaptive mesh refinement system that automatically adds refinement levels in specific regions of the simulation box, based on set

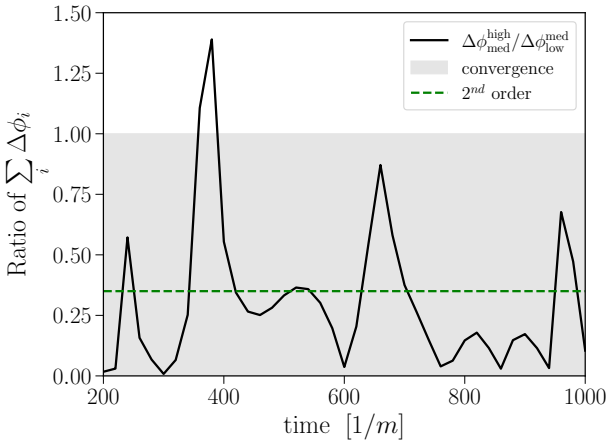

FIG. 10. Convergence testing using a stencil of 7 points centered in the middle of the simulation box. We plot the ratio of the difference in the scalar field ϕ value between the high and medium, and the medium and low resolution runs, summing over the stencil. Hence, all data points within the grey region indicate convergence. The simulation box size is $L = 1024m^{-1}$, and low, medium, and high resolution runs have $N^3 = 256^3$, $N^3 = 384^3$, and $N^3 = 512^3$ number of coarse grid points, respectively.

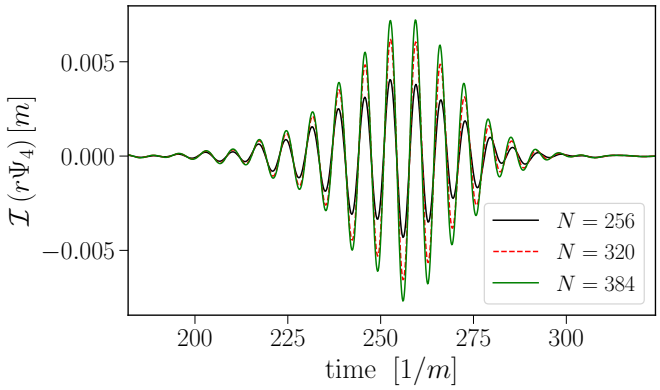

FIG. 11. Convergence testing of the gravitational wave waveform for the decay of a single star. The number of coarse grid points used for each resolution is shown in the legend. Convergence can be seen by eye as the higher resolutions (in green and red dashed) are closer together than the lower ones (red dashed and black). The waveforms were extracted at refinement level 2 at $r = 80m^{-1}$.

conditions and threshold values. However, the extraction of gravitational waves at a set radius and refinement level overrides the original, smooth refinement process by forcing a specific refinement layer on the simulation at each time step. As the boundaries of each layer introduce numerical errors to the simulation, we postulate that it is this regridding process that is responsible for the peak in our convergence plot. This was shown by running the same simulation without GW extraction, in which case the peak at around $t \sim 400m^{-1}$ disappeared. Moreover, the differences in the ϕ value as shown in Fig. 10 get smaller as the simulation progresses, which is consistent with convergence.

2. Gravitational wave convergence

In addition to testing the convergence of the bulk simulation, as explained above, we monitored the convergence of the gravitational wave waveforms, which is demonstrated in Fig. 11. The figure shows the imaginary part of the $l = 2, m = 0$ mode of the Weyl scalar, but we note that the real part followed a similar pattern. Convergence can be clearly seen by eye, as the difference between the high and medium resolution waveforms is smaller than that between the medium and the low resolutions.

Here we demonstrate the convergence for the GW signal from the decay of a single, stable star of mass $M_s = 0.60m^2_{\rm Pl}/m$. The merger GW signal (shown in Fig. 6) had better convergence. While Fig. 11 shows the signal from the decay of a single (non-excited) star, we also confirmed the convergence for the full combined merger and decay process. Due to the high frequency of the gravitational wave waveform of the decay, it was challenging to keep track of it, and indeed we found linear drift in the waveforms between different resolution runs for the decay after merger, corresponding to 3-4 wavelengths in time. However, the frequencies of the different resolution waveforms matched. Overall, despite the simulation and gravitational waveforms converging, we found some variation in the waveform amplitudes.

3. Regridding

In order to extract an overall clean waveform, we had to tune our regridding for the merger and the decay signal separately, using our adaptive mesh refinement code. The goal of regridding is to add higher resolution meshes in the simulation box areas where the interesting physics, and hence the need for higher resolution, is happening. For our simulations, this means that the star is resolved with a higher resolution grid than the empty space around it. (However, as mentioned above, the extraction of gravitational waves away from the star, closer to the boundaries of the box, means we also force a higher resolution at the extraction radius). In practice, this tuning of the regridding means that we had to change the threshold values for the variables with respect to which the refinement is happening (in our case, the scalar field ϕ and the conformal factor χ).

To get the full signal as shown in Fig. 6, we had to decrease the thresholds between the merger and the decay signal. The merger signal exhibited some numerical noise that was reduced with lesser regridding, while the

high oscillation frequency of the decay signal required more regridding and higher extraction levels. The decrease in the regridding thresholds (hence, more frequent regridding), moving from the merger to the decay, was 18% and 23%, for ϕ and χ, respectively. This regridding change had no effect on the overall evolution of the system, and demonstrates the difficulty of gravitational wave extraction from our oscillating scalar star.

Finally, we note that we found some linear drift in time in the energy fluxes and gravitational wave signals from the simulation due to this change of regridding in the middle of the run (between the merger and the decay of the merged star). Hence, the gravitational signal in Fig. 8 has been corrected to match the electromagnetic one, as we confirmed by running the simulation from the middle that those two indeed line up (our full GW signal displayed in Fig. 6 has the regridding change in the middle, as explained above).

Appendix C: Gravitational luminosity

The gravitational wave power (luminosity) was calculated according to the well-known equation (see e.g. [62] for similar use):

$$\frac{dE}{dt} = \lim_{r\to\infty} \frac{1}{16\pi} \sum_{l,m} \left| \int_{t_0}^{t} r\Psi_4^{lm} dt' \right|^2 , \qquad \text{(C1)}$$

where we used the modes up to $l = 6$ for the decay signal of the star and $l = 2$ for the merger signal of the star. To deal with the numerical error causing a cumulative drift in the total gravitational energy of the system, the integral of $r\Psi_4^{lm}$ was processed with a Butterworth high-pass filter (5th order), as the numerical error introduces low-frequency modes.

arXiv:2403.03723v1 [astro-ph.CO] 6 Mar 2024

LISA
CosWG-24-01

Prepared for submission to JHEP CERN-TH-2024-029

Gravitational waves from first-order phase transitions in LISA: reconstruction pipeline and physics interpretation

Chiara Caprini,[a,b] **Ryusuke Jinno,**[c] **Marek Lewicki,**[d,1] **Eric Madge,**[e,2] **Marco Merchand,**[f,g] **Germano Nardini,**[h,3] **Mauro Pieroni,**[b,4] **Alberto Roper Pol,**[a] **Ville Vaskonen**[i,j,k]

(For the LISA Cosmology Working Group)

[a] *Département de Physique Théorique and Center for Astroparticle Physics, Université de Genève, Quai E. Ansermet 24, CH-1211 Geneve 4, Switzerland*

[b] *Theoretical Physics Department, CERN, 1211 Geneva 23, Switzerland*

[c] *Research Center for the Early Universe (RESCEU), University of Tokyo, Hongo 7-3-1, Bunkyo-ku, Tokyo 113-003, Japan*

[d] *Faculty of Physics, University of Warsaw, ul. Pasteura 5, 02-093 Warsaw, Poland*

[e] *Department of Particle Physics and Astrophysics, Weizmann Institute of Science, Herzl Street 234, Rehovot, 7610001, Israel*

[f] *KTH Royal Institute of Technology, Department of Physics, SE-10691 Stockholm, Sweden*

[g] *The Oskar Klein Centre for Cosmoparticle Physics, AlbaNova University Centre, SE-10691 Stockholm, Sweden*

[h] *Department of Mathematics and Physics, University of Stavanger, NO-4036 Stavanger, Norway*

[i] *Dipartimento di Fisica e Astronomia, Università degli Studi di Padova, Via Marzolo 8, 35131 Padova, Italy*

[j] *Istituto Nazionale di Fisica Nucleare, Sezione di Padova, Via Marzolo 8, 35131 Padova, Italy*

[k] *Keemilise ja bioloogilise füüsika instituut, Rävala pst. 10, 10143 Tallinn, Estonia*

E-mail: chiara.caprini@unige.ch, ryusuke.jinno@resceu.s.u-tokyo.ac.jp, marek.lewicki@fuw.edu.pl, eric.madge-pimentel@weizmann.ac.il, marcomm@kth.se, germano.nardini@uis.no, mauro.pieroni@cern.ch, alberto.roperpol@unige.ch, ville.vaskonen@pd.infn.it

[1] Project coordinator: marek.lewicki@fuw.edu.pl
[2] Corresponding author: eric.madge-pimentel@weizmann.ac.il
[3] Project coordinator: germano.nardini@uis.no
[4] Corresponding author: mauro.pieroni@cern.ch

Abstract: We develop a tool for the analysis of stochastic gravitational wave backgrounds from cosmological first-order phase transitions with LISA: we initiate a template databank for these signals, prototype their searches, and forecast their reconstruction. The templates encompass the gravitational wave signals sourced by bubble collisions, sound waves and turbulence. Accounting for Galactic and extra-Galactic foregrounds, we forecast the region of the parameter space that LISA will reconstruct with better than $\sim 10\,\%$ accuracy, if certain experimental and theoretical uncertainties are solved by the time LISA flies. We illustrate the accuracy with which LISA can reconstruct the parameters on a few benchmark signals, both in terms of the template parameters and the phase transition ones. To show the impact of the forecasts on physics beyond the Standard Model, we map the reconstructed benchmark measurements into the parameter spaces of the singlet extension of the Standard Model and of the classically conformal invariant $U(1)_{B-L}$ model.

Contents

1 Introduction **2**

2 SGWB templates for first-order phase transitions **4**
2.1 Template I: broken power law for bubble collisions and highly relativistic fluid shells 5
2.2 Template II: double broken power law 7
2.2.1 Sound waves 7
2.2.2 Magnetohydrodynamic turbulence 10

3 Parameter reach and reconstruction **13**
3.1 LISA measurement channels 13
3.2 Data in each channel 14
3.3 Injected (and reconstructed) noises and signals 15
3.4 Data generation and analysis 17

4 Reconstruction of the geometric parameters **19**
4.1 Broken power law 19
4.2 Double broken power law 22
4.3 Synergy with other gravitational wave observatories 23

5 Reconstruction of the thermodynamic parameters **25**

6 Interpretation in terms fundamental particle physics models **33**
6.1 Gauge singlet extension with $\mathbb{Z}_2$ symmetry 34
6.2 Classically conformal U$(1)_{B-L}$ model 36

7 Conclusions **39**

1 Introduction

Cosmology and astrophysics are currently at the dawn of a new golden age thanks to the discovery of gravitational waves (GWs), which started with the first direct detections by the LIGO/Virgo/KAGRA (KAGRA) collaboration [1–9] of GWs emitted by black hole and neutron star mergers in the late Universe. Recently, Pulsar Timing Array (PTA) collaborations have presented strong evidence for the presence of a stochastic GW background (GW) at nano-Hertz frequencies [10–13]. The front-runner candidate for the source of this signal is associated with binaries of supermassive black holes, colliding relatively recently in cosmological terms [14–16], and interacting with their environment. However, at this stage, it is also possible that this signal is of primordial origin [15, 17–20]. The first detection of an SGWB gives hope that future GW observations will allow us to probe high-energy processes taking place in the early Universe.

Among the many candidates of primordial GW sources [21, 22], our analysis focuses on first-order phase transitions (PTs) in the early Universe. These are expected when a new minimum emerges in the effective potential of the theory as the Universe cools and thermal corrections to the potential diminish. If the PT is of first order, the new vacuum and the initial one are separated by a barrier that the scalar field will eventually cross through bubble nucleation. After nucleation, the bubbles grow due to the latent heat released from the difference between the true and the false vacua and eventually collide, filling the whole volume with the new phase. An SGWB is expected to be sourced by the anisotropic stresses due to the collisions of bubbles and highly relativistic fluid shells in very strong transitions [23–31], as well as the subsequent development of bulk fluid motion [32–34]. The latter initially takes the form of sound waves [35–41], but can also lead to the development of magnetohydrodynamic (MHD) turbulence [42–54]. Depending on the underlying PT model and the consequent bubble and plasma dynamics, any of these GW sourcing mechanisms may dominate the SGWB production, and we therefore include all of them in our analysis. Turbulence has often been neglected in previous analyses for two reasons: because it was considered subdominant, and because of the absence of a simulation-validated template for the GW signal [34]. However, it is now clear that the non-observation of turbulence in simulations of weakly first-order PTs does not imply that it is never formed or always subdominant, in particular, if the lifetime of the sound waves is shorter than one Hubble time [34, 55–57]. Furthermore, a simulation-validated template has been developed for the SGWB produced by fully developed turbulence [52, 54], which we will use in the following.

Our focus will be on the Laser Interferometer Space Antenna (LISA) mission [58], aimed at probing the currently unexplored GW frequency band around the milli-Hertz. In terms of cosmology, this band is associated with energies in the early Universe around the electroweak scale [22]. Many extensions of the Standard Model (SM) predict the electroweak PT to be of first order, which is a strong motivation to look for associated GW signals in LISA [33, 34]. In this work, we pursue two main goals. First, we select a set of templates for GW sourcing processes associated with first-order PTs, in order to initiate a template repository for the pipeline of SGWB searches that we have developed. We stress that some underlying assumptions and approximations still affect these templates. While

they cannot be considered as carved into stone, we are confident that they represent the best available choices combining simplicity and accuracy, given the state of the art in the field. Second, we implement these templates in the `SGWBinner` code [59, 60], and use them to produce forecasts of the sensitivity of LISA to SGWBs from first order PTs, studying in particular its impact on the reconstruction of the parameters of two examples of particle physics models underlying the transition.

With respect to previous works focused on the case of GW production by sound waves [61–64], we add parameter estimation also for the GW signals from bubble collisions and (MHD) turbulence. We assess the LISA sensitivity in terms of two different sets of parameters: in terms of thermodynamic parameters (cf. Sec. 5), such as the kinetic energy fraction, the temperature, and the duration of the transition, as well as in terms of geometric parameters (cf. Sec. 4), such as the frequency breaks and the amplitude of the SGWB and provide a mapping between the two sets. Compared to previous analyses [61–64], we go one step further in the process and translate the estimation of the SGWB template parameters into constraints on the parameter space of two specific particle physics models (cf. Sec. 6). Concerning the SGWB from sound waves, we adopt a somewhat simpler template than in Refs. [61–64], based on the results of Ref. [41]. The main features of the SGWB spectrum (spectral shape and position of the spectral breaks) are consistent with the results developed in Refs. [39, 61, 64]. However, the spectral slopes of the SGWB are taken from Ref. [41]. These are compatible with the recent results of Refs. [57, 65] (see also Ref. [54]). Note that the spectral shape of the SGWB sourced by sound waves in the context of the sound shell model [39, 66] is still a subject of active study [57, 65].

The LISA mission has recently been adopted by the European Space Agency (ESA) and its construction will start soon for a launch scheduled in the 2030s. Our results serve as a starting point for the main task ahead of the community in preparation of the experiment, which is the development of the pipelines for the data analysis and the physics interpretation. We make some simplifying assumptions in our analyses of the forecasts. We neglect the theoretical uncertainties associated with the computation of the transition parameters and the resulting GW signal in a given model [67–70]. However, this is an active research topic [71–78] and we assume significant progress will be made towards reducing this issue by the time the data becomes available. Another kind of theoretical uncertainty that we neglect are general relativity effects, important especially when the average bubble size is comparable in size to the Hubble scale [79]. Their exact effect on the SGWB spectra is still uncertain. Furthermore, we adopt a simple two-parameter noise model to predict the performance of the mission. While it is simplistic to assume that one can directly apply a pre-flight validated instrument noise model in a realistic search for the SGWB in real data, the development of methodologies to incorporate noise uncertainties in SGWB searches is a subject of ongoing study [80–82]. We plan to update our predictions as more realistic noise estimates, as well as methods of coincident noise and SGWB estimation, are produced by the LISA Consortium. We use simplified, template-based predictions for the astrophysical foregrounds. The impact of astrophysical foregrounds on the reach of LISA will very likely be significant [83–87]. Also in this aspect, we plan to improve our results in the future, when the methods for disentangling the primordial SGWB from the

astrophysical foregrounds improve further. We work on simulated data including only the SGWB, the foregrounds, and the instrument noise: therefore, we assume that the data stream can be perfectly cleaned from residuals due to the imperfect subtraction of the signals of other GWs sources. Finally, the data are also simulated adopting the very same templates for the noise, foregrounds and SGWB which we adopt in the reconstruction: hence, we also implicitly assume that any theoretical and experimental uncertainties are absent, and the models reproduce faithfully the reality of the signals and the noise.

This paper is organised as follows. In Sec. 2, we introduce the SGWB templates in terms of the "geometric parameters" such as the amplitude, characteristic frequencies, and spectral slopes, and specify how these depend on the "thermodynamic PT parameters" such as kinetic energy fraction in the plasma, the transition temperature and inverse timescale of the transition. Section 3 describes the `SGWBinner` code and the data analysis strategy. We then proceed with evaluating the parameter reconstruction for cosmological PTs in terms of different sets of parameters. In Sec. 4, we perform the SGWB spectrum reconstruction in terms of the geometric parameters. In Sec. 5, we address the reconstruction of the thermodynamic parameters related to the dynamics of the PT. Finally, Sec. 6 connects the PT parameters to two particular underlying particle physics models, reconstructing the "fundamental model parameters" such as masses and couplings. We conclude in Sec. 7.

2 SGWB templates for first-order phase transitions

Cosmological first-order PT generate GWs predominantly via three mechanisms: collisions of the vacuum bubble walls, sound waves in the primordial plasma, and turbulent motion. The corresponding SGWB spectra of the former can be modeled as a broken power law (BPL), whereas the latter two can be described in terms of double broken power laws (DBPLs). The respective amplitudes and frequency breaks depend on several parameters, which under some assumptions (to be clarified later for each source) can be related to the strength of the PT α, its inverse duration normalised to the Hubble rate β/H_*, the temperature T_* after the end of the transition, and the bubble wall velocity ξ_w [88]. Furthermore, the turbulence SGWB will also depend on the fraction of energy ε converted into turbulent motion in the PT.

The present-day frequencies and amplitudes are related to the quantities at the time of GW production (with subscript "*") via the relations

$$f = f_* \frac{a_*}{a_0} = H_{*,0} \frac{f_*}{H_*}\,, \qquad\qquad h^2\Omega = h^2 F_{\mathrm{GW},0}\,\Omega_*\,, \tag{2.1}$$

where $H_{*,0}$ is the Hubble rate at the time of GW production H_* redshifted to today,

$$H_{*,0} = \frac{a_*}{a_0} H_* \simeq 1.65\times 10^{-5}\,\mathrm{Hz}\,\left(\frac{g_*}{100}\right)^{\frac{1}{6}}\left(\frac{T_*}{100\,\mathrm{GeV}}\right), \tag{2.2}$$

and $F_{\mathrm{GW},0}$ is the red-shift factor for the fractional energy density,

$$h^2\,F_{\mathrm{GW},0} = h^2\left(\frac{a_*}{a_0}\right)^4\left(\frac{H_*}{H_0}\right)^2 \simeq 1.64\times 10^{-5}\left(\frac{100}{g_*}\right)^{1/3}, \tag{2.3}$$

with $H_0 = 100\,h$ km/s/Mpc. Here, g_* is the effective number of degrees of freedom at the end of the PT, which we assume to approximately be the same as the number of entropy degrees of freedom $g_* \approx g_{*s}$, as appropriate for $T_* > 0.1\,\mathrm{MeV}$ [89]. We will now proceed to describe the SGWB templates through both sets of geometric and thermodynamic parameters corresponding to the underlying sources, and refer to them as $\vec{\theta}_{\rm Cosmo}$ in each case.

2.1 Template I: broken power law for bubble collisions and highly relativistic fluid shells

Template I is a BPL that can be expressed as

$$\Omega_{\rm GW}^{\rm BPL}(f, \vec{\theta}_{\rm Cosmo}) = \Omega_b \left(\frac{f}{f_b}\right)^{n_1} \left[\frac{1}{2} + \frac{1}{2}\left(\frac{f}{f_b}\right)^{a_1}\right]^{\frac{n_2-n_1}{a_1}} , \tag{2.4}$$

where $\vec{\theta}_{\rm Cosmo} = \{\Omega_b, f_b\}$ is the set of free geometric parameters of the template, while n_1, n_2, and a_1 are geometric parameters fixed by the underlying modelling of the source, as described below. The amplitude is normalised such that $\Omega(f_b) = \Omega_b$. At $f \ll f_b$ the spectrum grows as f^{n_1}, and at $f \gg f_b$ it decreases (assuming $n_2 < 0$) as f^{n_2}. The parameter a_1 describes how broad is the transition around the spectral peak. Note that, in general, f_b does not coincide with the peak of the spectrum, located at $f_p = f_b\,(-n_1/n_2)^{1/a_1}$, and Ω_b does not correspond to the value of the spectrum at the peak (unless $n_1 = -n_2$), which is

$$\Omega_p = \Omega_b \left[\frac{1}{2}\left(-\frac{n_2}{n_1}\right)^{\frac{n_1}{n_1-n_2}} + \frac{1}{2}\left(-\frac{n_1}{n_2}\right)^{-\frac{n_2}{n_1-n_2}}\right]^{-\frac{n_1-n_2}{a_1}} . \tag{2.5}$$

Then, the SGWB spectrum can alternatively be expressed in terms of the spectral peak f_p and its value at the peak Ω_p,

$$\Omega_{\rm GW}^{\rm BPL}(f, \vec{\theta}_{\rm Cosmo}) = \Omega_p \frac{(n_1 - n_2)^{\frac{n_1-n_2}{a_1}}}{\left[-n_2\left(\frac{f}{f_p}\right)^{-\frac{n_1 a_1}{n_1-n_2}} + n_1\left(\frac{f}{f_p}\right)^{-\frac{n_2 a_1}{n_1-n_2}}\right]^{\frac{n_1-n_2}{a_1}}} . \tag{2.6}$$

While the functional form Eq. (2.6) is more commonly used in the literature [25, 30, 31, 90], in the following we will work with Eq. (2.4), which directly resembles the DBPL given in Eq. (2.8).

We use the BPL template, Eq. (2.4), for GW production in very strong PTs. These transitions are defined by the vacuum energy of the scalar field dominating over the radiation background, i.e. $\alpha \gg 1$. One possibility for the time evolution of the bubbles is that the walls interact sufficiently weakly with the surrounding plasma and thus most of the released vacuum energy goes to the bubble wall gradient and kinetic energies [91]. In such a transition, plasma motion can be neglected and the dominant source of GWs comes from the scalar field. The production of GWs in such a system was modelled with the envelope approximation [24, 92], in which the collided parts of the bubble walls are neglected in the thin wall limit, and further developed in, e.g. Refs. [25, 93, 94].

However, the collided part of the bubble walls has recently been found to be essential for a correct estimation of the SGWB spectrum, since in reality, the shells cannot lose their momentum instantaneously. Such a possibility has been pointed out in numerical simulations [26, 27, 95, 96] and from analogies with particle collisions [97]. While for maximally long-lived shells a modeling called bulk flow was proposed and has been studied numerically and analytically [90, 97], it is not obvious how the collided part decays in specific particle physics models. In this regard, we adopt a hybrid approach developed in Refs. [28, 30] for the time evolution of the collided walls and the resulting GW production. In these studies, time evolution of the momentum decay in the radial direction is embedded in multi-bubble nucleation and collision histories, allowing for the calculation of the SGWB spectrum in microphysics potentials that can realistically cause strongly supercooled PTs.

While the dominant energy carrier in the weak coupling limit is the scalar field, supercooled PTs can also proceed with relativistic detonations, in which the vacuum energy is dominantly transferred to highly relativistic fluid shells. In this energy transfer, particle splitting plays a key role [98–102]. As a result, the wall reaches a terminal velocity and the main energy carriers are the highly relativistic fluid shells surrounding the bubbles. The production of GWs for this case is expected to be qualitatively different from that of sound waves because, in the former case, the fluid shells become very thin and highly concentrated around the walls, and thus the macroscopic distribution of the energy-momentum tensor is expected to be rather similar to that of scalar walls [31, 32, 103]. In Ref. [31], the SGWB spectrum has been estimated by incorporating the radial time evolution of highly relativistic fluid shells. It was shown that the resulting SGWB spectrum is closer to the one found in the case of bubble wall collisions in models featuring the breaking of a gauge symmetry discussed in Ref. [30], which allows us to use the same SGWB template in both cases.

In this context, the peak amplitude and frequency at the present time are related to the parameters α, β/H_*, and T_* via

$$h^2\Omega_p = h^2 F_{\mathrm{GW},0}\, A_{\mathrm{str}}\, \tilde{K}^2 \left(\frac{H_*}{\beta}\right)^2 , \quad f_p \simeq 0.11\, H_{*,0}\, \frac{\beta}{H_*} , \tag{2.7}$$

where $\tilde{K} \equiv \alpha/(1+\alpha)$ is the fractional energy density of the GW source. The spectrum was computed assuming a very strong transition with $\alpha \gg 1$, corresponding to $\tilde{K} \approx 1$. However, we leave $\tilde{K}$ as a free parameter in the reconstruction (cf. Sec. 5) to take into account non-standard scenarios such as a PT taking part in a dark sector whose energy density is only a fraction of the total [104, 105]. We will focus on the most generic case of either gauged scalar field bubble collisions or highly relativistic fluid shells sourcing the SGWB. In this case, the numerical simulations of Ref. [31] indicate $A_{\mathrm{str}} \simeq 0.05$, and the 0.11 factor in f_p of Eq. (2.7). The corresponding parameters in Eq. (2.4) are found to be $n_1 = -n_2 \simeq 2.4$ and $a_1 \simeq 1.2$ [31]. In this case, $f_b = f_p$ and $\Omega_b = \Omega_p$. Note that at scales larger than the horizon scale at the time of the transition, the SGWB spectrum would be expected to scale as f^3 because the source is uncorrelated [106]. We do not directly include this effect because the spectra we use were computed with simulations that do not take into account the expansion and the exact impact is uncertain [31]. For convenience, Tab. 1

GW source	power law template	n_1	n_2	n_3	a_1	a_2
strong PT, Sec. 2.1	BPL, Eq. (2.4)	2.4	-2.4	—	1.2	—
sound waves, Sec. 2.2.1	DBPL, Eq. (2.8)	3	1	-3	2	4
turbulence, Sec. 2.2.2	DBPL, Eq. (2.8)	3	1	$-8/3$	4	2.15

Table 1: Spectral slopes of the BPL and DBPL templates used for the respective GW sources from PTs.

summarizes the spectral slopes used in this work for the respective contribution to the SGWB spectrum. The geometric free parameters $\{f_b, \Omega_b\}$ can be expressed through the thermodynamic free parameters $\vec{\theta}_{\rm Cosmo} = \{\tilde{K}, \beta/H_*, T_*\}$ via Eq. (2.7). The dependence of the spectrum on $\tilde{K}$, β/H_*, and T_* is illustrated in Fig. 1a.

2.2 Template II: double broken power law

Template II is a DBPL which takes the form

$$\Omega_{\rm GW}^{\rm DBPL}(f, \vec{\theta}_{\rm Cosmo}) = \Omega_{\rm int} \times S(f) = \Omega_2 \times S_2(f), \tag{2.8}$$
$$S(f) = N \left(\frac{f}{f_1}\right)^{n_1} \left[1 + \left(\frac{f}{f_1}\right)^{a_1}\right]^{\frac{-n_1+n_2}{a_1}} \left[1 + \left(\frac{f}{f_2}\right)^{a_2}\right]^{\frac{-n_2+n_3}{a_2}},$$

where the SGWB spectrum is decomposed into the amplitude $\Omega_{\rm int}$, corresponding to the value of the spectrum logarithmically integrated over the frequency, and the shape function $S(f)$. The spectrum behaves as $\Omega_{\rm GW}^{\rm DBPL} \propto f^{n_1}$ $(f < f_1)$, f^{n_2} $(f_1 < f < f_2)$, and f^{n_3} $(f_2 < f)$ from low to high frequencies. The parameters a_1 and a_2 describe how smoothly the power law behavior changes at $f \sim f_1$ and $f \sim f_2$, respectively. In principle, the normalization factor N is determined from $\int_{-\infty}^{\infty} {\rm d} \ln f \, S(f) = 1$. However, as we cannot write an analytical expression for N for arbitrary slopes and frequency breaks, we normalise the spectrum so that $S_2(f_2) = 1$, i.e. $S_2(f) = S(f)/S(f_2)$, and use the amplitude Ω_2 at the second frequency break instead of the integrated amplitude $\Omega_{\rm int}$. Thus, $\vec{\theta}_{\rm Cosmo} = \{\Omega_2, f_1, f_2\}$ is the set of free geometric parameters of this template, while n_1, n_2, n_3, a_1, and a_2 are parameters fixed by the underlying modelling of the source.

2.2.1 Sound waves

If the coupling between the bubble walls and plasma particles is large enough, the latent heat is transferred also to the bulk motion of the fluid. While the fluid motion in general has both compression and shear components, the former dominates the latter at the initial stage of the transition because of the initial condition set by expanding spherical bubbles. After bubbles collide, compression waves propagate acting as a source of GWs. This behavior is found in numerical simulations [35–38], and the sound shell model [39, 66] is proposed to explain it. The results show that both the sound shell thickness and the bubble size at the collision time are imprinted on the SGWB spectrum. At later times, vortical motion of the fluid can be produced by, for example, the non-linearities of the fluid or the presence of

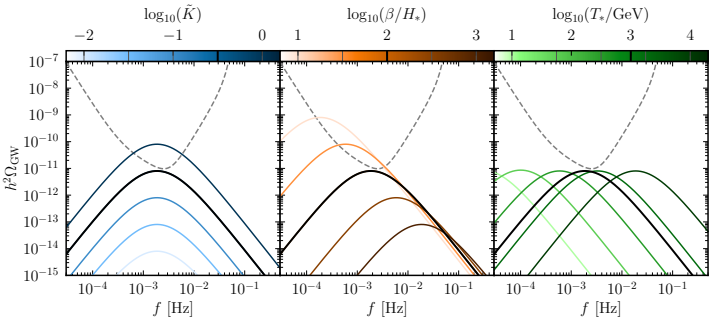

(a) bubble collisions and highly relativistic fluid shells (black: $\tilde{K} = 0.32$, $\beta/H_* = 100$, $T_* = 1\,\mathrm{TeV}$)

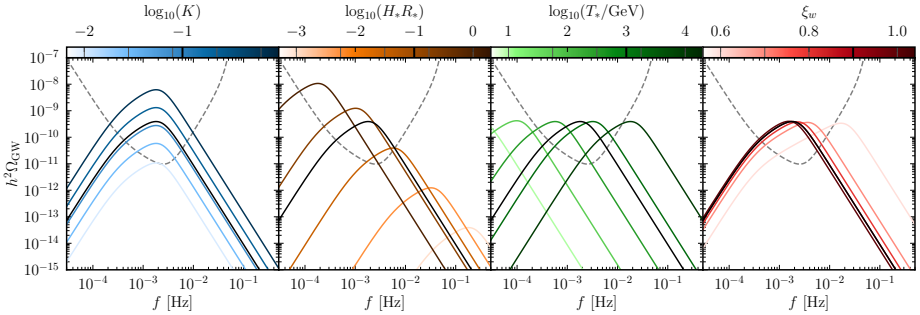

(b) sound waves (black: $K = 0.1$, $H_*R_* = 0.1$, $\xi_w = 0.9$, $T_* = 1\,\mathrm{TeV}$)

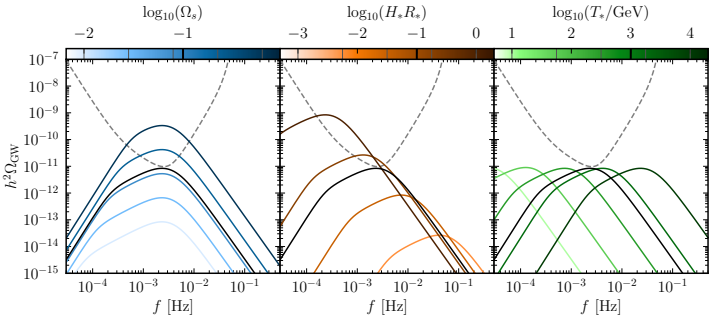

(c) turbulence (black: $\Omega_s = 0.1$, $H_*R_* = 0.1$, $T_* = 1\,\mathrm{TeV}$)

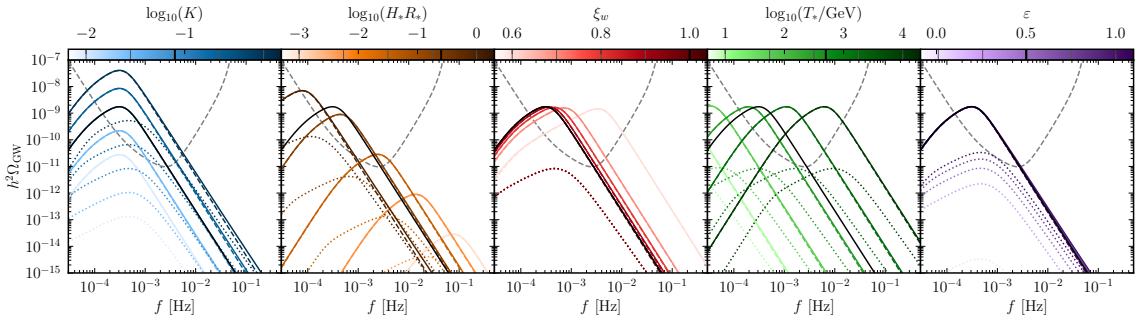

(d) sound waves + turbulence (black: $K = 0.08$, $H_*R_* = 0.25$, $\xi_w = 1$, $T_* = 500\,\mathrm{GeV}$, $\varepsilon = 0.5$)

Figure 1: The coloured lines show the parameter dependence of the SGWB templates for PTs in terms of the thermodynamic parameters, varying one parameter at a time. The remaining parameters are fixed to the benchmark values indicated in the subcaptions, corresponding to the black spectrum in each plot. From top to bottom we show bubble collisions, sound waves, turbulence, and sound waves + turbulence. For the latter, the spectra of the sound waves and turbulence contributions are shown as dashed and dotted lines, respectively. The dashed gray line is the LISA noise curve.

primordial magnetic fields. In this case, MHD turbulence would develop in the primordial plasma. This additional source of GWs is presented in the next subsection.

The aforementioned simulations solve the system of the fluid variables and the scalar field on a lattice, coupling both sectors via a phenomenological friction parameter. On the other hand, taking into account the large hierarchy between the scale of bubbles of cosmological size (with a sizable fraction of the Hubble radius) and that of the Higgs field, which varies within the bubble thickness (of the electroweak scale or higher), the effects of the Higgs field can be considered local to the bubble. Therefore, one can integrate out the dynamics of the Higgs field and treat the expansion of the true vacuum as a space- and time-dependent background, thus removing numerical difficulties associated with resolving the scalar field in the fluid dynamics, which can then be solved separately. Such a "Higgsless" approach has been pursued in Refs. [40, 41]. In these studies, shock waves in the plasma are also resolved with an appropriate numerical scheme [107] and are accurately incorporated into the simulation.

The SGWB spectrum from sound waves is well described by the DBPL of Eq. (2.8) that encodes the typical fluid shell thickness and the bubble size. In particular, the frequency breaks are found to be [41, 108]

$$f_1 \simeq 0.2\, H_{*,0}\, (H_* R_*)^{-1}\,, \qquad\qquad f_2 \simeq 0.5\, H_{*,0}\, \Delta_w^{-1}\, (H_* R_*)^{-1}\,, \tag{2.9}$$

where $\Delta_w = \xi_{\rm shell}/\max(\xi_w, c_s)$, with $\xi_{\rm shell}$ being the dimensionless sound shell thickness and c_s the speed of sound. $H_{*,0}$ is given in Eq. (2.2). For the integrated amplitude $\Omega_{\rm int}$, the parametric dependence is [41, 108]

$$h^2 \Omega_{\rm int} = h^2 F_{\rm GW,0}\, A_{\rm sw}\, K^2\, (H_* \tau_{\rm sw})\, (H_* R_*)\,, \tag{2.10}$$

where $F_{\rm GW,0}$ is given in Eq. (2.3). Here, $\tau_{\rm sw}$ is the duration of the sound wave source and R_* the average bubbles size, estimated as [34]

$$H_* R_* = (8\pi)^{1/3} \max(\xi_w, c_s)\, \frac{H_*}{\beta}\,. \tag{2.11}$$

The constant $A_{\rm sw} \simeq 0.11$ in Eq. (2.10) is computed from the average over the simulation data points with different values of α and ξ_w [41, 108]. The kinetic energy fraction is $K \simeq 0.6\, \kappa\, \alpha/(1+\alpha)$, where κ denotes the kinetic energy fraction of a single expanding bubble, derived in Ref. [88] for a perfect fluid with an ultra-relativistic equation of state, and with speed of sound $c_s^2 = 1/3$ (see Refs. [109, 110] for a generalization). The factor 0.6 accounts for the efficiency in producing kinetic energy in the bulk fluid motion with respect to the single bubble case, as found in Refs. [41, 108]. It constitutes a conservative estimate with respect to what was assumed, e.g. in Ref. [34].

The dependence of the other parameters entering the sound waves SGWB spectrum in Eqs. (2.9) and (2.10) is as follows. The dimensionless shell thickness is calculated from the profile of an expanding bubble as $\xi_{\rm shell} = \xi_{\rm front} - \xi_{\rm rear} = |\xi_w - c_s|$, where the last equality holds for subsonic deflagrations and detonations, the latter being the cases we focus on in this work, as we set ξ_w close to unity. The relative duration of the GW source,

$H_*\tau_{\rm sw} = \min\left[H_*\tau_{\rm sh}, 1\right]$, corresponds either to the estimated decay time into turbulence, $H_*\tau_{\rm sh} = H_*R_*/\sqrt{\bar{v}_f^2}$, if the latter is shorter than the Hubble time [34]; or to the Hubble time itself. The first case is expected for relatively strong transitions corresponding to large bulk fluid velocities [56]. Note that we will nevertheless adopt the average fluid velocity expression $\bar{v}_f^2 = \Gamma^{-1}\,K$ valid in the subrelativistic bulk velocity limit, where $\Gamma = \bar{w}/\bar{e}$ is the mean adiabatic index, which is $\Gamma = 4/3$ for a radiation fluid [34]. In the second case, i.e. when the sound source duration is comparable to the Hubble time, the scaling of the SGWB spectral amplitude becomes $\Omega_{\rm int} \propto (H_*R_*) \propto (H_*/\beta)$, in contrast to $\Omega_p \propto (H_*/\beta)^2$ for bubble collisions, indicating that the sourcing lasts longer for sound waves.

For the exponents we use the result of Ref. [41] and take $n_1 = 3$, $n_2 = 1$, $n_3 = -3$, $a_1 = 2$, and $a_2 = 4$, cf. Tab. 1. The amplitude at f_2 is then related to the integrated amplitude, Eq. (2.10), via

$$\Omega_2 = \frac{1}{\pi}\left(\sqrt{2} + \frac{2\,f_2/f_1}{1 + f_2^2/f_1^2}\right)\Omega_{\rm int} \approx 0.55\,\Omega_{\rm int}\,, \tag{2.12}$$

where the approximate sign holds for $\xi_w \approx 1$. The SGWB spectrum is then completely fixed once the thermodynamic free parameters $\vec{\theta}_{\rm Cosmo} = \{K, H_*R_*, \xi_w, T_*\}$ are set. The dependence of the SGWB spectrum on the input parameters K, H_*R_*, ξ_w, and T_* is illustrated in Fig. 1b.

2.2.2 Magnetohydrodynamic turbulence

The source of GWs from MHD turbulence is a combination of the anisotropic stresses produced by velocity and magnetic fields. Following Ref. [34], we insert an unknown parameter ε to represent the fraction of overall kinetic energy in bulk motion that is converted to MHD turbulence. We define the parameter

$$\Omega_s = \Omega_{\rm kin} + \Omega_{\rm mag} = \varepsilon K\,, \tag{2.13}$$

representing the total energy density fraction in the GW source from turbulence, where $\Omega_{\rm mag}$ and $\Omega_{\rm kin}$ are the corresponding magnetic (mag) and kinetic (kin) energy density fractions. Furthermore, we assume that the turbulence is fully developed at the beginning of the sourcing process and that equipartition between the turbulent kinetic and magnetic energies is reached [111], $\Omega_{\rm mag} \approx \Omega_{\rm kin}$, so that

$$\bar{v}_f^2 \approx \bar{v}_{\rm A}^2 \approx \Gamma^{-1}\varepsilon\,K = \frac{3}{4}\,\Omega_s\,, \tag{2.14}$$

where $\bar{v}_f$ is the characteristic fluid velocity and $\bar{v}_{\rm A}$ is the Alfvén speed, both approximated in the subrelativistic limit. The turbulence SGWB spectral peak is located at the energy injection scale, which we assume to be the bubbles separation at the end of the PT, R_* [46]. The characteristic length scale of the MHD turbulence relative to the Hubble scale at the moment of the GW sourcing determines the frequency at which the SGWB spectrum peaks, $f_p \simeq 1.4\,H_{*,0}\,(H_*R_*)^{-1}$ [52, 54], where $H_{*,0}$ and H_*R_* are given by Eqs. (2.2) and (2.11), respectively. Another important parameter in the model is the duration of the GW source, which can be inferred from MHD simulations and is of the order of a few eddy turnover

times, $\mathcal{N}\tau_{\rm e} = \mathcal{N}R_*/[2\pi \max(\bar{v}_f, \bar{v}_{\rm A})] \simeq \mathcal{N}R_*/(2\pi\bar{v}_{\rm A})$, with $\mathcal{N} \simeq 2$ [52, 54] (note that the definition of $\tau_{\rm e}$ differs from the one in Ref. [54] by a factor $1/2\pi$).

The SGWB from MHD turbulence can be written as [52, 54]

$$\Omega_{\rm GW}^{\rm MHD}(f, \vec{\theta}_{\rm Cosmo}) = 3\,\mathcal{A}\,\Omega_s^2\,F_{\rm GW}\,(H_*R_*)^3\,(f/H_{*,0})^3\,p_{\tilde{\Pi}}(f, H_*R_*)\,\mathcal{T}(f, \mathcal{N}H_*\tau_{\rm e}), \tag{2.15}$$

where the amplitude is[1] $\mathcal{A} \simeq 0.085$, the spectrum of the anisotropic stresses can be approximated as [54]

$$p_{\tilde{\Pi}}(f, H_*R_*) = \left[1 + \left(\frac{f}{f_2}\right)^{a_2}\right]^{-\frac{11}{3a_2}}, \quad \text{with} \quad f_2 \simeq 2.2\,\frac{H_{*,0}}{H_*R_*} \quad \text{and} \quad a_2 \simeq 2.15, \tag{2.16}$$

and the function $\mathcal{T}$ is [52, 54]

$$\mathcal{T}(f, \mathcal{N}H_*\tau_{\rm e}) = \begin{cases} \ln^2\left[1 + \mathcal{N}H_*\tau_{\rm e}\right], & \text{if } \ 2\pi f/H_{*,0} \leq (\mathcal{N}H_*\tau_{\rm e})^{-1}, \\ \ln^2\left[1 + H_{*,0}/(2\pi f)\right], & \text{if } \ 2\pi f/H_{*,0} > (\mathcal{N}H_*\tau_{\rm e})^{-1}. \end{cases} \tag{2.17}$$

The function $\mathcal{T}$ can be approximated to a BPL as

$$\mathcal{T}(f, \mathcal{N}H_*\tau_{\rm e}) = \left(\frac{H_{*,0}}{2\pi f_1}\right)^2 \left[1 + \left(\frac{f}{f_1}\right)^{a_1}\right]^{-\frac{2}{a_1}}, \tag{2.18}$$

where the position of the break f_1 and the smoothness parameter a_1, shown in Fig. 2, depend on the eddy turnover time,

$$f_1(\mathcal{N}\tau_{\rm e}) = \frac{H_{*,0}}{2\pi}\ln^{-1}\left(1 + \mathcal{N}H_*\tau_{\rm e}\right) \approx \frac{H_{*,0}}{2\pi\mathcal{N}H_*\tau_{\rm e}} = \frac{\bar{v}_{\rm A}}{\mathcal{N}}\,\frac{H_{*,0}}{H_*R_*}. \tag{2.19}$$

In the above equation, we have assumed that $\mathcal{N}H_*\tau_{\rm e} = \mathcal{N}H_*R_*/(2\pi\bar{v}_{\rm A}) \ll 1$: this holds in general whenever the MHD turbulence SGWB is large enough to be observable, i.e. in the regime where $\bar{v}_{\rm A} \sim \sqrt{\Omega_s}$ is large, meaning that the PT is strongly first order (large α). In this limit, the parameter a_1, can be approximated as a constant, $a_1 = 4$, for $\mathcal{N}H_*\tau_{\rm e} \lesssim 0.3$ (or, equivalently, for $H_*R_* \lesssim \bar{v}_{\rm A}$ since $\mathcal{N} \simeq 2$).

The resulting MHD turbulence SGWB can be expressed in terms of the DBPL model of Eq. (2.8) setting $n_1 = 3$, $n_2 = 1$, $n_3 = -8/3$, $a_1 = 4$, and $a_2 \simeq 2.15$,

$$\begin{aligned}\Omega_{\rm GW}^{\rm MHD}(f, \vec{\theta}_{\rm Cosmo}) = \frac{3\,\mathcal{A}\,\bar{v}_{\rm A}\,\Omega_s^2\,(H_*R_*)^2}{4\pi^2\mathcal{N}}\,F_{\rm GW,0} \\ \times\left(\frac{f}{f_1}\right)^3\left[1 + \left(\frac{f}{f_1}\right)^{a_1}\right]^{-\frac{2}{a_1}}\left[1 + \left(\frac{f}{f_2}\right)^{a_2}\right]^{-\frac{11}{3a_2}}.\end{aligned} \tag{2.20}$$

Note that expressed in this form, the amplitude of the SGWB seems to be proportional to $\bar{v}_{\rm A}\Omega_s^2 \sim \Omega_s^{\frac{5}{2}}$. This is actually not the case, because f_1 is a function of $\bar{v}_{\rm A}$. We find from Eqs. (2.16) and (2.19) that the ratio between the frequency breaks is

$$\frac{f_2}{f_1} = \frac{2.2\,\mathcal{N}}{\bar{v}_{\rm A}} \simeq \frac{2.5\,\mathcal{N}}{\sqrt{\Omega_s}} \gg 1. \tag{2.21}$$

[1] For simplicity and to take into account the average of the SGWB spectrum over oscillations in time, the parameter $\mathcal{A}$ here corresponds to $\mathcal{C}/(2\mathcal{A}^2)$ in Ref. [52], similar to Ref. [54].

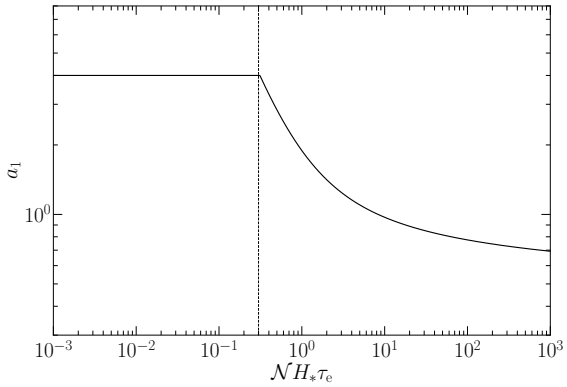

Figure 2: Smoothness parameter a_1 of the MHD turbulence SGWB as a function of the normalised eddy turnover time. It is set to 4 for values below the dashed vertical line corresponding to $\mathcal{N}H_*\tau_e = 0.3$ as larger values of a_1 do not significantly influence the DBPL template.

.

This ratio is in general large since $\bar{v}_A < 1$, so that $f_2/f_1 \gtrsim 5$ with $\mathcal{N} \simeq 2$. This property allows us to find the amplitude Ω_2 used in the DBPL template in Eq. (2.8). At frequencies $f/f_1 \gg 1$, the SGWB spectrum can be approximated by a single BPL,

$$\Omega_{\rm GW}^{\rm MHD}(f \gg f_1, \vec{\theta}_{\rm Cosmo}) = \frac{3\,\mathcal{A}\,\bar{v}_A\,\Omega_s^2\,(H_*R_*)^2}{4\pi^2\mathcal{N}} F_{\rm GW,0}\left(\frac{f}{f_1}\right)\left[1+\left(\frac{f}{f_2}\right)^{a_2}\right]^{-\frac{11}{3a_2}}, \tag{2.22}$$

from which one can derive

$$h^2\Omega_2 = h^2 F_{\rm GW,0}\,A_{\rm MHD}\,\Omega_s^2\,(H_*R_*)^2\,, \tag{2.23}$$

with $A_{\rm MHD} = 3\times 2.2\,\mathcal{A}/(4\pi^2)\times 2^{-11/(3a_2)} \simeq 4.37\times 10^{-3}$. Here the correct physical scaling $\Omega_2 \sim \Omega_s^2$ is recovered. Finally, using the value of Ω_2 in Eq. (2.23) and the expression for the SGWB in Eq. (2.20), we can reproduce the DBPL template in Eq. (2.8) with

$$S_2(f) = 2^{\frac{11}{3a_2}}\left(\frac{f_1}{f_2}\right)\left(\frac{f}{f_1}\right)^3\left[1+\left(\frac{f}{f_1}\right)^{a_1}\right]^{-\frac{2}{a_1}}\left[1+\left(\frac{f}{f_2}\right)^{a_2}\right]^{-\frac{11}{3a_2}}. \tag{2.24}$$

The peak of the SGWB spectrum in the template of Eq. (2.8) is not located exactly at f_2. Under the assumption $f_p/f_1 \sim f_2/f_1 \gg 1$, we can find the position of the spectral peak $f_p = f_2(-n_2/n_3)^{1/a_2} \simeq 0.6 f_2 \simeq 1.4\,H_{*,0}\,(H_*R_*)^{-1}$ [52, 54], and the SGWB amplitude at the peak using Eq. (2.5), $\Omega_p \simeq 1.2\,\Omega_2$.

To wrap up, the parameters that characterise the SGWB spectrum from MHD turbulence are Ω_s, H_*R_*, and T_*, from which we can derive the free geometric parameters of the DBPL,

$$\begin{gathered} f_1 = \frac{\sqrt{3\,\Omega_s}}{2\mathcal{N}}\,H_{*,0}\,(H_*R_*)^{-1}, \quad f_2 \simeq 2.2\,H_{*,0}\,(H_*R_*)^{-1}, \\ h^2\Omega_2 = h^2 F_{\rm GW,0}\,A_{\rm MHD}\,\Omega_s^2\,(H_*R_*)^2\,, \end{gathered} \tag{2.25}$$

with the exponents of the DBPL summarised in Tab. 1. Note that Ω_s and $H_* R_*$ can be related to the PT parameters using Eqs. (2.11) and (2.13), and the relation $K \simeq 0.6\,\kappa\,\alpha/(1+\alpha)$ given in Sec. 2.2.1.

The parameter dependence on Ω_s, $R_* H_*$, and T_* of the spectrum is depicted in Fig. 1c. In realistic scenarios of first-order PTs, the full SGWB spectrum consists of the sum of both contributions due to the fluid motion, sound waves and turbulence, in which case it can be parameterised in terms of $\vec{\theta}_{\rm Cosmo} = \{K, R_* H_*, \xi_w, T_*, \varepsilon\}$, as illustrated in Fig. 1d.

3 Parameter reach and reconstruction

The `SGWBinner` code has been originally designed to carry out agnostic searches and reconstructions of the primordial SGWB signal at LISA [59, 60], and used to quantify the instrument capabilities [112, 113]. In such agnostic searches, the code reconstructs the primordial signal as power laws in multiple bins of optimal widths, while using templates only for the astrophysical foregrounds. The agnostic search is flexible but sub-optimal when a precise template of the primordial signal is available. For this work (and the companion papers [114, 115]), we have developed a new functionality of the `SGWBinner`: a template-based analysis of the primordial signal. We present it below, starting with a review of the foundations of the LISA measurement. We also initiate a template bank within the code, including all the signals discussed in the previous section, preparing the tools to facilitate SGWB searches of cosmological first-order PTs in LISA.

3.1 LISA measurement channels

LISA consists of three satellites, $i = 1, 2, 3$, with relative distances L_{ij}. At every time t, the satellite i emits and receives a laser beam to and from the satellite $j \neq i$, and measures their phases. Due to the laser frequency instabilities, the direct comparison of the phase measurements is too noisy to perform interferometry sensitive to the expected GW signals. However, this noise contribution is largely suppressed by post-processing the data and performing time delay interferometry (TDI) [116], i.e. a comparison of the phase measurements at opportune different times. Different TDI approaches exist [117–125]. Here we consider the "first generation" one, which works under the assumption that the LISA satellites are in an equilateral configuration (i.e. $L_{ij} = L$ for any i, j) and have identical noise levels.[2] In the equilateral approximation, the laser phase emitted from the satellite j at time $t - L/c$ is recorded at time t in satellite i, with c being the light speed. We denote the phases $\eta_{ij}(t)$. Three measurements (suppressing the frequency instabilities) can be recast from these phases [118],

$$\mathrm{A} = \frac{\mathrm{Z} - \mathrm{X}}{\sqrt{2}}\,, \qquad \mathrm{E} = \frac{\mathrm{X} - 2\mathrm{Y} + \mathrm{Z}}{\sqrt{6}}\,, \qquad \mathrm{T} = \frac{\mathrm{X} + \mathrm{Y} + \mathrm{Z}}{\sqrt{3}}\,, \tag{3.1}$$

[2] The robustness of the results obtained in this simplified approach against the relaxation of both these assumptions has been investigated in Ref. [126]. Such work demonstrated that, for a power law signal, a non-equilateral LISA configuration and the inclusion of up to twelve noise parameters (one per each TM/laser noise component) do not affect the reconstruction of the signal parameters significantly. Further studies considering different signal templates, e.g. the ones considered in the present work, are required to generalise this statement.

where

$$\mathrm{X} = (1 - D_{13}D_{31})(\eta_{12} + D_{12}\eta_{21}) + (D_{12}D_{21} - 1)(\eta_{13} + D_{13}\eta_{31}) \,, \tag{3.2}$$

and the Y and Z variables are obtained through cyclic permutations of the indices. Here, $D_{ij}\eta_{kl}(t) = \eta_{kl}(t - L_{ij}/c)$ is the one-arm length delay operator. Remarkably, in the above approximations, the channels A, E, and T constitute three virtual, orthogonal GW interferometers, with the former two being identical and the latter being a (quasi-)null channel, i.e. a channel whose sensitivity to the signal is largely suppressed. The `SGWBinner` simulates and analyses the data in these three channels, and leverages the T channel property to reconstruct the satellite noise sources.

3.2 Data in each channel

The data collected via the A, E, and T channels will contain all the transient and non-transient signals. This includes individually resolvable GW emitting events and a stochastic component, given by the sum of all unresolved astrophysical sources, of the stochastic instrumental noise components, and of possible SGWB signals. The `SGWBinner` simulates data streams of the stochastic component and forecasts posteriors for the parameters of its aforementioned contributions, under the simplifying assumption that their correlations with the transient signals and transient noises are negligible. Thus, for our purpose, the data $\tilde{d}_i$ in the channel $i = \mathrm{A}, \mathrm{E}, \mathrm{T}$ reduce to

$$\tilde{d}_i(t) = \sum_\nu \tilde{n}_i^\nu(t) + \sum_\sigma \tilde{s}_i^\sigma(t) \,, \tag{3.3}$$

where the first sum includes the stochastic noise components, $\tilde{n}_i^\nu$, and the second sum runs over the signal contributions, $\tilde{s}_i^\sigma$. As we will clarify in Sec. 3.3, the noise components can be summarised in two contributions (from the test masses and the optical measurement systems), while we will focus on three signal contributions (two foregrounds and one primordial SGWB).

For simplicity, we assume all dominant noise sources to be practically stationary and Gaussian, with zero mean. Moreover, we expect the noise produced by a source common to different channels to create negligible correlations after TDI operations. In this way, the components $\tilde{n}_i^\nu$ effectively are independent, random, and Gaussian variables. In particular, $\tilde{n}_A^\nu$ and $\tilde{n}_E^\nu$ just differ by their statistical realization, while $\tilde{n}_A^\nu(t)$ (or $\tilde{n}_E^\nu(t)$) also differs from $\tilde{n}_T^\nu(t)$ due to their response function. Indeed, for identical satellites in an equilateral configuration, every satellite has statistically equivalent noise sources; furthermore, A and E have the same response functions, but A (or E) and T do not.

We also treat $\tilde{s}_i^\sigma(t)$ as independent, (zero-mean) Gaussian, and stationary variables. While this choice simplifies and speeds up the data simulation and analysis, it is suboptimal. Indeed, among our stochastic signals, the Galactic foreground is anisotropic in the cosmic microwave background (CMB) frame, yielding a non-stationary signal in the data due to the yearly rotation of the LISA satellites' plane. Averaging this non-stationary signal over several years effectively converts it to a broader Gaussian contribution that can be treated as stationary. This should not bias the whole parameter reconstruction but, at

least in principle, should be less precise than an analysis including the yearly variability (cf. Sec. 3.3 for details on the averaged Galactic foreground).

Within these assumptions, we Fourier transform the data in Eq. (3.3) from time to frequency domain,

$$d_i(f) = \int_{-\tau/2}^{\tau/2} \tilde{d}_i(t)\, \mathrm{e}^{-2\pi i f t}\, \mathrm{d}t \,, \tag{3.4}$$

with statistical properties

$$\langle d_i(f) \rangle = 0 \,, \qquad \langle d_i(f) d_j^*(f') \rangle = \delta_{ij} \frac{\delta(f-f')}{2} \left[P_{N,ii}(f) + P_{S,ii}(f) \right] \,, \tag{3.5}$$

where the brackets denote the ensemble average and τ is the time over which the Fourier transform is performed (as will be clarified in Sec. 3.4).[3] Moreover, $P_{N,ii}$ and $P_{S,ii}$ are the noise and signal power spectra. They are respectively the sum of the power spectra of each noise source ν and each signal σ recorded in the i-i correlator. $P_{N,ii}$ can be expressed in terms of the i-channel response function T_{ii}^{ν} relative to the strain S_{N}^{ν} of the noise sources ν, reading as

$$P_{N,ii}(f) = \sum_{\nu} T_{ii}^{\nu}(f) S_N^{\nu}(f) \,. \tag{3.6}$$

The same can be done for $P_{S,ii}$, with the peculiarity that all signal strain sources share the same response function:

$$P_{S,ii} = R_{ii}(f) \sum_{\sigma} S_S^{\sigma}(f) = \frac{3H_0^2}{4\pi^2 f^3} R_{ii}(f) \sum_{\sigma} h^2 \Omega_{\mathrm{GW}}^{\sigma}(f) \,, \tag{3.7}$$

with R_{ii} denoting the response function to the signals and S_S^{σ} the strain of the SGWBs.

For forecast studies and our level of approximations, it is reasonable to neglect the uncertainties in the response functions. For T_{ii}^{ν} and R_{ii} we thus adopt the response functions already implemented in the `SGWBinner` code, where all parameters have known values so that there is no need to fit for them. The explicit expressions can for instance be found in Ref. [60].[4]

3.3 Injected (and reconstructed) noises and signals

We now describe the noise and signal source strains we implement in `SGWBinner` for the present work. Regarding the signals, we only consider the astrophysical foregrounds whose presence in the LISA data is guaranteed from other observations, namely the Galactic foreground and the one from stellar-origin black hole binaries (SOBHBs). At the same time, we omit any potential cosmological SGWB besides the PT one.

[3] In Eq. (3.5), the Dirac delta only arises in the limit of infinite observation time. It is however a good approximation in the frequency regime $f \ll 1/\tau$ we are interested in. The Kronecker delta instead accounts for the orthogonality of the A, E, and T channel basis emerging in the case of three identical satellites in perfectly equilateral configuration.

[4] For studies on the response functions and their uncertainties see, e.g. Refs.[60, 125, 127].

Noise: LISA performs its measurements by monitoring the relative distances of the test masses (TMs) inside the satellites. The statistical errors in the GW detection are then primarily due to perturbations of the TM free fall regime, and uncertainties in the measurement of the TM relative positions. This qualitatively explains a well-investigated result: the dominant noise strains S_N^ν are given by the TM and the optical measurement system (OMS) strains [58, 128]

$$S_{ii}^{\rm TM}(f) = A^2 \left(1 + \left(\frac{0.4\,{\rm mHz}}{f}\right)^2\right)\left(1 + \left(\frac{f}{8\,{\rm mHz}}\right)^4\right)\left(\frac{1}{2\pi f c}\right)^2 \left(\frac{{\rm fm}^2}{{\rm s}^3}\right) , \quad (3.8)$$

$$S_{ii}^{\rm OMS}(f) = P^2 \left(1 + \left(\frac{2\times 10^{-3}\,{\rm mHz}}{f}\right)^4\right)\left(\frac{2\pi f}{c}\right)^2 \left(\frac{{\rm pm}^2}{{\rm Hz}}\right) , \quad (3.9)$$

where $S_{ii}^{\rm TM}$ models the noise relative to the non-free fall effects, and $S_{ii}^{\rm OMS}$ models the noise due to mismeasuring the TM distances.[5]

In our simulation, we inject the noise with the nominal values $A = 3$ and $P = 15$. In the parameter estimation of the noise and signals we adopt Gaussian priors centered on these nominal values and with 20 % width [58].

Extra-Galactic foreground: It results from the superposition of the SOBHBs and neutron-star binaries (NSBs) that are outside the Milky Way and that LISA does not individually resolve. LISA is sensitive to these sources when they are in the inspiral phase. Because of the statistical properties of the SOBHB and NSB populations as well as the LISA angular resolution, the extra-Galactic foreground in LISA can be approximated as an isotropic signal with a power law frequency shape [129–133]

$$h^2\Omega_{\rm GW}^{\rm Ext}(f) = h^2\Omega_{\rm Ext}\left(\frac{f}{1\,{\rm mHz}}\right)^{2/3} . \quad (3.10)$$

The fiducial value and prior for $\Omega_{\rm Ext}$ can be obtained from the population inference analyses at terrestrial interferometers [134]. By approximating one of the recent estimates [132], we use $\log_{10}(h^2\Omega_{\rm Ext}) = -12.38$ for the injections and a Gaussian prior around it, with $\sigma = 0.17$, for the parameter estimation.

Galactic foreground: The Compact Galactic Binary (CGB) population produces a loud signal in LISA coming from the Galactic disk [135]. After removing the CGBs that LISA can individually resolve, there remains a strong stochastic component which, in the LISA satellite's frame, originates from a sky patch that moves with time and has a cycle of one year (i.e. the yearly periodicity of the LISA orbit around the Sun). Thus, due to the angular dependence of the response functions, the unresolved CGB signal integrated over the whole sky dome exhibits a strength with a yearly modulation [85, 135]. To forecast the sensitivity to cosmological PTs, one would ideally leverage the yearly modulation to better separate the astrophysical signal

[5] Such an effective description must be accompanied by opportune manipulation of the response functions. The `SGWBinner` code includes them.

from the cosmological one, as done, e.g. in Refs. [63, 85]. This however requires data analysis techniques which are not yet implemented in the `SGWBinner`. In the following, we therefore only consider the whole sky-dome signal integrated over the total observing time of the mission, $T_{\rm obs}$. This assumption is a conservative one. For such a signal we adopt the following template [136]:

$$h^2\Omega_{\rm GW}^{\rm Gal}(f) = \frac{f^3}{2}\left(\frac{f}{1\,\mathrm{Hz}}\right)^{-\frac{7}{3}}\left[1+\tanh\left(\frac{f_{\rm knee}-f}{f_2}\right)\right]e^{-(f/f_1)^{\upsilon}}h^2\Omega_{\rm Gal}\,, \tag{3.11}$$

where

$$\begin{aligned}\log_{10}(f_1/\mathrm{Hz}) &= a_1\log_{10}(T_{\rm obs}/\mathrm{year})+b_1\,,\\ \log_{10}(f_{\rm knee}/\mathrm{Hz}) &= a_k\log_{10}(T_{\rm obs}/\mathrm{year})+b_k\,.\end{aligned} \tag{3.12}$$

For the injection, we use the fiducial values $a_1 = -0.15$, $b_1 = -2.72$, $a_k = -0.37$, $b_k = -2.49$, $\upsilon = 1.56$, $f_2 = 6.7\times10^{-4}\,\mathrm{Hz}$ and $\log_{10}(h^2\Omega_{\rm Gal}) = -7.84$ [136]. We assume all of them but $h^2\Omega_{\rm Gal}$ to be known in the parameter estimation and adopt a Gaussian prior on $\log_{10}(h^2\Omega_{\rm Gal})$ centered at -7.84 with width $\sigma = 0.21$.

PT SGWB: We implement Template I (i.e. the BPL representing the SGWB from bubble collisions and highly relativistic fluid shells) and Template II (i.e. the DBPL representing the SGWB from sound waves and MHD turbulence), given respectively in Secs. 2.1 and 2.2. We implement the templates both in terms of the geometric parameters that characterise the spectral templates and of the thermodynamic parameters that describe the PT and the subsequent fluid motion. The injection values and priors of the geometric and thermodynamic parameters are described in Secs. 4 and 5, respectively.

3.4 Data generation and analysis

LISA is planned to operate for at least 4.5 years up to a maximum of 10 years. However, due to antenna repointing and similar operations, some periodic data gaps are scheduled, yielding a duty cycle of about 82 % [113]. This would for instance correspond to interrupting the data acquisition for two days every two weeks. We consider an intermediate scenario and set the `SGWBinner` code to work with $N_d = 126$ data segments of duration $\tau = 11.4$ days each (see Eq. (3.4)), summing up to $T_{\rm obs} = 4$ effective years of data.

Furthermore, the `SGWBinner` works in frequency domain. We denote as $d_i^s(f_{\rm k})$ the Fourier-transformed datum of the segment $s = 1, ..., N_{\rm d}$ in the bin of frequency $f_{\rm k}$ and spacing $\Delta f = 1/\tau \simeq 10^{-6}\,\mathrm{Hz}$. To simulate the LISA data, for every signal and noise component described in Sec. 3.3, the `SGWBinner` code generates N_d Gaussian realizations at each frequency bin $f_{\rm k}$. These bins cover the whole LISA band, which in this work we assume to be $[3\times10^{-5}, 0.5]\,\mathrm{Hz}$, with the required resolution Δf.

The `SGWBinner` code then performs the analysis of the mock data. In our stationary approximation, one can analyse the average value at each frequency $f_{\rm k}$ after averaging over the N_d segments. In practice, we compute "segment-averaged" data defined as

$\mathcal{D}^{\rm k}_{ii} \equiv \sum_{s=1}^{N_d} d_i^s(f_{\rm k}) d_i^s(f_{\rm k})/N_d$. In addition, the resolution Δf is beyond the characteristic scale of the typical primordial SGWB frequency shape, making the data file heavy and slow to manipulate. For this reason, the `SGWBinner` code computes a new data set $D^{\rm k}_{ii}$, defined on a coarser set of frequencies $\bar{f}^{\rm k}_{ii}$ statistically equivalent to the original data [59, 60]. In practice, $\bar{f}^{\rm k}_{ii}$ and $D^{\rm k}_{ii}$ are computed through inverse variance weighting, and each of the new data points is associated with a weight $w^{\rm k}_{ii}$ that accounts for the number of high-resolution points (and their variance) falling into the coarse-grained bin.

For the parameter reconstruction, the code then probes the following likelihood:

$$\ln \mathcal{L}(\vec{\theta}) = \frac{1}{3} \ln \mathcal{L}_{\rm G}(\vec{\theta}|D^{\rm k}_{ii}) + \frac{2}{3} \ln \mathcal{L}_{\rm LN}(\vec{\theta}|D^{\rm k}_{ii}) \,, \tag{3.13}$$

with

$$\ln \mathcal{L}_{\rm G}(\vec{\theta}|D^{\rm k}_{ii}) = -\frac{N_d}{2} \sum_{\rm k} \sum_i w^{\rm k}_{ii} \left[1 - D^{\rm k}_{ii}/D^{\rm Th}_{ii}(\bar{f}^{\rm k}_{ii}, \vec{\theta})\right]^2 \,, \tag{3.14}$$

$$\ln \mathcal{L}_{\rm LN}(\vec{\theta}|D^{\rm k}_{ii}) = -\frac{N_d}{2} \sum_{\rm k} \sum_i w^{\rm k}_{ii} \ln^2 \left[D^{\rm Th}_{ii}(\bar{f}^{\rm k}_{ii}, \vec{\theta})/D^{\rm k}_{ii}\right] \,. \tag{3.15}$$

Here $D^{\rm Th}_{ii}(\bar{f}^{\rm k}_{ii}, \vec{\theta})$ denotes the data predicted in our theoretical model (i.e. our overall template of the injected noises and signals), while $\vec{\theta} = \{\vec{\theta}_S, \vec{\theta}_N\}$ is the vector of the free parameters involved in the injected noises and signals' templates, namely

$$\vec{\theta}_N = \{A, P\} \,, \qquad \vec{\theta}_S = \{\log_{10}(h^2\Omega_{\rm Gal}), \log_{10}(h^2\Omega_{\rm Ext}), \vec{\theta}_{\rm Cosmo}\} \,,$$

where $\vec{\theta}_{\rm Cosmo}$ denotes the thermodynamic or geometric parameters of the PT templates. Notice that $\ln \mathcal{L}_{\rm LN}$ is introduced to take into account the mild non-Gaussianity that the coarse graining introduces [137–140] and the Gaussian likelihood $\ln \mathcal{L}_{\rm G}$ does not properly treat. Moreover, the priors for the noises and SGWB signals should be added to Eq. (3.13) to obtain the posterior distributions, which the `SGWBinner` code determines and visualizes by calling `Polychord` [141, 142], `Cobaya` [143], and `GetDist` [144].

We finally remark that several forecast analyses use the signal-to-noise ratio (SNR) as a rule of thumb to assess whether a primordial SGWB can be detected. To help the comparison with these analyses, we will quote the SNRs of the injected PT signals. We compute it as [145]

$$\mathrm{SNR} = \sqrt{T_{\rm obs} \sum_i \int \left(\frac{S^{\rm Cosmo}_{\rm GW}}{S_{i,\rm N}}\right)^2 \mathrm{d}f} \,, \tag{3.16}$$

where the integral is over the LISA frequency range and $S^{\rm Cosmo}_{\rm GW}$ is related to $h^2\Omega^{\rm Cosmo}_{\rm GW}$ as in Eq. (3.7) and $\Omega^{\rm Cosmo}_{\rm GW}$ represents $\Omega^{\rm BPL}_{\rm GW}$ and $\Omega^{\rm DBPL}_{\rm GW}$ depending on the particular case.

We also perform a Fisher analysis, which corresponds to approximating the likelihood function $\mathcal{L}$ to be Gaussian. The relation between $\Delta\chi^2$ and the Fisher information matrix is given by

$$\Delta\chi^2 = \sum_{i,j} F_{ij} \Delta x_i \Delta x_j, \tag{3.17}$$

where $\Delta x_i \equiv x_{i,\text{postulated}} - x_{i,\text{fiducial}}$ and i, j run over the set of parameters. The Fisher information matrix F_{ij} is given by

$$F_{ij}(\vec{x}_{\text{fiducial}}) = \sum_{\alpha=A,E,T} T_{\text{obs}} \int \mathrm{d}f \left. \frac{(\partial_{x_i} h^2\Omega_\alpha)(\partial_{x_j} h^2\Omega_\alpha)}{(h^2\Omega_\alpha)^2} \right|_{\vec{x}=\vec{x}_{\text{fiducial}}} , \tag{3.18}$$

where $h^2\Omega_\alpha = h^2\Omega_{\text{GW}}^{\text{Cosmo}} + h^2\Omega_{\text{GW}}^{\text{Ext}} + h^2\Omega_{\text{GW}}^{\text{Gal}} + h^2\Omega_{N,\alpha}$ is the sum of the SGWBs, the foregrounds, and the fractional energy density noise $h^2\Omega_{N,\alpha} = \sum_\nu 4\pi^2 f^3 S_\alpha^\nu/(3H_0^2)$ with $\nu = \text{TM}, \text{OMS}$. The sum runs over the TDI AET channels. The projected relative uncertainty on the reconstruction of the parameters is then obtained from the diagonal values of the inverse of the Fisher information matrix, $\Delta x_i/x_i = \Delta \ln x_i = \ln 10 \times \Delta \log_{10} x_i = \ln 10 \times \sqrt{(F^{-1})_{ii}}$. Such errors represent the uncertainty on a given parameter after marginalizing over all the others.

4 Reconstruction of the geometric parameters

In this section, we discuss the prospect for the parameter reconstruction by LISA in terms of the geometric parameters, for the three templates presented in Secs. 2.1, 2.2.1 and 2.2.2. The geometric-parameter templates have the advantage of speeding up the likelihood exploration as their parametrization does not feature degeneracies. On the other hand, their non-trivial connection to PT parameters might lead to exploration of unphysical parts of the parameter space.

4.1 Broken power law

We start with very strong transitions, discussed in Sec. 2.1, leading to a SGWB from bubble collisions or highly relativistic fluid shells described by the BPL spectrum in Eq. (2.4). We fix the exponents to the values in Tab. 1, so that the geometric parameters of the model are $\vec{\theta}_{\text{Cosmo}} = (\log_{10} h^2\Omega_b, \log_{10} f_b/\text{Hz})$. In this case, we report the LISA sensitivity to the geometric parameters using both Fisher and Bayesian analyses.

As an example of the results of these analyses, Fig. 3 depicts the 68 % and 95 % confidence level (CL) expected reconstruction contours of a BPL signal from bubble collisions with a fiducial amplitude $h^2\Omega_b = 3 \times 10^{-12}$ and frequency $f_b = 1\,\text{mHz}$. We have chosen these values as they provide a signal in the ballpark of the maximum sensitivity of LISA. The priors used for the noise and foreground parameters are listed in Tab. 2, while those for the SGWB parameters are listed in Tab. 3, left column. In addition to the signal reconstruction, Fig. 3 also shows the posteriors of the noise parameters A and P, as well as those of the amplitudes of the Galactic and extra-Galactic binary foregrounds, provided in Sec. 3.3. The outcome of the Fisher analysis is shown in red, whereas the blue contours depict the reconstruction using `Polychord`. The inlay in the upper right shows the corresponding SGWB and foreground spectra, as well as the instrument sensitivity. The parameters of this example of signal are reconstructed with an accuracy within a few percent.

Let us now vary the values of the parameters f_b and Ω_b, and consider the corresponding reconstruction. The result is shown in Fig. 4. We display the relative uncertainty on

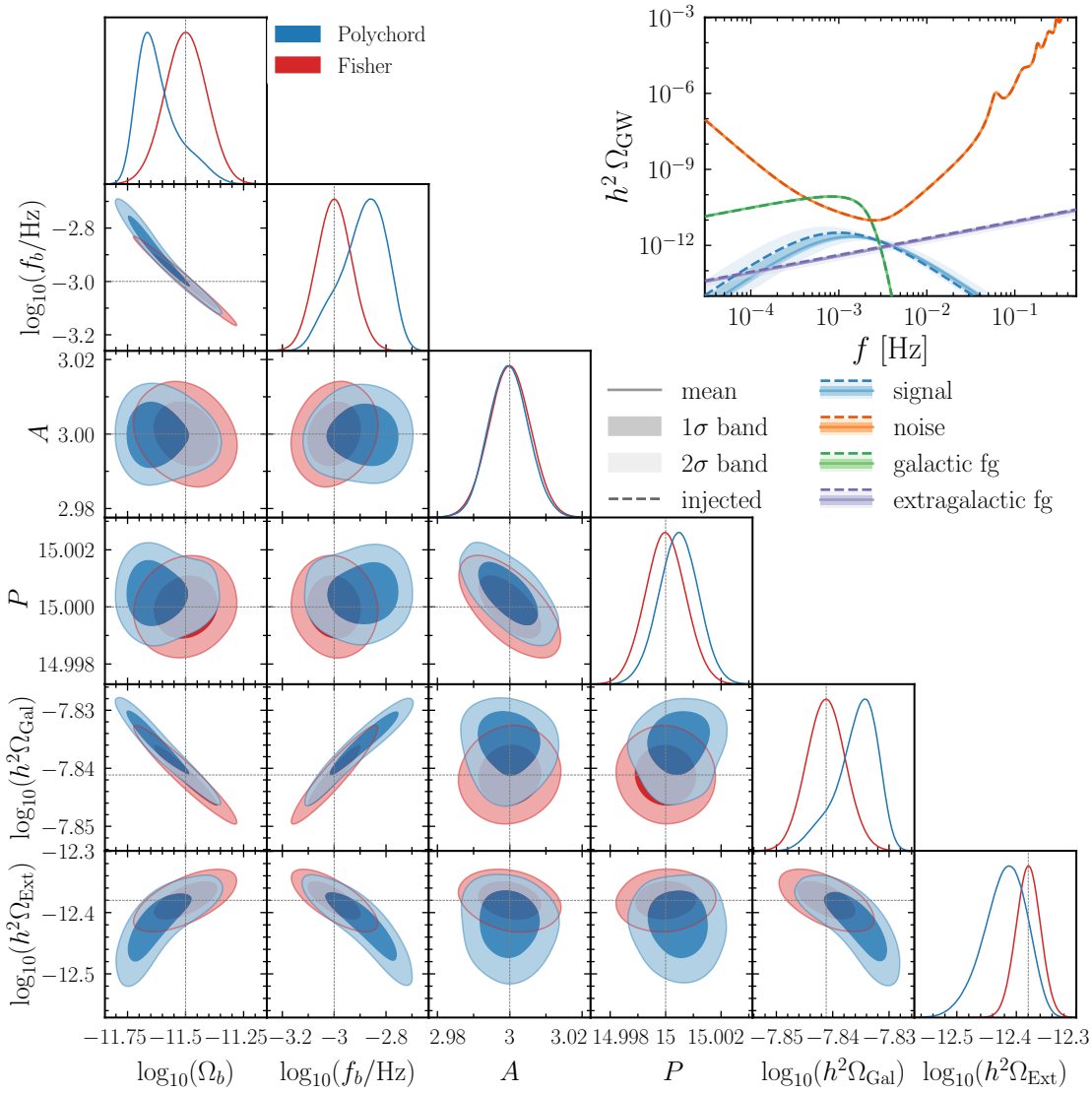

Figure 3: Triangle plot comparing the results of the Fisher analysis (red) and `Polychord` (blue) for a BPL spectrum corresponding to bubble collisions including noise and foregrounds. We fix the spectral exponents to the slopes for strong PTs in Tab. 1 and choose an injected signal with break frequency $f_b = 1\,\text{mHz}$ and amplitude $\log_{10}(h^2\Omega_b) = -11.5$. The plot in the top right corner visualizes the injected signals and noises as well as their reconstructions at 68 % (dark areas) and 95 % (light areas) CLs obtained with `Polychord`.

parameter	$\mu \pm \sigma$	parameter	$\mu \pm \sigma$
A	3 ± 0.6	$\log_{10}(h^2\Omega_{\rm Gal})$	-7.84 ± 0.21
P	15 ± 3	$\log_{10}(h^2\Omega_{\rm Ext})$	-12.38 ± 0.17

Table 2: Mean μ and standard deviation σ of the Gaussian priors used in `Polychord` for the noise parameters A and P as well as the amplitudes of the Galactic ($\log_{10}(h^2\Omega_{\rm Gal})$) and extra-Galactic ($\log_{10}(h^2\Omega_{\rm Ext})$) foregrounds. The injected values correspond to the mean.

parameter	prior range	parameter	prior range
$\log_{10}(h^2\Omega_b)$	$(-30, -5)$	$\log_{10}(h^2\Omega_2)$	$(-30, -5)$
$\log_{10}(f_b/\text{Hz})$	$(-7, 1)$	$\log_{10}(f_2/\text{Hz})$	$(-7, 1)$
		$\log_{10}(f_2/f_1)$	$(0, 2)$

Table 3: Ranges of the uniform priors used in `Polychord` for the parameters of the BPL (left) and DBPL (right). The spectral slopes are fixed to the values in Tab. 1 corresponding to the source under consideration.

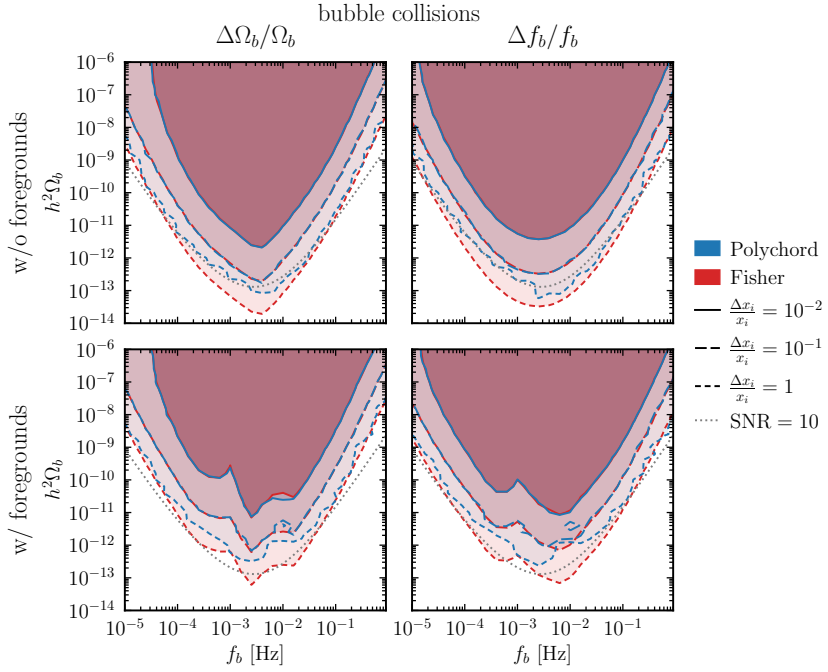

Figure 4: LISA sensitivity to the break frequency and amplitude of the BPL template using Fisher analysis (red) and `Polychord` (blue). The lower panel includes the foregrounds from Galactic and extra-Galactic binaries, whereas the upper panel is without foregrounds. The solid, long-dashed, and short-dashed lines correspond to a relative uncertainty of 1 %, 10 %, and 100 % in the reconstruction of the amplitude Ω_b (left) and the frequency f_b (right), respectively. The gray dotted line indicates an SNR of 10 (neglecting foregrounds) in LISA.

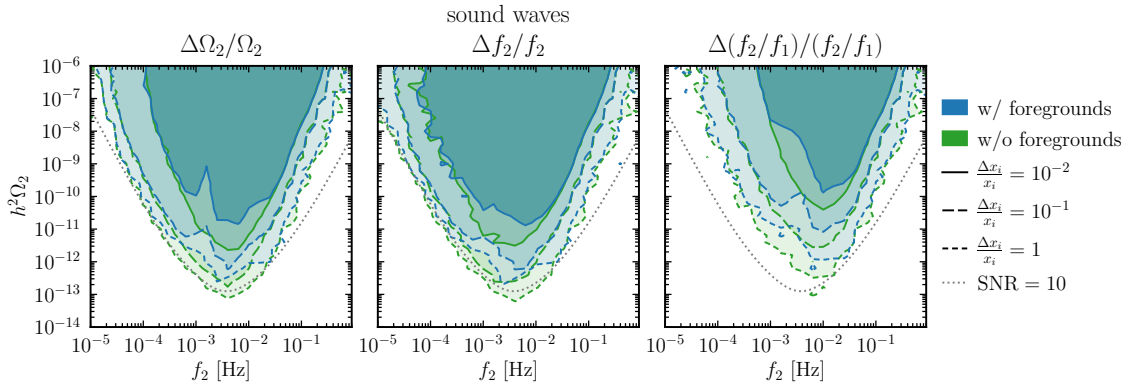

Figure 5: LISA sensitivity to the DBPL template parameters from `Polychord`. The blue regions correspond to the sensitivity including foregrounds, whereas the green curves only take into account the instrument noise. The fiducial point is taken from the sound wave template with $f_2/f_1 \simeq 2.5(\xi_w/\xi_{\rm shell}) \approx 5.9$ corresponding to a detonation with $\xi_w \approx 1$ and $c_s = 1/\sqrt{3}$, see Eq. (2.9).

the reconstructed values of the break amplitude $h^2\Omega_b$ (left) and frequency f_b (right) as a function of the fiducial values. The upper panel shows the result of the analysis when disregarding the foreground contributions, whereas the lower panel includes the expected foregrounds from unresolved Galactic and extra-Galactic binaries. The dark-red regions, delimited by solid lines, are reconstructed with an uncertainty of 1 %, the intermediate regions delimited by long-dashed lines have a reconstruction uncertainty of 10 %, whereas the light-red regions delimited by short-dashed lines are reconstructed within an order-one factor. For comparison, we again show the parameter estimation both from the Fisher analysis (in red), and with nested sampling, using the `Polychord` sampler (in blue). In the latter case, the relative uncertainty is calculated from the values of the diagonal of the covariance matrix of the `Polychord` samples. The priors for the amplitude and break frequency are assumed to be uniform, with the corresponding ranges listed in Tab. 3. The parameters yielding an SNR of 10 are further indicated by the dotted gray line. We find that the uncertainty in the Fisher analysis agrees well with `Polychord` reconstruction in the region where the parameters are reconstructed within $\sim$ 10 % or better. Slight deviations can be seen in the region where the reconstruction works only at $\mathcal{O}(1)$. The highest sensitivity is achieved for break frequencies around $f_b \sim (10^{-3} - 10^{-2})$ Hz.

4.2 Double broken power law

Here we analyse the case of an SGWB generated by bulk fluid motion, discussed in Sec. 2.2, which can be described by the DBPL spectrum of Eq. (2.8). In this case, we report the LISA sensitivity to the geometric parameters using the Bayesian approach only.

The results for the DBPL are shown in Figs. 5 and 6. We reconstruct the geometric parameters $\vec{\theta}_{\rm Cosmo} = \{\log_{10}(h^2\Omega_2), \log_{10}(f_2/{\rm Hz}), \log_{10}(f_2/f_1)\}$ and calculate the uncertainty of the reconstructed values from the corresponding values of the covariance matrix. In Fig. 5, we adapt the DBPL spectrum to the sound waves case, setting the

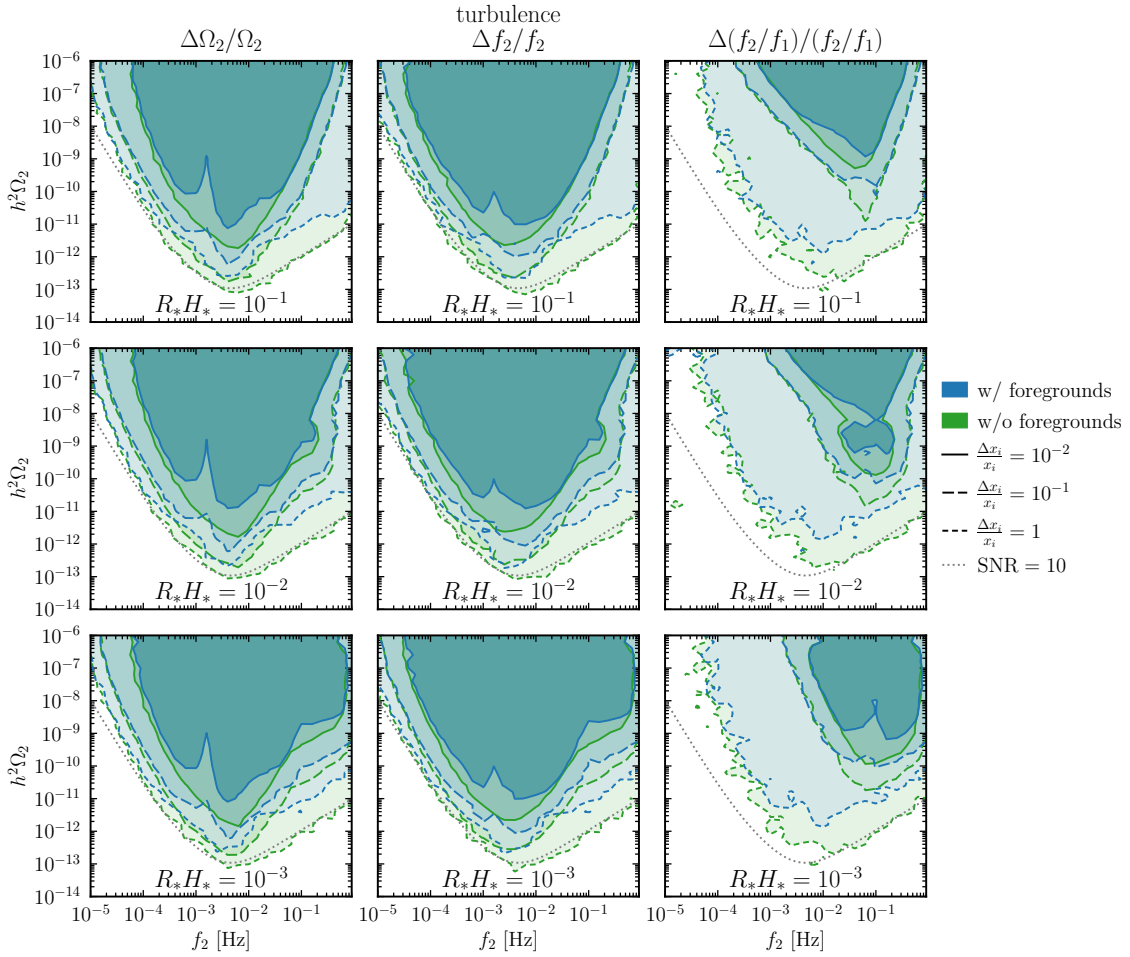

Figure 6: Same as Fig. 5. The fiducial point is taken from the turbulence template with $f_2/f_1 \simeq 80\,(R_*H_*)^{1/2}(h^2\Omega_2/10^{-12})^{-1/4}$, see Eq. (2.25). The rows correspond to different values of $R_*H_* = 10^{-1}$, 10^{-2}, and 10^{-3}.

break frequency ratio to $f_2/f_1 \simeq 2.5(\xi_w/\xi_{\rm shell}) \approx 5.9$, corresponding to a detonation with $\xi_w \approx 1$ and $c_s = 1/\sqrt{3}$, see Eq. (2.9). In Fig. 6, we adapt the DBPL spectrum to the MHD turbulence case, and by making use of Eq. (2.25) we set the frequency ratio to $f_2/f_1 \simeq 2.5\mathcal{N}\sqrt{R_*H_*}\,(F_{\rm GW,0}\,A_{\rm MHD}/\Omega_2)^{1/4} \simeq 80\,(R_*H_*)^{1/2}\,(h^2\Omega_2/10^{-12})^{-1/4}$ for $\mathcal{N} = 2$. Note that, by expressing the amplitude of the SGWB in terms of Ω_2 in the case of MHD turbulence one introduces a spurious dependence of the ratio f_2/f_1 on R_*H_*, while physically it only depends on the fractional energy Ω_s. Therefore, in Fig. 6 we present the reconstruction for a few fixed values of R_*H_*. The priors used for the amplitude and break frequencies are listed in Tab. 3.

4.3 Synergy with other gravitational wave observatories

In Fig. 7, we compare the reconstruction reach of LISA to the one of next-generation ground-based GW interferometers, in particular the Einstein Telescope (ET) [146], and

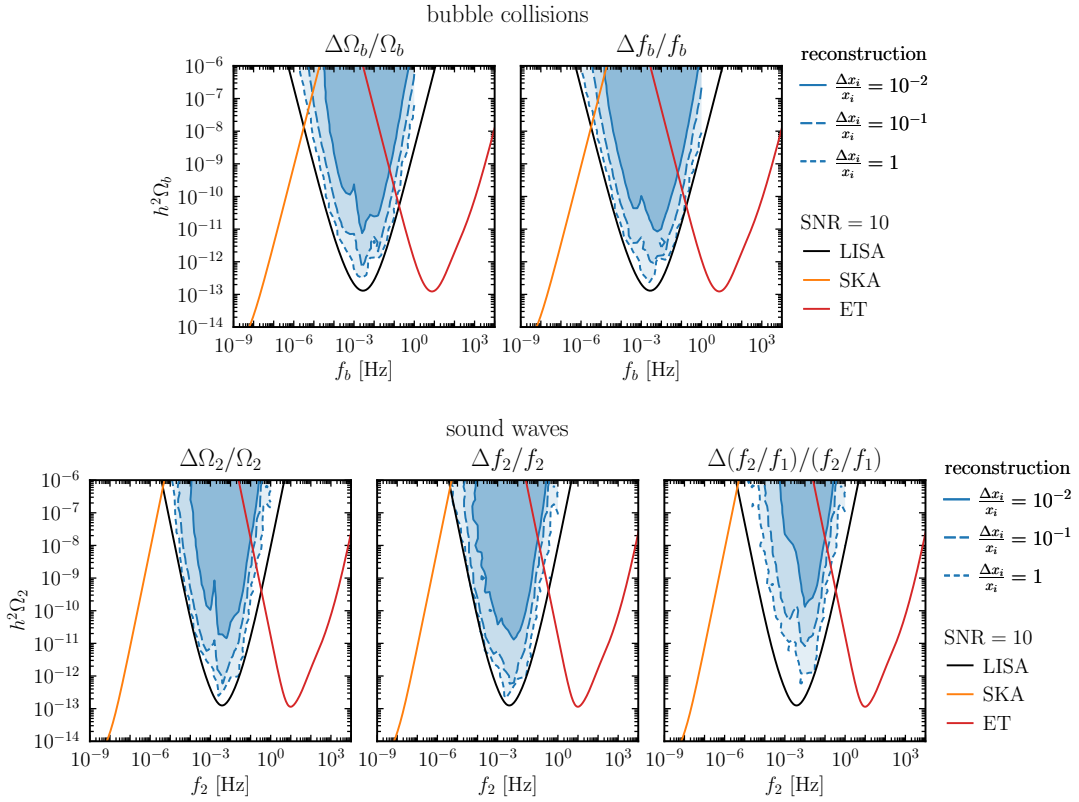

Figure 7: Relative uncertainty for the reconstruction of amplitude (left), frequency (top right or bottom center), and frequency ratio (bottom right, only for sound waves) in the cases of bubble collisions (top) and sound waves (bottom). The black (LISA), red (ET), and orange (SKA) lines correspond to an SNR of 10 for both templates.

to the one of future PTAs, in particular the Square Kilometre Array (SKA) [147]. The black line depicts the parameters that produce an SNR of 10 in LISA after an effective observation time of four years. The red line indicates the parameters leading to an SNR of 10 in ET, using the noise curve from Ref. [148], whereas the orange line corresponds to the SKA, assuming observation of 1000 pulsars over 20 years with a timing cadence of two weeks and timing uncertainty of 0.1 µs [149]. While synergies with ET are possible, simultaneous observation of a SGWB from a PT in the LISA and PTA bands requires unrealistically high amplitudes, due to the large separation between the frequency bands of the two experiments.

Another problem is the existence of foregrounds, which are not included in the SNR curves. The blue regions correspond to the respective reconstruction uncertainty estimated using `Polychord` including foregrounds in the LISA band (cf. Fig. 5), and a similar analysis would be required for the other experiments, which would further diminish the prospects for synergy between the experiments.

5 Reconstruction of the thermodynamic parameters

As shown in Secs. 2.1, 2.2.1 and 2.2.2, the SGWB signal from a first-order PT can be expressed in terms of a set of thermodynamical parameters, depending on the sourcing process. The SGWB from bubble collisions or highly relativistic fluid shells in strong first-order PTs is determined by the energy fraction $\tilde{K} \approx 1$, the relative inverse PT duration β/H_*, and the temperature at the end of the PT, T_*. The bubble wall speed does not enter, since in this case the bubble walls move close to the speed of light, $\xi_w \simeq 1$. In the case of a SGWB generated by both sound waves and turbulence, the parameters entering the spectrum are rather connected to the bulk fluid motion: the kinetic energy fraction K, the relative size of the bulk fluid motion $H_* R_*$, and the PT temperature T_*. For sound waves, the fluid shell thickness, which depends on the bubble walls speed ξ_w and on the sound speed c_s, also enters in the SGWB spectral shape; while for turbulence, there is an extra parameter, ε, representing the fraction of kinetic energy which is vortical rather than compressional. Note that the gradient and/or kinetic energy fractions $\tilde{K}$ and K can be related to the PT strength α, while the typical scale of the bulk fluid motion can be connected to the PT inverse duration β/H_* and the bubbles wall speed ξ_w (see Eq. (2.11)).

In this section, we develop two methods to reconstruct the thermodynamic parameters entering the SGWB signals, both based on parameter estimation with `Polychord` implemented in the `SGWBinner`: the first one consists in estimating the thermodynamic parameters directly; the second one consists in estimating the geometric parameters first, and then convert the reconstructed geometric parameters to the corresponding thermodynamic ones. Running the geometric-parameter reconstruction as a first step is efficient because they do not suffer from degeneracies.

While the SGWB spectra can be described in terms of three to five thermodynamic parameters, depending on the source, only two or three geometric parameters are present: the amplitude, and one or two break frequencies, depending on whether the power law is doubly or singly broken, i.e. whether the signal stems from strong transitions or is generated via interactions with the plasma. We are hence confronted with degeneracies when intending to infer the PT parameters from the signal. We will demonstrate that these degeneracies can be lifted if more than one contribution is reconstructed.

Bubble collisions and highly relativistic fluid shells In this case we have three independent thermodynamic parameters $(\tilde{K}, \beta/H_*, T_*)$ but only two geometric parameters: the break position and its amplitude $(f_b, h^2\Omega_b)$. The reconstruction of the thermodynamic parameters hence inevitably suffers from degeneracies. Fixing either of the three parameters, the other two can be determined uniquely. In particular, as strong transitions in sectors that are in equilibrium with the SM plasma have $\alpha \gg 1$, fixing $\tilde{K} \sim \frac{\alpha}{1+\alpha} \approx 1$ allows for the reconstruction of β/H_* and T_*. Alternatively, as shown by Eq. (2.7), we can obtain constraints on the combinations $T_*\beta/H_* \approx 54\,\mathrm{TeV}\, f_b/\mathrm{mHz}$ and $\tilde{K} H_*/\beta \approx \sqrt{10^6 h^2 \Omega_b}$.[6]

Figure 8 shows the reconstruction of the thermodynamic parameters of the SGWB spectrum from bubble collisions with $\tilde{K} = 1$, $\beta/H_* = 500$, and $T_* = 200\,\mathrm{GeV}$. As discussed

[6] Note that we fix $g_* = 106.75$ in these expressions.

parameter	input	prior range	parameter	input	prior range
$\log_{10}(\tilde{K})$	0.0	$(-4, 0)$	$\log_{10}(h^2\Omega_b)$	-11.5	$(-30, -5)$
$\log_{10}(\beta/H_*)$	2.7	$(0, 4)$	$\log_{10}(f_b/\mathrm{Hz})$	-2.7	$(-7, 1)$
$\log_{10}(T_*/\mathrm{GeV})$	2.3	$(0, 4)$			

Table 4: Input values and flat prior ranges for the injection and reconstruction of our bubble collisions benchmark spectrum in terms of the thermodynamic parameters (left) and the geometric parameters (right). The spectral slopes are set to $(n_1, n_2, a_1) = (2.4, -2.4, 1.2)$, see Tab. 1.

in Sec. 2.1, even though the spectrum we adopt in this work for bubble collisions was computed assuming $\tilde{K} \approx 1$, here we keep $\tilde{K}$ as a free parameter. The blue contours in Fig. 8 depict the reconstruction directly in terms of the thermodynamic parameters. The degeneracies between the parameters are clearly visible. In addition, the red contours show the reconstruction using a sample in terms of the break frequency f_b and amplitude $\log_{10}(h^2\Omega_b)$ of the corresponding BPL. The respective priors used in `Polychord` are listed in Tab. 4. In order to obtain the three thermodynamic parameters from the two geometric parameters, for each point in the sample, a random value for the transition temperature T_* was drawn according to the prior in Tab. 4, and the remaining parameters $\tilde{K}$ and β/H_* have been calculated assuming this temperature. The green contours indicate the Fisher analysis estimate in terms of the geometric parameters, converted to thermodynamic parameters using the same method.

The three approaches yield consistent results for the parameter estimation. Note that these methods are not completely equivalent, due to differences in the priors. However, as the relations between the logarithms of the parameters are mostly linear, except for deviations due to the temperature dependence of the effective degrees of freedom, the effects from the difference in priors are negligible. Details on how the differences in priors can be accounted for can be found in Ref. [64].

Sound waves The SGWB spectrum from sound waves is given in terms of three geometric parameters, the two frequency breaks and the amplitude at the second break, but four thermodynamic parameters, K, H_*R_*, T_*, and ξ_w. The relation between the geometric parameters f_1, f_2, and Ω_2 in the sound waves template and the thermodynamic parameters are given in Eqs. (2.9), (2.10) and (2.12). In this case, the frequencies depend on H_*R_*, ξ_w, and T_*, and the integrated amplitude Ω_{int} on K and H_*R_*, while Ω_2 also involves ξ_w through the ratio f_2/f_1 (both amplitudes Ω_2 and Ω_{int} also depend subdominantly on T_* via the degrees of freedom). This allows us to reconstruct the thermodynamic parameters in the following way: from the ratio of the frequency breaks, $f_2/f_1 = 2.5\,\Delta_w^{-1}(\xi_w)$ (see Eq. (2.9)), we can derive the compatible values of ξ_w (ξ_w might not be unique since $\Delta_w(\xi_w)$ is in general not invertible, so there can be one or two possible values of ξ_w for each Δ_w), from f_1 we can derive constraints (one for each value of ξ_w) on the ratio $T_*/(H_*R_*)$,

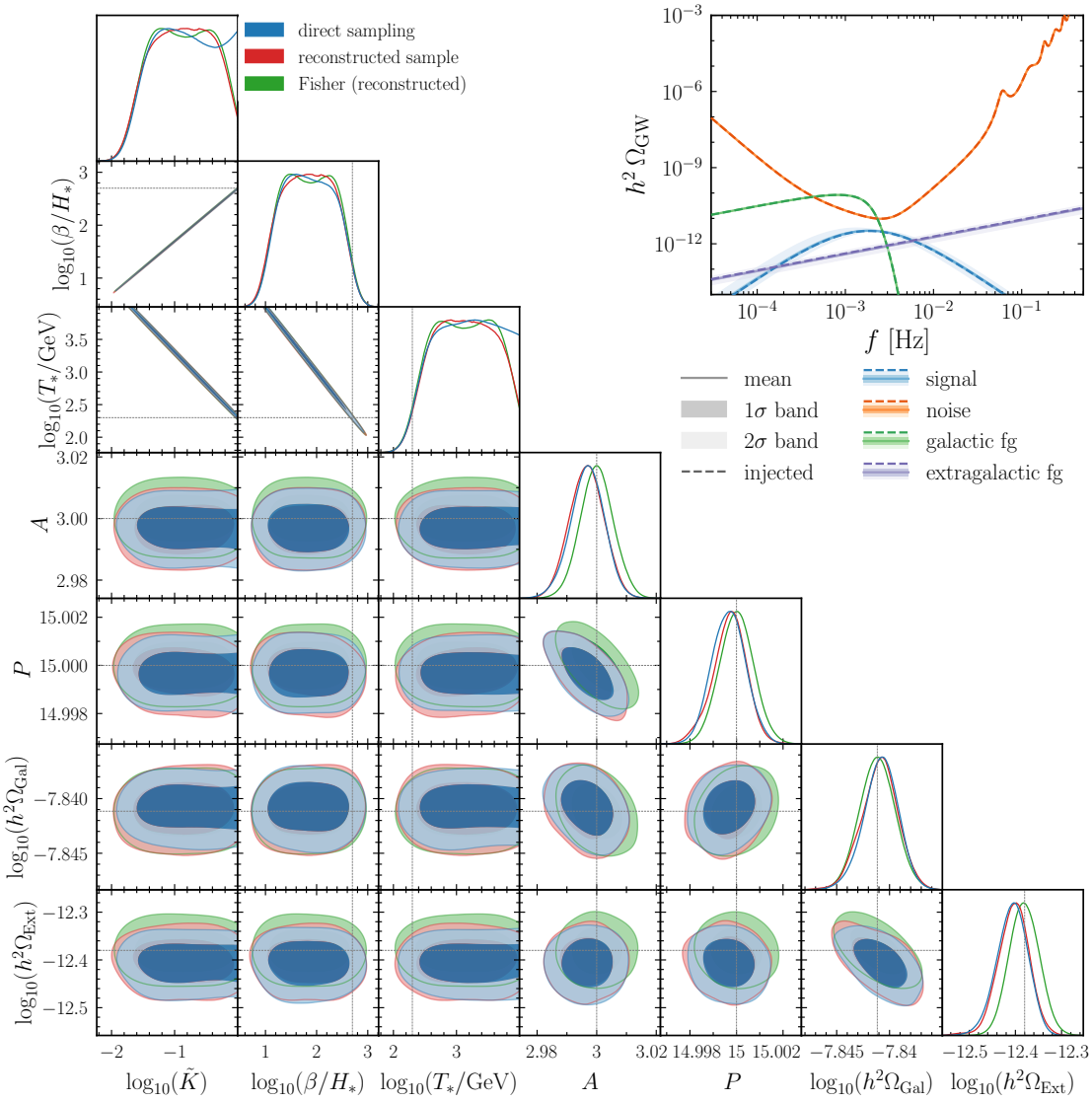

Figure 8: Reconstruction of the thermodynamic parameters of the GW spectrum from bubble collisions in a strong PT. The blue contours are sampled directly, whereas the red contour is reconstructed from a sample in terms of the geometric parameters of the BPL. The green contours are obtained from the Fisher analysis for the geometric parameters. The plot in the top right corner visualizes the injected signals and noises as well as their reconstructions at 68 % (dark areas) and 95 % (light areas) CLs obtained from direct sampling.

and from the amplitude Ω_2, combined with f_2/f_1 and f_1, we can derive a constraint on a combination of K and T_*. These constraints are

$$\frac{T_*}{H_* R_*} \simeq 30\,\mathrm{TeV}\,\frac{f_1}{\mathrm{mHz}} \quad \text{and} \quad \min\left[K^2\,H_* R_*,\ \frac{2}{\sqrt{3}} K^{\frac{3}{2}} (H_* R_*)^2\right] \simeq \frac{\Omega_{\rm int}}{1.8\times 10^{-6}}\,, \tag{5.1}$$

where $\Omega_{\rm int}$ is computed from f_2/f_1 and Ω_2 using Eq. (2.12). Hence, from the geometric parameters, we can only uniquely determine ξ_w (one or two values). The parameters $H_* R_*$ and T_* are degenerate since only the ratio $T_*/(H_* R_*)$ is reconstructed (one constraint for each value of ξ_w) using Eq. (5.1). Furthermore, $H_* R_*$ and K are also degenerate via Eq. (5.1). There are two possible degeneracies, due to the min function that appears in the computation of the sound wave time $\tau_{\rm sw}$ (cf. discussion in Sec. 2.2.1). Hence, either the product $K^2 H_* R_*$ or $K^{3/2}(H_* R_*)^2$ is constrained. Therefore, in general, the parameters K, $H_* R_*$, and T_* cannot be uniquely reconstructed from the geometric parameters of the sound waves template. However, the method described in the previous section and displayed in Fig. 8 can also be applied in this case.

Turbulence The geometric parameters f_1, f_2, and Ω_2 in the turbulence template are given in Eq. (2.25), and depend bijectively on Ω_s (from the ratio of the break frequencies), $H_* R_*$ (from the amplitude), and T_* (via $H_{*,0}$ in f_1). This gives

$$\varepsilon K = \Omega_s \simeq \frac{6.5\,\mathcal{N}^2}{(f_2/f_1)^2}\,, \tag{5.2a}$$

$$H_* R_* \simeq \frac{6\times 10^{-4}}{\mathcal{N}^2}\left(\frac{f_2}{f_1}\right)^2 \sqrt{\frac{h^2\Omega_2}{10^{-12}}}\,, \tag{5.2b}$$

$$T_* \simeq \frac{1.6\,\mathrm{GeV}}{\mathcal{N}^2}\frac{f_2}{\mathrm{mHz}}\left(\frac{f_2}{f_1}\right)^2 \sqrt{\frac{h^2\Omega_2}{10^{-12}}}\,. \tag{5.2c}$$

Hence, from the geometric parameters we can determine uniquely $H_* R_*$ and T_*, whereas K and ε are degenerate and only their product $\Omega_s = \varepsilon K$ is constrained.

Soundwaves + turbulence If we combine the SGWBs from sound waves and turbulence, $\Omega_{\rm GW} = \Omega_{\rm GW}^{\rm sw} + \Omega_{\rm GW}^{\rm turb}$, and use the fit as a DBPL for each of the components, we can break the degeneracies present separately for the sound waves and turbulence and reconstruct all the thermodynamic parameters $\{K, H_* R_*, \xi_w, T_*, \varepsilon\}$ when the geometric parameters $\{f_1^{\rm sw}, f_2^{\rm sw}, f_1^{\rm turb}, \Omega_2^{\rm turb}, \Omega_2^{\rm sw}\}$ can be inferred from the signal parameter estimation. Note that $f_2^{\rm turb} = 2.2\,H_{*,0}/(H_* R_*) \simeq 11 f_1^{\rm sw}$, such that $f_2^{\rm turb}$ does not add information as long as we know its exact relation with $f_1^{\rm sw}$. Indeed, one can see that given this relation, the first constraint in Eq. (5.1) and Eq. (5.2b) are equivalent if we use T_* from Eq. (5.2c).

From the sound waves geometric parameters we are able to reconstruct the possible value/s (one or two) of ξ_w from $f_2^{\rm sw}/f_1^{\rm sw}$, while we can reconstruct T_* from $\Omega_2^{\rm turb}$, $f_1^{\rm turb}$, and $f_1^{\rm sw}/f_1^{\rm turb}$ (see Eq. (5.2c)). We can solve for K for both cases in Eq. (5.1) and then check which solution also satisfies the corresponding condition on the sound wave lifetime. This could lead to one or two solutions for K. Then, for each solution of K, we can reconstruct $\varepsilon = \Omega_s/K$. In general, the reconstruction of the geometric parameters of a combined sound

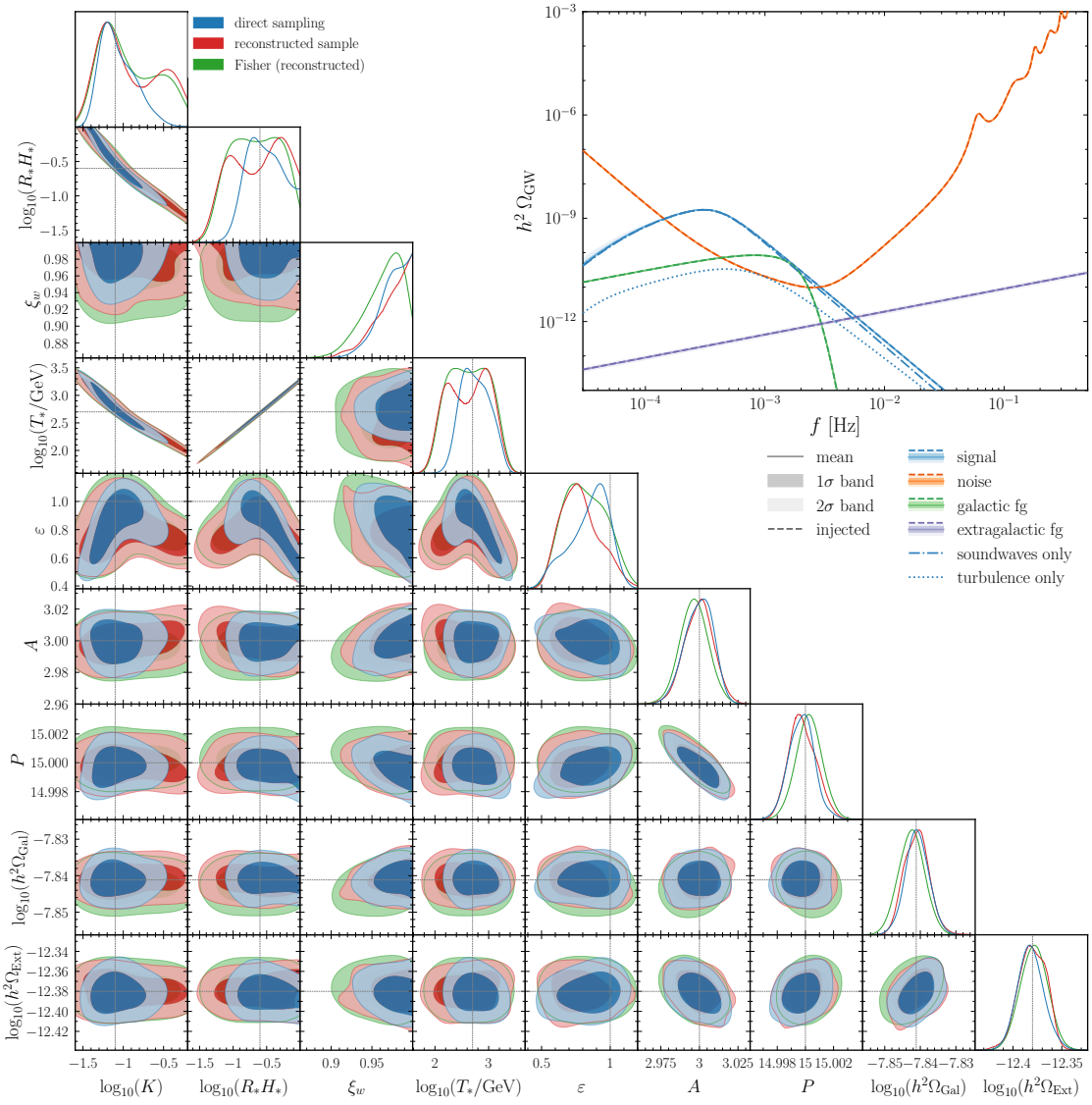

Figure 9: Reconstruction of the sum of the sound waves and turbulence SGWB spectra in terms of the thermodynamic parameters. The blue contours are sampled directly using `Polychord` in terms of the thermodynamic parameters, whereas the red contours are reconstructed from the sample in terms of the geometric parameters. The green contours are obtained from a Fisher analysis performed in terms of the geometric parameters.

parameter	input	prior range	parameter	input	prior range
$\log_{10}(K)$	-1.1	$(-4, -0.2)$	$\log_{10}(h^2\Omega_2^{\rm sw})$	-8.8	$(-30, -5)$
$\log_{10}(R_* H_*)$	-0.6	$(-3, 0)$	$\log_{10}(\Omega_2^{\rm turb}/\Omega_2^{\rm sw})$	-1.7	$(-5, 0)$
ξ_w	1.0	$(0.6, 1)$	$\log_{10}(f_2^{\rm sw}/{\rm Hz})$	-3.4	$(-5, -1)$
$\log_{10}(T_*/{\rm GeV})$	2.7	$(0, 4)$	$\log_{10}(f_2^{\rm sw}/f_1^{\rm sw})$	0.77	$(0, 2)$
ε	1.0	$(0.01, 1.2)$	$\log_{10}(f_1^{\rm turb}/f_1^{\rm sw})$	-0.21	$(-2, 2)$

Table 5: Input values and flat prior ranges for the injection and reconstruction of the turbulence plus sound waves benchmark spectrum in terms of the thermodynamic parameters (left) and of the geometric parameters (right). The ratio $f_2^{\rm turb}/f_1^{\rm sw}$ is fixed to 11 (cf. Eqs. (2.9) and (2.25)), whereas the spectral slopes are set to $(n_1, n_2, n_3, a_1, a_2) = (3, 1, -3, 2, 4)$ and $(n_1, n_2, n_3, a_1, a_2) = (3, 1, -8/3, 4, 2.15)$ for the sound waves and turbulence SGWB spectrum, respectively (cf. Tab. 1).

waves and turbulence template allows us to reconstruct all the thermodynamic parameters in a unique way.

Figure 9 depicts an example of parameter reconstruction in terms of the thermodynamic parameters of the PT featuring both the sound waves and the turbulence contributions. The blue contours correspond to directly sampling the thermodynamic parameters in `Polychord`. For the red contours, instead, we first sample over the geometric parameters and then convert the chains in terms of the thermodynamic parameters with the procedure previously described. Parameter points corresponding to unphysical values (ξ_w, K, or $R_* H_* > 1$) were discarded. The priors of the signal parameters in both cases are taken as uniform, with the corresponding ranges and the input values listed in Tab. 5. In addition, the green contours depict the result of the Fisher approach calculating the Fisher matrix in terms of the geometric parameters, creating samples using a multivariate Gaussian distribution according to the Fisher matrix, and then converting these to the thermodynamic parameters. While these approaches in principle differ in terms of the priors, we obtain consistent results.

Although in theory, the reconstruction of the sum of the two spectra should be unique, we can still see degeneracies between the kinetic energy fraction K, the bubble size $R_* H_*$, and the temperature T_*. These degeneracies arise since the first frequency break of the turbulence SGWB spectrum is hidden below the sound waves signal and the Galactic foreground, such that it cannot be reconstructed with enough precision. The corresponding loss of information inhibits the full reconstruction of the two spectra, leading to degeneracies, as one now needs to constrain five thermodynamic parameters from only four reconstructed geometric parameters. Furthermore, the two possible solutions for K, corresponding to the case where the SGWB generated from sound waves is cut off by their lifetime or at the Hubble time, lead to a kink in the 2D posteriors involving K or ε.

As a cross-check, Fig. 10 shows the reconstruction of the geometric parameters, i.e. the amplitudes and break frequencies of the two DBPLs, for the same input signal. The blue region now corresponds to directly sampling over the geometric parameters, whereas the

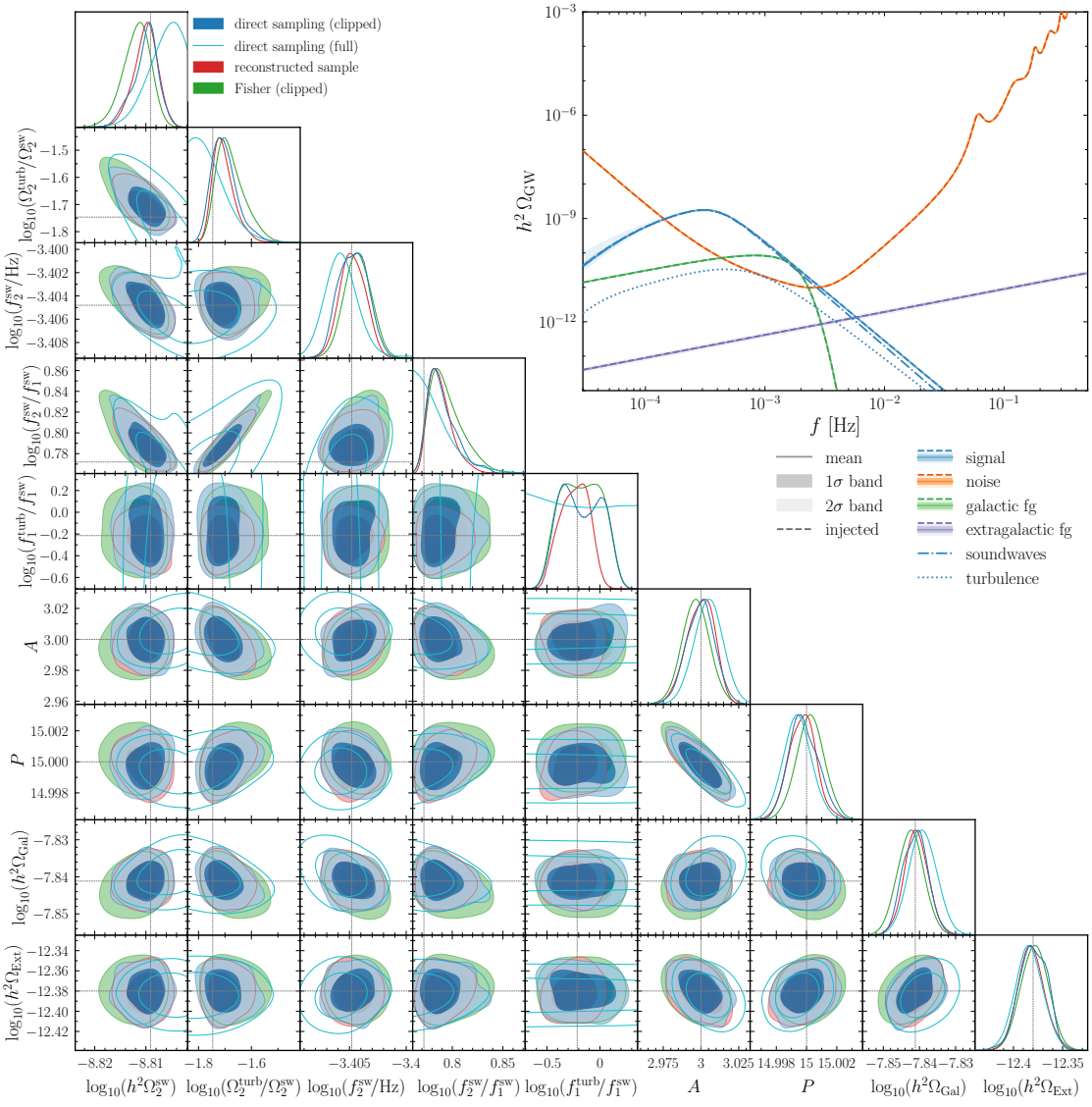

Figure 10: Reconstruction of the sum of two DBPLs in terms of the respective amplitudes and frequency breaks, assuming spectral slopes corresponding to the sum of the sound wave and turbulence spectra. The blue contours are sampled directly using `Polychord`, whereas the red contours are calculated from the sample in terms of the thermodynamic parameters. The green contours are obtained from Fisher analysis. Parameter points leading to unphysical thermodynamic parameters, i.e. ξ_w, K, or $H_* R_* > 1$ are discarded. These points are retained in the cyan contours.

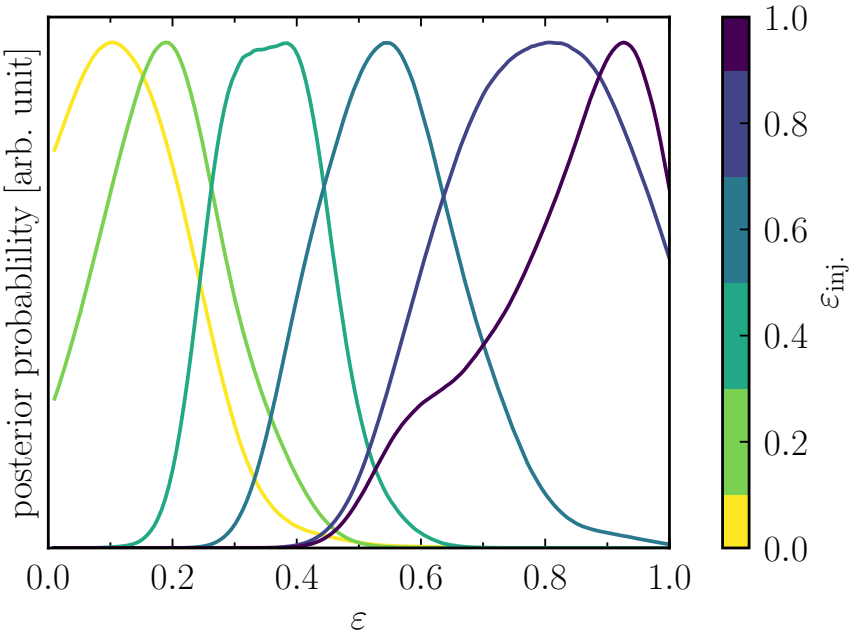

Figure 11: Posterior probability distributions for the reconstruction of ε using `Polychord` assuming $K = 0.08$, $H_* R_* = 0.25$, $\xi_w = 1$, and $T_* = 500\,\mathrm{GeV}$. The injected value of ε is varied between 0 and 1 in steps of 0.2.

red region shows the geometric parameters calculated from the sampling in terms of the thermodynamic parameters. The green region depicts the result from Fisher analysis. Note that we clipped the samples of the geometric parameters by removing parameter points that would yield unphysical values of ξ_w, K, or $R_* H_*$ when converted to thermodynamic parameters. While this would ideally be done directly in the priors or using other constraints, it turns out to be challenging to implement, due to the rather involved relations between the two sets of parameters. For reference, we further include the unclipped results as cyan contours, where the failure of the reconstruction of f_1^{turb}, which leads to the degeneracies in the thermodynamic parameters reconstruction, becomes apparent.

Above we have treated the fraction ε of bulk kinetic energy converted to turbulent motion as an additional independent parameter in our set. However, in principle we expect ε to depend on the PT parameters and on the properties of the primordial plasma. Therefore, if determined independently from an observed GW signal from a PT in LISA, it would improve our understanding of the SGWB source. In Fig. 11, we therefore depict the posteriors for the reconstruction of ε, where the colors indicate the injected value of ε. The remaining parameters are set to the ones listed in Tab. 5. While a precise determination of ε appears to be unrealistic, a strong SGWB signal from a PT can be used to at least roughly constrain the range of ε.

6 Interpretation in terms fundamental particle physics models

In this section, we provide two examples of how the PT SGWB reconstruction can be recast as compelling bounds on the parameter space of particle physics models. Performing parameter inference starting from the LISA SGWB data directly on the parameters of a beyond the SM (SM) Lagrangian is currently prohibitive. Indeed, computing the thermodynamic quantities governing the PT from the set of fundamental parameters within a given model requires numerical tools [150–152] that, at the moment, are not ready for intensive, fast, automatised applications. For instance, numerical instabilities and the computation time can represent obstacles for likelihood samplers.

For our reconstruction, we use a simple approach that circumvents these issues. We begin by scanning the parameter space of the models on a regular grid, and for each point, we determine the thermodynamic parameters. Next, we interpolate the data to find the parameters as smooth functions of the fundamental parameters of the model. These are then ready to be used in the reconstruction of the SGWB signal at LISA. We then map our reconstruction back onto the model parameter space. We do so for a handful of benchmarks of the SGWB spectrum, appropriately chosen so that the geometrical parameters of the SGWB can be well reconstructed.

We now proceed to explain how the PT parameters can be calculated from the models we consider. Below the critical temperature T_c the new minimum in the potential of the theory becomes deeper than the initial one. From that moment the probability that the field tunnels into the new minimum due to thermal fluctuations can be approximated by [153, 154]

$$\Gamma(T) = \left(\frac{S_3(T)}{2\pi T}\right)^{\frac{3}{2}} T^4 \mathrm{e}^{-S_3(T)}, \tag{6.1}$$

where $S_3(T)$ is the action of the field configuration driving the decay. The field configuration is obtained by solving the equation of motion of the field in a given potential assuming $O(3)$-symmetry as appropriate for thermal systems. The probability of a point to remain in the initial vacuum is given by [155]

$$P(t) = \exp\left[-\frac{4\pi}{3}\int_{t_c}^{t} \mathrm{d}t'\, \Gamma(t')\, a^3(t')\, r^3(t,t')\right], \tag{6.2}$$

where the comoving radius of a bubble reads

$$r(t,t') = \int_{t'}^{t} \frac{\xi_w(\tilde{t})}{a(\tilde{t})}\, \mathrm{d}\tilde{t}\,. \tag{6.3}$$

for a bubble with wall velocity $\xi_w(\tilde{t})$ growing up to time t and nucleated at t'. We assume the appropriate time to compute the thermodynamic quantities governing the GW production is percolation time, when bubbles collide to fill the volume (we assume instantaneous reheating after the transition). This moment can be approximated by $P(t_*) \approx 0.7$, which allows us to find the corresponding percolation temperature T_*. The strength of the PT is approximated as [34, 37]

$$\alpha \equiv \frac{1}{\rho_r}\left(\Delta V(T) - \frac{T}{4}\frac{\partial \Delta V(T)}{\partial T}\right)\Bigg|_{T=T_*}, \tag{6.4}$$

where $\Delta V(T)$ is the energy difference between the two coexisting minima, and ρ_r denotes the radiation energy density of the Universe. The inverse duration of the transition can be computed using the action of the solution

$$\frac{\beta}{H_*} \equiv T_* \frac{d}{dT}\left(\frac{S_3(T)}{T}\right)\Big|_{T=T_*}, \tag{6.5}$$

and related to the average bubble size via Eq. (2.11). Using the methods described in Refs. [156–160] we verify all the points of interest feature highly relativistic walls $\xi_w \approx 1$. In this case the efficiency factor reads [88]

$$\kappa = \frac{\alpha}{0.73 + 0.083\sqrt{\alpha} + \alpha}, \tag{6.6}$$

and with it, we have all the thermodynamic parameters needed to compute the SGWB spectrum from bubble collisions and highly relativistic fluid shells (see Sec. 2.1) as well as from sound waves (see Sec. 2.2.1).

We apply this procedure to two illustrative models, namely the SM supplemented with a neutral singlet, and the classically conformal $\mathrm{U}(1)_{B-L}$ extension of the SM. The former model is arguably the simplest SM extension allowing a strong first-order electroweak transition, while the latter is one of the minimal extensions featuring a wide parameter region with a very supercooled PT. Both extensions have few free parameters, making the scan of their whole parameter space feasible.

6.1 Gauge singlet extension with $\mathbb{Z}_2$ symmetry

One of the simplest extensions of the SM giving rise to PTs is that of an extra scalar singlet under the SM gauge group endowed with a $\mathbb{Z}_2$ symmetry [158, 160–173]. The tree-level potential in this model is written as

$$V_{\text{tree}}(\Phi, s) = -\mu_h^2 \Phi^\dagger\Phi + \lambda(\Phi^\dagger\Phi)^2 + \mu_s^2\frac{s^2}{2} + \frac{\lambda_s}{4}s^4 + \frac{\lambda_{hs}}{2}s^2\Phi^\dagger\Phi, \tag{6.7}$$

where $\Phi = (G^+, (h + iG^0)/\sqrt{2})^{\mathrm{T}}$ is the SM Higgs doublet while s is the singlet field. We consider a two-step transition where the singlet gets a non-zero vacuum expectation value at high temperature before the electroweak transition, and require that the global $T = 0$ minimum of the potential lies at the electroweak vacuum $(h, s) = (v, 0)$ with $v = 246\,\text{GeV}$. As usual, the minimisation conditions allow us to relate $\lambda = \mu_h^2/v^2$, $\mu_h^2 = m_h^2/2$, and $\mu_s^2 = m_s^2 - \lambda_{hs}v^2/2$, where m_h and m_s are the masses of the Higgs boson and the scalar singlet. The model is therefore described by the singlet mass m_s and the quartic couplings λ_s and λ_{hs}.

For a given value of singlet quartic coupling λ_s, the parameter space consistent with a first-order PT has a *banana* shape in the plane of m_s–λ_{hs}, such that larger λ_{hs} values are required for larger values of m_s. This shape arises from the requirements that the electroweak vacuum is the global minimum of the potential at $T = 0$, which gives an upper bound on λ_{hs}, and that the singlet gets a non-zero vacuum expectation value before the electroweak transition, which gives a lower bound on λ_{hs} [170]. The strength of the transition is controlled only by the Higgs-portal coupling and larger λ_{hs} values yield stronger

PTs. As the singlet mass increases and due to the *banana* shape of the parameter space, very large λ_{hs} values are required to produce sizable effects. Thus for sufficiently large m_s ($\approx 600\,\text{GeV}$) one reaches the perturbativity limit of the model.

The prospects of detection at colliders have been explored in Refs. [169, 172]. For scalar singlet masses in the range $65\,\text{GeV} < m_s < 300\,\text{GeV}$ the testability of this model by direct and indirect collider signatures is very limited and for this reason, it has been dubbed the *nightmare scenario* [169]. We restrict our attention to the parameter range $65\,\text{GeV} < m_s < 125\,\text{GeV}$ for which λ_{hs} remains well within the perturbativity limit. The simplified $\mathbb{Z}_2$ version of the model we consider also faces theoretical issues. Firstly, the entire parameter space capable of supporting a first-order PT predicts an amount of scalar dark matter (DM) which would already have been seen by direct detection experiments [172]. Secondly, this version predicts the presence of scalar domain walls before the electroweak transition which would influence the nature of the transition [174]. While this is a challenge when building self-contained models we can simply assume minimal changes that would not affect the transition we want to model in a significant way. We can easily add new particles coupled to the singlet which would destabilise the scalar DM and hide it from direct detection experiments while providing a DM candidate with a large enough abundance [175]. Adding even a very small $\mathbb{Z}_2$ breaking term would cause the domain walls to annihilate before the electroweak transition [176]. Thus the problems of the model can be fixed with minimal modifications that would not have a significant impact on the PT dynamics and our parameter reconstruction forecast.

We use the SGWB spectrum produced by the sound waves source (see Sec. 2.2.1) as our benchmark for this model, further choosing $h^2\Omega_2 = 10^{-11}$ and $f_2 = 0.4\,\text{mHz}$. We do not include the signal from MHD turbulence since no analysis so far has been able to predict the value of ε. We implement a modified version of the `CosmoTransitions` code [150] to scan the parameter space of this model. The reconstruction of the SGWB spectrum with LISA is shown in Fig. 12. The corresponding area translated into the parameter space of the model, using the `ChainConsumer` package [177], is shown in Figs. 13 to 15. The first one indicates the parameter space in terms of the scalar mass m_s and portal coupling λ_{hs} while the dependence on the scalar quartic is shown using three benchmark values $\lambda_s = 0.1, 0.5$, and 1 to indicate its impact. Figure 14 shows the entire parameter space populated by first-order PTs by the singlet model for a fixed value of the quartic $\lambda_s = 1$ with the red ellipsis indicating the reconstruction of our SGWB benchmark point. The future experimental sensitivities are shown as violet lines and these correspond to Higgs associated production σ_{Zh}, vector boson fusion (VBF) at a Future Circular Collider (FCC) and the high luminosity Large Hadron Collider (LHC) [55, 178]. Figure 15 again shows the entire parameter space populated by first-order PTs by the singlet model in terms of the geometric parameters of the spectrum Ω_2 and f_2 (see Sec. 2.2.1) with the three panels using each of our three benchmark values $\lambda_s = 0.1, 0.5$, and 1 with the red ellipsis indicating the reconstruction of our benchmark point in each panel.

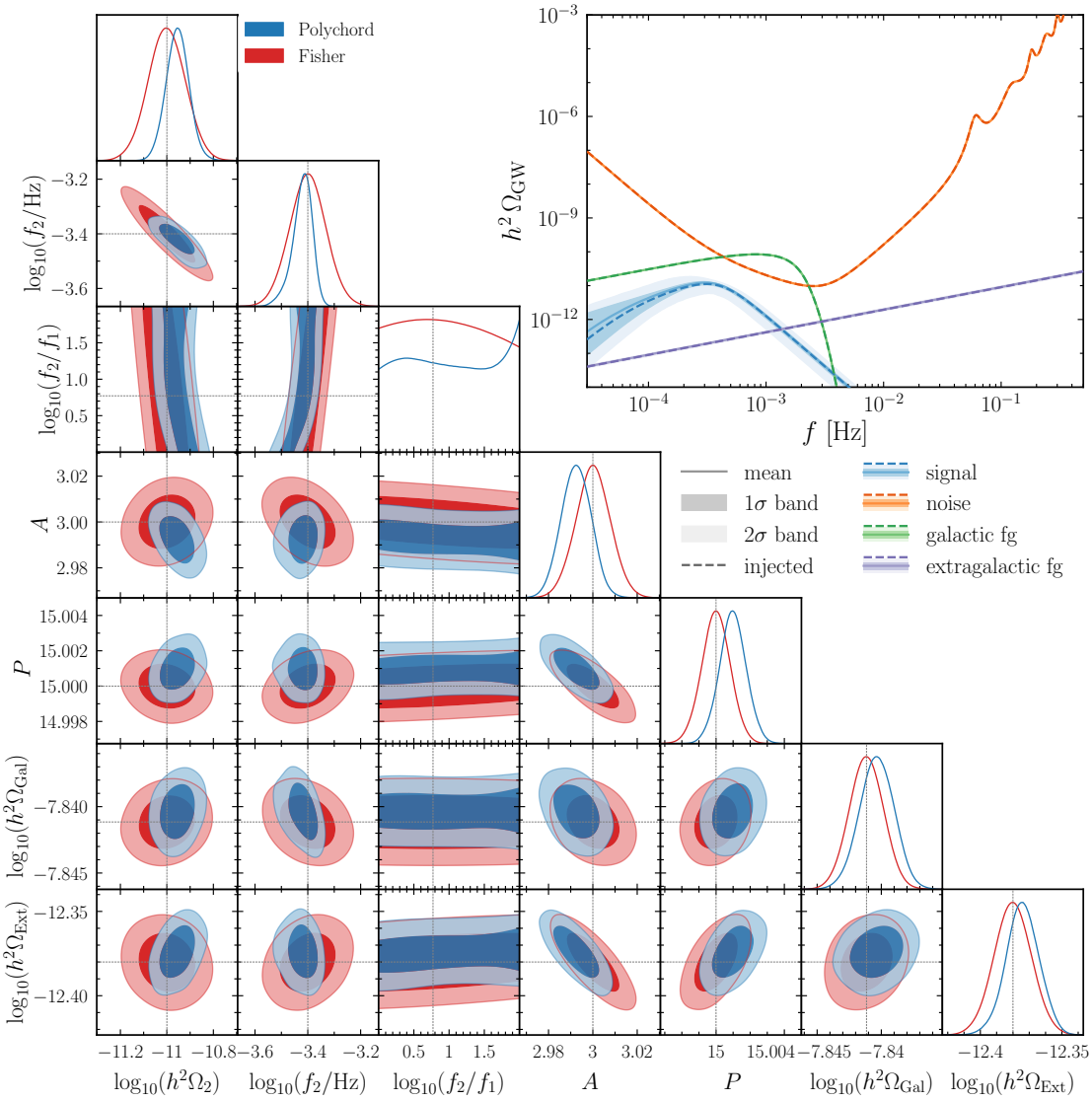

Figure 12: Reconstruction of the sound waves SGWB spectrum with $h^2\Omega_2 = 10^{-11}$ and $f_2 = 0.4\,\text{mHz}$, where the injected separation between the breaks $f_2/f_1 \approx 5.9$ is fixed by $\xi_w \approx 1$ (see Eq. (2.9)).

6.2 Classically conformal U(1)$_{B-L}$ model

The classically conformal U(1)$_{B-L}$ model [179–185] is characterised by the gauge symmetry SU(3)$_c \times$ SU(2)$_L \times$ U(1)$_Y \times$ U(1)$_{B-L}$ and the scalar potential that at tree level is scale-invariant,

$$V = \lambda_H (H^\dagger H)^2 + \lambda_\phi (\phi^\dagger \phi)^2 - \lambda_p (H^\dagger H)(\phi^\dagger \phi)\,, \tag{6.8}$$

where H is the Higgs SU(2)$_L$ doublet and ϕ is a complex scalar charged under U(1)$_{B-L}$. In addition to the SM parameters, this model includes three parameters: the U(1)$_{B-L}$ gauge coupling g_{B-L}, the U(1)$_{B-L}$ gauge boson mass $m_{Z'}$, and the gauge mixing parameter

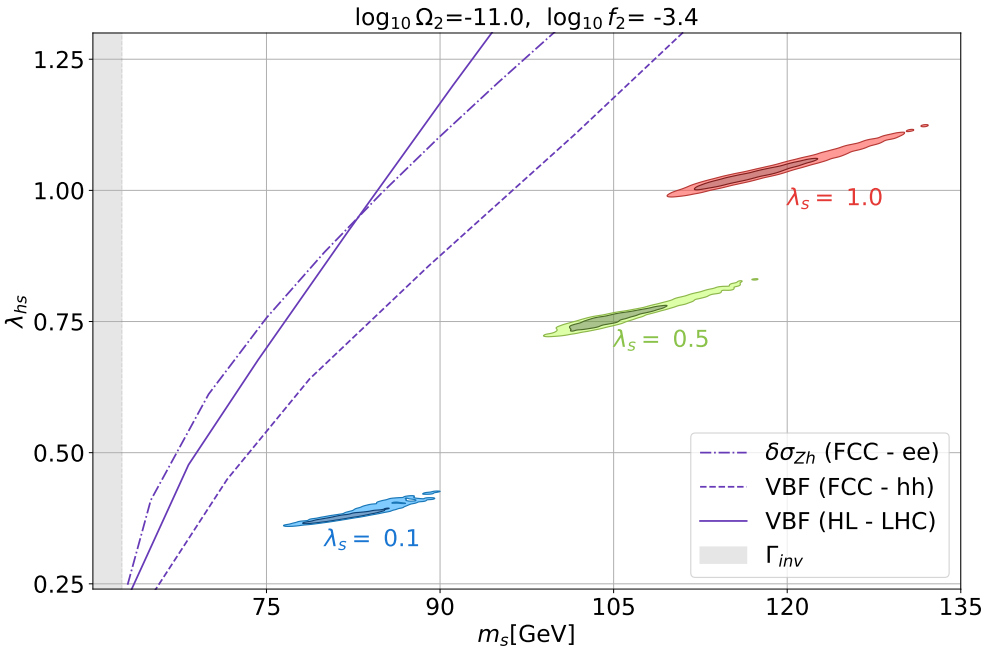

Figure 13: CL contours for different values of singlet quartic couplings. The violet curves are experimental upper limits from the FCC and the high luminosity LHC. The gray shaded region is excluded by the Higgs invisible decay.

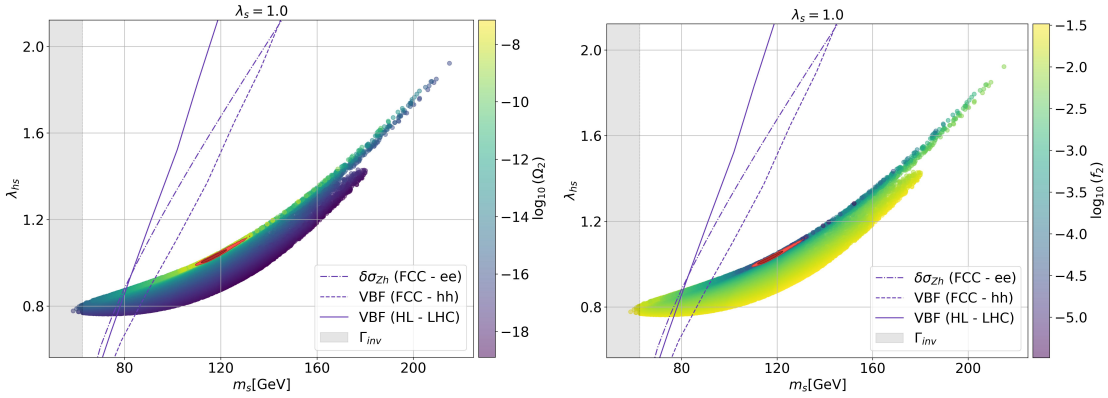

Figure 14: Parameter space of the singlet model. The colour bar displays the magnitude of the SGWB amplitude on the left panel and frequency on the right panel. The red region on top of the banana plots is the reconstructed ellipses.

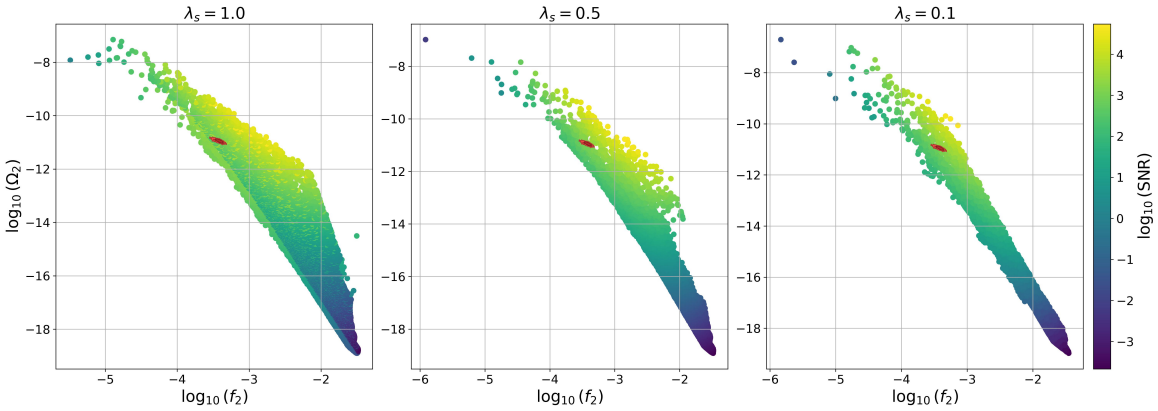

Figure 15: Geometric parameter space generated by the gauge singlet extension for different values of the singlet quartic coupling, displayed on top of each figure. The colour bar displays the SNR computed from the sound waves SGWB template. The small red ellipses on top of each plot are the CL contours.

between $\mathrm{U}(1)_Y$ and $\mathrm{U}(1)_{B-L}$, $\tilde{g}$ (all the quantities are computed at the renormalisation scale corresponding to the vacuum expectation value of ϕ). For $g_{\mathrm{B-L}} \gtrsim 0.1$, which is the region relevant for the GW searches (see Fig. 18), collider searches exclude $m_{Z'} \lesssim 4\,\mathrm{TeV}$ [186]. The PT dynamics is not very sensitive to the mixing parameter and we fix it to $\tilde{g} = -0.5$ that ensures perturbativity and vacuum stability of the model up to the Planck scale [183].

The PT dynamics and the resulting GW signal in this model have been studied, e.g. in Refs. [29, 181–184]. As typical for classically conformal models, the transition can be very strongly supercooled and, consequently, the GW signal arises from the bubble collisions and highly relativistic fluid shells.

We show the posteriors of the reconstruction in terms of the geometric parameters for two benchmark points with $h^2\Omega_b = 4 \times 10^{-12}$ and $f_b = 0.5\,\mathrm{mHz}$, and $h^2\Omega_b = 6 \times 10^{-10}$ and $f_b = 0.2\,\mathrm{Hz}$ in Fig. 16, and the corresponding posterior probability distributions in the model parameter space in Fig. 17. The first benchmark point, shown in the left panels, corresponds to a case where the peak of the SGWB spectrum is close to the best sensitivity of LISA and, consequently, the correlation in the reconstruction of Ω_b and f_b is small. This benchmark case is potentially within the reach of future collider experiments since the Z' gauge boson is not very heavy. For example, Ref. [183] estimated that the FCC could probe Z' masses up to 45 TeV [187].

The second benchmark point, shown in the right panel of Figs. 16 and 17, instead is at a much higher Z' mass and cannot be probed in colliders. In this case, the SGWB spectrum peak is in the high-frequency tail of the LISA sensitivity. Therefore, the reconstructed Ω_b and f_b are highly correlated. The SGWB spectrum in this case is, however, also in the reach of ET that will probe the opposite side of the GW spectrum than LISA, and combining these results will break the degeneracy in the reconstruction of Ω_b and f_b, consequently shrinking the posterior regions in the model parameter space. In Fig. 17, we show the

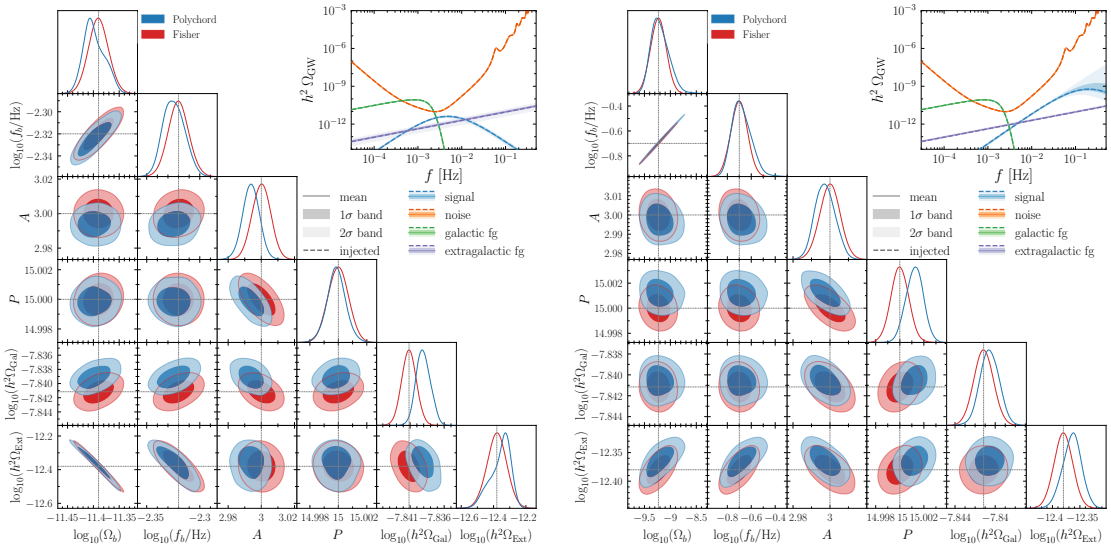

Figure 16: Reconstruction of the PT SGWB spectrum from bubble collisions and highly relativistic fluid shells with $h^2\Omega_b = 4\times10^{-12}$ and $f_b = 0.5\,\mathrm{mHz}$ (left), and $h^2\Omega_b = 6\times10^{-10}$ and $f_b = 0.2\,\mathrm{Hz}$ (right).

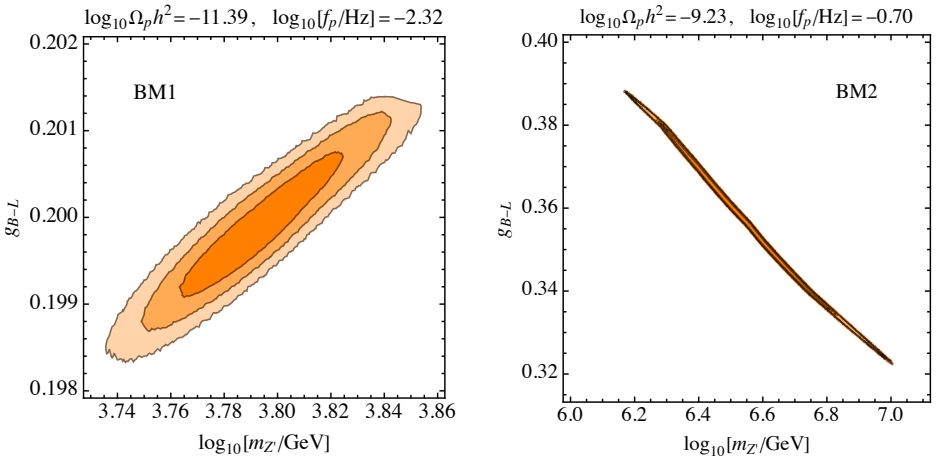

Figure 17: The shaded regions show the 1σ, 2σ, and 3σ CL regions of LISA in the $\mathrm{U}(1)_{B-L}$ model parameter space for the bubble collisions SGWB signal (gauged U(1) case) with the peak amplitude and frequency given above the plots.

peak amplitude and frequency of the SGWB spectrum and benchmark points on a broader range of the model parameters.

7 Conclusions

After the presence of an SGWB has been identified in the LISA data stream, an adequate interpretation of the SGWB origin must be based on templates, linking the frequency shape of the SGWB signal to the parameters of the sources. In the present and companion papers,

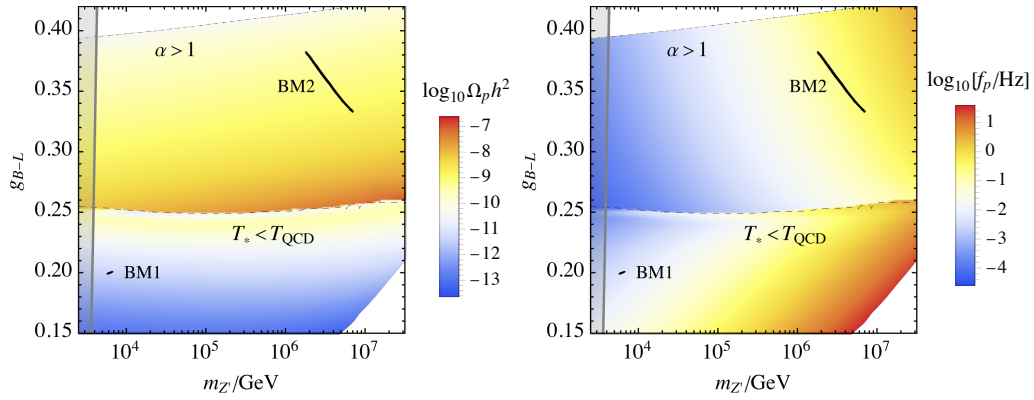

Figure 18: The colour coding shows in the left panel the peak amplitude and in the right panel the peak frequency of the SGWB spectrum in the $\mathrm{U}(1)_{B-L}$ model. In the white region at the top, $\alpha < 1$. Below the dashed curve, the transition is triggered by the confinement of quantum chromodynamics (QCD) and the gray region on the left is excluded by collider searches of Z'.

focusing on cosmic strings [114] and phenomena linked to inflation [115], we have selected a set of SGWB templates suitable for this purpose, and prototyped the LISA template-based data analysis pipeline in `SGWBinner`, a code which has been used and tested for agnostic SGWB reconstructions in previous LISA-related analyses [112, 113]. We forecast the detection and reconstruction of these sources. Although developed under simplifying assumptions, this program allows us to identify and quantify the bottlenecks that the LISA community will have to tackle in the next years.

In the present paper, we have reported the PT-related part of the above program. As a first step, we have designed and implemented the templates for the main first-order PT mechanisms sourcing an SGWB, namely bubble collisions, sound waves and (MHD) turbulence. The former typically dominates the SGWB signal in BSM scenarios where the first-order PT is extremely strong, while the others emerge in the case of mid-strength transition scenarios (weak transitions rarely lead to an observable signal at current GW detectors). We have then adapted the `SGWBinner` to simulate data of the PT SGWB together with the astrophysical foregrounds and instrumental noises, and then forecast their parameter estimation. Crucially, the models used for the injection perfectly match the templates of the noise, astrophysical foregrounds, and SGWBs employed in the reconstruction. The forecasts then quantify the SGWB parameter estimation that LISA will perform if, at the time LISA flies, the community will have shrunk the theoretical and experimental uncertainties below the statistical errors reconstructed in our analysis. In this sense, all our templates, although representing the current state of the art combining simplicity and accuracy, must be understood as placeholders of the precise templates that the community is urged to build in the next decade. On the other hand, our qualitative results are not expected to change if, as expected, the future templates will be similar to the current ones.

We have performed an analysis of detection prospects as a function of the SGWB template parameters, showing that for signals peaking around 3 mHz, the relative errors (at 68 % CL) in the parameter reconstruction are around or below 10 % if the signal's peak has an amplitude of $\Omega_p \gtrsim 10^{-12}$. This result, already remarkable on its own, does not leverage the yearly modulation of the Galactic foreground; if one optimistically assumes that this feature allows complete removal of this astrophysical foreground, the above-mentioned lower bound decreases to $\Omega_p \gtrsim 10^{-13}$. These two bounds have been obtained with the `SGWBinner` code accurately sampling the full likelihood. We have verified that the (fast and simple) Fisher approximation would lead to similar values for these two bounds. The observed tendency is that, in the reconstruction of the typical first-order PT signals, the values of the relative errors obtained with the Fisher approximation and with the full likelihood are in reasonably good agreement whenever they are about or below ten percent, while they quickly depart at higher values.

We have followed two approaches in the implementation of the first-order PT templates. In one case we have parameterised the templates in terms of parameters that describe the geometrical features of the SGWB signal frequency shape, i.e. the amplitude, frequency of the breaks, and the tilts of the spectrum. This parameterisation reduces the parameter degeneracies and, in turn, simplifies the sampling of the likelihood. In the second case, we have expressed the templates as a function of the thermodynamic parameters, describing the physics behind the signal such as the temperature of the transition, its duration, and the kinetic energy fraction. This implies parameter degeneracies but allows a more direct physics interpretation of the signal. For some benchmark signals with a satisfactory parameter reconstruction, we have verified that using the thermodynamic-parameter template leads to posteriors that are similar to those obtained by first using the geometric-parameter template and then converting the sampler chains into thermodynamic parameters. This is, however, only true provided one takes care to discard the regions corresponding to values of the geometric parameters leading to unphysical values for the thermodynamic ones.

The physics interpretation of the detection of (or upper bound on) the first-order PT SGWB cannot be limited to the thermodynamic parameters. Here we have proven that the SGWB reconstruction can lead to compelling bounds on particle physics models. Currently, performing parameter inference directly between a model Lagrangian and the LISA SGWB data is prohibitive, as calculating the PT (thermodynamic) parameters from a Lagrangian requires numerical tools that are not sufficiently automatised, fast or stable. We have shown how to circumvent the problem and applied the method to some concrete examples of BSM scenarios, namely the $\mathbb{Z}_2$-singlet extension and the scale-invariant $U(1)_{\mathrm{B-L}}$ extension. In the former model, with the detection of a first-order PT SGWB of amplitude $h^2\Omega_p \sim 10^{-11}$, LISA can constrain the singlet mass and the Higgs-singlet coupling with an accuracy of about ten percent (for a known singlet quartic coupling). In the latter model, with a similar first-order PT SGWB detection, LISA could bind the new gauge coupling with a relative error of one percent. The synergy with current and future particle physics experiments is manifest.

The synergy with other GW detectors is instead less clear. We have found that the joint detection of the same first-order PT signal both at LISA and SKA is unlikely. The

prospects are more optimistic with ET. The observation in both LISA and ET would require first-order PT signals with a peak frequency at $f_p \sim 0.1\,\mathrm{Hz}$, and peak amplitude $\Omega_p \gtrsim 10^{-10}$ for a vacuum-dominated transition and $\Omega_p \gtrsim 10^{-9}$ for sound waves and turbulence. This signal would indicate particle physics scenarios with a symmetry scale quite above the electroweak one. However, our synergy estimates with SKA and ET are likely optimistic, as they derive from SNR computations that do not account for technical limitations such as the presence of foregrounds in SKA and ET frequency bands. They can be considered as indicative of a possible synergistic detection of the first-order PT SGWB at SKA and ET, however, reaching robust conclusions would require dedicated studies.

In conclusion, the detection of the SGWB by LISA holds the potential for a historical, groundbreaking discovery. The precise reconstruction of this signal would further amplify the scientific impact of the observation. Our forecasts and their potential interpretations have highlighted this impact on scenarios featuring a first-order PT.

However, these results hinge on our simplifying assumptions concerning several theoretical and experimental issues. We assume that the data stream can be precisely cleaned from transient noise and signals. For the noise, foregrounds and SGWB, we use the same templates for the injection and reconstruction, meaning that we neglect the systematic errors due to the current theoretical and experimental uncertainties on the noise and signals. Thus, our results constitute an approximate upper bound for such systematic error: above this bound, the PT SGWB reconstruction will not be limited by the instrument itself but by the insufficient knowledge of its actual sensitivity, the theoretical understanding of the SGWB sources, and the data analysis capabilities. Ultimately, we intend this paper to serve as a call to action for the worldwide scientific community to address these challenges and unleash the full potential of LISA.

Acknowledgments

We acknowledge the LISA Cosmology Group members for seminal discussions. We especially thank the authors of Refs. [114, 115] for the collaborative developments of the `SGWBinner` code shared among this and those works. CC is supported by the Swiss National Science Foundation (SNSF Project Funding grant 212125). RJ is supported by JSPS KAKENHI Grant Numbers 23K17687 and 23K19048. The work of ML is supported by the Polish National Agency for Academic Exchange within the Polish Returns Programme under agreement PPN/PPO/2020/1/00013/U/00001 and the Polish National Science Center grant 2018/31/D/ST2/02048. EM acknowledges support from the Minerva foundation during the initial stage of the project. MM received support from the Swedish Research Council (Vetenskapsrådet) through contract no. 2017-03934. GN is partly supported by the grant Project. No. 302640 funded by the Research Council of Norway. MP acknowledges the hospitality of Imperial College London, which provided office space during some parts of this project. ARP is supported by the Swiss National Science Foundation (SNSF Ambizione grant no. 182044). VV is supported by the European Union's Horizon Europe research and innovation program under the Marie Skłodowska-Curie grant agreement

No. 101065736, and by the Estonian Research Council grants PRG803, RVTT3 and RVTT7 and the Center of Excellence program TK202.

Acronyms

BPL broken power law
BSM beyond the SM
CGB Compact Galactic Binary
CL confidence level
CMB cosmic microwave background
DBPL double broken power law
DM dark matter
ESA European Space Agency
ET Einstein Telescope
FCC Future Circular Collider
GW gravitational wave
KAGRA Kamioka Gravitational Wave Detector
LHC Large Hadron Collider
LIGO Laser Interferometer Gravitational Wave Observatory
LISA Laser Interferometer Space Antenna
LVK LIGO/Virgo/KAGRA
MHD magnetohydrodynamic
NSB neutron-star binary
OMS optical measurement system
PT phase transition
PTA Pulsar Timing Array
QCD quantum chromodynamics
SGWB stochastic GW background
SKA Square Kilometre Array
SM Standard Model
SNR signal-to-noise ratio
SOBHB stellar-origin black hole binary
TDI time delay interferometry
TM test mass
VBF vector boson fusion

References

[1] LIGO Scientific, Virgo collaboration, *Observation of Gravitational Waves from a Binary Black Hole Merger*, *Phys. Rev. Lett.* **116** (2016) 061102 [1602.03837].

[2] LIGO Scientific, Virgo collaboration, *GW151226: Observation of Gravitational Waves from a 22-Solar-Mass Binary Black Hole Coalescence*, *Phys. Rev. Lett.* **116** (2016) 241103 [1606.04855].

[3] LIGO Scientific, VIRGO collaboration, *GW170104: Observation of a 50-Solar-Mass Binary Black Hole Coalescence at Redshift 0.2*, *Phys. Rev. Lett.* **118** (2017) 221101 [1706.01812].

[4] LIGO Scientific, Virgo collaboration, *GW170608: Observation of a 19-solar-mass Binary Black Hole Coalescence*, *Astrophys. J. Lett.* **851** (2017) L35 [1711.05578].

[5] LIGO Scientific, Virgo collaboration, *GW170814: A Three-Detector Observation of Gravitational Waves from a Binary Black Hole Coalescence*, *Phys. Rev. Lett.* **119** (2017) 141101 [1709.09660].

[6] LIGO Scientific, Virgo collaboration, *GWTC-1: A Gravitational-Wave Transient Catalog of Compact Binary Mergers Observed by LIGO and Virgo during the First and Second Observing Runs*, *Phys. Rev. X* **9** (2019) 031040 [1811.12907].

[7] LIGO Scientific, Virgo collaboration, *GWTC-2: Compact Binary Coalescences Observed by LIGO and Virgo During the First Half of the Third Observing Run*, *Phys. Rev. X* **11** (2021) 021053 [2010.14527].

[8] LIGO Scientific, VIRGO collaboration, *GWTC-2.1: Deep Extended Catalog of Compact Binary Coalescences Observed by LIGO and Virgo During the First Half of the Third Observing Run*, 2108.01045.

[9] KAGRA, VIRGO, LIGO Scientific collaboration, *GWTC-3: Compact Binary Coalescences Observed by LIGO and Virgo during the Second Part of the Third Observing Run*, *Phys. Rev. X* **13** (2023) 041039 [2111.03606].

[10] NANOGrav collaboration, *The NANOGrav 15 yr Data Set: Evidence for a Gravitational-wave Background*, *Astrophys. J. Lett.* **951** (2023) L8 [2306.16213].

[11] EPTA collaboration, *The second data release from the European Pulsar Timing Array - I. The dataset and timing analysis*, *Astron. Astrophys.* **678** (2023) A48 [2306.16224].

[12] D. J. Reardon et al., *Search for an Isotropic Gravitational-wave Background with the Parkes Pulsar Timing Array*, *Astrophys. J. Lett.* **951** (2023) L6 [2306.16215].

[13] H. Xu et al., *Searching for the Nano-Hertz Stochastic Gravitational Wave Background with the Chinese Pulsar Timing Array Data Release I*, *Res. Astron. Astrophys.* **23** (2023) 075024 [2306.16216].

[14] NANOGrav collaboration, *The NANOGrav 15 yr Data Set: Constraints on Supermassive Black Hole Binaries from the Gravitational-wave Background*, *Astrophys. J. Lett.* **952** (2023) L37 [2306.16220].

[15] EPTA collaboration, *The second data release from the European Pulsar Timing Array: V. Implications for massive black holes, dark matter and the early Universe*, 2306.16227.

[16] J. Ellis, M. Fairbairn, G. Hütsi, J. Raidal, J. Urrutia, V. Vaskonen et al., *Gravitational Waves from SMBH Binaries in Light of the NANOGrav 15-Year Data*, 2306.17021.

[17] NANOGrav collaboration, *The NANOGrav 15 yr Data Set: Search for Signals from New Physics*, *Astrophys. J. Lett.* **951** (2023) L11 [2306.16219].

[18] D. G. Figueroa, M. Pieroni, A. Ricciardone and P. Simakachorn, *Cosmological Background Interpretation of Pulsar Timing Array Data*, 2307.02399.

[19] J. Ellis, M. Fairbairn, G. Franciolini, G. Hütsi, A. Iovino, M. Lewicki et al., *What is the source of the PTA GW signal?*, 2308.08546.

[20] E. Madge, E. Morgante, C. Puchades-Ibáñez, N. Ramberg, W. Ratzinger, S. Schenk et al., *Primordial gravitational waves in the nano-Hertz regime and PTA data — towards solving the GW inverse problem*, *JHEP* **10** (2023) 171 [2306.14856].

[21] C. Caprini and D. G. Figueroa, *Cosmological Backgrounds of Gravitational Waves*, *Class. Quant. Grav.* **35** (2018) 163001 [1801.04268].

[22] LISA Cosmology Working Group collaboration, *Cosmology with the Laser Interferometer Space Antenna*, *Living Rev. Rel.* **26** (2023) 5 [2204.05434].

[23] A. Kosowsky, M. S. Turner and R. Watkins, *Gravitational radiation from colliding vacuum bubbles*, *Phys. Rev. D* **45** (1992) 4514.

[24] A. Kosowsky and M. S. Turner, *Gravitational radiation from colliding vacuum bubbles: envelope approximation to many bubble collisions*, *Phys. Rev. D* **47** (1993) 4372 [astro-ph/9211004].

[25] S. J. Huber and T. Konstandin, *Gravitational Wave Production by Collisions: More Bubbles*, *JCAP* **09** (2008) 022 [0806.1828].

[26] D. Cutting, M. Hindmarsh and D. J. Weir, *Gravitational waves from vacuum first-order phase transitions: from the envelope to the lattice*, *Phys. Rev. D* **97** (2018) 123513 [1802.05712].

[27] D. Cutting, E. G. Escartin, M. Hindmarsh and D. J. Weir, *Gravitational waves from vacuum first order phase transitions II: from thin to thick walls*, *Phys. Rev. D* **103** (2021) 023531 [2005.13537].

[28] M. Lewicki and V. Vaskonen, *Gravitational wave spectra from strongly supercooled phase transitions*, *Eur. Phys. J. C* **80** (2020) 1003 [2007.04967].

[29] J. Ellis, M. Lewicki and V. Vaskonen, *Updated predictions for gravitational waves produced in a strongly supercooled phase transition*, *JCAP* **11** (2020) 020 [2007.15586].

[30] M. Lewicki and V. Vaskonen, *Gravitational waves from colliding vacuum bubbles in gauge theories*, *Eur. Phys. J. C* **81** (2021) 437 [2012.07826].

[31] M. Lewicki and V. Vaskonen, *Gravitational waves from bubble collisions and fluid motion in strongly supercooled phase transitions*, *Eur. Phys. J. C* **83** (2023) 109 [2208.11697].

[32] M. Kamionkowski, A. Kosowsky and M. S. Turner, *Gravitational radiation from first order phase transitions*, *Phys. Rev. D* **49** (1994) 2837 [astro-ph/9310044].

[33] C. Caprini et al., *Science with the space-based interferometer eLISA. II: Gravitational waves from cosmological phase transitions*, *JCAP* **04** (2016) 001 [1512.06239].

[34] C. Caprini et al., *Detecting gravitational waves from cosmological phase transitions with LISA: an update*, *JCAP* **03** (2020) 024 [1910.13125].

[35] M. Hindmarsh, S. J. Huber, K. Rummukainen and D. J. Weir, *Gravitational waves from the sound of a first order phase transition*, *Phys. Rev. Lett.* **112** (2014) 041301 [1304.2433].

[36] M. Hindmarsh, S. J. Huber, K. Rummukainen and D. J. Weir, *Numerical simulations of acoustically generated gravitational waves at a first order phase transition*, *Phys. Rev. D* **92** (2015) 123009 [1504.03291].

[37] M. Hindmarsh, S. J. Huber, K. Rummukainen and D. J. Weir, *Shape of the acoustic gravitational wave power spectrum from a first order phase transition*, *Phys. Rev. D* **96** (2017) 103520 [1704.05871].

[38] D. Cutting, M. Hindmarsh and D. J. Weir, *Vorticity, kinetic energy, and suppressed gravitational wave production in strong first order phase transitions*, *Phys. Rev. Lett.* **125** (2020) 021302 [1906.00480].

[39] M. Hindmarsh and M. Hijazi, *Gravitational waves from first order cosmological phase transitions in the Sound Shell Model*, *JCAP* **12** (2019) 062 [1909.10040].

[40] R. Jinno, T. Konstandin and H. Rubira, *A hybrid simulation of gravitational wave production in first-order phase transitions*, *JCAP* **04** (2021) 014 [2010.00971].

[41] R. Jinno, T. Konstandin, H. Rubira and I. Stomberg, *Higgsless simulations of cosmological phase transitions and gravitational waves*, *JCAP* **02** (2023) 011 [2209.04369].

[42] A. Kosowsky, A. Mack and T. Kahniashvili, *Gravitational radiation from cosmological turbulence*, *Phys. Rev. D* **66** (2002) 024030 [astro-ph/0111483].

[43] A. D. Dolgov, D. Grasso and A. Nicolis, *Relic backgrounds of gravitational waves from cosmic turbulence*, *Phys. Rev. D* **66** (2002) 103505 [astro-ph/0206461].

[44] G. Gogoberidze, T. Kahniashvili and A. Kosowsky, *The Spectrum of Gravitational Radiation from Primordial Turbulence*, *Phys. Rev. D* **76** (2007) 083002 [0705.1733].

[45] T. Kahniashvili, L. Campanelli, G. Gogoberidze, Y. Maravin and B. Ratra, *Gravitational Radiation from Primordial Helical Inverse Cascade MHD Turbulence*, *Phys. Rev. D* **78** (2008) 123006 [0809.1899].

[46] C. Caprini, R. Durrer and G. Servant, *The stochastic gravitational wave background from turbulence and magnetic fields generated by a first-order phase transition*, *JCAP* **12** (2009) 024 [0909.0622].

[47] A. Brandenburg, T. Kahniashvili, S. Mandal, A. Roper Pol, A. G. Tevzadze and T. Vachaspati, *Evolution of hydromagnetic turbulence from the electroweak phase transition*, *Phys. Rev. D* **96** (2017) 123528 [1711.03804].

[48] P. Niksa, M. Schlederer and G. Sigl, *Gravitational Waves produced by Compressible MHD Turbulence from Cosmological Phase Transitions*, *Class. Quant. Grav.* **35** (2018) 144001 [1803.02271].

[49] A. Roper Pol, S. Mandal, A. Brandenburg, T. Kahniashvili and A. Kosowsky, *Numerical simulations of gravitational waves from early-universe turbulence*, *Phys. Rev. D* **102** (2020) 083512 [1903.08585].

[50] T. Kahniashvili, A. Brandenburg, G. Gogoberidze, S. Mandal and A. Roper Pol, *Circular polarization of gravitational waves from early-Universe helical turbulence*, *Phys. Rev. Res.* **3** (2021) 013193 [2011.05556].

[51] A. Roper Pol, S. Mandal, A. Brandenburg and T. Kahniashvili, *Polarization of gravitational waves from helical MHD turbulent sources*, *JCAP* **04** (2022) 019 [2107.05356].

[52] A. Roper Pol, C. Caprini, A. Neronov and D. Semikoz, *Gravitational wave signal from primordial magnetic fields in the Pulsar Timing Array frequency band*, *Phys. Rev. D* **105** (2022) 123502 [2201.05630].

[53] P. Auclair, C. Caprini, D. Cutting, M. Hindmarsh, K. Rummukainen, D. A. Steer et al., *Generation of gravitational waves from freely decaying turbulence*, *JCAP* **09** (2022) 029 [2205.02588].

[54] A. Roper Pol, A. Neronov, C. Caprini, T. Boyer and D. Semikoz, *LISA and γ-ray telescopes as multi-messenger probes of a first-order cosmological phase transition*, 2307.10744.

[55] J. Ellis, M. Lewicki and J. M. No, *On the Maximal Strength of a First-Order Electroweak Phase Transition and its Gravitational Wave Signal*, *JCAP* **04** (2019) 003 [1809.08242].

[56] J. Ellis, M. Lewicki and J. M. No, *Gravitational waves from first-order cosmological phase transitions: lifetime of the sound wave source*, *JCAP* **07** (2020) 050 [2003.07360].

[57] A. Roper Pol, S. Procacci and C. Caprini, *Characterization of the gravitational wave spectrum from sound waves within the sound shell model*, 2308.12943.

[58] LISA collaboration, *Laser Interferometer Space Antenna*, 1702.00786.

[59] C. Caprini, D. G. Figueroa, R. Flauger, G. Nardini, M. Peloso, M. Pieroni et al., *Reconstructing the spectral shape of a stochastic gravitational wave background with LISA*, *JCAP* **11** (2019) 017 [1906.09244].

[60] R. Flauger, N. Karnesis, G. Nardini, M. Pieroni, A. Ricciardone and J. Torrado, *Improved reconstruction of a stochastic gravitational wave background with LISA*, *JCAP* **01** (2021) 059 [2009.11845].

[61] C. Gowling and M. Hindmarsh, *Observational prospects for phase transitions at LISA: Fisher matrix analysis*, *JCAP* **10** (2021) 039 [2106.05984].

[62] F. Giese, T. Konstandin and J. van de Vis, *Finding sound shells in LISA mock data using likelihood sampling*, *JCAP* **11** (2021) 002 [2107.06275].

[63] G. Boileau, N. Christensen, C. Gowling, M. Hindmarsh and R. Meyer, *Prospects for LISA to detect a gravitational-wave background from first order phase transitions*, *JCAP* **02** (2023) 056 [2209.13277].

[64] C. Gowling, M. Hindmarsh, D. C. Hooper and J. Torrado, *Reconstructing physical parameters from template gravitational wave spectra at LISA: first order phase transitions*, *JCAP* **04** (2023) 061 [2209.13551].

[65] R. Sharma, J. Dahl, A. Brandenburg and M. Hindmarsh, *Shallow relic gravitational wave spectrum with acoustic peak*, *JCAP* **12** (2023) 042 [2308.12916].

[66] M. Hindmarsh, *Sound shell model for acoustic gravitational wave production at a first-order phase transition in the early Universe*, *Phys. Rev. Lett.* **120** (2018) 071301 [1608.04735].

[67] D. Croon, O. Gould, P. Schicho, T. V. I. Tenkanen and G. White, *Theoretical uncertainties for cosmological first-order phase transitions*, *JHEP* **04** (2021) 055 [2009.10080].

[68] P. M. Schicho, T. V. I. Tenkanen and J. Österman, *Robust approach to thermal resummation: Standard Model meets a singlet*, *JHEP* **06** (2021) 130 [2102.11145].

[69] P. Athron, C. Balazs, A. Fowlie, L. Morris, G. White and Y. Zhang, *How arbitrary are perturbative calculations of the electroweak phase transition?*, *JHEP* **01** (2023) 050 [2208.01319].

[70] O. Gould and C. Xie, *Higher orders for cosmological phase transitions: a global study in a Yukawa model*, *JHEP* **12** (2023) 049 [2310.02308].

[71] O. Gould and J. Hirvonen, *Effective field theory approach to thermal bubble nucleation*, *Phys. Rev. D* **104** (2021) 096015 [2108.04377].

[72] P. Schicho, T. V. I. Tenkanen and G. White, *Combining thermal resummation and gauge invariance for electroweak phase transition*, *JHEP* **11** (2022) 047 [2203.04284].

[73] J. Löfgren, M. J. Ramsey-Musolf, P. Schicho and T. V. I. Tenkanen, *Nucleation at Finite Temperature: A Gauge-Invariant Perturbative Framework*, *Phys. Rev. Lett.* **130** (2023) 251801 [2112.05472].

[74] J. Hirvonen, J. Löfgren, M. J. Ramsey-Musolf, P. Schicho and T. V. I. Tenkanen, *Computing the gauge-invariant bubble nucleation rate in finite temperature effective field theory*, *JHEP* **07** (2022) 135 [2112.08912].

[75] A. Ekstedt, P. Schicho and T. V. I. Tenkanen, *DRalgo: A package for effective field theory approach for thermal phase transitions*, *Comput. Phys. Commun.* **288** (2023) 108725 [2205.08815].

[76] A. Ekstedt, O. Gould and J. Löfgren, *Radiative first-order phase transitions to next-to-next-to-leading order*, *Phys. Rev. D* **106** (2022) 036012 [2205.07241].

[77] A. Ekstedt, O. Gould and J. Hirvonen, *BubbleDet: a Python package to compute functional determinants for bubble nucleation*, *JHEP* **12** (2023) 056 [2308.15652].

[78] O. Gould and T. V. I. Tenkanen, *Perturbative effective field theory expansions for cosmological phase transitions*, *JHEP* **01** (2024) 048 [2309.01672].

[79] L. Giombi and M. Hindmarsh, *General relativistic bubble growth in cosmological phase transitions*, 2307.12080.

[80] Q. Baghi, N. Karnesis, J.-B. Bayle, M. Besançon and H. Inchauspé, *Uncovering gravitational-wave backgrounds from noises of unknown shape with LISA*, *JCAP* **04** (2023) 066 [2302.12573].

[81] M. Muratore, J. Gair and L. Speri, *Impact of the noise knowledge uncertainty for the science exploitation of cosmological and astrophysical stochastic gravitational wave background with LISA*, 2308.01056.

[82] F. Pozzoli, R. Buscicchio, C. J. Moore, F. Haardt and A. Sesana, *A weakly-parametric approach to stochastic background inference in LISA*, 2311.12111.

[83] G. Boileau, N. Christensen, R. Meyer and N. J. Cornish, *Spectral separation of the stochastic gravitational-wave background for LISA: Observing both cosmological and astrophysical backgrounds*, *Phys. Rev. D* **103** (2021) 103529 [2011.05055].

[84] M. Pieroni and E. Barausse, *Foreground cleaning and template-free stochastic background extraction for LISA*, *JCAP* **07** (2020) 021 [2004.01135].

[85] G. Boileau, A. Lamberts, N. J. Cornish and R. Meyer, *Spectral separation of the stochastic gravitational-wave background for LISA in the context of a modulated Galactic foreground*, *Mon. Not. Roy. Astron. Soc.* **508** (2021) 803 [2105.04283].

[86] M. Lewicki and V. Vaskonen, *Impact of LIGO-Virgo black hole binaries on gravitational wave background searches*, *Eur. Phys. J. C* **83** (2023) 168 [2111.05847].

[87] D. Racco and D. Poletti, *Precision cosmology with primordial GW backgrounds in presence of astrophysical foregrounds*, *JCAP* **04** (2023) 054 [2212.06602].

[88] J. R. Espinosa, T. Konstandin, J. M. No and G. Servant, *Energy Budget of Cosmological First-order Phase Transitions*, *JCAP* **06** (2010) 028 [1004.4187].

[89] E. W. Kolb and M. S. Turner, *The Early Universe*, vol. 69. 1990, 10.1201/9780429492860.

[90] T. Konstandin, *Gravitational radiation from a bulk flow model*, *JCAP* **03** (2018) 047 [1712.06869].

[91] D. Bodeker and G. D. Moore, *Can electroweak bubble walls run away?*, *JCAP* **05** (2009) 009 [0903.4099].

[92] A. Kosowsky, M. S. Turner and R. Watkins, *Gravitational waves from first order cosmological phase transitions*, *Phys. Rev. Lett.* **69** (1992) 2026.

[93] D. J. Weir, *Revisiting the envelope approximation: gravitational waves from bubble collisions*, *Phys. Rev. D* **93** (2016) 124037 [1604.08429].

[94] R. Jinno and M. Takimoto, *Gravitational waves from bubble collisions: An analytic derivation*, *Phys. Rev. D* **95** (2017) 024009 [1605.01403].

[95] H. L. Child and J. T. Giblin, Jr., *Gravitational Radiation from First-Order Phase Transitions*, *JCAP* **10** (2012) 001 [1207.6408].

[96] R. Jinno, T. Konstandin and M. Takimoto, *Relativistic bubble collisions—a closer look*, *JCAP* **09** (2019) 035 [1906.02588].

[97] R. Jinno and M. Takimoto, *Gravitational waves from bubble dynamics: Beyond the Envelope*, *JCAP* **01** (2019) 060 [1707.03111].

[98] D. Bodeker and G. D. Moore, *Electroweak Bubble Wall Speed Limit*, *JCAP* **05** (2017) 025 [1703.08215].

[99] S. Höche, J. Kozaczuk, A. J. Long, J. Turner and Y. Wang, *Towards an all-orders calculation of the electroweak bubble wall velocity*, *JCAP* **03** (2021) 009 [2007.10343].

[100] A. Azatov, M. Vanvlasselaer and W. Yin, *Baryogenesis via relativistic bubble walls*, *JHEP* **10** (2021) 043 [2106.14913].

[101] Y. Gouttenoire, R. Jinno and F. Sala, *Friction pressure on relativistic bubble walls*, *JHEP* **05** (2022) 004 [2112.07686].

[102] A. Azatov, G. Barni, R. Petrossian-Byrne and M. Vanvlasselaer, *Quantisation Across Bubble Walls and Friction*, 2310.06972.

[103] R. Jinno, H. Seong, M. Takimoto and C. M. Um, *Gravitational waves from first-order phase transitions: Ultra-supercooled transitions and the fate of relativistic shocks*, *JCAP* **10** (2019) 033 [1905.00899].

[104] M. Breitbach, J. Kopp, E. Madge, T. Opferkuch and P. Schwaller, *Dark, Cold, and Noisy: Constraining Secluded Hidden Sectors with Gravitational Waves*, *JCAP* **07** (2019) 007 [1811.11175].

[105] M. Fairbairn, E. Hardy and A. Wickens, *Hearing without seeing: gravitational waves from hot and cold hidden sectors*, *JHEP* **07** (2019) 044 [1901.11038].

[106] C. Caprini, R. Durrer, T. Konstandin and G. Servant, *General Properties of the Gravitational Wave Spectrum from Phase Transitions*, *Phys. Rev. D* **79** (2009) 083519 [0901.1661].

[107] A. Kurganov and E. Tadmor, *New High-Resolution Central Schemes for Nonlinear Conservation Laws and Convection–Diffusion Equations*, *J. Comput. Phys.* **160** (2000) 241.

[108] C. Caprini, R. Jinno, T. Konstandin, A. Roper Pol, H. Rubira and I. Stomberg, *To appear*, .

[109] F. Giese, T. Konstandin and J. van de Vis, *Model-independent energy budget of cosmological first-order phase transitions—A sound argument to go beyond the bag model*, *JCAP* **07** (2020) 057 [2004.06995].

[110] F. Giese, T. Konstandin, K. Schmitz and J. van de Vis, *Model-independent energy budget for LISA*, *JCAP* **01** (2021) 072 [2010.09744].

[111] R. Banerjee and K. Jedamzik, *The Evolution of cosmic magnetic fields: From the very early universe, to recombination, to the present*, *Phys. Rev. D* **70** (2004) 123003 [astro-ph/0410032].

[112] P. A. Seoane et al., *The effect of mission duration on LISA science objectives*, *Gen. Rel. Grav.* **54** (2022) 3 [2107.09665].

[113] M. Colpi et al., *LISA Definition Study Report*, 2402.07571.

[114] LISA Cosmology Working Group collaboration, *Gravitational waves from cosmic strings in LISA: reconstruction pipeline and science interpretation*, to appear.

[115] LISA Cosmology Working Group collaboration, *Gravitational waves from inflation in LISA: reconstruction pipeline and science interpretation*, to appear.

[116] M. Tinto and S. V. Dhurandhar, *Time-delay interferometry*, *Living Rev. Rel.* **24** (2021) 1.

[117] M. Tinto and J. W. Armstrong, *Cancellation of laser noise in an unequal-arm interferometer detector of gravitational radiation*, *Phys. Rev. D* **59** (1999) 102003.

[118] T. A. Prince, M. Tinto, S. L. Larson and J. W. Armstrong, *The LISA optimal sensitivity*, *Phys. Rev. D* **66** (2002) 122002 [gr-qc/0209039].

[119] D. A. Shaddock, *Operating LISA as a Sagnac interferometer*, *Phys. Rev. D* **69** (2004) 022001 [gr-qc/0306125].

[120] D. A. Shaddock, M. Tinto, F. B. Estabrook and J. W. Armstrong, *Data combinations accounting for LISA spacecraft motion*, *Phys. Rev. D* **68** (2003) 061303 [gr-qc/0307080].

[121] M. Tinto, F. B. Estabrook and J. W. Armstrong, *Time delay interferometry with moving spacecraft arrays*, *Phys. Rev. D* **69** (2004) 082001 [gr-qc/0310017].

[122] M. Vallisneri, *Geometric time delay interferometry*, *Phys. Rev. D* **72** (2005) 042003 [gr-qc/0504145].

[123] M. Muratore, D. Vetrugno and S. Vitale, *Revisitation of time delay interferometry combinations that suppress laser noise in LISA*, *Class. Quant. Grav.* **37** (2020) 185019 [2001.11221].

[124] M. Muratore, D. Vetrugno, S. Vitale and O. Hartwig, *Time delay interferometry combinations as instrument noise monitors for LISA*, *Phys. Rev. D* **105** (2022) 023009 [2108.02738].

[125] O. Hartwig and M. Muratore, *Characterization of time delay interferometry combinations for the LISA instrument noise*, *Phys. Rev. D* **105** (2022) 062006 [2111.00975].

[126] O. Hartwig, M. Lilley, M. Muratore and M. Pieroni, *Stochastic gravitational wave background reconstruction for a nonequilateral and unequal-noise LISA constellation*, *Phys. Rev. D* **107** (2023) 123531 [2303.15929].

[127] D. Q. Nam, Y. Lemiere, A. Petiteau, J.-B. Bayle, O. Hartwig, J. Martino et al., *TDI noises transfer functions for LISA*, 2211.02539.

[128] S. Babak, A. Petiteau and M. Hewitson, *LISA Sensitivity and SNR Calculations*, 2108.01167.

[129] E. S. Phinney, *A Practical theorem on gravitational wave backgrounds*, astro-ph/0108028.

[130] T. Regimbau, *The astrophysical gravitational wave stochastic background*, *Res. Astron. Astrophys.* **11** (2011) 369 [1101.2762].

[131] C. Périgois, C. Belczynski, T. Bulik and T. Regimbau, *StarTrack predictions of the stochastic gravitational-wave background from compact binary mergers*, *Phys. Rev. D* **103** (2021) 043002 [2008.04890].

[132] S. Babak, C. Caprini, D. G. Figueroa, N. Karnesis, P. Marcoccia, G. Nardini et al., *Stochastic gravitational wave background from stellar origin binary black holes in LISA*, *JCAP* **08** (2023) 034 [2304.06368].

[133] L. Lehoucq, I. Dvorkin, R. Srinivasan, C. Pellouin and A. Lamberts, *Astrophysical uncertainties in the gravitational-wave background from stellar-mass compact binary mergers*, *Mon. Not. Roy. Astron. Soc.* **526** (2023) 4378 [2306.09861].

[134] KAGRA, VIRGO, LIGO Scientific collaboration, *Population of Merging Compact Binaries Inferred Using Gravitational Waves through GWTC-3*, *Phys. Rev. X* **13** (2023) 011048 [2111.03634].

[135] S. Nissanke, M. Vallisneri, G. Nelemans and T. A. Prince, *Gravitational-wave emission from compact Galactic binaries*, *Astrophys. J.* **758** (2012) 131 [1201.4613].

[136] N. Karnesis, S. Babak, M. Pieroni, N. Cornish and T. Littenberg, *Characterization of the stochastic signal originating from compact binary populations as measured by LISA*, *Phys. Rev. D* **104** (2021) 043019 [2103.14598].

[137] J. R. Bond, A. H. Jaffe and L. E. Knox, *Radical compression of cosmic microwave background data*, *Astrophys. J.* **533** (2000) 19 [astro-ph/9808264].

[138] J. L. Sievers et al., *Cosmological parameters from Cosmic Background Imager observations and comparisons with BOOMERANG, DASI, and MAXIMA*, *Astrophys. J.* **591** (2003) 599 [astro-ph/0205387].

[139] WMAP collaboration, *First year Wilkinson Microwave Anisotropy Probe (WMAP) observations: Parameter estimation methodology*, *Astrophys. J. Suppl.* **148** (2003) 195 [astro-ph/0302218].

[140] S. Hamimeche and A. Lewis, *Likelihood Analysis of CMB Temperature and Polarization Power Spectra*, *Phys. Rev. D* **77** (2008) 103013 [0801.0554].

[141] W. J. Handley, M. P. Hobson and A. N. Lasenby, *polychord: next-generation nested sampling*, *Mon. Not. Roy. Astron. Soc.* **453** (2015) 4385 [1506.00171].

[142] W. J. Handley, M. P. Hobson and A. N. Lasenby, *PolyChord: nested sampling for cosmology*, *Mon. Not. Roy. Astron. Soc.* **450** (2015) L61 [1502.01856].

[143] J. Torrado and A. Lewis, *Cobaya: Code for Bayesian Analysis of hierarchical physical models*, *JCAP* **05** (2021) 057 [2005.05290].

[144] A. Lewis, *GetDist: a Python package for analysing Monte Carlo samples*, 1910.13970.

[145] J. D. Romano and N. J. Cornish, *Detection methods for stochastic gravitational-wave backgrounds: a unified treatment*, *Living Rev. Rel.* **20** (2017) 2 [1608.06889].

[146] B. Sathyaprakash et al., *Scientific Objectives of Einstein Telescope*, *Class. Quant. Grav.* **29** (2012) 124013 [1206.0331].

[147] G. Janssen et al., *Gravitational wave astronomy with the SKA*, *PoS* **AASKA14** (2015) 037 [1501.00127].

[148] S. Hild et al., *Sensitivity Studies for Third-Generation Gravitational Wave Observatories*, *Class. Quant. Grav.* **28** (2011) 094013 [1012.0908].

[149] A. Weltman et al., *Fundamental physics with the Square Kilometre Array*, *Publ. Astron. Soc. Austral.* **37** (2020) e002 [1810.02680].

[150] C. L. Wainwright, *CosmoTransitions: Computing Cosmological Phase Transition Temperatures and Bubble Profiles with Multiple Fields*, *Comput. Phys. Commun.* **183** (2012) 2006 [1109.4189].

[151] P. Basler and M. Mühlleitner, *BSMPT (Beyond the Standard Model Phase Transitions): A tool for the electroweak phase transition in extended Higgs sectors*, *Comput. Phys. Commun.* **237** (2019) 62 [1803.02846].

[152] P. Athron, C. Balázs, A. Fowlie and Y. Zhang, *PhaseTracer: tracing cosmological phases and calculating transition properties*, *Eur. Phys. J. C* **80** (2020) 567 [2003.02859].

[153] A. D. Linde, *Fate of the False Vacuum at Finite Temperature: Theory and Applications*, *Phys. Lett. B* **100** (1981) 37.

[154] A. D. Linde, *Decay of the False Vacuum at Finite Temperature*, *Nucl. Phys. B* **216** (1983) 421.

[155] A. H. Guth and E. J. Weinberg, *Could the Universe Have Recovered from a Slow First Order Phase Transition?*, *Nucl. Phys. B* **212** (1983) 321.

[156] B. Laurent and J. M. Cline, *Fluid equations for fast-moving electroweak bubble walls*, *Phys. Rev. D* **102** (2020) 063516 [2007.10935].

[157] J. M. Cline, A. Friedlander, D.-M. He, K. Kainulainen, B. Laurent and D. Tucker-Smith, *Baryogenesis and gravity waves from a UV-completed electroweak phase transition*, *Phys. Rev. D* **103** (2021) 123529 [2102.12490].

[158] M. Lewicki, M. Merchand and M. Zych, *Electroweak bubble wall expansion: gravitational waves and baryogenesis in Standard Model-like thermal plasma*, *JHEP* **02** (2022) 017 [2111.02393].

[159] B. Laurent and J. M. Cline, *First principles determination of bubble wall velocity*, *Phys. Rev. D* **106** (2022) 023501 [2204.13120].

[160] J. Ellis, M. Lewicki, M. Merchand, J. M. No and M. Zych, *The scalar singlet extension of the Standard Model: gravitational waves versus baryogenesis*, *JHEP* **01** (2023) 093 [2210.16305].

[161] J. McDonald, *Electroweak baryogenesis and dark matter via a gauge singlet scalar*, *Phys. Lett. B* **323** (1994) 339.

[162] J. R. Espinosa and M. Quiros, *The Electroweak phase transition with a singlet*, *Phys. Lett. B* **305** (1993) 98 [hep-ph/9301285].

[163] J. R. Espinosa and M. Quiros, *Novel Effects in Electroweak Breaking from a Hidden Sector*, *Phys. Rev. D* **76** (2007) 076004 [hep-ph/0701145].

[164] S. Profumo, M. J. Ramsey-Musolf and G. Shaughnessy, *Singlet Higgs phenomenology and the electroweak phase transition*, *JHEP* **08** (2007) 010 [0705.2425].

[165] J. R. Espinosa, T. Konstandin and F. Riva, *Strong Electroweak Phase Transitions in the Standard Model with a Singlet*, *Nucl. Phys. B* **854** (2012) 592 [1107.5441].

[166] V. Barger, D. J. H. Chung, A. J. Long and L.-T. Wang, *Strongly First Order Phase Transitions Near an Enhanced Discrete Symmetry Point*, *Phys. Lett. B* **710** (2012) 1 [1112.5460].

[167] J. M. Cline and K. Kainulainen, *Electroweak baryogenesis and dark matter from a singlet Higgs*, *JCAP* **01** (2013) 012 [1210.4196].

[168] T. Alanne, K. Tuominen and V. Vaskonen, *Strong phase transition, dark matter and vacuum stability from simple hidden sectors*, *Nucl. Phys. B* **889** (2014) 692 [1407.0688].

[169] D. Curtin, P. Meade and C.-T. Yu, *Testing Electroweak Baryogenesis with Future Colliders*, *JHEP* **11** (2014) 127 [1409.0005].

[170] V. Vaskonen, *Electroweak baryogenesis and gravitational waves from a real scalar singlet*, *Phys. Rev. D* **95** (2017) 123515 [1611.02073].

[171] G. Kurup and M. Perelstein, *Dynamics of Electroweak Phase Transition In Singlet-Scalar Extension of the Standard Model*, *Phys. Rev. D* **96** (2017) 015036 [1704.03381].

[172] A. Beniwal, M. Lewicki, J. D. Wells, M. White and A. G. Williams, *Gravitational wave, collider and dark matter signals from a scalar singlet electroweak baryogenesis*, *JHEP* **08** (2017) 108 [1702.06124].

[173] L. Niemi, P. Schicho and T. V. I. Tenkanen, *Singlet-assisted electroweak phase transition at two loops*, *Phys. Rev. D* **103** (2021) 115035 [2103.07467].

[174] S. Blasi and A. Mariotti, *Domain Walls Seeding the Electroweak Phase Transition*, *Phys. Rev. Lett.* **129** (2022) 261303 [2203.16450].

[175] A. Beniwal, M. Lewicki, M. White and A. G. Williams, *Gravitational waves and electroweak baryogenesis in a global study of the extended scalar singlet model*, *JHEP* **02** (2019) 183 [1810.02380].

[176] A. Azatov, G. Barni, S. Chakraborty, M. Vanvlasselaer and W. Yin, *Ultra-relativistic bubbles from the simplest Higgs portal and their cosmological consequences*, *JHEP* **10** (2022) 017 [2207.02230].

[177] S. R. Hinton, *ChainConsumer*, *The Journal of Open Source Software* **1** (2016) 00045.

[178] N. Craig, H. K. Lou, M. McCullough and A. Thalapillil, *The Higgs Portal Above Threshold*, *JHEP* **02** (2016) 127 [1412.0258].

[179] S. Iso, N. Okada and Y. Orikasa, *Classically conformal B^- L extended Standard Model*, *Phys. Lett. B* **676** (2009) 81 [0902.4050].

[180] S. Iso, N. Okada and Y. Orikasa, *The minimal B-L model naturally realized at TeV scale*, *Phys. Rev. D* **80** (2009) 115007 [0909.0128].

[181] R. Jinno and M. Takimoto, *Probing a classically conformal B-L model with gravitational waves*, *Phys. Rev. D* **95** (2017) 015020 [1604.05035].

[182] S. Iso, P. D. Serpico and K. Shimada, *QCD-Electroweak First-Order Phase Transition in a Supercooled Universe*, *Phys. Rev. Lett.* **119** (2017) 141301 [1704.04955].

[183] C. Marzo, L. Marzola and V. Vaskonen, *Phase transition and vacuum stability in the classically conformal B–L model*, *Eur. Phys. J. C* **79** (2019) 601 [1811.11169].

[184] J. Ellis, M. Lewicki, J. M. No and V. Vaskonen, *Gravitational wave energy budget in strongly supercooled phase transitions*, *JCAP* **06** (2019) 024 [1903.09642].

[185] L. Sagunski, P. Schicho and D. Schmitt, *Supercool exit: Gravitational waves from QCD-triggered conformal symmetry breaking*, *Phys. Rev. D* **107** (2023) 123512 [2303.02450].

[186] M. Escudero, S. J. Witte and N. Rius, *The dispirited case of gauged $U(1)_{B-L}$ dark matter*, *JHEP* **08** (2018) 190 [1806.02823].

[187] FCC collaboration, *FCC-hh: The Hadron Collider: Future Circular Collider Conceptual Design Report Volume 3*, *Eur. Phys. J. ST* **228** (2019) 755.

Controlling volume fluctuations for studies of critical phenomena in nuclear collisions

Romain Holzmann,[1,*] Volker Koch,[2,3,†] Anar Rustamov,[1,‡] and Joachim Stroth[4,1,5,§]

[1] *GSI Helmholtzzentrum für Schwerionenforschung, 64291 Darmstadt, Germany*
[2] *Nuclear Science Division Lawrence Berkeley National Laboratory Berkeley, CA, 94720, USA*
[3] *ExtreMe Matter Institute EMMI, GSI, 64291 Darmstadt, Germany*
[4] *Institut für Kernphysik, Goethe-Universität, 60438 Frankfurt am Main, Germany*
[5] *Helmholtz Research Academy Hesse for FAIR (HFHF), Campus Frankfurt , 60438 Frankfurt am Main, Germany*

We generalize and extend the recently proposed method [1] to account for contributions of system size (or volume/participant) fluctuations to the experimentally measured moments of particle multiplicity distributions. We find that in the general case there are additional biases which are not directly accessible to experiment. These biases are, however, parametrically suppressed if the multiplicity of the particles of interest is small compared to the total charged-particle multiplicity, e.g., in the case of proton number fluctuations at top RHIC and LHC energies. They are also small if the multiplicity distribution of charged particles per wounded nucleon is close to the Poissonian limit, which is the case at low energy nuclear collisions, e.g., at GSI/SIS18. We further find that mixed events are not necessarily needed to extract the correction for volume fluctuations, albeit it can help if event statistics is small, which is typically the case for reconstructing the higher-order cumulants. We provide the formulas to correct pure and mixed cumulants of particle multiplicity distributions up to any order together with their associated biases.

arXiv:2403.03598v1 [nucl-th] 6 Mar 2024

* r.holzmann@gsi.de
† vkoch@lbl.gov
‡ a.rustamov@gsi.de
§ j.stroth@gsi.de

I. INTRODUCTION

One of the main goals of studying relativistic heavy-ion collisions is to explore the structure of the QCD phase diagram. Fluctuations of observed particles carrying quantum numbers of conserved charges, baryon number (B), electric charge and strangeness, represent a powerful tool for this endeavor as the cumulants of their distributions measure the derivatives of the grand-canonical partition function, and thus the pressure (P), with respect to the associated chemical potentials. For example, for a thermal system of volume V and temperature T, the cumulants of the net baryon number distribution, within the Grand Canonical Ensemble (GCE), are given by [2]

$$\kappa_n[B] = \frac{\partial^n(\ln Z)}{\partial\,(\mu_B/T)^n} = \frac{V}{T}\frac{\partial^n P}{\partial\,(\mu_B/T)^n},$$

where Z is a GCE partition function and μ_B is a baryon chemical potential. Any nontrivial structures in the equation of state such as a possible phase transition [3–6] will result in potentially large derivatives of the pressure and thus in large values of the cumulants of conserved charges. In addition, as cumulants are derivatives of the pressure, they are accessible (at vanishing or small values of chemical potential) to Lattice QCD calculations [7, 8], which in principle enables a direct comparison of results from ab initio QCD calculations with experiment. For example, as pointed out in Ref. [9], the measurement of higher-order cumulants close to vanishing chemical potential may test the remnants of chiral criticality.

Measurements of fluctuations have meanwhile been carried out by many experiments. The STAR collaboration has measured cumulants of the net-proton number up to sixth order over the entire energy range available at RHIC [10, 11]. The HADES experiment has measured cumulants of proton number up to forth order at the low energy of $\sqrt{s_{\rm NN}} = 2.4\,\text{GeV}$ [12] and ALICE has measured the second- and third-order net-proton number cumulants at $\sqrt{s_{\rm NN}} = 2.76$ and $5.02\,\text{TeV}$ [13, 14].

When comparing cumulants measured in experiment with those obtained from lattice QCD or other field theoretical calculations [15] one needs to be aware of several key differences. While theoretical calculations are typically done in the grand canonical ensemble where charges can be exchanged with a heat bath and are only conserved on the average, in experiment charges are explicitly conserved on event by event basis and one has to account for global as well as local charge conservation [16–20]. Also, in experiments one usually is restricted to the measurement of net protons whereas theory can only calculate cumulants of the net baryon number. In the presence of many pions this difference can be corrected for [21]. Finally, and this will be the topic of the present paper, in experiment the size of the particle emitting system is not constant. Even under the tightest centrality selection criteria, this gives rise to so-called volume fluctuations [22] or, equivalently, fluctuations of the number of wounded nucleons [23]. Moreover, centrality is a concept assuming a strict correlation of event activity, i.e., charged particle multiplicity in a broad region around mid rapidity, with the size of the system. This requires a strict separation of the particles used to determine the fluctuation of conserved charges from the ones used for centrality determination. The effects due to volume fluctuations may be sizable, especially at lower energies where the charged particle multiplicity is dominated by the primordial protons, limiting the achievable resolution of the centrality selection. In Ref. [1] a novel and promising method based on event mixing has been proposed to experimentally determine and subtract the contributions to the cumulants caused by volume fluctuations. In the present work we will further elaborate on this topic, generalize the results, and provide the formulas for corrections of any higher-order cumulants.

This paper is organized as follows. In the next section we define the notation. We then present an analytical formulation of event mixing as proposed in Ref. [1]. We find that the cumulants of the the mixed events have additional bias terms which were assumed to vanish in the original work of [1], and we discuss the magnitude of these corrections for various scenarios. Next we extend our study to cumulants of higher order before we discuss and summarize our results.

II. NOTATION

In this paper we will mostly work within the wounded-nucleon model [24] to discuss volume or participant fluctuations. We would like to point out that this model has its limitations when applied to low collision energies because of the moderate separation of projectile and target rapidity and a multiplicity of created particles per wounded nucleon much smaller than unity. However, as we shall show later, the formalism can be easily applied also to the situation where one has generic volume fluctuations, as for example discussed in Refs. [22, 23]. Let us start with the expression

of the particle number cumulants $\kappa_j[N]$ in the presence of wounded-nucleon fluctuations (for details see Appendix A):

$$\kappa_1[N] = \langle N_w \rangle \kappa_1[n] = \langle N_w \rangle \langle n \rangle = \langle N \rangle \tag{1}$$

$$\kappa_2[N] = \langle N_w \rangle \kappa_2[n] + \langle n \rangle^2 \kappa_2[N_w] = \bar{\kappa}_2[N] + \langle N \rangle^2 \frac{\kappa_2[N_w]}{\langle N_w \rangle^2} \tag{2}$$

$$\kappa_3[N] = \langle N_w \rangle \kappa_3[n] + 3\langle n \rangle \kappa_2[n]\kappa_2[N_w] + \langle n \rangle^3 \kappa_3[N_w] = \bar{\kappa}_3[N] + 3\langle N \rangle \bar{\kappa}_2[N]\frac{\kappa_2[N_w]}{\langle N_w \rangle^2} + \langle N \rangle^3 \frac{\kappa_3[N_w]}{\langle N_w \rangle^3} \tag{3}$$

$$\begin{aligned}\kappa_4[N] &= \langle N_w \rangle \kappa_4[n] + 4\langle n \rangle \kappa_3[n]\kappa_2[N_w] + 3\kappa_2^2[n]\kappa_2[N_w] + 6\langle n \rangle^2 \kappa_2[n]\kappa_3[N_w] + \langle n \rangle^4 \kappa_4[N_w] \\ &= \bar{\kappa}_4[N] + 4\langle N \rangle \bar{\kappa}_3[N]\frac{\kappa_2[N_w]}{\langle N_w \rangle^2} + 3\bar{\kappa}_2^2[N]\frac{\kappa_2[N_w]}{\langle N_w \rangle^2} + 6\langle N \rangle^2 \bar{\kappa}_2[N]\frac{\kappa_3[N_w]}{\langle N_w \rangle^3} + \langle N \rangle^4 \frac{\kappa_4[N_w]}{\langle N_w \rangle^4}\end{aligned} \tag{4}$$

Here N refers to the particles of interest, say protons, and n to the number of these particles arising from one wounded nucleon; thus $\langle n \rangle$ is the average number of particles per wounded nucleon. The cumulants of the wounded-nucleon distribution are denoted by $\kappa_j[N_w]$ while the cumulants for the distribution of particles stemming from one wounded nucleon are $\kappa_j[n]$. The corresponding relations for cumulants of any order can be obtained with the provided software package [25].

The cumulants of interest are those at a fixed number of wounded nucleons. They reflect the true density fluctuations in a system at constant volume. We denote these cumulants for a system with fixed, i.e. non-fluctuating, number of $\langle N_w \rangle$ wounded nucleons as

$$\bar{\kappa}_j[N] = \langle N_w \rangle \kappa_j[n],$$

Below we will also deal with factorial cumulants, which we shall denote by C_j. Factorial cumulants, which measure the deviation from Poisson statistics, tell us about the true correlations in the system. As discussed in the Appendix B, they are linear combinations of the regular cumulants. For the first four orders we have

$$\begin{aligned}C_1[N] &= \kappa_1[N] = \langle N \rangle, \\ C_2[N] &= -\kappa_1[N] + \kappa_2[N], \\ C_3[N] &= 2\kappa_1[N] - 3\kappa_2[N] + \kappa_3[N], \\ C_4[N] &= -6\kappa_1[N] + 11\kappa_2[N] - 6\kappa_3[N] + \kappa_4[N].\end{aligned}$$

The expressions for the particle number factorial cumulants are similar to Eqs. 1- 4

$$C_1[N] = \langle N_w \rangle C_1[n] = \langle N_w \rangle \langle n \rangle = \langle N \rangle, \tag{5}$$

$$C_2[N] = \bar{C}_2[N] + \langle N \rangle^2 \frac{\kappa_2[N_w]}{\langle N_w \rangle^2}, \tag{6}$$

$$C_3[N] = \bar{C}_3[N] + 3\langle N \rangle \bar{C}_2[N]\frac{\kappa_2[N_w]}{\langle N_w \rangle^2} + \langle N \rangle^3 \frac{\kappa_3[N_w]}{\langle N_w \rangle^3}, \tag{7}$$

$$C_4[N] = \bar{C}_4[N] + 4\langle N \rangle \bar{C}_3[N]\frac{\kappa_2[N_w]}{\langle N_w \rangle^2} + 3\bar{C}_2^2[N]\frac{\kappa_2[N_w]}{\langle N_w \rangle^2} + 6\langle N \rangle^2 \bar{C}_2[N]\frac{\kappa_3[N_w]}{\langle N_w \rangle^3} + \langle N \rangle^4 \frac{\kappa_4[N_w]}{\langle N_w \rangle^4}. \tag{8}$$

Similar to the cumulants, we denote by

$$\bar{C}_k[N] = \langle N_w \rangle C_k[n]$$

the factorial cumulants for a system at constant volume or number of wounded nucleons, $\langle N_w \rangle$.

III. MIXED EVENTS

In Ref. [1] a mixed event is constructed such that it has the same total multiplicity as a given real event but each particle (track) is drawn from a different event, so that, by construction, the mixed events follow the same total multiplicity distribution as the original events. This is done in order to preserve volume flucutations as in real events. Since each particle (track) is chosen randomly from a random event, the distribution of particle species will follow a multinomial distribution with the Bernoulli probabilities $p_{\rm i} = \langle N_i \rangle / \langle M \rangle$ for particles of type i. Here $\langle N_i \rangle$ denotes the mean number of particles of type i and $\langle M \rangle$ the mean total multiplicity. Hence, the probability to find A particles

(successes) of type A and B particles of type B is given by the trinomial probability $B_3(A,B,M;p_{\rm A},p_{\rm B})$ and so on. Here M denotes the multiplicity of the event under consideration. Thus the distribution, $P_{mix}\left(A,B\right)$, of particles of species A and B in the mixed events is obtained by folding the multiplicity distribution $P_M(M)$ with a trinomial (in general multinomial) distribution:

$$P_{mix}\left(A,B\right)=\sum_M B_3(A,B,M;p_{\rm A},p_{\rm B})P_M(M)$$

with

$$p_{\rm A}=\frac{\langle A\rangle}{\langle M\rangle},\qquad p_{\rm B}=\frac{\langle B\rangle}{\langle M\rangle}.$$

and

$$B_3(A,B,M;p_{\rm A},p_{\rm B})=\frac{M!}{A!B!(M-A-B)!}\,p_{\rm A}^A\,p_{\rm B}^B\,(1-p_{\rm A}-p_{\rm B})^{M-A-B} \tag{9}$$

The factorial-cumulant generating function for this distribution is

$$\begin{aligned}g_{F,mx}\left(z_{\rm A},z_{\rm B}\right)&=\ln\left[\sum_{A,B}P_{mx}\left(A,B\right)\left(z_{\rm A}\right)^A\left(z_{\rm B}\right)^B\right]\\&=\ln\left[\sum_M\left[h_3\left(z_{\rm A},z_{\rm B}\right)\right]^M P_M(M)\right]\\&=G_{F,M}\left(h_3\left(z_{\rm A},z_{\rm B}\right)\right)\end{aligned} \tag{10}$$

where

$$h_3\left(z_{\rm A},z_{\rm B}\right)=\sum_{A,B}B_3(A,B;M=1;p_{\rm A},p_{\rm B})(z_{\rm A})^A(z_{\rm B})^B=(1-p_{\rm A}-p_{\rm B}+p_{\rm A}z_{\rm A}+p_{\rm B}z_{\rm B})$$

is the factorial-moment generating function for the trinomial distribution with one trial ($M=1$), and $G_{F,M}\left(z\right)$ is the factorial-cumulant generating function for the multiplicity distribution, $P_M(M)$ (see Eq.(B2)). The factorial cumulants are then obtained via

$$C_{i,j}^{mix}[mix]=\left.\frac{\partial^i\partial^j}{\partial(z_{\rm A})^i\partial(z_{\rm B})^j}G_{F,M}\left(h_3\left(z_{\rm A},z_{\rm B}\right)\right)\right|_{z_{\rm A}=z_{\rm B}=0}=p_{\rm A}^ip_{\rm B}^jC_{i+j}\left[M\right]$$

with $C_k[M]$ being the k^{th}-order factorial cumulant. Using the expression for the factorial cumulants of the multiplicity distribution derived in Appendix C, Eq. C5, we get within the wounded-nucleon model

$$\begin{aligned}C_1^{mix}[A]=\kappa_1^{mix}[A]&=p_{\rm A}\left\langle N_w\right\rangle\left\langle m\right\rangle\\C_2^{mix}[A]&=p_{\rm A}^2C_2[M]=p_{\rm A}^2\left[\kappa_2\left[N_w\right]\left\langle m\right\rangle^2+\left\langle N_w\right\rangle C_2[m]\right]\\C_{1,1}^{mix}\left[A,B\right]&=p_{\rm A}p_{\rm B}C_2[M]=p_{\rm A}p_{\rm B}\left[\kappa_2\left[N_w\right]\left\langle m\right\rangle^2+\left\langle N_w\right\rangle C_2[m]\right].\end{aligned} \tag{11}$$

For the corresponding cumulants up to second order we get accordingly

$$\begin{aligned}\kappa_1^{mix}[A]=C_1^{mix}[A]&=p_{\rm A}\left\langle N_w\right\rangle\left\langle m\right\rangle\\\kappa_2^{mix}[A]=C_2^{mix}[A]+C_1^{mix}[A]&=p_{\rm A}^2\left[\kappa_2\left[N_w\right]\left\langle m\right\rangle^2+\left\langle N_w\right\rangle\left(\kappa_2[m]-\kappa_1[m]\right)\right]+p_{\rm A}\left\langle N_w\right\rangle\left\langle m\right\rangle\\&=p_{\rm A}^2\left[\kappa_2\left[N_w\right]\left\langle m\right\rangle^2+\left\langle N_w\right\rangle\left(\kappa_2[m]-\left\langle m\right\rangle\right)\right]+p_{\rm A}\left\langle N_w\right\rangle\left\langle m\right\rangle\\cov^{mix}\left[A,B\right]=C_{1,1}^{mix}\left[A,B\right]&=p_{\rm A}p_{\rm B}\left[\kappa_2\left[N_w\right]\left\langle m\right\rangle^2+\left\langle N_w\right\rangle\left(\kappa_2[m]-\left\langle m\right\rangle\right)\right].\end{aligned} \tag{12}$$

With $\langle m\rangle$ denoting the mean number of total particles emitted by a wounded nucleon, we get $\langle a\rangle=p_{\rm A}\left\langle m\right\rangle$ and $\langle b\rangle=p_{\rm B}\left\langle m\right\rangle$ for the mean number of particles per wounded nucleon of type A and B, respectively, and recover the results of Ref.[1]. For that we have to assume that the multiplicity distribution per wounded nucleon is Poissonian,

i.e. that $C_2[m] = \kappa_2[m] - \langle m \rangle = 0$. This has been an implicit assumption in Ref. [1], which however is not valid in general as we shall discuss below.

The main benefit of the event mixing is to be able to relate the factorial cumulants of the various multiplicity distributions, as can be seen from Eq.11. All that enters is the second-order factorial cumulant, $C_2[M]$. The binomial probabilities, $p_{\rm A}$ and $p_{\rm B}$, are in the sense trivial as they can be determined without any mixed events. Thus we may express the fluctuations of the wounded nucleons in terms of the factorial cumulant of the track multiplicity distribution

$$\langle N \rangle^2 \frac{\kappa_2[N_w]}{\langle N_w \rangle^2} = \frac{\langle N \rangle^2}{\langle M \rangle^2} \left(C_2[M] - \langle N_w \rangle C_2[m] \right) = \frac{\langle N \rangle^2}{\langle M \rangle^2} \left(C_2[M] - \bar{C}_2[M] \right), \tag{13}$$

where $\bar{C}_2[M] = \langle N_w \rangle C_2[m]$ is the second-order factorial cumulant for a system of $\langle N_w \rangle$ wounded nucleons *without* wounded nucleon fluctuations and N stands now for the multiplicity of the particles of interest, i.e., either A or B. While the factorial cumulant of the multiplicity distribution, $C_2[M]$, is accessible to experiment, that of a non-fluctuating system, $\bar{C}_2[M]$, is not. Let us, therefore define a bias term, Δ_2, as

$$\Delta_2 \equiv \frac{\langle N \rangle^2}{\langle M \rangle^2} \bar{C}_2[M]. \tag{14}$$

In case of a Poissonian multiplicity distribution for one wounded nucleon the bias term vanishes, i.e., $\Delta_2 = 0$, since $\bar{C}_2[M] = \langle N_w \rangle C_2[m] = 0$ in this case, and we recover the results of Ref. [1]. Let us furthermore define the corrected cumulant, $\kappa_2^{corr}[N]$, which is based on measurable quantities only

$$\kappa_2^{corr}[N] = \kappa_2[N] - \frac{\langle N \rangle^2}{\langle M \rangle^2} C_2[M]. \tag{15}$$

Following Eq. 2 and using Eq. 6, the cumulant of the system *without* wounded nucleon fluctuations, $\bar{\kappa}_2[N]$, is given by

$$\bar{\kappa}_2[N] = \kappa_2[N] - \langle N \rangle^2 \frac{\kappa_2[N_W]}{\langle N_W \rangle^2} = \kappa_2^{corr}[N] + \Delta_2. \tag{16}$$

The bias, Δ_2, while not directly measurable, may be constrained by a fit to the track multiplicity distribution within the wounded-nucleon model [24], as it is commonly done [11, 26, 27]. In addition, we note that for protons at very high collision energies we have $\langle N_p \rangle \ll \langle M \rangle$ so that Δ_2 is suppressed parametrically. This behavior can indeed be illustrated with simulations as presented in Sec. V. Since cumulants scale with the system size, or in our case with the number of wounded nucleons, $\langle N_w \rangle$, it is instructive to scale the (factorial) cumulants with the mean number of particles

$$\frac{\bar{\kappa}_2[N]}{\langle N \rangle} = \frac{\kappa_2[N]}{\langle N \rangle} - \frac{\langle N \rangle}{\langle M \rangle} \left(\frac{C_2[M]}{\langle N \rangle} - \frac{\bar{C}_2[M]}{\langle N \rangle} \right) = \frac{\kappa_2^{corr}[N]}{\langle N \rangle} + \frac{\Delta_2}{\langle N \rangle} \tag{17}$$

The scaled bias is then given by

$$\frac{\Delta_2}{\langle N \rangle} = \frac{\langle N \rangle}{\langle M \rangle} \bar{c}_2[M]. \tag{18}$$

Typically, the scaled cumulants are of order unity, $\kappa_j[N] / \langle N \rangle \sim \mathcal{O}(1)$. In addition, the scaled factorial cumulants, $C_k[N] / \langle N \rangle$, are expected to depend only weakly on the multiplicity. Therefore, the scaled bias should be much smaller than one, $\Delta_2 / \langle N \rangle \ll 1$, for the volume correction to be reliable.

Finally, one may express the bias term Δ_2 also in terms of cumulants by using the relation between cumulants and factorial cumulants (see Appendix B), $C_2[M] = \kappa_2[M] - \langle M \rangle$ and and so forth. This gives,

$$\Delta_2 = \frac{\langle N \rangle^2}{\langle M \rangle^2} \left(\bar{\kappa}_2[M] - \langle M \rangle \right) \tag{19}$$

A note of caution may be useful in this context. One might be inclined to express the fluctuations of the wounded nucleon directly using the cumulants of the multiplicity distribution, in which case one would get

$$\langle N \rangle^2 \frac{\kappa_2[N_w]}{\langle N_w \rangle^2} = \frac{\langle N \rangle^2}{\langle M \rangle^2} \left(\kappa_2[M] - \langle N_w \rangle \kappa_2[m] \right).$$

And since $\langle N_W \rangle \kappa_2[m] = \bar{\kappa}_2[M]$ is not directly accessible to experiment, one may further assign the bias to be $\Delta_2 = \frac{\langle N \rangle^2}{\langle M \rangle^2} \bar{\kappa}_2[M]$. This, however, would considerably overestimate its true value, Eq. 19, as cumulants always contain a "trivial" component proportional to the number of particles, which in principle is measurable.

IV. HIGHER-ORDER RESULTS

Let us now discuss the corrections for volume fluctuations up to fourth order. Given the discussion in the previous section the strategy is straightforward. First we express the fluctuations of the wounded nucleons in terms of factorial cumulants of the multiplicity distribution. Then we identify the parts which are experimentally accessible and those which are not. The latter will be the bias while the former will be subtracted from the expression for the cumulants in order to remove most of the effect of volume fluctuations. The terms involving cumulants of the wounded-nucleon distribution as they appear in the expressions for the cumulants as $\kappa_j[N_w]/\langle N_w\rangle^j$, see Eqs. (6-8) are:

$$\frac{\kappa_2[N_w]}{\langle N_w\rangle^2} = \frac{C_2[M]-\bar{C}_2[M]}{\langle M\rangle^2} \tag{20}$$

$$\frac{\kappa_3[N_w]}{\langle N_w\rangle^3} = -3\frac{\bar{C}_2[M]}{\langle M\rangle^2}\frac{\kappa_2[N_w]}{\langle N_w\rangle^2} + \frac{C_3[M]-\bar{C}_3[M]}{\langle M\rangle^3} \tag{21}$$

$$\frac{\kappa_4[N_w]}{\langle N_w\rangle^4} = -6\frac{\bar{C}_2[M]}{\langle M\rangle^2}\frac{\kappa_3[N_w]}{\langle N_w\rangle^3} - \frac{4\bar{C}_3[M]\langle M\rangle + 3\bar{C}_2[M]^2}{\langle M\rangle^4}\frac{\kappa_2[N_w]}{\langle N_w\rangle^2} + \frac{C_4[M]-\bar{C}_4[M]}{\langle M\rangle^4} \tag{22}$$

We note that binomial efficiency corrections do not affect the results as both, numerators and denominators of the right hand side of the above expressions, scale with the same power of the efficiency.

Inserting these expressions into Eqs. (2-4) for the cumulants $\kappa_j[N]$, we can solve for the cumulants of the system with fixed number of wounded nucleons, namely the $\bar{\kappa}_j[N]$. The results are given in the following general form

$$\bar{\kappa}_j[N] = \kappa_j^{corr}[N] + \Delta_j[N] \tag{23}$$

with $\bar{\kappa}_j[N]$ the cumulant of order j for a system with fixed N_w nucleons, $\kappa_j^{corr}[N]$ the cumulant including the measurable corrections for volume fluctuations, and Δ_j the corresponding bias due to quantities that are not measurable. The second-order result we already derived in Sec. A, Eqs. (15) and (14), namely

$$\begin{aligned}\kappa_2^{corr}[N] &= \kappa_2[N] - \frac{\langle N\rangle^2}{\langle M\rangle^2}C_2[M]\\ \Delta_2 &= \frac{\langle N\rangle^2}{\langle M\rangle^2}\bar{C}_2[M].\end{aligned} \tag{24}$$

For the third order we have

$$\begin{aligned}\kappa_3^{corr}[N] &= \kappa_3[N] - \frac{3C_2[M]\kappa_2[N]\langle N\rangle}{\langle M\rangle^2} + \frac{3C_2[M]^2\langle N\rangle^3}{\langle M\rangle^4} - \frac{C_3[M]\langle N\rangle^3}{\langle M\rangle^3}\\ \Delta_3 &= \bar{C}_2[M]\left(\frac{3\kappa_2[N]\langle N\rangle}{\langle M\rangle^2} - \frac{3C_2[M]\langle N\rangle^3}{\langle M\rangle^4}\right) + \frac{\bar{C}_3[M]\langle N\rangle^3}{\langle M\rangle^3}.\end{aligned} \tag{25}$$

And the fourth order result reads

$$\begin{aligned}\kappa_4^{corr}[N] &= \kappa_4[N] - \left(\frac{6\kappa_2[N]\langle N\rangle^2\left(C_3[M]\langle M\rangle - 3C_2[M]^2\right)}{\langle M\rangle^4} + \frac{4C_2[M]\kappa_3[N]\langle N\rangle}{\langle M\rangle^2}\right.\\ &\left. + \frac{3C_2[M]\kappa_2(N)^2}{\langle M\rangle^2} + \frac{\langle N\rangle^4\left(-10C_3[M]C_2[M]\langle M\rangle + 15C_2[M]^3\right)}{\langle M\rangle^6} + \frac{C_4[M]\langle N\rangle^4}{\langle M\rangle^4}\right)\\ \Delta_4 &= \bar{C}_2[M]\left(-\frac{18C_2[M]\kappa_2[N]\langle N\rangle^2}{\langle M\rangle^4} + \frac{15C_2[M]^2\langle N\rangle^4}{\langle M\rangle^6} - \frac{4C_3[M]\langle N\rangle^4}{\langle M\rangle^5} + \frac{4\kappa_3[N]\langle N\rangle}{\langle M\rangle^2} + \frac{3\kappa_2[N]^2}{\langle M\rangle^2}\right)\\ &+ \bar{C}_3[M]\left(\frac{6\kappa_2[N]\langle N\rangle^2}{\langle M\rangle^3} - \frac{6C_2[M]\langle N\rangle^4}{\langle M\rangle^5}\right) + \frac{\bar{C}_4[M]\langle N\rangle^4}{\langle M\rangle^4}.\end{aligned} \tag{26}$$

The corresponding relations for correction and bias terms of any order can be obtained with the provided software package [25].

Equivalent expressions for the factorial cumulants, $C_n[N]$, and their related biases, $\Delta_{n,F}$, may then be obtained by using the relation between factorial cumulants and regular cumulants Eq. B6:

$$C_n^{corr}[N] = \sum_{j=1}^{n} B_{n,j}\left(1,-1,2,\ldots,(-1)^{j-1}(n-j+1)!\right)\ \kappa_j^{corr}[N]$$

$$\Delta_{n,F} = \sum_{j=1}^{n} B_{n,j}\left(1,-1,2,\ldots,(-1)^{j-1}(n-j+1)!\right)\ \Delta_j[N]$$

The results for the corrected factorial cumulants, C_k^{corr} and c_k^{corr}, and the associated biases, $\Delta_{k,F}$ and $\delta_{k,F}$, are given in Appendix E.

V. SIMULATIONS

Experimental data are usually analyzed in centrality percentiles, i.e. event classes corresponding to the $n\%$ most central collisions, by introducing selection criteria on e.g. the energy deposited in a forward detector system covering typically the projectile (target) spectator region or the multiplicity of charged particles emitted from the mid-rapidity region, with an acceptance reaching close to the projectile (target) rapidity regions in case of low beam energies [26, 27]. For the latter, care must be taken to ensure that the evaluated particles are not simultaneously used to determine the critical fluctuations [28]. The respective distributions, like e.g., the forward energy deposit or the charged particle

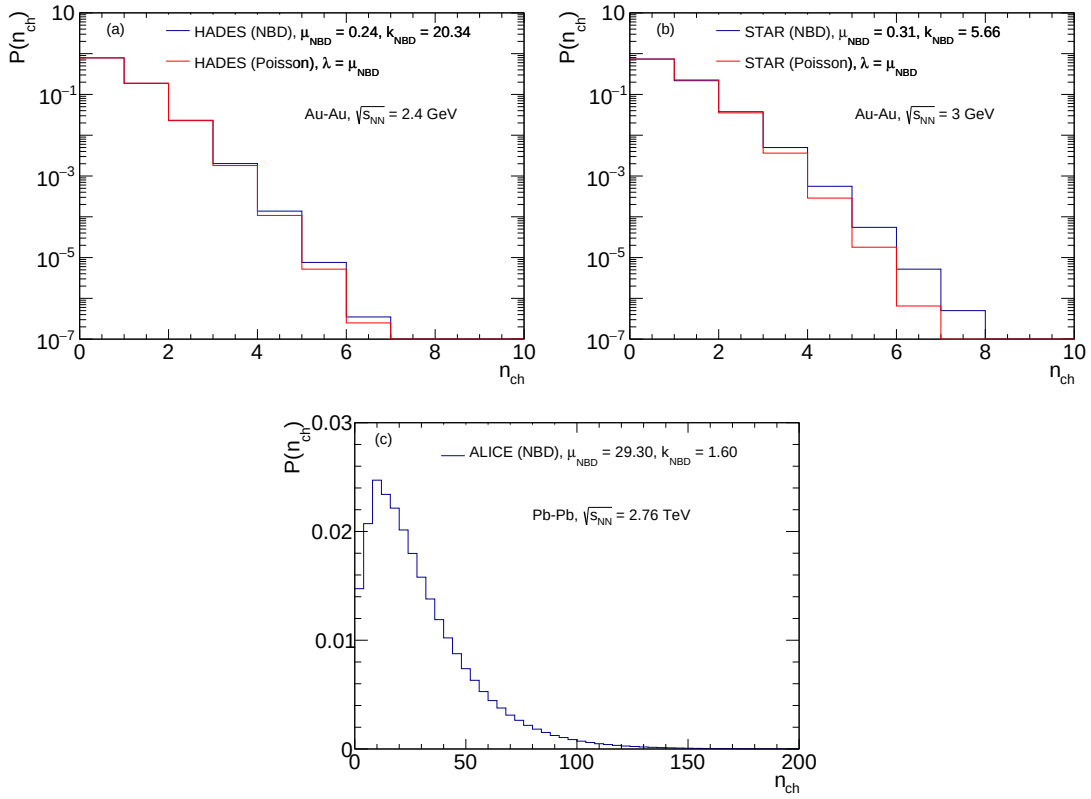

Figure 1. NBD adjusted to HADES (a), STAR (b) and ALICE (c) charged-particle multiplicity distributions (blue line), shown together with a Poisson distribution for the HADES and STAR data (red lines), the parameters used are listed in Table I.

multiplicity, are commonly modelled using the Glauber Monte Carlo Model [29]. The model provides event by event and for a given impact parameter the number of projectile/target nucleons which are "wounded" and responsible for the event activity (multiplicity), and those, which proceed nearly undisturbed into the phase space region covered by the forward detectors. To determine centrality using charged particle multiplicity the respective distribution is generally modelled assuming that particles are "produced" independently from distinct sources following a negative

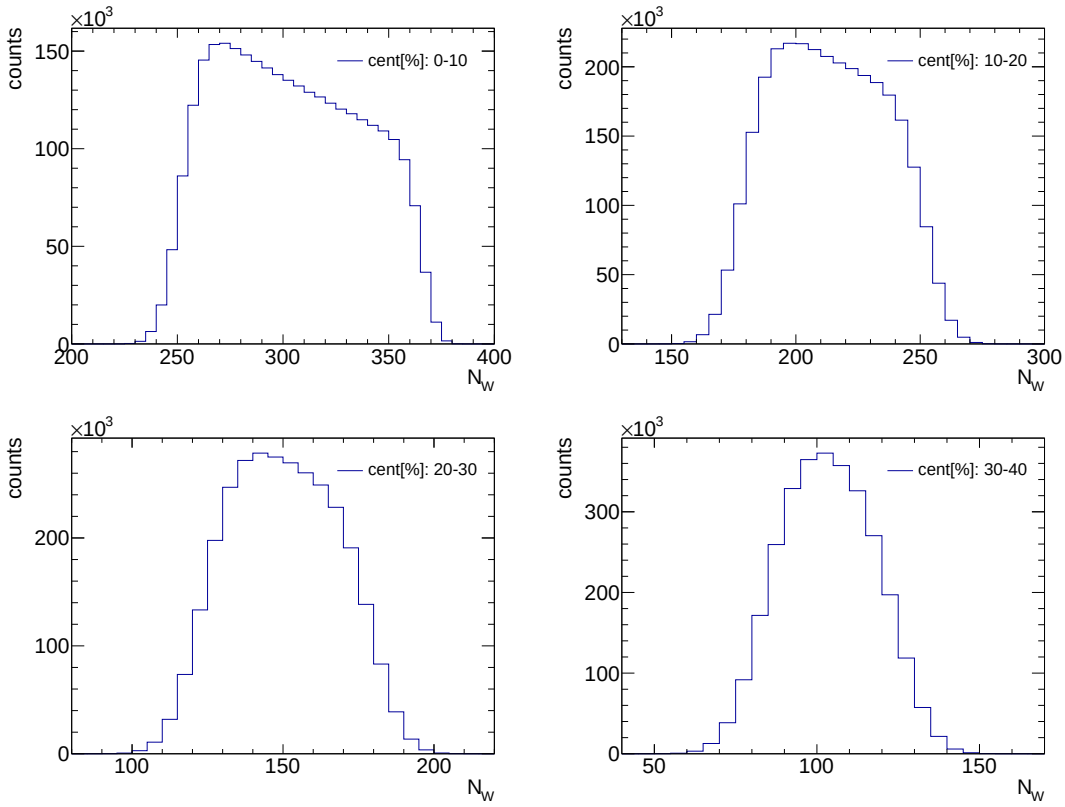

Figure 2. Distribution of wounded nucleons in Au+Au collisions at $\sqrt{s_{\rm NN}} = 2.4$ GeV for four selected centrality classes, as obtained from the Glauber Monte Carlo simulations.

binomial distribution (NBD). Its probability mass function is defined as

$$P(n;\mu,k) = \frac{\Gamma(n+k)}{\Gamma(n+1)\Gamma(k)} \left(\frac{\mu}{k}\right)^n \left(\frac{\mu}{k}+1\right)^{-(n+k)}, \tag{27}$$

where μ denotes the mean of the NBD, while the combination of μ and k determines its higher-order cumulants

$$\kappa_n^{NBD} = \left.\frac{\partial^n \ln M(t)}{\partial t^n}\right|_{t=0}, \tag{28}$$

with

$$M(t) = \sum_{n=0}^{\infty} e^{tn} P(n;\mu,k) = \left(\frac{k}{k+\mu(1-e^t)}\right)^k \tag{29}$$

being the moment-generating function of the NBD. The first four cumulants read

$$\kappa_1^{\rm NBD} = \mu, \tag{30}$$

$$\kappa_2^{\rm NBD} = \frac{\mu(k+\mu)}{k}, \tag{31}$$

$$\kappa_3^{\rm NBD} = \frac{\mu(k+\mu)(k+2\mu)}{k^2}, \tag{32}$$

$$\kappa_4^{\rm NBD} = \frac{\mu(k+\mu)(k^2+6k\mu+6\mu^2)}{k^3}, \tag{33}$$

The parameters of the NBD are fixed in each experiment by the fitting procedure. In a first step the number of particle-emitting sources n_s is determined according to [11, 27]

$$n_{\rm s} = fN_w + (1-f)N_{coll}, \tag{34}$$

where N_W and N_{coll} are the numbers of wounded nucleons and binary collisions, respectively. Sampling impact parameters according to $d\sigma = b\,db$ a list of number of sourses,n_s^i, is generated, with $i \in [1, \cdots, N_{\rm Event}]$. Then, for each event i, NBD is sampled n_s^i times and the parameters of the NBD, μ, k and f, are adjusted such that the obtained multiplicity distribution agrees with the corresponding experimental one. The mixing parameter f is introduced to improve the description by accounting also particles produced in hard (prompt) processes.

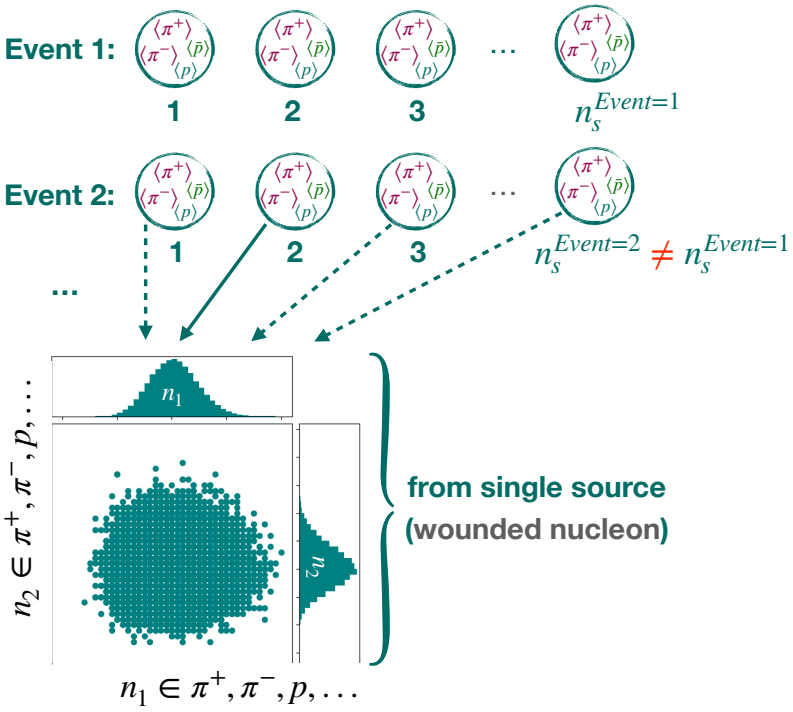

Figure 3. Simulation of particle production within the model of independent sources. The circles indicate the individual sources sampled according to Eq. 34. n_1 and n_2 show particle species used to sample emission from a single source. The distributions per single source can be chosen arbitrarily. See models A and B discussed below.

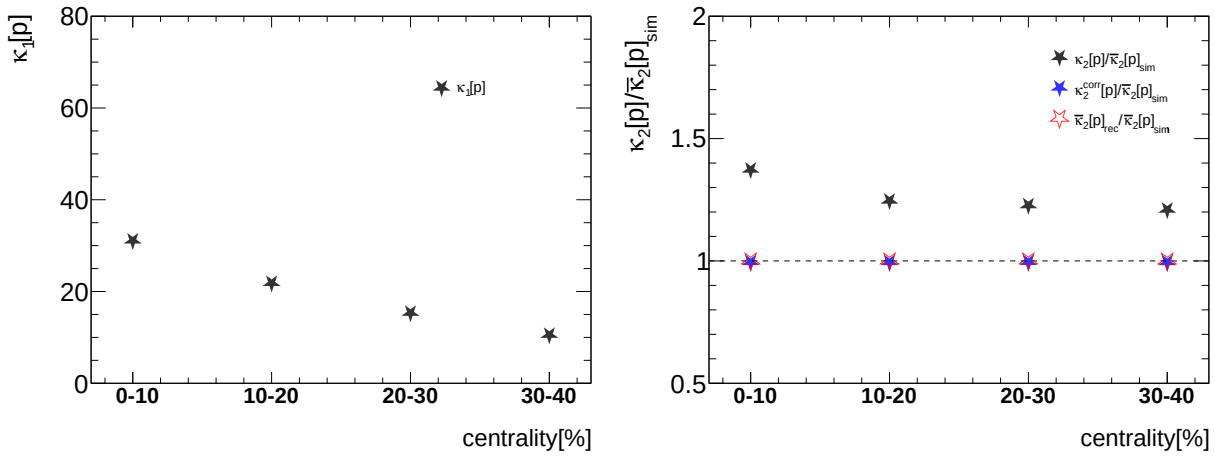

Figure 4. Left panel: Mean number of simulated protons used in Model A as a function of centrality. Right panel: Second-order cumulants of protons in Model A including volume fluctuations (black stars), corrected with Eq. 24 (blue stars) and reconstructed with Eq. 23 (open red stars). The results are normalized to $\bar{\kappa}_2[p]_{sim}$, corresponding to the second-order cumulants of protons in the absence of volume fluctuations.

Panel (a) of Fig. 1 represents the NBD distribution as observed by the HADES experiment for Au+Au collisions at $\sqrt{s_{\rm NN}} = 2.4\,$GeV, with parameters $\mu = 0.24$, $k = 20.34$, and $f = 1$ taken from [26]. For comparison, we also present a

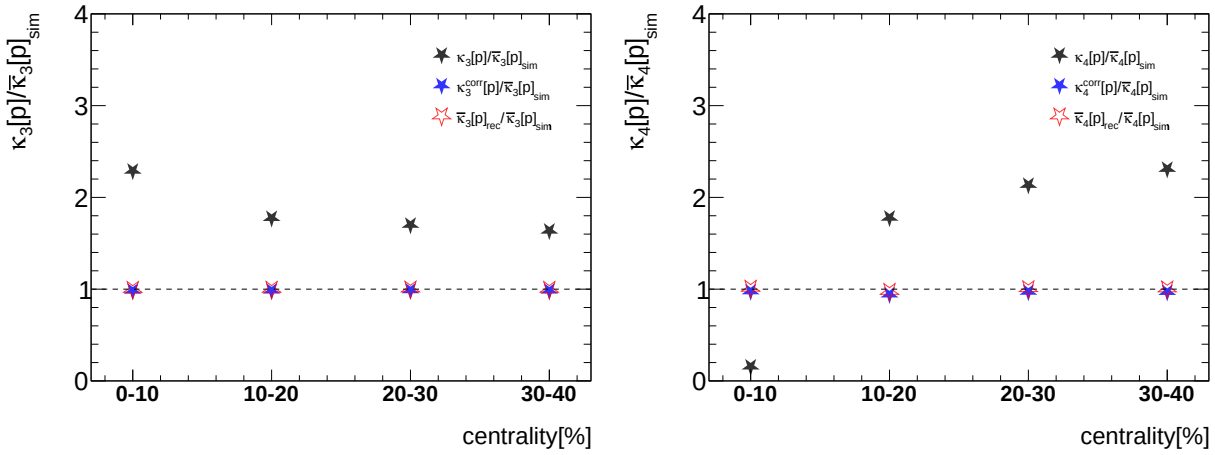

Figure 5. Left panel: Third order cumulants of protons in Model A including volume fluctuations (black stars), corrected with Eq. 25 (blue stars) and reconstructed with Eq. 23 (open red stars). The results are normalized to $\bar{\kappa}_3[p]_{\rm sim}$, corresponding to the second-order cumulants of protons in the absence of volume fluctuations. Right panel: Fourth order cumulants of protons in Model A including volume fluctuations (black stars), corrected with Eq. 26 (blue stars) and reconstructed with Eq. 23 (open red stars). The results are normalized to $\bar{\kappa}_4[p]_{\rm sim}$, corresponding to the fourth order cumulants of protons in the absence of volume fluctuations.

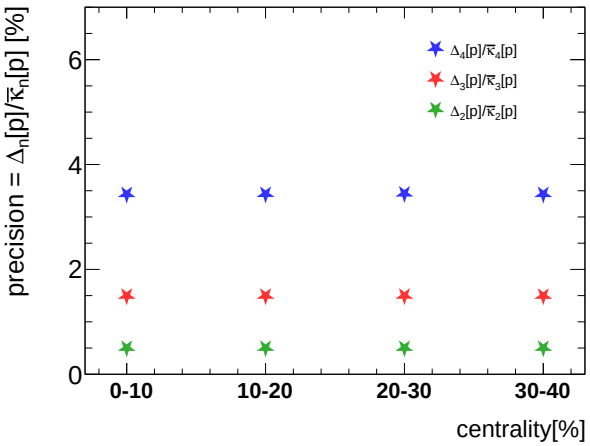

Figure 6. The normalised bias terms in Model A.

Poisson distribution with the same mean, μ. Similar distributions from the STAR [11] and ALICE [27] experiments are presented in panels (b) and (c). Figure 1 shows that at the HADES energy the fitted NBDs are very close to Poisson distributions. Quantitatively this can be seen by evaluating the cumulants of the HADES NBD ($\mu = 0.24$, $k = 20.34$)

$$\kappa_1^{\rm NBD}({\rm HADES}) = 0.24 \tag{35}$$
$$\kappa_2^{\rm NBD}({\rm HADES}) = 0.2428, \tag{36}$$
$$\kappa_3^{\rm NBD}({\rm HADES}) = 0.2486, \tag{37}$$
$$\kappa_4^{\rm NBD}({\rm HADES}) = 0.2602. \tag{38}$$

For a Poisson distribution all cumulants are equal to its mean and the HADES data are indeed close to fulfilling this condition. The statement, to a lesser extent, is also valid for the STAR Au+Au data at 3 GeV (see Fig. 1). The corresponding ALICE distribution, however, is much wider compared to the Poisson baseline, but the ALICE NBD is obtained for very different acceptance than that used for the cumulant analysis. In Table I we also provide the NBD parameters as obtained by the STAR and ALICE collaborations for Au+Au and Pb+Pb collisions at $\sqrt{s_{\rm NN}} = 3$ GeV and 2.76 TeV, respectively.

experiments	μ	k	f
HADES	0.24	20.34	1
STAR	0.31	5.66	0.94
ALICE	29.3	1.6	0.8

Table I. NBD parameters as extracted from Glauber fits to particle distributions observed in different experiments. For simulations, the distributions should be folded within the experimental acceptance in which the cumulants are measured.

In the following we test the proposed method using two different simulations referred to as Model A and Model B. While the sampling of wounded nucleons is the same for both models, in Model A we sample different particle species independently while in Model B we introduce correlations between pions and protons via cluster production and decay. We will concentrate on the HADES data. For both methods, we use the Glauber model to extract the distributions of wounded nucleons corresponding to four different centrality classes in Au+Au collisions at $\sqrt{s_{\rm NN}} = 2.4\,{\rm GeV}$. They are presented in Figure 2.

In both models particles are produced from independent sources (cf. Eq. 34). For the HADES data the extracted number of binary collision is zero ($f = 1$, see Table I), the number of sources per event are sampled exclusively from the wounded nucleon distributions presented in Fig. 2. The simulation process is schematically illustrated in Fig. 3.

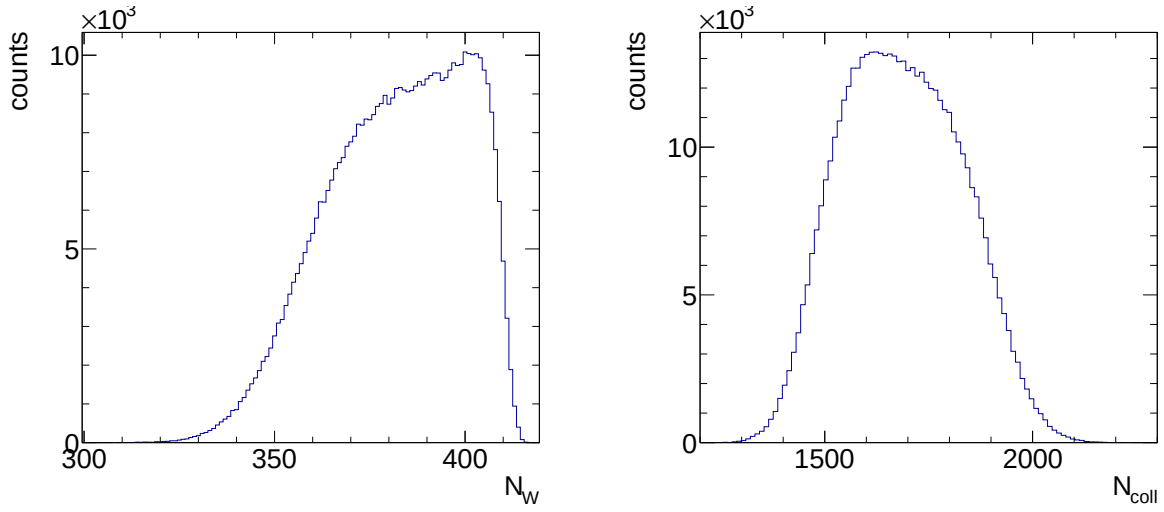

Figure 7. Number of wounded nucleons (left panel) and binary collisions (right panel) as generated with a Glauber Monte Carlo simulation using input from the ALICE experiment [27]. The selection corresponds to the 5% most central Pb-Pb collisions at $\sqrt{s_{\rm NN}} = 2.76$ TeV.

VI. MODEL A

In model A we first generate the charged-particle multiplicity for individual events using the NDB distribution as extracted by experimental measurements. In doing so we sample the NBD distribution n_s times. Different particle species are then taken as fractions of the total number of charged particles. For example, from a randomly sampled NBD distribution a respective fraction is assigned to protons. From the remaining charged particles another fraction is assigned to positively charged pions and the rest is taken as negatively charged pions. These fractions are chosen such that the overall probability of having protons, positively and negatively charged pions correspond to 75%, 9% and 16 % of all charged particles, respectively, based on the actual HADES measurement in Au+Au collisions (see [30] and references therein). In addition, we account for acceptance effects, because the NDB parameters are obtained in different acceptance than that used for the fluctuation analyses. We therefore fold the entire NDB distribution with a binomial distribution such that the experimentally measured mean multiplicities of particles in the acceptance used for fluctuation analysis are reproduced. Volume fluctuations are naturally accounted for as for each event the number of sources n_s are randomly sampled from the corresponding distributions.

The simulated mean numbers of protons are shown in the left panel of Fig. 4 for the four centrality classes. In the right panel of Fig. 4 the reconstructed second-order cumulants of protons are presented, normalized to the expected true cumulant, $\bar{\kappa}_2[p]_{sim}$. The black stars represent the results which include volume fluctuations. The values κ_2^{corr} as calculated using Eq. 15 are shown with blue stars, while the red stars correspond to $\bar{\kappa}_2[p] = \kappa_2^{corr}[p] + \Delta_2[p]$. The results for the third and fourth order cumulants are shown in Fig. 5. The corresponding normalized biases $\Delta_n/\bar{\kappa}_n$ are presented in Fig. 6. We find the normalized biases to be very small, of the order of a few present, so that the corrected cumulants, κ_n^{corr} are very close to their expected true values, $\bar{\kappa}_n$. As already discussed, this is to be expected since the multiplicity distribution per wounded nucleon in the present Model is close to Poisson.

A. High energy limit

In this section we apply the method to high energy collisions using ALICE data. In doing so we first run Glauber Monte Carlo simulations for Pb-Pb collisions at $\sqrt{s_{\rm NN}} = 2.76$ TeV. The input parameters are taken from Ref. [27]. Following the ALICE experiment [27], different centrality classes are chosen by introducing sharp cuts on the charged-particle distributions. The distributions of wounded nucleons and binary collisions corresponding to the 5% most central collisions are presented in Fig. 7 [23]. The reconstructed mean number of wounded nucleons and binary collisions, corresponding to the 5% most central collisions are $\langle N_W \rangle \approx 382$ and $\langle N_{coll} \rangle \approx 1685$, respectively, consistent with the numbers given in [27]. With these numbers one can estimate a mean number of particle emitting sources, yielding $\langle n_s \rangle \approx 642$ (see Eq. 34). The corresponding mean number of charged particles can be estimated as $\langle N_{ch} \rangle = \langle n_s \rangle \times \mu_{NBD} \approx 18811$. On the other hand, the total number of charged particles measured inside the ALICE acceptance is about 1601 [31]. We thus folded the ALICE NBD distribution with a binomial with the acceptance factor of $\epsilon = 1601/18811 \approx 8.5\%$ to obtain the distribution within the experimental acceptance.[1] The so obtained NDB distribution from ALICE is presented in Fig. 8. We further note that only the acceptance in rapidity is considered. Fluctuation analyses are performed within a finite momentum range. Inclusion of the latter will further reduce the discrepancy between NBD and the corresponding Poisson distribution shown with the red histogram in Fig. 8.

Finally using the NBD distribution presented in Fig. 8, and measured proton number, $\langle N_p \rangle \approx 35$ [31], we estimated $\Delta_2[p] \approx 1.2$. This corresponds to a bias of $\Delta_2[p]/\bar{\kappa}_2[p] \approx 3.3\%$.

VII. MODEL B

In model B we introduce correlations between charged particles, specifically pions and protons by generating clusters (or rather resonances). Especially for HADES energies most of the observed pions are believed to originate from decays of Delta resonances. Therefore, the effect of such decay correlations, while no treated quantitatively here, needs to be taken into account. Specifically, this is done by generating clusters of particles (e.g., resonances) from each source and letting them decay into two different particle species. Moreover, the clusters are generated from a Poisson distribution. In addition we produce independent particles from each source as well, sampled also from a Poisson distribution. Schematic illustration of the model for a single source is given in Fig. 9. Fluctuations of sources are introduced like in the model A. The input parameters for model B are given in Table II.

particles	mean numbers per source
clusters	0.03
independent protons	0.23
other particles	0.21

Table II. Parameters for model B are mean numbers of different particles species per source (see [30] and references therein). In addition, each cluster decays into one proton and one pion. Numbers of clusters, independent protons and other particles are sampled from independent Poisson distributions.

By construction the simulated protons, pions and clusters follow a Poisson distribution. However the distribution of the total number of particles does not, due to the correlation between pions and protons introduced via the cluster decay (see Appendix F).

[1] We note that binomial folding of the NDB distribution, with the acceptance factor ϵ, changes only the parameter μ of the original NDB distribution ($\mu \to \epsilon\mu$), while the parameter k stays unchanged.

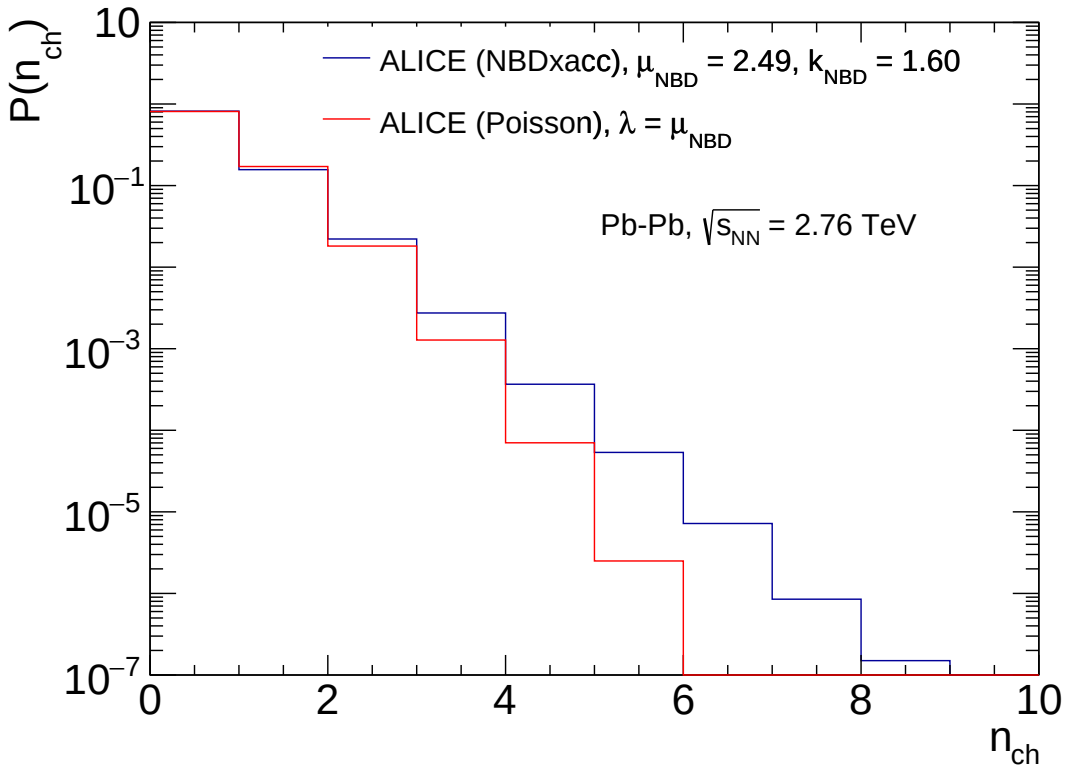

Figure 8. NDB distributions from ALICE as measured by fitting the signal amplitude in VZEROs (left panel) and after folding within the experimental acceptance 8.5% (see the text for details). The red histogram corresponds to a Poisson distribution with the same mean, μ as the folded NBD distribution. The original NBD distribution from ALICE is presented in the panel (c) of Fig. 1.

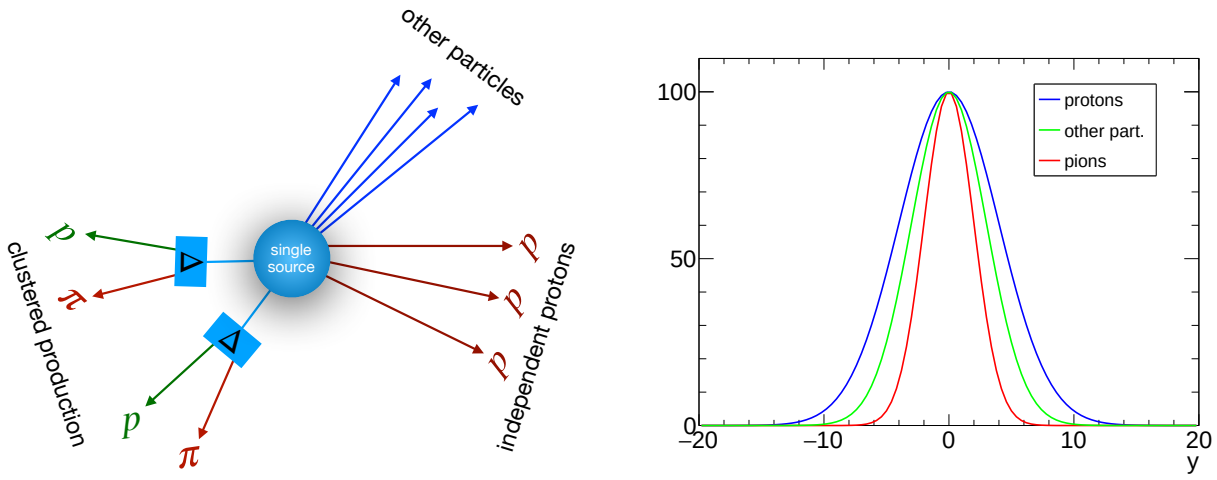

Figure 9. Left panel: Schematic illustration of model B. From a single source two clusters and three protons are produced. The clusters further decay to protons and pions. In simulations both, clusters and independent protons are sampled from Poisson distributions. The corresponding mean values of clusters and independent protons are provided in Table II. Right panel: Schematic rapidity distributions for different particles in order to study acceptance effects.

In experiments measurements are performed inside the finite acceptance by imposing selection criteria in momentum space, e.g., on rapidity and/or transverse momentum of particles. Moreover, such conditions typically lead to different

acceptances for different particle species. In order to study the impact of the finite acceptance on the presented formalism, we introduce arbitrary rapidity distributions for protons, pions and other particles as illustrated in the rigth panel of Fig. 9. To this end we generate rapidity values for protons, pions and other particles from the corresponding distributions presented in Fig. 9.

In the left panel of Fig. 10 we present mean multiplicities of protons produced via clusters (red circles) and independently (blue circles), while the black circles correspond to the total number of protons. In addition, we produce pions from clusters, and, by construction, their mean values are equal to those of protons from clusters. The right panel of Fig. 10 shows the second-order cumulants of protons divided by the expected value $\bar{\kappa}_2[p]_{sim}$. The black stars represent those including participant (volume) fluctuations, $\kappa_2[p]/\bar{\kappa}_2[p]_{sim}$. The corrected cumulants $\kappa_2^{corr}[p]/\bar{\kappa}_2[p]_{sim}$ (see Eq. 24) are shown with blue symbols, while the open red stars represent the true reconstructed values of fluctuations of protons $\bar{\kappa}_2[p]/\bar{\kappa}_2[p]_{sim}$ as calculated using Eq. 23. Similar results for the third and fourth order cumulants of protons are presented in Fig. 11 (see Eqs. 25, 26, 23). In Fig. 12 the normalized cumulants as a function of cumulant order are presented for the 10% most central collisions. The right panel of Fig. 12 corresponds to the full acceptance, while in the right panel the results in the finite acceptance, delimited as $|y| < 1$, are presented. One clearly observes that in the finite acceptance the precision of the method is significantly better. In Fig. 13 we show the magnitude of the corresponding normalized biases, $\Delta_n/\bar{\kappa}_n$, for the full acceptance (left panel) and for $|y| < 1$ (right panel). While the biases for the full acceptance may at first sight appear rather large ($\sim 40\%$) one should realize that for the most central events the uncorrected fourth order cumulant is more than a factor of 50 larger in magnitude than the true cumulants. In other words the proposed corrections, while not perfect are a huge improvement of the measurement. The situation gets better for the limited acceptance.

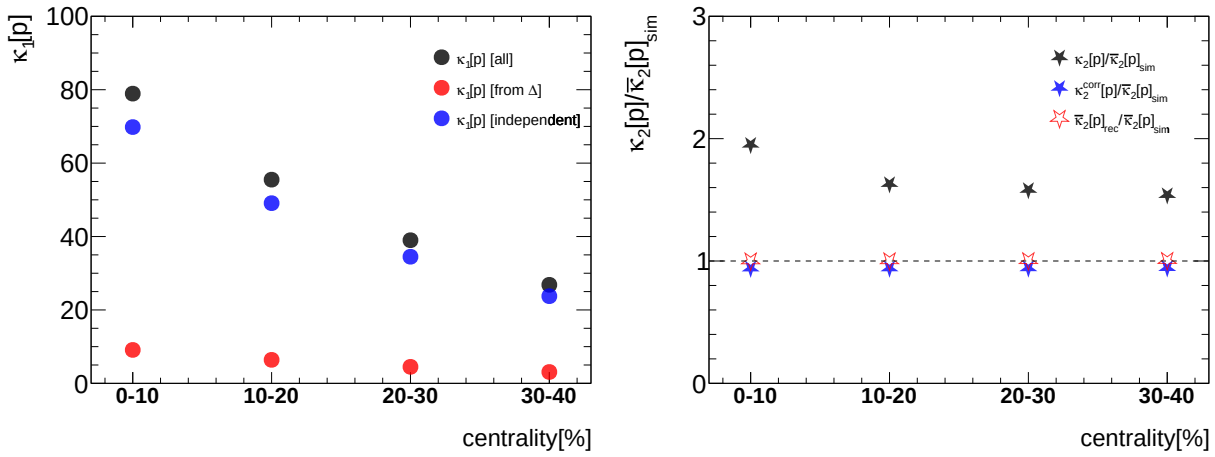

Figure 10. Left panel: Mean number of protons produced via clusters and independently are presented with the red and blue circles respectively. The black circles represent total multiplicity of protons. Pions are produced only via clusters. Right panel: Reconstructed second-order cumulants of protons including participant fluctuations (black stars). Corrected values for cumulants $\kappa_2^{corr}[p]$, i.e., without the bias term $\Delta_2[p]$ are presented with blue stars, while red stars represent fully corrected, against volume fluctuation. The results are normalized to the true second order cumulant, $\bar{\kappa}_2[p]_{sim}$.

VIII. SOFTWARE PACKAGE

A Python package is provided to derive analytical formulas for both mixed and pure cumulants of multiplicity distributions, including participant/volume fluctuations. The correction formulas and their bias terms can be derived as well. The dedicated graphical user interface is presented in Fig. 14 and can be downloaded via Ref. [25].

IX. DISCUSSION AND SUMMARY

- We have shown that using mixed events to determine the contributions of wounded nucleon or volume fluctuations is equivalent to extracting the latter from the track multiplicity distribution. However event mixing may offer an advantage since it allows to generate an almost arbitrarily large event ensemble with the same multiplicity distribution, and thus eliminate possible constraints due to limited event statistics.

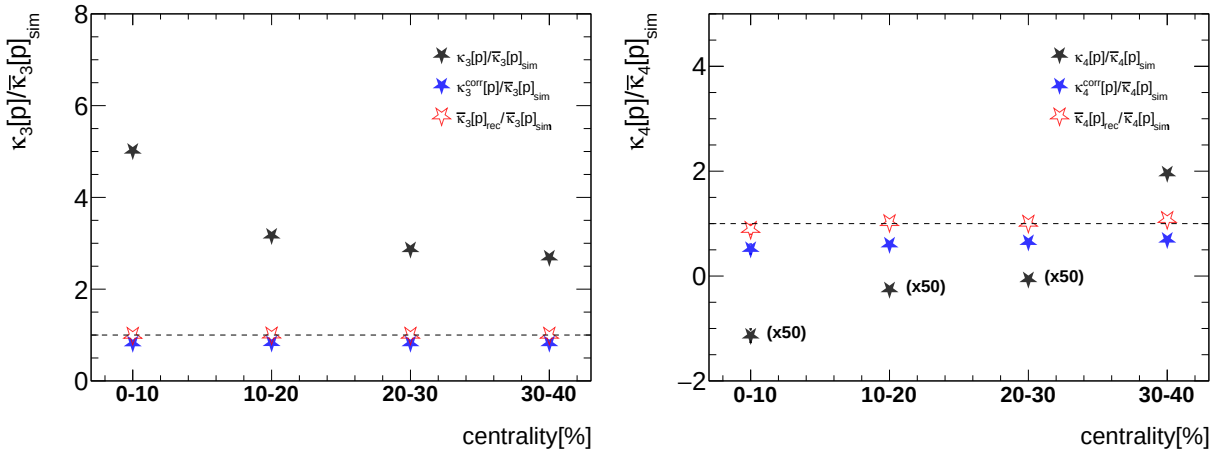

Figure 11. Left panel: Reconstructed third-order cumulants of protons including participant fluctuations (black stars) for model B. Corrected values for cumulants $\kappa_3^{corr}[p]$, i.e. without the bias term $\Delta_3[p]$ are presented with blue stars, while red stars represent fully corrected, against volume fluctuations, values $\bar{\kappa}_3[p]=\kappa_3^{corr}[p] + \Delta_3[p]$. Right panel: Similar to the left panel but for the fourth-order cumulants. Note that the values for the fourth-order cumulants with volume fluctuations (black stars) need to be multiplied by 50 for the first three centrality classes. The results are normalized to the true third or fourth order cumulant, $\bar{\kappa}_3[p]_{sim}$,$\bar{\kappa}_4[p]_{sim}$, respectively

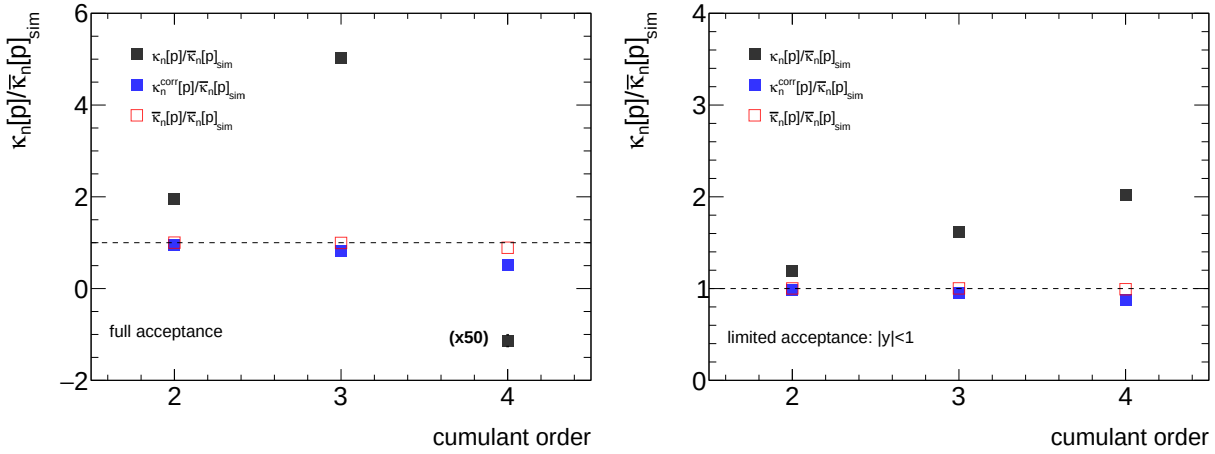

Figure 12. Left panel: Cumulants of protons in the full acceptance, presented for the 10% most central collisions (cf. Figs. 10 and 11). Right panel: Similar plot for the 10% most central collisions, but inside the finite acceptance delimited with the $|y| < 1$ criterion. The results are normalized to the true cumulants, $\bar{\kappa}_n[p]_{sim}$.

In either case, not all contributions can be accessed by a direct measurement. The remaining terms lead to biases, Δ_k, which depend on the multiplicity distribution per wounded nucleon. These biases are, however, parametrically suppressed by powers of $\langle N\rangle / \langle M\rangle$ depending on the order of the cumulants. The biases are also small if the multiplicity distribution per wounded nucleon is close to Poisson. In addition, we suggest to constrain these biases in experiment with fits to the observed multiplicity distribution within the wounded-nucleon model.

- We have worked here within the wounded nucleon model to formulate volume fluctuations. Alternatively, one may introduce generic volume fluctuations as done e.g. in [22]. It is easy to show (see Appendix D) that the resulting expressions for the corrected cumulants, κ_j^{corr}, and the biases, Δ_j, are identical to those derived here, i.e. Eqs. (24-26).

- We note that one gets similar expressions for the fluctuations from the wounded nucleons, Eqs. (20-22), in terms of the factorial cumulants of, for example, pions instead of the total track multiplicity. This has the advantage that the corrections do not involve the particles of interest, protons, in our case. Of course, this approach requires that sufficiently many pions are produced and thus may be limited to collisions at higher energies.

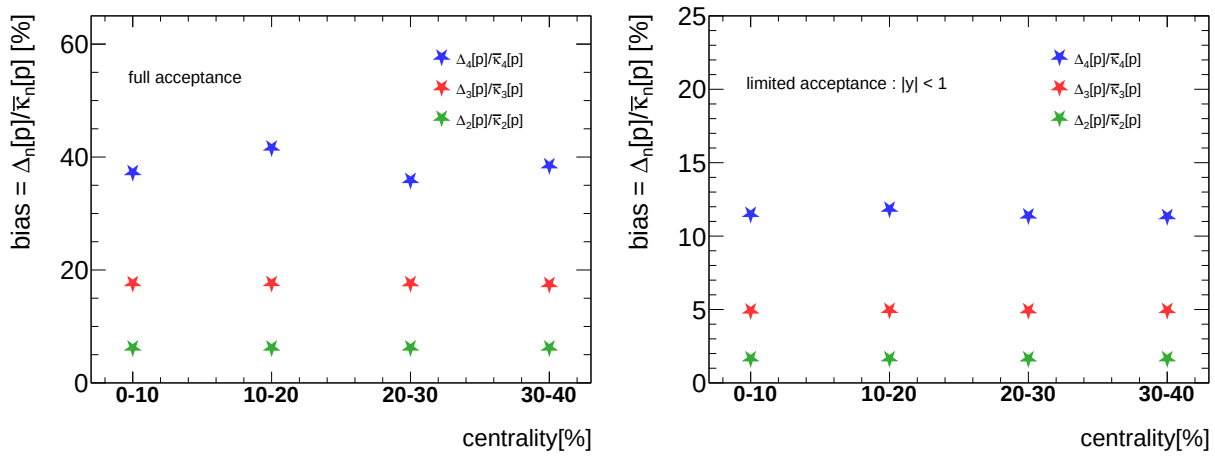

Figure 13. The bias terms for model B, in the full (left panel) and finite (right panel) acceptances. The acceptance, $|y| < 1$ is introduced using rapidity distributions of pions and protons as shown in Fig. 9.

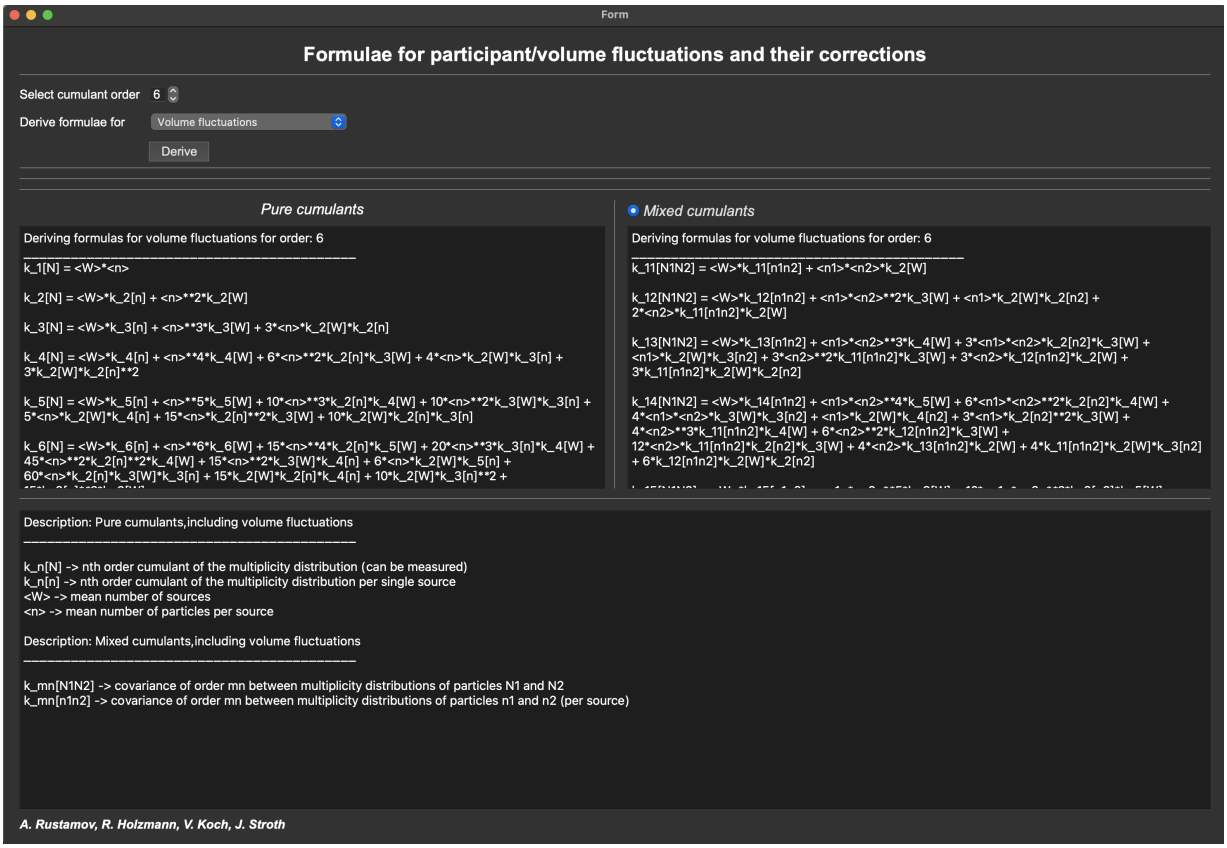

Figure 14. The GUI for deriving analytic formulas.

- We have checked that the proposed method also works if the multiplicity distribution is determined for a different acceptance than the particle distribution of interest. In this case all quantities in the expression for the corrected cumulants, Eqs.(24-26) involving the multiplicity should be evaluated in the multiplicity acceptance while all quantities involving the particles of interest, such as $\langle N \rangle$ or $\kappa_j[N]$ should be determined in the particle acceptance.

- We have verified that the proposed method is not affected by potentially different rapidity distributions for different particle types.

- We note that the correction term and bias for the second-order cumulant depends on the properties of the multiplicity distribution only while those for higher-order cumulants also involve the (uncorrected) cumulants of interest (at a lower order), $\kappa_n[N]$ (see Eq. (25,26).

- The proposed method is also applicable for mixed cumulants, such as the covariance between two particle species. The relevant formulas for mixed cumulants between species A and B up to $\kappa_{2,2}[A,B]$ are given in Appendix G.

  The corresponding relations for correction and bias terms for mixed cumulants of any order can be obtained with the provided software package [25].

- Here we have not explicitly discussed corrections for net proton cumulants. However, those can be easily obtained using the corrections to the mixed cumulants provided in Appendix G. For example, the second-order cumulant of the net proton distribution is given by

$$\kappa_2[N-\bar{N}] = \kappa_2[N] + \kappa_2[\bar{N}] - 2\kappa_{1,1}[N,\bar{N}] \tag{39}$$

  The corrected cumulant is the (using Eqs. (24, G8)

$$\kappa_2^{corr}[N-\bar{N}] = \kappa_2[N-\bar{N}] - \frac{\left(\langle N\rangle - \langle\bar{N}\rangle\right)^2}{\langle M\rangle^2} C_2[M] \tag{40}$$

  with the bias

$$\Delta = \frac{\left(\langle N\rangle - \langle\bar{N}\rangle\right)^2}{\langle M\rangle^2} \bar{C}_2[M] \tag{41}$$

  For systems at vanishing baryon number chemical potential, such as those created at very high collision energies, $\langle N\rangle = \langle\bar{N}\rangle$ so that the corrected cumulant is identical to the measured one (as discussed in [22]) and the bias vanishes.

In summary, we have presented a method to correct experimentally measured particle number cumulants for the effect of participant or volume fluctuations. The essential idea is to extract the contribution from the volume fluctuations from the distribution of charged particles which, after appropriate re-scaling, may be subtracted from the measured cumulants of interest. Our proposed method is not exact as there remains a bias or remnant which can not be accessed directly from experiment. However, we have shown by model calculations that this bias is very small compared to the contribution from participant fluctuations and we hence consider our method an important step towards measuring the true dynamical fluctuations of the system.

ACKNOWLEDGMENTS

V.K would like to thank GSI and the Institute for Nuclear Theory at the University of Washington for their kind hospitality and stimulating research environment. V.K. has been supported by the U.S. Department of Energy, Office of Science, Office of Nuclear Physics, under contract number DE-AC02-05CH11231, by the INT's U.S. Department of Energy grant No. DE-FG02-00ER41132, and by the ExtreMe Matter Institute EMMI at the GSI Helmholtzzentrum für Schwerionenforschung, Darmstadt, Germany.

Appendix A: Wounded-nucleon model

Here we briefly discuss the wounded-nucleon model following the Appendix of Ref. [32]. The wounded-nucleon model assumes that particles are produced by independent sources, called wounded nucleons or participants. Therefore, the probability to find A particles of type A and B particles of type B can be written as

$$P(A,B) = \sum_w W(w) \sum_{a_1,\cdots a_w} \sum_{b_1,\cdots b_w} p(a_1,b_1)\cdots p(a_w,b_w)\ \delta_{A,\sum_{k=1}^w a_k} \delta_{B,\sum_{k=1}^w b_k}. \tag{A1}$$

Here $W(w)$ denotes the probability to have w wounded nucleons, and $p(a,b)$ is the probability to have a particles of type A and b particles of type B from one wounded nucleon. The moment-generating function, $h\left(t_A,t_B\right)$ is then

$$\begin{aligned}
H\left(t_A,t_B\right) &= \sum_{A,B} e^{t_A A} e^{t_b B} P\left(A,B\right) \\
&= \sum_w W\left(w\right) \sum_{a_1,\cdots a_w} \sum_{b_1,\cdots b_w} p\left(a_1,b_1\right)\cdots p\left(a_w,b_w\right) e^{t_A \sum_{k=1}^{w} a_k} e^{t_B \sum_{k=1}^{w} b_k} \\
&= \sum_w W\left(w\right) \sum_{a_1,b_1} p\left(a_1,b_1\right) e^{t_A a_1 + t_b b_1} \cdots \sum_{a_w,b_w} p\left(a_w,b_w\right) e^{t_A a_w + t_B b_w} \\
&= \sum_w W\left(w\right) \left[\sum_{a,b} p\left(a,b\right) e^{t_A a + t_B b}\right]^w \\
&= \sum_w W\left(w\right) \left[h_w\left(t_A,t_B\right)\right]^w \\
&= \sum_w W\left(w\right) e^{w\, g_w(t_A,t_B)}
\end{aligned} \tag{A2}$$

where $h_w\left(t_A,t_B\right) = \sum_{a,b} p\left(a,b\right) e^{t_A a + t_B b}$ is the moment generating function and $g_w(t_A,t_B) = \ln\left[h_w\left(t_A,t_B\right)\right]$ the cumulant-generating function for one wounded nucleon, respectively. The cumulant-generating function, $G\left(t_A,t_B\right) = \ln\left(h\left(t_A,t_B\right)\right)$, is then given by

$$G\left(t_A,t_B\right) = \ln\left[H\left(t_A,t_B\right)\right] = \ln\left[\sum_w W\left(w\right) e^{w\, g_w(t_1,t_2)}\right] = G_W\left(g_w(t_A,t_B)\right) \tag{A3}$$

where $G_W(t) = \ln\left[\sum_w W\left(w\right) e^{w\,t}\right]$ in the cumulant-generating function for the wounded-nucleon distribution, $W(w)$. We note, that $g_w(0,0) = G_W(0) = 0$ by construction. The cumulants are then obtained as

$$\kappa_{j,k}[A,B] = \left.\frac{\partial^j \partial^k}{\partial t_A \partial t_B} g\left(t_A,t_B\right)\right|_{t_A=t_B=0}. \tag{A4}$$

For example:

$$\begin{aligned}
\kappa_1[A] &= \frac{\partial}{\partial t_A}\, G(t_A,0)|_{t_A=0} = \frac{dG_w}{dg_w}\, \left.\frac{dg_w(t_A,0)}{dt_A}\right|_{t_A=0} = \left.\frac{dG_w}{dg_w}\right|_{g_w=0} \left.\frac{dg_w(t_A,0)}{dt_A}\right|_{t_A=0} \\
&= \kappa_1[N_w]\kappa_1[a] = \left\langle N_w\right\rangle \left\langle a\right\rangle
\end{aligned} \tag{A5}$$

where $\kappa_1[n] = \langle a\rangle$ denotes the mean number of particles of type A per wounded nucleon and $\kappa_1[w] = \langle N_w\rangle$ the mean number of wounded nucleons. The second-order cumulant is

$$\begin{aligned}
\kappa_2[A] &= \frac{\partial^2}{\partial t_A^2}\, G(t_A,0)|_{t_A=0} \\
&= \frac{d^2G_w}{dg_w^2} \left.\left(\frac{dg_w(t_A,0)}{dt_A}\right)^2\right|_{t_A=0} + \frac{dG_w}{dg_w}\, \left.\frac{d^2g_w(t_A,0)}{dt_A^2}\right|_{t_1=0} \\
&= \kappa_2[N_w]\kappa_1[a]^2 + \kappa_1[N_w]\kappa_2[a] = \kappa_2[N_w]\left\langle a\right\rangle^2 + \left\langle N_w\right\rangle \kappa_2[a]
\end{aligned} \tag{A6}$$

The covariance is

$$\begin{aligned}
cov[A,B] &= \frac{\partial}{\partial t_A \partial t_B}\, G(t_A,t_B)|_{t_A,t_B=0} = \frac{\partial}{\partial t_B} \left.\left(\frac{dG_w}{dg_w}\frac{\partial g_w(t_A,t_B)}{\partial t_A}\right)\right|_{t_A,t_B=0} \\
&= \left.\frac{d^2G_w}{dg_w^2}\frac{\partial g_w(t_A,t_B)}{\partial t_A}\frac{\partial g_w(t_A,t_B)}{\partial t_B}\right|_{t_A,t_B=0} + \left.\left(\frac{dG_w}{dg_w}\frac{\partial^2 g_w(t_A,t_B)}{\partial t_A \partial t_B}\right)\right|_{t_A,t_B=0} \\
&= \kappa_2[N_W]\kappa_1[a]\kappa_1[a] + \kappa_1[N_w] cov[a,b] \\
&= \kappa_2[N_w]\left\langle a\right\rangle\left\langle b\right\rangle + \left\langle N_w\right\rangle cov[a,b]
\end{aligned} \tag{A7}$$

Using the relation between the cumulant and factorial cumulant generating function, Eq. B3 , the factorial cumulant generating function is given by

$$G_F\left(z_{\rm A},z_{\rm B}\right)=G\left(\ln(z_{\rm A}),\ln(z_{\rm B})\right)=G_W\left(g_w\left(\ln(z_{\rm A}),\ln(z_{\rm B})\right)\right)=G_W\left(g_{F,w}\left(z_{\rm A},z_{\rm B}\right)\right), \tag{A8}$$

with

$$g_{F,w}\left(z_{\rm A},z_{\rm B}\right)=\sum_{a,b}p\left(a,b\right)z_{\rm A}^{a}z_{\rm B}^{b}$$

the factorial cumulant generating function for the distribution of one wounded nucleon, $p\left(a,b\right)$. The structure is the same as for the cumulant generating function, except that now the argument of the wounded-nucleon cumulant-generating function is the factorial cumulant generating function, $g_{F,w}$. Thus the factorial cumulants are easily obtained by simply replacing all the cumulants of the particle distribution for a given wounded nucleon, $\kappa_{i,j}[a,b]$ with the corresponding factorial cumulants, with $C_1[X]=\kappa_1[X]=\langle X\rangle$

$$\begin{aligned}C_1[A]&=\frac{\partial}{\partial z_{\rm A}}\,g_F(z_{\rm A},1)|_{z_{\rm A}=1}=\kappa_1[N_w]C_1[a]=\langle N_w\rangle\,\langle a\rangle\\ C_2[A]&=\kappa_2[N_w]\,\langle a\rangle^2+\langle N_w\rangle\,C_2[a]\\ C_{1,1}[A,B]&=cov[A,B]\end{aligned} \tag{A9}$$

Appendix B: Cumulant and factorial cumulant generating functions

Given a multiplicity distribution for particles of type A and B, $P\left(A,B\right)$ the generating functions for cumulants, $g(t_A,t_B)$, and factorial cumulants. $g_F(t_A,t_B)$ are given by

$$g\left(t_A,t_B\right)=\ln[\sum_{A,B}P\left(A,B\right)e^{t_AA}e^{t_BB} \tag{B1}$$

$$g_F\left(z_{\rm A},z_{\rm B}\right)=\ln[\sum_{A,B}P\left(A,B\right)\left(z_{\rm A}\right)^A(z_{\rm B})^B. \tag{B2}$$

By construction, $g\left(t_A=0,t_B=0\right)=0$ and $g_F\left(z_{\rm A}=1,z_{\rm B}=1\right)=0$. Cumulants of order (i,j), $\kappa_{j,k}[A,B]$, are then obtained through

$$\kappa_{j,k}[A,B]=\left.\frac{\partial^j\partial^k}{\partial t_A\partial t_B}g\left(t_A,t_B\right)\right|_{t_A=t_B=0},$$

while the factorial cumulants, $C_{j,k}[A,B]$, are given by

$$C_{j,k}[A,B]=\left.\frac{\partial^j\partial^k}{\partial z_{\rm A}\partial z_{\rm B}}g\left(z_{\rm A},zt\right)\right|_{z_{\rm A}=z_{\rm B}=1}.$$

The generating functions are related through

$$g_F\left(z_{\rm A},z_{\rm B}\right)=g\left[\ln(z_{\rm A}),\ln(z_{\rm B})\right] \tag{B3}$$

or vice versa

$$g\left(t_A,t_B\right)=g_F\left(e^{t_B},e^{t_B}\right) \tag{B4}$$

These relations may also be used to convert cumulants into factorial cumulants and vice versa. For example, for the diagonal cumulants, $\kappa_n[A]$ we have

$$\kappa_n[A]=\sum_{j=1}^{n}S\left(n,j\right)C_j[A] \tag{B5}$$

where $S(n,j)$ denotes the Sterling numbers of the second kind. The inverse relation is

$$C_n[A] = \sum_{j=1}^{n} B_{n,j}\left(1, -1, 2, \ldots, (-1)^{j-1}(n-j+1)!\right)\ \kappa_j[A] \tag{B6}$$

with $B_{n,j}$ being Bell polynomials. For the first four orders this evaluates to

$$\begin{aligned}
\kappa_1 &= C_1 \\
\kappa_2 &= C_1 + C_2 \\
\kappa_3 &= C_1 + 3C_2 + C_3 \\
\kappa_4 &= C_1 + 7C_2 + 6C_3 + C_4
\end{aligned} \tag{B7}$$

and

$$\begin{aligned}
C_2 &= \kappa_2 - \kappa_1 \\
C_3 &= 2\kappa_1 - 3\kappa_2 + \kappa_3 \\
C_4 &= -6\kappa_1 + 11\kappa_2 - 6\kappa_3 + \kappa_4
\end{aligned} \tag{B8}$$

Appendix C: Multiplicity Distribution

The multiplicity distribution, $P(M)$, is given by summing over all (charged) particles,

$$P_M\left(M\right) = \sum_{A,B,X} P\left(A,B,X\right)\delta_{M,A+B+X}, \tag{C1}$$

where

$$P\left(A,B,X\right) = \sum_{w} W\left(w\right) \sum_{a_1,\cdots a_w} \sum_{b_1,\cdots b_w} \sum_{x_1.\cdots x_w} p\left(a_1,b_1,x_1\right)\cdots p\left(a_w,b_w,x_w\right)\ \delta_{A,\sum_{k=1}^{w} a_k}\delta_{B,\sum_{k=1}^{w} a_k}\delta_{X,\sum_{k=1}^{w} x_k}$$

is the distribution of particles of type A, B and all others, denoted by X. The distribution for particles A and B defined in Appendix A are then given by $P\left(A,B\right) = \sum_{X=0}^{\infty} P\left(A,B,X\right)$ while that for the particles per wounded nucleons are given by $p\left(a,b\right) = \sum_{x=0}^{\infty} p\left(a,b,x\right)$

The moment generating function is then given by (proceeding analogously to Eq. A2:

$$\begin{aligned}
H_M(t) &= \sum_{M} P_M(M)\, e^{tM} = \sum_{M,A,B,X} P(A,B,X)\delta_{M,A+B+X}\, e^{tM} = \sum_{A,B,X} P(A,B,X)\, e^{t(A+B+X)} \\
&= \sum_{w} W\left(w\right) \sum_{a_1,\cdots a_w} \sum_{b_1,\cdots b_w} \sum_{x_1.\cdots x_w} p\left(a_1,b_1,x_1\right)\cdots p\left(a_w,b_w,x_w\right) e^{t\sum_{k=1}^{w} a_k} e^{t\sum_{k=1}^{w} b_k} e^{t\sum_{k=1}^{w} x_k} \\
&= \sum_{w} W\left(w\right) \sum_{a_1}\sum_{b_1}\sum_{x_1} p\left(a_1,b_1,x_1\right) e^{t(a_1+b_1+c_1)} \cdots \sum_{a_w}\sum_{b_w}\sum_{x_w} p\left(a_w,b_w,x_w\right) e^{t(a_w+b_w+c_w)} \\
&= \sum_{w} W\left(w\right) \left[\sum_{a}\sum_{b}\sum_{x} p\left(a,b,x\right) e^{t(a+b+c)}\right]^{w} \\
&= \sum_{w} W\left(w\right) \left[h_{m,w}(t)\right]^{w} \\
&= \sum_{w} W\left(w\right) e^{w g_{m,w}(t)}
\end{aligned}$$

where, $h_{m,w}(t)$ the moment generating function and $g_{m,w}(t) = \ln\left[h_{m,w}(t)\right]$ the cumulant generating function of the multiplicity distribution for *one* wounded nucleon, $p(m) = \sum_{a,b,x} p(a,b,x)\delta_{m,a+b+c}$. The cumulant generating function, $G_M(t)$, for the multiplicity distribution, $P\left(M\right)$, is then given by

$$G_M(t) = \ln\left[H_M(t)\right] = \ln\left[\sum_{w} W\left(w\right) e^{w g_{m,w}(t)}\right] = G_W\left(g_{m,w}(t)\right) \tag{C2}$$

The cumulants of the multiplicity distribution are given by (following the analogous Eqs. A5 and A6)

$$\begin{aligned}\kappa_1[M] &= \langle N_w\rangle \langle m\rangle \\ \kappa_2[M] &= \kappa_2[N_w] \langle m\rangle^2 + \langle N_w\rangle \kappa_2[m]\end{aligned} \tag{C3}$$

where $\kappa_i[m]$ denote the cumulants of the multiplicity distribution of *one* wounded nucleon and $\kappa_i[N_W]$ those of the wounded nucleon distribution. Analogous to Eq. A8 the factorial cumulant generating function is readily obtained

$$G_{F,M}(z,) = G_M(\ln(z)) = G_W(g_{m,w}(\ln(z))) = G_W(g_{F,m,w}(z)), \tag{C4}$$

with

$$g_{F,m,w}(z) = \sum_m p(m) z^m$$

the factorial cumulant generating function for the multiplicity distribution of one nucleon, $p(m)$. Again, the factorial cumulants are obtained by replacing the cumulants of the distribution $p(m)$, $\kappa_i[m]$ with the corresponding factorial cumulants, $C_i[m]$, in Eq. C3 by the factorial cumulants

$$\begin{aligned}C_1[M] &= \langle N_w\rangle \langle m\rangle \\ C_2[M] &= \kappa_2[N_w] \langle m\rangle^2 + \langle N_w\rangle C_2[m]\end{aligned} \tag{C5}$$

Appendix D: Wounded Nucleon vs Volume Fluctuations

Here we will discuss the relation between wounded nucleon fluctuations and so-called volume fluctuations as they are discussed e.g. in [22]. Following Ref. [22] the cumulant generating function is given by

$$\Phi(t) = \ln\left[\int dV P(V) e^{V\xi(t)}\right] = \chi^V(\xi(t)) \tag{D1}$$

with $\chi^V(t)$ the cumulant generating function for the distribution of volumes, $P(V)$, and

$$\xi(t) = \frac{1}{V}\ln\left[\sum_N p(N;V) e^{Nt}\right] \tag{D2}$$

the generating function for scaled cumulants, κ/V, given for the distribution of particles at fixed volume, $p(N;V)$. Then, for a fixed volume V, the scaled cumulants are given by

$$\frac{\kappa_j}{V} = \frac{\partial^j}{\partial t^j}\,\xi(t)|_{t=0}\,. \tag{D3}$$

For the wounded nucleon model we have (see Appendix A)

$$G(t) = \ln\left[\sum_w W(w)\, e^{w\, g_w(t)}\right] = G_W(g_w(t)) \tag{D4}$$

with $G_W(t)$ the cumulant generating function for the wounded nucleon distribution, $W(w)$, and

$$g_w(t) = \ln\left[\sum_n p(n) e^{nt}\right] \tag{D5}$$

the generating function for the distribution of particles for one wounded nucleon. The cumulants per wounded nucleons for a fixed number of wounded nucleons, N_w, are given by

$$\frac{\kappa_j[N]}{N_w} = \kappa_j[n] = \frac{\partial^j}{\partial t^j}\, g_w(t)|_{t=0}\,. \tag{D6}$$

Comparing the above expressions, one finds that the cumulants for volume fluctuations can be obtained from those for the wounded-nucleon number by the following replacements

$$\kappa_j[N_w] \to \kappa_j[V]$$
$$\bar{\kappa}_j[N] = \langle N_w \rangle \kappa_j[N] \to \langle V \rangle \frac{\kappa_j}{V}$$

Indeed comparing the second-order cumulants for both scenarios we have

$$\kappa_2[N] = \langle N_w \rangle \kappa_2[n] + \langle n \rangle^2 \kappa_2[N_w] = \bar{\kappa}_2[N] + \langle N \rangle^2 \frac{\kappa_2[N_w]}{\langle N_w \rangle^2}$$
$$\kappa_2[N] = \langle V \rangle \frac{\kappa_2}{V} + \left(\frac{\kappa_1}{V}\right)^2 \kappa_2[V] = \bar{\kappa}_2[N] + \langle N \rangle^2 \frac{\kappa_2[V]}{\langle V \rangle^2}$$

where in the second line we used $\kappa_1 = \langle N \rangle$ and $\bar{\kappa}_2 = \langle V \rangle \frac{\kappa_2}{V}$. Obviously, analogous replacements also hold for the factorial cumulants

$$\bar{C}_j[N] = \langle N_w \rangle C_j[n] \to \langle V \rangle \frac{C_j}{V}$$

with C_j/V the volume scaled factorial cumulants.

Appendix E: Results for factorial cumulants

Here we provide the formulas for the corrected factorial cumulants, C_k^{corr} and c_k^{corr}, and the the associated biases, $\Delta_{k,F}$ and $\delta_{k,F}$. Both the factorial cumulants and the biases are related to the corresponding cumulants via the linear relation Eqs. B7 and B8. The corrected factorial cumulants and the associated biases are

$$C_2^{corr} = C_2[N] - \frac{\langle N \rangle^2}{\langle M \rangle^2} C_2[M] \tag{E1}$$
$$C_3^{corr} = C_3[N] - \frac{3C_2[M]C_2[N]\langle N \rangle}{\langle M \rangle^2} + \frac{3C_2[M]^2\langle N \rangle^3}{\langle M \rangle^4} - \frac{C_3[M]\langle N \rangle^3}{\langle M \rangle^3} \tag{E2}$$
$$C_4^{corr} = C_4[N] - \left(\frac{6C_2[N]\langle N \rangle^2 \left(C_3[M]\langle M \rangle - 3C_2[M]^2\right)}{\langle M \rangle^4} + \frac{4C_2[M]C_3[N]\langle N \rangle}{\langle M \rangle^2} \right. \tag{E3}$$
$$\left. + \frac{3C_2[M]C_2[N]^2}{\langle M \rangle^2} + \frac{\langle N \rangle^4 \left(-10C_3[M]C_2[M]\langle M \rangle + C_4[M]\langle M \rangle^2 + 15C_2[M]^3\right)}{\langle M \rangle^6} \right) \tag{E4}$$

$$\Delta_{2,F} = \frac{\langle N \rangle^2}{\langle M \rangle^2} \bar{C}_2[M] \tag{E5}$$
$$\Delta_{3,F} = \bar{C}_2[M] \left(\frac{3C_2[N]\langle N \rangle}{\langle M \rangle^2} - \frac{3C_2[M]\langle N \rangle^3}{\langle M \rangle^4} \right) + \frac{\bar{C}_3[M]\langle N \rangle^3}{\langle M \rangle^3} \tag{E6}$$
$$\Delta_{4,F} = \bar{C}_2[M] \left(\frac{4C_3[N]\langle N \rangle}{\langle M \rangle^2} + \frac{3C_2[N]^2}{\langle M \rangle^2} - \frac{18C_2[M]C_2[N]\langle N \rangle^2}{\langle M \rangle^4} - \frac{4C_3[M]\langle N \rangle^4}{\langle M \rangle^5} + \frac{15C_2[M]^2\langle N \rangle^4}{\langle M \rangle^6} \right) \tag{E7}$$
$$+ \bar{C}_3[M] \left(\frac{6C_2[N]\langle N \rangle^2}{\langle M \rangle^3} - \frac{6C_2[M]\langle N \rangle^4}{\langle M \rangle^5} \right) + \frac{\bar{C}_4[M]\langle N \rangle^4}{\langle M \rangle^4} \tag{E8}$$

For the scaled factorial cumulants we have

$$c_2^{corr} = c_2[N] - \frac{\langle N\rangle}{\langle M\rangle} c_2[M] \tag{E9}$$

$$c_3^{corr} = c_3[N] - 3\frac{\langle N\rangle}{\langle M\rangle} c_2[M]c_2[N] + \left(\frac{\langle N\rangle}{\langle M\rangle}\right)^2 \left(3c_2[M]^2 - c_3[M]\right) \tag{E10}$$

$$c_4^{corr} = c_4[N] - \frac{\langle N\rangle}{\langle M\rangle} \left(3c_2[M]c_2[N]^2 + 4c_2[M]c_3[N]\right) \tag{E11}$$

$$+ \left(\frac{\langle N\rangle}{\langle M\rangle}\right)^2 \left(18c_2[M]^2 c_2[N] - 6c_3[M]c_2[N]\right) \tag{E12}$$

$$+ \left(\frac{\langle N\rangle}{\langle M\rangle}\right)^3 \left(-15c_2[M]^3 + 10c_2[M]c_3[M] - c_4[M]\right) \tag{E13}$$

$$\delta_{2,F} = \frac{\langle N\rangle}{\langle M\rangle} \bar{c}_2[M] \tag{E14}$$

$$\delta_{3,F} = 3\frac{\langle N\rangle}{\langle M\rangle} c_2[N]\bar{c}_2[M] + \left(\frac{\langle N\rangle}{\langle M\rangle}\right)^2 \left(\bar{c}_3[M] - 3c_2[M]\bar{c}_2[M]\right) \tag{E15}$$

$$\delta_{4,F} = \frac{\langle N\rangle}{\langle M\rangle} \left(3c_2[N]^2\bar{c}_2[M] + 4c_3[N]\bar{c}_2[M]\right) \tag{E16}$$

$$+ \left(\frac{\langle N\rangle}{\langle M\rangle}\right)^2 \left(6c_2[N]\bar{c}_3[M] - 18c_2[M]c_2[N]\bar{c}_2[M]\right) \tag{E17}$$

$$+ \left(\frac{\langle N\rangle}{\langle M\rangle}\right)^3 \left(15c_2[M]^2\bar{c}_2[M] - 6c_2[M]\bar{c}_3[M] - 4c_3[M]\bar{c}_2[M] + \bar{c}_4[M]\right) \tag{E18}$$

Appendix F: Particle production through clusters

Let us assume that particles are produced via clusters and that each cluster further decays into two particles. Moreover, clusters are generated from a Poisson distribution. As each cluster decays into two particles the probability of measuring k particles is equivalent to measuring $k/2$ clusters and can be presented as:

$$p\left(k;\langle N_{cl}\rangle\right) = e^{-\langle N_{cl}\rangle} \frac{\langle N_{cl}\rangle^{k/2}}{(k/2)!} \tag{F1}$$

The corresponding moment generating function reads:

$$M(t) = \sum_{k/2=0}^{\infty} e^{tk} e^{-\langle N_{cl}\rangle} \frac{\langle N_{cl}\rangle^{k/2}}{(k/2)!} = e^{\langle N_{cl}\rangle\left(e^{2t}-1\right)}, \tag{F2}$$

where $\langle N_{cl}\rangle$ denotes mean number of clusters produced.

The cumulants of total particle number k can be computed as:

$$\kappa_n[k] = \left.\frac{\partial ln(M(t))}{dt}\right|_{t=0} \tag{F3}$$

For the first two cumulants one gets:

$$\kappa_1[k] = 2\langle N_{cl}\rangle \tag{F4}$$

$$\kappa_2[k] = 4\langle N_{cl}\rangle \tag{F5}$$

One clearly sees from Eqs. F4 and F5 that $\kappa_1(k) \neq \kappa_2(k)$, i.e the total number of particles does not follow a Poisson distribution, although the clusters do. Moreover, one observes that particle production through clusters enhances fluctuations. In general, for clusters following a Poisson distribution and decaying into m particles, the cumulants of total particle number can be written as:

$$\kappa_n[k] = m^n \langle N_{cl} \rangle \tag{F6}$$

Appendix G: Mixed Cumulants

Here we provide the relevant formulas for mixed cumulants. Given the generating function, Eq. A3, the mixed cumulants for particles of type A and B are given by (see Eq. A4)

$$\kappa_{j,k}[A,B] = \left. \frac{\partial^j \partial^k}{\partial t_A \partial t_B} g\left(t_A, t_B\right) \right|_{t_A = t_B = 0} \tag{G1}$$

The explicit formulas for the four lowest-order mixed cumulants are:

$$\kappa_{1,1}[A,B] = \bar{\kappa}_{1,1}[A,B] + \langle A \rangle \langle B \rangle \frac{\kappa_2\left[N_W\right]}{\langle N_W \rangle^2} \tag{G2}$$

$$\kappa_{2,1}[A,B] = \bar{\kappa}_{2,1}[A,B] + \left(2\langle A \rangle \bar{\kappa}_{1,1}[A,B] + \langle B \rangle \bar{\kappa}_{2,0}[A,B]\right) \frac{\kappa_2\left[N_W\right]}{\langle N_W \rangle^2} + \langle A \rangle^2 \langle B \rangle \frac{\kappa_3\left[N_W\right]}{\langle N_W \rangle^3} \tag{G3}$$

$$\kappa_{1,2}[A,B] = \bar{\kappa}_{1,2}[A,B] + \left(\langle A \rangle \bar{\kappa}_{0,2}[A,B] + 2\langle B \rangle \bar{\kappa}_{1,1}[A,B]\right) \frac{\kappa_2\left[N_W\right]}{\langle N_W \rangle^2} + \langle A \rangle \langle B \rangle^2 \frac{\kappa_3\left[N_W\right]}{\langle N_W \rangle^3} \tag{G4}$$

$$\begin{aligned} \kappa_{2,2}[A,B] = {} & \bar{\kappa}_{2,2}[A,B] + \left(\langle A \rangle^2 \bar{\kappa}_{0,2}[A,B] + 4\langle A \rangle \langle B \rangle \bar{\kappa}_{1,1}[A,B] + \langle B \rangle^2 \bar{\kappa}_{2,0}[A,B]\right) \frac{\kappa_3\left[N_W\right]}{\langle N_W \rangle^3} \\ & + \left(2\langle A \rangle \bar{\kappa}_{1,2}[A,B] + 2\langle B \rangle \bar{\kappa}_{2,1}[A,B] + 2\bar{\kappa}_{1,1}[A,B]^2 + \bar{\kappa}_{0,2}[A,B]\bar{\kappa}_{2,0}[A,B]\right) \frac{\kappa_2\left[N_W\right]}{\langle N_W \rangle^2} \\ & + \langle A \rangle^2 \langle B \rangle^2 \frac{\kappa_4\left[N_W\right]}{\langle N_W \rangle^4} \end{aligned} \tag{G5}$$

where, analogous to the notation for the regular cumulants, $\bar{\kappa}_{j,k}[A,B]$ denotes the mixed cumulant for constant number of wounded nucleons $\langle N_W \rangle$. Note, that $\kappa_{j,0}[A,B] = \kappa_j[A]$ and $\kappa_{0,j}[A,B] = \kappa_j[B]$ correspond to the regular cumulant for particles of type A and B respectively. The firs order mixed cumulant, $\kappa_{1,1}[A,B] = cov[A,B]$ is also referred to as the co-variance between the distributions of particles A and B. In order to obtain the corrected mixed cumulants we proceed in the same fashion as for the regular cumulant. We express the terms involving cumulants of the wounded nucleons, $\kappa_i\left[N_W\right] / \langle N_W \rangle^i$ in terms of the factorial cumulants of the multiplicity distribution (See Eqs. 20-22) and solve for the the mixed cumulants with fixed number of wounded nucleons, $\bar{\kappa}_{j,k}[A,B]$. Again, the results are given in the form

$$\bar{\kappa}_{j,k}[A,B] = \kappa_{j,k}^{corr}[A,B] + \Delta_{j,k} \tag{G6}$$

where $\kappa^{corr}_{j,k}[A,B]$ are the cumulants including the measurable corrections and $\Delta_{j,k}$ are the corresponding biases due to quantities which are not directly measurable.

$$\kappa^{corr}_{1,1}[A,B] = \kappa_{1,1}[A,B] - \frac{\langle A\rangle\langle B\rangle}{\langle M\rangle^2} C_2[M] \tag{G7}$$

$$\Delta_{1,1} = \frac{\langle A\rangle\langle B\rangle}{\langle M\rangle^2} \bar{C}_2[M] \tag{G8}$$

$$\kappa^{corr}_{2,1}[A,B] = \kappa_{2,1}[A,B] - \frac{\langle B\rangle C_2[M]\bar{\kappa}_{2,0}[A,B]}{\langle M\rangle^2} - \frac{2\langle A\rangle C_2[M]\kappa_{1,1}[A,B]}{\langle M\rangle^2} + \frac{\langle A\rangle^2\langle B\rangle\left(2C_2[M]^2 - \langle M\rangle C_3[M]\right)}{\langle M\rangle^4} \tag{G9}$$

$$\begin{aligned}\Delta_{2,1} = \frac{1}{\langle M\rangle^4}\big[&2\langle A\rangle\langle M\rangle^2\bar{C}_2[M]\kappa_{1,1}[A,B] + \langle B\rangle\langle M\rangle^2\bar{C}_2[M]\bar{\kappa}_{2,0}[A,B] \\ &-\langle A\rangle^2\langle B\rangle\left(\bar{C}_2[M]\left(\bar{C}_2[M] + C_2[M]\right) - \langle M\rangle\bar{C}_3[M]\right)\big]\end{aligned} \tag{G10}$$

$$\kappa^{corr}_{1,2}[A,B] = \kappa_{1,2}[A,B] - \frac{\langle A\rangle C_2[M]\bar{\kappa}_{0,2}[A,B]}{\langle M\rangle^2} - \frac{2\langle B\rangle C_2[M]\kappa_{1,1}[A,B]}{\langle M\rangle^2} + \frac{\langle B\rangle^2\langle A\rangle\left(2C_2[M]^2 - \langle M\rangle C_3[M]\right)}{\langle M\rangle^4} \tag{G11}$$

$$\begin{aligned}\Delta_{1,2} = \frac{1}{\langle M\rangle^4}\big[&2\langle B\rangle\langle M\rangle^2\bar{C}_2[M]\kappa_{1,1}[A,B] + \langle A\rangle\langle M\rangle^2\bar{C}_2[M]\bar{\kappa}_{0,2}[A,B] \\ &-\langle A\rangle\langle B\rangle^2\left(\bar{C}_2[M]\left(\bar{C}_2[M] + C_2[M]\right) - \langle M\rangle\bar{C}_3[M]\right)\big]\end{aligned} \tag{G12}$$

$$\begin{aligned}\kappa^{corr}_{2,2}[A,B] = \kappa_{2,2}[A,B] &+ \frac{2\langle A\rangle^2 C_2[M]^2\bar{\kappa}_{0,2}[A,B]}{\langle M\rangle^4} + \frac{2\langle B\rangle^2 C_2[M]^2\bar{\kappa}_{2,0}[A,B]}{\langle M\rangle^4} \\ &- \frac{C_2[M]\bar{\kappa}_{0,2}[A,B]\bar{\kappa}_{2,0}[A,B]}{\langle M\rangle^2} - \frac{\langle A\rangle^2 C_3[M]\bar{\kappa}_{0,2}[A,B]}{\langle M\rangle^3} - \frac{\langle B\rangle^2 C_3[M]\bar{\kappa}_{2,0}[A,B]}{\langle M\rangle^3} \\ &+ \frac{12\langle A\rangle\langle B\rangle C_2[M]^2\kappa_{1,1}[A,B]}{\langle M\rangle^4} - \frac{2C_2[M]\kappa_{1,1}[A,B]^2}{\langle M\rangle^2} - \frac{2\langle A\rangle C_2[M]\kappa_{1,2}[A,B]}{\langle M\rangle^2} \\ &- \frac{2\langle B\rangle C_2[M]\kappa_{2,1}[A,B]}{\langle M\rangle^2} - \frac{4\langle A\rangle\langle B\rangle C_3[M]\kappa_{1,1}[A,B]}{\langle M\rangle^3} - \frac{10\langle A\rangle^2\langle B\rangle^2 C_2[M]^3}{\langle M\rangle^6} \\ &+ \frac{8\langle A\rangle^2\langle B\rangle^2 C_3[M]C_2[M]}{\langle M\rangle^5} - \frac{\langle A\rangle^2\langle B\rangle^2 C_4[M]}{\langle M\rangle^4}\end{aligned} \tag{G13}$$

$$\begin{aligned}\Delta_{2,2} = &\bar{C}_2[M]^2\left(-\frac{\langle A\rangle^2\bar{\kappa}_{0,2}[A,B]}{\langle M\rangle^4} - \frac{\langle B\rangle^2\bar{\kappa}_{2,0}[A,B]}{\langle M\rangle^4} + \frac{3C_2[M]\langle A\rangle^2\langle B\rangle^2}{\langle M\rangle^6}\right) \\ &+ \bar{C}_2[M]\left(-\frac{C_2[M]\langle A\rangle^2\bar{\kappa}_{0,2}[A,B]}{\langle M\rangle^4} - \frac{C_2[M]\langle B\rangle^2\bar{\kappa}_{2,0}[A,B]}{\langle M\rangle^4} + \frac{\bar{\kappa}_{0,2}[A,B]\bar{\kappa}_{2,0}[A,B]}{\langle M\rangle^2}\right. \\ &- \frac{2\bar{C}_3[M]\langle A\rangle^2\langle B\rangle^2}{\langle M\rangle^5} - \frac{12C_2[M]\langle A\rangle\langle B\rangle\kappa_{1,1}[A,B]}{\langle M\rangle^4} + \frac{2\langle A\rangle\kappa_{1,2}[A,B]}{\langle M\rangle^2} + \frac{2\kappa_{1,1}[A,B]^2}{\langle M\rangle^2} \\ &\left.+\frac{2\langle B\rangle\kappa_{2,1}[A,B]}{\langle M\rangle^2} + \frac{6C_2[M]^2\langle A\rangle^2\langle B\rangle^2}{\langle M\rangle^6} - \frac{2C_3[M]\langle A\rangle^2\langle B\rangle^2}{\langle M\rangle^5}\right) \\ &+ \bar{C}_3[M]\left(\frac{\langle A\rangle^2\bar{\kappa}_{0,2}[A,B]}{\langle M\rangle^3} + \frac{\langle B\rangle^2\bar{\kappa}_{2,0}[A,B]}{\langle M\rangle^3} + \frac{4\langle A\rangle\langle B\rangle\kappa_{1,1}[A,B]}{\langle M\rangle^3} - \frac{4C_2[M]\langle A\rangle^2\langle B\rangle^2}{\langle M\rangle^5}\right) \\ &+ \frac{\bar{C}_2[M]^3\langle A\rangle^2\langle B\rangle^2}{\langle M\rangle^6} + \frac{\bar{C}_4[M]\langle A\rangle^2\langle B\rangle^2}{\langle M\rangle^4}\end{aligned} \tag{G14}$$

[1] A. Rustamov, J. Stroth, and R. Holzmann, Nucl. Phys. A **1034**, 122641 (2023), arXiv:2211.14849 [nucl-th].
[2] F. Gross *et al.*, Eur. Phys. J. C **83**, 1125 (2023), arXiv:2212.11107 [hep-ph].
[3] M. Stephanov, Phys.Rev.Lett. **102**, 032301 (2009), arXiv:0809.3450 [hep-ph].
[4] M. Stephanov, Phys.Rev.Lett. **107**, 052301 (2011), arXiv:1104.1627 [hep-ph].
[5] A. Bzdak, S. Esumi, V. Koch, J. Liao, M. Stephanov, and N. Xu, Phys. Rept. **853**, 1 (2020), arXiv:1906.00936 [nucl-th].
[6] M. Asakawa, S. Ejiri, and M. Kitazawa, Phys. Rev. Lett. **103**, 262301 (2009), arXiv:0904.2089 [nucl-th].
[7] A. Bazavov *et al.* (HotQCD), Phys. Rev. D **96**, 074510 (2017), arXiv:1708.04897 [hep-lat].
[8] S. Borsanyi, Z. Fodor, J. N. Guenther, S. K. Katz, K. K. Szabo, A. Pasztor, I. Portillo, and C. Ratti, JHEP **10**, 205 (2018), arXiv:1805.04445 [hep-lat].

[9] B. Friman, F. Karsch, K. Redlich, and V. Skokov, Eur.Phys.J. **C71**, 1694 (2011), arXiv:1103.3511 [hep-ph].
[10] M. Abdallah *et al.* (STAR), Phys. Rev. C **104**, 024902 (2021), arXiv:2101.12413 [nucl-ex].
[11] M. Abdallah *et al.* (STAR), Phys. Rev. C **107**, 024908 (2023), arXiv:2209.11940 [nucl-ex].
[12] J. Adamczewski-Musch *et al.* (HADES), Phys. Rev. (2020), arXiv:2002.08701 [nucl-ex].
[13] S. Acharya *et al.* (ALICE), Phys. Lett. B **807**, 135564 (2020), arXiv:1910.14396 [nucl-ex].
[14] S. Acharya *et al.* (ALICE), Phys. Lett. B **844**, 137545 (2023), arXiv:2206.03343 [nucl-ex].
[15] W.-j. Fu, J. M. Pawlowski, F. Rennecke, and B.-J. Schaefer, Phys. Rev. D **94**, 116020 (2016), arXiv:1608.04302 [hep-ph].
[16] M. Bleicher, S. Jeon, and V. Koch, Phys. Rev. **C62**, 061902 (2000), arXiv:hep-ph/0006201 [hep-ph].
[17] A. Bzdak, V. Koch, and V. Skokov, Phys. Rev. **C87**, 014901 (2013), arXiv:1203.4529 [hep-ph].
[18] P. Braun-Munzinger, A. Rustamov, and J. Stachel, Nucl. Phys. A **982**, 307 (2019), arXiv:1807.08927 [nucl-th].
[19] P. Braun-Munzinger, B. Friman, K. Redlich, A. Rustamov, and J. Stachel, Nucl. Phys. A **1008**, 122141 (2021), arXiv:2007.02463 [nucl-th].
[20] P. Braun-Munzinger, K. Redlich, A. Rustamov, and J. Stachel, (2023), arXiv:2312.15534 [nucl-th].
[21] M. Kitazawa and M. Asakawa, Phys. Rev. **C85**, 021901 (2012), arXiv:1107.2755 [nucl-th].
[22] V. Skokov, B. Friman, and K. Redlich, Phys. Rev. **C88**, 034911 (2013), arXiv:1205.4756 [hep-ph].
[23] P. Braun-Munzinger, A. Rustamov, and J. Stachel, Nucl. Phys. **A960**, 114 (2017), arXiv:1612.00702 [nucl-th].
[24] A. Bialas, M. Bleszynski, and W. Czyz, Nucl. Phys. B **111**, 461 (1976).
[25] `https://github.com/anarrustamov/VolumeFluctuations`.
[26] J. Adamczewski-Musch *et al.* (HADES), Eur. Phys. J. A **54**, 85 (2018), arXiv:1712.07993 [nucl-ex].
[27] B. Abelev *et al.* (ALICE), Phys. Rev. C **88**, 044909 (2013), arXiv:1301.4361 [nucl-ex].
[28] J. Adam *et al.* (STAR), Phys. Rev. Lett. **126**, 092301 (2021), arXiv:2001.02852 [nucl-ex].
[29] C. Loizides, J. Nagle, and P. Steinberg, SoftwareX **1-2**, 13 (2015), arXiv:1408.2549 [nucl-ex].
[30] S. Harabasz, J. Kołaś, R. Ryblewski, W. Florkowski, T. Galatyuk, M. Gumberidze, P. Salabura, J. Stroth, and H. P. Zbroszczyk, Phys. Rev. C **107**, 034917 (2023), arXiv:2210.07694 [nucl-th].
[31] B. Abelev *et al.* (ALICE), Phys. Rev. C **88**, 044910 (2013), arXiv:1303.0737 [hep-ex].
[32] A. Bzdak, V. Koch, and V. Skokov, Eur. Phys. J. **C77**, 288 (2017), arXiv:1612.05128 [nucl-th].

arXiv:2403.03503v1 [hep-th] 6 Mar 2024

Universality of pseudo-Goldstone damping near critical points

Yang-yang Tan,[1] Yong-rui Chen,[1] Wei-jie Fu,[1,2,*] and Wei-Jia Li[1,†]

[1] *School of Physics, Dalian University of Technology, Dalian, 116024, P.R. China*
[2] *Shanghai Research Center for Theoretical Nuclear Physics, NSFC and Fudan University, Shanghai 200438, China*

Recently, in studies of holographic models and hydrodynamics with spontaneous breaking of approximate symmetries, it has been proposed that the damping of pseudo-Goldstone modes at finite temperatures is universally constrained in the way that $\Omega_\varphi/m_\varphi^2 \simeq D_\varphi$ in the broken phase, where Ω_φ and m_φ are the relaxation rate at zero wavenumber and the mass of pseudo-Goldstones, D_φ is the Goldstone diffusivity in the limit of purely spontaneous breaking. In this paper, we investigate the pseudo-Goldstone damping in a purely relaxational O(N) model by performing the functional renormalization group calculations at the full quantum and stochastic level within the Schwinger-Keldysh formalism. We find that, away from the critical temperature, the proposed relation is always valid. When the temperature is very close to the critical value such that the mass of the Higgs mode is comparable to the mass of the pseudo-Goldstone modes, the pseudo-Goldstone damping displays a novel scaling behavior that follows $\Omega_\varphi/m_\varphi^2 \propto m_\varphi^{\Delta_\eta}$ with a correction Δ_η controlled by the critical universalities. Moreover, we study how the correction depends on the value of N and show that $\Delta_\eta \to 0$ when fluctuations are infinitely suppressed in the large N limit. In this case, the proposed relation works even in the critical region. Finally, we match our results to the dissipative sector of the pion dynamics near the chiral phase transition.

Introduction.– The notion of spontaneous symmetry breaking (SSB) plays a central role in modern physics. As is well known that when the broken symmetry is global and continuous, a gapless excitation called the Goldstone mode emerges and governs the long wavelength behavior of the system. Usually, symmetries are not exact. In these cases, the would be massless excitations acquire a slight mass gap which are often named the *pseudo-Goldstone modes*. These soft modes are ubiquitous in real world, ranging from the high-energy QCD matter to low energy condensed matter systems [1–10].

Over the years, the dynamic properties of pseudo-Goldstone modes have attracted a lot of attention, not only because they are crucial for our understanding of the nature, but also because they share remarkably universal features that do not depend on the details of microscopic physics or even types of broken approximate symmetries, e.g., the 'screening mass' of pseudo-Goldstone fields m_φ satisfying the so-called Gell-Mann-Oakes-Renner (GMOR) relation when the system is not very close to the critical point [11]. At finite temperatures, the real part of their dispersion relations(the propagation sector of the real-time response) can be completely determined by several thermodynamic quantities appeared in the static correlator [1, 2]. More recently, it was also noticed in the studies of hydrodynamics and holographic systems, that the relaxation rate of pseudo-Goldstones, Ω_φ, which is the imaginary part of their dispersion relation at zero wavenumber is also related to the transport coefficient and the screening mass in a universal form as follows [12, 13]

$$\frac{\Omega_\varphi}{m_\varphi^2} \simeq D_\varphi + \mathcal{O}(m_\varphi^2)\,, \tag{1}$$

where D_φ is the 'Goldstone diffusivity' in the purely SSB phase. The validity of this relation was later on verified for global U(1) and $\mathrm{SU(2)_L \times SU(2)_R}$ symmetries in the context of holography [14, 15], and quasicrystals in the effective field theory framework [16, 17]. In addition, a more general analysis on the universality of (1) has also be carried out within the hydrodynamic approach either by requiring the locality of equations of motion [18] or imposing the second law of thermodynamics [19] in presence of external sources [20]. This is again a concrete example that holography brought predictions, input and developments for other fields.

Nevertheless, neither the standard hydrodynamic approach nor the holographic method (in the large N limit) endows us a systematic treatment for the non-equilibrium fluctuations, and therefore the formula (1) so far can only be trusted in the region away from the criticality where the fluctuations are significantly suppressed. In this work, we will investigate the pseudo-Goldstone damping when non-equilibrium fluctuations become particularly pronounced near the critical point in the field theory approach. The main challenge here is twofold: On the one hand, one has to handle with the strong interaction problems, and on the other hand, the very important fluctuations in the critical region should be taken into account. To overcome the difficulty, we adopt the functional renormalization group (fRG) within the Schwinger-Keldysh formlism [21–31], which is a powerful method for nonperturbative continuum field theory at finite temperatures. In this approach quantum and thermal fluctuations of different modes are encoded successively with the evolution of the renormalization group

* wjfu@dlut.edu.cn
† weijiali@dlut.edu.cn

(RG) scale. After performing the fRG computation on a simple critical O(N) model [32] named 'model A' in the in Hohenberg-Halperin classification [33], it is found that the relation (1) is always satisfied even in the critical region as long as T is not so close to T_c that the Higgs mode fluctuates strongly. In addition, this relation is not obeyed in the vicinity of the critical point where the mass of Higgs mode $m_\sigma \sim m_\varphi$ for any finite N and finite m_φ. More preciously, in this region, the ratio $\Omega_\varphi/m_\varphi^2$ displays a universal scaling behavior

$$\frac{\Omega_\varphi}{m_\varphi^2} \propto m_\varphi^{\Delta_\eta}\,, \tag{2}$$

that is controlled by $\Delta_\eta \equiv \eta_t - \eta$, the difference between the dynamic anomalous exponent η_t and static anomalous exponent η due to the large fluctuating effects. To make a step further, we investigate the dependence of this anomalous scaling regime on the value of N, and find that such a regime fades away in the mean-field approximation that can be achieved by taking $N \to \infty$. This implies that the scaling behavior (2) is invisible in the mean-field systems or the strongly-coupled systems with classical gravity duals. Finally, we match the results of the $N = 4$ case to the dissipative sector of the real-time dynamics of pions which are the pseudo-Goldstone modes in high energy physics. To the best of our knowledge, this is the first time where universalities of the pseudo-Goldstone damping in a strongly coupled system has been ever discussed at full quantum and stochastic level.

A relaxational critical O(N) model.– We consider the critical dynamics of a N-component real order parameter $\phi_a(t,\boldsymbol{x})$ with $a = 0, 1, \cdots N-1$ at finite temperature, whose quantum effective action on the Schwinger-Keldysh contour is given by [34]

$$\Gamma[\phi_c,\phi_q] = \int d^4x \left(Z_a^{(t)}\,\phi_{a,q}\,\partial_t\,\phi_{a,c} - Z_a^{(i)}\,\phi_{a,q}\,\partial_i^2\,\phi_{a,c} + V'(\rho_c)\,\phi_{a,q}\,\phi_{a,c} - 2\,Z_a^{(t)}\,T\,\phi_{a,q}^2 - \sqrt{2}c\,\sigma_q \right). \tag{3}$$

This is a purely dissipative relaxation model classified as model A in the seminal paper [33]. The subscripts 'q' and 'c' denote the 'quantum' and 'classical' fields, $V(\rho_c)$ is the effective potential preserving the O(N) symmetry with $\rho_c \equiv \phi_c^2/4$ and $V'(\rho_c)$ denotes its derivative, the quadratic term of $\phi_{a,q}$ whose coefficient can be fixed by the fluctuation-dissipation theorem creates a Gaussian noise with temperature T. The last term linearly depending on $\sigma \equiv \phi_0$ plays the role of breaking the O(N) symmetry in the explicit manner with the constant c parametrizing the strength of symmetry breaking. In addition, $Z_a^{(t,i)}$ are wave function renormalizations in the temporal and spatial components, respectively, both of which depend on T and c. Note that in Eq. (3) the renormalization group (RG) scale k-dependence of the potential and wave functions is suppressed. When $c = 0$, this model allows us to reduce the symmetry from O(N) to O($N-1$) in the spontaneous manner for a potential $V(\rho_c)$ with the shape of a 'Mexican hat' in the UV, such that the fields take the expectation values $\bar{\phi}_{0,c} \equiv \bar{\sigma}_c \neq 0$ and $\bar{\phi}_{i,c} = 0$ ($i = 1, 2, \cdots N-1$) in the ground state. The expectation values of quantum fields are always vanishing, i.e., $\bar{\phi}_{a,q} = 0$. In the broken pattern, the fluctuating fields $\delta\sigma \equiv \delta\phi_0$ and $\varphi_i \equiv \delta\phi_i$ play roles of the *Higgs mode* and the *Goldstone modes*, respectively [35]. In the following, we will treat O(N) as an approximate symmetry (i.e., c is non-zero but takes small values) such that the would-be Goldstones acquire a small mass gap.

Here, we should point out that the model A in (3) neglects the fluctuations of the conserved density. Then, the dynamics is solely controlled by the order parameters. For this reason, we will see that our model cannot capture the propagating feature of the soft collective modes which is from the coupling of the pseudo-Goldstones and the almost conserved densities. However, in this work, we focus only on the dissipative sector that is sufficient for testing the proposed relation (1).

All the real-time correlators can be achieved from the effective action (3) [29]. Dispersion relations of excitations correspond to poles of retarded correlators which can be computed as follows

$$G_{ab}^R = \left(\frac{\delta^2\Gamma[\phi_c,\phi_q]}{\delta\phi_{a,q}\,\delta\phi_{b,c}} \right)^{-1}. \tag{4}$$

As a result, this gives rise to the retarded correlator of φ fields for small frequency ω and small wavenumber q in the following form,

$$G_{\varphi\varphi}^R(\omega,q) = \frac{1}{-\mathrm{i}Z_\varphi^{(t)}\omega + Z_\varphi^{(i)}\left(q^2 + m_\varphi^2\right)}\,, \tag{5}$$

with $m_\varphi^2 \equiv V'(\rho_{c,0})/Z_\varphi^{(i)}$, where $\rho_{c,0} = \rho_{c,0}(c)$ is the value of ρ_c corresponding to the minimum of $V(\rho_c)$ when $c \neq 0$. Due to the presence of c, $V'(\rho_{c,0})$ is no longer equal to zero. Then, the Goldstone modes acquire a small mass m_φ when c is sufficiently small. In this work, we calculate $Z_\varphi^{(t,i)}$ and m_φ numerically using the fRG method. Note that the non-zero m_φ means that the static correlator $G_{\varphi\varphi}^R(0,q)$ contains a damping factor $\sim e^{-m_\varphi|x|}$ in the real space. Following the QCD language, we call it the screening mass of the pseudo-Goldstone modes. The dispersion relation can be directly read from the zero of denominator in (5). We find a damped mode

$$\omega(q) = -\mathrm{i}\,\frac{Z_\varphi^{(i)}}{Z_\varphi^{(t)}}\left(m_\varphi^2 + q^2\right), \tag{6}$$

which implies that the relaxation rate of the pseudo-Goldstone modes (which is the damping coefficient at zero wavenumber) is

$$\Omega_\varphi \equiv -\mathrm{Im}\,\omega(q=0) = \frac{Z_\varphi^{(i)}}{Z_\varphi^{(t)}}\,m_\varphi^2\,. \tag{7}$$

In consequence, the relaxation rate and the screening mass are related with each other only via the ratio of the two wave function renormalizations. Note that this is a rigid result for all temperatures and all values of m_φ (or c).

When the broken O(N) symmetry is exact, i.e., $m_\varphi \to 0$, we have that $\Omega \to 0$ and (6) becomes a standard diffusive dispersion with the transport coefficient

$$D_\varphi(T) \equiv \frac{Z_\varphi^{(i)}(T, c=0)}{Z_\varphi^{(t)}(T, c=0)} \,. \tag{8}$$

In this limit, the physical meaning of the two coefficients $Z_\varphi^{(t,i)}$ are manifest. It is obvious to see from (5) that $1/Z_\varphi^{(t)}$ plays the role of the 'Goldstone conductivity' which satisfies the Kubo formula for the Goldstone fields[36]

$$\sigma_\varphi \equiv \frac{1}{Z_\varphi^{(t)}(T, c=0)} = \lim_{\omega\to 0} \omega \, \mathrm{Im}\, G^R_{\varphi\varphi}(\omega, 0) \,, \tag{9}$$

and $1/Z_\varphi^{(i)}(T, c=0)$ should be understood as the 'Goldstone susceptibility'[15]. Then, Eq.(8) is essentially an Einstein relation.

Next, we consider the effect from a non-zero m_φ (or c). To show how the ratio $Z_\varphi^{(i)}/Z_\varphi^{(t)}$ depends on T and c explicitly, we start with the O(4) model. After that, we generalize the discussions into the models with other values of N. Depending on whether the system is close to the critical temperature or not, we shall separate our discussions as follows:

When T is far below the critical temperature T_c (but we still require that $T \gg m_\varphi$), the effect of the Higgs field $\delta\sigma$ can be negelected in the low energy description. In this region, one would expect that $Z_\varphi^{t,i}$ only receive corrections from the small parameter m_φ/T in an analytic way. If this is the case, $\Omega_\varphi/m_\varphi^2$ should take the following expansion

$$\frac{\Omega_\varphi}{m_\varphi^2} \simeq D_\varphi(T) + \mathcal{O}\left(\frac{m_\varphi^2}{T^2}\right), \quad m_\varphi \ll T \ll T_c \,. \tag{10}$$

The analyticity of the expansion (10) can be verified in the full numeric approach (see Fig. 4 in S.2.). Then, the deviation of $\Omega_\varphi/m_\varphi^2$ from the value of D_φ is parametrically suppressed for small c and the proposed relation (1) is obeyed in the whole hydrodynamic regime where the pseudo-Goldstone mass is necessary to be small.

When T approaches to the critical temperature from below, T_c sets a new scale for the system [37]. In this region, the system exhibits critical behaviors known as the *static universality* and *critical slowing down* which are insensitive to the microscopic physics but characterized by static critical exponents ($\alpha, \beta, \gamma, \delta, \nu, \eta$, only two of them are independent) as well as the dynamic critical exponent z, respectively [33]. For the convenience, we introduce a reduced temperature $t \equiv (T_c - T)/T_c$ which is appeared as a new small parameter and a scaling variable $\mathbb{z} \equiv t c^{-1/(\beta\delta)}$. In the critical region, the two wave function renormalizations in Eq. (7) read

$$Z_\varphi^{(i)} = t^{-\nu\eta} f^{(i)}(\mathbb{z}) \,, \qquad Z_\varphi^{(t)} = t^{-\nu\eta_t} f^{(t)}(\mathbb{z}) \,, \tag{11}$$

where $f^{(i)}(\mathbb{z})$ and $f^{(t)}(\mathbb{z})$ are universal scaling functions. In the case of $c \to 0$, the two scaling functions approach towards constants, which leave us with

$$\frac{Z_\varphi^{(i)}}{Z_\varphi^{(t)}} \propto t^{\nu(\eta_t - \eta)} \,. \tag{12}$$

In the other case of $t \to 0$, that is our most concern in this work, the variable t in (11) has to be eliminated by virtue of the scaling functions. Then, we arrive at

$$\frac{Z_\varphi^{(i)}}{Z_\varphi^{(t)}} \propto c^{\frac{\nu}{\beta\delta}(\eta_t - \eta)} \propto m_\varphi^{(\eta_t - \eta)} \,. \tag{13}$$

which is exactly Eq. (2). Note that in the last step in (13) the scaling behavior of the Goldstone mass, i.e.,

$$m_\varphi^2 \propto c^{\frac{2\nu}{\beta\delta}} \,, \tag{14}$$

is utilized, which is detailed in S.3. Since m_φ does no longer depend on c linearly, it violates the standard GMOR relation. This was also observed in the numerical results of the holographic AdS/QCD model close to the chiral phase transition [15]. It has also been shown that the mass of the Higgs mode shares the same scaling dependence on c as the mass of the pseudo-Goldstones and the condition $m_\varphi \ll m_\sigma$ is no longer maintained and the Higgs mode fluctuates strongly in this region. Using the fRG method, we fix $\eta \approx 0.0374$ and $\eta_t \approx 0.0546$ in the O(4) model. Then, $\Delta_\eta \equiv \eta_t - \eta \approx 0.0172 \neq 0$ implies the relation (1) is not followed.

It is found that the prediction above from the scaling theory perfectly matches the result of the dispersion relation achieved in the fully numeric approach. In Fig. 1, we plot $\Omega_\varphi/m_\varphi^2$ as a function of the strength of the explicit symmetry breaking at several fixed values of temperature as well as a variational temperature with $t = \bar{c}^{1/\beta\delta}$ with $\bar{c} = c/c_0$, where c_0 denotes the value of c corresponding to the physical pion mass in QCD as shown in the supplement. For $\bar{c} \ll t^{\beta\delta}$, the ratio $\Omega_\varphi/m_\varphi^2$ approaches to the value of D_φ as $c \to 0$. On the contrary, when $\bar{c} \gtrsim t^{\beta\delta}$, the anomalous scaling regime (2) takes over, resulting in a strong breakdown of the relation (1). At the critical temperature $T = T_c$, the scaling regime stretches to $\bar{c} = 0$, and therefore the relation (1) breaks down for any $c \neq 0$. In Fig. 1 we also show the scaling line $\sim \bar{c}^{\frac{\nu}{\beta\delta}(\eta_t - \eta)}$, where the critical exponents are computed through fixed-point equations within the fRG approach, see the supplement for their values and more details. It is found that the numerical results at $T = T_c$ are in excellent agreement with the scaling line when the chiral limit is approached, i.e., $c \to 0$. More importantly, one finds that a deviation between the numerical results and the scaling line

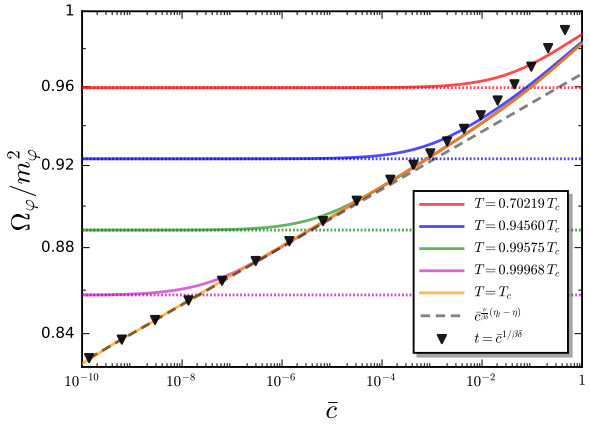

FIG. 1. Ratio $\Omega_\varphi/m_\varphi^2$ as a function of $\bar{c}=c/c_0$ for various temperatures close to T_c, where c_0 denotes the value of c with physical pion mass in QCD as shown in S.1. The dotted lines correspond to values of $D_\varphi(T)$ in the pure SSB limit. The triangle points stands for results with a variational temperature with $t=\bar{c}^{1/\beta\delta}$. The gray dashed line denotes the scaling line $\sim \bar{c}^{\frac{\nu}{\beta\delta}(\eta_t-\eta)}$.

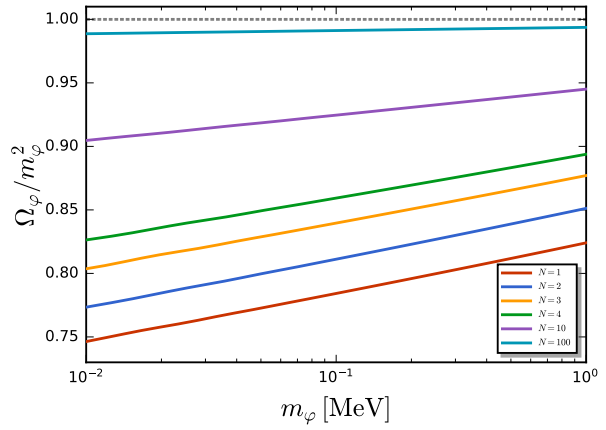

FIG. 2. Ratio $\Omega_\varphi/m_\varphi^2$ as a function of m_φ for different values of N at $T=T_c$, where the gray dashed line denotes the value of $D_\varphi(T_c)$ in the large N limit.

takes place when $\bar{c}\gtrsim 10^{-6}\sim 10^{-4}$, corresponding to the pion mass at very low temperature $m_{\pi 0}\gtrsim 0.1\sim 1$ MeV [38], from which one can estimate the size of the dynamic critical region, that is $m_{\pi 0}\lesssim 0.1\sim 1$ MeV.

Finally, our statement can be formulated as that the proposed relation (1) works as long as the critical fluctuations can be neglected which is always true in the hydrodynamic regime. We may name it 'hydrodynamic universality'. When T is sufficiently close to T_c that the Higgs mass becomes of the same order as the mass of the pseudo-Goldstones, the critical slowing down has to be taken into account and the anomalous scaling behavior (2) emerges. Note that such a universality governed by the critical point is of course beyond the standard hydrodynamic regime and should be called 'critical universality'.

Since the scaling exponent Δ_η depends on the anomalous dimensions, the effects caused by critical fluctuations cannot ignored in order to obtain a non-trivial scaling. In the following, we turn to study the general O(N) model and show explicitly that, for the large N model, $\Delta_\eta\to 0$ and the relation (1) is satisfied everywhere in the broken phase. For this reason, the absence of the anomalous scaling regime in holographic models should just be a result of the large N limit where the dynamic critical exponent reduces into $z=2+\eta_t-\eta=2$, exactly matching the result from the conventional mean-field theory (See discussions on the universality class of holographic systems in [39, 40].).

From finite N's to the large N limit.– The O(N) critical model can be widely applied to describe various interacting systems. The paradigmatic examples include the Ising model ($N=1$), the XY model ($N=2$), the Heisenberg antiferromagnet ($N=3$) and the low energy QCD ($N=4$) matter, etc.

We redo the fRG calculations with different values of N. The relevant results of the ratio Ω/m_φ^2 as a function of the symmetry breaking strength at $T=T_c$ are shown in Fig. 2. The tendency is that the scaling exponent Δ_η becomes smaller for larger values of N. In the limit of large N, one is able to obtain analytic η and η_t for $d+1$-dimensional systems which are detailed in S.4. As a result, both the anomalous dimensions approach to zero in the way that $(\eta,\,\eta_t)\sim N^{-1}$ when $N\to\infty$. Despite that there is still critical slowing down, the non-equilibrium fluctuations become negligible and Ω/m_φ^2 becomes c-independent in the large N limit. Moreover, we find that its value approaches to the value of D_φ. In this case, the proposed relation (1) is valid everywhere even beyond the scope of the standard hydrodynamic regime (as long as c is small) . Therefore, one should not expect that the anomalous scaling regime (2) can be observed in 'mean-field systems'.

Damping of pions near the chiral phase transition.– It is well-known that the QCD matter below the critical temperature of chiral phase transition possesses a broken approximate symmetry $\mathrm{SU}(2)_\mathrm{L}\times\mathrm{SU}(2)_\mathrm{R}\simeq\mathrm{O}(4)$. Then the dynamics of pions (the associated pseudo-Goldstones in the broken phase) is often investigated via the O(4) model. To that end, we adopt the identification that $\delta\sigma$ as the sigma meson and $\varphi\equiv\pi$ as pions.

In Fig. 3, we plot the ratio $\Omega_\pi/(D_\pi\, m_\pi^2)$ as a function of the temperature for different values of the physical pion mass $m_{\pi 0}$ at very low temperatures. Indeed, it is found that the ratio is very close to unity at all temperatures far below T_c. Its value becomes very sensitive to the value of $m_{\pi 0}$ near the critical point when $t\ll 1$. For the experiment result $m_{\pi 0}\approx 138$ MeV, we expect that the deviation from 1 becomes obvious ($\sim 10\%$) at $T\approx 0.994\,T_c$. When $T\to T_c$, we find that the deviation

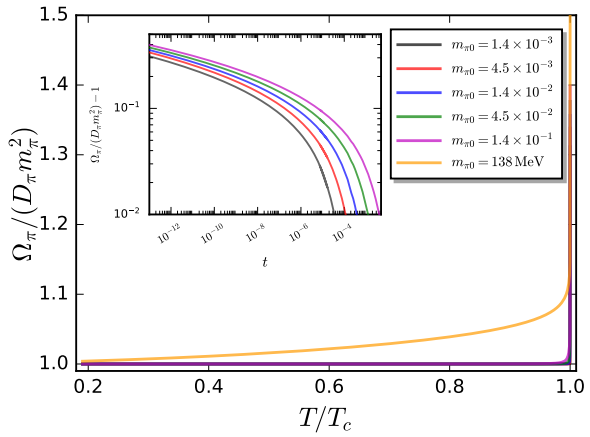

FIG. 3. Ratio $\Omega_\pi/(D_\pi\, m_\pi^2)$ as a function of the temperature for different values of $m_{\pi 0}$.

displays a scaling growth

$$\frac{\Omega_\pi}{D_\pi m_\pi^2} - 1 \propto t^{(\eta-\eta_t)\nu}, \tag{15}$$

leading to $\Omega_\pi \gg D_\pi m_\pi^2$ very close to the chiral phase transition. Note that this cannot be observed in the AdS/QCD model where the large N limit was taken [15].

Conclusion and Outlook.– In this work, we investigate the real-time dynamics of pseudo-Goldstones in a relaxational O(N) model by applying the SK formalism of the fRG, aiming to extend the scope of the study on the damping rate to the critical region. As verified in this paper, the relation (1) governed by the hydrodynamic regime is always valid in the broken phase away from the critical point. While, in the vicinity of the critical point where the mass of the Higgs mode becomes comparable to the screening mass of the pseudo-Goldstone modes, $\Omega_\varphi/m_\varphi^2$ is no longer equal to the Goldstone diffusivity but instead displays a novel universal scaling behavior (2) controlled by the critical slowing down as well as the non-equilibrium fluctuations.

Despite the fact that this work is based on a specific model, we believe that our conclusion should be applicable to general interacting systems with spontaneously broken approximate symmetries. Nevertheless, as we mentioned, this model fails to capture the propagating feature of the pseudo-Goldstones. To make the it more realistic, it is necessary to couple the order parameter ϕ_a to an almost conserved charge which generates a pair of soft modes with a finite sound speed as well as a finite pole mass. Furthermore, it should also be interesting to verify our result using other methods which allows us to handle the critical fluctuations. For instance, one can include stochastic forces in the hydrodynamic equations following the line of [2, 41–44] or calculate the 'hydrodynamic loops' using the Schwinger-Keldysh field theory of fluctuating hydrodynamics [45–51]. Another direction is that one can enlarge the hydrodynamic description by considering the effects of Higgs mode in holographic systems near critical points [52, 53] and verify if the relation (1) is aways satisfied up to T_c in the large N limit.

Acknowledgements.– We would like to thank Matteo Baggioli, Blaise Goutéraux, Jan M. Pawlowski, Fabian Rennecke, Nicolas Wink and Hongbao Zhang for inspiring discussions and reading a previous version of this manuscript. This work is supported by the National Natural Science Foundation of China (NSFC) under Grant No.12175030, No.12147101, No.12275038 and No.12047503. W.J.L. also acknowledges the sponsorship from the Peng Huanwu Visiting Professor Program in 2023 and Institute of Theoretical Physics, Chinese Academy of Sciences for the warm hospitality during which part of this work was completed.

[1] D. T. Son and M. A. Stephanov, Pion propagation near the QCD chiral phase transition, Phys. Rev. Lett. **88**, 202302 (2002), arXiv:hep-ph/0111100.
[2] D. T. Son and M. A. Stephanov, Real time pion propagation in finite temperature QCD, Phys. Rev. D **66**, 076011 (2002), arXiv:hep-ph/0204226.
[3] G. Gruner, The dynamics of spin-density waves, Rev. Mod. Phys. **66**, 1 (1994).
[4] M. M. Fogler and D. A. Huse, Dynamical response of a pinned two-dimensional Wigner crystal, Phys. Rev. B. **62**, 7553 (2000).
[5] W.-j. Fu, J. M. Pawlowski, and F. Rennecke, QCD phase structure at finite temperature and density, Phys. Rev. D **101**, 054032 (2020), arXiv:1909.02991 [hep-ph].
[6] F. Gao and J. M. Pawlowski, Chiral phase structure and critical end point in QCD, Phys. Lett. B **820**, 136584 (2021), arXiv:2010.13705 [hep-ph].
[7] N. Dupuis, L. Canet, A. Eichhorn, W. Metzner, J. M. Pawlowski, M. Tissier, and N. Wschebor, The nonperturbative functional renormalization group and its applications, Phys. Rept. **910**, 1 (2021), arXiv:2006.04853 [cond-mat.stat-mech].
[8] P. J. Gunkel and C. S. Fischer, Locating the critical endpoint of QCD: Mesonic backcoupling effects, Phys. Rev. D **104**, 054022 (2021), arXiv:2106.08356 [hep-ph].
[9] W.-j. Fu, QCD at finite temperature and density within the fRG approach: an overview, Commun. Theor. Phys. **74**, 097304 (2022), arXiv:2205.00468 [hep-ph].
[10] J. Braun *et al.*, Soft modes in hot QCD matter, (2023), arXiv:2310.19853 [hep-ph].
[11] This relation was firstly derived in the chiral perturbative theory for pions in QCD [54] and its validity for other symmetries has been discussed in specific holographic systems [12, 14, 15, 55–58] and within more formal ap-

proaches [59, 60] in recent years.
[12] A. Amoretti, D. Areán, B. Goutéraux, and D. Musso, Universal relaxation in a holographic metallic density wave phase, Phys. Rev. Lett. **123**, 211602 (2019), arXiv:1812.08118 [hep-th].
[13] A. Amoretti, D. Areán, B. Goutéraux, and D. Musso, Diffusion and universal relaxation of holographic phonons, JHEP **10**, 068, arXiv:1904.11445 [hep-th].
[14] M. Ammon, D. Arean, M. Baggioli, S. Gray, and S. Grieninger, Pseudo-spontaneous $U(1)$ symmetry breaking in hydrodynamics and holography, JHEP **03**, 015, arXiv:2111.10305 [hep-th].
[15] X. Cao, M. Baggioli, H. Liu, and D. Li, Pion dynamics in a soft-wall AdS-QCD model, JHEP **12**, 113, arXiv:2210.09088 [hep-ph].
[16] M. Baggioli, Homogeneous holographic viscoelastic models and quasicrystals, Phys. Rev. Res. **2**, 022022 (2020), arXiv:2001.06228 [hep-th].
[17] M. Baggioli and M. Landry, Effective Field Theory for Quasicrystals and Phasons Dynamics, SciPost Phys. **9**, 062 (2020), arXiv:2008.05339 [hep-th].
[18] L. V. Delacrétaz, B. Goutéraux, and V. Ziogas, Damping of Pseudo-Goldstone Fields, Phys. Rev. Lett. **128**, 141601 (2022), arXiv:2111.13459 [hep-th].
[19] J. Armas, A. Jain, and R. Lier, Approximate symmetries, pseudo-Goldstones, and the second law of thermodynamics, Phys. Rev. D **108**, 086011 (2023), arXiv:2112.14373 [hep-th].
[20] Before that, this relation was noticed in QCD based on the argument of positivity of entropy production [41].
[21] J. Berges and G. Hoffmeister, Nonthermal fixed points and the functional renormalization group, Nucl. Phys. B **813**, 383 (2009), arXiv:0809.5208 [hep-th].
[22] T. Gasenzer and J. M. Pawlowski, Towards far-from-equilibrium quantum field dynamics: A functional renormalisation-group approach, Phys. Lett. B **670**, 135 (2008), arXiv:0710.4627 [cond-mat.other].
[23] J. M. Pawlowski and N. Strodthoff, Real time correlation functions and the functional renormalization group, Phys. Rev. D **92**, 094009 (2015), arXiv:1508.01160 [hep-ph].
[24] L. Corell, A. K. Cyrol, M. Heller, and J. M. Pawlowski, Flowing with the temporal renormalization group, Phys. Rev. D **104**, 025005 (2021), arXiv:1910.09369 [hep-th].
[25] S. Huelsmann, S. Schlichting, and P. Scior, Spectral functions from the real-time functional renormalization group, Phys. Rev. D **102**, 096004 (2020), arXiv:2009.04194 [hep-ph].
[26] Y.-y. Tan, Y.-r. Chen, and W.-j. Fu, Real-time dynamics of the $O(4)$ scalar theory within the fRG approach, SciPost Phys. **12**, 026 (2022), arXiv:2107.06482 [hep-ph].
[27] J. V. Roth, D. Schweitzer, L. J. Sieke, and L. von Smekal, Real-time methods for spectral functions, Phys. Rev. D **105**, 116017 (2022), arXiv:2112.12568 [hep-ph].
[28] J. Braun *et al.*, Renormalised spectral flows, SciPost Phys. Core **6**, 061 (2023), arXiv:2206.10232 [hep-th].
[29] Y.-r. Chen, Y.-y. Tan, and W.-j. Fu, Critical dynamics within the real-time fRG approach, (2023), arXiv:2312.05870 [hep-ph].
[30] J. V. Roth and L. von Smekal, Critical dynamics in a real-time formulation of the functional renormalization group, JHEP **10**, 065, arXiv:2303.11817 [hep-ph].
[31] L. Batini, E. Grossi, and N. Wink, Dissipation dynamics of a scalar field, Phys. Rev. D **108**, 125021 (2023), arXiv:2309.06586 [hep-th].
[32] We will show that this model is, though, not able to describe the propagation features of pseudo-Goldstone modes, is sufficient for the discussions on the proposed relation of their damping.
[33] P. Hohenberg and B. Halperin, Theory of Dynamic Critical Phenomena, Rev. Mod. Phys. **49**, 435 (1977).
[34] In the fRG approach, we focus on quantities depending the renormalization scale (which is often denoted as k). For more details about the setup, one can refer to S.1.
[35] Since the $N-1$ Goldtones are identical in this model, we will omit the subscript 'i' hereafter.
[36] Eq. (9) can also be re-expressed as the standard Kubo formula for the correlator of $\partial_t\varphi$ instead of φ field like in [18].
[37] Throughout the work, T_c is defined as the critical temperature in the purely SSB limit, namely $c = 0$.
[38] Here, we use an extra subscript '0' to denote values of the observables at very low temperatures.
[39] K. Maeda, M. Natsuume, and T. Okamura, Universality class of holographic superconductors, Phys. Rev. D **79**, 126004 (2009), arXiv:0904.1914 [hep-th].
[40] M. Natsuume and T. Okamura, Dynamic universality class of large-N gauge theories, Phys. Rev. D **83**, 046008 (2011), arXiv:1012.0575 [hep-th].
[41] E. Grossi, A. Soloviev, D. Teaney, and F. Yan, Transport and hydrodynamics in the chiral limit, Phys. Rev. D **102**, 014042 (2020), arXiv:2005.02885 [hep-th].
[42] E. Grossi, A. Soloviev, D. Teaney, and F. Yan, Soft pions and transport near the chiral critical point, Phys. Rev. D **104**, 034025 (2021), arXiv:2101.10847 [nucl-th].
[43] A. Soloviev, Transport near the chiral critical point, EPJ Web Conf. **258**, 05008 (2022), arXiv:2111.11375 [nucl-th].
[44] A. Florio, E. Grossi, A. Soloviev, and D. Teaney, Dynamics of the $O(4)$ critical point in QCD, Phys. Rev. D **105**, 054512 (2022), arXiv:2111.03640 [hep-lat].
[45] M. Crossley, P. Glorioso, and H. Liu, Effective field theory of dissipative fluids, JHEP **09**, 095, arXiv:1511.03646 [hep-th].
[46] F. M. Haehl, R. Loganayagam, and M. Rangamani, Topological sigma models & dissipative hydrodynamics, JHEP **04**, 039, arXiv:1511.07809 [hep-th].
[47] H. Liu and P. Glorioso, Lectures on non-equilibrium effective field theories and fluctuating hydrodynamics, PoS **TASI2017**, 008 (2018), arXiv:1805.09331 [hep-th].
[48] X. Chen-Lin, L. V. Delacrétaz, and S. A. Hartnoll, Theory of diffusive fluctuations, Phys. Rev. Lett. **122**, 091602 (2019), arXiv:1811.12540 [hep-th].
[49] A. Jain and P. Kovtun, Late Time Correlations in Hydrodynamics: Beyond Constitutive Relations, Phys. Rev. Lett. **128**, 071601 (2022), arXiv:2009.01356 [hep-th].
[50] A. Jain, P. Kovtun, A. Ritz, and A. Shukla, Hydrodynamic effective field theory and the analyticity of hydrostatic correlators, JHEP **02**, 200, arXiv:2011.03691 [hep-th].
[51] A. Donos and P. Kailidis, Nearly critical superfluids in Keldysh-Schwinger formalism, JHEP **01**, 110, arXiv:2304.06008 [hep-th].
[52] A. Donos and C. Pantelidou, Higgs/amplitude mode dynamics from holography, JHEP **08**, 246, arXiv:2205.06294 [hep-th].
[53] A. Donos and P. Kailidis, Nearly critical holographic superfluids, JHEP **12**, 028, [Erratum: JHEP 07, 232

(2023)], arXiv:2210.06513 [hep-th].
[54] M. Gell-Mann, R. J. Oakes, and B. Renner, Behavior of current divergences under SU(3) x SU(3), Phys. Rev. **175**, 2195 (1968).
[55] T. Andrade and A. Krikun, Coherent vs incoherent transport in holographic strange insulators, JHEP **05**, 119, arXiv:1812.08132 [hep-th].
[56] M. Ammon, M. Baggioli, and A. Jiménez-Alba, A Unified Description of Translational Symmetry Breaking in Holography, JHEP **09**, 124, arXiv:1904.05785 [hep-th].
[57] A. Donos, P. Kailidis, and C. Pantelidou, Dissipation in holographic superfluids, JHEP **09**, 134, arXiv:2107.03680 [hep-th].
[58] Y.-Y. Zhong and W.-J. Li, Transverse Goldstone mode in holographic fluids with broken translations, Eur. Phys. J. C **82**, 511 (2022), arXiv:2202.05437 [hep-th].
[59] R. Argurio, A. Marzolla, A. Mezzalira, and D. Musso, Analytic pseudo-Goldstone bosons, JHEP **03**, 012, arXiv:1512.03750 [hep-th].
[60] A. Amoretti, D. Areán, R. Argurio, D. Musso, and L. A. Pando Zayas, A holographic perspective on phonons and pseudo-phonons, JHEP **05**, 051, arXiv:1611.09344 [hep-th].
[61] Y.-y. Tan, C. Huang, Y.-r. Chen, and W.-j. Fu, Criticality of the $O(N)$ universality via global solutions to nonperturbative fixed-point equations, (2022), arXiv:2211.10249 [hep-ph].

Supplemental Materials

The supplemental materials provide some details in sequence in line with the main text.

S.1. Setup of the relaxation model within the fRG

From the real-time effective action in Eq. (3), one can obtain the flow equation of the effective potential within the functional renormalization group (fRG) approach, which reads

$$\partial_\tau u'(\bar\rho) = (-2+\eta)u'(\bar\rho) + (1+\eta)\bar\rho u^{(2)}(\bar\rho) - \frac{1}{4\pi^2}\frac{2}{3}\Big(1-\frac{\eta}{5}\Big)\left[\frac{3u^{(2)}(\bar\rho)+2\bar\rho u^{(3)}(\bar\rho)}{\big(1+u'(\bar\rho)+2\bar\rho u^{(2)}(\bar\rho)\big)^2} + (N-1)\frac{u^{(2)}(\bar\rho)}{\big(1+u'(\bar\rho)\big)^2}\right], \tag{16}$$

where we have defined the dimensionless, renormalized field and potential, viz.,

$$\bar\rho = Z_\varphi^{(i)} T^{-1} k^{-1}\rho\,, \qquad u(\bar\rho) = T^{-1}k^{-3}V(\rho)\,, \tag{17}$$

with the temperature T and the renormalization group (RG) scale k. Here we have used ρ instead of ρ_c for simplicity for the subscript of 'classical' field. The flow in Eq. (16) is formulated in terms of the RG time $\tau = \ln(k/\Lambda)$, where Λ is some reference scale, e.g., an ultraviolet (UV) cutoff scale. Note that in order to arrive at the flow equation in Eq. (16) as well as those in what follows, we have used the optimized infrared (IR) regulator in fRG, see, e.g., [29] for more details.

The static and dynamic anomalous dimensions are related to the spatial and temporal wave function renormalizations through

$$\eta = -\frac{\partial_\tau Z_\varphi^{(i)}}{Z_\varphi^{(i)}}\,, \qquad \eta_t = -\frac{\partial_\tau Z_\varphi^{(t)}}{Z_\varphi^{(t)}}\,, \tag{18}$$

respectively. Within the modified local potential approximation to the effective action in Eq. (3), usually called the LPA′ truncation, one finds for the two anomalous dimensions

$$\eta = \frac{2}{3\pi^2}\frac{\bar\rho_0\big(u^{(2)}(\bar\rho_0)\big)^2}{\big(1+u'(\bar\rho_0)\big)^2\big(1+u'(\bar\rho_0)+2\bar\rho_0 u^{(2)}(\bar\rho_0)\big)^2}\,, \tag{19}$$

$$\begin{aligned}\eta_t =& \frac{1}{30\pi^2}(5-\eta)\bar\rho_0^2\big(u^{(2)}(\bar\rho_0)\big)^2\big(1+u'(\bar\rho_0)\big)^{-2}\big(1+u'(\bar\rho_0)+2\bar\rho_0 u^{(2)}(\bar\rho_0)\big)^{-2}\big(1+u'(\bar\rho_0)+\bar\rho_0 u^{(2)}(\bar\rho_0)\big)^{-2}\\ &\times\Big[\big(1+u'(\bar\rho_0)\big)^2 + 4\big(1+u'(\bar\rho_0)\big)\big(1+u'(\bar\rho_0)+2\bar\rho_0 u^{(2)}(\bar\rho_0)\big) + \big(1+u'(\bar\rho_0)+2\bar\rho_0 u^{(2)}(\bar\rho_0)\big)^2\Big]\,,\end{aligned} \tag{20}$$

where the potential is computed on the expectation value of the field $\bar\rho_0$, which satisfies the equation of motion (EoM) as follows

$$\sqrt{2\rho_0}V'(\rho_0) - c = 0\,, \tag{21}$$

Observables	Values [MeV]	Parameters
f_π	93.5	$\Lambda = 430\,\mathrm{MeV}$
m_π	137.2	$\rho_\Lambda = 3.84 \times 10^3\,\mathrm{MeV}^2$
m_σ	567.2	$\lambda_\Lambda = 17.5$
f_π^χ	87.4	$c = 1.76 \times 10^6\,\mathrm{MeV}^3$

TABLE I. Observables and parameters in the relaxational O(4) model within the functional renormalization group approach.

with $\bar{\rho}_0 = Z_\varphi^{(i)} T^{-1} k^{-1} \rho_0$. The EoM in Eq. (21) results from the effective action in Eq. (3) by differentiating with respect to the 'quantum' field.

In our numerical calculations, the flow equation of effective potential in Eq. (16) is integrated on a grid of the potential from an UV initial value Λ to the IR limit $k \to 0$. This integral is iterated with a value of the static anomalous dimension in Eq. (19) updated for each iteration, until a convergence is observed. At the initial UV cutoff $k = \Lambda$, the effective potential is parameterized as

$$V'_{k=\Lambda}(\rho) = \lambda_\Lambda(\rho - \rho_\Lambda)\,. \tag{22}$$

Note only the derivative of potential is relevant, that is the reason why V' rather than V is specified in Eq. (22). The initial UV scale Λ, the parameters ρ_Λ and λ_Λ in the potential at the initial scale, and the strength of explicit symmetry breaking c as shown in the effective action in (3) constitute the set of parameters for the relaxation model within the fRG. The values of model parameters adopted in this work are collected in Tab. I, where the observables produced at low temperature, say $T = 1$ MeV, are also presented. In Tab. I the mass of pseudo-Goldstones, i.e., the pion mass in low energy QCD, $m_\varphi \equiv m_\pi = 137.2$ MeV, is the physical mass in the real world. m_σ denotes the mass of sigma mode. The pion decay constant at physical pion mass is given by $f_\pi = \sqrt{2\rho_{c0}}$, and f_π^χ stands for the pion decay constant in the chiral limit, to wit, vanishing pion mass. Moreover, within the parameters in Tab. I one finds for the critical temperature of phase transition in the chiral limit $T_c = 141.633955(10)$ MeV. This precision of T_c is necessary for the scaling analysis in this work. Note that the anomalous damping of the pseudo-Goldstone modes in the critical region found in the main text does not depend on the specific values of model parameters.

The values of critical exponents in the LPA$'$ truncation are found to be $\eta_t = 0.054424$, $\eta = 0.037320$, $\nu = 0.78110$, $\beta = 0.40513$, $\delta = 4.7841$, which are calculated by solving the fixed-point equation, i.e., $\partial_\tau u' = 0$ in Eq. (16), see, e.g., [61] for more details.

S.2. Numerical verification of Eq. (10) in the main text

In Fig. 4 we show the dependence of $\Omega_\varphi/m_\varphi^2$ on the mass of pseudo-Goldstones, where the temperature is chosen a value, $T = 0.3\,T_c$ far lower than the critical temperature. The subleading term of the expansion in Eq. (10) is shown in the inlay, from which one can extract the exponent α

$$\Omega_\varphi/m_\varphi^2 - D_\varphi(T) \propto (m_\varphi/T)^\alpha\,, \tag{23}$$

with $\alpha = 2.0056$, which is equal to 2 within errors.

S.3. Scaling behavior of the pseudo-Goldstone mass and Higgs mass

Employing the EoM of fields in Eq. (21), one arrives at the mass of the pseudo-Goldstone modes immediately as

$$m_\varphi^2 = \frac{V'(\rho_0)}{Z_\varphi^{(i)}} = \frac{c}{\sigma_0 Z_\varphi^{(i)}}\,, \tag{24}$$

where the order parameter $\sigma_0 = \sqrt{2\rho_0}$ plays the role of magnetization. When the reduced temperature $t \to 0$ and in the critical region, one has $\sigma_0 \sim c^{1/\delta}$. Moreover, one finds from the scaling function of the spatial wave function renormalization in Eq. (11) $Z_\varphi^{(i)} \sim c^{-\nu\eta/(\beta\delta)}$. Consequently, in the case of $t \to 0$ one is led to

$$m_\varphi^2 \sim \frac{c}{c^{\frac{1}{\delta}} c^{-\frac{\nu\eta}{\beta\delta}}} = c^{\frac{2\nu}{\beta\delta}}\,, \tag{25}$$

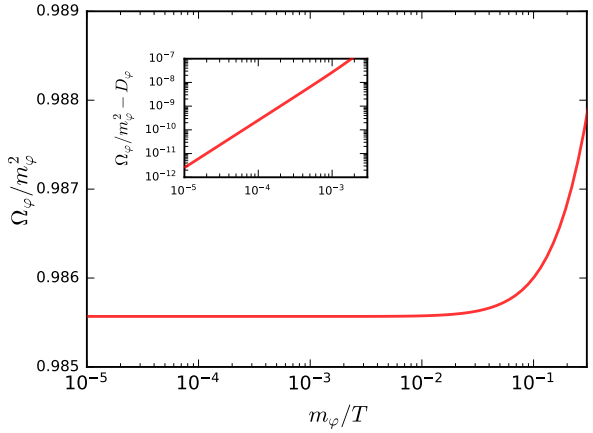

FIG. 4. Ratio $\Omega_\varphi/m_\varphi^2$ as a function of m_φ/T with $T = 0.3\,T_c$ and $N = 4$. The inset shows the subleading term of mass correction, i.e., $\Omega_\varphi/m_\varphi^2 - D_\varphi$ as a function of m_φ/T.

which is Eq. (14) in the main text. In the last step of Eq. (25) we have used the scaling relations for different critical exponents as follows

$$\beta = \frac{\nu}{2}(d-2+\eta)\,, \qquad \delta = \frac{d+2-\eta}{d-2+\eta}\,, \tag{26}$$

where d denotes the spatial dimension.

We proceed with the scaling analysis of the mass of sigma mode. It is very known that the sigma mass is related to the correlation length ξ through $m_\sigma = \xi^{-1}$, and the correlation length behaves as $\xi \sim t^{-\nu}$. Thus, one finds for the scaling behavior of the sigma mass

$$m_\sigma^2 = t^{2\nu} f^\sigma(\mathbb{z})\,, \tag{27}$$

with the scaling variable $\mathbb{z} = tc^{-1/(\beta\delta)}$ and the scaling function $f^\sigma(\mathbb{z})$. In the case of $t \to 0$, the reduced temperature in Eq. (27) has to be eliminated by the scaling function, which leaves use with

$$m_\sigma^2 \sim c^{\frac{2\nu}{\beta\delta}}\,. \tag{28}$$

Comparing Eq. (25) and Eq. (28), we find that both the Goldstone and sigma masses have the same scaling dependence on the strength of symmetry breaking c in the critical region.

S.4. Large N limit

In this section we discuss the large N limit for the relaxation model in Section S.1. In the large N limit, the flow of effective potential in Eq. (16) is simplified as

$$\partial_\tau u'(\bar\rho) = (-2+\eta)u'(\bar\rho) + (1+\eta)\bar\rho u^{(2)}(\bar\rho) - \frac{1}{4\pi^2}\frac{2}{3}\left(1-\frac{\eta}{5}\right)(N-1)\frac{u^{(2)}(\bar\rho)}{\left(1+u'(\bar\rho)\right)^2}\,. \tag{29}$$

We are interested in the fixed-point solution of the flow equation above, i.e., $\partial_\tau u'_*(\bar\rho) = 0$. The fixed-point equation in (29) can be solved analytically through an implicit formulation, whose solution reads

$$\bar\rho = \frac{1}{30\pi^2}\frac{(5-\eta)}{1+\eta}(N-1)\,{}_2F_1\left(2, 1+\frac{3}{\eta-2}; \frac{2\eta-1}{\eta-2}; -u'_*(\bar\rho)\right) + \mathcal{C}u'_*(\bar\rho)^{\frac{1+\eta}{2-\eta}}\,, \tag{30}$$

with a constant $\mathcal{C}$ to be determined, where ${}_2F_1$ is a hypergeometric function with a general notation ${}_pF_q\left(a_1,\ldots,a_p; b_1,\ldots,b_q; z\right)$. As for the last term Eq. (30), since the exponent $(1+\eta)/(2-\eta)$ is not an integer in general, which would result in a branch cut for $u'_*(\bar\rho) < 0$. In consequence, the constant $\mathcal{C}$ has to be vanishing to

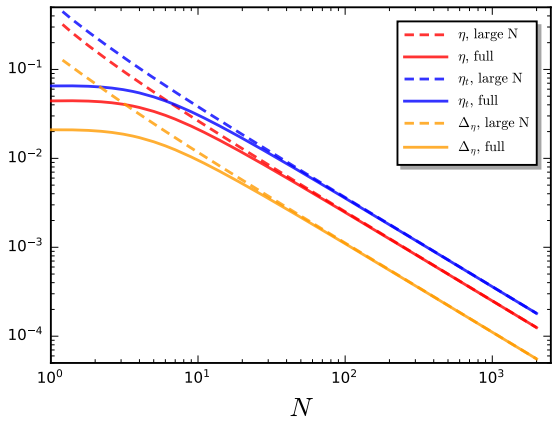

FIG. 5. Dynamic anomalous dimension η_t, static anomalous dimension η and their difference $\Delta_\eta \equiv \eta_t - \eta$ as functions of N. Here, the solid lines denote the full numeric results and the dashed ones denote the scaling lines from Eq. (32) at large N.

make sure that the potential is analytic. The minimal point of the potential is determined by the EoS in Eq. (21). In the chiral limit one has $u'_*(\bar{\rho}_0) = 0$, which leaves us with

$$\bar{\rho}_0 = \frac{1}{30\pi^2}\frac{(5-\eta)}{(1+\eta)}(N-1)\,, \qquad u^{(2)}_*(\bar{\rho}_0) = 15\pi^2\frac{(1-2\eta)}{(5-\eta)}\frac{1}{(N-1)}\,. \tag{31}$$

Inserting the expressions above as well as $u'_*(\bar{\rho}_0) = 0$ into Eq. (19) and Eq. (20), one obtains analytic expressions of the static and dynamic anomalous dimensions as follows

$$\eta = \frac{5}{N-1}\frac{(1+\eta)(1-2\eta)^2}{(5-\eta)(2-\eta)^2}\,, \qquad \eta_t = \frac{1}{9(N-1)}\frac{(1-2\eta)^2(13+15\eta-2\eta^3)}{(2-\eta)^2}\,. \tag{32}$$

These are implicit functions. But one can still see clearly that $\eta \to 0$ and $\eta_t \to 0$ when $N \to \infty$. Then, the scaling exponent $\Delta_\eta \equiv \eta_t - \eta$ also becomes trivial in the large N limit. Numerical calculations of Eq. (32) are presented in Fig. 5.

In the following we adopt the method of eigenperturbations to calculate the critical exponent ν in the large N limit, cf. e.g., [61]. A small perturbation of the effective potential around the fixed point can be described as

$$u(\bar{\rho}) = u_*(\bar{\rho}) + \epsilon\, \mathrm{e}^{-\omega\tau} v(\bar{\rho})\,, \tag{33}$$

with a small parameter ϵ, where ω and $v(\bar{\rho})$ stand for the eigenvalue and eigenfunction of the perturbation, respectively. Substituting Eq. (33) into Eq. (29), one is led to

$$\omega v(\bar{\rho}) = 3v(\bar{\rho}) - (1+\eta)\bar{\rho}\, v'(\bar{\rho}) + \frac{5-\eta}{30\pi^2}\frac{(N-1)v'(\bar{\rho})}{\left(1+u'_*(\bar{\rho})\right)^2}\,. \tag{34}$$

This equation can be solved analytically, and its solution is given by

$$v(\bar{\rho}) = \mathcal{C}_v\left[u'_*(\bar{\rho})\right]^{\frac{3-\omega}{2-\eta}}\,, \tag{35}$$

with a constant $\mathcal{C}_v$. Since the Wilson-Fisher fixed point has the property $u'_*(\bar{\rho}=0) < 0$, in order to warrant that the eigenfunction in Eq. (35) is analytic, one has to choose the exponent there to be positive integers, i.e.,

$$\frac{3-\omega_n}{2-\eta} = n+1\,, \qquad n = 0, 1, 2, \cdots\,. \tag{36}$$

Thus, we are led to

$$\omega_n = 3 - (n+1)(2-\eta)\,. \tag{37}$$

As we have show above, $\eta \to 0$ when $N \to \infty$. So, only the first eigenvalue is relevant, i.e., $\omega_0 = 1 + \eta > 0$. The critical exponent reads

$$\nu = \frac{1}{\omega_0} = \frac{1}{1+\eta}\,. \tag{38}$$

Prepared for submission to JCAP

arXiv:2403.03338v1 [astro-ph.CO] 5 Mar 2024

Correlated scalar perturbations and gravitational waves from axion inflation

Sofia P. Corbà and Lorenzo Sorbo

Amherst Center for Fundamental Interactions, Department of Physics, University of Massachusetts, Amherst, MA 01003, U.S.A.

E-mail: spcorba@umass.edu, sorbo@umass.edu

Abstract. The scalar and tensor fluctuations produced during inflation can be correlated, if arising from the same underlying mechanism. In this paper we investigate such correlation in the model of axion inflation, where the rolling inflaton produces quanta of a $U(1)$ gauge field which, in turn, source scalar and tensor fluctuations. We compute the primordial correlator of the curvature perturbation, ζ, with the amplitude of the gravitational waves squared, $h_{ij}h_{ij}$, at frequencies probed by gravitational wave detectors. This two-point function receives two contributions: one arising from the correlation of gravitational waves with the scalar perturbations generated by the standard mechanism of amplification of vacuum fluctuations, and the other coming from the correlation of gravitational waves with the scalar perturbations sourced by the gauge field. Our analysis shows that the latter effect is generally dominant. The correlator, normalized by the amplitude of ζ and of $h_{ij}h_{ij}$, turns out to be of the order of $10^{-2} \times (f_{\rm NL}^{\rm equil})^{1/3}$, where $f_{\rm NL}^{\rm equil}$ measures the scalar bispectrum sourced by the gauge modes.

Contents

1 Introduction **1**

2 Review of scalar and tensor perturbations from axion inflation **3**

3 The correlator between scalar fluctuations and gravitational waves **7**
3.1 Correlation with amplified vacuum scalar fluctuations 8
3.2 Correlation with sourced scalar fluctuations 9

4 Discussion and conclusions **11**

1 Introduction

The theory of inflation constitutes the dominant paradigm of primordial cosmology. Besides solving the most important problems of the standard Hot Big Bang model, it is able to provide an explanation, in excellent agreement with observations, for the origin of the temperature anisotropies present in the Cosmic Microwave Background (CMB) radiation and of the density fluctuations that characterize the large scale structure of the Universe. Among the many different inflationary scenarios, axion inflation is one of those giving a satisfying solution to the problem of UV sensitivity of the inflaton potential. In this model, proposed for the first time in 1990 as natural inflation [1], the inflaton is a pseudo-Nambu–Goldstone Boson that enjoys a (softly broken) shift symmetry, i.e., a symmetry under the transformation $\phi \to \phi + \text{const}$, which protects its potential against large radiative corrections.

The axionic inflaton is naturally coupled to gauge fields through the operator $\phi F_{\mu\nu}\tilde{F}^{\mu\nu}/f$, where f is the axion decay constant [2]. In the presence of such coupling, the rolling zero mode of the inflaton acts as a source for the modes of the gauge field. As a result, quanta of the gauge field are amplified into classical modes, which in turn source, through a process of inverse decay, both scalar and tensor fluctuations. Since, due to the pseudoscalar nature of the inflaton, only one of the two helicities of the gauge field experiences a tachyonic instability, the spectra of the tensor modes of different helicities have different amplitudes. This scenario has multiple phenomenological predictions, including nongaussianities [3], deviations from scale invariance [4], formation of a population of primordial black holes [5], generation of primordial chiral gravitational waves at CMB [6] or interferometer [7] frequencies, baryogenesis [8], as well as the possible generation of cosmologically relevant magnetic fields [9] - see [10] for a review.

By comparing these phenomenological predictions with observations we can constrain the relevant parameters characterizing the models of axion inflation. More specifically, there are two significant observational lengthscales to examine. At large scales, probed by CMB measurements, the primary constraint arises from the non-observation of primordial nongaussianities for the scalar fluctuations. In axion inflation the sourced scalar fluctuations are highly nongaussian. Consequently, for a viable model, we must require that the sourced component of scalar modes is subdominant compared to that generated by the standard amplification of vacuum fluctuations. This is equivalent to stating that the amplitude of the gauge field, which sources the scalar and tensor fluctuations, must be relatively small. Therefore, the sourced component of tensor fluctuations is also small at this stage.

At smaller scales, corresponding to modes that left the horizon closer to the end of inflation, the situation becomes more interesting. For simple inflationary potentials, the inflaton's velocity increases as inflation progresses and therefore the population of gauge quanta, whose amplitude depends exponentially on the inflaton's velocity, becomes more sizable towards the end of inflation. As a consequence, sourced gravitational waves of shorter wavelengths, which are remarkably those probed by gravitational wave experiments, can have a much larger amplitude and might even be directly detectable [7] by a variety of observatories. Also in this regime we need the scalar fluctuations to remain bounded to avoid an overproduction of primordial black holes [10, 11].

A natural follow-up to the recent observational evidence [12–14] of a stochastic gravitational wave background (SGWB) is the search for anisotropies, in analogy to the scalar anisotropies observed in the CMB (see, e.g., [15] for a recent analysis of LIGO/Virgo/KAGRA and [16] for LISA's reach in this respect). Study of these anisotropies can allow us to distinguish between the astrophysical and cosmological origin of the SGWB. Furthermore, cosmological tensor anisotropies may be correlated with the scalar anisotropies of the CMB if they arise from the same underlying mechanisms [17]. Exploring such correlations can give important information about the cosmological background of gravitational waves, thus providing insights about the physics of the Early Universe. Reference [18] performed a study of the statistics of these anisotropies while [19] studied the consequences of a non-trivial primordial scalar-tensor-tensor nongaussianity on the energy density of gravitational waves.

In this work we compute the correlation between the curvature perturbation $\zeta(\mathbf{x})$ and the squared amplitude of the tensor modes $h_{ij}(\mathbf{x})\, h_{ij}(\mathbf{x})$ within the framework of axion inflation. The computation is conducted at frequencies tested by gravitational detectors, and the correlator is normalized by both the square root of the scalar power spectrum and the tensor power spectrum. The two point function receives two contributions, reflecting the fact that scalar fluctuations are generated both from the vacuum, through the standard amplification process, and by modes of the gauge field, through the inverse decay process. More specifically, we will study the two following situations:

- the rolling inflaton has fluctuations that are generated by the standard mechanism of amplification of vacuum fluctuations in an expanding Universe. The rolling inflaton then sources quanta of the gauge field, which in turn source gravitational waves. The fluctuations in the inflaton are thus imprinted in the fluctuations in the gravitational waves. We study this correlator in Section 3.1;

- the rolling inflaton sources quanta of the gauge field, which in turn source *both* scalar fluctuations and gravitational waves. Since these modes are produced by the same population of gauge modes, they are correlated. We study this correlator in Section 3.2.

As we will see, the second effect is generally dominant over the first one, and can lead to a primordial cross-correlation of the order of $(f_{\rm NL}^{\rm equil}/10^6)^{1/3}$, where $f_{\rm NL}^{\rm equil}$ measures the scalar bispectrum at CMB scales in the equilateral configuration generated by the gauge field dynamics.

The correlator studied in this work is the one between scalar perturbations at CMB scales, corresponding to modes that left the horizon early during inflation and gravitational waves at interferometer scales, which correspond to modes that left the horizon later during inflation. Even though these gravitational waves have relatively short (i.e., non cosmological) wavelengths, their *anisotropies* are at large, cosmological scales.

During the last stages of axion inflation the large amplitude acquired by the gauge modes implies that they can have strong backreaction effects on the inflating background. The nonperturbative inflaton-gauge field dynamics, studied in numerous papers including [20–29], is rich, complicated, and not yet fully understood. The production of gravitational waves, although generated during the phase of strong backreaction, is treated at the perturbative level. Reference [28] derived spectra of gravitational waves produced during this stage keeping into account the nonperturbative dynamics of the inflaton-gauge field system, even if it ignored inflaton inhomogeneities. Reference [30] performed an analogous study for the case of an $SU(2)$ gauge sector. The results of [28] suggest that, even though strong backreaction effects complicate significantly the dynamics of the inflaton and of the gauge quanta, if the inflaton evolution $\phi(t)$ is known, then the resulting gravitational wave spectra reflect quite accurately the shape of the function $\dot{\phi}(t)$. For the scope of our calculation, since we will formulate our results in terms of $\dot{\phi}(t)$ without referring to the specific dynamics that led to that expression, our results should be valid even in the strong backreaction regime, at least as long as the inflaton inhomogeneities are ignored. Moreover, there are reasons to expect that our results will not change even once inflaton gradients are accounted for, since causality will prevent the late strong dynamics from affecting physics at scales that have left the horizon at much earlier times.

This paper is organized as follows. Section 2 contains a review of the amplification process that quanta of gauge field undergo as the inflaton rolls down its potential, together with the generation of curvature perturbations and of gravitational waves. Then, in Section 3, we calculate the two contributions to the correlator between scalar fluctuations and the squared amplitude of the gravitational waves: in Subsection 3.1 we study the correlation of gravitational waves with the amplified vacuum scalar fluctuations and in Subsection 3.2 the correlation of gravitational waves with sourced scalar fluctuations. Finally, in Section 4 we discuss our results and we conclude.

2 Review of scalar and tensor perturbations from axion inflation

Our system consists of a pseudoscalar inflaton ϕ and a $U(1)$ gauge field A_μ in interaction with each other and with gravity through the action

$$\mathcal{S} = \int d^4x\sqrt{-g}\left[\frac{M_P^2}{2}R - \frac{1}{2}\partial_\mu\phi\,\partial^\mu\phi - V(\phi) - \frac{1}{4}F_{\mu\nu}\,F^{\mu\nu} - \frac{\phi}{8\,f}\frac{\epsilon^{\mu\nu\rho\lambda}}{\sqrt{-g}}F_{\mu\nu}\,F_{\rho\lambda}\right], \tag{2.1}$$

where $g = \det(g_{\mu\nu})$, $F_{\mu\nu} = \partial_\mu A_\nu - \partial_\nu A_\mu$, f is a constant with dimensions of mass, R is the Ricci scalar, and $\epsilon^{\mu\nu\rho\lambda}$ is the totally antisymmetric tensor defined by $\epsilon^{0123} = +1$. We will not make any assumption about the shape of the potential $V(\phi)$, other than it is flat enough to be able to support inflation.

Concerning the metric, we will assume that it is of the form of de Sitter space in flat slicing plus tensor perturbations (repeated latin indices are understood to be summed upon)

$$\begin{aligned} ds^2 &= a^2(\tau)\left[-d\tau^2 + (\delta_{ij} + h_{ij}(\mathbf{x},\,\tau))\,dx^i\,dx^j\right], \\ a(\tau) &= -\frac{1}{H\,\tau}, \qquad h_{ii} = \partial_i h_{ij} = 0\,. \end{aligned} \tag{2.2}$$

We perturb the inflaton as

$$\phi(\mathbf{x},\,\tau) \equiv \phi_0(\tau) + \delta\phi(\mathbf{x},\,\tau)\,, \tag{2.3}$$

so that the curvature perturbation is given by $\zeta \equiv -\frac{H}{\dot{\phi}_0}\delta\phi$. We will denote the derivative with respect to conformal time τ by a prime and that with respect to the cosmic time t, defined through $dt = a(\tau)\, d\tau$, by an overdot. We set the scale factor to be equal to unity at the end of inflation, i.e., inflation will end at $\tau_{\rm end} = -1/H$.

We treat the homogeneous inflaton $\phi_0(\tau)$ and the scale factor $a(\tau)$ as background quantities, and we work with the following canonically normalized perturbations

$$\begin{aligned} & A_\mu(\mathbf{x},\,\tau) \qquad \text{with} \qquad A_0(\mathbf{x},\,\tau) = 0\,, \quad \partial_i A_i(\mathbf{x},\,\tau) = 0\,, \\ & \Phi(\mathbf{x},\,\tau) \equiv a(\tau)\,\delta\phi(\mathbf{x},\,\tau)\,, \\ & H_{ij}(\mathbf{x},\,\tau) \equiv \frac{M_P}{2}\,a(\tau)\,h_{ij}(\mathbf{x},\,\tau)\,. \end{aligned} \tag{2.4}$$

Neglecting the mass of the inflaton, our perturbed Lagrangian takes the form

$$\begin{aligned} \mathcal{L} = & \left(\frac{1}{2}\Phi'^2 - \frac{1}{2}\partial_k\Phi\,\partial_k\Phi + \frac{a''}{2\,a}\Phi^2\right) + \left(\frac{1}{2}H'_{ij}\,H'_{ij} - \frac{1}{2}\partial_k H_{ij}\,\partial_k H_{ij} + \frac{a''}{2\,a}H_{ij}\,H_{ij}\right) \\ & + \left(\frac{1}{2}A'_i\,A'_i - \frac{1}{2}\partial_k A_i\,\partial_k A_i - \frac{\phi_0}{f}\epsilon^{ijk}\,A'_i\,\partial_j A_k\right) \\ & - \frac{H_{ij}}{a\,M_P}\,\left[A'_i\,A'_j - (\partial_i A_k - \partial_k A_i)\,(\partial_j A_k - \partial_k A_j)\right] - \frac{\Phi}{f\,a}\epsilon^{ijk}\,A'_i\,\partial_j A_k\,, \end{aligned} \tag{2.5}$$

where the first line describes the free scalar and free tensor perturbations, the second line describes the free gauge field modes, and the last line contains the interactions that lead to processes of the form $A_iA_j \to H_{ij}$ and $A_iA_j \to \Phi$.

By varying the Lagrangian (2.5) with respect to Φ, H_{ij} and A_i, we obtain the equations of motion

$$\Phi'' - \frac{a''}{a}\Phi - \nabla^2\Phi + \frac{1}{f\,a}\epsilon^{ijk}\,A'_i\,\partial_j A_k = 0\,, \tag{2.6}$$

$$H''_{ij} - \frac{a''}{a}H_{ij} - \nabla^2 H_{ij} + \frac{1}{a\,M_P}\,\left[A'_i\,A'_j - (\partial_i A_k - \partial_k A_i)\,(\partial_j A_k - \partial_k A_j)\right] = 0\,, \tag{2.7}$$

$$A''_i - \nabla^2 A_i - \frac{\phi'_0}{f}\epsilon^{ijk}\,\partial_j A_k = 0\,. \tag{2.8}$$

The solution of eq. (2.6) splits into two parts: the solution of the homogeneous equation, denoted as $\Phi_{\rm V}$, and the particular solution, denoted as $\Phi_{\rm S}$. The solution of the homogeneous equation represents the usual vacuum fluctuations generated during inflation due to the accelerated expansion of the background, while the particular solution is induced by the inverse decay of the gauge fields. The homogeneous solution can be quantized through the standard quantization of the free Lagrangian, using the first line of eq. (2.5), as

$$\begin{aligned} & \Phi_{\rm V}(\mathbf{x},\,\tau) = \int \frac{d\mathbf{k}}{(2\pi)^{3/2}} e^{i\mathbf{k}\mathbf{x}}\,\left[\Phi_{\rm V}(k,\,\tau)\,\hat{a}(\mathbf{k}) + \Phi^*_{\rm V}(k,\,\tau)\,\hat{a}^\dagger(-\mathbf{k})\right]\,, \\ & \Phi_{\rm V}(k,\,\tau) \equiv \frac{1}{\sqrt{2k}}\left(1 - \frac{i}{k\tau}\right)\,e^{-ik\tau}\,, \end{aligned} \tag{2.9}$$

where the creation/annihilation operators $\hat{a}^\dagger(\mathbf{k})/\hat{a}(\mathbf{k})$ satisfy the usual commutation relations $\left[\hat{a}(\mathbf{k}),\,\hat{a}^\dagger(\mathbf{q})\right] = \delta(\mathbf{k}-\mathbf{q})$, $\left[\hat{a}(\mathbf{k}),\,\hat{a}(\mathbf{q})\right] = \left[\hat{a}^\dagger(\mathbf{k}),\,\hat{a}^\dagger(\mathbf{q})\right] = 0$.

The power spectrum of the curvature perturbation, $\mathcal{P}_\zeta$, defined through the two point function

$$\langle \zeta(\mathbf{k})\, \zeta(\mathbf{q})\rangle \equiv \frac{2\pi^2}{k^3}\, \mathcal{P}_\zeta(\mathbf{k})\, \delta(\mathbf{k}+\mathbf{q})\,, \tag{2.10}$$

results in the sum of the power spectra corresponding to the homogeneous and the particular solutions, denoted as $\mathcal{P}_{\zeta,\,\mathrm{V}}$ and $\mathcal{P}_{\zeta,\,\mathrm{S}}$, respectively.

Specifically, the homogeneous solution, corresponding to the scalar perturbations associated to the mode functions (2.9), yields, at the end of inflation and for large scales,

$$\mathcal{P}_{\zeta,\,\mathrm{V}} = \frac{k^3}{2\pi^2}\frac{H^2}{\dot{\phi}_0^2}\,|\Phi_{\mathrm{V}}(k,\,\tau_{\mathrm{end}})|^2 \xrightarrow[k\ll H]{} \frac{H^4}{4\pi^2\,\dot{\phi}_0^2}\,. \tag{2.11}$$

An analogous discussion holds also for the tensor perturbations $H_{ij}(\mathbf{x},\,\tau)$, whose vacuum component gives rise to $\mathcal{P}_{h,\,\mathrm{V}} = \frac{2\,H^2}{\pi^2\,M_P^2}$.

In order to find the sourced components of the scalar and tensor power spectra we need to take into account the generation of the electromagnetic field by the rolling pseudoscalar. In order to do that, we start with the quantization of the vector field $A_i(\mathbf{x},\,\tau)$:

$$A_i(\mathbf{x},\,\tau) = \int \frac{d\mathbf{k}}{(2\pi)^{3/2}} \sum_{\lambda=\pm} e_i^{\lambda}(\widehat{\mathbf{k}})\, e^{i\mathbf{k}\mathbf{x}} \left[A_\lambda(k,\,\tau)\,\hat{a}_\lambda(\mathbf{k}) + A_\lambda^*(k,\,\tau)\,\hat{a}_\lambda^\dagger(-\mathbf{k})\right]\,, \tag{2.12}$$

where the helicity projectors $e_i^{\pm}(\widehat{\mathbf{k}})$ satisfy the relations

$$\begin{aligned} &k_i\, e_i^{\lambda}(\widehat{\mathbf{k}}) = 0\,, && e_i^{\lambda}(\widehat{\mathbf{k}})^* = e_i^{-\lambda}(\widehat{\mathbf{k}}) = e_i^{\lambda}(-\widehat{\mathbf{k}})\,,\\ &i\epsilon_{ijk}k_j e_k^{\lambda}(\widehat{\mathbf{k}}) = \lambda\, k\, e_i^{\lambda}(\widehat{\mathbf{k}})\,, && e_i^{\lambda}(\widehat{\mathbf{k}}) e_i^{\lambda'}(\widehat{\mathbf{k}}) = \delta_{\lambda,\,-\lambda'}\,. \end{aligned} \tag{2.13}$$

Inserting the decomposition (2.12) into eq. (2.8) we obtain the equation of motion for the mode functions $A_\lambda(k,\,\tau)$,

$$A_\lambda''(k,\,\tau) + \left(k^2 - \lambda\frac{\phi_0'}{f}k\right)\, A_\lambda(k,\,\tau) = 0\,, \tag{2.14}$$

which can be solved explicitly in terms of special functions if $\dot{\phi}_0 =$ constant. However, we do not need the exact solution. Defining

$$\xi \equiv \frac{\dot{\phi}_0}{2\,f\,H}\,, \tag{2.15}$$

we can rewrite eq. (2.14) as

$$\frac{d^2\,A_\lambda}{d(k\,\tau)^2} + \left(1 + 2\,\lambda\,\frac{\xi}{k\,\tau}\right)\, A_\lambda = 0\,, \tag{2.16}$$

so that, assuming $\xi > 0$, the helicity $\lambda = -1$ in eq. (2.16) has always real frequencies that are adiabatically evolving (remember that $\tau < 0$). As a consequence, the mode A_- stays in its vacuum and we will neglect it from now on. On the other hand, the positive helicity mode A_+ has imaginary frequencies for a range of values of $k\tau$ and is therefore exponentially amplified.

In the WKB approximation, the leading term in the solution of the tachyonic modes of A_+ reads [2]

$$A_+(k,\,\tau) \simeq \frac{1}{\sqrt{2\,k}}\left(-\frac{k\,\tau}{2\,\xi}\right)^{1/4} e^{-2\,\sqrt{-2\xi k\tau}+\pi\,\xi}\,, \tag{2.17}$$

which is strictly speaking valid only in the range [3] $\frac{1}{8\,\xi} \lesssim |k\,\tau| \lesssim 2\,\xi$ (we will assume $\xi \gtrsim O(1)$ throughout this paper). However, since the momenta in this range dominate the contributions to the observables we will be interested in, we will apply the expression (2.17) to the entire range $0 < |k\,\tau| < \infty$. Eq. (2.17) shows that the $\lambda = +$ helicity of the gauge field is amplified by a factor $e^{\pi\xi}$, which can be very large even for moderate values of ξ.

We are now in position to compute the leading order contribution of the amplified gauge field to the curvature perturbation ζ. Taking the Fourier of eq. (2.6), we obtain the equation

$$\Phi''(\mathbf{q},\,\tau) + q^2\Phi(\mathbf{q},\,\tau) - \frac{2}{\tau^2}\Phi(\mathbf{q},\,\tau) - i\,\frac{H\tau}{f}\,\epsilon^{ijk}\int\frac{d\mathbf{p}}{(2\pi)^{3/2}}\,A_i'(\mathbf{p},\,\tau)\,(\mathbf{q}-\mathbf{p})_j A_k(\mathbf{q}-\mathbf{p},\,\tau) = 0\,. \tag{2.18}$$

The particular solution of this equation, $\Phi_{\rm S}$, which corresponds to the sourced component of scalar fluctuations, can be found using the retarded propagator

$$\Phi_{\rm S}(\mathbf{q},\,\tau) \equiv i\int d\tau'\,G_q(\tau,\,\tau')\frac{H\tau'}{f}\,\epsilon^{ijk}\int\frac{d\mathbf{p}}{(2\pi)^{3/2}}\,A_i'(\mathbf{p},\,\tau')\,(\mathbf{q}-\mathbf{p})_j A_k(\mathbf{q}-\mathbf{p},\,\tau')\,. \tag{2.19}$$

Given that we are assuming an exact de Sitter background, the retarded propagator can be written explicitly as

$$G_k(\tau,\tau') = \frac{(1+k^2\,\tau\,\tau')\,\sin(k\,(\tau-\tau')) + k\,(\tau'-\tau)\,\cos(k\,(\tau-\tau'))}{k^3\,\tau\,\tau'}\,\Theta(\tau-\tau')\,, \tag{2.20}$$

where Θ denotes the Heaviside step function.

The sourced component of the scalar fluctuations induces an additional contribution to the power spectrum of the curvature perturbation, that for $\xi \gtrsim 3$, is well approximated by the formula [3]

$$\mathcal{P}_{\zeta,\,\rm S} = \frac{k^3}{2\pi^2}\frac{H^2}{\dot\phi_0^2}\,|\Phi_{\rm S}(k,\,\tau_{\rm end})|^2 \xrightarrow[k\ll H]{} 4.8\times10^{-8}\,\frac{H^8}{\dot\phi_0^4}\,\frac{e^{4\pi\xi}}{\xi^6}\,. \tag{2.21}$$

A commonly used measure of nongaussianity is the parameter $f_{\rm NL}$, which measures the amplitude of the bispectrum of the curvature perturbation and is defined via

$$\langle\zeta(\mathbf{k}_1)\,\zeta(\mathbf{k}_2)\,\zeta(\mathbf{k}_3)\rangle = \frac{3}{10}\,(2\pi)^{5/2}\,f_{\rm NL}(k_1,\,k_2,\,k_3)\,\mathcal{P}_\zeta^2\,\delta(\mathbf{k}_1+\mathbf{k}_2+\mathbf{k}_3)\,\frac{k_1^3+k_2^3+k_3^3}{k_1^3\,k_2^3\,k_3^3}\,. \tag{2.22}$$

For single field, slow-roll inflation, the bispectrum has a small amplitude, and $f_{\rm NL}$ is of the order of the slow-roll parameters [31]. On the other hand, the sourced component of the curvature perturbation, since it results from a $2 \to 1$ process, obeys an intrinsically nongaussian statistics. Since such nongaussianities originate from some sub-horizon dynamics, the bispectrum is peaked on equilateral configurations, i.e., for $k_1 = k_2 = k_3$, with [3]

$$f_{\rm NL}^{\rm equil} \simeq 7.1\times10^5\,\frac{H^{12}}{\dot\phi^6}\,\frac{e^{6\pi\xi}}{\xi^9}\,, \tag{2.23}$$

for $\xi \gtrsim 3$ and in the regime $\mathcal{P}_{\zeta,\mathrm{S}} \ll \mathcal{P}_{\zeta,\mathrm{V}}$. In the regime of large ξ, where $\mathcal{P}_{\zeta,\mathrm{S}} \gg \mathcal{P}_{\zeta,\mathrm{V}}$, $f_{\mathrm{NL}}^{\mathrm{equil}}$ converges to a value of the order of 10^4, which exceeds by a $O(10^3)$ factor the constraints from Planck. This limits severely the value ξ_{CMB} taken by ξ when Cosmic Microwave Background scales are leaving the horizon, leading to [32] $\xi_{\mathrm{CMB}} \lesssim 2.5$.

The excited modes of the vector field are also a source of gravitational waves. To leading order, production of gravitational waves via this process is described by the equation

$$H_{ij}''(\mathbf{q},\,\tau) + q^2 H_{ij}(\mathbf{q},\,\tau) - \frac{2}{\tau^2} H_{ij}(\mathbf{q},\,\tau) = \frac{H\,\tau}{M_P} \int \frac{d\mathbf{p}}{(2\pi)^{3/2}} \left(A_i'(\mathbf{p},\,\tau)\, A_j'(\mathbf{q}-\mathbf{p},\,\tau) - F_{ik}(\mathbf{p},\,\tau) F_{jk}(\mathbf{q}-\mathbf{p},\,\tau) \right) , \tag{2.24}$$

where $F_{ij}(\mathbf{p},\,\tau) \equiv i\,\mathbf{p}_i A_j(\mathbf{p},\tau) - i\,\mathbf{p}_j A_i(\mathbf{p},\tau)$. As a consequence of the functional dependence of A_+ on $k\,\tau$ and on ξ, the electric field is stronger than the magnetic field by a factor $\sim \xi \gtrsim 1$. For this reason we will neglect the term $F_{ik}(\mathbf{p},\,\tau) F_{jk}(\mathbf{q}-\mathbf{p},\,\tau)$ in eq. (2.24). Using again the Green's function (2.20) we eventually obtain

$$H_{ij,\,\mathrm{S}}(\mathbf{q},\,\tau) \equiv \int d\tau'\, G_q(\tau,\tau')\, \frac{H\,\tau'}{M_P} \int \frac{d\mathbf{p}}{(2\pi)^{3/2}}\, A_i'(\mathbf{p},\,\tau')\, A_j'(\mathbf{q}-\mathbf{p},\,\tau') \,. \tag{2.25}$$

The resulting power spectrum for the tensor modes reads [6]

$$\mathcal{P}_h = \mathcal{P}_{h,\,\mathrm{V}} + \mathcal{P}_{h,\,\mathrm{S}} \simeq \frac{2\,H^2}{\pi^2\,M_P^2} + 8.7 \times 10^{-8} \frac{H^4}{M_P^4}\, \frac{e^{4\pi\xi}}{\xi^6} \,. \tag{2.26}$$

It is worth stressing that the sourced component of the gravitational waves is almost fully chiral, as a consequence of the fact that only the + helicity of the gauge field is excited. While this fact can lead to a rich and interesting phenomenology, we will not be concerned with it here.

The constraint on the parameter ξ coming from the limits on nongaussianities implies that $\mathcal{P}_{h,\,\mathrm{V}} \gg \mathcal{P}_{h,\,\mathrm{S}}$. This constraint, however, holds only for the value ξ_{CMB} taken by ξ when CMB scales left the horizon. The quantity ξ is slowly evolving, typically increasing, during inflation. Since the sourced component of the gravitational wave spectrum has an exponential dependence on ξ, it is possible that at later times $\mathcal{P}_{h,\,\mathrm{V}}$ is actually overwhelmed by $\mathcal{P}_{h,\,\mathrm{S}}$. We will denote by $\xi_{\mathrm{LATE}} > \xi_{\mathrm{CMB}}$ the value taken by ξ at this later stage. In particular, this leads to the possibility that gravitational waves sourced by the vector field have such large amplitude to be directly detectable by current or future gravitational detectors [7].

In the next section we will describe two mechanisms that induce correlation between the curvature perturbation and the gravitational waves produced in axion inflation.

3 The correlator between scalar fluctuations and gravitational waves

We define the normalized correlator of scalar fluctuations and gravitational waves as

$$\begin{aligned} \mathcal{C}_{h\zeta}(\mathbf{k},\,\tau) &= \frac{1}{\mathcal{P}_h\,\sqrt{\mathcal{P}_\zeta}}\, \frac{k^3}{2\pi^2} \int \frac{d\mathbf{y}}{(2\pi)^{3/2}} e^{-i\mathbf{k}\mathbf{y}} \langle h_{ij}(\mathbf{x}+\mathbf{y},\,\tau)\, h_{ij}(\mathbf{x}+\mathbf{y},\,\tau)\, \zeta(\mathbf{x},\,\tau) \rangle \\ &= \frac{1}{\mathcal{P}_h\,\sqrt{\mathcal{P}_\zeta}}\, \frac{k^3}{2\pi^2} \int \frac{d\mathbf{p}}{(2\pi)^3} \langle h_{ij}(\mathbf{k}-\mathbf{p},\,\tau)\, h_{ij}(\mathbf{p},\,\tau)\, \zeta(-\mathbf{k},\,\tau) \rangle' \,, \end{aligned} \tag{3.1}$$

where $\langle \ldots \rangle'$ denotes the correlator stripped of the Dirac delta associated to momentum conservation, i.e.,

$$\langle h_{ij}(\mathbf{k}_1,\tau)\, h_{ij}(\mathbf{k}_2,\tau)\, \zeta(\mathbf{k}_3,\tau)\rangle \equiv \langle h_{ij}(\mathbf{k}_1,\tau)\, h_{ij}(\mathbf{k}_2,\tau)\, \zeta(\mathbf{k}_3,\tau)\rangle'\, \delta(\mathbf{k}_1+\mathbf{k}_2+\mathbf{k}_3)\,. \tag{3.2}$$

The correlator (3.1) receives two different contributions: the first is the result of the correlation of gravitational waves with the amplified vacuum scalar fluctuations; the second is due to the correlation of gravitational waves with the sourced scalar fluctuations. In the following we will examine the two cases separately.

3.1 Correlation with amplified vacuum scalar fluctuations

The spectrum $\mathcal{P}_{h,\,\mathrm{S}}$ of gravitational waves sourced by the gauge field depends on the values of ϕ and $\dot\phi$ evaluated approximately at the time when the tensor modes under consideration left the horizon, and where, in slow-roll approximation, $\dot\phi$ is a function of ϕ. As a consequence, long wavelength perturbations in the values of ϕ will lead to correlated long wavelength perturbations in the spectrum of gravitational waves. Schematically, in the long wavelength approximation we can write

$$\begin{aligned}
&\left\langle [h_{ij}h_{ij}]_{\mathrm{S}}\,(\mathbf{x}+\mathbf{y})\zeta_{\mathrm{V}}(\mathbf{x})\right\rangle \simeq \left\langle [h_{ij}h_{ij}(\phi(\mathbf{x}+\mathbf{y}))]_{\mathrm{S}}\,\zeta_{\mathrm{V}}(\mathbf{x})\right\rangle \\
&\simeq \left\langle [h_{ij}h_{ij}(\phi_0)]_{\mathrm{S}}\,\zeta_{\mathrm{V}}(\mathbf{x})\right\rangle + \left\langle \frac{d\ [h_{ij}h_{ij}(\phi_0)]_{\mathrm{S}}}{d\phi_0}\,\delta\phi_{\mathrm{V}}(\mathbf{x}+\mathbf{y})\zeta_{\mathrm{V}}(\mathbf{x})\right\rangle ,
\end{aligned} \tag{3.3}$$

where the first correlator in the second line vanishes since it is equal to $\left\langle [h_{ij}h_{ij}(\phi_0)]_{\mathrm{S}}\right\rangle \langle\zeta_{\mathrm{V}}(\mathbf{x})\rangle$ with $\langle\zeta_{\mathrm{V}}(\mathbf{x})\rangle = 0$. Since $[h_{ij}h_{ij}(\phi_0)]_{\mathrm{S}}$ is proportional to $e^{4\pi\,\xi_{\mathrm{LATE}}}$, the dominant contribution to its variation, in the large-ξ limit, is given by

$$\frac{d\ [h_{ij}h_{ij}(\phi_0)]_{\mathrm{S}}}{d\phi_0} \simeq 4\pi\ [h_{ij}h_{ij}(\phi_0)]_{\mathrm{S}}\ \frac{d\xi_{\mathrm{LATE}}}{d\phi_0}\,, \tag{3.4}$$

where in slow roll, assuming $\dot\phi_0 > 0$, $V' < 0$,

$$\xi \equiv \frac{\dot\phi_0}{2\,fH} \simeq -\frac{V'}{6\,fH^2} = -\frac{M_P^2}{2\,f}\frac{V'}{V}\,. \tag{3.5}$$

As a consequence,

$$\frac{d\xi_{\mathrm{LATE}}}{d\phi_0} = -\frac{M_P^2}{2\,f}\left(\frac{V''}{V} - \frac{V'^2}{V^2}\right) = \left(\epsilon_{\mathrm{LATE}} - \frac{\eta_{\mathrm{LATE}}}{2}\right)\frac{1}{f}\,, \tag{3.6}$$

where we have defined as usual the slow-roll parameters as

$$\epsilon = \frac{M_P^2}{2}\,\frac{V'^2}{V^2}\,, \qquad\qquad \eta = M_P^2\frac{V''}{V}\,. \tag{3.7}$$

The above results allow us to write the contribution to $\mathcal{C}_{h\zeta}$ from the amplified vacuum fluctuations of the scalar spectrum, which we denote as $(\mathcal{C}_{h\zeta})_{\mathrm{V}}$, as

$$\begin{aligned}
(\mathcal{C}_{h\zeta})_{\mathrm{V}} &= \frac{1}{\mathcal{P}_h\,\sqrt{\mathcal{P}_\zeta}}\frac{k^3}{2\pi^2}\int\frac{d\mathbf{y}}{(2\pi)^{3/2}}e^{-i\mathbf{k}\mathbf{y}}\langle h_{ij,\,\mathrm{S}}(\mathbf{x}+\mathbf{y},\,\tau)\,h_{ij,\,\mathrm{S}}(\mathbf{x}+\mathbf{y},\,\tau)\,\zeta_{\mathrm{V}}(\mathbf{x},\,\tau)\rangle \\
&\simeq \frac{1}{\mathcal{P}_h\,\sqrt{\mathcal{P}_\zeta}}\frac{k^3}{2\pi^2}\int\frac{d\mathbf{y}}{(2\pi)^{3/2}}\,e^{-i\mathbf{k}\mathbf{y}}\frac{4\pi}{f}\left(\epsilon_{\mathrm{LATE}} - \frac{\eta_{\mathrm{LATE}}}{2}\right)\,\langle h_{ij}h_{ij}\rangle_{\mathrm{S}}\,\langle\delta\phi_{\mathrm{V}}(\mathbf{x}+\mathbf{y})\,\zeta_{\mathrm{V}}(\mathbf{x})\rangle\ .
\end{aligned} \tag{3.8}$$

Then using $\delta\phi = -\dot{\phi}_0\,\zeta/H$, where ζ, being evaluated at superhorizon scales, is constant, and writing $\langle h_{ij}h_{ij}\rangle_{\rm S} \propto \mathcal{P}_{h,\,\rm S} \simeq \mathcal{P}_h$, we obtain

$$(\mathcal{C}_{h\zeta})_{\rm V} = -\frac{1}{\sqrt{\mathcal{P}_\zeta}}\frac{k^3}{2\pi^2}\int\frac{d\mathbf{y}}{(2\pi)^{3/2}}\,e^{-i\mathbf{k}\mathbf{y}}\,\frac{4\pi}{f}\left(\epsilon_{\rm LATE}-\frac{\eta_{\rm LATE}}{2}\right)\frac{\dot{\phi}_{0,\,\rm LATE}}{H_{\rm LATE}}\,\langle\zeta_{\rm V}(\mathbf{x}+\mathbf{y})\,\zeta_{\rm V}(\mathbf{x})\rangle\,, \tag{3.9}$$

with

$$\int\frac{d\mathbf{x}}{(2\pi)^{3/2}}\,e^{-i\mathbf{k}\mathbf{x}}\,\langle\zeta_{\rm V}(\mathbf{x}+\mathbf{y})\zeta_{\rm V}(\mathbf{y})\rangle = \frac{1}{(2\pi)^{3/2}}\,\langle\zeta_{\rm V}(\mathbf{k})\zeta_{\rm V}(-\mathbf{k})\rangle' = \frac{1}{(2\pi)^{3/2}}\frac{2\pi^2}{k^3}\mathcal{P}_{\zeta,\,\rm V}\,, \tag{3.10}$$

so that we finally get

$$(\mathcal{C}_{h\zeta})_{\rm V} = 8\pi\,\xi_{\rm LATE}\frac{\sqrt{\mathcal{P}_{\zeta,\,\rm V}}}{(2\pi)^{3/2}}\left(\frac{\eta_{\rm LATE}}{2}-\epsilon_{\rm LATE}\right)\,. \tag{3.11}$$

To estimate our result for $(\mathcal{C}_{h\zeta})_{\rm V}$ we note that both $\epsilon_{\rm LATE}$ and $\eta_{\rm LATE}$ must be smaller than 1. Moreover, $\xi_{\rm LATE}$ is typically of the order of 10 or so. Using $\mathcal{P}_{\zeta,\,\rm V} \simeq \mathcal{P}_\zeta \simeq 2\times10^{-9}$ (consistency with observations requires the sourced contribution to $\mathcal{P}_\zeta$ to be negligible), we finally obtain the upper bound

$$\left|(\mathcal{C}_{h\zeta})_{\rm V}\right| \lesssim O(10^{-3})\,, \tag{3.12}$$

which is very small and, as we will see, subdominant with respect to the correlation between sourced tensors and sourced scalar perturbations, that we will study now.

3.2 Correlation with sourced scalar fluctuations

In order to calculate the correlator between the sourced scalar and tensor fluctuations, that we denote as $(\mathcal{C}_{h\zeta})_{\rm S}$, we use eqs. (2.4), (2.19) and (2.25) to find $\langle h_{ab,\,\rm S}(\mathbf{k}_1,\tau)\,h_{ab,\,\rm S}(\mathbf{k}_2,\tau)\,\zeta_{\rm S}(\mathbf{k}_3,\tau)\rangle$ in terms of the canonically normalized perturbations as

$$\begin{aligned}
&\langle h_{ab,\,\rm S}(\mathbf{k}_1,\tau)\,h_{ab,\,\rm S}(\mathbf{k}_2,\tau)\,\zeta_{\rm S}(\mathbf{k}_3,\tau)\rangle = -\frac{4\,H(\tau)}{M_P^2\,\dot{\phi}_0(\tau)\,a^3(\tau)}\langle H_{ab,\,\rm S}(\mathbf{k}_1,\tau)\,H_{ab,\,\rm S}(\mathbf{k}_2,\tau)\,\Phi_{\rm S}(\mathbf{k}_3,\tau)\rangle\\
&= \frac{4\,H(\tau)}{M_P^4\,\dot{\phi}_0(\tau)\,a^3(\tau)\,f}\int_{-\infty}^{\tau}\frac{d\tau_1}{a(\tau_1)}\,\frac{d\tau_2}{a(\tau_2)}\,\frac{d\tau_3}{a(\tau_3)}\,G_{k_1}(\tau,\tau_1)\,G_{k_2}(\tau,\tau_2)\,G_{k_3}(\tau,\tau_3)\\
&\times\int\frac{d\mathbf{q}_1\,d\mathbf{q}_2\,d\mathbf{q}_3}{(2\pi)^{9/2}}\,e_a^+(\widehat{\mathbf{q}_1})\,e_b^+(\widehat{\mathbf{k}_1-\mathbf{q}_1})\,e_a^+(\widehat{\mathbf{q}_2})\,e_b^+(\widehat{\mathbf{k}_2-\mathbf{q}_2})\,e_i^+(\widehat{\mathbf{q}_3})\,e_i^+(\widehat{\mathbf{k}_3-\mathbf{q}_3})\,|\mathbf{k}_3-\mathbf{q}_3|\\
&\times\langle A'_+(q_1,\tau_1)\,A'_+(|\mathbf{k}_1-\mathbf{q}_1|,\tau_1)\,A'_+(q_2,\tau_2)\,A'_+(|\mathbf{k}_2-\mathbf{q}_2|,\tau_2)\,A'_+(q_3,\tau_3)\,A_+(|\mathbf{k}_3-\mathbf{q}_3|,\tau_3)\rangle\,,
\end{aligned} \tag{3.13}$$

where we have assumed that only the positive helicity photons contribute because, from eq. (2.14), A_+ is the only helicity that is amplified, and therefore

$$\begin{aligned}
&i\,\epsilon^{ijk}A'_i(\mathbf{q}_3,\tau_3)\,(\mathbf{k}_3-\mathbf{q}_3)_j\,A_k(\mathbf{k}_3-\mathbf{q}_3,\tau_3) =\\
&|\mathbf{k}_3-\mathbf{q}_3|\,e_i^+(\widehat{\mathbf{q}_3})\,e_i^+(\widehat{\mathbf{k}_3-\mathbf{q}_3})\,A'_+(q_3,\tau_3)\,A_+(|\mathbf{k}_3-\mathbf{q}_3|,\tau_3)\,,
\end{aligned} \tag{3.14}$$

and

$$A'_a(\mathbf{q}_1,\tau_1)\,A'_b(\mathbf{k}_1-\mathbf{q}_1,\tau_1) = e_a^+(\widehat{\mathbf{q}_1})\,e_b^+(\widehat{\mathbf{k}_1-\mathbf{q}_1})\,A'_+(q_1,\tau_1)\,A'_+(|\mathbf{k}_1-\mathbf{q}_1|,\tau_1)\,. \tag{3.15}$$

Using Wick's theorem to decompose the last line of eq. (3.13) and inserting it back into (3.1) we obtain

$$(\mathcal{C}_{h\zeta})_{\rm S}\,(\mathbf{k},\,\tau) = \frac{2\,k^3\,H(\tau)}{\pi^2\,M_P^4\,\dot\phi_0(\tau)\,a^3(\tau)\,f\,\mathcal{P}_h\,\sqrt{\mathcal{P}_\zeta}}\int\frac{d\mathbf{p}}{(2\pi)^3}\Bigg[\int_{-\infty}^{\tau}\frac{d\tau_1}{a(\tau_1)}\,\frac{d\tau_2}{a(\tau_2)}\,\frac{d\tau_3}{a(\tau_3)}$$
$$G_{k_1}(\tau,\tau_1)\,G_{k_2}(\tau,\tau_2)\,G_{k_3}(\tau,\tau_3)\int\frac{d\mathbf{q}\,\mathcal{A}(\mathbf{q},\mathbf{k}_1-\mathbf{q},\mathbf{k}_2+\mathbf{q})}{(2\pi)^{9/2}}\Big(|\mathbf{k}_2+\mathbf{q}|\,A'_+(q,\tau_1)\,A'_+(|\mathbf{k}_1-\mathbf{q}|,\tau_1)$$
$$A'_+(q,\tau_2)\,A'_+(|\mathbf{k}_1-\mathbf{q}|,\tau_3)\,A'_+(|\mathbf{k}_2+\mathbf{q}|,\tau_2)\,A_+(|\mathbf{k}_2+\mathbf{q}|,\tau_3)+|\mathbf{k}_1-\mathbf{q}|\,A'_+(q,\tau_1)\,A'_+(q,\tau_2)$$
$$A'_+(|\mathbf{k}_1-\mathbf{q}|,\tau_1)\,A_+(|\mathbf{k}_1-\mathbf{q}|,\tau_3)\,A'_+(|\mathbf{k}_2+\mathbf{q}|,\tau_2)\,A'_+(|\mathbf{k}_2+\mathbf{q}|,\tau_3)\Big)\Bigg]_{\substack{\mathbf{k}_1=\mathbf{k}-\mathbf{p}\\ \mathbf{k}_2=\mathbf{p}\\ \mathbf{k}_3=-\mathbf{k}}}, \tag{3.16}$$

where we have collected the angular part inside the expression $\mathcal{A}$:

$$\mathcal{A}(\mathbf{k}_1,\mathbf{k}_2,\mathbf{k}_3) = \delta_{ac}\,\delta_{bd}\,((e_a^+(\widehat{\mathbf{k}_1})\,e_c^+(\widehat{-\mathbf{k}_1})\,e_b^+(\widehat{\mathbf{k}_2})\,e_i^+(\widehat{-\mathbf{k}_2})\,e_d^+(\widehat{\mathbf{k}_3})\,e_i^+(\widehat{-\mathbf{k}_3})+(a\leftrightarrow b))+(c\leftrightarrow d))\,.$$

Using the explicit form of the gauge field (2.17), the expression (3.16) becomes

$$(\mathcal{C}_{h\zeta})_{\rm S}\,(\mathbf{k},\,\tau) = -\frac{k^3\,H^4(\tau)\,e^{2\pi\xi_1}\,e^{2\pi\xi_2}\,e^{2\pi\xi_3}}{2\,\pi^2\,(2\pi)^{9/2}\,M_P^4\,\dot\phi_0(\tau)\,f\,a^3(\tau)\,\mathcal{P}_h\,\sqrt{\mathcal{P}_\zeta}}$$
$$\times\int\frac{d\mathbf{p}}{(2\pi)^3}\int_{-\infty}^{\tau}d\tau_1\,d\tau_2\,d\tau_3\,\xi_1^{1/2}\,\xi_2^{1/2}\,\sqrt{\tau_1\,\tau_2}\,\tau_3\,G_p(\tau,\tau_2)\,G_{|\mathbf{k}-\mathbf{p}|}(\tau,\tau_1)\,G_k(\tau,\tau_3)$$
$$\times\int d\mathbf{q}\,\mathcal{A}(\mathbf{q},\mathbf{k}-\mathbf{p}-\mathbf{q},\mathbf{p}+\mathbf{q})q^{1/2}\,|\mathbf{k}-\mathbf{p}-\mathbf{q}|^{1/2}\,|\mathbf{p}+\mathbf{q}|^{1/2}(|\mathbf{k}-\mathbf{p}-\mathbf{q}|^{1/2}+|\mathbf{p}+\mathbf{q}|^{1/2})$$
$$\times e^{-2\sqrt{-2\,\xi_1\,q\,\tau_1}-2\sqrt{-2\,\xi_2\,q\,\tau_2}-2\sqrt{-2\,\xi_1\,|\mathbf{k}-\mathbf{p}-\mathbf{q}|\,\tau_1}-2\sqrt{-2\,\xi_2\,|\mathbf{p}+\mathbf{q}|\,\tau_2}-2\sqrt{-2\,\xi_3\,|\mathbf{p}+\mathbf{q}|\,\tau_3}-2\sqrt{-2\,\xi_3\,|\mathbf{k}-\mathbf{p}-\mathbf{q}|\,\tau_3}} \tag{3.17}$$

where we have also allowed for the parameter ξ to be time-dependent, albeit adiabatically, and we have denoted $\xi_i \equiv \xi(\tau_i)$. In order to perform the calculation we set the time at the end of inflation to be $\tau_{\rm end} = -1/H$ and we measure all the integration variables in units of k, i.e. $\mathbf{q}' = \mathbf{q}/k$, $\mathbf{p}' = \mathbf{p}/k$, $\hat{\mathbf{k}} = \mathbf{k}/k$, $x_i = -k\,\tau_i$. Then we can further simplify the expression by performing the change of variables $\tilde{\mathbf{q}} = \mathbf{q}'+\mathbf{p}'$ and by taking the limit $k/H \to 0$. Subsequently we use the expressions

$$\int_0^\infty dx\,x^3\,e^{-a\,\sqrt{x}} = \frac{2}{a^8}\Gamma(8)\,,$$
$$\int_0^\infty dx\,x^{5/2}\,e^{-a\,\sqrt{x}} = \frac{2}{a^7}\Gamma(7)\,, \tag{3.18}$$

where the object a depends on ξ and is in principle time-dependent, but we assume it to be constant as the integral gets contributions only from a relatively narrow range of times. Since the integration variables τ_1 and τ_2 are associate to the sourced tensor modes, whereas τ_3 is associated to the scalar modes, we can set $\xi_1 = \xi_2 = \xi_{\rm LATE}$ and $\xi_3 = \xi_{\rm CMB}$. We thus finally obtain

$$(\mathcal{C}_{h\zeta})_{\rm S} = \frac{4\,H^7\,e^{4\pi\,\xi_{\rm LATE}}\,e^{2\pi\,\xi_{\rm CMB}}\,\Gamma(8)\,\Gamma(7)^2}{27\,\pi^2\,(2\pi)^{15/2}\,f\,(2\sqrt{2})^{22}\,\xi_{\rm LATE}^6\,\xi_{\rm CMB}^4\,M_P^4\,\dot\phi_0\,\mathcal{P}_h\,\sqrt{\mathcal{P}_\zeta}}\times\mathcal{I}\,, \tag{3.19}$$

where

$$\mathcal{I} = \int d\mathbf{p}'\int d\tilde{\mathbf{q}}\,\frac{\mathcal{A}(\tilde{\mathbf{q}}-\mathbf{p}',\hat{\mathbf{k}}-\tilde{\mathbf{q}},\tilde{\mathbf{q}})\,|\tilde{\mathbf{q}}-\mathbf{p}'|^{1/2}\,|\hat{\mathbf{k}}-\tilde{\mathbf{q}}|^{1/2}\,\tilde{q}^{1/2}}{(|\hat{\mathbf{k}}-\tilde{\mathbf{q}}|^{1/2}+\tilde{q}^{1/2})^7\,(|\tilde{\mathbf{q}}-\mathbf{p}'|^{1/2}+\tilde{q}^{1/2})^7\,(|\tilde{\mathbf{q}}-\mathbf{p}'|^{1/2}+|\hat{\mathbf{k}}-\tilde{\mathbf{q}}|^{1/2})^7}\,, \tag{3.20}$$

with

$$\mathcal{A}(\mathbf{k}_1,\,\mathbf{k}_2,\,\mathbf{k}_3)=\frac{1}{4}\Bigg(2+3\,(\widehat{\mathbf{k}_2}\cdot\widehat{\mathbf{k}_3})^2-5\,\widehat{\mathbf{k}_2}\cdot\widehat{\mathbf{k}_3}+(\widehat{\mathbf{k}_1}\cdot\widehat{\mathbf{k}_3})^2+(\widehat{\mathbf{k}_1}\cdot\widehat{\mathbf{k}_2})^2-\widehat{\mathbf{k}_1}\cdot\widehat{\mathbf{k}_3}+\widehat{\mathbf{k}_1}\cdot\widehat{\mathbf{k}_2}$$
$$-(\widehat{\mathbf{k}_1}\cdot\widehat{\mathbf{k}_3})(\widehat{\mathbf{k}_1}\cdot\widehat{\mathbf{k}_2})-(\widehat{\mathbf{k}_2}\cdot\widehat{\mathbf{k}_3})(\widehat{\mathbf{k}_1}\cdot\widehat{\mathbf{k}_2})+(\widehat{\mathbf{k}_2}\cdot\widehat{\mathbf{k}_3})(\widehat{\mathbf{k}_1}\cdot\widehat{\mathbf{k}_3})$$
$$-(\widehat{\mathbf{k}_1}\cdot\widehat{\mathbf{k}_2})(\widehat{\mathbf{k}_1}\cdot\widehat{\mathbf{k}_3})(\widehat{\mathbf{k}_2}\cdot\widehat{\mathbf{k}_3})-i\,\epsilon_{dil}\,\widehat{\mathbf{k}_1}_d\,\widehat{\mathbf{k}_2}_i\,\widehat{\mathbf{k}_3}_l\,(\widehat{\mathbf{k}_1}\cdot\widehat{\mathbf{k}_2}-\widehat{\mathbf{k}_1}\cdot\widehat{\mathbf{k}_3}-\widehat{\mathbf{k}_2}\cdot\widehat{\mathbf{k}_3}+1)\Bigg)\,. \quad (3.21)$$

The integral can be computed numerically and evaluates to $\mathcal{I}\simeq 6\times10^{-4}$. After having substituted $\sqrt{\mathcal{P}_\zeta}\simeq\sqrt{\mathcal{P}_{\zeta,\,\mathrm{V}}}=H^2/(2\pi\,\dot{\phi}_0)$ and $\mathcal{P}_h\simeq\mathcal{P}_{h,\mathrm{S}}$ from (2.26), the expression (3.19) takes the simple form

$$(\mathcal{C}_{h\zeta})_{\mathrm{S}}\simeq 2\times10^{-4}\,\frac{e^{2\pi\,\xi_{\mathrm{CMB}}}\,H}{\xi^4_{\mathrm{CMB}}\,f}\,. \quad (3.22)$$

Finally, we use eq. (2.23) together with the measured amplitude of the scalar perturbations $\mathcal{P}_{\zeta,\,\mathrm{V}}\simeq 2\times10^{-9}$ to obtain

$$(\mathcal{C}_{h\zeta})_{\mathrm{S}}\simeq 1.5\times10^{-2}\,(f_{\mathrm{NL}}^{\mathrm{equil}})^{1/3}\,. \quad (3.23)$$

4 Discussion and conclusions

An important component of current and future gravitational wave research is the detection and characterization of the stochastic gravitational wave background. This background may originate from astrophysical sources or have a cosmological origin. Specifically, identifying a cosmological gravitational wave background will provide important information about the very early universe.

A powerful approach to distinguish between astrophysical and cosmological backgrounds involves studying their anisotropies. Notably, it has been shown that these anisotropies are correlated with the anisotropies in the CMB [33, 34]. The exploration of such correlations can significantly contribute to the interpretation of the CMB and SGWB measurements.

In the present paper we have investigated the correlator between the curvature perturbation and the amplitude squared of the tensor modes, computed at the end of inflation, within the axion inflation model. In this model, scalar fluctuations are generated through two distinct mechanisms: first, from the vacuum via the standard amplification process, and second, as a consequence of the production of gauge fields through a process of inverse decay. Consequently, the correlator exhibits two distinct components.

Our analysis reveals that the correlation of gravitational waves with sourced scalar fluctuations is approximately of the order of $\sim 1.5\times10^{-2}\,(f_{\mathrm{NL}}^{\mathrm{equil}})^{1/3}$, where $f_{\mathrm{NL}}^{\mathrm{equil}}$ measures the amplitude of the bispectrum, in the equilateral configuration, of the scalar perturbations induced at CMB scales by the gauge field population. Observations [35] constrain $f_{\mathrm{NL}}^{\mathrm{equil}}\lesssim O(50)$. Notably, this correlation turns out to be larger than the correlation with the vacuum scalar fluctuations. The correlator saturates to $\mathcal{C}_{h\zeta}=O(1)$ when $f_{\mathrm{NL}}^{\mathrm{equil}}=O(10^5)$, which is indeed the maximum value attainable by $f_{\mathrm{NL}}^{\mathrm{equil}}$ in the perturbative regime.

Our main result, provided by eq. (3.23), corresponds to the initial correlation between the tensor and scalar fluctuations in the model of axion inflation. The formalism of [36–38] can then be applied to derive potentially observable quantities. The actual observability of such correlators, subject to instrumental noise as well as to the intrinsic variance of the isotropic component [39, 40], will depend on the amplitude of the anisotropies in the gravitational wave

spectra. Such an amplitude is encoded in the correlator $\langle h_{ij}(\mathbf{x})\, h_{ij}(\mathbf{x})\, h_{ab}(\mathbf{y}) h_{ab}(\mathbf{y})\rangle$, whose calculation, in the model of axion inflation, requires the evaluation of the gauge field's eight-point function – a calculation that we leave to future work. However, we expect anisotropies to have a potentially detectable amplitude. For instance, the lattice study of [41] showed that the spectrum of gravitational waves induced by preheating at the end of inflation display anisotropies with an amplitude of the order of $\sim 10^{-2}$.

Acknowledgments

We thank Marco Peloso for interesting discussions. This work is partially supported by the US-NSF grant PHY-2112800.

References

[1] K. Freese, J. A. Frieman and A. V. Olinto, "Natural inflation with pseudo - Nambu-Goldstone bosons," Phys. Rev. Lett. **65** (1990), 3233-3236 doi:10.1103/PhysRevLett.65.3233

[2] M. M. Anber and L. Sorbo, "N-flationary magnetic fields," JCAP **10**, 018 (2006) doi:10.1088/1475-7516/2006/10/018 [arXiv:astro-ph/0606534 [astro-ph]].

[3] N. Barnaby and M. Peloso, "Large Nongaussianity in Axion Inflation," Phys. Rev. Lett. **106**, 181301 (2011) doi:10.1103/PhysRevLett.106.181301 [arXiv:1011.1500 [hep-ph]].

[4] R. Namba, M. Peloso, M. Shiraishi, L. Sorbo and C. Unal, "Scale-dependent gravitational waves from a rolling axion," JCAP **01**, 041 (2016) doi:10.1088/1475-7516/2016/01/041 [arXiv:1509.07521 [astro-ph.CO]].

[5] A. Linde, S. Mooij and E. Pajer, "Gauge field production in supergravity inflation: Local non-Gaussianity and primordial black holes," Phys. Rev. D **87** (2013) no.10, 103506 doi:10.1103/PhysRevD.87.103506 [arXiv:1212.1693 [hep-th]].

[6] L. Sorbo, "Parity violation in the Cosmic Microwave Background from a pseudoscalar inflaton," JCAP **06**, 003 (2011) doi:10.1088/1475-7516/2011/06/003 [arXiv:1101.1525 [astro-ph.CO]].

[7] J. L. Cook and L. Sorbo, "Particle production during inflation and gravitational waves detectable by ground-based interferometers," Phys. Rev. D **85**, 023534 (2012) [erratum: Phys. Rev. D **86**, 069901 (2012)] doi:10.1103/PhysRevD.85.023534 [arXiv:1109.0022 [astro-ph.CO]].

[8] M. M. Anber and E. Sabancilar, "Hypermagnetic Fields and Baryon Asymmetry from Pseudoscalar Inflation," Phys. Rev. D **92**, no.10, 101501 (2015) doi:10.1103/PhysRevD.92.101501 [arXiv:1507.00744 [hep-th]].

[9] W. D. Garretson, G. B. Field and S. M. Carroll, "Primordial magnetic fields from pseudoGoldstone bosons," Phys. Rev. D **46**, 5346-5351 (1992) doi:10.1103/PhysRevD.46.5346 [arXiv:hep-ph/9209238 [hep-ph]].

[10] E. Pajer and M. Peloso, "A review of Axion Inflation in the era of Planck," Class. Quant. Grav. **30**, 214002 (2013) doi:10.1088/0264-9381/30/21/214002 [arXiv:1305.3557 [hep-th]].

[11] J. Garcia-Bellido, M. Peloso and C. Unal, "Gravitational waves at interferometer scales and primordial black holes in axion inflation," JCAP **12**, 031 (2016) doi:10.1088/1475-7516/2016/12/031 [arXiv:1610.03763 [astro-ph.CO]].

[12] G. Agazie *et al.* [NANOGrav], Astrophys. J. Lett. **951**, no.1, L8 (2023) doi:10.3847/2041-8213/acdac6 [arXiv:2306.16213 [astro-ph.HE]].

[13] J. Antoniadis *et al.* [EPTA and InPTA:], "The second data release from the European Pulsar Timing Array - III. Search for gravitational wave signals," Astron. Astrophys. **678**, A50 (2023) doi:10.1051/0004-6361/202346844 [arXiv:2306.16214 [astro-ph.HE]].

[14] D. J. Reardon, A. Zic, R. M. Shannon, G. B. Hobbs, M. Bailes, V. Di Marco, A. Kapur, A. F. Rogers, E. Thrane and J. Askew, *et al.* "Search for an Isotropic Gravitational-wave Background with the Parkes Pulsar Timing Array," Astrophys. J. Lett. **951**, no.1, L6 (2023) doi:10.3847/2041-8213/acdd02 [arXiv:2306.16215 [astro-ph.HE]].

[15] R. Abbott *et al.* [KAGRA, Virgo and LIGO Scientific], "Search for anisotropic gravitational-wave backgrounds using data from Advanced LIGO and Advanced Virgo's first three observing runs," Phys. Rev. D **104**, no.2, 022005 (2021) doi:10.1103/PhysRevD.104.022005 [arXiv:2103.08520 [gr-qc]].

[16] N. Bartolo *et al.* [LISA Cosmology Working Group], "Probing anisotropies of the Stochastic Gravitational Wave Background with LISA," JCAP **11**, 009 (2022) doi:10.1088/1475-7516/2022/11/009 [arXiv:2201.08782 [astro-ph.CO]].

[17] M. Geller, A. Hook, R. Sundrum and Y. Tsai, "Primordial Anisotropies in the Gravitational Wave Background from Cosmological Phase Transitions," Phys. Rev. Lett. **121** (2018) no.20, 201303 doi:10.1103/PhysRevLett.121.201303 [arXiv:1803.10780 [hep-ph]].

[18] F. Schulze, L. Valbusa Dall'Armi, J. Lesgourgues, A. Ricciardone, N. Bartolo, D. Bertacca, C. Fidler and S. Matarrese, "GW_CLASS: Cosmological Gravitational Wave Background in the Cosmic Linear Anisotropy Solving System," [arXiv:2305.01602 [gr-qc]].

[19] P. Adshead, N. Afshordi, E. Dimastrogiovanni, M. Fasiello, E. A. Lim and G. Tasinato, "Multimessenger cosmology: Correlating cosmic microwave background and stochastic gravitational wave background measurements," Phys. Rev. D **103**, no.2, 023532 (2021) doi:10.1103/PhysRevD.103.023532 [arXiv:2004.06619 [astro-ph.CO]].

[20] S. L. Cheng, W. Lee and K. W. Ng, "Numerical study of pseudoscalar inflation with an axion-gauge field coupling," Phys. Rev. D **93**, no. 6, 063510 (2016) [arXiv:1508.00251 [astro-ph.CO]].

[21] A. Notari and K. Tywoniuk,"Dissipative Axial Inflation," JCAP **1612**, 038 (2016) [arXiv:1608.06223 [hep-th]].

[22] O. O. Sobol, E. V. Gorbar and S. I. Vilchinskii, "Backreaction of electromagnetic fields and the Schwinger effect in pseudoscalar inflation magnetogenesis," Phys. Rev. D **100**, no.6, 063523 (2019) [arXiv:1907.10443 [astro-ph.CO]].

[23] G. Dall'Agata, S. González-Martín, A. Papageorgiou and M. Peloso, "Warm dark energy," JCAP **08**, 032 (2020) [arXiv:1912.09950 [hep-th]].

[24] V. Domcke, V. Guidetti, Y. Welling and A. Westphal, "Resonant backreaction in axion inflation," JCAP **09**, 009 (2020) [arXiv:2002.02952 [astro-ph.CO]].

[25] A. Caravano, E. Komatsu, K. D. Lozanov and J. Weller, "Lattice simulations of axion-U(1) inflation," Phys. Rev. D **108**, no.4, 043504 (2023) doi:10.1103/PhysRevD.108.043504 [arXiv:2204.12874 [astro-ph.CO]].

[26] M. Peloso and L. Sorbo, "Instability in axion inflation with strong backreaction from gauge modes," JCAP **01**, 038 (2023) doi:10.1088/1475-7516/2023/01/038 [arXiv:2209.08131 [astro-ph.CO]].

[27] D. G. Figueroa, J. Lizarraga, A. Urio and J. Urrestilla, "Strong Backreaction Regime in Axion Inflation," Phys. Rev. Lett. **131**, no.15, 151003 (2023) doi:10.1103/PhysRevLett.131.151003 [arXiv:2303.17436 [astro-ph.CO]].

[28] J. Garcia-Bellido, A. Papageorgiou, M. Peloso and L. Sorbo, "A flashing beacon in axion inflation: recurring bursts of gravitational waves in the strong backreaction regime," [arXiv:2303.13425 [astro-ph.CO]].

[29] R. von Eckardstein, M. Peloso, K. Schmitz, O. Sobol and L. Sorbo, "Axion inflation in the

strong-backreaction regime: decay of the Anber-Sorbo solution," JHEP **11**, 183 (2023) doi:10.1007/JHEP11(2023)183 [arXiv:2309.04254 [hep-ph]].

[30] O. Iarygina, E. I. Sfakianakis, R. Sharma and A. Brandenburg, "Backreaction of axion-SU(2) dynamics during inflation," [arXiv:2311.07557 [astro-ph.CO]].

[31] J. M. Maldacena, "Non-Gaussian features of primordial fluctuations in single field inflationary models," JHEP **05**, 013 (2003) doi:10.1088/1126-6708/2003/05/013 [arXiv:astro-ph/0210603 [astro-ph]].

[32] N. Barnaby, R. Namba and M. Peloso, "Phenomenology of a Pseudo-Scalar Inflaton: Naturally Large Nongaussianity," JCAP **04**, 009 (2011) doi:10.1088/1475-7516/2011/04/009 [arXiv:1102.4333 [astro-ph.CO]].

[33] A. Ricciardone, L. V. Dall'Armi, N. Bartolo, D. Bertacca, M. Liguori and S. Matarrese, "Cross-Correlating Astrophysical and Cosmological Gravitational Wave Backgrounds with the Cosmic Microwave Background," Phys. Rev. Lett. **127** (2021) no.27, 271301 doi:10.1103/PhysRevLett.127.271301 [arXiv:2106.02591 [astro-ph.CO]].

[34] M. Braglia and S. Kuroyanagi, "Probing prerecombination physics by the cross-correlation of stochastic gravitational waves and CMB anisotropies," Phys. Rev. D **104**, no.12, 123547 (2021) doi:10.1103/PhysRevD.104.123547 [arXiv:2106.03786 [astro-ph.CO]].

[35] Y. Akrami *et al.* [Planck], "Planck 2018 results. IX. Constraints on primordial non-Gaussianity," Astron. Astrophys. **641**, A9 (2020) doi:10.1051/0004-6361/201935891 [arXiv:1905.05697 [astro-ph.CO]].

[36] V. Alba and J. Maldacena, "Primordial gravity wave background anisotropies," JHEP **03**, 115 (2016) doi:10.1007/JHEP03(2016)115 [arXiv:1512.01531 [hep-th]].

[37] C. R. Contaldi, "Anisotropies of Gravitational Wave Backgrounds: A Line Of Sight Approach," Phys. Lett. B **771**, 9-12 (2017) doi:10.1016/j.physletb.2017.05.020 [arXiv:1609.08168 [astro-ph.CO]].

[38] N. Bartolo, D. Bertacca, S. Matarrese, M. Peloso, A. Ricciardone, A. Riotto and G. Tasinato, "Characterizing the cosmological gravitational wave background: Anisotropies and non-Gaussianity," Phys. Rev. D **102**, no.2, 023527 (2020) doi:10.1103/PhysRevD.102.023527 [arXiv:1912.09433 [astro-ph.CO]].

[39] G. Mentasti, C. R. Contaldi and M. Peloso, "Intrinsic Limits on the Detection of the Anisotropies of the Stochastic Gravitational Wave Background," Phys. Rev. Lett. **131**, no.22, 221403 (2023) doi:10.1103/PhysRevLett.131.221403 [arXiv:2301.08074 [gr-qc]].

[40] Y. Cui, S. Kumar, R. Sundrum and Y. Tsai, "Unraveling cosmological anisotropies within stochastic gravitational wave backgrounds," JCAP **10**, 064 (2023) doi:10.1088/1475-7516/2023/10/064 [arXiv:2307.10360 [astro-ph.CO]].

[41] L. Bethke, D. G. Figueroa and A. Rajantie, "Anisotropies in the Gravitational Wave Background from Preheating," Phys. Rev. Lett. **111**, no.1, 011301 (2013) doi:10.1103/PhysRevLett.111.011301 [arXiv:1304.2657 [astro-ph.CO]].

Know your footprint - Evaluation of the professional carbon footprint for individual researchers in high energy physics and related fields

Valerie Lang[a,1,*], Naman Kumar Bhalla[a], Simran Gurdasani[a], Pardis Niknejadi[b]

[a]*Albert-Ludwigs-Universität, Freiburg, Germany*
[b]*Deutsches Elektronensynchrotron (DESY), Hamburg, Germany*

arXiv:2403.03308v1 [physics.soc-ph] 5 Mar 2024

Abstract

Understanding the environmental impact of professional activities is becoming paramount in current times, especially within sectors that historically have had significant resource utilisation, such as High Energy Physics (HEP) and related fields. The *young High Energy Physicists* (yHEP) association launched the *Know your footprint* (Kyf) campaign to evaluate the CO_2-equivalent emissions generated by HEP-related research. This study delves into the carbon footprints associated with four distinct categories: *Experiments*, tied to extensive collaborations with substantial infrastructure; *Institutional*, representing the resource consumption of research institutes and universities; *Computing*, focusing on simulations and data analysis; and *Travel*, covering professional trips such as to conferences, meetings, and workshops. The findings in this assessment are integrated into a tool for self-evaluation, the *Know-your-footprint* (Kyf) calculator, which allows colleagues to assess their personal and professional footprint, and optionally share their data with the yHEP association. The aim of the Kyf campaign is to heighten awareness, foster sustainability, and inspire the community to adopt more environmentally-responsible research methodologies.

Keywords: High Energy Physics, CO_2 emissions, Know your footprint, yHEP

1. Introduction

The impact of the atmospheric presence of CO_2 on the ground temperature of the Earth was first predicted in 1896 [1], indicating temperature variations as a function of the amount of CO_2 (at the time denoted as carbonic acid), the time of the year and the latitude. For Europe, the prediction for doubling the atmospheric CO_2 content amounted to an average temperature increase of around 6 °C.

In 2023, the measured CO_2 content in the atmosphere has reached nearly 425 ppm [2], compared to a maximum of about 300 ppm over the last 800 000 years before industrial age. The CO_2 content in the atmosphere has thus increased by a factor of about 1.4 compared to the maximum, and around 1.9 compared to the mean over the last 800 000 years [3]. The average temperature in Europe in 2023 has climbed up by 1.90 °C compared to pre-industrial levels (reference years: 1850-1900) [4], which is also used as reference for temperature differences in the following. The year 2023 is in direct competition with the year 2020 which was the warmest year on record in Europe with a 2.07 °C increase. Globally, 2023 surpassed the previously warmest year 2016 (1.32 °C increase), reaching an increase of 1.48 °C.

Scientific research has thus been drawing a consistent picture for more than 100 years, with continuously refined measurements and scenario predictions. Decisive actions counteracting the changes to the atmosphere and the planetary ecosystem, however, have been and are still lacking.

According to the Sixth Assessment Report (AR6) by the Intergovernmental Panel on Climate Change (IPCC), Summary for Policymakers (SPM) [5], *"[i]t is unequivocal that human influence has warmed the atmosphere, ocean and land"*, leading to changes across the climate system that are *"unprecedented over many centuries to many thousands of years"*.

Relevant for changes of the climate are the cumulative CO_2 emissions. Part of the CO_2 emissions are re-absorbed by carbon sinks on land and ocean, but the higher the cumulative CO_2 emissions are, the lower is the fraction of absorption by land and ocean carbon sinks. This results in higher contributions for both the fraction and the absolute amount that remain in the atmosphere.

The IPCC AR6 SPM estimates historical cumulative anthropogenic CO_2 emissions from 1850 to 2019 to (2390±240) Gigatonnes of CO_2 ($GtCO_2$). In order to achieve a likelihood of 67 % to limit human-induced global warming to a maximum increase of 1.5 °C (2.0 °C), which are the two thresholds explicitly mentioned in the Paris Agreement 2015 [6] to reduce risks and impacts of climate change, only 400 $GtCO_2$ (1150 $GtCO_2$) remain to be emitted. This remaining carbon budget is defined, starting from the beginning of 2020 until global net zero CO_2 emissions are reached.

Using the most naive assumption of equal yearly emissions until 2050, i.e. for 30 years, and a static population of 8 billion people, which was reached on 15 November 2022 [7], the remaining carbon budget per person per year accumulates to 1.7 tCO_2 (4.8 tCO_2) for a maximum temperature increase of 1.5 °C (2.0 °C).

In Germany, the average CO_2 emissions accumulate to

*Corresponding author
[1]Email: valerie.lang@physik.uni-freiburg.de

around 10–11 tCO_2 per person per year [8, 9], i.e. more than a factor of two above what is required for the scenario limiting global warming to an increase of 2.0 °C. This, however, only summarises emissions from private life. For researchers in the area of high energy physics (HEP), emissions resulting from research activities need to be added on top.

The first step for reducing emissions is to quantify current emissions and raise awareness. The *Know your footprint* (Kyf) campaign by the *young High Energy Physicists* (yHEP) association [10] targets these aspects for the professional footprint of researchers in the area of HEP and related fields. While scientific research and development activities contribute only a fraction of the carbon footprint compared to industrial activities, it is crucial for the scientific community to understand and mitigate the environmental impact of their research. Knowledge of the own carbon footprint will allow to identify areas requiring most urgent action and indicate possible starting points for action to reduce the footprint. This paper discusses the data sources and calculations conducted to evaluate the CO_2-equivalent emissions for researchers in HEP for yHEP's Kyf campaign and Kyf calculator.

2. General setup

The Kyf campaign by the yHEP association evaluates the carbon footprint of researchers in HEP, mostly in, or associated to, Germany. For emissions of private life in Germany, we refer to the *Carbon Calculator* by the German Federal Environment Agency (*Umweltbundesamt* - UBA) [8, 9, 11].

For the professional footprint, we target four distinct categories: *Experiments*, *Institutions*, *Computing* and *Travel*.

The *experimental* footprint comprises the emissions from (large) research infrastructures, collaborations or research projects, i.e. especially in experimental physics, the experimental setup. The *institutional* footprint summarises the emissions from the home university or research centre of the individual researcher, which should be understood as the institution where the researcher spends the larger part of her/his working time. *Computing* focuses on the individual researcher's footprint of running simulations and data analysis, optionally considering data storage impacts as well. *Travel* covers the individual's professional trips such as to conferences, meetings, or workshops.

The footprints in each category are broken down to the level of the individual researcher so that they can be placed in relation to each other as well as to the individual's emissions for private life. Several options in each category allow adjusting to the researcher's individual situation, although some simplifications are needed to allow for sufficient user-friendliness and manageable scope of the first version of the Kyf calculator by the yHEP association. Refinements are considered possible in the future. The Kyf calculator is published on the webpage of the yHEP association [10].

The calculations that form the basis of the Kyf calculator are discussed in detail in Sections 3 to 6. An example footprint is given in Section 7. The Kyf calculator provides feedback to individual researchers regarding their own professional carbon footprint, and optionally allows to share the data anonymously with the yHEP association. This data will be used by the yHEP association to obtain and later publish an overview of the professional footprint of researchers in HEP and related fields in, and associated to, Germany. The focus on Germany implies that numbers for the German electricity grid, German institutions, etc. will be used in the calculations, where applicable. Other institutions or interest groups are encouraged to transfer the considerations by yHEP's Kyf campaign to different countries, citing this publication as basis for their considerations. In case of questions, contact can be established with us as authors directly, or with the yHEP association through the webpage [10].

3. Experiment, collaboration or project footprint

The experiment, collaboration or project footprint strongly depends on the corresponding experiment, collaboration or project. In order to provide a rough estimate, we use the experiments at the Large Hadron Collider (LHC) as benchmark for large HEP experiments, DESY electricity consumption (excluding the European XFEL) as benchmark for smaller HEP experiments and the European Southern Observatory (ESO) as benchmark for experimental research in astronomy.

To evaluate the per-researcher environmental footprint, two numbers are needed: an estimate of the total amount of emissions by the experiment, collaboration or project in tonne-CO_2-equivalent (tCO_2e), and the number of people that the footprint should be distributed over. The ratio of these two numbers provides the per-person benchmark footprint.

The design of experimental setups in HEP has traditionally been driven, mainly, by the scientific question that is to be answered, without systematic consideration for minimising its carbon footprint. The scientific output is credited to the authors of the scientific publications. In the area of HEP, authorship on the publications typically requires membership in the experimental collaboration. We therefore assign the carbon footprint of the experiment to the members of the experimental collaboration, or the users (and operators) of the experimental facility, where corresponding numbers are available.

More indirect beneficiaries of the knowledge gained in the experiment, collaboration, or project, such as *the industry* or *the public*, are not considered here. These categories are too vague to provide a good reference for the carbon footprint of an experimental collaboration, and do not allow for well-defined boundaries of the organisation, i.e. the experiment, collaboration or project. In contrast to a company, where the footprint could alternatively be assigned to the "product" of the company and could thus be attributed to the "consumer", *knowledge* as a "product" of scientific experiments is not easily quantifiable and thus not distributable to "consumers". In order to maintain the responsibility for the emissions with those who can impact their reduction, we estimate the per-researcher footprint without consideration of such indirect benefits. This approach is not intended to scrutinise scientists for the environmental impact of their research, but rather aims to highlight key areas where the

scientific community can focus its sustainability efforts, ensuring a more environmentally responsible approach to advancing knowledge.

3.1. LHC experiments

The LHC [12] is the largest particle accelerator housed at CERN [13] colliding proton beams at the location of four major particle detectors: ATLAS [14], CMS [15], ALICE [16] and LHCb [17]. While ATLAS and CMS are large general-purpose detectors, ALICE and LHCb are specialised for specific investigations. Due to different sizes of the detectors, it is expected that the larger experiments also have higher annual CO_2 emissions compared to the two smaller experiments. Hence, the Kyf calculator aims at estimating separate values for annual emissions per person for the larger (ATLAS and CMS) and smaller (ALICE and LHCb) LHC experiments.

Since 2017, CERN publishes a biennial environmental report listing its CO_2 emissions. In order to estimate the annual footprints for this benchmark scenario, the environmental reports for 2017–18 [18], 2019–20 [19] and 2021–22 [20] were used to get an estimate of years with, as well as without, the LHC in operation. In addition, the latest technical design report from the LHCb collaboration, which includes a section on environment protection and safety, was used to estimate the difference in CO_2 emissions between the larger and smaller LHC experiments [21]. In this section, the annual emissions are distributed into two phases: Run phase (2017, 2018 and 2022) and Shutdown phase (2019–21).

CERN categorises its CO_2 emissions into three scopes: scope 1 for direct emissions from sources such as detector operations and heating, scope 2 for indirect emissions primarily arising from electricity consumption, and scope 3 for emissions from other indirect sources such as travel, commute, waste, catering and procurement. For the estimation of the footprint for affiliation to the LHC experiments, only scopes 1 and 2 are relevant with the following corrections applied:

- Scope 1: CERN includes the emissions from heating, non-LHC experiments and others into scope 1. Since this estimate is only for LHC experiments, the corrected scope 1 value, corresponding to LHC experiments (particle detection and cooling) are extracted using `PlotDigitizer` [22] (see Appendix A) from the figure: *CERN scope 1 emissions for 2017–2022 by category*, on page 18 in CERN's environmental report 2021–2022 [20]. These total and corrected scope 1 values for all years are listed in Table 1.

- Scope 2: The scope 2 contribution of CERN's CO_2 emissions include the electricity consumption of the Meyrin and Prevessin sites, which do not correspond to the consumption for powering the LHC and should be corrected for. CERN's environmental report 2021–2022 mentions that powering the CERN campus corresponds to 5% of the total energy consumption which was used as the correction factor for the scope 2 values [20]. Since, the scope 2 emissions for 2017–20 were recalculated for the 2021–22 environment report, but given only in a figure without the final values, they were extracted using `PlotDigitizer` [22] from the figure: *CERN scope 2 emissions for 2017–2022*, on page 19 in CERN's environmental report 2021–2022 [20]. The values for 2021 and 2022 were directly listed in the same report. The total and corrected scope 2 values are listed in Table 2.

	Year	Total	Corrected
Run	2017	193 600	168 293
	2018	192 100	162 718
	2022	184 173	152 444
	Mean	-	161 151
Shutdown	2019	78 169	56 446
	2020	98 997	75 958
	2021	123 174	89 547
	Mean	-	73 984

Table 1: Total and corrected scope 1 contribution to CERN's total emissions for the various years in Run and Shutdown phases [18, 19, 20]. The corrected values were extracted using `PlotDigitizer` [22] from the figure: *CERN scope 1 emissions for 2017–2022 by category*, on page 18 in CERN's environmental report 2021–2022 [20]. All emission values are provided in tCO_2e.

	Year	Total	Corrected
Run	2017	66 667	63 333
	2018	74 884	71 140
	2022	63 161	60 003
	Mean	-	64 825
Shutdown	2019	28 527	27 101
	2020	26 202	24 891
	2021	56 382	53 563
	Mean	-	35 185

Table 2: Total and corrected scope 2 contribution to CERN's total emissions for the various years in Run and Shutdown phases [20]. Values for 2017–20 were not given and were extracted using `PlotDigitizer` [22] from the figure: *CERN scope 2 emissions for 2017–2022*, on page 19 in CERN's environmental report 2021–2022 [20]. The corrected value is 95% of the total value. All emission values are provided in tCO_2e.

The technical design report of the LHCb experiment lists their total emission for 2022 to be $4400\,tCO_2e$ of which 51% is assigned to scope 1 [21], i.e.

$$\begin{aligned} S1^{\text{Run}}_{\text{Small}} &= 0.51 \times 4400\,tCO_2e \\ &= 2244\,tCO_2e\,. \end{aligned}$$

Since the LHC was operating in 2022, $S1^{\text{Run}}_{\text{Small}}$ is defined as the scope 1 contribution for the smaller experiments in the Run phase. In order to estimate the scope 1 contribution for the smaller experiments in the Shutdown phase ($S1^{\text{SD}}_{\text{Small}}$), it is assumed that the emissions for larger and smaller experiments scale by the same factor between the two phases. This factor ($S1^{\text{Run/SD}}$) can be calculated from the mean corrected scope 1

contribution for the two phases from Table 1 as

$$\mathrm{S1}^{\mathrm{Run/SD}} = \frac{161\,151}{73\,984} = 2.18\,.$$

This results in $\mathrm{S1}^{\mathrm{SD}}_{\mathrm{Small}}$ being estimated as

$$\mathrm{S1}^{\mathrm{SD}}_{\mathrm{Small}} = \frac{\mathrm{S1}^{\mathrm{Run}}_{\mathrm{Small}}}{\mathrm{S1}^{\mathrm{Run/SD}}} = \frac{2244\,\mathrm{tCO_2e}}{2.18} = 1030\,\mathrm{tCO_2e}\,.$$

The scope 1 contribution for the larger experiments ($\mathrm{S1_{Large}}$) for each phase can be estimated using the mean corrected scope 1 contribution for all LHC experiments ($\mathrm{S1_{All}}$) from Table 1 and $\mathrm{S1_{Small}}$. This is done by assuming an equal contribution from both the smaller experiments and an equal contribution also from the two larger experiments and calculated as

$$\mathrm{S1_{All}} = 2 \times \mathrm{S1_{Small}} + 2 \times \mathrm{S1_{Large}} \quad (1)$$

$$\mathrm{S1_{Large}} = \frac{\mathrm{S1_{All}} - 2 \times \mathrm{S1_{Small}}}{2}\,. \quad (2)$$

The resulting values for the larger experiments are

$$\mathrm{S1}^{\mathrm{Run}}_{\mathrm{Large}} = 78\,332\,\mathrm{tCO_2e} \text{ and}$$
$$\mathrm{S1}^{\mathrm{SD}}_{\mathrm{Large}} = 35\,962\,\mathrm{tCO_2e}\,.$$

To estimate the scope 2 contribution of individual experiments, it is assumed that all four experiments share an equal contribution to the mean corrected scope 2 emissions of all experiments ($\mathrm{S2_{All}}$) given in Table 2. This assumption is based on the premise that the dominant scope 2 emissions come from the electricity consumption for running the entire accelerator complex, up to and including the LHC, which is equally necessary for all four experiments. In reality, the electricity consumed by the four experiments might vary and could be refined in the future if more data becomes available. The scope 2 contributions for the smaller ($\mathrm{S2_{Small}}$) and larger ($\mathrm{S2_{Larger}}$) experiments, calculated individually for the Run and Shutdown phases, are given as

$$\mathrm{S2_{Small}} = \mathrm{S2_{Large}} = \frac{\mathrm{S2_{All}}}{4}\,. \quad (3)$$

Using this relation, the scope 2 contributions for the Run and Shutdown phases can be calculated as

$$\mathrm{S2}^{\mathrm{Run}}_{\mathrm{Small}} = \mathrm{S2}^{\mathrm{Run}}_{\mathrm{Large}} = \frac{64\,825\,\mathrm{tCO_2e}}{4} = 16\,206\,\mathrm{tCO_2e}\,,$$

and

$$\mathrm{S2}^{\mathrm{SD}}_{\mathrm{Small}} = \mathrm{S2}^{\mathrm{SD}}_{\mathrm{Large}} = \frac{35\,185\,\mathrm{tCO_2e}}{4} = 8796\,\mathrm{tCO_2e}\,.$$

After summing the contributions from scopes 1 and 2 to obtain the total footprint of smaller and larger experiments in the Run and Shutdown phases, a weighted mean of the two phases is taken assuming a Run phase of 4 years and Shutdown phase of 3 years,

$$\text{Overall annual emission} = \frac{4 \times \mathrm{Total}^{\mathrm{Run}} + 3 \times \mathrm{Total}^{\mathrm{SD}}}{7}\,. \quad (4)$$

The values for the individual scopes in the Run and Shutdown phases for smaller and larger experiments are summarised in Table 3 along with the total values for each phase and the overall values calculated using Equation 4.

	Phase	Scope 1	Scope 2	Total
Small	Run	2244	16 206	18 450
	SD	1030	8796	9826
	Overall	-	-	14 754
Large	Run	78 332	16 206	94 538
	SD	35 962	8796	44 758
	Overall	-	-	73 204

Table 3: Contribution from individual scopes in the Run and Shutdown phases for smaller and larger experiments along with the total values for each phase, calculated as Total = Scope 1 + Scope 2, and the overall values calculated using Equation 4.

Finally, to calculate the per person annual footprint for someone affiliated with one of the smaller (larger) LHC experiments, the overall contribution from Table 3 is divided by the mean of total members listed on the public webpages of ALICE [23] and LHCb [24] (CMS [25] and ATLAS [26]) experiments. These values are listed in Table 4. The overlap of members between the four experiments is assumed to be negligible. The annual emission per person for smaller (larger) LHC experiments are estimated to be 8.76 $\mathrm{tCO_2e}$ (11.91 $\mathrm{tCO_2e}$).

	Experiment	Members	Mean	Emissions
Small	ALICE	1968 [23]	1684	8.76 $\mathrm{tCO_2e}$
	LHCb	1400 [24]		
Large	CMS	6288 [25]	6144	11.91 $\mathrm{tCO_2e}$
	ATLAS	6000 [26]		

Table 4: Total members affiliated to the four LHC experiments. The values in the *Mean* column is calculated independently for the two smaller and two larger LHC experiments. The *Emissions* column lists the per person annual emission for the smaller and larger LHC experiments. This is calculated by dividing the Overall emissions from Table 3 by the respective values in the *Mean* column.

3.2. DESY

The research centre *Deutsches Elektronensynchrotron* (DESY) in Hamburg, Germany, is the German national laboratory for accelerator development and operation, photon science, particle physics and astroparticle physics. Due to the presence of a significant accelerator and experimental complex,

emissions from DESY are used as proxy for emissions from smaller HEP experiments.

The first DESY sustainability report for 2019–2021 [27] has been published in 2022, but does not include detailed numbers on the emissions from scope 1, 2 or 3 sources as provided in the CERN environmental reports [18, 19, 20]. The DESY webpage, however, provides a figure on the energy consumption at DESY in 2021 [28] which is reproduced in Figure 1.

Electricity consumption in the year 2021 at DESY, excluding the electricity needed for the European XFEL, amount to 152.5 GWh. This includes: the accelerator complex with the accelerators: PETRA, FLASH, LINAC, HERA and DESY (55%), cryogenics (25%), as well as offices, workshops and laboratories, computing centre, cooling centre, canteen and others (20%). Subtracting the contribution from offices, workshops and laboratories, canteen and others as institute footprint, and the computing centre as computing footprint, which are treated separately in the Kyf calculator, the remaining experimental electricity consumption is 128.3 GWh for 2021, which is considered as representative for the annual consumption.

Two conversion factors for electricity consumption to CO_2 emissions are employed, based on data of Ref. [29]: The specific CO_2 emissions averaged over the German grid in 2023 correspond to 416 gCO_2e/kWh; emissions from green energy production assume 100 % photovoltaic (PV)-based electricity production with a footprint of 35 gCO_2e/kWh. Emissions from wind- (13 gCO_2e/kWh) and water- (11 gCO_2e/kWh) based production are lower, so 100 % PV-based production is considered to be a conservative estimate for green electricity production.

The number of guest scientists using the DESY facilities is listed as 3000 in the DESY environmental report [27], which is complemented by an additional 200 accelerator operators. The latter is based on an internal estimate by one accelerator operator, and is considered reasonable given the size of the DESY facilities. Refinements of these numbers are possible in a future version of the Kyf calculator.

Based on the above conversion factors and the number of scientists and operators, the total emissions from DESY are 53 372.8 tCO_2e (4490.5 tCO_2e) for conventional (green) electricity production, corresponding to 16.68 tCO_2e (1.40 tCO_2e) emissions per person per year, given a conventional (green) electricity supply. DESY itself switched to a green electricity contract at the start of 2023, significantly reducing its environmental footprint.

3.3. European Southern Observatory

Since 2020, the annual reports for ESO include a section on the environmental impact of the observatory [30, 31, 32]. In order to estimate the annual CO_2 emissions per person, only the emissions for 2021 were used to stay with the most up-to-date values. This, however, involves contributions from business travels, commute and waste, which do not fit well under this category and need to be subtracted. The breakdown for the various categories was extracted using `PlotDigitizer` [22] from the figure: *ESO* CO_2 *emissions 2018–2021*, on page 111 in ESO's annual report 2022 [32] and is shown in Table 5. The overall emission after correcting for the contributions from business travels, commute and waste is estimated to be 19 363 tCO_2e.

Category	**Emission**
Energy (E)	8599
Purchase (P)	5924
Freight (F)	2675
Travel (T)	191
Commuting (C)	1083
Capital Goods (CG)	2166
Waste (W)	127
Total	20 764
Corrected	19 363

Table 5: Breakdown of the total CO_2 emissions of ESO for 2021. The contribution of the various categories are extracted using `PlotDigitizer` [22] from the figure: *ESO* CO_2 *emissions 2018–2021*, on page 111 in ESO's annual report 2022 [32]. The corrected value is calculated as Corrected = Total − T − C − W. All emission values are provided in tCO_2e.

The public webpage of ESO lists more than 22 000 users of the observatory who share this overall emission [33]. The average annual emission per person is hence estimated as 19 363 $tCO_2e/22\,000$ = 0.88 tCO_2e.

More refined evaluation of individual ESO facilities and experiments would be very interesting for future versions of the Kyf calculator, if additional information becomes available.

4. Institute or research centre footprint

Institutes within universities or research centres, as key academic institutions, are an integral part of a researcher's environmental footprint. As benchmarks, the University of Freiburg, Leibniz University Hannover, and CERN are considered. The choice is based on the location of the universities in Germany, or CERN as central European HEP laboratory, and the publication of environmental reports by the institutions with sufficient information for a calculation.

In the Kyf calculator, the estimate from the University of Freiburg is used as proxy for a German university, the estimate for CERN is used as proxy for a research centre. Our analysis is based on the respective environmental reports, covering the years 2017–2019 for the Leibniz University Hannover, the years 2019–2020 for the University of Freiburg, and the years 2021–2022 for CERN. We base our estimate of the institutional footprint on one example year each (outside of the COVID-19 pandemic), and consider this to be representative for the annual footprint. Future assessments will test this assumption.

The carbon footprint of the institutions is assessed across several categories including electricity, heating/cooling, water, waste, and procurement. The section offers a detailed comparison between these entities, highlighting the diversity and scale of their emissions. Special attention is given to the significant role of procurement in contributing to the overall carbon footprint of universities and research centres.

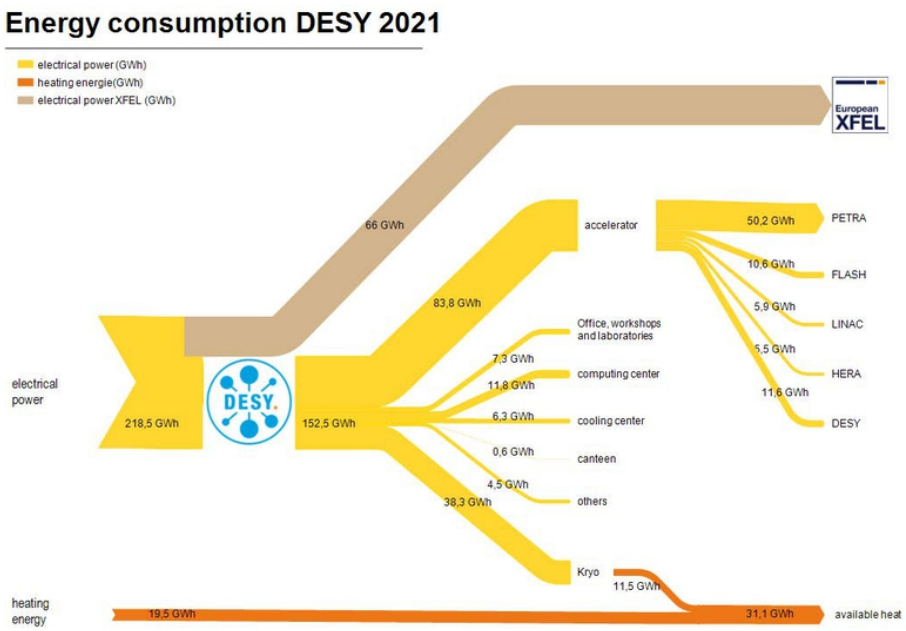

Figure 1: DESY energy consumption in 2021 [28]. Electrical power consumption (yellow) is split into consumption by the European XFEL (brown) and DESY (yellow). Heat consumption (orange) contains a contribution from heat recovery from cryogenics plants which is provided for heating and hot water supply to buildings on the DESY campus.

4.1. University of Freiburg

The environmental footprint for the University of Freiburg is based on the environmental report for 2019/2020 [34], published in 2021. The numbers for 2019 are used as the most recent, pre-pandemic numbers considered to be representative for the annual consumption of the university.

Emissions of the University of Freiburg are included for the categories: Electricity, heating/cooling, water, waste, and procurement. Numbers for vehicle fleet and business travel are provided as well, but are considered separately in the Kyf calculator and are therefore not listed here. The numbers provided for each of the used categories are reproduced in Table 6. Additional detail on the numbers for procurement can be found in Appendix B.

Category	**Emissions** [tCO_2e]
Electricity	2431 (19 224)
Heating/Cooling	13 584
Water	14
Waste	577
Procurement	14 486
Total	31 092 (47 885)

Table 6: Breakdown of the total CO_2 emissions of the University of Freiburg for 2019 [34], summing all categories except *Vehicle fleet + business travel* which is considered separately in the Kyf calculator. Electricity values are provided nominally using green electricity supply. The values in brackets provide the numbers using electricity produced with the German electricity mix. The conversions to tCO_2e are conducted by the University of Freiburg.

The total annual footprint of the University of Freiburg, excluding vehicle fleet and business travel which are considered separately in the Kyf calculator, is estimated as 31 092 tCO_2e (47 885 tCO_2e) using green electricity (the German electricity grid mix). The University of Freiburg obtains green electricity from certified water-power plants [34]. The largest individual contributor for the University of Freiburg, when considering green electricity supply, is procurement which corresponds to 87 % of the emissions from other categories (excl. vehicle fleet + business travel).

The environmental footprint of the University of Freiburg is distributed over the members of the university (students and employees) which are determined as 31 147 from the environmental report [34]. The institutional footprint per person per year therefore amounts to 1.00 tCO_2e (1.54 tCO_2e) using green electricity (the German electricity grid mix).

4.2. Leibniz University Hannover

The environmental footprint of the Leibniz University Hannover is estimated based on the environmental report for 2017–2019 [35], using numbers from 2019 for direct comparison to the numbers from the University of Freiburg in Section 4.1. Numbers for the Leibniz University Hannover, provided in the environmental report, largely specify the original consumption, hence the conversion to tCO_2e is performed in this study.

Emissions for the Leibniz University Hannover are provided for the categories: Electricity, Heating/Cooling, Water, and Waste. Numbers for procurement are not provided. While the total footprint is therefore not comparable to the one from the University of Freiburg, for the categories except procurement, the numbers from the Leibniz University Hannover provide an interesting cross-check.

Consumption numbers, as provided by the Leibniz University Hannover, conversion factors and CO_2 emissions

are listed in Table 7. The conversion factors for green (conventional) electricity are used as 35 gCO_2e/kWh (416 gCO_2e/kWh) [29] as in Section 3.2. The conversion factor of 98.7 $kgCO_2e/MWh$ [36] (including green house gas emissions other than CO_2) for heating is obtained from the energy provider *enercity* of the Leibniz University Hannover, which is specified to use district heating. The climate impact for water consumption assumes that the used water is drinking water, and the conversion factor of 0.35 gCO_2e/l is obtained from a study comparing the climate impact of bottled vs. tap water [37]. The total amount of waste in 2019, as well as the amount of toxic waste (*Sonderabfall*) in 2019, are read off from two figures contained in the environmental report 2017–2019 by the Leibniz University Hannover [35]. The conversion factors for the CO_2 emissions for waste are not provided in that report, however, in the environmental report by the University of Freiburg [34] sufficient information is provided to calculate conversion factors[2].

The total emissions for the Leibniz University Hannover are estimated to be 8001 tCO_2e (30 351 tCO_2e), with green (conventional) electricity production. Comparing only the equivalent categories, the emissions of 8001 tCO_2e in case of green electricity are in contrast with 16 606 tCO_2e for the University of Freiburg. The main difference results from the emissions for heating/cooling, where district heating for the Leibniz University Hannover generates significantly fewer emissions than the heating/cooling used at the University of Freiburg. In the latter case, the usage of ground water for cooling is specified, but no information on the type of heating by the University of Freiburg is provided.

The number of students at the Leibniz University Hannover is given in the environmental report 2017–2019 [35] as 29 781, and the number of employees as 4948, summing to 34 729 members of the Leibniz University Hannover. This results in emissions per person per year of 0.23 tCO_2e (0.87 tCO_2e) with green (conventional) electricity supply, with the caveat of not accounting for procurement.

Given the lack of information on procurement for the Leibniz University Hannover, the larger emissions for heating/cooling by the University of Freiburg and approximate similarity in the required other numbers, the values obtained for the University of Freiburg are used as conservative estimate for the institutional footprint of a university.

4.3. Research centre CERN

The environmental footprint for CERN as research centre is based on the values for 2022 (post-pandemic), listed in the newest environmental report for 2021–2022, published in 2023 [20].

The categories considered are similar to the ones for University of Freiburg and Leibniz University Hannover: *Electricity*, *Heating (gas+fuel)* and *Other (scope 1)*, *Water purification*, *Waste*, *Procurement*. A value for business travel is provided as well, but will be considered separately in the professional footprint of the Kyf calculator and is therefore dropped here. Values for catering and personal commutes are provided by the CERN environmental report, in addition; however, in the Kyf calculator, food, diet choices and commute are considered as part of the personal footprint, and are therefore removed from the institutional footprint to avoid double counting. The numbers for each of the employed categories are provided in Table 8.

Emissions for electricity correspond to 5 % of the total electricity-related emissions for 2022, which is specified in the CERN environmental report 2021–2022 [20] as electricity component required for powering the campus. Though not explicitly specified in the report, the effective conversion factor for electricity consumption to CO_2 emissions can be derived as 52 tCO_2e/GWh(= gCO_2e/kWh) from the total electricity consumption in 2022 of 1215 GWh, corresponding to emissions of 63 161 tCO_2e, specified for scope 2 in 2022. Electricity at CERN largely comes from low-carbon nuclear-power plants from France, resulting in a conversion factor significantly lower than the one from the conventional German grid mixture, but still slightly larger than electricity based on renewables, discussed in Section 3.2. The numbers for *Heating (gas+fuel) and Other* (scope 1) are obtained from the total scope-1 emissions minus emissions for *LHC experiments: Particle detection* and *LHC experiments: Detector cooling* as well as *Other experiments*, where the LHC-related emissions are considered as part of the experimental contribution, discussed in Section 3.1. The value for the sum of the LHC and non-LHC experimental contributions has been obtained using `PlotDigitizer` [22] (also see Appendix A). Additional detail on the composition of the procurement category are given in Appendix B.

The total emissions for CERN as a research centre in 2022 sum to 121 433 tCO_2e (16 459 tCO_2e) including (excluding) procurement. They are dominated by the footprint of procurement, followed by heating (gas+fuel), where heating reaches a similar level as for the University of Freiburg. A split up of the emissions from procurement is provided by the CERN environmental report 2021–2022 [20], and discussed further in Appendix B. It is important to note that the emissions from procurement at CERN do not only cover those related to CERN as an institute, but also those related to the experiments, accelerator facilities, as well as future accelerator developments. Some procurement categories such as *Civil engineering, building and technical services* appear more related to the infrastructure of the accelerator and experimental complex; different categories such as *Other* that includes office supplies, furniture, etc. seem more related to CERN as an institute. A clear separation of the procurement categories belonging to CERN as an institute is however not possible. In the future, improved assignment can be done if more granular information becomes available. For the moment, procurement is fully assigned to the CERN institute footprint.

Emissions from electricity and waste play a smaller role in

[2] For the University of Freiburg, 88 t of toxic waste are specified to correspond to 24 % of the total amount of emissions from waste, which are given as 577 tCO_2e. This results in a conversion factor of 1.57 tCO_2e/t for toxic waste. The remaining 1019 t of waste for the University of Freiburg are specified to generate 76 % of the emissions, resulting in a conversion factor of 0.43 tCO_2e/t for other waste. These conversion factors are transferred to the waste of the Leibniz University Hannover, assuming implicitly a similar waste composition within the two categories and a similar treatment by the two universities.

Category	Consumption	Conversion factor	Emissions [tCO_2e]
Electricity	58.66 GWh	35 gCO_2e/kWh (416 gCO_2e/kWh) [29]	2053 (24 403)
Heating/Cooling	50.01 GWh	98.7 $kgCO_2e$/MWh [36]	4936
Water	696 000 m^3	0.35 g/l [37]	244
Waste	1620 t		
... Toxic waste	63 t	1.57 tCO_2e/t [34]	99
... Other waste	1557 t	0.43 tCO_2e/t [34]	670
Total			8001 (30 351)

Table 7: Breakdown of the total CO_2 emissions of the Leibniz University Hannover. Consumption values are taken from the environmental report 2017–2019 [35]. Electricity values are provided nominally using green electricity supply. The values in brackets provide the numbers using electricity produced with the German electricity mix. Sources for the conversion factors are indicated, and further explained in the text. Note that the sums are calculated with more decimal places than indicated, resulting in small differences to the sums of the listed values.

Category	Emissions [tCO_2e]
Electricity	3158
Heating (gas+fuel) + Other	11 250
Water purification	176
Waste	1875
Procurement	104 974
Total	121 433
Total without Procurement	16 459

Table 8: Breakdown of the total CO_2 emissions of CERN as research institute for 2022 [20]. The categories Business travel and Personnel commutes are considered separately in the Kyf calculator, and thus not listed here. The conversions to tCO_2e are conducted by CERN.

the carbon footprint of CERN as an institute. Differences in the electricity consumption to the university footprints can be primarily attributed to different conversion factors for the type of used electricity. The electricity consumption of the CERN campus in GWh is comparable to that of the University of Freiburg and the Leibniz University Hannover[3].

The evaluation of an *effective CERN population* needs to consider that at any time during the year, a certain fraction of CERN users is present at CERN, using electricity, water, heating, etc. and thus contributing to the institutional footprint. The total number of CERN personnel employed by CERN (Employed Members of Personnel - MPE) in 2022 amounts to $N_{\mathrm{MPE}} = 3558$ [38], including staff and CERN fellows. The total number of Associated Members of Personnel (MPA), including CERN users as largest subcategory, corresponds to $N_{\mathrm{MPA}} = 13\,376$ in 2022 [38]. The average presence for MPAs at CERN is evaluated as a weighted average of the *Yearly Presence* of CERN users at CERN, using the midpoint of the percentage bins in Table 11 of Ref. [38] for weighting. This results in an average presence $\bar{p} = 27.9\,\%$ for MPAs at CERN. The effective CERN population, N_{eff}, is thus calculated as:

$$N_{\mathrm{eff}} = N_{\mathrm{MPE}} + \bar{p} \cdot N_{\mathrm{MPA}} \,,$$

and, numerically, determined to be $N_{\mathrm{eff}} = 7295$.

The institutional footprint per person per year for CERN as research institute is estimated to be 16.65 tCO_2e (2.26 tCO_2e) including (excluding) procurement. This is, also excluding procurement, larger than the institute footprint of the University of Freiburg, discussed in Section 4.1. Given the larger experimental facilities at the research centre, higher per-researcher emissions at a research centre compared to a university are expected. The impact of procurement at CERN as an institute is artificially increased, since it also includes contributions relevant to the experiments, accelerators and future developments, which cannot be separated at the moment. The estimate of emissions from procurement at CERN are based on the Greenhouse Gas Protocol spend-based method, which – though already rather advanced – is acknowledged in the CERN environmental report 2021-2022 [20] to have limitations and variable degrees of uncertainty. CERN started the *Environmentally Responsible Procurement Policy Project (CERP3)* in September 2021, to improve the environmental impact of procurement in the future.

5. Computing footprint

Most of research in physical sciences today relies on having High Performance Computing (HPC) Clusters to enable breakthroughs and make advancements within the various sub-fields of physics. Hence, it is essential to consider the environmental impact of such computing clusters. Sustainable research and accelerating scientific progress is very much dependent on rise of awareness of our resource usage [39].

Typical HPC usage involves researchers submitting jobs to computational clusters via a scheduler or interactively. For each job, specific requirements are defined, including the number of CPU-cores or GPUs [4] needed and a defined time window for execution. For a carbon footprint, average idle times as well as

[3] The electricity consumption for the CERN campus is 5 % of 1215 GWh in 2022, corresponding to 60.75 GWh vs. about 50 GWh for the University of Freiburg and 58.66 GWh for the Leibniz University Hannover

[4] We do not detail GPU power consumption by individual CUDA cores [40] for two main reasons: the standard power specification of 250W for a PCIe A100 GPU offers a reliable estimate, and the real-world application of GPUs does not involve partitioning by CUDA cores, rendering such a breakdown impractical here.

surplus-power, e.g. due to HPC cooling, need to be considered as well.

The carbon footprint averaged over a year is thus estimated as:

$$\text{Total Footprint [tCO}_2\text{e]} = f_{\text{PUE}} \cdot f_{\text{overh}} \cdot n_{\text{WPC}} \cdot f_{\text{conv}}\,, \quad (5)$$

where f_{PUE} denotes the HPC's *Power Usage Effectiveness* (PUE) [41], f_{overh} is an overhead factor to account for power consumption of the HPC when its computing cores are idle[5], n_{WPC} accounts for the *Workload Power Consumption* (WPC), and f_{conv} is the conversion factor from kWh to gCO_2e.

The yearly WPC is estimated taking into account the usage of CPUs and GPUs separately as:

$$n_{\text{WPC}} = p_{\text{CPU-core}} \cdot l_{\text{core-h, CPU}} + p_{\text{GPU}} \cdot l_{\text{h, GPU}}\,, \quad (6)$$

where $p_{\text{CPU-core}}$ is the power consumption in kW for each CPU core and $l_{\text{core-h, CPU}}$ is the CPU workload measured in core hours. GPU usage is calculated with p_{GPU} representing the power consumption in kW per GPU and $l_{\text{h, GPU}}$ is the total number of hours the GPU is used for.

For the Kyf calculator, the following values are used as default values for an individual researcher's computing footprint. For f_{PUE}, a value of 1.5 has been chosen, which is listed in the CERN environmental report 2021–2022 [20] as global average PUE for large data centres, and which has been declared as the target to be reached by 1 July 2027 for computing centres starting operations before 1 July 2026 in the German law for the improvement of energy efficiency (*Energieeffizienzgesetz* - EnEfG, §11(1)) [42]. The idle-time overhead factor f_{overh} has been estimated by comparing the system power consumption of the *Hawk* supercomputer at the HPC Stuttgart [43] at full load (LinPack operation) (4.1 MW) to normal operation (3.5 MW). The resulting factor of 1.17 is used as default idle-time overhead factor. As conversion factor f_{conv}, the same values as discussed in Section 3.2 are employed, based on Ref. [29]: 416 $\text{gCO}_2\text{e/kWh}$ (35 $\text{gCO}_2\text{e/kWh}$) for a conventional (green) electricity provision at the HPC. Finally, 7.25 W is the default value set for the CPU power consumption per core along with a default power consumption of 250 W per GPU. The CPU value is obtained from the DESY Maxwell cluster with AMD EPYC 75F3 CPU cores [44]. The GPU value is the median of a range, 150–350 W, reported on a forum of NVIDIA GPU users [45]. Both these systems are fairly recent, so the power usages should be representative of newer HPC processing units. The usage load in core-hours for CPU and GPU usage, $l_{\text{core-h, CPU}}$ and $l_{\text{h, GPU}}$, needs to be provided by the researcher when using the Kyf calculator.

The computing footprint estimate can be further personalised by adjusting f_{PUE}, if calculations have been done, for example, at the very new CERN computing centre which targets a PUE value of 1.1 [20], or by changing f_{overh} to a different value, if better or worse HPC load factors have been obtained. It can also be switched to green electricity, with conventional electricity being used as default.

In recent years, HPC centres have been implementing system-generated reports that inform their users about their usage with high transparency. Resources like the *Production and Distributed Analysis* (PanDA) client [46] or API [47] can also be used by users or software developers to monitor group or individual workload on a system. If the annual carbon footprint is thus known precisely, this can also be entered directly in tCO_2e.

For convenience, four scenarios discussed in the following are provided, based on the estimated usage level: low, medium, high and extremely high. Several factors come into play when deciding whether to utilise a CPU or a GPU for a particular computational task. These factors include the availability of suitable software and libraries, memory requirements, considerations related to parallelisation, as well as potential bottlenecks in data transfer rates. As a result, simulations and analyses are tailored to the specific needs and research objectives of individual researchers. The provided examples thus serve as rough approximations only, and CPU vs. GPU usage cannot necessarily be interchanged easily.

- Case for low usage

  Example: A graduate student submits several jobs per week each needing between one to four CPU cores. The consumption corresponds to an an average of 4000 CPU core-h used per month resulting in an annual footprint as follows:

$$\begin{aligned}\text{Footprint} &= 1.5 \times 1.17 \times 0.007\,25\,\text{kW} \\ &\quad \times 12 \times 4000\,\text{CPU core-h/month} \\ &\quad \times 416\,\text{gCO}_2\text{e/kWh} \\ &\quad = 0.25\,\text{tCO}_2\text{e}\end{aligned}$$

- Case for medium usage

  Example: A doctoral student or post-doctoral researcher, involved in data analysis 70-100% of their time, submits jobs over the year. For this case, the top five ranked users at the Uni-Freiburg HPC called the Black-Forest Grid (BFG) are used as a blueprint, giving 30 000 CPUcore-h per month. The resulting annual footprint is as follows:

$$\begin{aligned}\text{Footprint} &= 1.5 \times 1.17 \times 0.007\,25\,\text{kW} \\ &\quad \times 12 \times 30\,000\,\text{CPU core-h/month} \\ &\quad \times 416\,\text{gCO}_2\text{e/kWh} \\ &\quad = 1.91\,\text{tCO}_2\text{e}\end{aligned}$$

- Case for high usage

  Example: An accelerator scientist studies accelerator performance with particle tracking codes and semi particle-in-cell (PIC) codes. The studies are both memory and computationally demanding. We assume 2500 GPU h

[5] Generally, an HPC has to estimate the number of cores it operates by predicting the requirements by its users. If too few cores are operated, it leads to long waiting times for jobs to start, but no idle operation time. It too many cores are available, idle times become too large. HPCs will thus aim for a small fraction of idle time, which needs to be considered in the carbon footprint.

used per month with code optimised for GPUs (equivalent to 80 000 CPU core-h per month).

$$\begin{aligned}\text{Footprint} &= 1.5 \times 1.17 \times 0.25\,\text{kW} \\ &\quad \times 12 \times 2500\,\text{GPU h/month} \\ &\quad \times 416\,\text{gCO}_2\text{e/kWh} \\ &= 5.48\,\text{tCO}_2\text{e}\end{aligned}$$

- Case for extremely high usage

  Example: A researcher runs PIC simulations or high-resolution imaging analysis. This corresponds to a usage of 8000 GPU h per month (equivalent to 300 000 core-h per month on CPUs).

$$\begin{aligned}\text{Footprint} &= 1.5 \times 1.17 \times 0.25\,\text{kW} \\ &\quad \times 12 \times 8000\,\text{GPU h/month} \\ &\quad \times 416\,\text{gCO}_2\text{e/kWh} \\ &= 17.52\,\text{tCO}_2\text{e}\end{aligned}$$

It is important to acknowledge that the calculations presented here are based on the assumption of optimal core utilisation in HPCs. In practice, however, it is often the case that not all cores are used efficiently, leading to unnecessary energy consumption.

The environmental costs associated with data centres for long-term storage require significant amounts of electricity and water to operate servers and cooling systems. The large scale resources used by experimental collaborations or at institutes are assumed to be accounted for within their respective categories. Within the individual computing footprint, the environmental contribution of data storage is assumed to be small compared to that of actively running jobs and is therefore neglected. If we obtain data that such costs for an individual are high, we will include this contribution in future iterations. If significant amounts of data are stored at a location other than the institute, such as on a commercial cloud, e.g. Microsoft OneDrive [48] or Google Drive [49], an additional CO_2 emission contribution can however be added, based e.g. on the Microsoft emissions impact dashboard [50], or the Google's Carbon Footprint app [51].

6. Business travel footprint

Travel constitutes another crucial component of High Energy Physics (HEP). The importance of in-person events became notably evident during the COVID-19 pandemic, where their absence made discussions and collaborations more challenging, prompting a reconsideration of our methodologies. In light of this realisation, a meticulous assessment of travel-associated CO_2 emissions is imperative. Business travel, including transportation and accommodations, significantly contributes to CO_2 footprints. Efforts to comprehend and mitigate these emissions involve scrutinising various transportation modes, such as long-distance buses, trains, personal cars, and air travel, each exerting diverse impacts on our environmental footprint [11, 52]. Comparison of CO_2 emissions from various modes of transport are briefly discussed in Appendix C. Additionally, the emissions from factors such as accommodation and event venues play a role, emphasising the need to evaluate the average CO_2 emissions of hotel rooms per night and event venues per day for an individual [53]. Benchmark values used for the Kyf calculator are documented in Table 9. These values are estimated using travel, hotel stay and meeting room usage scenarios in Germany. The footprint corresponding to the event venue assumes an area of 4 m^2 per person.

Source of Emission	**Emission Factor**	
Long-distance Buses	0.031	$kgCO_2e/km$
Long-distance Trains	0.031	$kgCO_2e/km$
Personal Car	0.17	$kgCO_2e/km$
Flights within Europe	130	$kgCO_2e/h$
Transcontinental Flights	170	$kgCO_2e/h$
Hotel room	12	$kgCO_2e/night$
Event venue	0.19	$kgCO_2e/day$

Table 9: List of dominant contributors to the CO_2 footprint of a business trip with the respective CO_2-equivalent emission value for an average individual in the German scenario.

It is important to note that some institutes, such as the University of Freiburg, compensate for all flights taken by its employees for business trips. The Kyf calculator provides an option for showing the amount of carbon footprint, which was compensated. This might be extended to other sections of the Kyf calculator in future iterations.

Using the values from Table 9, it is possible to obtain a rudimentary estimate for a business trip. Three benchmark scenarios are presented here.

6.1. Train travel within Europe

For someone in Freiburg attending a conference in Hamburg lasting 5 days and travelling by long-distance trains, the total CO_2 emissions are a sum of the following three contributions:

- Travel: Given a one-way distance of 800 km, the footprint for the travel with long-distance trains (both ways) is:

$$\begin{aligned}\text{Footprint (travel)} &= 2 \times 800\,\text{km} \times 0.031\,\text{kgCO}_2\text{e/km} \\ &= 49.6\,\text{kgCO}_2\text{e}\,.\end{aligned}$$

- Hotel: For a conference from Monday to Friday, a hotel reservation of 5 nights with check-in on Sunday and check-out on Friday is assumed. The footprint for the hotel room is:

$$\begin{aligned}\text{Footprint (hotel)} &= 5\,\text{nights} \\ &\quad \times 12\,\text{kgCO}_2\text{e/night} \\ &= 60\,\text{kgCO}_2\text{e}\,.\end{aligned}$$

- Venue: Assuming that the conference venue is occupied for 8 hours on all 5 days of the conference, the footprint

for the event venue is:

$$\begin{aligned}\text{Footprint (venue)} &= 5\,\text{days} \times 0.19\,\text{kgCO}_2\text{e/day} \\ &= 0.95\,\text{kgCO}_2\text{e}\,.\end{aligned}$$

The total CO_2 emission for this benchmark scenario is given by the sum of the three contributions:

$$\begin{aligned}\text{Total Footprint} &= \text{Footprint(travel + hotel + venue)} \\ &= 49.6\,\text{kgCO}_2\text{e} + 60\,\text{kgCO}_2\text{e} + 0.95\,\text{kgCO}_2\text{e} \\ &\approx 111\,\text{kgCO}_2\text{e}\,.\end{aligned}$$

6.2. Flight travel within Europe

Considering the same scenario as in the previous benchmark, but changing the mode of transport from train to flight, which requires 1.5 hours for the same distance of 800 km one way, the travel contribution increases to:

$$\begin{aligned}\text{Footprint (travel)} &= 2 \times 1.5\,\text{h} \times 130\,\text{kgCO}_2\text{e/h} \\ &= 390\,\text{kgCO}_2\text{e}\,.\end{aligned}$$

The change to flight as transport mode therefore yields a travel footprint that is 5.4 times larger compared to travel by train. The total footprint for the entire business trip in this case is estimated as:

$$\begin{aligned}\text{Total Footprint} &= 390\,\text{kgCO}_2\text{e} + 60\,\text{kgCO}_2\text{e} \\ &\quad + 0.95\,\text{kgCO}_2\text{e} \\ &\approx 451\,\text{kgCO}_2\text{e}\,.\end{aligned}$$

To consider an example where travelling by train would not be considered practical, another scenario for a person based in Freiburg attending a conference lasting 5 days in Thessaloniki, Greece is considered. A direct flight from Basel to Thessaloniki takes about 2.5 hours for one way. This results in a travel contribution of:

$$\begin{aligned}\text{Footprint (travel)} &= 2 \times 2.5\,\text{h} \times 130\,\text{kgCO}_2\text{e/h} \\ &= 650\,\text{kgCO}_2\text{e}\,.\end{aligned}$$

Taking the same contributions for hotel and venue calculated in Section 6.1, the total footprint for the entire business trip in this case is estimated as:

$$\begin{aligned}\text{Total Footprint} &= 650\,\text{kgCO}_2\text{e} + 60\,\text{kgCO}_2\text{e} \\ &\quad + 0.95\,\text{kgCO}_2\text{e} \\ &\approx 711\,\text{kgCO}_2\text{e}\,.\end{aligned}$$

6.3. Flight travel across continents

This benchmark scenario considers a person travelling to Seoul (South Korea) from Freiburg for a summer school lasting 2 weeks. As in the previous benchmark scenarios, the three contributions are estimated as follows:

- Travel: A one-way travel requires a long-distance train from Freiburg to Frankfurt (275 km) followed by an transcontinental flight from Frankfurt to Seoul (12 hours). The footprint of the return trip is estimated as:

$$\begin{aligned}\text{Footprint (travel)} &= 2 \times (275\,\text{km} \times 0.031\,\text{kgCO}_2\text{e/km} \\ &\quad + 12\,\text{h} \times 170\,\text{kgCO}_2\text{e/h}) \\ &= 4097\,\text{kgCO}_2\text{e}\,.\end{aligned}$$

- Hotel: For a summer school lasting 2 weeks, a Hotel reservation of 14 nights is assumed. The footprint for the hotel room is:

$$\begin{aligned}\text{Footprint (hotel)} &= 14\,\text{nights} \\ &\quad \times 12\,\text{kgCO}_2\text{e/night} \\ &= 168\,\text{kgCO}_2\text{e}\,.\end{aligned}$$

- Venue: Assuming that the conference venue is occupied for 8 hours on all 10 business days of the summer school, the footprint for the event venue is:

$$\begin{aligned}\text{Footprint (venue)} &= 10\,\text{days} \times 0.19\,\text{kgCO}_2\text{e/day} \\ &= 1.9\,\text{kgCO}_2\text{e}\,.\end{aligned}$$

The total footprint for the entire trip is estimated as:

$$\begin{aligned}\text{Total Footprint} &= 4097\,\text{kgCO}_2\text{e} + 168\,\text{kgCO}_2\text{e} \\ &\quad + 1.9\,\text{kgCO}_2\text{e} \\ &\approx 4267\,\text{kgCO}_2\text{e}\,.\end{aligned}$$

The duration of this trip is extended from the typical 5 day duration observed in other scenarios to recognise that longer-distance trips often require more justification to be funded, e.g. longer educational programs. It must be noted however, that the footprint of hotel stay and event venue remains small compared to that of the travel itself. This implies that the carbon footprint of a shorter trip would be similar as long as the footprint of the flight travel is not compensated. Note that hotel and venue footprints are based on German numbers and are assumed to be valid in the international context as well. This assumption might be refined in a future version of the Kyf calculator.

7. Professional footprint example

An example professional footprint of an early-career researcher in Germany is calculated for a benchmark doctoral student working on one of the large LHC experiments at CERN, being employed by a university in Germany, which is supplied with conventional electricity, medium computing level, where the HPC also uses conventional electricity, and who does two 1-week trips in Germany by train (for example, a DPG spring meeting and a national collaboration meeting), one flight travel within Europe for a week (for example, a conference in Thessaloniki, Greece), and one two-week flight travel across continents (for example, a summer school in Seoul, South Korea) during one particular year. The combined professional footprint

is listed in Table 10, and shown in Figure 2, in comparison with the personal footprint and the remaining carbon budget per person per year, given the climate warming limitation goals discussed in Section 1.

Category	**Emissions** [tCO_2e]
Large LHC experiment	11.91
University (German electricity mix)	1.54
Computing (medium)	1.91
Travel (2xT, 1xF(E), 1xF(C))	5.20
Total	20.56

Table 10: Professional CO_2 footprint of a benchmark doctoral researcher, working on one of the large LHC experiments, employed by a German university, with medium computing usage level and two intra-Germany travels by train (T), one intra-Europe flight travel (F(E)) and one cross-continental flight travel (F(C)) per year.

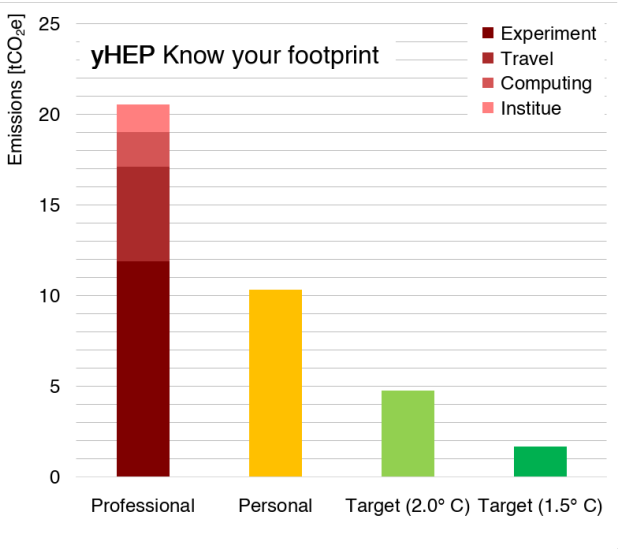

Figure 2: Professional CO_2 footprint of a benchmark doctoral researcher, working on one of the large LHC experiments, employed by a German university, with medium computing usage level and travel as discussed in the text, in comparison with the average personal footprint in Germany, as well as the remaining carbon budget per person per year of 1.7 tCO_2e (4.8 tCO_2e) for a maximum temperature increase of 1.5 °C (2.0 °C).

The annual professional footprint of the benchmark doctoral researcher amounts to 20.56 tCO_2e, which can be compared to the average private footprint of 10–11 tCO_2e per person per year in Germany [8, 9, 11]. The professional footprint is clearly dominated by work in a large LHC experiment, followed by travel. Work on a smaller HEP experiment using a green electricity supply or an astronomy experiment would have resulted in a smaller experimental footprint, leaving the travel footprint dominant. Several cross-continental business travels per year also would result in a significantly larger travel footprint, turning it into the leading contribution. A high or extremely high usage computing level would significantly increase the computing footprint, making it instead the leading contribution. Similarly, employment at a research centre with larger laboratory facilities could result in the institutional footprint becoming dominant.

For the benchmark doctoral researcher and several other scenarios, the professional footprint thus exceeds the personal footprint, both of which by far exceed the remaining carbon budget per person per year of 1.7 tCO_2e (4.8 tCO_2e) for a maximum temperature increase of 1.5 °C (2.0 °C), as discussed in Section 1 and displayed in Figure 2. It is therefore crucial, that not only personal consumption patterns, including the societal boundaries and incentives, are adjusted, but that also the way research is performed is transformed towards a more sustainable and environmentally friendly practice. The Kyf calculator provides a first idea for an individual researcher where these transformations have to happen first and most urgently, such that the biggest and easiest contributions are addressed first, immediately followed by tackling the more challenging ones. Environmental reports by universities, research centres, experiments, computing centres, etc. provide key information for this purpose, and should become mandatory as soon as possible, followed by action (plans) for the reduction of the carbon footprint. It is clear that changes towards a more sustainable research practice require resources, both financially and personnel-wise. This fact needs to be considered by funding agencies in their future decision-making. The costs for inaction will eventually be higher than those for coordinated and targeted action now.

8. Conclusions

Know your footprint is an essential early step in tackling climate change and for motivating sustainable behaviour. This holds both in the personal as well as in professional life.

In an energy-hungry sector, such as High Energy Physics (HEP) and related fields, awareness is key to start moving towards a more sustainable research practice. The *young High Energy Physicists* (yHEP) association launched the *Know your footprint* (Kyf) campaign to evaluate the CO_2-equivalent emissions generated by HEP-related research.

In the four categories: *Experiments*, *Institutes*, *Computing* and *Travel*, we have evaluated the carbon footprint of research activities. A user-oriented tool is provided [10] to allow for the simple evaluation of the professional footprint of an individual researcher in, or associated to, Germany. The results show that for various combinations, the professional footprint significantly exceeds the personal footprint of an average citizen in Germany, which already exceeds the maximal remaining carbon budget per person per year, allowed for a maximum temperature increase of 1.5 °C (2.0 °C), by factors of around 6 (around 2). Targeted and prompt action is therefore essential. Every gram of CO_2 saved makes a difference.

While it is encouraging to see a growing awareness among individuals and institutions of their carbon footprint, our study shows that significant work in the HEP-related research lies before us. Given that the next 10–20 years will be crucial to mitigate global warming, this work needs to start now. Carbon-footprint accounting provides us with the data to shape strategies and target measures in order to effectively reduce our carbon footprint. Scientific research, starting now, needs

to ensure that our pursuit of scientific and technological progress aligns harmoniously with a strong commitment to environmental sustainability.

Acknowledgements

Our warm thanks go to Ruth Jacobs, Srijan Sehgal, and Dima El Khechen from the yHEP management board for their constructive input on this paper and to Michael Lupberger from the yHEP management board on his feedback to the Kyf calculator. Many thanks also go to further current and former yHEP management board members for their support and constructive input to the Kyf campaign efforts: Farah Afzal, Leonel Morejon, Meike Küßner, Felipe Peña, Philipp Krönert, Alina Nasr-Esfahani, Annika Thiel. Additionally, we would like to express our gratitude for feedback on the paper and the calculator to the following colleagues: Lutz Feld (for the committee for particle physics (KET) in Germany), Uli Katz (for the committee for astro-particle physics (KAT) in Germany), Michael Block (for the committee for physics of nucleons and hadrons (KHuK) in Germany), Eric Bründermann (for the committee for accelerator physics (KfB) in Germany), Denise Völker (as head of the DESY Sustainability group), Sonja Kleiner and Luisa Ulrici (as leaders of the CERN Environment group), Frank Schlünzen (for computing inputs), and Maria Zeitz (from KlimAktiv). We thank KlimAktiv especially for the permission to reference and forward to the UBA carbon calculator for the private footprint. The authors of this paper take responsibility for any errors in this paper.

Appendix A. Digitisation of CERN scope 1 emissions

Numbers from the digitisation of the figure: *CERN scope 1 emissions for 2017–2022 by category*, from page 18 of the CERN environmental report 2021–2022 [20], reproduced in Figure A.3, can be found in Table A.11. The total scope 1 emissions from 2022 determined with `PlotDigitizer` [22] agree within 0.05 % with the numerical value for the total 2022 scope 1 emissions stated in the environmental report. Given resolution precision, this is considered sufficiently close.

Appendix B. Emissions from procurement

Procurement is a major source of emissions, in particular for organisations such as a university, whose core functionalities: research, teaching and knowledge transfer, can be assigned to the services sector.

The procurement-related emissions by the University of Freiburg, discussed in Section 4.1 and obtained from the environmental report 2019/2020 [34], are based on procurement data from 2017, analysed in a master thesis [54], which is unfortunately not available online. A subsequent report is accessible in Ref. [55], for which the relevant figure has been reproduced. Figure B.4 displays the scope 3 procurement distribution of the categories *Goods and services* and *Capital goods*, contained in Ref. [55]. The combined emissions listed as 15 100 tCO_2e do

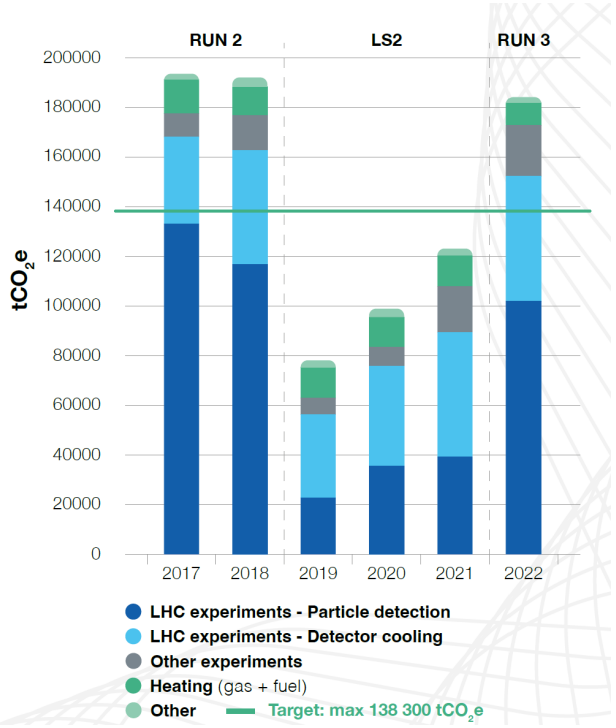

Figure A.3: CERN scope 1 emissions for 2017–2022 by category [20]. The category *Other* includes air conditioning, electrical insulation, emergency generators and the fuel consumption of the CERN vehicle fleet.

not exactly equal the value of 14 486 tCO_2e, quoted in the environmental report 2019/2020 by the University of Freiburg [34], but are very close. The displayed split-up can therefore be seen as representative of the value, quoted in the environmental report 2019/2020.

Largest contributors to the emissions from procurement are the categories: *Chemicals* (3700 tCO_2e), *Medical & Precision Instruments* (3000 tCO_2e), *Furniture & Goods n.e.c.* (1700 tCO_2e), and *Machinery n.e.c.* (1200 tCO_2e), which amount to about 64 % of the procurement-related emissions.

The large number of categories gives an idea of how difficult it is to address the reduction of procurement-related emissions; due to its large overall contribution, it remains critical though. Two approaches are possible for this purpose: demand management by the university, and *green* procurement. The choice of the best approach might differ depending on the category.

Details on procurement-related emissions by CERN are provided in the environmental report 2021–2022 [20]. The figure *Emissions by procurement family 2021–2022* from page 23 of the CERN environmental report 2021–2022 [20] is reproduced in Figure B.5.

The largest contributors to procurement-related emissions in 2022 are the following categories: *Civil engineering, building and technical services*, *Permanent services on the CERN site*, and *Mechanical engineering and raw materials*. These could be related to construction regarding buildings or machinery, which can be seen either as part of the infrastructure of the accelerator complex, usual construction and maintenance of buildings of an organisation, or engineering work, which could also be

Category	Cumulative emissions [tCO_2e]
LHC experiments: Particle detection	101 981
LHC experiments: Detector cooling	152 444
Other experiments	172 923
Heating (gas+fuel)	181 857
Other	184 090
Total (specified in the report)	184 173

Table A.11: Digitised values for 2022 of the CERN scope 1 emissions, extracted with `PlotDigitizer` [22] from Figure A.3. The values correspond to the upper edge of the bar including the specified category. The value for *Other* should therefore correspond to the total scope 1 emissions value specified in the CERN environmental report 2021–2022 [20], listed under *Total (specified in the report)*, which - given resolution precision - is sufficiently close.

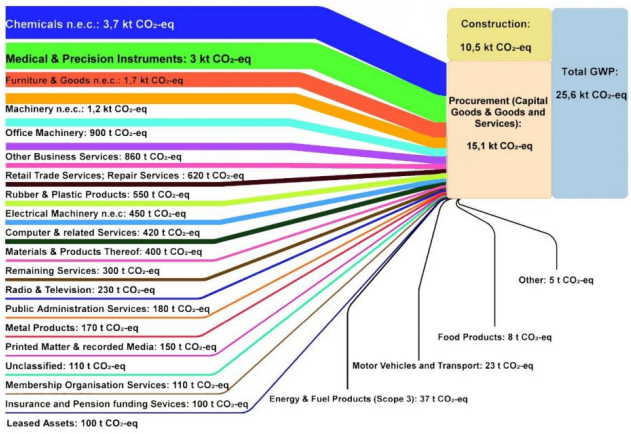

Figure B.4: Distribution of scope 3 greenhouse gas emissions of the two categories *Goods and services* and *Capital goods* for the University of Freiburg in 2017 [55]. *Construction* is listed as separate scope 3 category for comparison, but it is unclear which category in the environmental report 2019/2020 [34] this has been added to.

performed at a university. It is not possible to explicitly assign the procurement categories to the footprints of accelerators, experiments, upgrade activities, or CERN as an institute.

A direct comparison of the procurement categories to those of the University of Freiburg is not possible.

Appendix C. Emissions for various transportation modes

The German Federal Environtment Agency (*Umweltbundesamt* - UBA) provides a comparison of CO_2 emissions for various modes of transport per person per kilometre in a table on their webpage [52]. This table represents the data collected for 2022 and is reproduced in Table C.12. For the calculation of the average emission values, an average occupancy is also estimated to obtain a comparable value for an individual across all modes of transport.

For the first version of the Kyf calculator, only long-distance trains (*Eisenbahn, Fernverkehr*), long-distance buses (*Linienbus, Fernverkehr*) and personal car (*Pkw*) were considered. The CO_2 emissions for intra-Europe and transcontinental flights were obtained from Ref. [11] in order to have the emission values corresponding to the duration of the flight rather than the distance covered by it. This was considered to be more user-friendly for the Kyf calculator. Other modes of transportation listed in Table C.12 are primarily relevant for short-distance commute and were therefore not incorporated in the first version of the Kyf calculator. These could potentially be included in future iterations.

References

[1] S. Arrhenius, *XXXI. On the influence of carbonic acid in the air upon the temperature of the ground*, The London, Edinburgh, and Dublin Philosophical Magazine and Journal of Science 41 (251) (1896) 237–276. doi:10.1080/14786449608620846.
URL https://doi.org/10.1080/14786449608620846

[2] UC San Diego and SCRIPPS Institution of Oceanography, *The Keeling Curve - Full Record*, accessed: 2023-10-22 (2023).
URL https://keelingcurve.ucsd.edu

[3] D. Lüthi, M. Le Floch, B. Bereiter, et al., *High-resolution carbon dioxide concentration record 650,000–800,000 years before present*, Nature 453 (2008) 379–382. doi:https://doi.org/10.1038/nature06949.

[4] Copernicus Climate Change Service/ECMWF, *Surface air temperature for December 2023*, accessed: 2024-02-09 (2023).
URL https://climate.copernicus.eu/surface-air-temperature-december-2023

[5] Intergovernmental Panel on Climate Change (IPCC), Climate Change 2021 – The Physical Science Basis: Working Group I Contribution to the Sixth Assessment Report of the Intergovernmental Panel on Climate Change, Cambridge University Press, 2023, Ch. *Summary for Policymakers*, pp. 3–32. doi:10.1017/9781009157896.001.

[6] United Nations, *Paris Agreement*, United Nations Treaty Series 3156 (2015) 79.
URL https://treaties.un.org/doc/Treaties/2016/02/20160215%2006-03%20PM/Ch_XXVII-7-d.pdf

[7] United Nations, *Global issues: Population*, accessed: 2023-10-22 (2023).
URL https://www.un.org/en/global-issues/population

[8] K. Schächtele, H. Hertle, *Die CO_2 Bilanz des Bürgers - Recherche für ein internetbasiertes Tool zur Erstellung persönlicher CO2 Bilanzen*, Umweltbundesamt Förderkennzeichen: 206 42 110 (2007).
URL https://www.umweltbundesamt.de/sites/default/files/medien/publikation/long/3327.pdf

[9] S. Schunkert, J. Siewert, P. Pitz, et al., *Der UBA-CO_2-Rechner für Privatpersonen - Hintergrundinformationen*, Umweltbundesamt Forschungskennzahl: 3718 16 313 0 (2022).
URL https://www.umweltbundesamt.de/sites/default/files/medien/479/publikationen/texte_97-2022_der_uba-co2-rechner_fuer_privatpersonen.pdf

[10] young High Energy Physicists Association (yHEP), *Know your footprint*, accessed: December 2023.
URL https://yhep.desy.de/sustainability/

[11] Umweltbundesamt, *Carbon Calculator*, accessed: 2023-11-01 (2023).
URL https://uba.co2-rechner.de/en_GB/

[12] *LHC Machine*, JINST 3 (2008) S08001. doi:10.1088/1748-0221/3/08/S08001.

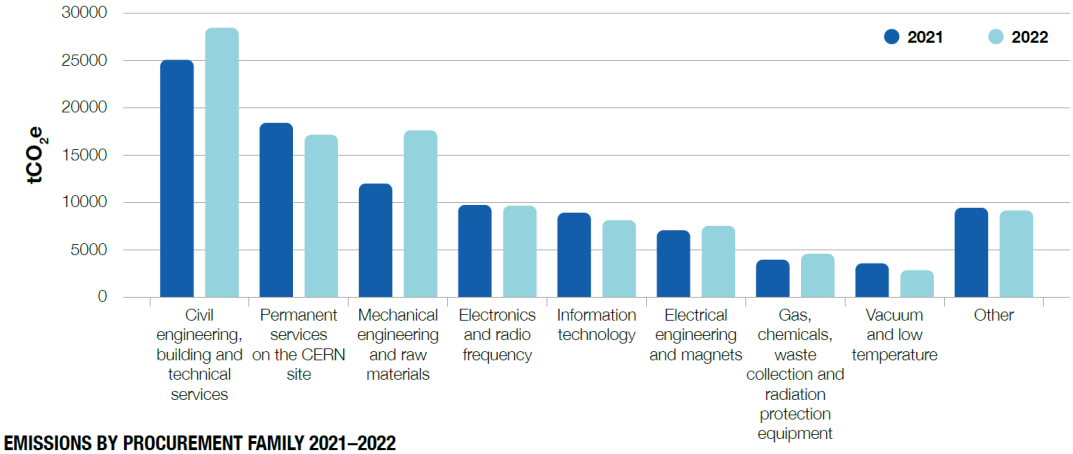

EMISSIONS BY PROCUREMENT FAMILY 2021–2022

"Other" includes: office supplies, furniture, transport, handling and vehicles; centralised expenses and codes for internal use; particle and photon detectors; health, safety and environment; optics and photonics.

Figure B.5: Emissions by procurement family 2021–2022 [20]. The category *Other* includes office supplies, furniture, transport, handling and vehicles; centralised expenses and codes for internal use; particle and photon detectors; health, safety and environment; optics and photonics.

Vergleich der durchschnittlichen Emissionen einzelner Verkehrsmittel des Linien- und Individualverkehrs im Personenverkehr in Deutschland 2022

Quelle: Umweltbundesamt, TREMOD 6.51

Verkehrsmittel		Treibhausgase [1]	Stickoxide	Partikel [4]	Auslastung
Pkw [2]	g / Pkm	**166**	**0,32**	**0,013**	**1,4 Pers./Pkw**
└ davon Elektro-Pkw		*79*	*0,08*	*0,004*	
└ davon Hybrid-Pkw		*121*	*0,10*	*0,008*	
└ davon Diesel-Pkw		*173*	*0,52*	*0,015*	
└ davon Benzin-Pkw		*165*	*0,17*	*0,012*	
Flugzeug, Inland		**238** [3]	**1,03**	**0,011**	**57 %**
Eisenbahn, Fernverkehr		**31**	**0,04**	**0,002**	**46 %**
Linienbus, Fernverkehr		**31**	**0,03**	**0,002**	**52 %**
Eisenbahn, Nahverkehr		**58**	**0,18**	**0,005**	**24 %**
└ davon Dieseltraktion		*90*	*0,68*	*0,015*	
└ davon Elektrotraktion		*49*	*0,05*	*0,002*	
Linienbus, Nahverkehr [5]		**93**	**0,25**	**0,008**	**16 %**
└ davon Elektrobusse		*72*	*0,07*	*0,003*	
└ davon Dieselbusse		*96*	*0,27*	*0,008*	
Straßen-, Stadt- und U-Bahn		**63**	**0,06**	**0,003**	**15 %**
E-Bike		**3**	**0,00**	**0,000**	**1 Pers./E-Bike**

g/Pkm = Gramm pro Personenkilometer, inkl. der Emissionen aus der Bereitstellung und Umwandlung der Energieträger in Strom, Benzin, Diesel , Flüssig- und Erdgas sowie Kerosin; sämtliche für Elektroantrieb ausgewiesenen Emissionsfaktoren basieren auf Werten zum durchschnittlichen Strom-Mix in Deutschland - Emissionsfaktoren, die auf unternehmens- oder sektorbezogenen Strombezügen basieren (siehe z. B. "CO2Kompass" der Deutschen Bahn AG), können daher von den in der Tabelle dargestellten Werten abweichen

[1] CO_2, CH_4 und N_2O angegeben in CO_2-Äquivalenten gemäß AR5 (5. Sachstandsbericht des IPCC)

[2] alle Antriebe (Benzin, Diesel, Elektro, Flüssig- und Erdgas, Hybride)

[3] inkl. Nicht-CO2-Effekte, EWF 1,1 (Hauptverkehrsflughäfen)

[4] ohne Abrieb von Reifen, Straßenbelag, Bremsen, Oberleitungen

[5] alle Antriebe (Diesel, Elektro, Hybride, Erdgas)

Für Informationen zu den Emissionen aus Infrastruktur- und Fahrzeugbereitstellung siehe UBA-Broschüre "Umweltfreundlich mobil!"

Table C.12: Comparison of average CO_2-equivalent emissions for various modes of transport in Germany for 2022 listed in gCO_2e [52]. For the first version of the Kyf calculator, only long-distance trains (*Eisenbahn, Fernverkehr*), long-distance buses (*Linienbus, Fernverkehr*) and personal car (*Pkw*) were used.

[13] Home — cern, accessed: 2024-02-09.
URL https://home.cern/

[14] ATLAS Collaboration, *The ATLAS Experiment at the CERN Large Hadron Collider*, JINST 3 (2008) S08003. doi:10.1088/1748-0221/3/08/S08003.

[15] CMS Collaboration, *The CMS Experiment at the CERN LHC*, JINST 3 (2008) S08004. doi:10.1088/1748-0221/3/08/S08004.

[16] ALICE Collaboration, *The ALICE experiment at the CERN LHC*, JINST 3 (2008) S08002. doi:10.1088/1748-0221/3/08/S08002.

[17] LHCb Collaboration, *The LHCb Detector at the LHC*, JINST 3 (2008) S08005. doi:10.1088/1748-0221/3/08/S08005.

[18] CERN, *CERN Environment Report – Rapport sur l'environnement 2017–2018* (2020). doi:10.25325/CERN-Environment-2020-001.
URL https://doi.org/10.25325/CERN-Environment-2020-001

[19] CERN, *CERN Environment Report – Rapport sur l'environnement 2019–2020* (2021). doi:10.25325/CERN-Environment-2021-002.
URL https://doi.org/10.25325/CERN-Environment-2021-002

[20] CERN, *CERN Environment Report – Rapport sur l'environnement 2021–2022* (2023). doi:10.25325/CERN-Environment-2023-003.
URL https://doi.org/10.25325/CERN-Environment-2023-003

[21] LHCb Collaboration, Framework TDR for the LHCb Upgrade II: Opportunities in flavour physics, and beyond, in the HL-LHC era (2021).

[22] Plotdigitizer: Version 3.1.5 (2024).
URL https://plotdigitizer.com

[23] ALICE Collaboration, *Collaboration Map*, accessed: 2024-01-05 (2024).
URL https://alice-collaboration.web.cern.ch/collaboration/map

[24] LHCb Collaboration, *The LHCb Collaboration*, accessed: 2024-01-05 (2021).
URL https://lhcb-outreach.web.cern.ch/collaboration/

[25] CMS Collaboration, *People Statistics*, accessed: 2024-01-05 (2022).
URL https://cms.cern/index.php/collaboration/people-statistics

[26] ATLAS Collaboration, *The Collaboration*, accessed: 2024-01-05 (2024).
URL https://atlas.cern/Discover/Collaboration

[27] DESY, *First Sustainability report* (2022).
URL https://nachhaltigkeit.desy.de/sustainability_report/index_eng.html

[28] DESY, *Energy monitoring*, accessed: 2024-01-07 (2023).
URL https://nachhaltigkeit.desy.de/energy_management/energy_monitoring/index_eng.html

[29] Electricity maps, *Germany*, accessed: 2024-01-07 (2023).
URL https://app.electricitymaps.com/zone/DE

[30] European Organisation for Astronomical Research in the Southern Hemisphere, *ESO Annual Report 2020*, accessed: 2023-10-16 (2021).
URL https://www.eso.org/public/products/annualreports/ar_2020/

[31] European Organisation for Astronomical Research in the Southern Hemisphere, *ESO Annual Report 2021*, accessed: 2023-10-16 (2022).
URL https://www.eso.org/public/products/annualreports/ar_2021/

[32] European Organisation for Astronomical Research in the Southern Hemisphere, *ESO Annual Report 2022*, accessed: 2023-10-23 (2023).
URL https://www.eso.org/public/products/annualreports/ar_2022/

[33] European Southern Observatory, *About ESO*, accessed: 2024-01-03 (2023).
URL https://www.eso.org/public/about-eso/

[34] University of Freiburg, *Umweltbericht 2019/2020* (2021).
URL https://www.nachhaltige.uni-freiburg.de/de/umweltberichte/umweltbericht-2019-2020-2

[35] Leibniz University Hannover, *Umweltbericht 2017-2019* (2021).
URL https://www.uni-hannover.de/fileadmin/luh/content/webredaktion/universitaet/publikationen/umweltbericht/umweltbericht_17_19.pdf

[36] Technische Universität Dresden, *Certification for the district heating system from enercity AG Hannover* (2022).
URL https://www.enercity.de/assets/cms/enercity-de/Privatkunden/Produkte/Waerme/Fernwaerme/Downloads/FW309-6.pdf

[37] GUTcert, *Vergleich des* CO_2*-Fußabdrucks von Mineral- und Trinkwasser* (2020).
URL https://atiptap.org/files/studie_gutcert_pcf_wasser.pdf

[38] CERN Annual Personnel Statistics 2022CERN Annual Personnel Statistics 2022 (2022).
URL https://cds.cern.ch/record/2858688

[39] B. Bruers, M. Cruces, M. Demleitner, et al., Resource-aware research on universe and matter: Call-to-action in digital transformation (2023). arXiv:2311.01169.

[40] Nvidia cuda cores explained, accessed: 2024-03-04.
URL https://www.techcenturion.com/nvidia-cuda-cores/

[41] Pue: A comprehensive examination of the metric, accessed: 2024-01-16 (2014).
URL https://www.thegreengrid.org/en/resources/library-and-tools/20-PUE:-A-Comprehensive-Examination-of-the-Metric

[42] Gesetz zur steigerung der energieeffizienz in deutschland, effective date: 18 November 2023.
URL https://www.gesetze-im-internet.de/enefg/BJNR1350B0023.html

[43] Hpe apollo (hawk), accessed: 2024-01-24.
URL https://www.hlrs.de/solutions/systems/hpe-apollo-hawk

[44] F. Schluenzen, Computing cluster power consumption data, private communication (2023).

[45] How much electricity does the a100 gpu use?, accessed: 2024-01-16.
URL https://wifocusonenergy.com/optimizing-power-consumption-understanding-the-nvidia-a100s-energy-usage

[46] Panda dashboard, accessed: 2024-01-16.
URL https://bigpanda.cern.ch/dash/region/

[47] Panda system python api reference, accessed: 2024-01-16 (2020).
URL https://panda-wms.readthedocs.io/en/latest/client/rest.html

[48] Microsoft onedrive, https://www.microsoft.com/en-us/microsoft-365/onedrive/online-cloud-storage.

[49] Google drive, https://www.google.com/drive/.

[50] Microsoft onedrive emisions impact dashboard, https://www.microsoft.com/en-us/sustainability/emissions-impact-dashboard.

[51] Google drive footprint calculator, https://cloud.google.com/carbon-footprint.

[52] Umweltbundesamt, Emissionsdaten, accessed: 2024-02-12 (2023).
URL https://www.umweltbundesamt.de/themen/verkehr/emissionsdaten

[53] UBA CO2-Rechner für Veranstaltungen (2024), accessed: 2024-03-02 (2024).
URL https://uba-event-free.co2-rechner.pro/de_DE/

[54] M. Eichler, *Evaluating Environmental Impacts of University Procurements – An Environmentally Extended Multiregional Input Output Analysis of Albert-Ludwigs-Universität Freiburg* (2020).

[55] S. Pauliuk, M. Eichler, B. E. Durán, et al., *Treibhausgasbilanz der Universität Freiburg im Breisgau 2017*, Industrial Ecology Freiburg (IEF) Working Paper 1 (2021). doi:10.6094/UNIFR/176419.
URL https://www.blog.industrialecology.uni-freiburg.de/wp-content/uploads/2021/03/Klimabilanz_Uni_Freiburg_IEF_Working_Paper_1_2021.pdf

arXiv:2403.03256v1 [hep-th] 5 Mar 2024

Impossible Symmetries and Conformal Gravity

Kurt Hinterbichler,[a*] Austin Joyce,[b†] and Grégoire Mathys,[c,d‡]

[a] *CERCA, Department of Physics, Case Western Reserve University, 10900 Euclid Ave, Cleveland, OH 44106, USA*

[b] *Kavli Institute for Cosmological Physics, Department of Astronomy and Astrophysics University of Chicago, Chicago, IL 60637, USA*

[c] *Department of Physics, Cornell University, Ithaca, NY 14850, USA*

[d] *Fields and Strings Laboratory, Institute of Physics Ecole Polytechnique Fédérale de Lausanne (EPFL) Route de la Sorge, CH-1015 Lausanne, Switzerland*

Abstract

We explore the physics of relativistic gapless phases defined by a mixed anomaly between two generalized conserved currents. The gapless modes can be understood as Goldstone modes arising from the nonlinear realization of (generically higher-form) symmetries arising from these currents. In some cases, the anomaly cannot be reproduced by any local and unitary theory, indicating that the corresponding symmetries are impossible, in the sense that they cannot appear in a Lorentzian physical system. We consider many examples of the general construction. Most notably, we study conformal gravity from this perspective, describing the higher-form symmetries of the linear theory and showing how it can be understood in terms of anomalies. Along the way we clarify some aspects of electric-magnetic duality in linear conformal gravity.

*kurt.hinterbichler@case.edu

†austinjoyce@uchicago.edu

‡gregoire.mathys@epfl.ch

Contents

1 Introduction **3**

2 Symmetries and gapless phases **5**
- 2.1 Currents and cohomology 5
- 2.2 Anomalies and gapless modes 10
- 2.3 Effective field theory 11

3 Scalar examples **13**
- 3.1 Superfluid 13
- 3.2 Galileonic superfluid 14
- 3.3 Conformal scalar 17

4 Spin-2 examples **22**
- 4.1 Einstein gravity 22
- 4.2 Conformal gravity 25

5 Conclusions **30**

A Conformal gravity **31**
- A.1 Nonlinear conformal gravity 31
- A.2 Linearized conformal gravity 33

B Spectral decompositions **35**
- B.1 Projectors 35
- B.2 Spectral decomposition 35

References **37**

1 Introduction

Symmetries help to delineate the boundaries between the possible and the impossible. For example, selection rules tell us that transitions between certain states cannot happen. As we will see, sometimes symmetries *themselves* are impossible: certain patterns of symmetries cannot be unitarily realized by any low-energy effective field theory (EFT).

One of the goals of physics is to understand the possible phases that the degrees of freedom that make up our universe can be in. In this pursuit, the Landau paradigm and effective field theory serve as powerful organizing principles which allow us to describe a wide variety of phenomena using a unified language. From this perspective, we classify phases both by their symmetries and by how these symmetries are realized on the light degrees of freedom of the system. Recently, the horizons of the Landau paradigm have been significantly broadened by a commensurate expansion of our conceptions of symmetries themselves. It has been understood that ordinary symmetries admit vast generalizations in many directions, from higher forms [1, 2] to higher groups [3, 4] and even to non-invertible and categorical settings [5–11]. These formal structures have already proven to be useful in phenomenological applications [12–18] and the interplay between these structures and the principles of effective field theory is just beginning to be explored [19–30]. In this regard, understanding what symmetries can consistently appear in effective descriptions is essential.

In light of these developments, it is worthwhile to reconsider what actually defines an effective field theory, or a phase of matter, in order to fully realize the potential of the Landau paradigm. A natural operational definition is to specify the local conserved currents, along with their compatibility, as expressed by the structure of 't Hooft anomalies in the presence of background sources. This viewpoint is surprisingly powerful, making it possible to describe phenomena as varied as superfluids and superconductors [23, 24] to gravity [29–32] in a unified language. Given these successes, one might imagine that any pattern of symmetries and anomalies can be realized by *some* quantum field theory. But, quite remarkably, it has long been known that certain apparently consistent effective field theories do not admit ultraviolet completions, satisfying certain requirements [33].[1]

In this paper, we explore this ultraviolet-infrared (UV-IR) interplay in the context of the *symmetries* that arise in a low-energy field theory. Following [23, 29], we define an EFT via its conserved currents. We allow for these currents to be generalized (i.e., they can be operators in arbitrary mixed-symmetry representations of the Lorentz group, satisfying general conservation conditions involving one or more derivatives acting in various ways). We consider situations where a relativistic system possesses two of these generalized currents in the IR: one current, K, which we call "magnetic," and one current, J, which we call "electric". These currents can have a mixed anomaly between them—one of the two conservation conditions must necessarily be broken in the presence of background gauge fields for the currents, or equivalently, conservation must be broken at coincident points in correlators. By assuming such a non-vanishing mixed anomaly between the currents, we show that the system must necessarily be in a gapless phase. The properties of the massless degrees of freedom are then determined by the structure of the currents and their con-

[1] A thematically related line of inquiry is the "swampland" program [34], which is concerned with the constraints placed on EFTs by the requirement that they can consistently be ultraviolet completed by quantum gravity. A difference, however, is that swampland constraints are not supposed to be visible within the EFT itself.

servation conditions. We will see that sometimes these gapless modes are necessarily non-unitary, which means that the corresponding combinations of conserved currents and anomalies cannot be realized by any unitary field theory. This then implies that these symmetries are impossible in the sense that they cannot arise in the low-energy description of any unitary and Lorentz invariant microphysical theory. These symmetries need not be exact symmetries of the underlying microphysical theory—and indeed in general we would not expect them to be. Rather, they can be emergent at low energies. Remarkably, even this possibility is not allowed.

In order to illustrate the features of the construction, we consider several examples where the gapless mode is a scalar degree of freedom, and show how they can be understood in a uniform way. In addition to the familiar example of an ordinary superfluid [23], and the slightly more exotic galileon superfluid considered in [29], we also consider the theory of a higher-derivative conformal scalar. This theory is structurally similar to conformal gravity, and the corresponding gapless phase is necessarily non-unitary, providing a simple example of a theory with "impossible" symmetries.

Perhaps one of the more interesting applications—and our original motivating example—is to conformal gravity. Weyl-squared gravity is a four-derivative theory of gravity which propagates more degrees of freedom than Einstein gravity. In four spacetime dimensions it is Weyl invariant and is known as conformal gravity [35–38]. Famously, some of its propagating modes necessarily have a wrong sign kinetic term (as can be seen explicitly around an (A)dS background [39–42]) so that the theory is non-unitary. We will describe the higher-form symmetries of linearized Weyl-squared gravity (which is Weyl and conformally invariant in all dimensions, in contrast to its nonlinear version), and show how it can be thought of as a relativistic gapless phase with a particular structure of symmetries and anomalies. Unsurprisingly, this structure cannot be realized by any unitary theory, showing more abstractly that (linearized) conformal gravity cannot arise as the low-energy description of a unitary QFT. We also consider conserved charges in this theory, and elucidate the structure of its electric-magnetic duality in $D = 4$.

These results form a version of a UV-IR connection. Given our ignorance of UV physics as low-energy observers, we might imagine that it is possible for the microscopic theory that describes our world to have essentially any symmetries.[2] The examples we study give obstructions to certain symmetries being present in the UV, assuming unitarity and relativistic invariance of the IR theory. We expect that these insights will help to more broadly understand the systematics of generalized symmetries in the context of EFT.

Outline: In Section 2 we describe the general construction of relativistic gapless phases in terms of a pair of conserved currents with a mixed anomaly. In Section 3 we illustrate this construction with several scalar field examples, including one that is conceptually similar to conformal gravity. In Section 4 we review the higher-form symmetries of linearized Einstein gravity then describe the higher-form symmetries of linear conformal gravity and cast it as a gapless phase. We conclude in Section 5. In Appendix A we briefly review some of the salient features of both nonlinear and linear conformal gravity. In Appendix B we describe the spectral decomposition of the two-point functions of interest, and explain how they cannot be reproduced by purely unitary representations.

[2] Presumably these symmetries would be only approximate at some energy scale, given the expectation that quantum gravity breaks all global symmetries.

Conventions: Throughout we will work in Euclidean signature for simplicity, despite the fact that we are primarily interested in Lorentzian physics. Our curvature conventions are those of [43]. We denote the spacetime dimension by D, and denote symmetrization of indices by $(\cdots)$ and antisymmetrization by $[\cdots]$. We denote the fully traceless symmetrization by $(\cdots)_T$ and all indices are (anti)symmetrized with weight 1. In many places we employ Young diagrams and Young tableaux to represent the index symmetries of various tensors. We denote Young diagrams by $[r_1, r_2, \ldots, r_n]$, where r_a are the lengths of the various rows. Our conventions are such that all Young diagrams are first symmetrized and then antisymmetrized with respect to the relevant indices (so that all tableaux are in the manifestly antisymmetric presentation). We also define the Hodge star $*$ such that it dualizes the first column of a given tableau. We denote Young projectors onto the diagram $[r_1, r_2, \ldots, r_n]$ by $\mathcal{Y}_{[r_1,r_2,\ldots,r_n]}$, and we denote projectors onto the space of traceless tensors by $\mathcal{Y}^T$. Note that essentially all tensors in this paper are traceless. Typically there is only one nonzero way to assign indices to be compatible with a given Young projector, so when there is no ambiguity we do not explicitly display the indices involved in the projector.

2 Symmetries and gapless phases

In this section we describe the general structure of the relativistic gapless phases of interest, before considering some concrete examples in Sections 3 and 4. The physics of these phases is controlled by a pair of generalized conserved currents that have a particular mixed anomaly between them. The presence of gapless modes is mandated by this anomaly, and we will see through the examples that in some cases the anomaly cannot be reproduced in any unitary theory.

2.1 Currents and cohomology

A phase will be defined by specifying both a generalized "magnetic" current, K, and a generalized "electric" current, J, along with the generalized conservation conditions that they each satisfy. The Lorentz representation of these currents and their conservation conditions do not need to be the same, and will generically not be. In general, there will be a mixed anomaly between the two symmetries, whose precise form can also be thought of as an input. A signal of the anomaly will be the impossibility of sourcing one of these currents via a background gauge field without violating conservation of the other current. As is usually the case with anomalies, the failure of conservation can be shifted between the currents by adjusting local counterterms in the theory. As a matter of convention, we will choose the anomaly to appear in the magnetic current's conservation equation. We will see that this mixed anomaly governs the structure of the phase. At the practical level, we will specify the properties of the gauge field that the current J couples to, rather than the current itself, and this indirectly defines the conservation equation J satisfies. This will both allow us to define the conservation equation for the current J, and the gauge-invariant field strength that will ultimately appear in the anomaly equation for K.

2.1.1 Generalized cochain complexes

The currents can transform in arbitrary representations of the Lorentz group, and satisfy generalized conservation laws [44]. In order to describe the systematics, it is convenient to introduce a cochain complex that generalizes the familiar de Rham complex for antisymmetric tensors to more general representations [45–48] (also known as BGG complexes [49–51]). Each of the currents, or its background gauge field, will be an element of one of these complexes, and its conservation law will be described by a generalized exterior derivative that maps between successive elements of the complex. Under the assumption that the cohomology of this complex is trivial, as it is in flat space, we will be able to understand the features of the mixed anomaly of the currents' conservation, the structure of the gauge invariances of external sources, and the structure of the low energy EFT.

It is simplest to consider the elements of the complex as fully traceless tensors, which therefore carry irreducible $\mathrm{SO}(D)$ representations in generic D. We label the elements by their index symmetries, so that members of the a^{th} element of the complex will have the index symmetries of the Young diagram $\mathbb{Y}^{(a)}$. We can therefore write the cochain complex of interest schematically as

$$\mathbb{Y}^{(1)} \xrightarrow{\mathrm{d}_{(1)}} \mathbb{Y}^{(2)} \xrightarrow{\mathrm{d}_{(2)}} \mathbb{Y}^{(3)} \xrightarrow{\mathrm{d}_{(3)}} \mathbb{Y}^{(4)} \xrightarrow{\mathrm{d}_{(4)}} \cdots \quad . \tag{2.1}$$

The differential maps $\mathrm{d}_{(a)}$ will be described shortly; they will map between elements of the complex in such a way that $\mathrm{d}_{(a+1)}\mathrm{d}_{(a)} = 0$.

We now describe the symmetry types $\mathbb{Y}^{(a)}$ of the elements that can appear in the complex. The starting point can be chosen freely. It is an arbitrary tensor with index symmetries given by the Young tableau $\mathbb{Y}^{(1)}$:

$\mathbb{Y}^{(1)} \in$ 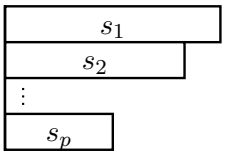

, (2.2)

where the integers $s_1, \ldots, s_p$ label the lengths of the rows of the tableau. The only requirement is that these lengths are non-increasing: $s_1 \geq s_2 \geq \cdots \geq s_p$, so that $\mathbb{Y}^{(1)} \in [s_1, \ldots, s_p]$. In order to obtain the subsequent elements of the complex (2.1), we add more boxes to the tableaux row-by-row using the integers r_a that we will describe below: to get $\mathbb{Y}^{(2)}$, we add r_1 boxes to the first row of $\mathbb{Y}^{(1)}$, to get $\mathbb{Y}^{(3)}$, we add r_2 boxes to the second row of $\mathbb{Y}^{(2)}$, and so on. So in general, to obtain $\mathbb{Y}^{(a+1)}$, we add r_a boxes to the a-th row of $\mathbb{Y}^{(a)}$.

The data that we need to completely specify all of the $\mathbb{Y}^{(a)}$ is the first element of the cochain $\mathbb{Y}^{(1)}$, and the number $r_1 > 0$ of boxes that are added to the first row of $\mathbb{Y}^{(1)}$ in order to obtain $\mathbb{Y}^{(2)}$. In order to obtain r_2, r_3, etc. we use the following formula:

$$r_a = s_{a-1} - s_a + 1, \quad \text{for} \quad a = 2, 3, \cdots \quad , \tag{2.3}$$

where s_a is the number of boxes in the a-th row of the initial tableau $\mathbb{Y}^{(1)}$. In particular, this implies that if the starting tableau has p non-zero rows, then $\mathbb{Y}^{(p+3)}$ will have a last row with just a single box, and all the subsequent steps of the algorithm will just add a new one-box row at the

bottom of the diagram. We can visualize the complex as

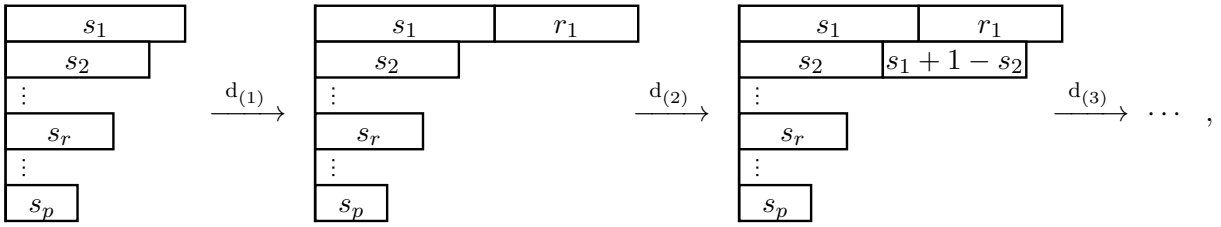

which can equivalently be written in terms of the row lengths as

$$[s_1, s_2, s_3, \cdots, s_p] \xrightarrow{\mathrm{d}_{(1)}} [s_1+r_1, s_2, s_3, \cdots, s_p] \xrightarrow{\mathrm{d}_{(2)}} [s_1+r_1, s_1+1, s_3, \cdots, s_p] \xrightarrow{\mathrm{d}_{(3)}} [s_1+r_1, s_1+1, s_2+1, \ldots, s_p] \xrightarrow{\mathrm{d}_{(4)}} \cdots \quad . \tag{2.4}$$

We now turn to describing the differential maps $\mathrm{d}_{(a)}$ that take us between succesive element of the complex. The operator $\mathrm{d}_{(a)}$ contains r_a derivatives and maps tensors of type $\mathbb{Y}^{(a)}$ into tensors of type $\mathbb{Y}^{(a+1)}$: operationally, we obtain $\mathbb{Y}^{(a+1)}$ by associating derivatives to the r_a new boxes that are present in $\mathbb{Y}^{(a+1)}$ but not in $\mathbb{Y}^{(a)}$, putting $\mathbb{Y}^{(a)}$ into the remaining boxes and then Young projecting to $\mathbb{Y}^{(a+1)}$ and removing all traces. We can think of the additional boxes present in the Young diagram $\mathbb{Y}^{(a+1)}$ compared to $\mathbb{Y}^{(a)}$ as being the derivatives in $\mathrm{d}_{(a)}$. Due to the fact that derivatives in successive steps are being added to different rows, and the fact that indices in the same column are antisymmetrized, it is straightforward to see that these operators satisfy the central condition of a cochain complex, that the composition of two successive maps vanishes,

$$\mathrm{d}_{(a+1)}\mathrm{d}_{(a)} = 0, \tag{2.5}$$

because derivatives end up being antisymmetrized. By assuming the cohomology of this cochain is trivial, we can say that if a tensor $T^{(a)}$ of symmetry type $\mathbb{Y}^{(a)}$ satisfies $\mathrm{d}_{(a)}T^{(a)} = 0$, then it can be written as $T^{(a)} = \mathrm{d}_{(a-1)}T^{(a-1)}$ for some tensor $T^{(a-1)}$ of symmetry type $\mathbb{Y}^{(a-1)}$. In the following, the magnetic conserved current and the gauge field source for the electric current will be elements of complexes of this type.[3]

Examples: Here we give some examples of the above generalized cochain complexes that will be relevant for some of the theories that we study below.

- As a familiar first example, consider the starting tensor to be a scalar $\mathbb{Y}^{(1)} = \bullet$, and take $r_1 = 1$, which gives

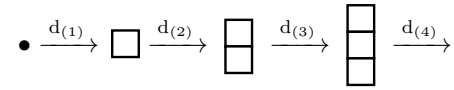

(2.6)

  This is the standard de Rham complex for p-forms, and plays a role in the construction of ordinary superfluids, reviewed in Section 3.1.

[3]Note that these complexes are the same ones underlying the on-shell gauge invariances and Bianchi identities of general mixed-symmetry partially massless fields on (A)dS [52, 53].

- Another useful complex that will appear in several places takes the same starting point $\mathbb{Y}^{(1)} = \bullet$, but adds two indices in the first step ($r_1 = 2$), which leads to

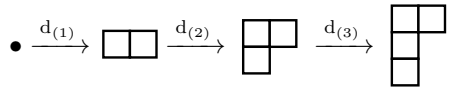

(2.7)

This complex will be relevant when we study a scalar analogue of conformal gravity in Section 3.3, and also appears in the construction of a galileonic superfluidin Section 3.2. This is also the cochain complex underlying the gauge invariances of the partially massless graviton [54, 55].

- If we take $\mathbb{Y}^{(1)} = [1]$, and $r_1 = 1$, we find

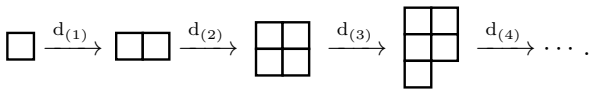

(2.8)

This is the chain complex underlying the diffeomorphism invariance of the linearized massless graviton, and the conserved magnetic current of linearized gravity fits into this complex, as we review in Section 4.1. It will also appear in the construction of the galileon superfluid (Section 3.3) and in both the magnetic current and gauge field of the conformal graviton in Section 4.2.

- As a final example, we can take $\mathbb{Y}^{(1)} = [1, 1]$ and $r_1 = 1$. The corresponding complex is then

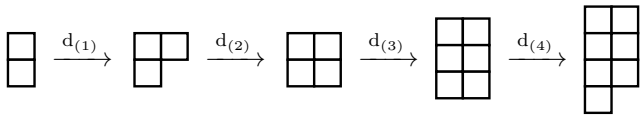

(2.9)

This complex is relevant for the electric gauge field of linearized Einstein gravity, as we will see in Section 4.1.

2.1.2 Electric and magnetic currents

We now want to describe how to use this complex to construct the electric and magnetic currents that we will use to define the phases of interest. Two objects will play a central role in the construction: a (magnetic) current, K, and a gauge field, A which sources the electric current J, and so defines it indirectly. K and A each fit into a complex of the form (2.4). For each, the choice of complex and the position into which it fits is equivalent to choosing the Lorentz representation and conservation equations for the currents.

Magnetic current: We begin by considering the magnetic current K. There are two features that we have to specify: its index symmetries, and the conservation condition that it satisfies. We specify its index symmetries via the Young diagram $\mathbb{Y}^{(K)}$ and we take it to be completely traceless. In order to specify its conservation conditions, we specify the complex (2.4) that the magnetic current K belongs to:

$$\cdots \longrightarrow \mathbb{Y}^{(\phi)} \xrightarrow{\mathrm{d}_{(\phi)}} \mathbb{Y}^{(K)} \xrightarrow{\mathrm{d}_{(K)}} \mathbb{Y}^{(\mathcal{C})} \xrightarrow{\mathrm{d}_{(\mathcal{C})}} \cdots . \tag{2.10}$$

Here K is the current of interest, ϕ will end up being the field theory degree of freedom that realizes

the relevant pattern of symmetries when we construct an EFT, and $\mathcal{C}$ is a tensor that will appear in the anomalous conservation equation of the magnetic current in the presence of a background gauge field for J. We will see that typically K corresponds to $\mathbb{Y}^{(2)}$ in (2.1)—or $\mathbb{Y}^{(3)}$ in cases involving irreducible gauge fields—but in general, we can take K to be a member of any complex that contains an element with the right index symmetries. (In general, if the current is in the representation $\mathbb{Y}^{(r)}$ then we'll get an EFT involving a gauge field with $r-3$ levels of reducibility.)

The differential operators in the complex are essentially generalized curls or Bianchi identities, so specifying the conservation of K by the differential complex that it fits into may seem somewhat abnormal (usually we think of conserved currents as satisfying divergence-like conditions), but it is actually more natural from the point of view of generating conserved quantities/symmetry operators. Recall that in the familiar case of a conserved current (which satisfies $\partial_\mu J^\mu = 0$), we actually use the dual current $K = *J$ (which satisfies $\mathrm{d}K = 0$) to define a conserved quantity by integrating over a codimension-1 surface. Here we are specifying this current that satisfies an exterior derivative-like conservation condition directly.[4] Of course one could translate these conditions into divergence-like conditions on the Hodge dual of K, fitting into a dual complex, if desired.

Electric gauge field: Next we specify the background gauge field A that couples to the conserved "electric" current J. We will take A to be traceless with the index symmetries of a tableau $\mathbb{Y}^{(A)}$. The current then has the same index symmetries: $J \in \mathbb{Y}^{(A)}$. Like the magnetic current, we then have to specify what complex of the form (2.4) the gauge field A is a member of. In this case, the complex determines the gauge transformation rule for A:

$$\cdots \longrightarrow \mathbb{Y}^{(\Lambda)} \xrightarrow{\mathrm{d}_{(\Lambda)}} \mathbb{Y}^{(A)} \xrightarrow{\mathrm{d}_{(A)}} \mathbb{Y}^{(F)} \xrightarrow{\mathrm{d}_{(F)}} \cdots . \tag{2.11}$$

In this complex, A is the background gauge field, Λ is a gauge parameter with the index symmetries of the tableau $\mathbb{Y}^{(\Lambda)}$, so that A transforms as

$$\delta A_{\mathbb{Y}^{(A)}} = \mathrm{d}_{(\Lambda)} \Lambda_{\mathbb{Y}^{(\Lambda)}} , \tag{2.12}$$

and F is the field strength with the with the index symmetries of the tableau $\mathbb{Y}^{(F)}$, which is gauge invariant by virtue of (2.5),

$$\delta F_{\mathbb{Y}^{(F)}} = 0 . \tag{2.13}$$

Specifying the pattern of gauge symmetry for A is equivalent to specifying the conservation condition for J: since A couples to the current J, the current must satisfy a conservation equation of the form

$$* \, \mathrm{d}_{(A)} * J_{\mathbb{Y}^{(A)}} = 0 , \tag{2.14}$$

in order for the coupling to be gauge invariant.

[4] Note that this is a slightly different perspective/convention from that employed in [29], where the magnetic current called K here would be called $*K*$ there in the generic case.

2.2 Anomalies and gapless modes

Fully defining the phases of interest requires one additional piece of information: the systems have two conserved currents, J and K, and we have to specify the compatibility of their conservation laws. A priori, it is not guaranteed in the presence of a source for one of these conserved currents that the other will continue to be conserved. Indeed, in many cases conservation will fail, in which case we say there is a mixed 't Hooft anomaly between these symmetry currents. By specifying a particular structure of this anomaly, we will see that the system must be in a gapless phase.

In the presence of the background gauge field A (which sources J), both K and J are promoted to gauge-invariant versions $\mathcal{J}$ and $\mathcal{K}$. Conservation of the current $\mathcal{J}$ can be maintained by adding appropriate local counterterms, but the magnetic current $\mathcal{K}$ will generically not be conserved. It will instead satisfy the anomalous conservation equation[5]

$$\mathrm{d}_{(K)}\mathcal{K}_{\mathbb{Y}(K)} = -\mathcal{C}_{\mathbb{Y}(\mathcal{C})}\,, \tag{2.15}$$

where $\mathcal{C}$ is a tensor built from the gauge-invariant field strength F appearing in (2.11) and which has the index symmetries $\mathbb{Y}^{(\mathcal{C})}$ of the tensor appearing in (2.10).[6] In many cases F and $\mathcal{C}$ do not have the same symmetry type. If this happens, since F is traceless, the only possible way to construct a tensor with the correct symmetry properties is by taking derivatives of F.

The failure of conservation encapsulated by (2.15) is the sign of a mixed anomaly between the electric and magnetic symmetries. The structure of the phase is essentially dictated by this anomaly. One way to understand this is to consider the two-point function between the currents J and K. It is fixed by the requirements that J and K be conserved at separated points, and by the anomaly equation (2.15), which specifies the contact terms that spoil conservation of the current K at coincident points. (The fact that it is impossible to have both currents conserved even at coincident points is another way of expressing the anomaly.) The spectral decomposition of the two point function $\langle JK\rangle$ then provides us with information about the degrees of freedom in this phase. In all cases of interest in this paper, K has the same symmetry type as J, and the Källén–Lehmann spectral decomposition of their two-point function will require the presence of gapless modes, whose precise identity depends on the symmetry type and conservation conditions of the currents, along with the anomaly equation.[7]

Certain gapless phases can therefore be *defined* by their structure of conserved currents and anomalies. It would not be possible to match the two-point function of these currents without gapless modes present in the system. We will see in some cases that the two-point function cannot

[5] The $-$ sign is conventional, and we normalize the anomaly so that properly quantized operators charged under K have unit charge.

[6] In all the cases we consider, the anomaly can be written in terms of a gauge-invariant field strength. This is because the anomalies that we consider are "Abelian". For non-Abelian anomalies, it is typically not possible to write the anomaly in terms of a gauge-invariant combination that also satisfies the Wess–Zumino consistency conditions [56].

[7] This structure of anomalies is what appears in generic spacetime dimension. However, there can be certain special dimensions where interesting additional features appear. In particular, it is sometimes possible to construct gauge-invariant topological terms out of the gauge field A, which can generate trace anomalies for the currents of interest (particularly $\mathcal{J}$). Some examples of these trace anomalies were discussed in [29]. We will not consider them further, but it would be very interesting to understand whether these topological terms contain any interesting information about the global structure of the manifolds on which they are defined.

be matched by any spectrum of unitary representations of the Poincaré group, implying that the relevant pattern of symmetries cannot arise as the effective description of any unitary quantum system, i.e. it is *impossible*.

2.3 Effective field theory

It is often desirable to have an effective description of small fluctuations around the ground state of a system in a given phase. We now turn to the construction of such an EFT description of the phases of interest, which realizes the symmetry and anomaly structure. This discussion will be somewhat abstract, but we will later provide a number of concrete examples.

To build an effective field theory, we need to introduce some local field theory degrees of freedom ϕ from which the currents J and K will be built. Since the anomaly (2.15) involves the magnetic current, K, it is convenient to realize this current as a "topological" current, whose conservation is trivialized by the parameterization of degrees of freedom. This is a choice: by choosing appropriate counterterms, we could instead make the anomaly appear in the conservation of J, and instead realize J as a topological current in dual variables. This would change the presentation of the EFT, but would not change any of the actual long distance physics of the system. With this choice, the magnetic conserved current will not get deformed in the presence of abelian interactions, so that the anomaly structure is reliable in the interacting theory. Looking at the complex (2.10), we see that if we define

$$K \equiv \mathrm{d}_{(\phi)}\phi\,, \tag{2.16}$$

then conservation of K will be automatic: $\mathrm{d}_{(K)}K = \mathrm{d}_{(K)}\mathrm{d}_{(\phi)}\phi = 0$.

Reproducing the relevant anomaly in this effective description is fairly straightforward. We promote the magnetic current to its gauge invariant version:

$$K \to \mathcal{K} \equiv K - C\,, \tag{2.17}$$

where C is a tensor built out of the gauge field A with the same index symmetries as K. This tensor is uniquely defined by the requirement that $\mathcal{K}$ is gauge invariant. In the presence of C, $\mathcal{K}$ is no longer annihilated by $\mathrm{d}_{(K)}$, and instead satisfies (2.15) with $\mathcal{C} = \mathrm{d}_{(K)}C$. Note also that $\mathcal{C}$ can be written in terms of (possibly derivatives of) the gauge-invariant field strength F associated to A.

We now want to construct a Lagrangian involving ϕ whose equations of motion imply the conservation of the current J. There are two conceptually different structures that the effective field theory can have. The first is *Maxwell-like*, where the effective action is just given by powers of (2.16)

$$S = \int \mathrm{d}^D x \left(\frac{1}{2} \left(\mathrm{d}_{(\phi)}\phi\right)^2 + c_1 \left(\mathrm{d}_{(\phi)}\phi\right)^3 + \cdots \right) . \tag{2.18}$$

In effective field theories of this type, the tensor C is actually just directly the gauge field A. Consequently, building the action out of powers of K guarantees that the interacting EFT can be consistently coupled to the gauge field A. The corresponding current is J, which therefore satisfies the conservation condition (2.14).[8]

[8] Notice also that the form of the action guarantees that it will have the shift symmetry

$$\phi \mapsto \phi + \alpha_{\mathbb{Y}(\phi)}\,, \tag{2.19}$$

In some cases the equations of motion following from (2.18) involve more than two derivatives. This may be undesirable, and we may want to find theories with the same degrees of freedom and symmetries but with lower-order equations of motion. This can sometimes be achieved by constructing an EFT that is *Chern–Simons-like*, i.e., using terms that are not constructed solely from K yet are still invariant under (2.19) up to a total derivative (often known as Wess–Zumino terms). To our knowledge there is no classification of such terms for totally generic symmetry types (though many scalar cases are known [57–59]), and so we will just cover the cases of later interest.

What we require in these cases is an analogue of the Einstein tensor. This can be constructed by considering the trace-ful analogue of the complex that the current K fits into. We can then define the relevant Einstein tensor as the traceless part of the single trace of K in this complex:

$$G = \mathcal{Y}^{T}_{\mathbb{Y}(\mathrm{tr}\,K)}\,\mathrm{tr}\,K\,, \tag{2.20}$$

where K can be written in terms of ϕ. In all the cases of interest ϕ will have two fewer indices than K, and so it is possible to contract ϕ with G,[9] producing an action of the form

$$S = \int \mathrm{d}^D x \Big(\phi\, G + c_1 \left(\mathrm{d}_{(\phi)}\phi\right)^2 + c_2 \left(\mathrm{d}_{(\phi)}\phi\right)^3 + \cdots \Big)\,, \tag{2.21}$$

where we have allowed for the possibility of irrelevant corrections built out of ϕ, which may also be of Wess–Zumino type. It is somewhat non-obvious, but this action will have the same global symmetries as (2.18), but with the Einstein term being invariant only up to a total derivative. The equation of motion following from this action is a partial flatness condition on the trace-ful version of the curvature K, in contrast to the wave equation-like condition following from (2.18).

We will see versions of both of these types of EFT in the following examples. Heuristically, one can think of the Maxwell-like EFTs as being more like electromagnetism, and the Chern–Simons-like EFTs as being more like Einstein gravity. While the precise EFT construction may seem like somewhat of a choice at the level of global symmetries, there actually is no freedom once one specifies the anomaly structure that the EFT is to reproduce. One way to understand this is that in the deep IR, the two currents J and K coincide, and so the two-point function of these currents is determined by the free theory, and the number of derivatives in the quadratic action will affect the form of this two-point function. Since the two-point function of the theory is completely determined by the conservation conditions and anomalies, different quadratic actions must have different anomaly structures. Thus, the anomaly that we are trying to reproduce dictates the kinetic structure that must be present. In Section 3 we will see an explicit example, where the current K will be the same in two different theories, but the current J will satisfy different conservation conditions depending on the kinetic term of the theory, and correspondingly the theories can be coupled to different background gauge fields and will produce different anomalies.

---

where α is a tensor with the same symmetry type as ϕ, which also satisfies $\mathrm{d}_{(\phi)}\alpha = 0$. This signals that the symmetry associated with J is spontaneously broken in this phase, and ϕ serves as the corresponding Goldstone boson.

[9] This is the difficulty in describing the totally generic construction for currents of any symmetry type, because ϕ and G will not always have the same indices.

3 Scalar examples

We now turn to some concrete examples of the preceding abstract discussion. In this section we present the simplest possible cases: a scalar field realizing various patterns of symmetries and anomalies which fit into the general framework presented in Section 2.

3.1 Superfluid

One of the simplest examples of a gapless quantum system is a superfluid. The massless phonon in this phase can be understood as a consequence of a mixed anomaly between the shift symmetry acting on the phonon and an (emergent) winding symmetry, under which the superfluid's vortices are charged [23]. Here we review this in the context of the general construction of Section 2.

Currents and anomalies: In the language of Section 2, the two objects of interest are a magnetic 1-form current K_μ and a 1-form gauge field A_μ, which sources an electric current J_μ. Both the current K_μ and gauge field A_μ can be thought of as elements of the ordinary de Rham complex

$$\bullet \xrightarrow{\mathrm{d}} \square \xrightarrow{\mathrm{d}} \begin{array}{|c|}\hline \\ \hline \\ \hline \end{array} \xrightarrow{\mathrm{d}} \cdots . \tag{3.1}$$

Here, the presence of K_μ in this complex signals that it is closed $\partial_{[\mu}K_{\nu]} = 0$, which implies that its dual $(*K)_{\mu_1\cdots\mu_{D-1}}$ is conserved in the ordinary sense, $\partial^{\mu_1}(*K)_{\mu_1\cdots\mu_{D-1}} = 0$. The fact that A_μ is part of this complex implies that it has the usual gauge transformation rule $\delta A_\mu = \partial_\mu \Lambda$, and thus sources a current J_μ which is conserved in the ordinary sense, $\partial_\mu J^\mu = 0$. These equations are true as operator statements at separated points, but they cannot both be chosen to be true at coincident points in correlation functions. Contact terms necessarily spoil conservation of at least one of them. The structure of these contact terms is dictated by the anomaly equation[10]

$$\partial_{[\mu}\mathcal{K}_{\nu]} = -\frac{1}{2}F_{\mu\nu}\,, \tag{3.2}$$

where $F_{\mu\nu} = \partial_\mu A_\nu - \partial_\nu A_\mu$ is the field strength that is part of the complex (3.1), and $\mathcal{K}_\mu$ is the gauge-invariant version of K in the presence of A_μ. So we see here that the gauge-invariant field strength directly plays the role of $\mathcal{C}$ in (2.15).

In order to see how this pattern of symmetries and anomalies defines the superfluid phase, we note that the Fourier-space two-point function between J and K is completely fixed by their conservation and mixed anomaly (3.2) to be [23]

$$\langle J_\mu K_\nu \rangle = \frac{1}{p^2}\left(p_\mu p_\nu - p^2\eta_{\mu\nu}\right)\,. \tag{3.3}$$

The pole at $p^2 \to 0$ indicates the presence of a gapless excitation in the spectrum, and a more careful spectral decomposition reveals that this excitation is a scalar particle [23, 29]. From this

[10] As mentioned above, we have chosen to put the anomaly in the conservation equation for K_μ. We could instead choose a renormalization scheme that shuffles the anomaly into the conservation equation for J. This other choice would be more natural in dual variables where the superfluid phonon is packaged into a $(D-2)$-form (see e.g., [60]).

perspective, the superfluid Goldstone mode is forced upon us by the currents and the structure of their anomaly.

Effective field theory: It is straightforward to construct an EFT that reproduces this physics and describes the superfluid phonon directly [61]. Recall that the (magnetic) current satisfies $\mathrm{d}K = 0$. From the complex (3.1) we see that we can trivialize this conservation law by writing

$$K_\mu = \partial_\mu \phi \,, \tag{3.4}$$

for some scalar field ϕ. Our goal is then to construct a field theory for ϕ that has a conserved (electric) current. In this case the relevant EFT is Maxwell-like, and we can write

$$S = \int \mathrm{d}^D x \left(\frac{1}{2}(\partial\phi)^2 + \frac{1}{4\Lambda^D}(\partial\phi)^4 + \cdots \right) , \tag{3.5}$$

where Λ is a dimension-ful scale. The existence of a conserved electric current that is conserved on-shell follows from the shift symmetry $\phi \mapsto \phi + c$ of the action,

$$J_\mu = \partial_\mu \phi \left[1 + \frac{1}{\Lambda^D}(\partial\phi)^2 + \cdots \right] . \tag{3.6}$$

We can couple this current to a background gauge field A_μ by promoting everywhere

$$\partial_\mu \phi \;\; \mapsto \;\; \partial_\mu \phi - A_\mu \,, \tag{3.7}$$

after which the action is invariant under the gauge transformations $\delta\phi = \xi(x)\,, \delta A_\mu = \partial_\mu \xi(x)$. In this case, the magnetic current (3.4) fails to be gauge invariant, and we then see that the gauge invariant version of this current

$$\mathcal{K}_\mu \equiv \partial_\mu \phi - A_\mu \,, \tag{3.8}$$

no longer is anti-symmetrically conserved, but instead displays the expected anomaly (3.2). We therefore see that the EFT (3.5) captures the low-lying excitations of this phase, with ϕ acting as the superfluid phonon.

Two dimensions: A small interesting feature appears in the linearized theory in two dimensions. In this case, the linear equations of motion are

$$\partial_\mu J^\mu = 0 \,, \qquad\qquad \partial_{\mu_1} (*J)^{\mu_1 \cdots \mu_{D-1}} = 0 \,. \tag{3.9}$$

so we see that precisely in $D = 2$ these are electric-magnetic duals of each other.

3.2 Galileonic superfluid

As another example with the same degrees of freedom as an ordinary superfluid—but with different symmetries—we now consider a "galileon superfluid," which is an exotic version of a superfluid with a spacetime-dependent shift symmetry [29, 62].

Currents and anomalies: As before, we begin by introducing the magnetic current and the electric gauge field, which will be used to define the phase. In this case, the magnetic current is a traceless symmetric two-index tensor

$$K_{\mu\nu} \;\in\; \square\square \,. \tag{3.10}$$

We consider K to be part of the complex

$$\bullet \xrightarrow{\mathrm{d}_{(\phi)}} \ydiagram{2} \xrightarrow{\mathrm{d}_{(K)}} \ydiagram{2,2} \longrightarrow \cdots , \tag{3.11}$$

where the maps appearing are

$$(\mathrm{d}_{(\phi)}\phi)_{\mu\nu} = \partial_{(\mu}\partial_{\nu)_T}\phi \,, \tag{3.12}$$

$$(\mathrm{d}_{(K)}K)_{\alpha\mu\nu} = 3\mathcal{Y}^T_{[2,1]}\partial_\alpha K_{\mu\nu} = \partial_\alpha K_{\mu\nu} + \cdots \,, \tag{3.13}$$

so that the conservation condition satisfied by K is $\mathrm{d}_{(K)}K = 0$, which involves projecting onto the traceless $[2,1]$ tableau.

We specify the electric current by defining a symmetric traceless gauge field $A_{\mu\nu}$, which is an element of the complex,

$$\ydiagram{1} \xrightarrow{\mathrm{d}_{(\Lambda)}} \ydiagram{2} \xrightarrow{\mathrm{d}_{(A)}} \ydiagram{2,2} \xrightarrow{\mathrm{d}_{(F)}} \cdots \quad . \tag{3.14}$$

This implies that the gauge transformation rule for A is $\mathrm{d}_{(\Lambda)}\Lambda$ which can be written as

$$\delta A_{\mu\nu} = 2\partial_{(\mu}\Lambda_{\nu)_T} \,, \tag{3.15}$$

and the gauge-invariant field strength $F = \mathrm{d}_{(A)}A$ has the symmetries of the Weyl tensor

$$F_{\mu\nu\alpha\beta} = \frac{3(D-1)}{2(D-3)}\mathcal{Y}^T_{[2,2]}\ \partial_\mu\partial_\alpha A_{\nu\beta} = \frac{(D-1)}{(D-3)}\partial_\mu\partial_\alpha A_{\nu\beta} + \cdots \,, \tag{3.16}$$

where we have chosen the normalization for later convenience. The gauge field A sources the electric current $J_{\mu\nu}$. The current $J_{\mu\nu}$ therefore has the same symmetry properties (symmetric traceless) and the gauge transformation (3.15) implies that it satisfies the conservation condition

$$\partial^\nu J_{\mu\nu} = 0. \tag{3.17}$$

In the presence of the background gauge field A, the gauge-improved current $\mathcal{J}$ continues to be conserved, but the magnetic current no longer satisfies (3.13), but rather obeys the anomalous conservation equation

$$\mathcal{Y}^T_{[2,1]}\,\partial_\alpha \mathcal{K}_{\mu\nu} = -\mathcal{C}_{\alpha\mu\nu} \,, \tag{3.18}$$

where the right-hand side is built from the field strength (3.16) as

$$\mathcal{C}_{\alpha\mu\nu} = -\partial^\beta F_{\beta\nu\alpha\mu} = \frac{3}{2}\mathcal{Y}^T_{[2,1]}\partial_\alpha\, C_{\mu\nu} \,, \tag{3.19}$$

where

$$C_{\mu\nu} = \frac{D-1}{D-2}\left[2\partial^\alpha\partial_{(\mu}A_{\nu)_T\alpha} - \Box A_{\mu\nu}\right]. \tag{3.20}$$

Notice that the tensor appearing in the anomaly $\mathcal{C}_{\alpha\mu\nu}$ is not directly $F_{\mu\nu\alpha\beta}$ because of the mismatch in index structures: since $\mathcal{C}$ has one fewer index than F, it must be constructed using one derivative, and (3.19) is the unique way of making something with the index symmetries of $\mathcal{C}$ out of a derivative

of F. Similarly to the ordinary superfluid, this anomaly fixes the two-point function between the currents $J_{\mu\nu}$ and $K_{\mu\nu}$ to be

$$\langle J_{\mu_1\mu_2}K_{\nu_1\nu_2}\rangle = \frac{D-1}{D-2}\Bigg[p^2\eta_{\mu_1(\nu_2}\eta_{\nu_1)\mu_2} - \frac{1}{D-1}\Big(p^2\eta_{\mu_1\mu_2}\eta_{\nu_1\nu_2} - \eta_{\mu_1\mu_2}p_{\nu_1}p_{\nu_2} - \eta_{\nu_1\nu_2}p_{\mu_1}p_{\mu_2}\Big) \\ - \eta_{\mu_2(\nu_2}p_{\nu_1)}p_{\mu_1} - \eta_{\mu_1(\nu_2}p_{\nu_1)}p_{\mu_2} + \frac{D-2}{D-1}\frac{p_{\mu_1}p_{\mu_2}p_{\nu_1}p_{\nu_2}}{p^2}\Bigg], \tag{3.21}$$

and the Källén–Lehmann spectral decomposition once again reveals that the gapless excitation in the system is a Poincaré scalar [29].

In $D = 2$ there is a topological term that can be built out of the gauge field $A_{\mu\nu}$ which has no free indices (it is the linearized Ricci tensor $\partial^\mu\partial^\nu A_{\mu\nu}$, thinking of $A_{\mu\nu}$ as a traceless version of the graviton). This topological term can appear in the trace equations $\mathrm{tr}\mathcal{J} = \mathrm{tr}\mathcal{K} = 0$, leading to additional anomalies [29].

Effective field theory: We would now like to construct an EFT that reproduces the anomaly structure and describes this phase. From the complex (3.11), we see that we can trivialize the magnetic conservation equation by defining

$$K_{\mu\nu} = \partial_{(\mu}\partial_{\nu)_T}\phi = \partial_\mu\partial_\nu\phi - \frac{1}{D}\eta_{\mu\nu}\Box\phi\,. \tag{3.22}$$

Recall that for this current, the desired conservation equation is that the antisymmetric derivative of $K_{\mu\nu}$ with all traces removed vanishes, as dictated by the complex (3.11), and this is guaranteed by writing K in this way. As expected, the relevant degree of freedom in this phase is a scalar field ϕ. We now want to construct an action that leads to the conservation of the electric current $J_{\mu\nu}$. Notice that $K_{\mu\nu}$ is invariant under the transformation [62]

$$\delta\phi = c_\mu x^\mu\,, \tag{3.23}$$

and so it is natural to imagine that $J_{\mu\nu}$ will be the Noether current for this symmetry.[11] More specifically, we want to construct an EFT that has a global symmetry $\delta\phi = \partial_\mu\xi^\mu$, where ξ^μ is a conformal Killing vector that also satisfies $\partial_\mu\partial_\nu\partial_\alpha\xi^\beta = 0$ [29]. One way to guarantee that this will be a symmetry of the action is to construct the action out of powers of $K_{\mu\nu}$, which would be analogous to the Maxwell-like EFT of a superfluid (3.5). However, this action will necessarily have higher-derivative equations of motion, and it would not reproduce the anomaly (3.18). We therefore are motivated to ask whether it is possible to construct an EFT with the same symmetries, but which has second order linearized equations of motion. This turns out to indeed be possible. Notice that the linearized action

$$S = -\int \mathrm{d}^D x\,\frac{1}{2}\phi\Box\phi\,, \tag{3.24}$$

[11] Notice that this EFT is still written in terms of a scalar field, despite the fact that it has *more* symmetry than the superfluid (it is also clearly invariant under $\delta\phi = \text{const.}$). The fact that a single degree of freedom can realize multiple symmetries is a manifestation of the so-called inverse Higgs effect [63].

is also invariant under the symmetry (3.23), despite having fewer derivatives.[12] This is possible because the action is invariant up to a total derivative under the symmetry—there also exist interactions with the same property, so called galileon terms [62, 64]. We can gauge the symmetry (3.23) by promoting $\Box\phi$ to

$$\mathcal{G} = -\Box\phi + \partial_\mu\partial_\nu A^{\mu\nu}\,, \tag{3.25}$$

after which the linearized action can be put in the form

$$S = \frac{1}{2}\int \mathrm{d}^D x\Big(\phi\,\mathcal{G} + A^{\mu\nu}\mathcal{J}_{\mu\nu}\Big)\,. \tag{3.26}$$

Here $\mathcal{J}_{\mu\nu}$ is the electric current

$$\mathcal{J}_{\mu\nu} = \partial_{(\mu}\partial_{\nu)_T}\phi - C_{\mu\nu}\,, \tag{3.27}$$

where $C_{\mu\nu}$ is given by (3.20). In the linearized theory, it happens that $\mathcal{K}_{\mu\nu} = \mathcal{J}_{\mu\nu}$, but this will not be true generically once interactions are included. Taking the antisymmetric derivative, we reproduce (3.18) [29]. The action (3.26) is invariant under the gauge transformation

$$\delta\phi = \frac{2(D-1)}{D}\partial^\mu\xi_\mu\,, \tag{3.28}$$

for ϕ, along with the transformation (3.15) for A.

Interactions can be introduced similarly by taking arbitrary powers of $\mathcal{K}_{\mu\nu}$, which coincides with (3.27). The magnetic current (and anomaly) do not change. The electric current will receive corrections from the interaction terms, but will continue to exist as long as the interactions respect the symmetry (3.23) (or equivalently gauge invariance in the presence of A). Note that this theory and the ordinary superfluid have the same kinetic term. The difference between them lies only in the symmetries that are demanded, and thus in the spectrum of operators and in the types of irrelevant interactions that we are allowed to include.[13]

Two dimensions: Here again there is a version of electric-magnetic duality in two dimensions. This case is similar to the ordinary superfluid, but just with an extra index. The two equations of motion are

$$\partial_\mu J^{\mu\nu} = 0\,, \qquad\qquad \partial_{\mu_1}(*J)^{\mu_1\cdots\mu_{D-1}\,\nu} = 0\,, \tag{3.30}$$

where $*J$ is dualized over its μ index. We again see that these equations are duals of each other in $D = 2$.

3.3 Conformal scalar

We now want to consider a more novel example, which is a conformal scalar that shares many similarities with conformal gravity. Here we meet our first example of a theory with "impossible"

[12] We can construct the "Einstein scalar" $G = -\Box\phi$ from the trace-ful version of the complex (3.11). In this complex, we would have $K_{\mu\nu} = \partial_\mu\partial_\nu\phi$, which has G as its nonzero trace.

[13] Note that if we had not included the $\phi\mathcal{G}$ term and instead built the EFT directly out of powers of $\mathcal{K}$, we would see that $\mathcal{K}$ has an anomaly of the form

$$\mathcal{Y}^T_{[2,1]}\,\partial_\alpha\mathcal{K}_{\mu\nu} \sim -\Box\,\mathcal{C}_{\alpha\mu\nu}\,, \tag{3.29}$$

rather than (3.18), and correspondingly this EFT would have a different two-point function.

symmetries, where the structure of anomalies cannot be matched by a unitary theory. Consequently we will find that the EFT that captures the dynamics and reproduces the anomalies necessarily involves higher-order derivatives.

Currents and anomalies: In the previous examples, the currents of interest satisfied single-derivative conservation equations. In this example we will have an electric current that satisfies a higher-derivative condition.

The magnetic current is the same as in the galileon superfluid example

$$K_{\mu\nu} \in \square\!\square \,, \tag{3.31}$$

which then fits into the same complex

$$\bullet \xrightarrow{\mathrm{d}_{(\phi)}} \square\!\square \xrightarrow{\mathrm{d}_{(K)}} \begin{array}{ll}\square & \square \\ \square & \end{array} \longrightarrow \cdots \quad . \tag{3.32}$$

In this complex, the maps are the same as (3.12) and (3.13), and the conservation condition that K satisfies is $\mathrm{d}_{(K)}K = 0$.

The novelty in this case compared with the superfluid is the electric gauge field: it is once again a two-index traceless tensor $A_{\mu\nu}$, but it is now part of the complex

$$\bullet \xrightarrow{\mathrm{d}_{(\Lambda)}} \square\!\square \xrightarrow{\mathrm{d}_{(A)}} \begin{array}{ll}\square & \square \\ \square & \end{array} \xrightarrow{\mathrm{d}_{(F)}} \cdots \,. \tag{3.33}$$

Under a gauge transformation, A shifts as

$$\delta A_{\mu\nu} = \partial_{(\mu}\partial_{\nu)_T}\Lambda \,, \tag{3.34}$$

and the field strength $F_{\mu\nu\alpha}$ is defined as

$$F_{\mu\nu\alpha} = \partial_{[\mu}A_{\nu]\alpha} - \frac{1}{D-1}\eta_{\alpha[\mu}\partial^{\beta}A_{\nu]\beta} \,. \tag{3.35}$$

These two equations are the maps in (3.33) expressed in indices. The gauge transformation (3.34) implies that the electric current satisfies the conservation condition

$$\partial_\mu\partial_\nu J^{\mu\nu} = 0 \,. \tag{3.36}$$

Note that the single divergence of J does not necessarily vanish, $\partial_\nu J^{\mu\nu} \neq 0$.

In the presence of the background gauge field $A_{\mu\nu}$, the electric current $\mathcal{J}_{\mu\nu}$ continues to be conserved, but the magnetic current instead satisfies the anomalous conservation equation

$$\mathcal{Y}^{T}_{[2,1]}\,\partial_\alpha \mathcal{K}_{\mu\nu} = -F_{\alpha\mu\nu} \,. \tag{3.37}$$

Since $F_{\alpha\mu\nu}$ has the correct index symmetries, it can appear directly on the right-hand side of this equation, playing the role of $\mathcal{C}_{\alpha\mu\nu}$ in (2.15). In this sense the mixed anomaly for this theory is conceptually more similar to that of the ordinary superfluid than the galileon superfluid, despite the fact that the magnetic current has the same index symmetries as in the galileonic example.

As in the previous examples, the conservation condition $\partial_\mu\partial_\nu J^{\mu\nu} = 0$ along with the mixed anomaly (3.37) completely fixes the Fourier-space two-point function between the two currents:

$$\langle J_{\mu\nu}K_{\rho\sigma}\rangle = \frac{D}{D-1}\frac{1}{p^4}\left[p_\mu p_\nu p_\rho p_\sigma - \frac{D-1}{D}p^4\eta_{\mu(\sigma}\eta_{\rho)\nu} + \frac{p^2}{D}\left(p^2\eta_{\mu\nu}\eta_{\rho\sigma} - p_\mu p_\nu\eta_{\rho\sigma} - p_\rho p_\sigma\eta_{\mu\nu}\right)\right] . \tag{3.38}$$

Notice that this two-point function has a p^{-4} divergence as $p \to 0$, which already suggests that this theory cannot be unitary. This can be formalized by an explicit spectral decomposition, but the result is the expected one—the higher-order pole cannot be matched by any unitary Poincaré representation, and instead reveals the existence of a so-called "dipole ghost" state [65–67]. More details are provided in Appendix B. We therefore see that any theory with this pattern of symmetries and anomalies must necessarily be non-unitary—they are impossible symmetries.

Effective field theory: Let us now reproduce this physics from an effective field theory. We can again trivialize conservation of the magnetic current by writing

$$K_{\mu\nu} = \partial_{(\mu}\partial_{\nu)_T}\phi\,. \tag{3.39}$$

We now want to find an action for ϕ from which the (double) conservation of $J_{\mu\nu}$ follows. The appearance of the gauge-invariant field strength itself in the anomaly equation (3.37) suggests that the relevant EFT will be Maxwell-like, and indeed this is the case. We consider the EFT

$$S = -\frac{1}{2}\int \mathrm{d}^D x\left(K_{\mu\nu}K^{\mu\nu} + \frac{1}{\Lambda^D}K_{\mu\nu}^4 + \cdots\right) , \tag{3.40}$$

where $K_{\mu\nu}^4$ stands schematically for all index contractions, and Λ is an energy scale (not to be confused with the gauge parameter). Notice that the kinetic term for ϕ that comes from (3.40) is higher derivative

$$S = -\int \mathrm{d}^D x\left(\frac{D-1}{2D}\phi\,\Box^2\phi + \cdots\right) . \tag{3.41}$$

We can then understand the presence of the electric current $J_{\mu\nu}$ as a consequence of the fact $K_{\mu\nu}$, can be coupled a background gauge field by promoting it to

$$K_{\mu\nu} \to \mathcal{K}_{\mu\nu} \equiv \partial_{(\mu}\partial_{\nu)_T}\phi - A_{\mu\nu}\,, \tag{3.42}$$

which is then invariant under the gauge transformations

$$\delta\phi = \xi\,, \tag{3.43}$$

$$\delta A_{\mu\nu} = \partial_{(\mu}\partial_{\nu)_T}\xi\,. \tag{3.44}$$

with a scalar gauge parameter $\xi(x)$. The gauge field $A_{\mu\nu}$ will then couple to the electric current $\mathcal{J}_{\mu\nu}$:

$$\begin{aligned}\mathcal{J}_{\mu\nu} &\equiv \frac{\delta S}{\delta A^{\mu\nu}} \\ &= \partial_{(\mu}\partial_{\nu)_T}\phi - A_{\mu\nu} + \cdots\,,\end{aligned} \tag{3.45}$$

which will be doubly conserved (because of the gauge transformation of A). The presence of this conserved current also guarantees that the action will have certain global symmetries, which we detail in the following inset.

Symmetries: We can use the current $J_{\mu\nu}$ to construct ordinary Noether currents that correspond to the global symmetries of the EFT (3.40). Let us illustrate this in the special case of the free theory. In this case, the doubly conserved electric current is

$$J_{\mu\nu} = \partial_{(\mu}\partial_{\nu)_T}\phi\,, \tag{3.46}$$

which is doubly conserved as a consequence of the higher-derivative equations of motion. Note that, as expected, the current $J_{\mu\nu}$ in a generic EFT agrees with $K_{\mu\nu}$ in the deep IR.

To obtain an ordinary conserved current from $J_{\mu\nu}$, we can start from (3.46) and contract it with a conformal Killing scalar χ, which satisfies $\partial_{(\mu}\partial_{\nu)_T}\chi = 0$. The current

$$J_\mu[\chi] = J_{\mu\nu}\partial^\nu\chi + \partial^\nu J_{\mu\nu}\chi\,, \tag{3.47}$$

will then be conserved. We can then consider the free conformal scalar Lagrangian, and write it in the form

$$\mathcal{L} = -\frac{1}{2}J_{\mu\nu}^2 = -\frac{1}{2}\left[\partial_{(\mu}\partial_{\nu)_T}\phi\right]^2. \tag{3.48}$$

In this form, it is manifestly invariant under a shift by a conformal Killing scalar,

$$\delta\phi = \chi. \tag{3.49}$$

The Noether current for this symmetry is

$$\mathcal{J}^\mu = -\delta\phi\partial_\nu\frac{\partial\mathcal{L}}{\partial(\partial_\mu\partial_\nu\phi)} + \frac{\partial\mathcal{L}}{\partial(\partial_\mu\partial_\nu\phi)}\partial_\nu\delta\phi = -\partial^\mu\partial_\nu\phi\partial^\nu\chi + \frac{1}{D}\partial^\mu\chi\Box\phi + \frac{(D-1)}{D}\chi\partial^\mu\Box\phi, \tag{3.50}$$

which gives exactly $-J^\mu[\chi]$.

The independent conformal Killing scalars are

$$c, \quad b_\mu x^\mu, \quad x^2, \tag{3.51}$$

such that these include the usual constant shift, galileon symmetry, as well as shifty by x^2, which is not a symmetry of the $(\partial\phi)^2$ kinetic term, but which *is* a symmetry of (3.40).

The electric current defined by (3.45) is guaranteed to be double conserved, but the (topological) magnetic current (3.42) will no longer satisfy the conservation equation $\mathrm{d}_{(K)}K = 0$, but will instead produce the anomaly (3.37). As expected, the EFT (3.41) that reproduces the general physics of this phase is manifestly non-unitary, having fourth-order equations of motion.

Electric-magnetic duality: The linearized version of this effective field theory displays a version of electric-magnetic duality in $D = 2$. In generic dimension, we can think of the theory as being defined by the equations

$$\partial^\mu\partial^\nu J_{\mu\nu} = 0\,, \tag{3.52}$$

$$\mathcal{Y}^T_{[2,1]}\,\partial_\alpha J_{\mu\nu} = 0\,, \tag{3.53}$$

which are valid at separated points, and where $J_{\mu\nu} = K_{\mu\nu}$ in the linear theory. Recalling that $J_{\mu\nu}$

is part of the complex (3.32), equation (3.53) implies that we can write[14]

$$J_{\mu\nu} = \partial_{(\mu}\partial_{\nu)_T}\phi\,. \tag{3.54}$$

The equation of motion $\Box^2\phi = 0$ then follows from (3.52).

Two dimensions: Something special happens in $D = 2$. Tensors with the symmetry type $\begin{array}{|c|c|}\hline\multicolumn{1}{|c}{}\\[-1em]\hline\end{array}$ vanish identically, such that the equation (3.53) is trivially satisfied in $D = 2$. We must therefore additionally impose the two-derivative equation

$$\partial_{[\alpha}\partial^{\nu}\mathcal{J}_{\mu]\nu} = -\partial_{[\alpha}\partial^{\nu}A_{\mu]\nu}\,, \tag{3.55}$$

in order to fix the overall normalization of the two-point function. The standard de Rham complex can be used to infer from (3.55) that

$$\partial^{\nu}J_{\mu\nu} = \partial_{\mu}f\,, \tag{3.56}$$

while the identically satisfied equation (3.53) implies that $f = \Box\phi$. Then, we see that $\Box^2\phi = 0$ from (3.52). The takeaway is that the two equations

$$\partial_{\mu}\partial_{\nu}J^{\mu\nu} = 0\,, \tag{3.57}$$

$$\partial_{\mu}\partial_{\nu}(*J)^{\mu\nu} = 0 \implies \partial_{[\alpha}\partial^{\nu}J_{\mu]\nu} = 0\,, \tag{3.58}$$

are equivalent at separated points in $D = 2$, and completely fix this theory (along with the particular anomaly (3.55) at coincident points). Here the dualization is defined with respect to the μ index. In two dimensions, the equation (3.57) is equivalent to its dual, so this is a manifestly electric-magnetic duality invariant formulation of the theory.

Note, of course, that the choice of which equation to make anomalous at coincident points breaks electric-magnetic duality, which will appear in the contact terms of the theory. The equation (3.58) is actually only true at separated points. Inside correlation functions there is an anomaly, which–for example—fixes the normalization of the two point function. The two-point function (3.38) is not correct in $D = 2$. Instead we find

$$\langle J_{\mu\nu}K_{\rho\sigma}\rangle|_{D=2} = \frac{2}{p^4}\left[p_\mu p_\nu p_\rho p_\sigma - \frac{p^2}{2}\left(p_\mu p_{(\rho}\eta_{\sigma)\nu} + \eta_{\mu(\rho}p_{\sigma)}p_\nu\right)\right]\,, \tag{3.59}$$

where the overall normalization is fixed by the anomaly in the equation (3.58), and again this correlator implies the presence of a massless scalar.

[14]Note that, from the CFT point of view, this current is not a primary operator, so it does not appear among the multiply-conserved currents of the $\Box^2$ theory classified in [68].

4 Spin-2 examples

In the preceding section, we saw several examples of the general construction described in Section 2, and saw how the same scalar degree of freedom can realize different patterns of symmetries and anomalies, some of which cannot arise in a unitary theory. Similar constructions can lead to massless spin-1 [2, 3, 20, 21] excitations, or higher p-form excitations. In this section we wish to present some other examples where the gapless degree of freedom has spin two. We first review the symmetries of the EFT of a linearized graviton, before describing the higher-form symmetries of linearized conformal gravity. Conformal gravity is well-known to be non-unitary, and we will see that this is a property shared by any theory with the same generalized symmetries as (linear) conformal gravity.

4.1 Einstein gravity

We first review the anomaly structure of (linearized) Einstein gravity [29–31] and show how it fits into the general framework described in Section 2.

Currents and anomalies: The magnetic current of interest has four indices $K_{\mu_1\mu_2\nu_1\nu_2}$, with the symmetry type of the Weyl tensor

$$K_{\mu_1\mu_2\nu_1\nu_2} \in \ydiagram{2,2} \,. \tag{4.1}$$

This current is an element of the complex

$$\ydiagram{1} \xrightarrow{\mathrm{d}_{(\xi)}} \ydiagram{2} \xrightarrow{\mathrm{d}_{(h)}} \ydiagram{2,2} \xrightarrow{\mathrm{d}_{(K)}} \ydiagram{3,2,1} \longrightarrow \cdots \,, \tag{4.2}$$

where the various maps are defined by

$$\left(\mathrm{d}_{(\xi)}\xi\right)_{\mu\nu} = 2\partial_{(\mu}\xi_{\nu)_T} \,, \tag{4.3}$$

$$\left(\mathrm{d}_{(h)}h\right)_{\mu\nu\alpha\beta} = -3\mathcal{Y}^T_{[2,2]}\,\partial_\mu\partial_\alpha h_{\nu\beta} = -\partial_\mu\partial_\alpha h_{\nu\beta} + \cdots \,, \tag{4.4}$$

$$\left(\mathrm{d}_{(K)}K\right)_{\rho\mu\nu\alpha\beta} = 3\mathcal{Y}^T_{[2,2,1]}\partial_\rho K_{\mu\nu\alpha\beta} = \partial_\rho K_{\mu\nu\alpha\beta} + \cdots \,. \tag{4.5}$$

Using this complex, the conservation condition that is satisfied by the magnetic current is

$$\mathrm{d}_{(K)}K = 0 \,, \tag{4.6}$$

which is the same form as the traceless part of the Bianchi identity for the Weyl tensor.

The gauge field that couples to the electric current is $A_{\mu\nu\alpha\beta}$ and also has the symmetries of the Weyl tensor. It is part of the complex

$$\ydiagram{1,1} \longrightarrow \ydiagram{2,1,1} \xrightarrow{\mathrm{d}_{(\Lambda)}} \ydiagram{2,2} \xrightarrow{\mathrm{d}_{(A)}} \ydiagram{3,3} \xrightarrow{\mathrm{d}_{(F)}} \cdots \,. \tag{4.7}$$

Here the gauge parameter is a mixed-symmetry tensor $\Lambda_{\mu\nu\alpha}$, and the differential operators are defined explicitly as

$$\left(\mathrm{d}_{(\Lambda)}\Lambda\right)_{\mu\nu\alpha\beta} = 12\mathcal{Y}^T_{[2,2]}\partial_\mu\Lambda_{\alpha\beta\nu} = \partial_\mu\Lambda_{\alpha\beta\nu} + \cdots\,, \tag{4.8}$$

$$\left(\mathrm{d}_{(A)}A\right)_{\mu\nu\rho\alpha\beta\sigma} = 18\mathcal{Y}^T_{[2,2,2]}\partial_\rho\partial_\sigma A_{\mu\nu\alpha\beta} = \partial_\rho\partial_\sigma A_{\mu\nu\alpha\beta} + \cdots\,, \tag{4.9}$$

so that under a gauge transformation the field transforms as[15]

$$\delta A_{\mu\nu\alpha\beta} = \partial_\mu\Lambda_{\alpha\beta\nu} + \cdots\,, \tag{4.10}$$

and the gauge-invariant field strength is,

$$F = \mathrm{d}_{(A)}A\,. \tag{4.11}$$

This encodes the fact that the electric current is ordinarily conserved,

$$\partial_\mu J^{\mu\nu\alpha\beta} = 0. \tag{4.12}$$

In the presence of this background gauge field, the electric current continues to be conserved, while the magnetic current satisfies the anomaly equation

$$3\mathcal{Y}^T_{[2,2,1]}\partial_{[\rho}\mathcal{K}_{\mu\nu]\alpha\beta} = -\mathcal{C}_{\mu\nu\rho\alpha\beta}\,, \tag{4.13}$$

where the anomaly can be written in terms of the gauge-invariant field strength of A as[16]

$$\mathcal{C}_{\mu\nu\rho\alpha\beta} = -\frac{(D-3)}{8(D-5)}\,\partial^\sigma F_{\mu\nu\rho\alpha\beta\sigma} = 3\mathcal{Y}^T_{[2,2,1]}\partial_\rho C_{\mu\nu\alpha\beta}\,, \tag{4.14}$$

which also can be written in terms of the auxiliary tensor

$$C_{\mu\nu\alpha\beta} = \frac{D-3}{D-4}\mathcal{Y}^T_{[2,2]}\left(\partial^\rho\partial_\mu A_{\nu\alpha\beta\rho} - \frac{1}{4}\Box A_{\mu\nu\alpha\beta}\right)\,. \tag{4.15}$$

As in the scalar examples, the symmetries/anomalies of this system completely fix the two point function involving the electric and magnetic currents. Explicitly, it takes the form [29].

$$\begin{aligned}\langle J_{\mu_1\mu_2\nu_1\nu_2}K_{\alpha_1\alpha_2\beta_1\beta_2}\rangle = \mathcal{P}\Bigg[&\frac{9(D-4)}{D-3}\frac{p_{\mu_1}p_{\mu_2}p_{\alpha_1}p_{\alpha_2}\eta_{\nu_1\beta_1}\eta_{\nu_2\beta_2}}{p^2}\\ &+\frac{3}{4}p^2\eta_{\mu_1\alpha_1}\eta_{\mu_2\alpha_2}\eta_{\nu_1\beta_1}\eta_{\nu_2\beta_2} - 3p_{\mu_1}p_{\alpha_1}\eta_{\mu_2\alpha_2}\eta_{\nu_1\beta_1}\eta_{\nu_2\beta_2}\Bigg]\,,\end{aligned} \tag{4.16}$$

where $\mathcal{P}\equiv\mathcal{Y}^T_{[2,2]}\mathcal{Y}^T_{[2,2]}$ is a Young projector onto the tableau that has the symmetries of a symmetric product of Weyl tensors

$$\begin{array}{|c|c|}\hline\mu_1&\nu_1\\\hline\mu_2&\nu_2\\\hline\end{array}\;\otimes\;\begin{array}{|c|c|}\hline\alpha_1&\beta_1\\\hline\alpha_2&\beta_2\\\hline\end{array}\,. \tag{4.17}$$

[15] Note that the fact that $\Lambda_{\alpha\beta\nu}$ is itself the derivative of another tensor in (4.7) implies that the gauge transformation is reducible, any gauge parameter that is the symmetric derivative of a 2-form will automatically have $\delta A = 0$.

[16] The slightly strange normalizations are chosen for convenience when matching to the EFT description. Note that the apparently singular behavior in $D = 5$ is due to the fact that the field strength (4.9) vanishes identically in five dimensions, and so it is not possible to write the anomaly in terms of it. Nevertheless, it is possible to write it in terms of (4.15) by dividing by $D - 5$.

Note that only the first term of (4.16) is nonlocal. Performing a spectral decomposition on the two-point function (4.16) implies that there is a gapless spin-2 mode—the linearized graviton—in the spectrum [29]. From this perspective, the graviton is a Goldstone for a (higher-form) symmetry, which is nonlinearly realized.

Effective field theory: We now want to review how this structure of anomalies is reproduced in effective field theory [29, 30]. As before, the strategy is to trivialize the magnetic conservation condition by writing the magnetic current in terms of a potential field

$$K_{\mu_1\mu_1\nu_1\nu_2} = -3\mathcal{Y}^T_{[2,2]}\partial_{\mu_1}\partial_{\nu_1}h_{\mu_2\nu_2}\,, \tag{4.18}$$

where $h_{\mu\nu}$ is a traceless symmetric tensor. Of course this is just the linearized Weyl tensor where $h_{\mu\nu}$ is the linearized metric in a gauge where $h^\mu{}_\mu = 0$. Notice that the complex (4.2) implies that this tensor is invariant under the gauge transformation

$$\delta h_{\mu\nu} = 2\partial_{(\mu}\xi_{\nu)_T}\,, \tag{4.19}$$

which is nothing but the linearized diffeomorphism invariance that preserves $h^\mu{}_\mu = 0$. We see that gauge invariance in this language is an inevitable consequence of choosing to write one of the currents locally in terms of field variables that trivialize its conservation.[17]

We now want to construct an action whose equation of motion implies the conservation of the electric current $J_{\mu_1\mu_1\nu_1\nu_2}$. This current can be seen as the Noether current for the shift

$$\delta h_{\mu\nu} = 2\partial^\alpha\Lambda_{\alpha(\mu\nu)}\,, \tag{4.20}$$

where Λ is a traceless mixed-symmetry tensor and we must require that $K[\delta h]_{\mu\nu\alpha\beta} = 0$ in order for this to be a symmetry. (This condition is the analogue of the 1-form symmetry in electromagnetism requiring that we shift by a flat connection.)

As in the galileon superfluid example discussed in Section 3.2, the most naive action built directly from K will have fourth-order equations of motion, and the wrong anomaly. It is, however, possible to construct a kinetic term with lower-order equations of motion:

$$S = -\int \mathrm{d}^D x\,\frac{1}{2}h^{\mu\nu}\Big(\Box h_{\mu\nu} - 2\partial^\alpha\partial_{(\mu}h_{\nu)\alpha}\Big)\,, \tag{4.21}$$

whose equation of motion sets the traceless linearized Einstein tensor to zero $G_{(\mu\nu)_T} = 0$. Note that this is a non-standard presentation of linearized gravity, written in terms of an identically traceless tensor (see section 2.4 of [69]). The electric current in this linearized theory is also the Weyl tensor

$$W_{\mu_1\mu_1\nu_1\nu_2} = -3\mathcal{Y}^T_{[2,2]}\partial_{\mu_1}\partial_{\nu_1}h_{\mu_2\nu_2}\,, \tag{4.22}$$

which is conserved on-shell. As before, the electric current happens to coincide with K, but this is again an accident of the linearized theory. We can introduce interactions, which are naturally built from powers of K. The electric current will then receive corrections (but will continue to be

[17] We would have seen a similar phenomenon in the scalar examples if we had decided to trivialize the electric current conservation, which would have introduced a $(D-2)$-form field carrying the gapless mode.

conserved on-shell), while the magnetic current will be unchanged. These will be interactions of the "pseudo-linear" type [70–74]. It is an open question how to extend this framework to describe the non-abelian interactions of full Einstein–Hilbert gravity.

We can gauge the symmetry (4.20) by introducing $A_{\mu\nu\alpha\beta}$ into the action (4.21) as

$$\begin{aligned} S = \int \mathrm{d}^D x \Big(& \frac{1}{2}\partial_\alpha h_{\mu\nu}\partial^\alpha h^{\mu\nu} - \partial^\mu h_{\mu\alpha}\partial_\nu h^{\nu\alpha} - A_{\mu\nu\rho\sigma}\partial^\mu\partial^\rho h^{\nu\sigma} \\ & - \frac{D-3}{8(D-4)}\partial^\mu A_{\nu\rho\sigma\alpha}\partial_\mu A^{\nu\rho\sigma\alpha} + \frac{D-3}{2(D-4)}\partial^\mu A_{\nu\rho\sigma\mu}\partial_\alpha A^{\nu\rho\sigma\alpha}\Big) , \end{aligned} \tag{4.23}$$

which is invariant under the following gauge transformations

$$\delta_\Lambda A_{\mu\nu\alpha\beta} = 12\mathcal{Y}^T_{[2,2]}\partial_\mu\Lambda_{\alpha\beta\nu} = \partial_\mu\Lambda_{\nu\beta\alpha} + \cdots \tag{4.24}$$

$$\delta_\Lambda h_{\mu\nu} = \frac{6(D-3)}{D-2}\partial^\alpha\Lambda_{\alpha(\mu\nu)} . \tag{4.25}$$

This action can be written more simply as

$$S = -\frac{1}{2}\int \mathrm{d}^d x \Big(h^{\mu\nu}\mathcal{G}_{\mu\nu} + A^{\mu\nu\rho\sigma}\mathcal{J}_{\mu\nu\rho\sigma}\Big) , \tag{4.26}$$

where we have introduced the gauge-improved (traceless) Einstein tensor and electric current

$$\mathcal{G}_{\mu\nu} = \Box h_{\mu\nu} - 2\partial^\alpha\partial_{(\mu}h_{\nu)_T\alpha} - \partial^\alpha\partial^\beta A_{\mu\alpha\nu\beta} , \tag{4.27}$$

$$\mathcal{J}_{\mu\nu\alpha\beta} = \frac{1}{4}W_{\mu\nu\alpha\beta} - C_{\mu\nu\alpha\beta} . \tag{4.28}$$

In the absence of the gauge field, the electric current is just the linearized Weyl tensor, and in the gauge-invariant version the C tensor is the same as in (4.15). In the linearized theory, the magnetic current is equal to the electric current, so we also have

$$\mathcal{K}_{\mu\nu\alpha\beta} = \frac{1}{4}W_{\mu\nu\alpha\beta} - C_{\mu\nu\alpha\beta} . \tag{4.29}$$

One can then check that the antisymmetric derivative of this current reproduces the anomaly (4.13), where we have

$$\mathcal{C}_{\mu\nu\rho\alpha\beta} = 3\mathcal{Y}^T_{[2,2,1]}\partial_\rho C_{\mu\nu\alpha\beta} . \tag{4.30}$$

Gauge-invariant interactions of the pseudo-linear type are introduced by including higher-order contractions of $\mathcal{K}$. Then, in the full theory $\mathcal{K}$ (and hence its anomaly) will remain unchanged, while the electric current $\mathcal{J}_{\mu\nu\alpha\beta}$ will be modified by the interactions.

4.2 Conformal gravity

We now turn to (linearized) conformal gravity. This theory shares many features with the conformal scalar example encountered in (3.3): both its magnetic current and electric gauge field will be governed by the same differential complex, and the mixed anomaly between conservation of the two symmetries will imply that the theory is non-unitary. Of course the non-unitarity of conformal

gravity is well known, but this perspective casts this fact as an inevitable consequence of symmetry, and indeed exposes the (higher-form) symmetries of conformal gravity itself. As a byproduct of our analysis, we elucidate the fate and structure of electric-magnetic duality for linearized conformal gravity in four spacetime dimensions. (See Appendix A for more details about (linearized) conformal gravity.)

Currents and anomalies: We start by defining the magnetic current in the same way as in linearized Einstein gravity (4.1). The index symmetries of $K_{\mu_1\mu_2\nu_1\nu_2}$ are identical and it fits into the same differential complex (4.2). The essential difference with the linearized GR case is that we take the gauge field $A_{\mu\nu\alpha\beta}$ to be part of this same differential complex,

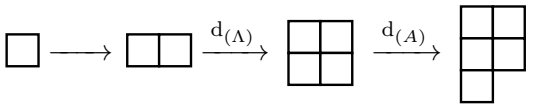

(4.31)

Here the relevant maps involved can be written explicitly as

$$\left(\mathrm{d}_{(\Lambda)}\Lambda\right)_{\mu\nu\alpha\beta} = 3\mathcal{Y}^T_{[2,2]}\,\partial_\mu\partial_\alpha\Lambda_{\nu\beta}\,, \tag{4.32}$$

$$\left(\mathrm{d}_{(A)}A\right)_{\rho\mu\nu\alpha\beta} = 6\mathcal{Y}^T_{[2,2,1]}\,\partial_\rho A_{\mu\nu\alpha\beta}\,. \tag{4.33}$$

In particular this implies that under a gauge transformation the gauge field transforms as

$$\delta A_{\mu\nu\alpha\beta} = \mathcal{Y}^T_{[2,2]}\,\partial_\mu\partial_\alpha\Lambda_{\nu\beta}, \tag{4.34}$$

and there is a gauge-invariant field strength

$$F_{\rho\mu\nu\alpha\beta} = \mathcal{Y}^T_{[2,2,1]}\,\partial_\rho A_{\mu\nu\alpha\beta}\,. \tag{4.35}$$

The fact that A has a gauge transformation involving two derivatives implies that the electric current that it couples to satisfies the double conservation condition

$$\partial_{\mu_1}\partial_{\nu_1}J^{\mu_1\mu_2\nu_1\nu_2} = 0\,. \tag{4.36}$$

The presence of the background gauge field A that sources the electric current J preserves this conservation condition, but causes K to satisfy the anomalous conservation equation

$$\mathcal{Y}^T_{[2,2,1]}\partial_\rho\mathcal{K}_{\mu_1\mu_2\nu_1\nu_2} = -F_{\rho\mu_1\mu_2\nu_1\nu_2}\,, \tag{4.37}$$

where F is the gauge-invariant field strength (4.35) built out of A. Notice that in this case the field strength has the right index symmetries to appear on the right hand side of the anomaly equation without needing to take derivatives. In this sense, conformal gravity is conceptually quite similar to the conformal scalar example discussed in Section 3.3.

Two-point function and spectrum: As in the other examples, the combined requirements of conservation of the electric current at all points, and the 't Hooft anomaly (4.37) entirely fixes the two-point functions between these currents to be

$$\begin{aligned}\langle J_{\mu_1\mu_2\mu_3\mu_4}K_{\nu_1\nu_2\nu_3\nu_4}\rangle = -\mathcal{P}\Bigg[&\frac{p_{\mu_1}p_{\alpha_1}\eta_{\nu_1\beta_1}}{p^4}\left(-6p_{\mu_2}p_{\beta_2}\eta_{\nu_2\alpha_2}+p^2\eta_{\mu_2\alpha_2}\eta_{\nu_2\beta_2}\right)\\&+\frac{3}{4}\eta_{\mu_1\alpha_1}\eta_{\mu_2\alpha_2}\eta_{\nu_1\beta_1}\eta_{\nu_2\beta_2}-\frac{3p_{\mu_1}p_{\alpha_1}\eta_{\mu_2\alpha_2}\eta_{\nu_1\beta_1}\eta_{\nu_2\beta_2}}{p^2}\\&+\frac{9(D-4)}{D-3}\frac{p_{\mu_1}p_{\mu_2}p_{\alpha_1}p_{\alpha_2}\eta_{\nu_1\beta_1}\eta_{\nu_2\beta_2}}{p^4}\Bigg]\,,\end{aligned} \tag{4.38}$$

where $\mathcal{P}$ is the same projector as in (4.16). Notice that this two point function has a p^{-4} pole. This pole cannot be reproduced by any unitary representation in the Källén–Lehmann decomposition of this correlator. We therefore conclude that any theory with this pattern of symmetries must necessarily be non-unitary. In the next section we will see that the EFT description of this physics is linearized conformal gravity, which is entirely consistent with the theory being non-unitary.

Effective field theory: We now want to see how we can reproduce the physics of this phase using effective field theory. Once again the magnetic current's conservation can be trivialized by writing the current as (4.18). We further notice that this current is again invariant under the shift symmetry (4.20). In this case, we must use a Maxwell-type action to realize the relevant symmetries. This Maxwell-type action is quadratic in the magnetic current K,

$$S = \frac{1}{4}\int \mathrm{d}^D x\, K_{\mu\nu\alpha\beta}K^{\mu\nu\alpha\beta}\,. \tag{4.39}$$

The action (4.39) is of course the action of linearized conformal gravity in a gauge in which the linearized Weyl symmetry is used to make $h_{\mu\nu}$ traceless, with K the linearized Weyl tensor. As in the Einstein gravity case, we could include higher-order interaction terms involving powers of the Weyl tensor. This would leave the magnetic current unchanged, but would modify the electric current.

In order to understand the structure of anomalies, we want to gauge the symmetry (4.20) by introducing a gauge field that couples to the electric current. We can construct a gauge-invariant action as (now writing $\mathcal{K}$ in terms of the Weyl tensor),

$$S = \frac{1}{4}\int \mathrm{d}^D x\, \big(W_{\mu\nu\alpha\beta} - A_{\mu\nu\alpha\beta}\big)\big(W^{\mu\nu\alpha\beta} - A^{\mu\nu\alpha\beta}\big)\,, \tag{4.40}$$

which is just the square of the gauge-invariant magnetic current,

$$\mathcal{K}_{\mu\nu\rho\sigma} = W_{\mu\nu\rho\sigma} - A_{\mu\nu\rho\sigma}\,. \tag{4.41}$$

This is invariant under the following gauge transformations of the fields,

$$\delta h_{\mu\nu} = \Lambda_{\mu\nu}\,, \tag{4.42}$$

$$\delta A_{\mu\nu\alpha\beta} = -3\mathcal{Y}^T_{[2,2]}\,\partial_\nu\partial_\beta\Lambda_{\mu\alpha}\,, \tag{4.43}$$

where $\Lambda_{\mu\nu}$ is a symmetric traceless gauge parameter. In the presence of $A_{\mu\nu\alpha\beta}$, the electric current that couples to A will be conserved, but the magnetic current now obeys the anomalous equation (4.37). So we see that this effective field theory precisely reproduces the structure of symmetries and anomalies that we want. If desired, we can incorporate interactions by adding higher powers of $\mathcal{K}$ to the action.

As anticipated, this effective field theory involves a higher-derivative action, and it is known to be non-unitary, consistent with our statement that the symmetries (4.36) and (4.37) cannot arise in a unitary EFT.

4.2.1 Charges

Here we discuss some conserved currents and charges that arise from the conserved electric current in conformal gravity. $W_{\mu\nu\alpha\beta}$ is a double conserved ($\partial^\nu\partial^\beta W_{\mu\nu\alpha\beta}=0$) traceless operator, with the symmetries of the Young diagram $\square\!\square$. From this we can construct 2-form conserved currents $J_{\mu\nu}[\xi]$ by contracting with a conformal killing vector ξ^μ satisfying the conformal Killing equation $\partial_{(\mu}\xi_{\mu)_T}=0$ as follows,

$$J_{\mu\nu}[\xi]=W_{\mu\nu\alpha\beta}\partial^\alpha\xi^\beta-2\partial^\alpha W_{\mu\nu\alpha\beta}\,\xi^\beta\,. \tag{4.44}$$

These currents are conserved: $\partial^\nu J_{\mu\nu}[\xi]=0$, as we show in the following inset.

Conservation of $J_{\mu\nu}[\xi]$: To see that $J_{\mu\nu}[\xi]$ defined in (4.44) is conserved, act with ∂^ν and use the fact that W is double conserved to give

$$\partial^\nu J_{\mu\nu}[\xi]=\partial^\nu W_{\mu\nu\alpha\beta}\partial^\alpha\xi^\beta+W_{\mu\nu\alpha\beta}\partial^\nu\partial^\alpha\xi^\beta-2\partial^\alpha W_{\mu\nu\alpha\beta}\,\partial^\nu\xi^\beta\,. \tag{4.45}$$

We can treat $\partial^\mu\xi^\nu$ as anti-symmetric—since the symmetric traceless part vanishes by the conformal Killing equation—and the trace part vanishes upon contracting with the traceless W. So, the second term, which has two derivatives on ξ, can be written as

$$W_{\mu\nu\alpha\beta}\partial^\nu\partial^\alpha\xi^\beta=-W_{\mu\beta\alpha\nu}\partial^\alpha\partial^\nu\xi^\beta\,, \tag{4.46}$$

which then vanishes due to the symmetry of the two derivatives and the antisymmetry of W. Now, looking at the two terms in (4.45) with one derivative on ξ, we can write them as

$$\partial^\nu W_{\mu\nu\alpha\beta}\partial^\alpha\xi^\beta-2\partial^\alpha W_{\mu\nu\alpha\beta}\,\partial^\nu\xi^\beta=\partial^\nu\left(W_{\mu\nu\alpha\beta}-2W_{\mu\alpha\nu\beta}\right)\partial^\alpha\xi^\beta\,. \tag{4.47}$$

Again treating $\partial^\mu\xi^\nu$ as anti-symmetric, we can manipulate this as follows,

$$\begin{aligned}\partial^\nu\left(W_{\mu\nu\alpha\beta}-2W_{\mu\alpha\nu\beta}\right)\partial^\alpha\xi^\beta&=\partial^\nu\left(W_{\mu\nu\alpha\beta}-W_{\mu\alpha\nu\beta}+W_{\mu\beta\nu\alpha}\right)\partial^\alpha\xi^\beta\\&=\partial^\nu\left(W_{\mu\nu\alpha\beta}+W_{\mu\alpha\beta\nu}+W_{\mu\beta\nu\alpha}\right)\partial^\alpha\xi^\beta\,,\end{aligned} \tag{4.48}$$

which now vanishes upon using the mixed-symmetry condition $W_{\mu[\nu\alpha\beta]}=0$.

Due to the fourth order nature of the conformal gravity field equations, solutions to Einstein gravity are also solutions to conformal gravity, but the converse is not true: it would be interesting to study linearized black hole solution in conformal gravity that are not also solutions of Einstein gravity [75, 76], to see if and how they carry these charges, and study their topology, along the lines of [29, 77, 78].

4.2.2 Electric-magnetic duality

In this section, we describe the electric-magnetic-like duality invariance of linearized conformal gravity in $D=4$, which is quite similar to the conformal scalar in $D=2$ discussed in Section 3.3. Recall that linearized conformal gravity is on-shell equivalent to the equations

$$\partial_{\mu_1}\partial_{\nu_1}J^{\mu_1\mu_2\nu_1\nu_2}=0\,, \tag{4.49}$$

$$\partial^{\mu_1}(*J)_{\mu_1\cdots\mu_{D-2}\nu_1\nu_2}=0\implies\mathcal{Y}^T_{[2,2,1]}\partial_{[\mu_1}J_{\mu_1\mu_3]\nu_1\nu_2}=0\,, \tag{4.50}$$

where the tensor $J_{\mu_1\mu_2\nu_1\nu_2}$ has the symmetries of the window-shaped tableau $\square\!\square$. The Hodge dual is defined with respect to the first two indices of J so that $(*J)_{\mu_1\cdots\mu_{D-2}\nu_1\nu_2} = \frac{1}{2}\epsilon_{\mu_1\mu_2\cdots\mu_{D-2}\alpha\beta}J^{\alpha\beta}{}_{\nu_1\nu_2}$. In general dimension $J_{\mu_1\mu_2\nu_1\nu_2}$ is nothing but the Weyl tensor, and we can use the fact that it fits into the complex (4.31) along with (4.50) write

$$J_{\mu_1\mu_2\nu_1\nu_2} = \mathcal{Y}^T_{[2,2]}\,\partial_{\mu_1}\partial_{\nu_1}h_{\mu_2\nu_2}\,, \tag{4.51}$$

so that (4.49) is the wave equation satisfied by the conformal graviton (A.22).

In $D = 4$, the equation (4.50) is trivially satisfied, and so the equation (4.49) is not sufficient to completely fix the theory. In this case, we have to additionally impose

$$\partial^{\mu_1}\partial^{\nu_1}(*J)_{\mu_1\mu_2\nu_1\nu_2} = 0\,. \tag{4.52}$$

The equations (4.49) and (4.52) are sufficient to fix the two-point function of the current to be that of conformal gravity. We can also reproduce the equations of motion by noting that we can equivalently write this equation as

$$\partial_{[\mu_1}\partial^{\nu_1}J_{\mu_1\mu_3]\nu_1\nu_2} = 0\,. \tag{4.53}$$

Then, the fact that the mixed-symmetry tensor appearing in this equation fits into the complex (3.32) implies that we can write

$$\partial^{\nu_1}J_{\mu_1\mu_2\nu_1\nu_2} = \partial_{[\mu_1}S_{\mu_2]\nu_2}\,, \tag{4.54}$$

where S is a symmetric tensor. We can also use the trivial equation (4.50) to deduce that

$$J_{\mu_1\mu_2\nu_1\nu_2} = \mathcal{Y}^T_{[2,2]}\,\partial_{\mu_1}\partial_{\nu_1}h_{\mu_2\nu_2}\,. \tag{4.55}$$

Combining these equations, we find that

$$S_{\mu\nu} = -2\Box h_{\mu\nu} + 2\partial^\alpha\partial_{(\mu}h_{\nu)\alpha}\,. \tag{4.56}$$

Then, applying (4.49), we find the linearized wave equation of conformal gravity. All together, we see that in $D = 4$, linearized conformal gravity is equivalent to the two equations

$$\partial_{\mu_1}\partial_{\nu_1}J^{\mu_1\mu_2\nu_1\nu_2} = 0\,, \tag{4.57}$$

$$\partial_{\mu_1}\partial_{\nu_1}(*J)^{\mu_1\mu_2\nu_1\nu_2} = 0\,, \tag{4.58}$$

which are clearly Hodge duals of each other. The same conclusion was reached by [79] via a slightly different chain of reasoning.[18] As in the scalar case, the anomaly appearing in (4.58) at coincident points (which we have not written explicitly) is necessary to fully fix the normalization of the two-point function.

[18] See [48, 55] for discussions of the duality-invariant formulation of linearized Einstein gravity.

5 Conclusions

We have explored the properties of relativistic gapless phases defined by a pair of generalized conserved currents with a mixed anomaly between them. We have given a unified description of these systems, and have considered several examples, both old and new, and shown how they fit into the general framework. Perhaps the most conceptually nontrivial aspect of these examples is that some current and anomaly structures cannot possibly arise in a unitary (Lorentzian) quantum field theory: these symmetries are impossible.

Along the way, we elucidated the structure of symmetries in conformal gravity, giving a definition of the linearized theory in terms of higher-form symmetries. This theory is one with impossible symmetries, reflecting the well-known fact that conformal gravity is non-unitary. We have also considered some aspects of the conserved charges in this theory, and elucidated some aspects of the electric-magnetic duality of linear conformal gravity. A similar construction should exist for the massless higher spin fields described by the Fronsdal action [80], as well as the Fradkin–Tseytlin fields [81, 82], which are higher-spin generalizations of linearized conformal gravity, and would give a new perspective on these theories. In these cases, there is a generalized Weyl tensor satisfying conservation equations whose anomalies should characterize the theory, and give an interpretation of each massless high spin as a Goldstone boson.

A number of questions are raised by this construction. Philosophically, one could ask why some symmetries are impossible, and whether we could predict a priori when currents are incompatible. One avenue to further elucidate this structure would be to connect these statements to more familiar theorems that forbid the presence of certain conserved currents: either the Weinberg–Witten [83, 84] or Maldacena–Zhiboedov [85] theorems. By invoking standard unitarity, we had in mind the relativistic setting, where the constraints of Lorentz invariance imply a certain rigidity, but for condensed matter applications, it would be useful to relax this assumption and study whether these patterns of symmetries can be realized by physical systems that are interpreted as statistical ensembles (i.e. as Euclidean field theories). In any setting, it would be interesting to understand if there is a more abstract and general characterization of impossible symmetries.

There is a complementary perspective on impossible symmetries that comes from recent developments in the study of positivity bounds. By studying scattering amplitudes away from the forward limit, it is possible to obtain two-sided bounds on the Wilson coefficients of EFTs [86–88]. One way of phrasing the lesson is that large hierarchies in dimensionless parameters in an EFT usually cannot descend from a standard Lorentz invariant UV completion. As a concrete example, scalar field theories with amplitudes that are parametrically softer than E^2 in the forward limit cannot arise from such a completion. In particular, this rules out models of galileons [62] arising in this way. This is, in a sense, another statement about "impossible" symmetries, as the galileon realizes a particular low-energy symmetry which is responsible for the softness of its amplitudes. It would be very interesting if one could understand these violations of positivity by using the extended operators or higher-form currents present in the theory of a galileon, or in more general EFTs.

We are just beginning to understand the interplay between generalized symmetries and the structure of EFT. A number of novel and interesting phenomena have already been uncovered, and we expect that there is a wealth of additional insights to be gained.

Acknowledgements: We would like to thank Clifford Cheung and Diego Hofman for helpful discussions. KH acknowledges support from DOE grant DE-SC0009946. AJ is supported in part by DOE (HEP) Award DE-SC0009924. GM is supported in part by the Simons Foundation grant 488649 (Simons Collaboration on the Nonperturbative Bootstrap) and the Swiss National Science Foundation through the project 200020 197160 and through the National Centre of Competence in Research SwissMAP. GM also acknowledges support from NSF grant PHY-1748958 for participation in a KITP workshop. Part of this work was performed in part at the Aspen Center for Physics, which is supported by NSF grant PHY-2210452.

A Conformal gravity

Here we review some aspects of both nonlinear and linearized conformal gravity that are useful in the main text.

A.1 Nonlinear conformal gravity

We begin by considering nonlinear Weyl-squared gravity. The action of this theory is given by[19]

$$S_{\mathrm{W}^2} = -\frac{1}{8}\int \mathrm{d}^D x\sqrt{g}\, W_{\mu\nu\rho\sigma}W^{\mu\nu\rho\sigma}\,, \tag{A.2}$$

where $W_{\mu\nu\rho\sigma}$ is the Weyl tensor, which is the traceless part of the Riemann tensor,

$$\begin{aligned} W_{\mu\nu\rho\sigma} &= R_{\mu\nu\rho\sigma} - \frac{2}{D-2}\left(g_{\mu[\rho}R_{\sigma]\nu} - \eta_{\nu[\rho}R_{\sigma]\mu}\right) + \frac{2}{(D-1)(D-2)}\eta_{\mu[\rho}\eta_{\sigma]\nu}R \\ &= R_{\mu\nu\rho\sigma} - 2(g_{\mu[\rho}S_{\sigma]\nu} - g_{\nu[\rho}S_{\sigma]\mu})\,. \end{aligned} \tag{A.3}$$

In the second line, we have expressed it in terms of the Schouten tensor, which is defined as

$$S_{\mu\nu} = \frac{1}{D-2}\left(R_{\mu\nu} - \frac{1}{2(D-1)}g_{\mu\nu}R\right)\,. \tag{A.4}$$

The Weyl tensor shares the same index symmetries as the Riemann tensor, $W_{\mu\nu\rho\sigma} = -W_{\nu\mu\rho\sigma} = -W_{\mu\nu\sigma\rho} = W_{\rho\sigma\mu\nu}$, and the algebraic Bianchi identity $W_{[\mu\nu\rho]\sigma} = 0$, and it is completely traceless i.e., it has the symmetries of the traceless $[2,2]$ tableau $\begin{array}{|c|c|}\hline \mu & \sigma \\ \hline \nu & \rho \\ \hline \end{array}$.

The divergence of the Weyl tensor can be written as

$$\nabla^\mu W_{\mu\nu\rho\sigma} = -\frac{(D-3)}{(D-2)}C_{\nu\rho\sigma}\,, \tag{A.5}$$

where $C_{\nu\rho\sigma}$ is the Cotton tensor, which can be written as

$$C_{\nu\rho\sigma} = 2(D-2)\nabla_{[\sigma}S_{\rho]\nu} = -2\nabla_{[\rho}R_{\sigma]\nu} - \frac{1}{D-1}g_{\nu[\rho}\nabla_{\sigma]}R\,. \tag{A.6}$$

[19] Given the definition of the Weyl tensor, this action can equivalently be written in terms of the Riemann tensor as

$$S_{W^2} = -\frac{1}{8}\int \mathrm{d}^D x\sqrt{g}\left(R_{\mu\nu\alpha\beta}R^{\mu\nu\alpha\beta} - \frac{4}{D-2}R_{\mu\nu}R^{\mu\nu} + \frac{2}{(D-1)(D-2)}R^2\right)\,. \tag{A.1}$$

The Cotton tensor is fully traceless and has the symmetry of a $[2,1]$ tableau $\begin{array}{|c|c|}\hline \rho & \nu \\ \hline \sigma \\ \cline{1-1}\end{array}$.

The Weyl tensor with one index raised is invariant under Weyl transformations, that is, if we define

$$g_{\mu\nu} = \Omega^2(x)\tilde{g}_{\mu\nu}\,, \tag{A.7}$$

then the Weyl tensors of these two metrics are equivalent,

$$W^{\mu}{}_{\nu\alpha\beta} = \tilde{W}^{\mu}{}_{\nu\alpha\beta}\,. \tag{A.8}$$

This implies that in $D = 4$, the action (A.2) is invariant under Weyl transformations $\delta g_{\mu\nu} \mapsto \Omega^2(x) g_{\mu\nu}$ because the transformation of the inverse metrics needed to contract indices cancel against the measure. Taking $\Omega(x) = e^{\sigma(x)}$, infinitesimally the Weyl transformation reads

$$\delta g_{\mu\nu} = 2\sigma(x) g_{\mu\nu}\,. \tag{A.9}$$

Due to this Weyl invariance, In $D = 4$, we call (A.2) conformal gravity. In other dimensions, the action (A.2) is *not* Weyl invariant.[20]

The equation of motion derived from the action (A.2) in $D = 4$ is $B_{\mu\nu} = 0$, where B is the Bach tensor[21]

$$B_{\mu\nu} \equiv \frac{1}{D-3}\left(\nabla^\rho\nabla^\sigma + \frac{D-3}{D-2}R^{\rho\sigma}\right) W_{\rho\mu\sigma\nu} \tag{A.13}$$

$$= S^{\alpha\beta}W_{\mu\alpha\nu\beta} + \nabla^2 S_{\mu\nu} - \nabla^\rho\nabla_{(\mu}S_{\nu)\rho}. \tag{A.14}$$

The structure of nonlinear conformal gravity is quite interesting: any maximally symmetric spacetime is a solution, and the propagating degrees of freedom around these solutions form an irreducible

[20] In higher dimensions, there are multiple independent Weyl invariants [89], so it is not immediately obvious what one should mean by conformal gravity for $D > 4$. For D even, there is a natural candidate; it is a D-derivative theory that when expanded around (A)dS contains a massless, partially massless, and $\frac{D-4}{2}$ massive, spin-2 degrees of freedom (see e.g., [90]). Its linearized action is the linearization of $\sim \int \mathrm{d}^D x\, W_{\mu\nu\alpha\beta}\Box^{\frac{D-4}{2}}W^{\mu\nu\alpha\beta}$, which is a spin 2 Fradkin–Tseytlin field [81, 82].

[21] Note that in the literature, there exist different definitions for the Bach tensor in general dimension $D > 4$. One choice is to define the Bach tensor as the tensor that is set to zero by the equations of motion derived from the action (A.2),

$$\overline{B}_{\mu\nu} \equiv -2\frac{\delta S_{W^2}}{\delta g^{\mu\nu}} = -\nabla^{(\rho}\nabla^{\sigma)}W_{\mu\rho\nu\sigma} - \frac{1}{2}W_\mu{}^{\rho\sigma\alpha}W_{\nu\rho\sigma\alpha} - \frac{1}{D-2}R^{\rho\sigma}W_{\mu\rho\nu\sigma} + \frac{1}{8}g_{\mu\nu}W^2_{\mu\nu\rho\sigma}\,. \tag{A.10}$$

This tensor is divergenceless ($\nabla^\mu\overline{B}_{\mu\nu} = 0$) in any dimension, as required by diffeomorphism invariance, but only traceless in $D = 4$.

Another commonly used definition of the Bach tensor in general dimension is $B_{\mu\nu}$ that we presented in the main text in equation (A.14) and (A.13). The tensor $B_{\mu\nu}$ in (A.13) is now traceless in any dimension, but its divergence is

$$\nabla^\mu B_{\mu\nu} = (D-4)S^{\alpha\beta}\left(\nabla_\nu S_{\alpha\beta} - \nabla_\alpha S_{\nu\beta}\right)\,, \tag{A.11}$$

which vanishes in $D = 4$.

These two definitions coincide in $D = 4$ (in showing this, it is useful to add the variation of the Gauss–Bonnet term, which vanishes in $D = 4$). Moreover, in $D = 4$ the Bach tensor is Weyl covariant,

$$\delta B_{\mu\nu} = 2\sigma B_{\mu\nu}\,, \tag{A.12}$$

under infinitesimal Weyl transformations $\delta g_{\mu\nu} = 2\sigma g_{\mu\nu}$.

SO(2, 4) representation. Around flat space, this representation is a (non-unitary) Poincaré representation that cannot be split apart. Around de Sitter or Anti-de Sitter space, the representation can be split into a pair of (A)dS representations, which are that of a massless spin-2, and a partially massless (PM) spin-2 [39, 40]. On AdS, the PM representation is by itself non-unitary, but on de Sitter space, the reason that conformal gravity is not unitary is that there is a relative minus sign between the kinetic terms of the massless spin-2 and PM spin-2 degrees of freedom. It is possible to project out the PM part of the representation, and obtain the wavefunction in Einstein gravity from that of conformal gravity [39, 91].

A.2 Linearized conformal gravity

We now discuss some of the features of linearized conformal gravity. This theory can be straightforwardly obtained from the nonlinear Weyl-squared theory (A.2) by linearizing around flat space,

$$g_{\mu\nu} = \eta_{\mu\nu} + 2h_{\mu\nu}\,. \tag{A.15}$$

The linearized Riemann and Schouten tensors are given explicitly by

$$R^{(L)}_{\mu\nu\rho\sigma} = -\partial_\mu\partial_\rho h_{\nu\sigma} - \partial_\nu\partial_\sigma h_{\mu\rho} + \partial_\mu\partial_\sigma h_{\nu\rho} + \partial_\nu\partial_\rho h_{\mu\sigma}\,, \tag{A.16}$$

$$S^{(L)}_{\mu\nu} = \frac{1}{D-2}\left(-\partial_\mu\partial_\nu h - \Box h_{\mu\nu} + 2\partial^\alpha\partial_{(\mu}h_{\nu)\alpha}\right) - \eta_{\mu\nu}\frac{1}{D-1}\left(2\partial_\alpha\partial_\beta h^{\alpha\beta} - \Box h\right)\,, \tag{A.17}$$

and the linearized Weyl tensor is:

$$W^{(L)}_{\mu\nu\rho\sigma} = R^{(L)}_{\mu\nu\rho\sigma} - 2(\eta_{\mu[\rho}S^{(L)}_{\sigma]\nu} - \eta_{\nu[\rho}S^{(L)}_{\sigma]\mu})\,. \tag{A.18}$$

In contrast to the nonlinear theory, the action

$$S = \frac{1}{4}\int \mathrm{d}^D x\, W^{(L)}_{\mu\nu\rho\sigma}W^{\mu\nu\rho\sigma}_{(L)}\,, \tag{A.19}$$

is invariant under both linearized diffeomorphisms and linearized Weyl transformations in *all* dimensions:

$$\delta h_{\mu\nu} = \partial_\mu\xi_\nu + \partial_\nu\xi_\mu\,, \tag{A.20}$$

$$\delta h_{\mu\nu} = \Omega(x)\eta_{\mu\nu}\,, \tag{A.21}$$

and so it makes sense to call this linearized conformal gravity in any dimension. In fact, the linearized Weyl tensor itself is gauge invariant under both of these transformations. Much like in Einstein gravity, an important difference between the linear and nonlinear theories is that the linear theory has gauge-invariant local operators. The linearized Weyl tensor is the basic such operator (see [92–94] for formalisms that reveal the operator spectrum of linear conformal gravity).

The equation of motion following from (A.19) is

$$\partial_\mu\partial_\rho W^{\mu\nu\rho\sigma}_{(L)} = 0\,. \tag{A.22}$$

Because of the relation (A.23), which at the linearized level reads

$$\partial^{\mu} W^{(L)}_{\mu\nu\rho\sigma} = -\frac{(D-3)}{(D-2)} C^{(L)}_{\nu\rho\sigma} \,, \tag{A.23}$$

where the linearized Cotton tensor is

$$C^{(L)}_{\nu\rho\sigma} = 2(D-2)\partial_{[\sigma} S^{(L)}_{\rho]\nu} \,, \tag{A.24}$$

we can also write (A.22) as the vanishing of the divergence of the linearized Cotton tensor

$$\partial^{\rho} C^{(L)}_{\nu\rho\sigma} = 0 \,. \tag{A.25}$$

Much like Einstein gravity, in $D = 4$ linearized conformal gravity is electric-magnetic duality invariant, as we discussed in Section 4.2.

It is possible to include irrelevant interaction terms in this effective field theory, paralleling the EFT of linearized Einstein gravity. Any interaction terms built out of the linearized Weyl tensor will preserve all the symmetries of the theory. As we discuss in Section 4.2, we can think of this EFT as being the gapless phase mandated by the anomaly (4.37), or equivalent we can think of it as the Goldstone theory for the breaking of the electric 1-form shift symmetry of the conformal graviton.

B Spectral decompositions

Spectral decompositions of the current-current two-point functions play an important role in the main text. In particular, by analyzing the properties of the two-point functions that are fixed by the symmetry structure, we infer properties of the spectrum of the theory. In this appendix we provide some additional details about the Källén–Lehmann decomposition, particularly in theories where the two-point functions indicates that they are not unitary. The overall strategy mirrors that of [23, 29], where the decomposition of the current-current two-point function is used to discern the spectrum of the theory.

In this appendix we focus in particular on the case of the conformal scalar and illustrate how the spectral decomposition can be used to infer that the theory is not unitary. The general lessons can be abstracted straightforwardly to cases with spin.

B.1 Projectors

This first step involves rewriting the two-point function (3.38) in terms of projectors that split up the various components of the two-point function. These projectors are defined in terms of the simpler objects:

$$\pi^{(0)}_{\mu\nu} = \frac{p_\mu p_\nu}{p^2}\,, \qquad \pi^{(1)}_{\mu\nu} = \eta_{\mu\nu} - \frac{p_\mu p_\nu}{p^2}\,. \tag{B.1}$$

A basis of projectors is given by

$$\Pi^{(0)}_{\mu_1\mu_2\nu_1\nu_2} = \frac{D}{D-1}\left(\pi^{(0)}_{\mu_1\mu_2} - \frac{\eta_{\mu_1\mu_2}}{D}\right)\left(\pi^{(0)}_{\nu_1\nu_2} - \frac{\eta_{\nu_1\nu_2}}{D}\right)\,, \tag{B.2}$$

$$\Pi^{(1)}_{\mu_1\mu_2\nu_1\nu_2} = \frac{1}{2}\left(\pi^{(0)}_{\mu_1\nu_1}\pi^{(1)}_{\mu_2\nu_2} + \pi^{(0)}_{\mu_1\nu_2}\pi^{(1)}_{\mu_2\nu_1} + \pi^{(1)}_{\mu_1\nu_1}\pi^{(0)}_{\mu_2\nu_2} + \pi^{(1)}_{\mu_1\nu_2}\pi^{(0)}_{\mu_2\nu_1}\right)\,, \tag{B.3}$$

$$\Pi^{(2)}_{\mu_1\mu_2\nu_1\nu_2} = \frac{1}{2}\left(\pi^{(1)}_{\mu_1\nu_1}\pi^{(1)}_{\mu_2\nu_2} + \pi^{(1)}_{\mu_1\nu_2}\pi^{(1)}_{\mu_2\nu_1} - \frac{1}{D-1}\pi^{(1)}_{\mu_1\mu_2}\pi^{(1)}_{\nu_1\nu_2}\right)\,, \tag{B.4}$$

which satisfy the orthonormality conditions

$$\Pi^{(i)}_{\mu_1\mu_2\rho_1\rho_2}\Pi^{(j)\rho_1\rho_2}{}_{\nu_1\nu_2} = \delta^{ij}\Pi^{(i)}_{\mu_1\mu_2\nu_1\nu_2}\,, \tag{B.5}$$

with $i, j = 0, 1, 2$, and the completeness relation

$$\Pi^{(0)}_{\mu_1\mu_2\rho_1\rho_2} + \Pi^{(1)}_{\mu_1\mu_2\rho_1\rho_2} + \Pi^{(2)}_{\mu_1\mu_2\rho_1\rho_2} = \frac{1}{2}\left(\eta_{\nu_1\mu_2}\eta_{\mu_1\nu_2} + \eta_{\mu_1\nu_1}\eta_{\mu_2\nu_2}\right) - \frac{1}{D}\eta_{\nu_1\nu_2}\eta_{\mu_1\mu_2}\,, \tag{B.6}$$

where the tensor on the right-hand side is the identity on the space of symmetric traceless tensors. We can think of $\Pi^{(i)}$ as the projector onto the spin-i representation within this space.

B.2 Spectral decomposition

We now argue that the conformal scalar theory is non-unitary using the spectral decomposition of the two-point function (3.38). This correlator is easily rewritten in terms of the projectors (B.2)–(B.4). This yields

$$\langle J_{\mu\nu}K_{\rho\sigma}\rangle = -\left(\Pi^{(1)}_{\mu\nu\rho\sigma} + \Pi^{(2)}_{\mu\nu\rho\sigma}\right)\,. \tag{B.7}$$

Our starting point is the spectral decomposition for a correlator of two symmetric traceless tensors

$$\langle J_{\mu\nu} K_{\rho\sigma} \rangle = \int_0^\infty \mathrm{d}s \, \frac{s}{p^2 + s} \left(\rho_0(s) \tilde{\Pi}^{(0)}_{\mu\nu\rho\sigma} + \rho_1(s) \tilde{\Pi}^{(1)}_{\mu\nu\rho\sigma} + \rho_2(s) \tilde{\Pi}^{(2)}_{\mu\nu\rho\sigma} \right) . \tag{B.8}$$

Here $\rho_j(s)$ are the spin j components of the spectral density (the only massless representation that can couple to a symmetric conserved current is a scalar, so the spectral densities of the spin-1 and spin-2 states must go to zero as $p^2 \to 0$). Implicit in the spectral decompostion (B.8) is the assumption that the representations contributing to the correlator have propagators that go like p^{-2} [95], which is satisfied by all unitary Poincaré representations. As usual [29], the tensors $\tilde{\Pi}^{(i)}$ that appear in (B.8) are not quite the projectors (B.2)–(B.4), but are instead off-shell versions of the projectors that are obtained by replacing $p^2 \to -s$ in (B.2)–(B.4). Hence, they depend on s and reduce to the projectors when $s \to -p^2$.

In order to perform the spectral decomposition, the goal is to match (B.8) to (B.7), and solve for the three spectral densities ρ_j. In this case, there is no choice of the $\rho_j(s)$ that works. At its core, this is because we are trying to match a two-point function that goes like p^{-4} with a sum of propagators that go like p^{-2}. Since all unitary representations have propagators that scale like this, this is already enough to see that the theory is not unitary. Of course, we could generalize the Källén–Lehmann representation to allow for totally generic behavior of the Feynman propagator of the exchanged representations (and therefore allow all possible non-unitary irreducible representations to be exchanged as well). In this case it would be possible to match the two point function and extract the spectrum of the theory. It would actually be quite interesting to do this, as the properties of non-unitary Poincaré representations are not particularly well understood. But for our purposes, it suffices to conclude that there must be non-unitary representations in the theory.

Not that the structure of anomalies completely fixes the nonlocal part of the current-current two-point function, so the structure of these poles is intrinsic to the anomaly. There is an ambiguity about where to put the anomaly in a conservation equation, but this freedom only changes the contact terms appearing in the correlator, i.e. the terms analytic in p^μ, and so cannot modify the structure of the poles.

Note that the essential tension has nothing to do with the spin of the fields involved, it was merely the difficulty of matching a two-point function that scales like p^{-4} to a spectral decomposition where each of the constituents have a propagator that scales like p^{-2}. These same ingredients are present in the conformal gravity case. There, the two-point function scales like p^{-4}, and it is similarly impossible to match it to the Källén–Lehmann decomposition under the assumption that all of the states have ordinary p^{-2} propagators (which all unitary representations do). We can therefore conclude that the theory is non-unitary also in that case.

References

[1] A. Kapustin and R. Thorngren, "Higher symmetry and gapped phases of gauge theories," arXiv:1309.4721 [hep-th].

[2] D. Gaiotto, A. Kapustin, N. Seiberg, and B. Willett, "Generalized Global Symmetries," *JHEP* **02** (2015) 172, arXiv:1412.5148 [hep-th].

[3] C. Córdova, T. T. Dumitrescu, and K. Intriligator, "Exploring 2-Group Global Symmetries," *JHEP* **02** (2019) 184, arXiv:1802.04790 [hep-th].

[4] F. Benini, C. Córdova, and P.-S. Hsin, "On 2-Group Global Symmetries and their Anomalies," *JHEP* **03** (2019) 118, arXiv:1803.09336 [hep-th].

[5] E. P. Verlinde, "Fusion Rules and Modular Transformations in 2D Conformal Field Theory," *Nucl. Phys. B* **300** (1988) 360–376.

[6] C.-M. Chang, Y.-H. Lin, S.-H. Shao, Y. Wang, and X. Yin, "Topological Defect Lines and Renormalization Group Flows in Two Dimensions," *JHEP* **01** (2019) 026, arXiv:1802.04445 [hep-th].

[7] Z. Komargodski, K. Ohmori, K. Roumpedakis, and S. Seifnashri, "Symmetries and strings of adjoint QCD_2," *JHEP* **03** (2021) 103, arXiv:2008.07567 [hep-th].

[8] Y. Choi, C. Cordova, P.-S. Hsin, H. T. Lam, and S.-H. Shao, "Noninvertible duality defects in 3+1 dimensions," *Phys. Rev. D* **105** no. 12, (2022) 125016, arXiv:2111.01139 [hep-th].

[9] J. Kaidi, K. Ohmori, and Y. Zheng, "Kramers-Wannier-like Duality Defects in (3+1)D Gauge Theories," *Phys. Rev. Lett.* **128** no. 11, (2022) 111601, arXiv:2111.01141 [hep-th].

[10] I. n. García Etxebarria and N. Iqbal, "A Goldstone theorem for continuous non-invertible symmetries," *JHEP* **09** (2023) 145, arXiv:2211.09570 [hep-th].

[11] S.-H. Shao, "What's Done Cannot Be Undone: TASI Lectures on Non-Invertible Symmetry," arXiv:2308.00747 [hep-th].

[12] Y. Choi, H. T. Lam, and S.-H. Shao, "Noninvertible Global Symmetries in the Standard Model," *Phys. Rev. Lett.* **129** no. 16, (2022) 161601, arXiv:2205.05086 [hep-th].

[13] C. Cordova and K. Ohmori, "Noninvertible Chiral Symmetry and Exponential Hierarchies," *Phys. Rev. X* **13** no. 1, (2023) 011034, arXiv:2205.06243 [hep-th].

[14] C. Cordova, S. Hong, S. Koren, and K. Ohmori, "Neutrino Masses from Generalized Symmetry Breaking," arXiv:2211.07639 [hep-ph].

[15] C. Cordova, S. Hong, and L.-T. Wang, "Axion Domain Walls, Small Instantons, and Non-Invertible Symmetry Breaking," arXiv:2309.05636 [hep-ph].

[16] Y. Choi, M. Forslund, H. T. Lam, and S.-H. Shao, "Quantization of Axion-Gauge Couplings and Non-Invertible Higher Symmetries," arXiv:2309.03937 [hep-ph].

[17] M. Reece, "Axion-gauge coupling quantization with a twist," *JHEP* **10** (2023) 116, arXiv:2309.03939 [hep-ph].

[18] P. Agrawal and A. Platschorre, "The Monodromic Axion-Photon Coupling," arXiv:2309.03934 [hep-th].

[19] S. Grozdanov, D. M. Hofman, and N. Iqbal, "Generalized global symmetries and dissipative magnetohydrodynamics," *Phys. Rev. D* **95** no. 9, (2017) 096003, arXiv:1610.07392 [hep-th].

[20] E. Lake, "Higher-form symmetries and spontaneous symmetry breaking," arXiv:1802.07747 [hep-th].

[21] D. M. Hofman and N. Iqbal, "Goldstone modes and photonization for higher form symmetries," *SciPost Phys.* **6** no. 1, (2019) 006, arXiv:1802.09512 [hep-th].

[22] P. Glorioso and D. T. Son, "Effective field theory of magnetohydrodynamics from generalized global symmetries," arXiv:1811.04879 [hep-th].

[23] L. V. Delacrétaz, D. M. Hofman, and G. Mathys, "Superfluids as Higher-form Anomalies," *SciPost Phys.* **8** (2020) 047, arXiv:1908.06977 [hep-th].

[24] R. Thorngren, T. Rakovszky, R. Verresen, and A. Vishwanath, "Higgs Condensates are Symmetry-Protected Topological Phases: II. $U(1)$ Gauge Theory and Superconductors," arXiv:2303.08136 [cond-mat.str-el].

[25] J. McGreevy, "Generalized Symmetries in Condensed Matter," arXiv:2204.03045 [cond-mat.str-el].

[26] S. Vardhan, S. Grozdanov, S. Leutheusser, and H. Liu, "A new formulation of strong-field magnetohydrodynamics for neutron stars," arXiv:2207.01636 [astro-ph.HE].

[27] M. J. Landry and H. Liu, "A systematic formulation of chiral anomalous magnetohydrodynamics," arXiv:2212.09757 [hep-ph].

[28] A. Das, N. Iqbal, and N. Poovuttikul, "Towards an effective action for chiral magnetohydrodynamics," arXiv:2212.09787 [hep-th].

[29] K. Hinterbichler, D. M. Hofman, A. Joyce, and G. Mathys, "Gravity as a gapless phase and biform symmetries," *JHEP* **02** (2023) 151, arXiv:2205.12272 [hep-th].

[30] V. Benedetti, P. Bueno, and J. M. Magan, "Generalized Symmetries for Generalized Gravitons," *Phys. Rev. Lett.* **131** no. 11, (2023) 111603, arXiv:2305.13361 [hep-th].

[31] V. Benedetti, H. Casini, and J. M. Magan, "Generalized Symmetries of the Graviton," arXiv:2111.12089 [hep-th].

[32] C. M. Hull, "Magnetic Charges for the Graviton," arXiv:2310.18441 [hep-th].

[33] A. Adams, N. Arkani-Hamed, S. Dubovsky, A. Nicolis, and R. Rattazzi, "Causality, analyticity and an IR obstruction to UV completion," *JHEP* **10** (2006) 014, arXiv:hep-th/0602178.

[34] E. Palti, "The Swampland: Introduction and Review," *Fortsch. Phys.* **67** no. 6, (2019) 1900037, arXiv:1903.06239 [hep-th].

[35] H. Weyl, "Gravitation and electricity," *Sitzungsber. Preuss. Akad. Wiss. Berlin (Math. Phys.)* **1918** (1918) 465.

[36] H. Weyl, "A New Extension of Relativity Theory," *Annalen Phys.* **59** (1919) 101–133.

[37] H. Weyl, "Reine Infinitesimalgeometrie," *Math. Z.* **2** no. 3-4, (1918) 384–411.

[38] R. Bach, "Zur Weylschen Relativitätstheorie und der Weylschen Erweiterung des Krümmungstensorbegriffs," *Math. Z.* **9** no. 1, (1921) 110–135.

[39] J. Maldacena, "Einstein Gravity from Conformal Gravity," arXiv:1105.5632 [hep-th].

[40] S. Deser, E. Joung, and A. Waldron, "Partial Masslessness and Conformal Gravity," *J. Phys. A* **46** (2013) 214019, arXiv:1208.1307 [hep-th].

[41] S. Deser, E. Joung, and A. Waldron, "Gravitational- and Self- Coupling of Partially Massless Spin 2," *Phys. Rev. D* **86** (2012) 104004, arXiv:1301.4181 [hep-th].

[42] E. Joung, W. Li, and M. Taronna, "No-Go Theorems for Unitary and Interacting Partially Massless Spin-Two Fields," *Phys. Rev. Lett.* **113** (2014) 091101, arXiv:1406.2335 [hep-th].

[43] S. M. Carroll, *Spacetime and Geometry: An Introduction to General Relativity*. Cambridge University Press, 7, 2019.

[44] Y. Pano, A. Puhm, and E. Trevisani, "Symmetries in Celestial CFT$_d$," *JHEP* **07** (2023) 076, arXiv:2302.10222 [hep-th].

[45] P. J. Olver, "Differential hyperforms i," *Univ. of Minnesota report* (1982) 82–101.

[46] M. Dubois-Violette and M. Henneaux, "Generalized cohomology for irreducible tensor fields of mixed Young symmetry type," *Lett. Math. Phys.* **49** (1999) 245–252, arXiv:math/9907135.

[47] M. Dubois-Violette and M. Henneaux, "Tensor fields of mixed Young symmetry type and N complexes," *Commun. Math. Phys.* **226** (2002) 393–418, arXiv:math/0110088.

[48] X. Bekaert and N. Boulanger, "Tensor gauge fields in arbitrary representations of GL(D,R): Duality and Poincare lemma," *Commun. Math. Phys.* **245** (2004) 27–67, arXiv:hep-th/0208058.

[49] A. Čap, J. Slovák, and V. Souček, "Bernstein-gelfand-gelfand sequences," *Annals of Mathematics* **154** no. 1, (2001) 97–113, arXiv:math/0001164 [math.DG]. http://www.jstor.org/stable/3062111.

[50] M. G. Eastwood, "Variations on the de rham complex," *Notices AMS* **46** (1999) 1368–1376.

[51] D. N. Arnold and K. Hu, "Complexes from complexes," *Foundations of Computational Mathematics* **21** (2020) 1739 – 1774. https://api.semanticscholar.org/CorpusID:218889263.

[52] E. D. Skvortsov and M. A. Vasiliev, "Geometric formulation for partially massless fields," *Nucl. Phys. B* **756** (2006) 117–147, arXiv:hep-th/0601095.

[53] E. D. Skvortsov, "Gauge fields in (A)dS(d) and Connections of its symmetry algebra," *J. Phys. A* **42** (2009) 385401, arXiv:0904.2919 [hep-th].

[54] K. Hinterbichler, "Manifest Duality Invariance for the Partially Massless Graviton," *Phys. Rev. D* **91** no. 2, (2015) 026008, arXiv:1409.3565 [hep-th].

[55] K. Hinterbichler and A. Joyce, "Manifest Duality for Partially Massless Higher Spins," *JHEP* **09** (2016) 141, arXiv:1608.04385 [hep-th].

[56] W. A. Bardeen and B. Zumino, "Consistent and Covariant Anomalies in Gauge and Gravitational Theories," *Nucl. Phys. B* **244** (1984) 421–453.

[57] G. Goon, K. Hinterbichler, A. Joyce, and M. Trodden, "Galileons as Wess-Zumino Terms," *JHEP* **06** (2012) 004, arXiv:1203.3191 [hep-th].

[58] K. Hinterbichler and A. Joyce, "Goldstones with Extended Shift Symmetries," *Int. J. Mod. Phys. D* **23** no. 13, (2014) 1443001, arXiv:1404.4047 [hep-th].

[59] T. Griffin, K. T. Grosvenor, P. Horava, and Z. Yan, "Scalar Field Theories with Polynomial Shift Symmetries," *Commun. Math. Phys.* **340** no. 3, (2015) 985–1048, arXiv:1412.1046 [hep-th].

[60] B. Horn, A. Nicolis, and R. Penco, "Effective string theory for vortex lines in fluids and superfluids," *JHEP* **10** (2015) 153, arXiv:1507.05635 [hep-th].

[61] D. T. Son, "Low-energy quantum effective action for relativistic superfluids," arXiv:hep-ph/0204199.

[62] A. Nicolis, R. Rattazzi, and E. Trincherini, "The Galileon as a local modification of gravity," *Phys. Rev. D* **79** (2009) 064036, arXiv:0811.2197 [hep-th].

[63] E. A. Ivanov and V. I. Ogievetsky, "The Inverse Higgs Phenomenon in Nonlinear Realizations," *Teor. Mat. Fiz.* **25** (1975) 164–177.

[64] D. B. Fairlie and J. Govaerts, "Euler hierarchies and universal equations," *J. Math. Phys.* **33** (1992) 3543–3566, arXiv:hep-th/9204074.

[65] M. Karowski, "Dipole ghosts and unitarity," *Nuovo Cim. A* **23** (1974) 126–136.

[66] B. T. Binegar, "On The State Space Of The Dipole Ghost," *Lett. Math. Phys.* **8** (1984) 149.

[67] N. Berkovits and E. Witten, "Conformal supergravity in twistor-string theory," *JHEP* **08** (2004) 009, arXiv:hep-th/0406051.

[68] C. Brust and K. Hinterbichler, "Free $\Box^k$ scalar conformal field theory," *JHEP* **02** (2017) 066, arXiv:1607.07439 [hep-th].

[69] J. Bonifacio, P. G. Ferreira, and K. Hinterbichler, "Transverse diffeomorphism and Weyl invariant massive spin 2: Linear theory," *Phys. Rev. D* **91** (2015) 125008, arXiv:1501.03159 [hep-th].

[70] R. M. Wald, "Spin-2 Fields and General Covariance," *Phys. Rev. D* **33** (1986) 3613.

[71] W. Li, "A unifying framework for ghost-free Lorentz-invariant Lagrangian field theories," *Phys. Lett. B* **779** (2018) 485–491, arXiv:1508.03247 [gr-qc].

[72] A. Chatzistavrakidis, F. S. Khoo, D. Roest, and P. Schupp, "Tensor Galileons and Gravity," *JHEP* **03** (2017) 070, arXiv:1612.05991 [hep-th].

[73] D. Bai and Y.-H. Xing, "On the uniqueness of ghost-free special gravity," *Commun. Theor. Phys.* **68** no. 3, (2017) 329, arXiv:1702.05756 [hep-th].

[74] J. Bonifacio, K. Hinterbichler, and L. A. Johnson, "Pseudolinear spin-2 interactions," *Phys. Rev. D* **99** no. 2, (2019) 024037, arXiv:1806.00483 [hep-th].

[75] R. J. Riegert, "Birkhoff's Theorem in Conformal Gravity," *Phys. Rev. Lett.* **53** (1984) 315–318.

[76] P. D. Mannheim and D. Kazanas, "Exact Vacuum Solution to Conformal Weyl Gravity and Galactic Rotation Curves," *Astrophys. J.* **342** (1989) 635–638.

[77] K. Hinterbichler and R. A. Rosen, "Partially Massless Monopoles and Charges," *Phys. Rev. D* **92** no. 10, (2015) 105019, arXiv:1507.00355 [hep-th].

[78] C. Hull, M. L. Hutt, and U. Lindström, "Charges and topology in linearised gravity," arXiv:2401.17361 [hep-th].

[79] H. F. Snethlage and S. Hörtner, "Manifest electric-magnetic duality in linearized conformal gravity," *Phys. Rev. D* **103** (2021) 105014, arXiv:2101.04705 [hep-th].

[80] C. Fronsdal, "Massless Fields with Integer Spin," *Phys. Rev. D* **18** (1978) 3624.

[81] E. S. Fradkin and A. A. Tseytlin, "Conformal Supergravity," *Phys. Rept.* **119** (1985) 233–362.

[82] A. Y. Segal, "Conformal higher spin theory," *Nucl. Phys. B* **664** (2003) 59–130, arXiv:hep-th/0207212.

[83] S. Weinberg and E. Witten, "Limits on Massless Particles," *Phys. Lett. B* **96** (1980) 59–62.

[84] V. Benedetti, H. Casini, and J. M. Magan, "Generalized symmetries and Noether's theorem in QFT," arXiv:2205.03412 [hep-th].

[85] J. Maldacena and A. Zhiboedov, "Constraining Conformal Field Theories with A Higher Spin Symmetry," *J. Phys. A* **46** (2013) 214011, arXiv:1112.1016 [hep-th].

[86] B. Bellazzini, J. Elias Miró, R. Rattazzi, M. Riembau, and F. Riva, "Positive moments for scattering amplitudes," *Phys. Rev. D* **104** no. 3, (2021) 036006, arXiv:2011.00037 [hep-th].

[87] A. J. Tolley, Z.-Y. Wang, and S.-Y. Zhou, "New positivity bounds from full crossing symmetry," *JHEP* **05** (2021) 255, arXiv:2011.02400 [hep-th].

[88] S. Caron-Huot and V. Van Duong, "Extremal Effective Field Theories," *JHEP* **05** (2021) 280, arXiv:2011.02957 [hep-th].

[89] N. Boulanger, J. François, and S. Lazzarini, "A classification of global conformal invariants," *J. Phys. A* **52** no. 11, (2019) 115201, arXiv:1809.05445 [math-ph].

[90] E. Joung, K. Mkrtchyan, and G. Poghosyan, "Looking for partially-massless gravity," *JHEP* **07** (2019) 116, arXiv:1904.05915 [hep-th].

[91] G. Anastasiou and R. Olea, "From conformal to Einstein Gravity," *Phys. Rev. D* **94** no. 8, (2016) 086008, arXiv:1608.07826 [hep-th].

[92] T. Basile, "A note on rectangular partially massless fields," *Universe* **4** no. 1, (2018) 4, arXiv:1710.10572 [hep-th].

[93] T. Basile, X. Bekaert, and E. Joung, "Conformal Higher-Spin Gravity: Linearized Spectrum = Symmetry Algebra," *JHEP* **11** (2018) 167, arXiv:1808.07728 [hep-th].

[94] E. Joung, M.-g. Kim, and Y. Kim, "Unfolding conformal geometry," *JHEP* **12** (2021) 092, arXiv:2108.05535 [hep-th].

[95] S. Weinberg, *The Quantum theory of fields. Vol. 1: Foundations*. Cambridge University Press, 6, 2005.

arXiv:2403.03255v1 [nucl-th] 5 Mar 2024

QCD critical point and hydrodynamic fluctuations in relativistic fluids*

Mikhail Stephanov

Department of Physics and Laboratory for Quantum Theory at the Extremes, University of Illinois, Chicago, IL 60607

Kadanoff Center for Theoretical Physics, University of Chicago, Chicago, IL 60637

Received March 7, 2024

These lecture notes consist of two major connected parts. The first part (Sections 1, 2), after a brief historical introduction, deals with the physics of critical points in thermodynamic *equilibrium*. The features of the fluctuations relevant for the QCD critical point search are highlighted. The second part (Sections 3, 4) focuses on the recent developments in the description of the fluctuation *dynamics* especially relevant for the QCD critical point search in heavy-ion collisions.

1. Introduction

Almost exactly 200 years ago Cagniard de la Tour performed an experiment which led to the discovery of critical points in a number of liquids [1]. One can think about this groundbreaking experiment as an attempt to address the following question: What happens if a liquid is heated in a sealed container to such (temperature and pressure) conditions that its propensity to evaporate competes with its propensity to expand, as illustrated in Fig. 1.

Cagniard de la Tour discovered that the boundary (meniscus) separating liquid and gas phases disappears. This phenomenon occurred for all liquids he experimented with, including water. He also described the phenomenon now called *critical opalescence*.

Michael Faraday, at the time, was working on the problem of liquefying gases — his report on the liquefaction of chlorine appears in the same issue with the English translation of Cagniard de la Tour's article [1]. Faraday took great interest in Cagniard de la Tour's discovery, in particular, in its

* Presented at the 63rd Cracow School of Theoretical Physics, Zakopane, Poland, September 17-23, 2023

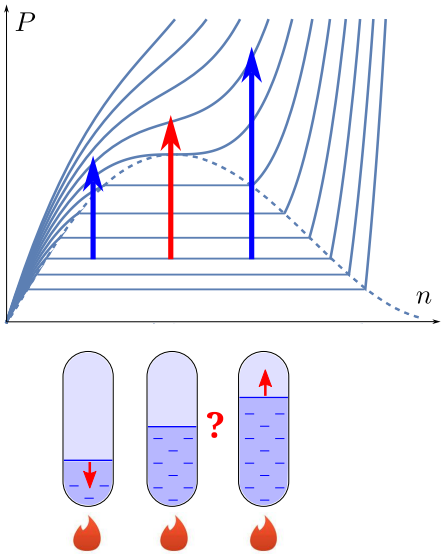

Fig. 1. A schematic representation of Cagniard de la Tour's experiment, with the heating "histories" indicated by the vertical (fixed volume) lines on the pressure-density diagram (solid lines are isotherms). One can think of this experiment as a (density) scan of the phase diagram. On the left: if a small amount of fluid is placed in a sealed container and heated the fluid evaporates and the meniscus goes down. On the right: if the fluid fills most of the container the fluid expands and the meniscus goes up. There must be a certain intermediate, critical filling fraction at which evaporation and expansion compete. What happens to the meniscus at this point?

intriguing implication of the continuity between liquid and gaseous phases. Curiously, Faraday was frustrated that Cagniard de la Tour had not named the novel phenomenon and struggled to come up with a name he needed to refer to a "point at which the fluid & its vapour become one according to a law of continuity" [2].

Full understanding of the ubiquity of the phenomenon and its logical consequence – continuity between "liquid and gaseous states" was solidified after systematic quantitative studies by Thomas Andrews [3], who also coined the name "critical point" we use today.

The desire to explain the liquid-gas continuity and the critical point led Leiden University Ph.D. student van der Waals [4] to discover a model of the equation of state based on, revolutionary at the time, molecular description of matter. The law of corresponding states formulated by van der Waals to describe near-critical fluids paved the way to the concept of universality of critical phenomena.

The phenomenon of critical opalescence was understood by Smoluchowski [5] as an effect of density fluctuations. This discovery was followed by quantitative theoretical description by Einstein [6].

The ubiquity of critical phenomena led Landau to develop the well-known classical theory of phase transitions [7]. But it took much more work to understand the crucial role of fluctuations. This work includes the pioneering contributions by Fisher, Kadanoff, and Wilson, which lead to the modern understanding of the (fluctuating) field theory (including quantum field theory) in terms of such essential concepts as scaling and renormalization group.

Thermodynamic critical points are ubiquitous in Nature. Not only practically all fluids possess such a point, but similar phenomena occur in completely different physical systems, such as, e.g., ferromagnets. The universality of critical phenomena extends over a vast range of physically different systems.

Hot and dense QCD matter dominating the Universe moments after the Big Bang, or recreated in heavy-ion collision experiments, is a fluid. It is natural to ask if this fluid also possesses a critical point. This is a non-trivial question first of all because this fluid, unlike the fluids in which critical points have been observed so far, is *relativistic*. In that respect, we are especially interested in the critical point which is related to deconfinement and chiral restoration transition, and we call this point QCD critical point.[1]

There are two necessary prerequisites for the existence of the critical point. One of them is the existence of two phases (e.g., liquid and gas). QCD matter does, indeed, possess such two phases, shown in Fig. 2 – Hadron Resonance Gas (HRG) and Quark Gluon Plasma (QGP), the latter having liquid properties [9]. Another prerequisite is the continuity between these two phases. Such a continuity has been, indeed, by now rather firmly established by first-principle lattice calculations at zero net baryon density, or $\mu_B = 0$ [10].

Does the crossover separating the two QCD phases at zero μ_B turn into a first order transition at some finite value of μ_B, and what is that value? I.e., where is the critical point on the QCD phase diagram (see Fig. 2)? Unfortunately, this question cannot, at this time, be answered by a lattice calculation due to the notorious sign problem.

However, this question can be addressed experimentally, by scanning QCD phase diagram in heavy-ion collision experiments [11], as illustrated in Fig. 2. The sought signatures of the critical point are based on the

[1] The critical point of nuclear matter (see Fig. 2) is also of interest. However, its existence is not in question and its location at temperature of order 10 MeV (commensurate with the binding energy of nuclear matter), much smaller than nucleon rest energy, makes it somewhat similar to non-relativistic liquid-gas critical points.

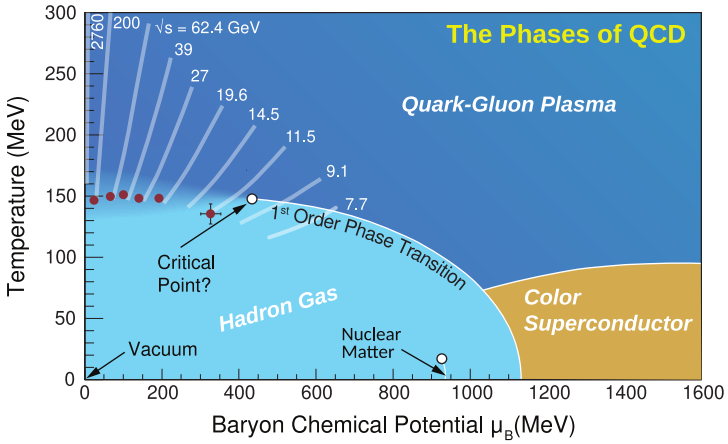

Fig. 2. A schematic rendering of the QCD phase diagram as it is currently understood or conjectured [8]. Superimposed are expansion "histories" of fireballs created in heavy-ion collisions at varying energies used in the bean-energy scan experiments (white lines labeled by $\sqrt{s_{\rm NN}}$ in GeV). The experimental freezeout points (red) are illustrating the dependence of the freezeout point on $\sqrt{s_{\rm NN}}$.

non-monotonic dependence of fluctuations on the collision energy, $\sqrt{s_{\rm NN}}$ [8, 12, 13].

While fluctuations in thermodynamic *equilibrium* near critical points, and their role in such critical phenomena as critical opalescence have been long and well understood, heavy-ion collisions present an additional challenge – fluctuation dynamics.

QCD matter (QGP) fireball created in heavy-ion collisions evolves sufficiently slowly that it can be described by hydrodynamics. However, the separation of scales is not astronomical, as in usual condensed matter contexts. As a result, fluctuations, which take time to relax to evolving equilibrium during the expansion, could deviate substantially from equilibrium values at freezeout.

After a brief introduction to equilibrium fluctuations (which can be also found elsewhere, e.g., [8]) these lectures will describe the recent progress achieved in the dynamical description of fluctuations.

2. Fluctuations in thermodynamics, critical fluctuations

2.1. Relation between equation of state and fluctuations

In thermodynamic equilibrium (by definition) the probability of the system to be found in a given *microscopic*, i.e., quantum, state depends only on the conserved quantum numbers of this state, such as energy, momen-

tum, charge, etc. Therefore, the probability of a given *macroscopic* state, characterized by a given set of macroscopic variables, such as energy, is proportional to the number of microscopic states with these values of the macroscopic variables. That probability is equal to the exponential of the entropy, by definition. Therefore, the dependence of the entropy on energy, etc, i.e., the equation of state (EOS), determines the probability of the fluctuations for a system in thermodynamic equilibrium [14].

This fundamental relationship between fluctuations and EOS is at the core of Einstein's description [6] of the density fluctuations, whose singular behavior near critical points explains the phenomenon of critical opalescence [5].

The entropy in question is the entropy of the open system which can exchange conserved quantities, such as energy and charge with the surroundings (thermodynamic bath) at temperature T and chemical potential μ. The corresponding probability distribution for the values of energy density ϵ and charge density n is given by

$$\mathcal{P}(\epsilon, n) \sim \exp\left\{V[s(\epsilon, n) - \beta\epsilon + \alpha n]\right\} \tag{1}$$

where $\beta = 1/T$, $\alpha = \mu/T$ and V is the volume of the thermodynamic system. In the thermodynamic limit, i.e., for large V, the probability is sharply peaked around the maximum determined by the familiar conditions:

$$\left(\frac{\partial s}{\partial \epsilon}\right)_n - \beta = 0, \quad \left(\frac{\partial s}{\partial n}\right)_\epsilon + \alpha = 0. \tag{2}$$

I.e., the entropy $s(\epsilon, n)$ determines the relationship between conserved densities ϵ, n and the corresponding thermodynamic quantities T and μ.

The quadratic form of second derivatives of the entropy must be negative to ensure thermodynamic stability. This form can be diagonalized using variables $m \equiv s/n$ (specific entropy) and p (pressure). The probability of small fluctuations in terms of these variables is given by

$$\mathcal{P} \sim \exp\left\{-\frac{V}{2}\left(\frac{n^2}{c_p}(\delta m)^2 + \frac{\beta}{w c_s^2}(\delta p)^2 + \dots\right)\right\} \tag{3}$$

Specific heat $c_p = Tn(\partial m/\partial T)_p$ diverges at the critical point. This corresponds to the probability of fluctuations developing a "flat direction" along which $\delta p = 0$, where the fluctuations of the specific entropy $V\langle(\delta m)^2\rangle = c_p/n^2$ become large. [2] The non-monotonic behavior of fluctuations as the

[2] Other thermodynamic quantities also develop large fluctuations at the critical point. For example, $V\langle(\delta n)^2\rangle = \chi_T T$, where $\chi_T = (\partial n/\partial \mu)_T$ is also divergent. The specific entropy $m = s/n$ is special from the hydrodynamic point of view. Unlike, e.g., baryon density, $m = s/n$ is a normal hydrodynamic mode in ideal hydrodynamics, i.e., being a ratio of conserved densities specific entropy is a diffusive mode which does not mix with propagating sound modes.

critical point is being approached and passed during the QCD phase diagram scan has been proposed as a signature of the QCD critical point [12,15].

Before proceeding, let us pause to note that in these lectures we focus on the fluctuations intrinsic in any system which affords local thermodynamic, statistical description. These fluctuations are determined by the equation of state, as discussed above. In the context of heavy-ion collisions we must distinguish these fluctuations from the fluctuations which are determined by the initial state of the system. For example, from the fluctuations of the initial geometry of the system. In experiments, such separation is not always trivial. Typically it involves selecting collisions with similar centrality, i.e., similar collision geometry. The effects of the initial fluctuations are also qualitatively different from those of thermodynamic fluctuations in that the correlations induced by initial fluctuations are longer range (in longitudinal rapidity space) than the thermodynamic fluctuations we discuss [16]. Most importantly, the $\sqrt{s_{\rm NN}}$ dependence of the initial fluctuations does not reflect the *non-monotonicity* inherent in the thermodynamic fluctuations in the vicinity of the critical point.

2.2. Universality and non-Gaussianity of critical fluctuations

Since the equation of state is universal near critical points, the fluctuation phenomena are also universal. In this section we shall describe some universal properties of the fluctuations which are relevant for the search for the QCD critical point in heavy-ion collisions.

Since the coefficient of the $(\delta m)^2$ term in Eq. (3) vanishes at the critical point, non-Gaussian terms in Eq. (3), such as δm^3, δm^4 etc., become important. This makes non-Gaussianity of fluctuations a telltale signature of the critical point [17].

Similarly, the vanishing of the coefficient of δm^2 in Eq. (3) makes gradient terms, such as $(\boldsymbol{\nabla}\delta m)^2$, important and leads to the divergence of the correlation length ξ of the fluctuations at the critical point. The non-Gaussianity of fluctuations and the divergence of the correlation length go hand in hand since the limit $V/\xi^3 \to \infty$, which ensures the Gaussianity of the fluctuations via central limit theorem, is in obvious conflict with $\xi \to \infty$.

The fluctuations at length scales of order the correlation length cannot be described by the variable δm, or by the uniform "mean field" δm, alone. Instead, the fluctuating spatially varying field $\delta m(x)$ must be considered. The corresponding scalar field theory — ϕ^4 theory in three dimensions, is universal in that it describes a wide range of critical phenomena from liquid-gas critical points to uniaxial (Ising) ferromagnets. The full details of the universal theory of critical phenomena are beyond the scope of these lectures, and are covered in many textbooks and reviews on critical phenom-

ena [18, 19]. Here we shall emphasize only the basic properties which are most relevant for the critical point search in the beam-energy scan heavy-ion collision experiments.

The universality means that we can consider fluctuations of m, or any other quantity, whose fluctuations diverge at the critical point, such as baryon number, or entropy density (and in the case of ferromagnets, magnetization density) as an order parameter and map it onto the field variable ϕ in the ϕ^4 theory, i.e.,

$$\Delta m \equiv m - m_{\rm c} \sim \phi, \tag{4}$$

where $m_{\rm c}$ is the value of m at the critical point and the implicit coefficient of proportionality is determined by the normalization of the field ϕ. The universality of the critical point phenomena means that the probability of fluctuations can be expressed in terms of the field ϕ:

$$\mathcal{P}[\phi] \sim \exp\left\{-V\left(-h\phi + \frac{r}{2}\phi^2 + \frac{\lambda}{4}\phi^4 + \frac{1}{2}(\boldsymbol{\nabla}\phi)^2 \dots\right)\right\} \tag{5}$$

where we expanded in powers of ϕ and kept the leading non-Gaussian term ϕ^4 as well as the leading gradient term $(\boldsymbol{\nabla}\phi)^2$. At the critical point the ordering field h and the reduced temperature r vanish. The probability becomes non-Gaussian and, at the same time, the correlation length ξ, proportional to $r^{-1/2}$ in the mean-field approximation (i.e., neglecting fluctuations), diverges. The cumulants of the order parameter ϕ also diverge, according to

$$\langle\phi^2\rangle \sim \xi^{2.}\,, \quad \langle\phi^3\rangle \sim \xi^{4.5}\,, \quad \langle\phi^4\rangle^{\rm c} \sim \xi^{7.}\,, \tag{6}$$

with (approximate) powers different from mean-field values due to fluctuations.

It is important that, unlike the variance $\langle\phi^2\rangle$, which measures the width of the probability distribution, the cubic and quartic cumulants, which measure the shape, are not positive definite. The cubic cumulant, measuring the skewness of the probability distribution $\mathcal{P}$, has the sign determined by the sign of h. The sign of the quartic cumulant can be understood by looking at the value of the cumulant along the crossover line $r > 0$ at $h = 0$, as illustrated in Fig. 3. The distribution along this line starts off as Gaussian away from the critical point and then splits into two maxima on the phase coexistence (first-order phase transition) line for $r < 0$. As $r \to +0$ the distribution becomes "flatter" which is represented by the negative value of the quartic cumulant. [3]

[3] The quartic cumulant is related to kurtosis, K: $K = \langle\phi^4\rangle/\langle\phi^2\rangle^2$, which has an advantage of canceling overall normalization of ϕ.

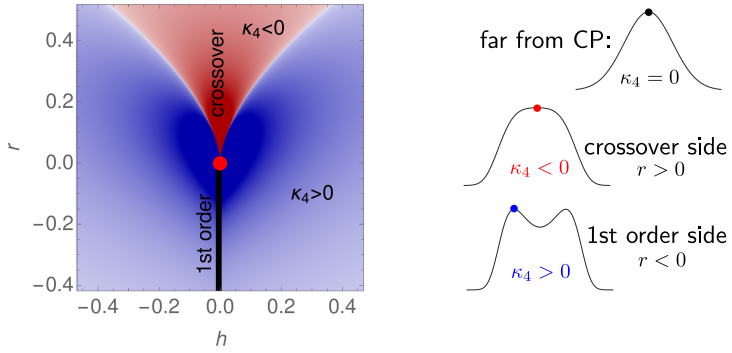

Fig. 3. *Left:* The sign of the quartic cumulant $\kappa_4 \equiv \langle\phi^4\rangle^c$ as a function of ϕ^4 (Ising model) field theory parameters h and r. *Right:* Schematic representation of the probability distribution $\mathcal{P}[\phi]$ in Eq. (5) at different points on the $h = 0$ line.

For $r < 0$, on the coexistence line, while the distribution is symmetric, the symmetry is spontaneously broken and the fluctuations occur around one of the maxima. This skewness effect dominates the quartic cumulant making it positive (see, e.g., [20] for more details).

The linear mapping from the Ising model variables h and r and the QCD variables μ and T captures the singular behavior of the QCD thermodynamics due to the fluctuations of the order parameter field ϕ, as well as due to the next-to-leading relevant operator (ϕ^2 in the mean-field approximation) [21–23].

Such a mapping has been standardized in Ref. [24] using 6 parameters: T_c, μ_{Bc}, w, ρ, α_1 and α_2. The parameters T_c and μ_{Bc} set the location of the QCD critical point, while α_1 is the angle of the slope of the coexistence line (first-order phase transition line) at the critical point in the T vs μ_B plane. It is also the slope of $m = m_c$ (critical isentrope) line at the critical point and is obtained by mapping the zero magnetization line $\phi = 0$ (i.e., zero magnetic field $h = 0$) of the Ising model onto the QCD phase diagram. The angle α_2 is the angle of the line on the QCD phase diagram onto which the constant temperature line passing through the Ising critical point maps.

The non-Gaussian cumulants of the order parameter such as m are proportional to those in the Ising model (or ϕ^4 theory, see Eq. (4)), but mapped into the QCD phase diagram. In particular, these cumulants contain singular contributions which diverge at the critical point with universal powers of the correlation length, given approximately by [17]

$$\Delta\langle(\delta m)^2\rangle \sim \xi^{2.}, \quad \Delta\langle(\delta m)^3\rangle \sim \xi^{4.5}, \quad \Delta\langle(\delta m)^4\rangle^c \sim \xi^{7.} \tag{7}$$

where Δ reminds us that this is a *contribution* to cumulants, singular at the critical point. There is, of course, less singular and regular contribu-

tions, or baseline. The search for the critical point is aimed at detecting the non-monotonic dependence of fluctuations measures on the collision energy $\sqrt{s_{\rm NN}}$ as the critical point is approached and passed, i.e., as the correlation length increases and then shrinks back to non-critical background, or baseline, values.

For example, the quartic cumulant around the QCD critical point is illustrated in Fig. 4(a). [20] The resulting dependence on the collision energy, as it is varied in the region where the freeze-out occurs near the critical point, is illustrated in Fig. 4(b). The characteristic non-monotonicity of this cumulant is one of the signatures of the critical point searched for in the Beam Energy scan experiments [8].

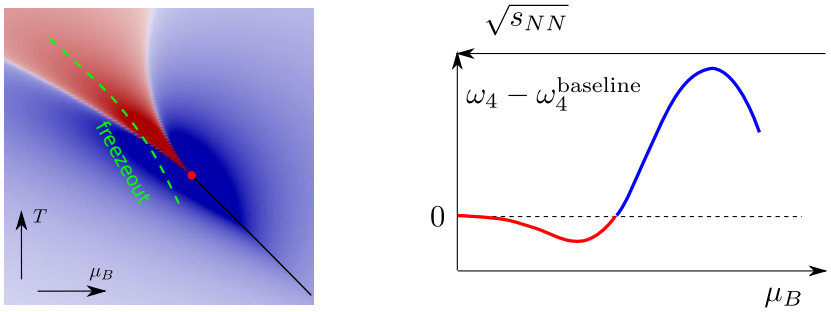

(a) (b)

Fig. 4. The equilibrium expectation for the quartic cumulant of fluctuations as a function of temperature and baryon chemical potential on the QCD phase diagram in the vicinity of the critical point. Red and blue colors reflect the sign of the cumulant – negative and positive respectively. Compare to Fig. 3. The sign changes as the QCD phase diagram is scanned by varying $\sqrt{s_{\rm NN}}$, and thus T and μ_B, along the freeze-out "trajectory" (dashed green line).

The most recently published experimental measurements of quartic cumulants by STAR collaboration indicate a non-monotonic dependence of the type similar to the one shown in Fig. 4(b) (see, e.g., Fig.4(2) in Ref. [25]). While the magnitude of the cumulant sensitively depends on the EOS, and thus hard to predict (hence the lack of the vertical scale on Fig. 4(b)) the experimental results indicate that monotonic dependence is excluded at 3.1σ level [25–27]. While not yet a definitive indication of the presence of the QCD critical point, this intriguing result motivates the second phase of the beam energy scan (BES-II) program which has collected higher statistics data being processed and analyzed currently.

We shall focus on the recent progress achieved in connecting these equilibrium fluctuations to the experimental measurements. There are at least

two steps that need to be made to get from the equilibrium thermodynamic fluctuations to the experimental observables:

First, like thermodynamic variables themselves, the fluctuations of these variables evolve. This evolution is subject to conservation laws which may lead to significant memory effects, i.e., the lag of the fluctuations behind the instantaneous equilibrium values.

Second, the thermodynamic/hydrodynamic quantities are not measured by experiments directly. An important step is connecting the fluctuations of these quantities to the observables, such as measures of particle multiplicity fluctuations and correlations.

The following two sections will review the recent development towards accomplishing these two steps necessary for connecting the theory and the experiment.

3. Fluctuations in hydrodynamics

3.1. Stochastic hydrodynamics

There has been significant recent progress in understanding and describing the *dynamics* of local thermodynamic fluctuations in hot *relativistic* fluids, such as the QCD matter making up a heavy-ion collision fireball.

The evolution of the QCD matter in the heavy-ion fireball is successfully described in the framework of hydrodynamics. This description is inherently statistical, and therefore, fluctuations are an essential part of this description. One can also understand this fact by invoking fluctuation-dissipation theorem according to which dissipative systems (such as non-ideal hydrodynamics) have to be stochastic.

There are two complementary approaches for describing dynamics of fluctuations, which we shall refer to as stochastic and deterministic. Both begin with the Landau-Lifshits theory of hydrodynamic fluctuations [28]. In this theory, generalized to relativistic context in Ref. [16] , the equations of hydrodynamics are *stochastic*.

Hydrodynamic description exists because of the separation of scales. The timescale of relaxation to local equilibrium (typical microscopic time, such as inter-collision time) is much shorter that the time needed to transport conserved quantities and establish global equilibrium. This is typically a diffusion time proportional to the square of the size of inhomogeneities in the system. This latter slow evolution process is essentially governed by conservation equations, which we can write generically as

$$\partial_\mu \breve{\mathcal{J}}^\mu = 0 \tag{8}$$

by combining all conserved currents into an array

$$\breve{\mathcal{J}}^\mu \equiv \{\breve{N}_q^\mu, \breve{T}^{\mu\nu}\}\,. \tag{9}$$

We use 'breve' accent to denote stochastic (fluctuating) quantities. For QCD such conserved currents include currents of energy and momentum, $T^{\mu\nu}$, as well as conserved charge currents, N_q^μ, among which we shall focus on the baryon charge $q = B$.

While each current involves one time and three spatial components, there is only one equation for each current in (8). Therefore, to close the system of equations we need to express all 4 current components in terms of 1 variable – the conserved density. To maintain relativistic covariance, we want this density to be a covariant object (scalar for the baryon charge density, or vector for energy-momentum density). The density in the lab frame would not do.

The fluid itself, however, allows us to define (in each space-time point) a reference frame associated with fluid's motion. This frame is often referred as the "local rest frame" of the fluid. Following Landau, we chose for that purpose the frame in which the momentum density vanishes. The 4-velocity of such a frame solves the following equation (known as "Landau condition"):

$$\breve{T}^\mu_{\ \nu}\breve{u}^\nu = \breve{\epsilon}\breve{u}^\mu. \tag{10}$$

Since $\breve{T}^\mu_{\ \nu}$ fluctuates, so does $\breve{u}^\mu$. Eq. (10) also defines the energy density $\breve{\epsilon}$ in the fluid's rest frame. The rest frame charge density is defined similarly $\breve{n}_q = \breve{u}_\mu \breve{N}_q^\mu$.

It is convenient to define an array of these covariant variables – one for each conservation equation in (8):

$$\breve{\Psi} \equiv \breve{u}_\mu \breve{\mathcal{J}}^\mu = \{\breve{n}_q, \breve{\epsilon}\breve{u}^\nu\}\,. \tag{11}$$

In order to close the system of equations we need to express all components of the currents in $\breve{\mathcal{J}}^\mu$ in terms of the covariant variables in $\breve{\Psi}$. The separation of scales in hydrodynamics means that this relationship is *local*. I.e., the currents $\breve{\mathcal{J}}(x)$ are functions of variables $\Psi(x)$ and its gradients at the same point x:

$$\mathcal{J}^\mu[\Psi] = \{nu^\mu, \epsilon u^\mu u^\nu - p(g^{\mu\nu} - u^\mu u^\nu)\} + \text{diffusive/viscous gradients}\,. \tag{12}$$

The key point of the Landau-Lifshits theory of hydrodynamic fluctuations is that the constitutive relations such as (12) are only satisfied *on average* – hence the absence of 'breve' in Eq. (12). For fluctuating quantities there is random discrepancy, which is due to the microscopic degrees of freedom excluded from hydrodynamic description. Hence,

$$\breve{\mathcal{J}}^\mu = \mathcal{J}^\mu[\breve{\Psi}] + \breve{\mathcal{I}}^\mu\,, \tag{13}$$

where $\breve{\mathcal{I}}^\mu$ is the local noise, $\langle\breve{\mathcal{I}}^\mu\rangle = 0$, whose correlation function,

$$\langle\breve{\mathcal{I}}^\mu(x_1)\breve{\mathcal{I}}^\nu(x_2)\rangle \sim \delta^{(4)}(x_1 - x_2)\,, \tag{14}$$

is determined by the fluctuation dissipation theorem, ensuring that the equilibrium fluctuations and correlations have the correct magnitudes in agreement with thermodynamics.

The evolution of fluctuations can be then described by, for example, directly solving this system of stochastic equations (8), (13). In a numerical simulation, this *stochastic* approach, however, produces a problem (also known as infinite noise problem) due to the fact that the noise is singular at $x_1 = x_2$ in Eq. (14). The resulting solutions are dependent on the hydrodynamic cutoff, i.e., the finite elementary hydrodynamic cell size, b, complicating the "continuum limit" $b \to 0$. Some solutions to this problem within a numerical simulation have been proposed and implemented in the literature [29, 30], but we shall not discuss them here.

3.2. Deterministic approach to hydrodynamic fluctuations

The approach which deals with the infinite noise problem *before* the actual numerical simulation is performed has been also developed recently for Bjorken flow [31–33], for arbitrary relativistic flow [34–36], and for non-Gaussian fluctuations [37, 38]. In this *deterministic* approach one expands in fluctuations around the average $\Psi \equiv \langle\breve{\Psi}\rangle$:

$$\breve{\Psi} = \Psi + \delta\Psi\,, \tag{15}$$

thus obtaining stochastic equations for the fluctuations $\delta\Psi$ on the deterministically evolving inhomogeneous fluctuation averaged background $\Psi(x)$. These equations can then be used to derive *deterministic* equations obeyed by the *correlation functions* of the fluctuations, i.e., by averages of the products of the fluctuations, such as $\langle\delta\Psi(x_1)\delta\Psi(x_2)\rangle$.

The short-distance singularity of the noise results in ultraviolet divergences in the deterministic equations – the infinite noise problem. Indeed expanding constitutive equations (13) to quadratic order and averaging one finds:

$$\langle\breve{\mathcal{J}}^\mu(x)\rangle = \mathcal{J}^\mu[\Psi(x)] + \frac{1}{2}\frac{\partial^2\mathcal{J}^\mu}{\partial\Psi_a\partial\Psi_b}\langle\delta\Psi_a(x)\delta\Psi_b(x)\rangle + \dots \tag{16}$$

where a, b index hydrodynamic variables in the array (11). The last term in Eq. (16) is singular because the correlator of hydrodynamic variables is evaluated at coinciding points, and in (and near) equilibrium $\langle\delta\Psi_a(x_1)\delta\Psi_b(x_2)\rangle \sim \delta(x_1 - x_2)$. The support of the delta function is of the size of the hydrodynamic cell b, over which the operators defining conserved densities are averaged to obtain classical (stochastic) hydrodynamic variables $\breve{\Psi}$.

The key observation is that these singular (divergent in the limit $b \to 0$) contributions are *local* due to the hydrodynamic separation of scales we discussed already. Thus the divergent terms in Eq. (16) must simply renormalize the local terms already present in the "bare" constitutive relations in Eq. (12). The resulting system of renormalized equations for hydrodynamic evolution of the renormalized average densities, as well as the correlation functions, is ultraviolet finite, i.e., cutoff independent, and the continuum limit can be taken (see, Refs. [35, 36] for more detail).

After the renormalization, the averaged hydrodynamic equations keep the form of usual hydrodynamic equations to first order in gradients with renormalized, i.e., physical, equation of state and transport coefficients. However, finite (i.e., cutoff independent) fluctuation contributions appear beyond that order. These terms introduce contributions non-local in space (effectively being of order 3/2 in gradients) and also non-local in time, leading to the phenomena known as "long-time tails". Near the critical point these fluctuation effects also lead to critical slowing down of the relaxation to equilibrium [34] and the related divergence of kinetic coefficients, most notably, of bulk viscosity [34, 36, 39].

3.3. Multipoint Wigner transform

Because fluctuations occur on shorter length scales than the hydrodynamic evolution of the background [31, 34, 35] it is convenient to consider Wigner-transformed equal-time correlation functions. For a fluid at rest globally, the Wigner transform definition is straightforward:

$$W_{ab}(t, \boldsymbol{x}; \boldsymbol{q}) = \int d^3\boldsymbol{y} \left\langle \delta\Psi_a \left(t, \boldsymbol{x} + \frac{\boldsymbol{y}}{2}\right) \delta\Psi_b \left(t, \boldsymbol{x} - \frac{\boldsymbol{y}}{2}\right) \right\rangle e^{-i\boldsymbol{q}\cdot\boldsymbol{y}} , \tag{17}$$

where $\delta\Psi_a$ is the fluctuation of a hydrodynamic field from array (11) labeled by index a.

Non-Gaussianity of fluctuations, important for the critical point search, is described by *connected* correlation functions of $k > 2$ fluctuation fields:

$$H_{a_1 \dots a_k}(t, \boldsymbol{x}_1, \dots, \boldsymbol{x}_k) \equiv \langle \delta\Psi_{a_1}(t, \boldsymbol{x}_1) \dots \delta\Psi_{a_k}(t, \boldsymbol{x}_k) \dots \rangle^{\text{connected}} \tag{18}$$

The corresponding generalization of Wigner transform was introduced in Ref. [37] in terms of the Fourier integral with fixed midpoint

$$\boldsymbol{x} \equiv \frac{\boldsymbol{x}_1 + \dots + \boldsymbol{x}_k}{k} , \tag{19}$$

i.e.,

$$W_{a_1\ldots a_k}(t,\boldsymbol{q}_1,\ldots,\boldsymbol{q}_k) \equiv \int d^3\boldsymbol{y}_1\, e^{-i\boldsymbol{q}_1\cdot\boldsymbol{y}_1}\ldots \int d^3\boldsymbol{y}_k\, e^{-i\boldsymbol{q}_k\cdot\boldsymbol{y}_k} \times \delta^{(3)}\left(\frac{\boldsymbol{y}_1+\cdots+\boldsymbol{y}_k}{k}\right) H_{ab\ldots}(t,\boldsymbol{x}+\boldsymbol{y}_1,\ldots,\boldsymbol{x}+\boldsymbol{y}_k) \quad (20)$$

Due to the delta-function factor in Eq. (20), the function W does not change if all $\boldsymbol{q}$'s are shifted by the same vector. This means that one of the $\boldsymbol{q}$ arguments is redundant. In practice, it is sufficient to know the function W at all values of $\boldsymbol{q}$ which add up to zero. In particular, the correlator $H_{a_1\ldots a_k}$ can be obtained via inverse transformation:

$$H_{a_1\ldots a_k}(t,\boldsymbol{x}_1,\ldots,\boldsymbol{x}_k) = \int \frac{d^3\boldsymbol{q}_1}{(2\pi)^3}\, e^{i\boldsymbol{q}_1\cdot\boldsymbol{y}_1}\ldots \int \frac{d^3\boldsymbol{q}_k}{(2\pi)^3}\, e^{i\boldsymbol{q}_k\cdot\boldsymbol{y}_k} \times (2\pi)^3\delta^{(3)}\left(\boldsymbol{q}_1+\cdots+\boldsymbol{q}_k\right) W_{a_1\ldots a_k}(t,\boldsymbol{x};\boldsymbol{q}_1\ldots\boldsymbol{q}_k)\,. \quad (21)$$

where $\boldsymbol{y}_i \equiv \boldsymbol{x}_i - \boldsymbol{x}$. For $k=2$ the generalized Wigner function $W_{ab}(t,-\boldsymbol{q},\boldsymbol{q})$ coincides with the usual 2-point Wigner function defined in Eq. (17).

3.4. Evolution equations for fluctuations in a diffusion problem

The hierarchy of evolution equations was derived in Ref. [37] for fluctuations of density in a diffusion problem, where the only hydrodynamic variable is the diffusing charge density n which obeys conservation equation and the Fick's law with local noise

$$\partial_t n = -\boldsymbol{\nabla}\cdot\boldsymbol{N}, \quad \boldsymbol{N} = -\lambda(n)\boldsymbol{\nabla}\alpha(n) + \text{noise}\,. \quad (22)$$

The evolution equations describe the relaxation of the k-point functions W_k of fluctuations of density n to equilibrium values given by thermodynamics in terms of the equation of state $\alpha(n)$ (chemical potential divided by temperature):

$$\partial_t W_2(\boldsymbol{q}) = -2\left[\gamma\boldsymbol{q}^2 W_2(\boldsymbol{q}) - \lambda\boldsymbol{q}^2\right]\,, \quad (23a)$$

$$\partial_t W_3(\boldsymbol{q}_1,\boldsymbol{q}_2,\boldsymbol{q}_3) = -3\left[\gamma\boldsymbol{q}_1^2 W_3(,\boldsymbol{q}_2,\boldsymbol{q}_3) + \gamma'\boldsymbol{q}_1^2 W_2(\boldsymbol{q}_2)W_2(\boldsymbol{q}_3) + 2\lambda'\boldsymbol{q}_1\cdot\boldsymbol{q}_2 W_2(\boldsymbol{q}_3)\right]_{\overline{123}}\,, \quad (23b)$$

$$\partial_t W_4(\boldsymbol{q}_1,\boldsymbol{q}_2,\boldsymbol{q}_3,\boldsymbol{q}_4) = -4\left[\gamma\boldsymbol{q}_1^2 W_4(,\boldsymbol{q}_2,\boldsymbol{q}_3,\boldsymbol{q}_4) + 3\gamma'\boldsymbol{q}_1^2 W_2(\boldsymbol{q}_2)W_3(,\boldsymbol{q}_3,\boldsymbol{q}_4) + \gamma''\boldsymbol{q}_1^2 W_2(\boldsymbol{q}_2)W_2(\boldsymbol{q}_3)W_2(\boldsymbol{q}_4) + 3\lambda'\boldsymbol{q}_1\cdot\boldsymbol{q}_2 W_3(,\boldsymbol{q}_3,\boldsymbol{q}_4) + 3\lambda''\boldsymbol{q}_1\cdot\boldsymbol{q}_2 W_2(\boldsymbol{q}_3)W_2(\boldsymbol{q}_4)\right]_{\overline{1234}}\,, \quad (23c)$$

where $\gamma = \lambda\alpha'$ is the diffusion coefficient. In Eqs. (23) we suppressed arguments t and $\boldsymbol{x}$, as they are the same for all functions W_k. Furthermore, note that all arguments of each function W_k add up to zero – reminiscent of the momentum conservation in Feynman diagrams. Therefore, to save space, we omitted the first argument in W_k where this argument can be inferred from the condition $\boldsymbol{q}_1 + \cdots + \boldsymbol{q}_k = 0$. For example, $W_2(\boldsymbol{q}) \equiv W_2(,\boldsymbol{q}) \equiv W_2(-\boldsymbol{q},\boldsymbol{q})$ or $W_3(,\boldsymbol{q}_3,\boldsymbol{q}_4) \equiv W_3(-\boldsymbol{q}_3-\boldsymbol{q}_4,\boldsymbol{q}_3,\boldsymbol{q}_4)$. The symbol $[\dots]_{\overline{1\dots k}}$ denotes the sum over all permutations of $\boldsymbol{q}_1,\dots,\boldsymbol{q}_k$ divided by $1/k!$, i.e., the average over all permutations. Diagrammatic representation of Eqs. (23) is given in Ref. [37] (see also Fig. 5).

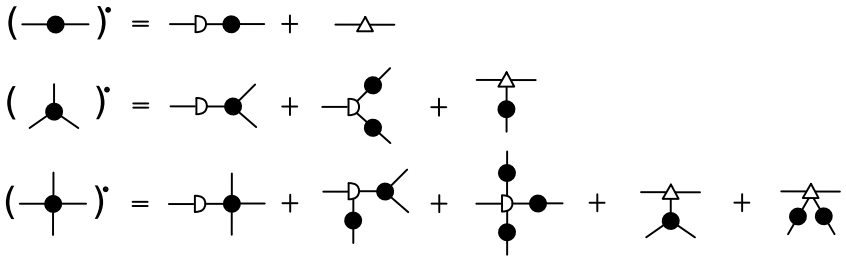

Fig. 5. Diagrammatic representation of Eqs. (23). See Refs. [37, 38].

Equations (23) represent the leading order in hydrodynamic gradient expansion. The next order would correspond to loop diagrams (in terms of the diagrammatic technique used in Fig. 5). It represents the feedback of fluctuations. For two-point functions, such feedback have been considered in Refs. [31–36] and the corresponding renormalization of hydrodynamic equations has been shown to remove cutoff dependence due to "infinite noise" problem, as discussed above in Section 3.2.

3.5. Confluent formalism for arbitrary relativistic flow

For a *relativistic* fluid with nontrivial velocity gradients the definition of the equal-time correlator in Eq. (18) and its Wigner transform are insufficient since the rest frame of the fluid is different at different space-time points, and the concept of "equal time" is thus ambiguous. To maintain Lorentz covariance in the description of fluctuations, Ref. [35], and for non-Gaussian fluctuations, Ref. [38], propose to use averaged local rest frame of the fluid at the midpoint $x \equiv (t,\boldsymbol{x})$ of the correlator to define "equal time". The same locally defined frame is also used to define, or measure, fluctuations of velocity.

The idea is to equip every space-time point x with an orthonormal triad of basis 4-vectors $e_{\mathring{a}}(x)$, $\mathring{a} = 1,2,3$, or $\boldsymbol{e}(x)$, spatial in the local rest frame

of the fluid at that point, i.e.,

$$\boldsymbol{e}(x) \cdot u(x) = \mathbf{0}. \tag{24}$$

One can then define equal-time k-point correlators as functions of k space-time points expressed as

$$x_1 = x + \boldsymbol{e}(x) \cdot \boldsymbol{y}_1, \quad \ldots \quad , \quad x_k = x + \boldsymbol{e}(x) \cdot \boldsymbol{y}_k, \tag{25}$$

in terms of the midpoint x and the separation 3-vectors $\boldsymbol{y}_1, \ldots, \boldsymbol{y}_k$, which sum to zero: $\boldsymbol{y}_1 + \ldots + \boldsymbol{y}_k = 0$.

Some of the fields in the correlator may not be Lorentz scalars, for example, fluctuations of velocity, δu. One would like to express such fluctuations in a frame associated with the fluid, such as the local rest frame, rather than in an arbitrary lab frame. The local rest frame of the fluid is, however, different for different points $x_1, \ldots, x_k$. To use the same frame for all points while making sure that fluctuations represent deviations from fluid at rest locally, we boost the fluctuation variables (if they are not scalars) from the rest frame at the point they occur, say, at $x + y_1$, to that at the midpoint x of the correlator. This operation leads to the *confluent correlator* defined as:

$$H_{a_1 \ldots a_k}(x_1, \ldots, x_k) \equiv \left\langle [\Lambda(x, x_1)\delta\Psi(x_1)]_{a_1} \ldots [\Lambda(x, x_k)\delta\Psi(x_k)]_{a_k} \right\rangle^{\mathrm{c}} \tag{26}$$

where $\Lambda(x, x_1)$ performs the boost on the corresponding fluctuation field $\delta\Psi(x_1)$ such that the 4-velocities in points x_1 and x are related by

$$\Lambda(x, x_1)u(x_1) = u(x). \tag{27}$$

Superscript 'c' means "connected" as in Eq. (18).

We can now take the multipoint Wigner transform of the confluent correlator we just defined in Eq. (26) with respect to the 3-vectors $\boldsymbol{y}_1, \ldots, \boldsymbol{y}_k$ describing separation of the points in the local basis at point x (cf. Eq. (20)):

$$\begin{aligned} W_{a_1 \ldots a_k}(x; \boldsymbol{q}_1, \ldots, \boldsymbol{q}_k) \equiv \int d^3\boldsymbol{y}_1 \, e^{-i\boldsymbol{q}_1 \cdot \boldsymbol{y}_1} \ldots \int d^3\boldsymbol{y}_k \, e^{-i\boldsymbol{q}_k \cdot \boldsymbol{y}_k} \\ \times \, \delta^{(3)}\left(\frac{\boldsymbol{y}_1 + \cdots + \boldsymbol{y}_k}{k} \right) H_{a_1 \ldots a_k}(x + \boldsymbol{e}(x) \cdot \boldsymbol{y}_1, \ldots, x + \boldsymbol{e}(x) \cdot \boldsymbol{y}_k) \end{aligned} \tag{28}$$

The inverse is given by (cf. Eq. (21))

$$\begin{aligned} H_{a_1 \ldots a_k}(x + \boldsymbol{e}_1(x) \cdot \boldsymbol{y}_1, \ldots, x + \boldsymbol{e}_k(x) \cdot \boldsymbol{y}_k) \\ = \int \frac{d^3\boldsymbol{q}_1}{(2\pi)^3} \, e^{i\boldsymbol{q}_1 \cdot \boldsymbol{y}_1} \ldots \int \frac{d^3\boldsymbol{q}_k}{(2\pi)^3} \, e^{i\boldsymbol{q}_k \cdot \boldsymbol{y}_k} \\ \times \, \delta^{(3)}\left(\frac{\boldsymbol{q}_1 + \cdots + \boldsymbol{q}_k}{2\pi} \right) W_{a_1 \ldots a_k}(x; \boldsymbol{q}_1, \ldots, \boldsymbol{q}_k) \, . \end{aligned} \tag{29}$$

Care must be taken also in defining a derivative with respect to the midpoint of such a correlation function in order to maintain the "equal-time in local rest frame" condition. The local rest frame is different in points x and $x+\Delta x$ used to define the derivative. A derivative which maintains "equal-time" condition is introduced in Ref. [35, 36] and termed *confluent derivative*. It is defined via the $\Delta x \to 0$ limit of the following equation:

$$\Delta x \cdot \bar{\nabla} W_{a_1\dots a_k}(x;\boldsymbol{q}_1,\dots,\boldsymbol{q}_k) \equiv \Lambda(x,x+\Delta x)^{b_1}_{a_1}\dots\Lambda(x,x+\Delta x)^{b_k}_{a_k} \times W_{b_1\dots b_k}(x;\boldsymbol{q}'_1,\dots,\boldsymbol{q}'_k) - W_{a_1\dots a_k}(x;\boldsymbol{q}_1,\dots,\boldsymbol{q}_k)\,, \quad (30)$$

where

$$\boldsymbol{q}' = \boldsymbol{e}(x+\Delta x)\cdot[\Lambda(x+\Delta x,x)\boldsymbol{e}(x)\cdot\boldsymbol{q}] \equiv R(x+\Delta x,x)\boldsymbol{q}\,. \quad (31)$$

In Eq. (30) the (non-scalar) fluctuation fields are boosted from point $x+\Delta x$ back to point x, similarly to the definition of the confluent correlator in Eq. (26). In addition, at $x+\Delta x$ we evaluate the function using the set of 3-wavevectors $\boldsymbol{q}'_i$ given by Eq. (31), different from the set $\boldsymbol{q}_i$ used at point x. The new set is obtained by representing each vector $\boldsymbol{q}$ as a *4-vector* orthogonal to $u(x)$, $\boldsymbol{e}(x)\cdot\boldsymbol{q}$, then boosting this vector to the rest frame at point $x+\Delta x$ and then expressing it again as a 3-vector, but now in the basis $\boldsymbol{e}(x+\Delta x)$ orthogonal to $u(x+\Delta x)$. The resulting transformation of vector $\boldsymbol{q}$ is a rotation, denoted by R in Eq. (31).

Taking the limit $\Delta x \to 0$ in Eq. (30) one can express confluent derivative as follows:

$$\bar{\nabla}_\mu W_{a_1\dots a_2} = \partial_\mu W_{a_1\dots a_2} + k\left(\mathring{\omega}^{\mathring{a}}_{\mu\mathring{b}} q_{1\mathring{a}}\frac{\partial}{\partial q_{1\mathring{b}}} W_{a_1\dots a_k} - \bar{\omega}^{b}_{\mu a_1} W_{b a_2\dots a_k}\right)_{\overline{1\dots k}}\,, \quad (32)$$

where the confluent connection $\bar{\omega}$ is a generator of the infinitesimal boost Λ and $\mathring{\omega}$ is a generator of the infinitesimal rotation R:

$$\Lambda(x+\Delta x,x)^a{}_b = \delta^a_b - \Delta x^\mu \bar{\omega}^a_{\mu b}, \quad (33)$$

$$R(x+\Delta x,x)^{\mathring{a}}{}_{\mathring{b}} = \delta^{\mathring{a}}_{\mathring{b}} - \Delta x^\mu \mathring{\omega}^{\mathring{a}}_{\mu\mathring{b}}\,. \quad (34)$$

The indices $a, b, a_1 \dots a_k$ label fluctuating fields. The confluent connection $\bar{\omega}^a_{\mu b}$ is nonzero when indices a, b refer to different components of a Lorentz vector (such as δu). In this case the connection satisfies

$$\bar{\nabla}_\mu u^\alpha \equiv \partial_\mu u^\alpha + \bar{\omega}^\alpha_{\mu\beta} u^\beta = 0, \quad (35)$$

(local velocity is "confluently" constant), which follows from Eqs. (27) and (33).[4]

[4] For a scalar field (e.g., energy density, pressure fluctuations, etc) the confluent connection is, of course, zero. E.g., $\bar{\nabla}_\mu \delta m = \partial_\mu \delta m$.

The rotation connection $\mathring{\omega}$ is determined by Eqs. (31) and (34):

$$\mathring{\omega}^{\mathring{b}}_{\mu\mathring{a}} = e^{\mathring{b}}_{\alpha}\left(\partial_\mu e^{\alpha}_{\mathring{a}} + \bar{\omega}^{\alpha}_{\mu\beta} e^{\beta}_{\mathring{a}}\right) . \tag{36}$$

Naturally, it satisfies:

$$\bar{\nabla}_\mu e^{\alpha}_{\mathring{a}} \equiv \partial_\mu e^{\alpha}_{\mathring{a}} + \bar{\omega}^{\alpha}_{\mu\beta} e^{\beta}_{\mathring{a}} - \mathring{\omega}^{\mathring{b}}_{\mu\mathring{a}} e^{\alpha}_{\mathring{b}} = 0 \tag{37}$$

(local basis vectors are confluently constant).

The boost Λ is not defined uniquely by Eq. (27) – only up to a rotation keeping u unchanged. The simplest choice is the boost without additional rotation, which corresponds to confluent connection given explicitly by

$$\bar{\omega}^{\alpha}_{\mu\beta} = u_\beta \partial_\mu u^\alpha - u^\alpha \partial_\mu u_\beta \, . \tag{38}$$

For this choice of the confluent connection the rotation connection also simplifies to

$$\mathring{\omega}^{\mathring{b}}_{\mu\mathring{a}} = e^{\mathring{b}}_{\alpha} \partial_\mu e^{\alpha}_{\mathring{a}} \, . \tag{39}$$

3.6. Evolution equations for hydrodynamic fluctuations

There are five normal hydrodynamics modes, which can be described as two propagating modes and three diffusive.[5] The propagating modes correspond to fluctuations of pressure mixed with the fluctuations of the longitudinal (with respect to the wave vector $\boldsymbol{q}$) velocity. The frequency of these modes is $c_s|\boldsymbol{q}|$. The diffusive modes are the fluctuations of the specific entropy $m \equiv s/n$ at fixed pressure and transverse velocity. The relaxation rate of these modes is proportional to the square of their wavenumber $\boldsymbol{q}^2$. The slowest diffusive mode near the critical point is specific entropy because its diffusion constant vanishes at the critical point.

In this review we shall focus on the slowest diffusive mode m for two reasons. First, because it is the slowest and therefore the furthest from equilibrium mode. Second, in equilibrium this mode shows the fluctuations of the order parameter (i.e., $\delta m \sim \delta\phi$, Eq. (4)), divergent at the critical point.

The evolution equation for the Wigner-transformed confluent two-point correlator of the specific entropy fluctuations, $\langle \delta m \delta m \rangle$, derived in Ref. [36] reads:

$$\mathcal{L}[W_{mm}(\boldsymbol{q})] = (\partial \cdot u) W_{mm}(\boldsymbol{q}) - 2\gamma_{mm}\boldsymbol{q}^2 \left[W_{mm}(\boldsymbol{q}) - \frac{c_p}{n^2}\right] . \tag{40}$$

[5] We focus on hydrodynamics involving baryon charge. Each additional charge adds one diffusive mode to the count.

where $\gamma_{mm} \equiv \kappa/c_p$ – the heat diffusion constant, and $\mathcal{L}$ is the Liouville operator given by

$$\mathcal{L}[W_{mm}] \equiv \left[u \cdot \bar{\nabla} - \partial_\nu u^\mu (\boldsymbol{e}_\mu \cdot \boldsymbol{q}) \left(\boldsymbol{e}^\nu \cdot \frac{\partial}{\partial \boldsymbol{q}}\right)\right] W_{mm}\,. \tag{41}$$

The first term is the confluent derivative along the flow of the fluid, while the second describes stretching and/or rotation of the vectors $\boldsymbol{q}$ due to the expansion and/or rotation of the fluid. In the case of expansion one can think of this term as describing the Hubble-like "red shift" of the fluctuation wavevector $\boldsymbol{q}$. For example, for Bjorken flow the Liouville operator takes the form

$$\mathcal{L}_{\rm Bj} = \partial_\tau - \frac{q_3}{\tau}\frac{\partial}{\partial q_3}, \tag{42}$$

where the second term describes the "stretching" of the fluctuations, i.e., the "red shift" of the wave number q_3 due to longitudinal expansion.[6]

The first term on the r.h.s. of Eq. (40), describes the scaling of the fluctuation magnitude with the volume of a hydrodynamic cell, as the cell expands at the rate $\partial \cdot u$. This trivial rescaling could be absorbed by multiplying W by a conserved density, such as the baryon density, n. The equation for a rescaled function $N_{mm} \equiv nW_{mm}$ is the same as in Eq. (40), but without the $\partial \cdot u$ term.

$$\mathcal{L}[N_{mm}(\boldsymbol{q})] = -2\gamma_{mm}\boldsymbol{q}^2\left[N_{mm}(\boldsymbol{q}) - \frac{c_p}{n}\right]. \tag{43}$$

The last term in Eq. (40) describes diffusive relaxation of fluctuations towards equilibrium given by thermodynamic quantity c_p/n^2 (or c_p/n for N_{mm}).

It is instructive to compare Eq. (40) for W_{mm} (or the corresponding Eq. (43) for N_{mm}) to Eq. (23a) for the density-density correlator $\langle \delta n \delta n \rangle$ in the diffusion problem. The main difference is that the time derivative is replaced by the Liouville operator, which takes into account the flow of the fluid. The $(\partial \cdot u)$ term on the r.h.s. (absent when Eq. (40) is written in terms of N_{mm}, Eq. (43)) is also an effect of the flow – expansion. The diffusive relaxation terms are different because the correlated quantities are different, $\delta m \delta m$ in Eq. (40) and $\delta n \delta n$ in Eq. (23a). The coefficients, however, can be mapped onto each other via substitution

$$n \to m, \quad \gamma = \lambda\alpha' \to \gamma_{mm} = \frac{\kappa}{c_p}, \quad \lambda \to \frac{\kappa}{n}, \quad W_2 \to N_{mm}. \tag{44}$$

[6] Naturally, we have chosen the triad of the 4 vectors $\boldsymbol{e}$ in such a way that the spatial part of the 4-vector e_3 points along the direction of the longitudinal flow, while the e_1 and e_2 are constant. In this case the rotation connection ($\mathring{\omega}$) terms vanish in the confluent derivative in Eq. (32). The confluent connection ($\bar{\omega}$) terms are absent already for arbitrary flow because the fluctuating quantity, m, is a scalar.

The evolution equations for non-Gaussian correlators W_{mmm} and W_{mmmm} (or $N_{mmm} \equiv n^2 W_{mmm}$ and $N_{mmmm} \equiv n^3 W_{mmmm}$) are qualitatively similar to those in the diffusion problem in Eq. (23b) and (23c). However, unlike the case of W_{mm}, where the whole equation (43) can be obtained from Eq. (23a) for W_2 by the substitution given by Eq. (44), only the terms containing leading singularities at the critical point can be obtained from Eq. (23b) and (23c) by the substitution (44) (with $W_3 \to N_{mmm}$ and $W_4 \to N_{mmmm}$). There are subleading singularities, which are due to the nonlinearity of the mapping $n \to m$. These terms are written explicitly in Ref. [38].

4. Freeze-out of fluctuations and observables

The previous section was devoted to recent progress in describing the evolution of fluctuations in hydrodynamics using correlators of hydrodynamic variables in *coordinate* space. Heavy-ion collision experiments do not measure such densities, or their correlations, directly. Instead the particle multiplicities and their correlations in *momentum* space are measured. In this section we describe how to connect the theoretical description in terms of fluctuating hydrodynamics to these experimental observables.

4.1. Event-by-event fluctuations and their experimental measures

Typical experimental measures are cumulants of the event-by-event fluctuations or correlations of particle multiplicities. For example, if N_p is the proton number in an event, its fluctuation in the event is $\delta N_p \equiv N_p - \langle N_p \rangle$ and $\langle (\delta N)^2 \rangle$ is its quadratic cumulant, or variance, where $\langle \dots \rangle$ is the event average. Higher-order cumulants, measuring non-Gaussianity of fluctuations, are constructed similarly (see, e.g., Ref. [8] for a review).

In addition, correlations between particles can be also measured, such as $\langle \delta N_p \delta N_\pi \rangle$ – a correlation between proton and pion multiplicities. Such measures can also include higher-order correlators [40]. Similarly to correlations between species one can also consider correlations between particles with different momenta.

The number of particles d^3N_i in a given momentum cell d^3p is given by the well-know Cooper-Frye formula [41]

$$d^3 N_i = \frac{d^3 p}{(2\pi)^3} \frac{p^\mu}{p^0} \int_\Sigma d^3 \Sigma_\mu(x) f_i(x,p) \tag{45}$$

in terms of the phase space distribution function $f_i(x,p)$ integrated over the freeze-out hypersurface Σ. Therefore the correlations between different momentum cells and/or between different species, can be expressed in terms of the correlation functions of fluctuations of $f_i(x,p)$: $\delta f \equiv f - \langle f \rangle$.

To simplify and shorten notations we shall combine the species index (which includes all discrete quantum numbers, such as mass, spin, isospin, etc.) together with the coordinate and momentum into a single composite index $A = \{i, x, p\}$. Therefore, the general correlator which, upon integration over the freeze-out hypersurface, gives the observable correlation measures has the form

$$\langle \delta f_{i_1}(x_1, p_1) \dots \delta f_{i_k}(x_k, p_k) \rangle \equiv \langle \delta f_{A_1} \dots \delta f_{A_k} \rangle \,. \tag{46}$$

Usually the Cooper-Frye prescription (45) is applied to determine the event-by-event *averaged* number of particles in terms of the averaged distribution function $\langle f_A \rangle$. This averaged function is expressed in terms of the hydrodynamic variables, or fields, $T(x)$ and $\mu(x)$:

$$\langle f_A \rangle \equiv \langle f_{i_A}(x_A, p_A) \rangle = \left[\exp\left\{ \beta(x) u(x) \cdot p_A - \alpha(x) q_A \right\} - (-1)^{2s_A} \right]^{-1} \tag{47}$$

where $\beta = 1/T$, $\alpha = \mu/T$, q_A is the charge of the particle A with respect to the chemical potential μ (baryon charge, for example) and s_A is the spin of the particle.

In order to convert hydrodynamic *fluctuations* into particle event-by-event fluctuations we need an analogous freeze-out prescription for *correlators* in Eq. (46).

4.2. Freeze-out of fluctuations and the maximum entropy method

The generalization of the Cooper-Frye freeze-out to fluctuations has been first considered in Ref. [16]. In the approach of Ref. [16] the fluctuations of the phase space distribution function $f(x, p)$ are assumed to be caused by fluctuations of the hydrodynamic variables/fields $T(x)$ and $\mu(x)$ on which $f(x, p)$ depends, as in Eq. (47). As a result, coordinate space correlations in $T(x)$ and $\mu(x)$ translate into the phase space correlations in $f(x, p)$.

This approach has an important flaw, which becomes obvious if one considers fluctuations in an (almost) ideal gas. In this case, there are fluctuations of hydrodynamic variables, such as charge density $n(x)$, but there are no momentum space correlations of $f(x, p)$, which would, nevertheless, be produced if the approach of Ref. [16] were to be applied. Instead, the hydrodynamic fluctuations of $n(x)$ are matched on the particle side by trivial (Poisson, in the ideal gas case) *uncorrelated* fluctuations of the occupation numbers in each phase-space point.

This problem has been addressed in Refs. [42, 43] by subtracting this trivial ideal gas contribution from hydrodynamic fluctuations of $n(x)$ before applying the procedure of Ref. [16] to the remainder, which is due to interactions and out-of-equilibrium dynamics.

Generalization of this approach to fluctuations of other hydrodynamic variables, and to non-Gaussian fluctuations, proved elusive until the principle of maximum entropy for fluctuations was proposed and implemented in Ref. [23]. In this approach the matching of conserved hydrodynamic densities such as $\breve{\epsilon}(x)$ and $\breve{n}_q(x)$, defined in Eqs. (10), (11), is done on an event-by-event basis. For example, we have to match the fluctuations of conserved charge density:

$$\delta n_q(x) = \sum_i \int_p q_i \delta f_i(x,p) \equiv \int_{\tilde{A}} q_A \delta f_A(x) \equiv \int_A q_A \delta^{(3)}(x - x_A)\delta f_A \,, \quad (48)$$

where $\int_p$ is a 3-integral over momenta with the Lorentz-invariant measure and $\sum_i$ is a sum over the species of particles with id label i (corresponding to mass, spin, isospin, etc.) carrying charge q_i corresponding to density n_q (e.g., baryon charge when $n_q = n_B$ is the baryon density). We have also introduced a convenient shorthand $\int_{\tilde{A}}$, which denotes the sum and the momentum space integral together (but no space integration). One can think of the composite index A as describing not only the particle "id" (i.e., mass, spin, etc) but also its position in the phase space (as if each particle species has its own phase space): $A \equiv \{i_A, p_A, x_A\}$. Finally, we also introduced $\int_A$, which includes integration over the whole phase space (momentum p_A *and* coordinate x_A) of each particle species, and a convenient shorthand $f_A \equiv f_A(x_A)$. The delta function simply reflects the locality of freeze-out (i.e., each hydrodynamic cell at point x is converted into particles located at the same position $x_A = x$). Similarly, matching of the energy-momentum density requires

$$\delta(\epsilon(x)u^\mu(x)) = \int_{\tilde{A}} p^\mu \delta f_A(x) \equiv \int_A p^\mu \delta^{(3)}(x - x_A)\delta f_A \,. \quad (49)$$

It is convenient to organize equations such as (48) and (49) into an indexed array, where lowercase index a runs through five hydrodynamic variables $\delta\Psi_a = \delta\{n_q, \epsilon u^\mu\}$, similar to Eq. (11):

$$\delta\Psi_a \equiv \delta\Psi_a(x_a) = \int_A P_a^A \delta f_A \,, \quad (50)$$

where

$$P_a^A = \{q_A, p_A^\mu\}\delta^{(3)}(x_a - x_A) \quad (51)$$

is the array of the contributions of a single particle at point x_A to hydrodynamic densities $\Psi_a = \{n, \epsilon u^\mu\}$ in a cell around point x_a on the freeze-out surface. Similarly to particle index A it is convenient to view hydrodynamic

field index a as a composite index labeling both the field and the point on the freeze-out surface where the value of this field is measured.

Eq. (50) for fluctuations imply relationships between the hydrodynamic correlators in space points $x_{a_1} \dots x_{a_k}$,

$$H_{a_1 \dots a_k} \equiv \langle \delta\Psi_{a_1} \dots \delta\Psi_{a_k} \rangle \,, \tag{52}$$

and particle correlators in phase-space points $A_1 \dots A_k$,

$$G_{A_1 \dots A_k} \equiv \langle \delta f_{A_1} \dots \delta f_{A_k} \rangle \,, \tag{53}$$

which have the form:

$$H_{a_1 \dots a_k} = \int_{A_1 \dots A_k} G_{A_1 \dots A_k} P^{A_1}_{a_1} \dots P^{A_k}_{a_k} \,. \tag{54}$$

Equations (54) represent constraints on the particle correlators $G_{AB\dots}$ imposed by conservation laws. These constraints alone are not enough to completely determine $G_{AB\dots}$ simply because there are more "unknowns" $G_{AB\dots}$ then the constraints. The situation is similar already for ensemble (i.e., event) averaged quantities, or one-point functions. In this case the knowledge of the averaged energy, momentum and baryon density is not sufficient alone to determine the particle distribution functions f_A. Additional input is needed.

In the absence of additional information, the most natural solution is the one which maximizes the entropy of the resonance gas into which the hydrodynamically evolved fireball freezes out. That entropy is given by the functional of f_A:

$$S[f_A] = \int_A (\theta_A^{-1} + f_A) \ln(1 + \theta_A f_A) - f_A \ln f_A \,, \tag{55}$$

where $\theta_A = (-1)^{2s_A}$ is determined by the particle spin s_A. [7] Maximizing $S[f_A]$, subject to the constraints on f_A imposed by conservation laws, produces the well-known equilibrium distribution f_A given in Eq. (47), underlying the Cooper-Frye freeze-out procedure, which has been widely and successfully used for describing experimental data for half a century. This observation have been also used recently to describe systematically deviations from equilibrium due to viscous or diffusive gradients in Ref. [44].

In order to apply the maximum entropy approach to *fluctuation* freeze-out, on needs the entropy of fluctuations as a functional of f_A as well as

[7] Neglecting quantum statistics, i.e., taking $\theta_A \to 0$ one obtains the familiar Boltzmann entropy $S[f_A] = \int_A f_A(1 - \ln f_A)$.

correlators G_{AB}, G_{ABC}, etc. Conceptually, this entropy, $S[f_A, G_{AB}, \dots]$ represents the (logarithm) of the number of the microscopic states in the resonance gas ensemble with the given set of correlators. The single-particle entropy $S[f_A]$ is the value of $S[f_A, G_{AB}, \dots]$ when all correlators $G_{AB\dots}$ are given by their values in the equilibrium resonance gas.

The expression for the functional $S[f_A, G_{AB}, \dots]$ was found in Ref. [23]. For example, keeping only terms with out-of-equilibrium two-point correlators it reads [8]

$$S_2[f, G] = S[f] + \frac{1}{2}\mathrm{Tr}\,[\log(CG) - CG + 1]\,. \tag{56}$$

The last term is always negative except for $G = C^{-1} \equiv \bar{G}$ which is the equilibrium value of the correlator G, where $C_{AB} = -\delta^2 S[f]/(\delta f_A \delta f_B)$. When $G = \bar{G}$ the last term vanishes and S_2 is maximized with respect to G.

However, maximizing the entropy in Eq. (56) with respect to G under constraints in Eq. (54) gives

$$(G^{-1})^{AB} = (\bar{G}^{-1})^{AB} + (H^{-1} - \bar{H}^{-1})^{ab}\, P_a^A\, P_b^B\,. \tag{57}$$

In this equation and below the repeated lower case indices a, b, etc. imply summation over the set hydrodynamic variables Ψ_a, Ψ_b *and* volume integration over hydrodynamic cells at points x_a, x_b. Due to the delta functions in the definition of P_a^A in Eq. (51), these implied integrals in Eq. (57) simply set the spatial arguments of $(G^{-1})^{AB}$ to those of $(H^{-1})^{ab}$, i.e., $x_A = x_a$ and $x_B = x_b$. When hydrodynamic correlator H equals its equilibrium value $\bar{H}$ in the resonance gas, the particle correlator G equals $\bar{G}$ — its value in the resonance gas (i.e., $f_A \delta_{AB}$, neglecting quantum statistics).

If deviations of fluctuations from equilibrium resonance gas are small, the equation (57) can be linearized in such deviations. The deviations could be due to non-equilibrium effects, which have to be small for hydrodynamics to apply, or due to effects of the critical point. Linearized equation relates deviations of the particle correlators $\Delta G_{AB} = G_{AB} - \bar{G}_{AB}$ to the deviations of the hydrodynamics correlators $\Delta H_{ab} = H_{ab} - \bar{H}_{ab}$ from the resonance gas values:

$$\Delta G_{AB} = \Delta H_{ab} (\bar{H}^{-1} P \bar{G})^a_A (\bar{H}^{-1} P \bar{G})^b_B, \tag{58}$$

Similarly, the non-Gaussian cumulants $G_{ABC\dots}$ of particle fluctuations can be expressed in terms of the non-Gaussian cumulants of the hydrodynamic variables $H_{abc\dots}$. Such non-linear relations similar to Eq. (57) can be

[8] The calculation of the entropy of fluctuations along these lines for a two-point correlator of *hydrodynamic* variables can be found in Ref. [34], and it is *mathematically* similar to the 2-PI action in quantum field theory [45–49].

derived from the corresponding entropy functional found in Ref. [23] and we will not reproduce them here.

Linearized relations valid for small deviations from the equilibrium resonance gas, however, are simple and instructive. The relationship is similar to Eq. (58), but instead of the "raw" deviations from equilibrium $\Delta G_{AB...}$ and $\Delta H_{ab...}$, i.e. correlations relative to equilibrium, the proportionality relation holds between *irreducible* relative correlators $\hat{\Delta} G_{AB...}$ defined in Ref. [23]. An irreducible correlator $\hat{\Delta} G$ is different from the "raw", or reducible, relative correlator ΔG by subtraction of correlations involving only a smaller subset of the points $AB\ldots$. The irreducible ΔH differs from ΔH similarly. The resulting linear relation generalizes Eq. (58):

$$\widehat{\Delta} G_{A_1 \ldots A_k} = \widehat{\Delta} H_{a_1 \ldots a_k} (\bar{H}^{-1} P \bar{G})^{a_1}_{A_1} \ldots (\bar{H}^{-1} P \bar{G})^{a_k}_{A_k}, \tag{59}$$

where $\widehat{\Delta} G$ and $\widehat{\Delta} H$ denote *irreducible* relative correlators for particles and for hydrodynamic variables, respectively. For two-point (Gaussian) correlators $\hat{\Delta} G = \Delta G$ and $\hat{\Delta} H = \Delta H$ and Eq. (57) reproduces Eq. (57).

Eq. (58) thus solves the problem of translating fluctuations in hydrodynamics into correlations between particles at freeze-out, in such a way as to obey the conservation laws on event-by-event basis (by satisfying constraints in Eq. (54)). As one can see, it systematically eliminates spurious "self-correlations" discussed in the beginning of this section not only for Gaussian, but also for non-Gaussian cumulants.

Similarly to the way the maximum entropy approach reproduces and generalizes Cooper-Frye prescription for event *averaged* observables, the maximum entropy approach to fluctuations reproduces, justifies, and generalizes prior approaches to freezing out fluctuations, in particular, of critical fluctuations, as shown in Ref. [23]. Such a prior approach involving fluctuating background field σ was introduced in Ref. [15], generalized to non-Gaussian fluctuations in Refs. [20, 40], and then further generalized to *non-equilibrium* fluctuations in Ref. [50].

The σ-field approach [15,20,40], however, besides the knowledge of QCD EOS, requires the knowledge of the properties of the field σ such as its correlation length as well as its coupling to observed particles. These properties would depend on the nature of this field – an *a priori* unknown mixture of scalar fields such as chiral condensate, energy and baryon number densities. It was also not clear how to deal with non-critical fluctuations or contributions of lower point correlations to higher-point correlators. All these uncertainties are absent in the maximum entropy approach. The correlations described by Eq. (59) are very similar to the correlations induced by the σ field given by a mixture of hydrodynamic fields determined by the QCD EOS itself.

The maximum entropy approach thus provides a direct connection between the fluctuations of the hydrodynamic quantities and the observed particle multiplicities, with their fluctuations. This connection is determined by the EOS of QCD in the resonance gas phase where the freeze-out occurs. The effects of the critical point and non-equilibrium are encoded in the non-trivial correlations described quantitatively by Eq. (59).

5. Summary and conclusions

These lecture notes describe recent theory developments aimed at mapping QCD phase diagram and the search for the critical point in heavy-ion collisions.

The existence and location of the QCD critical point is a major unanswered question about the QCD phase diagram. Universality of critical phenomena allows us to draw predictions which do not require precise microscopic knowledge of QCD dynamics.

In particular, singular behavior of the fluctuations at critical points should manifest itself in non-monotonic dependence of the fluctuation measures in heavy-ion collisions as the critical point is approached and then passed in the course of the beam-energy scan. This dependence is especially pronounced for non-Gaussian fluctuation measures.

The dynamical nature of the heavy-ion collision fireball requires treatment of fluctuations *beyond equilibrium* thermodynamics. This means not only that we need to be able to describe fluctuations of hydrodynamic variables, but also that we need to be able to translate those hydrodynamic fluctuations into the fluctuations and correlations of particle multiplicities observable in experiments. The understanding of how to do this in a way consistent with hydrodynamics, in particular, with conservation laws, has only emerged recently. And these recent developments are the focus of the lectures.

As is often the case with a developing field of research, these lectures can only attempt to capture a snapshot of the current state of the art. Some questions still require more careful analyses, and some tools, such as fully-fledged simulation of the heavy-ion collision with fluctuations, still need to be developed before comparison to experiment can become quantitative and reliable. Naturally, much of the future development of the field will be informed by the experimental data from the BES-II program at RHIC as well as from experiments at planned future heavy-ion collision facilities [51].

I would like to express my gratitude to the organizers of the 63rd Cracow School of Theoretical Physics for their warm hospitality in Zakopane. This work is supported by the U.S. Department of Energy, Office of Science, Office of Nuclear Physics Award No. DE-FG0201ER41195.

REFERENCES

[1] C. Cagniard de la Tour, *On the effect of heat and compression*, *Annals of Philosophy, new series* **5** 290–294 (1823).

[2] Y. Goudaroulis, *Searching for a name: the development of the concept of the critical point (1822-1869)*, *Revue d'histoire des sciences* **47** 353–379 (1994).

[3] T. Andrews, *The Bakerian Lecture. — On the continuity of the gaseous and liquid states of matter*, *Phil. Trans. Roy. Soc.* **159** 575 (1869).

[4] J. van der Waals, *Over de Continuïteit van den Gas en Vloeistoftoestand*, (Ph.D. Thesis, Leiden Univ., 1873).

[5] M. v. Smoluchowski, *Molekular-kinetische theorie der opaleszenz von gasen im kritischen zustande, sowie einiger verwandter erscheinungen*, *Annalen der Physik* **330** 205–226 (1908), [https://onlinelibrary.wiley.com/doi/pdf/10.1002/andp.19083300203].

[6] A. Einstein, *Theorie der opaleszenz von homogenen flüssigkeiten und flüssigkeitsgemischen in der nähe des kritischen zustandes*, *Annalen der Physik* **338** 1275–1298 (1910), [https://onlinelibrary.wiley.com/doi/pdf/10.1002/andp.19103381612].

[7] L. D. Landau, *On the theory of phase transitions*, *Zh. Eksp. Teor. Fiz.* **7** 19–32 (1937).

[8] A. Bzdak, S. Esumi, V. Koch, J. Liao, M. Stephanov and N. Xu, *Mapping the Phases of Quantum Chromodynamics with Beam Energy Scan*, *Phys. Rept.* **853** 1–87 (2020), [1906.00936].

[9] W. Zajc, *The fluid nature of quark-gluon plasma*, *Nuclear Physics A* **805** 283c–294c (2008).

[10] Y. Aoki, G. Endrodi, Z. Fodor, S. D. Katz and K. K. Szabo, *The Order of the quantum chromodynamics transition predicted by the standard model of particle physics*, *Nature* **443** 675–678 (2006), [hep-lat/0611014].

[11] STAR collaboration, M. M. Aggarwal et al., *An Experimental Exploration of the QCD Phase Diagram: The Search for the Critical Point and the Onset of De-confinement*, 1007.2613.

[12] M. A. Stephanov, K. Rajagopal and E. V. Shuryak, *Signatures of the tricritical point in QCD*, *Phys. Rev. Lett.* **81** 4816–4819 (1998), [hep-ph/9806219].

[13] M. A. Stephanov, *QCD Phase Diagram and the Critical Point*, *Prog. Theor. Phys. Suppl.* **153** 139–156 (2004), [hep-ph/0402115].

[14] L. Landau and E. Lifshitz, *Statistical Physics: Volume 5*, (Elsevier Science, 2013).

[15] M. A. Stephanov, K. Rajagopal and E. V. Shuryak, *Event-by-event fluctuations in heavy ion collisions and the QCD critical point*, *Phys. Rev. D* **60** 114028 (1999), [hep-ph/9903292].

[16] J. I. Kapusta, B. Muller and M. Stephanov, *Relativistic Theory of Hydrodynamic Fluctuations with Applications to Heavy Ion Collisions*, *Phys. Rev. C* **85** 054906 (2012), [1112.6405].

[17] M. A. Stephanov, *Non-Gaussian fluctuations near the QCD critical point*, *Phys. Rev. Lett.* **102** 032301 (2009), [0809.3450].

[18] D. J. Amit, *Field theory, the renormalization group, and critical phenomena*, (Singapore, World Scientific, 1984).

[19] A. Pelissetto and E. Vicari, *Critical phenomena and renormalization group theory*, *Phys. Rept.* **368** 549–727 (2002), [cond-mat/0012164].

[20] M. A. Stephanov, *On the sign of kurtosis near the QCD critical point*, *Phys. Rev. Lett.* **107** 052301 (2011), [1104.1627].

[21] J. J. Rehr and N. D. Mermin, *Revised Scaling Equation of State at the Liquid-Vapor Critical Point*, *Phys. Rev.* **A8** 472–480 (1973).

[22] J. F. Nicoll, *Critical phenomena of fluids: Asymmetric Landau-Ginzburg-Wilson model*, *Phys. Rev.* **A24** 2203–2220 (1981).

[23] M. S. Pradeep and M. Stephanov, *Maximum Entropy Freeze-Out of Hydrodynamic Fluctuations*, *Phys. Rev. Lett.* **130** 162301 (2023), [2211.09142].

[24] P. Parotto, M. Bluhm, D. Mroczek, M. Nahrgang, J. Noronha-Hostler, K. Rajagopal et al., *QCD equation of state matched to lattice data and exhibiting a critical point singularity*, *Phys. Rev. C* **101** 034901 (2020), [1805.05249].

[25] STAR collaboration, J. Adam et al., *Nonmonotonic Energy Dependence of Net-Proton Number Fluctuations*, *Phys. Rev. Lett.* **126** 092301 (2021), [2001.02852].

[26] STAR collaboration, M. Abdallah et al., *Cumulants and correlation functions of net-proton, proton, and antiproton multiplicity distributions in Au+Au collisions at energies available at the BNL Relativistic Heavy Ion Collider*, *Phys. Rev. C* **104** 024902 (2021), [2101.12413].

[27] STAR collaboration, M. S. Abdallah et al., *Measurements of Proton High Order Cumulants in $\sqrt{s_{\rm NN}}$ = 3 GeV Au+Au Collisions and Implications for the QCD Critical Point*, *Phys. Rev. Lett.* **128** 202303 (2022), [2112.00240].

[28] L. Landau and E. Lifshitz, *Statistical Physics, Part 2*, vol. 9 of *Course of Theoretical Physics*, (Elsevier Science, 2013).

[29] M. Singh, C. Shen, S. McDonald, S. Jeon and C. Gale, *Hydrodynamic Fluctuations in Relativistic Heavy-Ion Collisions*, *Nucl. Phys. A* **982** 319–322 (2019), [1807.05451].

[30] C. Chattopadhyay, J. Ott, T. Schaefer and V. Skokov, *Dynamic scaling of order parameter fluctuations in model B*, *Phys. Rev. D* **108** 074004 (2023), [2304.07279].

[31] Y. Akamatsu, A. Mazeliauskas and D. Teaney, *Kinetic regime of hydrodynamic fluctuations and long time tails for a bjorken expansion*, *Phys. Rev. C* **95** 014909 (2017).

[32] Y. Akamatsu, A. Mazeliauskas and D. Teaney, *Bulk viscosity from hydrodynamic fluctuations with relativistic hydrokinetic theory*, *Phys. Rev. C* **97** 024902 (2018).

[33] M. Martinez and T. Schaefer, *Stochastic hydrodynamics and long time tails of an expanding conformal charged fluid*, 1812.05279.

[34] M. Stephanov and Y. Yin, *Hydrodynamics with parametric slowing down and fluctuations near the critical point*, *Phys. Rev. D* **98** 036006 (2018), [1712.10305].

[35] X. An, G. Basar, M. Stephanov and H.-U. Yee, *Relativistic Hydrodynamic Fluctuations*, *Phys. Rev. C* **100** 024910 (2019), [1902.09517].

[36] X. An, G. Başar, M. Stephanov and H.-U. Yee, *Fluctuation dynamics in a relativistic fluid with a critical point*, *Phys. Rev. C* **102** 034901 (2020), [1912.13456].

[37] X. An, G. Başar, M. Stephanov and H.-U. Yee, *Evolution of Non-Gaussian Hydrodynamic Fluctuations*, *Phys. Rev. Lett.* **127** 072301 (2021), [2009.10742].

[38] X. An, G. Basar, M. Stephanov and H.-U. Yee, *Non-Gaussian fluctuation dynamics in relativistic fluids*, *Phys. Rev. C* **108** 034910 (2023), [2212.14029].

[39] A. Onuki, *Phase Transition Dynamics*, (Cambridge University Press, 2002).

[40] C. Athanasiou, K. Rajagopal and M. Stephanov, *Using Higher Moments of Fluctuations and their Ratios in the Search for the QCD Critical Point*, *Phys. Rev. D* **82** 074008 (2010), [1006.4636].

[41] F. Cooper and G. Frye, *Comment on the Single Particle Distribution in the Hydrodynamic and Statistical Thermodynamic Models of Multiparticle Production*, *Phys. Rev. D* **10** 186 (1974).

[42] B. Ling, T. Springer and M. Stephanov, *Hydrodynamics of charge fluctuations and balance functions*, *Phys. Rev. C* **89** 064901 (2014), [1310.6036].

[43] J. I. Kapusta and C. Plumberg, *Causal Electric Charge Diffusion and Balance Functions in Relativistic Heavy Ion Collisions*, *Phys. Rev. C* **97** 014906 (2018), [1710.03329].

[44] D. Everett, C. Chattopadhyay and U. Heinz, *Maximum entropy kinetic matching conditions for heavy-ion collisions*, *Phys. Rev. C* **103** 064902 (2021), [2101.01130].

[45] J. M. Luttinger and J. C. Ward, *Ground state energy of a many fermion system. 2.*, *Phys. Rev.* **118** 1417–1427 (1960).

[46] G. Baym, *Selfconsistent approximation in many body systems*, *Phys. Rev.* **127** 1391–1401 (1962).

[47] J. M. Cornwall, R. Jackiw and E. Tomboulis, *Effective Action for Composite Operators*, *Phys. Rev. D* **10** 2428–2445 (1974).

[48] R. E. Norton and J. M. Cornwall, *On the Formalism of Relativistic Many Body Theory*, *Annals Phys.* **91** 106 (1975).

[49] J. Berges and J. Serreau, *Progress in nonequilibrium quantum field theory*, in *5th International Conference on Strong and Electroweak Matter*, pp. 111–126, 2003. hep-ph/0302210. DOI.

[50] M. Pradeep, K. Rajagopal, M. Stephanov and Y. Yin, *Freezing out fluctuations in Hydro+ near the QCD critical point*, *Phys. Rev. D* **106** 036017 (2022), [2204.00639].

[51] NSAC, *A New Era of Discovery: The 2023 Long Range Plan for Nuclear Science*, https://nuclearsciencefuture.org/wp-content/uploads/2023/11/NSAC-LRP-2023-v1.3.pdf, (2023).

arXiv:2403.03246v1 [astro-ph.HE] 5 Mar 2024

Listening to the long ringdown: a novel way to pinpoint the equation of state in neutron-star cores

Christian Ecker[1], Tyler Gorda[1,2,3], Aleksi Kurkela[4], Luciano Rezzolla[1,5,6]

[1]Institut für Theoretische Physik, Goethe Universität, 60438, Frankfurt am Main, Germany.
[2]ExtreMe Matter Institute EMMI, GSI Helmholtzzentrum für Schwerionenforschung GmbH, 64291, Darmstadt, Germany.
[3]Department of Physics, Technische Universität Darmstadt, 64289 Darmstadt, Germany.
[4]Faculty of Science and Technology, University of Stavanger, Stavanger, 4036, Stavanger, Norway.
[5]Frankfurt Institute for Advanced Studies, 60438, Frankfurt, Germany.
[6]School of Mathematics Trinity College, Dublin 2, Ireland.

Abstract

Multimessenger signals from binary neutron star (BNS) mergers are promising tools to infer the largely unknown properties of nuclear matter at densities that are presently inaccessible to laboratory experiments. The gravitational waves (GWs) emitted by BNS merger remnants, in particular, have the potential of setting tight constraints on the neutron-star equation of state (EOS) that would complement those coming from the late inspiral, direct mass-radius measurements, or ab-initio dense-matter calculations. To explore this possibility, we perform a representative series of general-relativistic simulations of BNS systems with EOSs carefully constructed so as to cover comprehensively the high-density regime of the EOS space. From these simulations, we identify a novel and tight correlation between the ratio of the energy and angular-momentum losses in the late-time portion of the post-merger signal, i.e., the "long ringdown", and the properties of the EOS at the highest pressures and densities in neutron-star cores. When applying this correlation to post-merger GW signals, we find a significant reduction of the EOS uncertainty at densities several times the nuclear saturation density, where no direct constraints are currently available. Hence, the long ringdown has the potential of providing new and stringent constraints on the state of matter in neutron stars in general and, in particular, in their cores.

The densest matter in the observable universe is found in the cores of neutron stars (NSs), where gravity compresses it to supernuclear densities, exceeding manyfold the nuclear density of $n_{\rm sat} = 0.16$ baryons/fm^3. While the behaviour of pressure and density in such cores, that is, the equation of state (EOS) of strongly interacting matter, remains an open question, a precise determination of the EOS of NSs would provide precious insights on the phase diagram of Quantum Chromodynamics (QCD).

In recent years, there have been remarkable advances in the inference of the EOS thanks to rapidly advancing observations of NSs and theoretical ab-initio calculations (see, e.g., [1]). In addition, the observation of the GW signal from the late inspiral of the BNS merger event GW170817 demonstrated the potential of GW measurements to constrain the EOS by setting limits on the tidal deformabilities of the inspiralling NSs, which are tightly correlated with the EOS at densities $\sim 3\, n_{\rm sat}$ and reached by NSs prior to merger (see, e.g., Refs. [2–4] for reviews). Finally, the analysis of the electromagnetic counterpart associated with GW170817 provided convincing evidence for the formation of a hypermassive neutron star (HMNS) that ultimately collapsed into a black hole approximately one second after the merger [5]. Because HMNSs are expected to reach densities that are significantly higher than those in the stars before the merger, the study of their properties opens up the opportunity to directly determine the EOS up to the highest densities in the observable Universe.

This potential will be fully realized with the upcoming third-generation GW observatories [6, 7], whose high sensitivity at frequencies larger than 1 kHz allows them to detect with high signal-to-noise ratios (SNR) also the post-merger signal from the HMNS [2–4]. This has important consequences, as a number of studies have shown that the most prominent features of the spectral power density (PSD) of the post-merger signal, i.e., the $f_1 - f_3$ "peaks" of the spectrum, correlate with the underlying EOS models (see, e.g., [8–13]). We here propose an improvement on this approach that concentrates on a specific and late part of the post-merger signal and that allows for a direct determination of the EOS at the highest densities.

More specifically, just like the ringdown of a perturbed black hole contains precise information on the black-hole properties, we show that the late-time, attenuated GW signal produced by the HMNSs between ~ 1 and $\sim 15\,{\rm ms}$ holds a similar potential in showing a clear correlation with the maximum densities and pressures of the EOS. We refer to this late-time signal as to the "*long ringdown*" since its characteristic damping time is much longer than the typical damping time of a black hole with similar mass. The origin of this long ringdown is to be found in the fact that $\sim 10\,{\rm ms}$ after the merger – when the GW amplitude is still comparatively large – the HMNS exhibits a quasi-stationary dynamics, with a mostly axisymmetric equilibrium and small $\ell = 2, m = 2$ deformations that are responsible for an almost constant-frequency, constant-amplitude GW emission. Under these conditions, a simple toy model, as that introduced in Ref. [9], is sufficient to show that thanks to the equilibrium achieved during this stage, the radiated GW energy and angular momentum follow a linear relation and correlate strongly with the EOS at high densities. Hence, the observation of the long ringdown at a large SNR represents a novel and faithful probe of the largest densities and pressures of the remnant's EOS.

In order to quantify this novel correlation, we perform a suite of general-relativistic simulations of BNS mergers with EOSs carefully constructed so as to comprehensively cover the currently allowed space of parameters. More precisely, we employ a large posterior sample of model-agnostic, Gaussian-process (GP) based, zero-temperature EOSs of NS matter

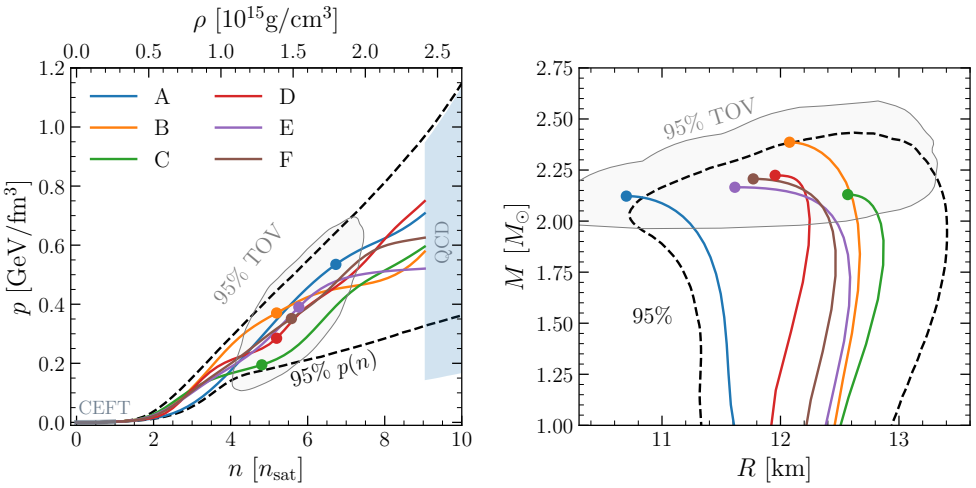

Fig. 1 The "golden" EOSs. *Left panel:* Solid lines of different colors show the six golden EOSs (A–F) in the (p, n) plane. The dashed black lines show the 95% credible intervals of all possible EOSs, while the CEFT and QCD bounds are shown with shaded areas (gray and light blue, respectively). Colored filled circles show the TOV points of the golden EOSs, while the solid light gray line is the 95% credible interval for all TOVs. *Right panel:* The same as in the left but shown in the (M, R) plane.

from [14] that is conditioned with constraints from the tidal-deformability measurement of GW170817, radio measurements of high-mass pulsars, combined mass-radius measurements from X-ray pulse-profile modeling of isolated NSs, as well as with low-energy nuclear-theory constraints from chiral effective field theory (CEFT) and high-energy particle-theory bounds from perturbative QCD. The significant breadth of EOSs in the ensemble reflects the current level of uncertainty in the determination of the EOS. Because it is computationally prohibitively expensive to scan a large number of EOSs, we reduce the full ensemble to a smaller sample of six "golden" EOSs that maximizes the variation in the following four NS parameters: the maximum (TOV) mass of an isolated, nonrotating NS $M_{\rm TOV}$, its compactness $C_{\rm TOV} := M_{\rm TOV}/R_{\rm TOV}$, where $R_{\rm TOV}$ is the corresponding radius, the central pressure $p_{\rm TOV}$, and the radius of a typical $1.4\,M_\odot$ NS $R_{1.4}$. By performing a principal-component analysis [see supplemental material (SM) for details], we select six EOSs that are located in the center (EOS labeled F) and distributed on the boundary (EOSs labelled A – E) of the 68%-credible region in the four-dimensional space spanned by the NS parameters (see Fig. 5 of SM).

These six EOSs are shown in Fig. 1 in the pressure–number density (p, n) plane (left panel), along with the corresponding mass-radius relationships for nonrotating stars (right panel). We note that, by construction, our global sample of EOSs, and hence also the golden EOSs, do not contain strong phase transitions, which could lead to a larger EOS space consistent with astrophysical bounds [15]. This choice allows us to focus our attention on smooth EOSs and to build an understanding of their phenomenology, leaving the exploration of EOSs with phase transitions to a subsequent work where we will employ the approach in [16, 17].

While NSs during the inspiral stage can be described also when neglecting the temperature dependence of the EOS, during and after the merger shock-heating effects can lead

to temperatures of tens of MeV inside the merger remnant [18–24]. To model and approximate these heating effects, the zero-temperature EOSs selected in our sample are modified in what is normally referred to as a "hybrid EOS", where the cold part of the EOS is combined with an ideal-gas EOS, thus providing an effective-temperature contribution. While this is an approximation, it does not affect the properties of the correlation and we have adopted an adiabatic-index value of $\Gamma_{\rm th} = 1.75$ [25], which on average mimics well the temperature dependence of microscopic constructions [26] (see SM for details). We have verified that all of the qualitative properties of the GW emission from the HMNS presented here are preserved when considering also self-consistent temperature-dependent EOSs, such as the V-QCD [26] or the HS-DD2 EOS [27] (see SM).

Using these six golden EOSs, we performed a series of general-relativistic BNS merger simulations and extracted the emitted GW signal starting from about 15 ms before merger until 30 ms after. From these simulations, we compute the instantaneous GW frequency $f_{\rm GW}$, the radiated energy $E_{\rm GW}$, and angular momentum $J_{\rm GW}$. The binaries have been constructed with parameters that are consistent with those measured for GW170817, i.e., with fixed chirp mass $\mathcal{M}_{\rm chirp} = 1.18\,M_\odot$ and three different ratios $q := M_2/M_1 = 0.7, 0.85, 1$ of the binary constituent masses M_1 and M_2. From a qualitative point of view, the dynamics of the six binaries reflects what has been found by a large number of works (e.g., [9, 18–24, 28]), with an HMNS attaining a mestastable equilibrium a few milliseconds after the merger and then emitting GW radiation at frequency that is almost constant in time and around the characteristic f_2 frequency of the post-merger PSD [10]. However, what has not been appreciated so far is the behaviour of the rates at which energy and angular momentum are radiated by the HMNS when it has reached a quasi-stationary equilibrium at about 10 ms after the merger.

Figure 2 displays the most salient results of the six equal-mass binaries by showing in the top part the evolution of the radiated GW energy $E_{\rm GW}$ and angular momentum $J_{\rm GW}$ normalized by their values from the start of the simulations till the merger[1], $E^{\rm mer}_{\rm GW}$ and $J^{\rm mer}_{\rm GW}$, where, as customary, $t_{\rm mer}$ is defined as the moment of maximum-amplitude strain. Note the significant change in the evolution between the inspiral phase and the post-merger. In the former, all binaries – indicated with the same color convention as in Fig. 1 – follow essentially the same trajectory in the $(E_{\rm GW}, J_{\rm GW})$ plane, which is well captured by the post-Newtonian (PN) approximation shown as a black dashed line (we use a reference tidal deformability $\tilde{\Lambda} = 580$ in the 5PN-order Taylor-T2 model of the PyCBC library [31]). Obviously, there are differences in evolution of the six binaries that are generated by the different tidal deformabilities, but these differences are minute when compared with those that emerge after the merger, when the different evolutions become visibly distinct. More importantly, it is remarkable that in the latter part of the signal, i.e., in the long ringdown, the normalized radiative losses in $E_{\rm GW}$ and $J_{\rm GW}$ are linearly related, as clearly shown in the inset reporting a magnification of the long ringdown. This apparently striking behaviour has a rather simple explanation in terms of the Newtonian quadrupole formula applied to a rotating system with an $\ell = 2 = m$ deformation, as in the toy model of Ref. [9]. In this case, one can show the identity $\dot{E}_{\rm GW}/\dot{J}_{\rm GW} = dE_{\rm GW}/dJ_{\rm GW} = f_{\rm GW}/(2\pi)$, where we use a dot to indicate a time derivative (see SM). Stated differently, during the long ringdown, the HMNS behaves essentially as a rotating $m = 2$ deformed quadrupole and radiates GW energy and angular

[1] The specific starting time of the simulation, or the time when the signal enters the detector's sensitivity curve, are not relevant here, since the energy and angular momentum radiated in the entire inspiral phase are negligibly small compared to the losses during and after the merger [29, 30].

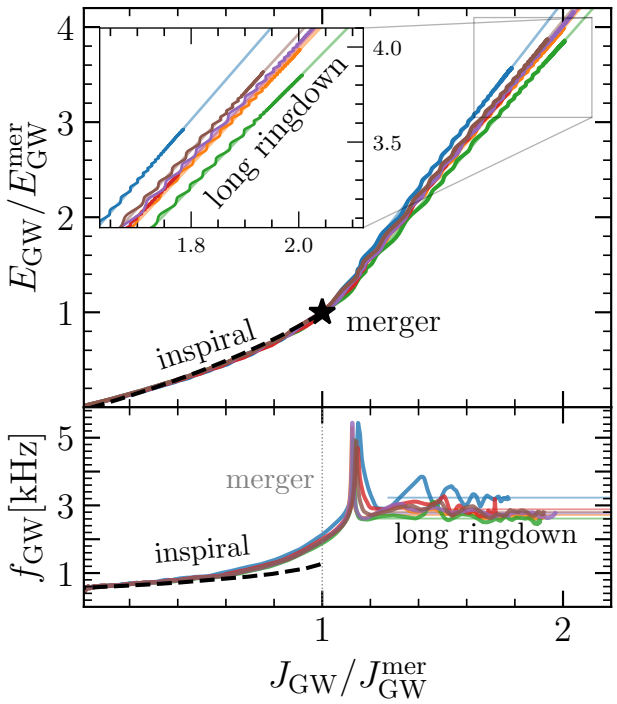

Fig. 2 Radiated GW energy and angular momentum. *Top panel:* Using the same color convention as in Fig. 1, we report the energy $E_{\rm GW}$ and angular momentum $J_{\rm GW}$ emitted in GWs for the golden EOSs when normalized to the values at merger, indicated by a star. The evolution expected from the post-Newtonian inspiral is shown with a dashed black line. The inset offers a magnification of the long ringdown with the corresponding linear slopes indicated by thin lines of the same color. *Lower panel:* As in the top panel but in terms of the instantaneous GW frequency $f_{\rm GW}$. The data refers to equal-mass binaries but very similar behaviour is found also for unequal-mass binaries (see Fig. 9 in the SM for details).

momentum that are linearly related. Indeed, we have verified that more than 97% of the gravitational wave amplitude arises from this dominant mode. We note that while Fig. 2 refers to equal-mass binaries, a perfectly analogous behaviour is also realized by unequal-mass binaries, which we do not show here for clarity, but that can be found in the SM (see Fig. 9).

The importance of the results summarised in Fig. 2 is that binaries whose HMNS signal can be measured with high SNR, and hence for which the slope between the radiated GW energy and angular momentum can be measured accurately, offer a key to access the properties of the EOS at the highest densities and pressures, i.e., $n_{\rm TOV}$ and $p_{\rm TOV}$. Before discussing how this can be done and to what precision, we need to make a few important remarks. First, the physical picture presented in Fig. 2 in terms of the slope between $E_{\rm GW}$ and $J_{\rm GW}$ can also be drawn in terms of the instantaneous GW frequency $f_{\rm GW}$, which is instead presented in the bottom part of Fig. 2. This panel shows in fact that during the long ringdown $f_{\rm GW}$ also asymptotes to an essentially constant value, $f_{\rm GW} = f_{\rm rd} \simeq$ const., and, of course, this is the same value that can be deduced from the slope between $E_{\rm GW}$ and $J_{\rm GW}$. Hence, while measuring $f_{\rm rd}$ in the long ringdown is conceptually analogous to measuring the slope, we have found that the latter is more robust as it is easier to fit an

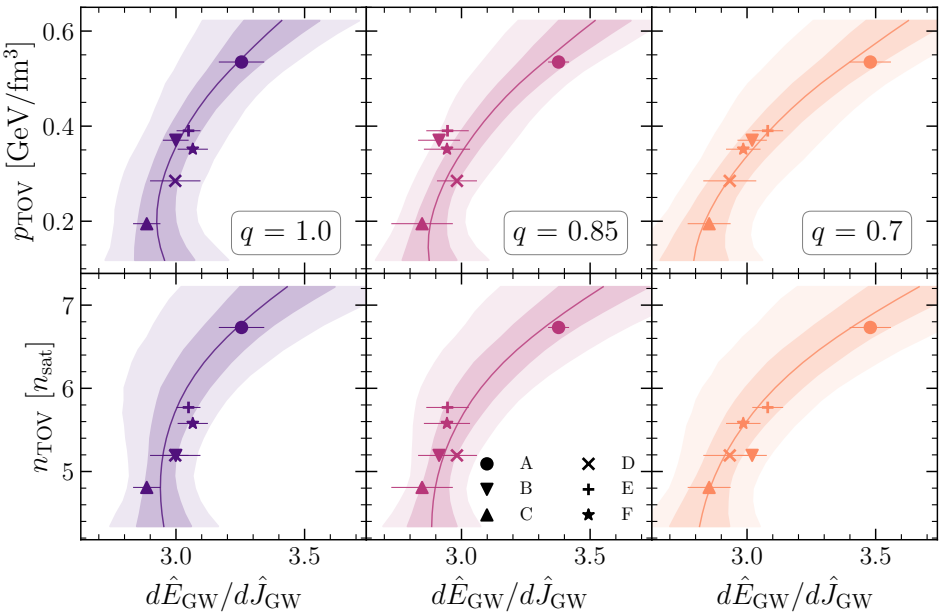

Fig. 3 Correlation between the long-ringdown slope and the TOV properties. Data and fits illustrating the correlations between the slope of the radiated quantities $\widehat{E}_{\rm GW}$ and $\widehat{J}_{\rm GW}$ normalized to the merger values, and $p_{\rm TOV}$ (top row) or $n_{\rm TOV}$ (bottom row), and for different mass ratios (different columns). The dark (light) shaded regions denote 68%(95%) credible intervals for the bilinear model (1), while the solid lines denote the mean value. A marginalization over the remaining EOS quantity in the bilinear model was performed.

approximately linear function, i.e., $E_{\rm GW}$ vs $J_{\rm GW}$, than the average of an oscillating and potentially noisy function, i.e., $f_{\rm GW}$ (see SM for a discussion); the extrapolated slopes are shown with transparent lines of the corresponding color in Fig. 2. Second, the long-ringdown frequency $f_{\rm rd}$ is close to but different from the main-peak frequency in the post-merger PSD, i.e., f_2, which is traditionally advocated as a good proxy for the EOS [8–12, 32]. This is because $f_{\rm GW}$ oscillates wildly right after the merger and hence f_2 collects power from frequencies that are both larger and smaller than $f_{\rm rd}$ (see lower part of Fig. 2), thus increasing the uncertainty in its measurement. Finally, our analysis reveals that the correlations between the GW signatures (i.e., f_2 and $f_{\rm rd}$) and the properties of the EOS (i.e., $n_{\rm TOV}$ and $p_{\rm TOV}$) are statistically different. In particular, we have measured the Pearson-correlation coefficients to be respectively $r(dE_{\rm GW}/dJ_{\rm GW}, p_{\rm TOV}) = 0.877$ and $r(f_2, p_{\rm TOV}) = 0.792$ and $r(dE_{\rm GW}/dJ_{\rm GW}, n_{\rm TOV}) = 0.917$ and $r(f_2, n_{\rm TOV}) = 0.865$, thus indicating that there is a strong correlation in both cases, but also that this is stronger for the long-ringdown frequency.

To illustrate how to make use of the long ringdown to set constraints on the EOS at the highest densities and pressures, Fig. 3 shows the tight correlation between the normalized slope during the long ringdown $d\widehat{E}_{\rm GW}/d\widehat{J}_{\rm GW}$, where $\widehat{E}_{\rm GW} := E_{\rm GW}/E^{\rm mer}_{\rm GW}$ and $\widehat{J}_{\rm GW} := J_{\rm GW}/J^{\rm mer}_{\rm GW}$, and the highest pressure $p_{\rm TOV}$ and density $n_{\rm TOV}$ reached in nonrotating NSs. The six different panels of Fig. 3 are organized so as to show in the three columns the correlations for the three different mass ratios considered ($q = 1, 0.85$ and 0.70 from

left to right) and in the two rows the variation with the maximum pressure (top row) and the maximum density (bottom row). It is straightforward to appreciate from the six panels that correlation is strong and we find it quite remarkable that measuring long-ringdown slope of a low-mass NS can provide such precise information on the properties of the EOS at much larger densities and pressures than those of the low-mass star.

To quantify the strength of the correlation, we consider a bilinear model fit to the data from our simulations

$$\frac{d\widehat{E}_{\rm GW}}{d\widehat{J}_{\rm GW}} = \beta_0 + \beta_1\, p_{\rm TOV} + \beta_2\, n_{\rm TOV} + \beta_3\, q + \beta_4\, q\, p_{\rm TOV} + \beta_5\, q\, n_{\rm TOV} + \beta_6\, p_{\rm TOV}\, n_{\rm TOV}\,. \tag{1}$$

Note that the ansatz (1) ignores quadratic terms in $q, p_{\rm TOV}$, and $n_{\rm TOV}$ as these provide only marginal improvements to the fit (for q) or break it (for $p_{\rm TOV}, n_{\rm TOV}$). After fitting this model over the time window $t - t_{\rm mer} \in [1, 30]\,{\rm ms}$, we obtain a probability distribution for the model parameters β_i and, in turn, for the long-ringdown slope given the parameters of the EOS $P(d\widehat{E}_{\rm GW}/d\widehat{J}_{\rm GW}|p_{\rm TOV}, n_{\rm TOV}, q)$, which we use to produce the 68% (95%) credible intervals for $d\widehat{E}_{\rm GW}/d\widehat{J}_{\rm GW}$ shown in dark (light) shading in each of the panels in Fig. 3. These intervals are produced by marginalizing over the other EOS variables using the underlying probability distribution $P(p_{\rm TOV}, n_{\rm TOV})$ from the EOS ensemble.

Clearly, the bilinear model (1) reproduces well long-ringdown slopes, where the distribution of model parameters $\boldsymbol{\beta} := (\beta_0, \ldots, \beta_6)$ are given by a multivariate Gaussian distribution with a mean $\bar{\boldsymbol{\beta}} = (1.78, 0.72, -1.44, 1.90, -1.74, -1.14, 3.61)$ and a covariance matrix ${\rm cov}(\boldsymbol{\beta})$ reported in Table 2 of the SM, with $p_{\rm TOV}$ and $n_{\rm TOV}$ expressed in units of ${\rm GeV/fm}^3$ and ${\rm fm}^{-3}$, respectively.

Having pointed out a novel correlation between the properties of the long-term GW signal from a merger remnant and after having quantified the strength of this correlation in terms of the properties of the EOS at the *highest density*, we now take our analysis a step further and show how our results, in conjunction with a future post-merger GW detection, can be used to constrain the EOS at *all densities*. More specifically, to demonstrate the effect of a future measurement of $d\widehat{E}_{\rm GW}/d\widehat{J}_{\rm GW}$, we use Bayes's theorem to infer the combined EOS and NS properties

$$P({\rm EOS}, {\rm NSs}|{\rm data}) = \frac{P({\rm data}|{\rm EOS}, {\rm NSs})P({\rm EOS}, {\rm NSs})}{P({\rm data})}\,. \tag{2}$$

In particular, we can use as an additional piece of the likelihood function $P({\rm data}|{\rm EOS}, {\rm NSs})$ the integral of our bilinear model over the likelihood of the measurement (see SM for the details). Assuming a Gaussian measurement of the long-ringdown slope, as well as a uniform distribution on the mass ratio $q \in [0.7, 1.0]$ from the measurement, we display in Fig. 4 the resulting constraints at 68% credibility.

The left panel of Fig. 4 considers three values of the measured long-ringdown slope, i.e., $d\widehat{E}_{\rm GW}/d\widehat{J}_{\rm GW} = 2.9, 3.2$ and 3.4 with an error estimate of 8%, *joint* with the measurements of the frequency $f_2 = 2.6, 3.0, 3.4\,{\rm kHz}$ with an error of 8% [32, 33]. Using different colors for the different measurements, it is then apparent that smaller (larger) values of the slope would constrain the EOS to have higher (lower) pressures at 2–4 times nuclear saturation density while also having a smaller (larger) pressure and density for the maximally

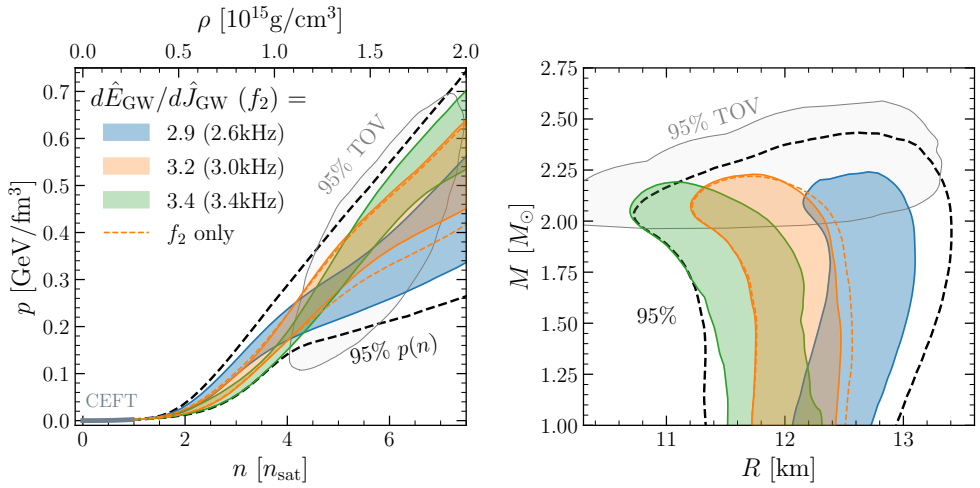

Fig. 4 Impact of slope measurements on the EOS and NS properties. *Left panel* Using the same convention as in Fig. 1, we show the 68% credibility values on the (p, n) plane from potential *joint* measurements of the long-ringdown slope and f_2 assuming a flat distribution for $q \in [0.7, 1]$ and an uncertainty of $\pm 4\%$ on the slope and $\pm 4\%$ on f_2. Shown with a dashed line is the result for using only the f_2 measurement. *Right panel* the same but in the (M, R) plane.

massive NSs. In turn, this leads to larger (smaller) radii for the most massive stars, as shown in the right panel of Fig. 4. Note also how the measurement of the long ringdown provides a considerable improvement of the corresponding posteriors obtained when measuring the f_2 frequency only (see dashed orange lines for the representative case of $d\widehat{E}_{\rm GW}/d\widehat{J}_{\rm GW} = 3.2$, $f_2 = 3.2\,{\rm kHz}$).

Our concluding remarks are about the robustness of the new correlation. We have already commented that the results apply qualitatively unchanged when considering unequal-mass binaries or EOSs with a consistent temperature dependence (see SM for details). In addition, we have also verified that the same is true when considering different values for the chirp mass. More specifically, taking $\mathcal{M}_{\rm chirp} = 1.13, 1.22\,M_\odot$ instead of our fiducial value of 1.18 leads to differences in the slope that are significantly smaller than those introduced by considering different EOSs (see SM for details). Finally, and importantly, the long-ringdown slope is essentially insensitive to different choices in the adiabatic index $\Gamma_{\rm th}$, as we have verified by replacing our fiducial value of 1.75 with $\Gamma_{\rm th} = 1.5$ or 2 (see SM for details).

The preliminary study carried out here can be improved in a number of ways, e.g., by estimating the impact that large spins, strong magnetic fields, neutrino emission, and temperature-dependent EOSs have on the long-ringdown slope. However, already now our new correlation between the radiated energy and angular momentum during the long ringdown has the realistic potential of significantly reducing the EOS uncertainty at the highest densities realized in NSs for which no alternative observational constraints are available to date. This potential may already be exploited by the ongoing and near-future observations by the LIGO-Virgo-Kagra collaboration, but it will surely play a fundamental role in third-generation GW detectors, where the combined network of Cosmic Explorer and Einstein Telescope are expected to detect 180 BNS signals per year with post-merger ${\rm SNR} > 8$ [7].

The potential that these detectors have in measuring the long ringdown will be explored in a forthcoming work.

Acknowledgements. It is a pleasure to thank M. Cassing, M. Chabanov, C. Musolino, H. H.-Y. Ng, and K. Topolski for numerous discussions and comments during the development of this work. Partial funding comes from the Deutsche Forschungsgemeinschaft (DFG, German Research Foundation) project-ID 279384907–SFB 1245, the State of Hesse within the Research Cluster ELEMENTS (Project ID 500/10.006), by the ERC Advanced Grant "JETSET: Launching, propagation and emission of relativistic jets from binary mergers and across mass scales" (Grant No. 884631). C. E. acknowledges support by the DFG through the CRC-TR 211 "Strong-interaction matter under extreme conditions"– project number 315477589 – TRR 211. L. R. acknowledges the Walter Greiner Gesellschaft zur Förderung der physikalischen Grundlagenforschung e.V. through the Carl W. Fueck Laureatus Chair. The simulations were performed on the local ITP Supercomputing Clusters Iboga and Calea and on HPE Apollo HAWK at the High Performance Computing Center Stuttgart (HLRS) under the grant BNSMIC.

Methods

In what follows we provide additional details on a number of aspects of our analysis that we have omitted in the main text for compactness. These refer to the approach followed for the selection of the golden EOSs, the numerical techniques employed to simulate the binaries and extract the GW signal, and a number of validations highlighting the robustness of the correlation found between the EOS and the long-ringdown slope.

Selection of the golden EOSs

For the agnostic construction of cold EOSs, we begin from the GP setup presented in [14], which we briefly review here. Below densities of $n = 0.57\, n_{\rm sat}$, we use the crust model by Baym, Pethick, and Sutherland [34]. Above this density, in the interval $n = [0.57, 10]\, n_{\rm sat}$, a GP regression is performed in an auxiliary variable $\phi(n) := -\ln(1/c_s^2(n) - 1)$, where c_s is the sound speed, and where the prior for $\phi(n)$ is drawn from a multivariate Gaussian distribution

$$\phi(n) \sim \mathcal{N}\big(-\ln(1/\bar{c}_s^2 - 1), K(n, n')\big)\,, \tag{3}$$

with a Gaussian kernel $K(n, n') = \eta \exp\big(-(n - n')^2/2\ell^2\big)$ [14]. The hyper-parameters η, ℓ, and $\bar{c}_s^2$ within these definitions are themselves drawn from probability distributions

$$\eta \sim \mathcal{N}(1.25, 0.2^2)\,, \quad \ell \sim \mathcal{N}(1.0\, n_{\rm sat}, (0.25\, n_{\rm sat})^2)\,, \quad \bar{c}_s^2 \sim \mathcal{N}(0.5, 0.25^2)\,. \tag{4}$$

Below a density of $1.1\, n_{\rm sat}$, the GP is conditioned with the CEFT results from [35]. In particular, the average between the "soft" and "stiff" results from that work are taken as the mean, while the difference between them is taken as the 90% credible interval for the conditioning [14]. From this GP, we draw sample of 120,000 EOSs.

We impose the astrophysical observations referred to as "Pulsars + $\tilde{\Lambda}$" in [14]. Explicitly, we use the following three sets of observations:

1. heavy-pulsar mass constraints from radio astronomy. In particular, we use the constraints from PSR J0348+0432 with $M = 2.01 \pm 0.04\,M_\odot$ [36] and PSR J1624−2230 with $M = 1.928 \pm 0.017\,M_\odot$ [37]. We approximate the uncertainties from these measurements as normal distributions, which holds to good accuracy.
2. joint tidal-deformability and mass-ratio constraints from GW observations. We use the two-dimensional (2D) joint probability distribution for the tidal deformability and mass ratio using the `PhenomPNRT` waveform model with low-spin priors from Fig. 12 of [38].
3. joint mass-radius measurements from X-ray pulse profile modeling. We use the 2D joint probability distribution for the mass and radius for PSR J0740+6620 using the NICER + XMM-Newton data from the right panel of Fig. 1 of [39].

Within each of these measurements, we assume as our mass prior $P_0(M|\mathrm{EOS})$ a uniform distribution between $0.5\,M_\odot$ and $M_{\rm TOV}$.

Lastly, the GP is conditioned using information from high-density perturbative QCD calculations, which are under theoretical control at densities with baryon number chemical potential $\mu = 2.6\,\mathrm{GeV}$, corresponding to $n \approx 40 n_{\rm sat}$. This information is included in a conservative way, excluding those EOSs which cannot be connected to the perturbative densities using any causal, mechanically stable, and thermodynamically consistent interpolation in the density interval $[10, 40]\,n_{\rm sat}$ [40]. This is done by conditioning the GP with the QCD likelihood function of [14], where the uncertainty in the pQCD calculation at $\mu = 2.6\,\mathrm{GeV}$ is taken into account by marginalizing over the unphysical renormalization scale $X := 2\Sigma/(3\mu)$ in the range $[0.5, 2]$, with Σ the renormalization scale in the modified minimal subtraction scheme.

We consider the posterior in the 4D space of $(M_{\rm TOV},\, C_{\rm TOV},\, \ln p_{\rm TOV},\, R_{1.4})$, within which we perform a modified principal-component analysis to select a small sample of EOSs that characterize the 68% credible region of the distribution. This is done as follows:

1. construct a normalized set of variables defined by $\widehat{x} := (x - \mu_x)/\sigma_x$, with μ_x, σ_x the mean and standard deviation for the variable x.
2. construct the 4×4 covariance matrix of these normalized variables.
3. calculate the eigenvalues λ_i and eigenvectors v_i of this covariance matrix, ordered by the magnitude on the eigenvalues.

The orthogonal vectors v_i define the principal components of the distribution in the original 4D space, while the λ_i characterize the variance of the distribution in each of these directions.

Figure 5 shows on the left the components of the v_i in the normalized coordinate system, while the right panel shows the posterior distribution in the v_i coordinate system. As seen in this figure, the distribution is primarily 3D, with a prominent triangular component within the plane spanned by the components v_0 and v_1. This behaviour of the distribution clearly explains a well-known aspect to anyone constructing agnostic models of EOSs, namely, that while it is reasonable to model the variation in EOSs in terms of stiffness, i.e., $\widehat{R}_{1.4}$, this choice does not cover all of the possible space of parameters, which can be determined for instance in a principal-component analysis. Finally, we select the six golden EOSs from our ensemble by choosing EOSs that are near the extrema of the 68% credible region and one near the origin. With a standard principal-component analysis, these points would be given by $\pm\sqrt{\lambda_i} v_i$ (no summation), which we modify slightly to capture the triangular shape within the plane spanned by v_0 and v_1. In this plane, we use the directions that extremize the 95% credible regions. Having identified the relevant points in the parameter space, we then select

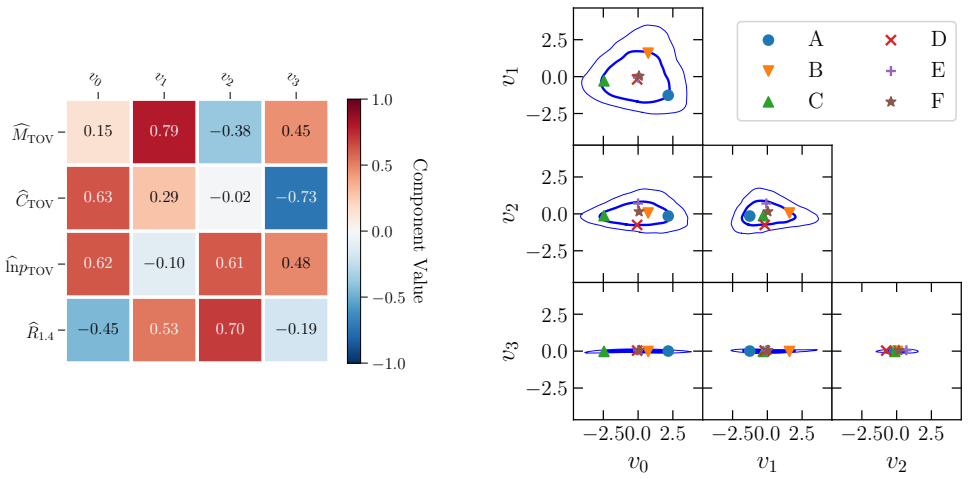

Fig. 5 Principal-Component Analysis. *Left panel:* Components of the principal-component vectors v_i in terms of the original (normalized) coordinates $(\widehat{M}_{\rm TOV}, \widehat{C}_{\rm TOV}, \widehat{\ln p}_{\rm TOV}, \widehat{R}_{1.4})$. *Right panel:* Posterior distribution in the PCA coordinate system. Shown are 95% (thin lines) and 68% (thick lines) credible regions. Also shown are the six golden EOSs, with A–E lying on the 68% contour by construction, and F lying at the center.

the golden EOSs corresponding to one of these six points by finding the 30 closest EOSs using the Euclidean metric in the full 4D space and selecting the one with the highest posterior likelihood. We note that using the reduced 3D metric obtained by dropping the v_3 component leads to the same final golden EOSs.

Figure 6 shows the golden EOSs selected by this procedure as curves in the (p, n) and (M, R) planes (thick solid colored lines), as well as the five next-highest likelihood EOSs from the 30 nearby EOSs (thin solid colored lines). Note that at least for densities $n \leq n_{\rm TOV}$, the selection procedure is robust, with the nearby EOSs having a similar structure to the corresponding golden EOSs. Table 1, instead, provides a concise summary of the most salient properties of the binaries with the golden EOSs that have been simulated, together with the characteristic GW frequencies f_2 and $f_{\rm rd}$.

Merger Simulations and GW Analysis

The initial data in our simulations is computed using the spectral-solver code `FUKA` [41] to generate equal and non-equal mass irrotational BNS initial data with a separation of $\approx 45\,{\rm km}$. `FUKA` uses the so-called extended conformal thin-sandwich formulation of Einstein's field equations to solve for binaries in the quasi-circular orbit approximation. In addition, residual eccentricities are reduced by applying estimates for the orbital and radial infall velocities at 3.5PN order [41].

For the evolution we instead make use of the `Einstein-Toolkit` [42] that includes the fixed-mesh box-in-box refinement framework `Carpet` [43]. More specifically, we use six refinement levels with the finest grid having a spacing of $295\,{\rm m}$ and impose reflection symmetry across the orbital plane. This intermediate resolution allows us to explore a reasonable part of the EOS and BNS parameter space, while keeping the computational costs affordable.

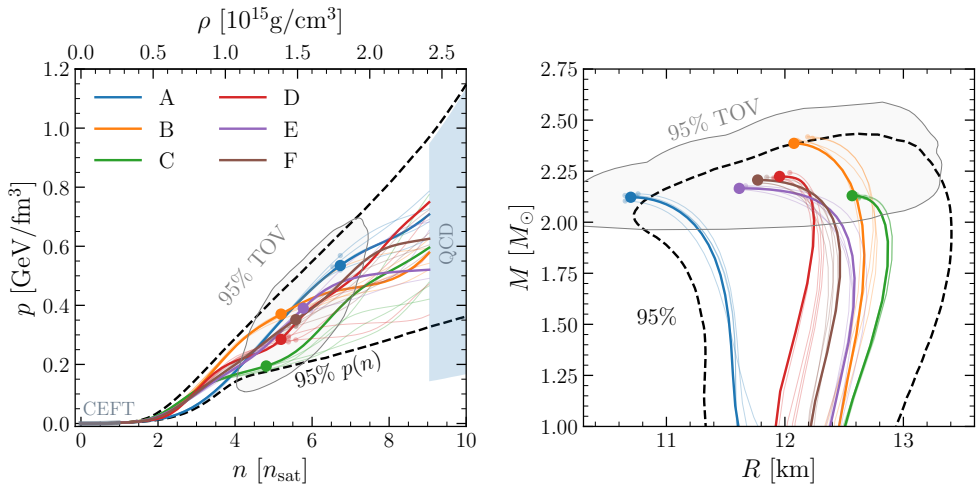

Fig. 6 Golden and nearby EOSs. Similar to Fig. 1, with the golden EOSs shown in thick colored lines and the TOV points shown with large filled points. Additionally shown with thin lines are the five next-highest likelihood EOSs from the 30 closest EOSs to the points on the 68% contour (see text in SM for more details). The TOV points for these nearby EOSs are also shown with small filled points.

EOS	$M_{\rm TOV}$ [$M_\odot$]	$C_{\rm TOV}$	$R_{1.4}$ [km]	$p_{\rm TOV}$ [GeV/fm^3]	$n_{\rm TOV}$ [$n_{\rm sat}$]	q	$\tilde{\Lambda}$	f_2 [Hz]	$f_{\rm rd}$ [Hz]	$d\widehat{E}_{\rm GW}/d\widehat{J}_{\rm GW}$
A	2.12	0.293	11.55	0.535	6.73	0.70	286	3380	3366	3.48
						0.85	301	3245	3344	3.38
						1.00	303	3205	3229	3.25
B	2.39	0.292	12.57	0.370	5.19	0.70	528	2600	2587	3.02
						0.85	538	2710	2601	2.91
						1.00	566	2725	2716	3.00
C	2.13	0.250	12.72	0.195	4.81	0.70	520	2495	2471	2.85
						0.85	577	2615	2695	2.85
						1.00	627	2635	2611	2.89
D	2.22	0.275	12.06	0.285	5.19	0.70	352	2680	2677	2.93
						0.85	358	2900	2759	2.98
						1.00	434	2850	2883	3.00
E	2.17	0.275	12.53	0.390	5.77	0.70	520	2665	2637	3.08
						0.85	540	2700	2687	2.95
						1.00	562	2756	2761	3.05
F	2.21	0.277	12.37	0.352	5.58	0.70	456	2680	2662	2.99
						0.85	494	2735	2625	2.94
						1.00	502	2815	2802	3.06

Table 1 EOS and NS properties. For each EOS, we list the TOV-mass $M_{\rm TOV}$, the TOV compactness $C_{\rm TOV}$, the radii of a 1.4 $M_\odot$ NS $R_{1.4}$, the TOV pressure $p_{\rm TOV}$, the TOV number density $n_{\rm TOV}$, the binary tidal deformability $\tilde{\Lambda}$, the post-merger frequencies f_2, the long-ringdown frequency $f_{\rm rd}$ and the corresponding slope $d\widehat{E}_{\rm GW}/d\widehat{J}_{\rm GW}$.

The computational domain has an outer boundary at $\pm 1512\,\mathrm{km}$, which allows us to compute GWs accurately and impose suitable boundary conditions.

For the spacetime evolution we use `Antelope` [44], which solves a constraint damping formulation of the Z4 system [45], while we evolve matter using the `FIL` general-relativistic magnetohydrodynamic code [44]. `FIL` implements fourth-order conservative finite-differencing methods, enabling a precise hydrodynamic evolution even at the intermediate resolution used here. Furthermore, `FIL` is able to handle tabulated EOSs that are dependent on temperature and electron-fraction, and includes a neutrino transport scheme that can handle neutrino cooling and weak interactions [46]. To maintain our description as simple as reasonably possible, we have considered zero magnetic fields and neglected the radiative transfer of neutrinos; while we do not expect qualitative changes from either magnetic fields or neutrinos, it is reasonable to expect will play a quantitative role in establishing the long-ringdown slope.

As discussed in the main text, our agnostic EOS construction provides the "cold" (i.e., $T = 0$, where T is the temperature) part of the EOSs, while the "thermal" part is added during the evolution to account for shock-heating effects during and after the merger [18]. More specifically, the total pressure is given by the sum of the cold EOS $p_{\rm c} = p_{\rm c}(\rho)$ and a thermal component $p_{\rm th} = p_{\rm th}(\rho, T) = \rho T$, where $\rho := m_{\rm B} n$ is the rest-mass density and $m_{\rm B} = 931.5\,\mathrm{MeV}$ the atomic mass unit. Analogously, the total specific internal energy can be separated into a cold $\epsilon_{\rm c} = \epsilon_{\rm c}(\rho)$ and a thermal part $\epsilon_{\rm th} = \epsilon_{\rm th}(T)$. Here, $\epsilon_{\rm c}(\rho) = e_c(\rho)/\rho - 1$ and $\epsilon_{\rm th}(T) := T/(\Gamma_{\rm th} - 1)$, where $e_c(\rho)$ is the energy density of the cold EOS and $\Gamma_{\rm th}$ is the thermal adiabatic index, which we choose to take the constant value $\Gamma_{\rm th} = 1.75$ [25]. As a result, the total pressure and total internal energy density are given by

$$p(\rho, T) = p_c(\rho) + \rho T\,, \qquad \epsilon(\rho, T) = \frac{e_c(\rho)}{\rho} - 1 + \frac{T}{\Gamma_{\rm th} - 1}\,, \tag{5}$$

where the cold contributions $e_c(\rho)$ and $p_c(\rho)$ are provided in tabulated form by the GP construction explained above. The entropy can then be expressed as

$$s(\rho, T) = \frac{1}{\Gamma_{\rm th} - 1} \ln\left(\frac{\bar{\epsilon}_{\rm th}}{\rho^{\Gamma_{\rm th}-1}}\right)\,, \tag{6}$$

where $\bar{\epsilon}_{\rm th} := \max(\epsilon_{\rm th}, s_{\rm min})$, with some numeric lower bound for the entropy $s_{\rm min} = 10^{-10}$.

For the GW analysis, we use the Newman-Penrose formalism to relate the Weyl curvature scalar ψ_4 to the second time derivative of the polarization amplitudes of the GW strain $h_{+,\times}$ via [47]

$$\ddot{h}_+ + i\ddot{h}_\times = \psi_4 := \sum_{\ell=2}^{\infty} \sum_{m=-\ell}^{m=\ell} \psi_4^{\ell,m}\, {}_{-2}Y_{\ell,m}\,, \tag{7}$$

where ${}_sY_{\ell,m}(\theta, \phi)$ are spin-weighted spherical harmonics of weight $s = -2$. From our simulations, we extract the multipoles $\psi_4^{\ell,m}$ with a sampling rate of $\approx 634\,\mathrm{kHz}$ from a spherical surface with radius $\approx 574\,\mathrm{km}$ centred at the origin of our computational domain and extrapolate the result to the estimated luminosity distance of $40\,\mathrm{Mpc}$ of the GW170817 event [48]. In addition, we fix the angular dependence of the spherical harmonics by considering a viewing

angle $\theta = 15^\circ$, as inferred determined from the jet of GW170817 [49] and set $\phi = 0^\circ$ without loss of generality. We restrict our analysis to the multipoles $\ell \leq 4$ of the expansion (7) and note that the $\ell = |m| = 2$ modes represent the dominant contribution in our analysis; indeed the relative difference in the maximum GW amplitude when considering multipoles with $\ell \leq 4$ and $\ell = 2$ is less than 3%. Furthermore, we report all results as functions of the retarded time $t - t_{\rm mer}$, where $t_{\rm mer}$ is defined as the time of the global maximum of the GW amplitude $\sqrt{h_+^2 + h_\times^2}$.

An important quantity in our analysis is the instantaneous GW frequency $f_{\rm GW}$, defined as

$$f_{\rm GW} := \frac{1}{2\pi}\frac{d\phi}{dt}\,, \qquad\qquad \phi := \arctan\left(\frac{h_\times^{2,2}}{h_+^{2,2}}\right)\,. \tag{8}$$

The radiated power is given by the integral expression [47]

$$\dot{E}_{\rm GW} = \frac{r^2}{16\pi}\sum_{\ell=2}^{\infty}\sum_{m=-\ell}^{\ell}\left|\int_{-\infty}^{t} dt'\,\psi_4^{\ell m}\right|^2\,, \tag{9}$$

where the total emitted GW energy follows from another time integration $E_{\rm GW}(t) := \int_{-\infty}^{t} dt' \dot{E}_{\rm GW}(t')$. Similarly, the rate of radiated angular momentum is defined as [47]

$$\dot{J}_{\rm GW} := \frac{r^2}{16\pi}{\rm Im}\left\{\sum_{\ell=2}^{\infty}\sum_{m=-\ell}^{\ell} m\left(\int_{-\infty}^{t} dt'\psi_4^{\ell m}\right)\int_{-\infty}^{t} dt'\int_{-\infty}^{t'} dt''\,\bar{\psi}_4^{\ell m}\right\}\,, \tag{10}$$

where r is the observer distance and where $\bar{\psi}_4$ is the complex conjugate of ψ_4 and the total emitted angular momentum follows again from another time integration $J_{\rm GW}(t) := \int_{-\infty}^{t} dt' \dot{J}_{\rm GW}(t')$.

In the main text we work with dimensionless energies $E_{\rm GW}(t)/E_{\rm GW}^{\rm mer}$ and angular momenta $J_{\rm GW}(t)/J_{\rm GW}^{\rm mer}$ obtained by normalizing with the respective values at merger time $E_{\rm GW}^{\rm mer} := E_{\rm GW}(t_{\rm mer})$ and $J_{\rm GW}^{\rm mer} := J_{\rm GW}(t_{\rm mer})$. When expressed in terms of strain components, and in full generality, the ratio of the radiated energy and angular-momentum rates $dE_{\rm GW}/dJ_{\rm GW}$ is similar to the instantaneous GW frequency

$$\frac{dE_{\rm GW}}{dJ_{\rm GW}} = \frac{\dot{E}_{\rm GW}}{\dot{J}_{\rm GW}} = \frac{\dot{h}_+^2 + \dot{h}_\times^2}{h_+\dot{h}_\times - \dot{h}_+ h_\times}\,, \qquad\qquad f_{\rm GW} = \frac{1}{2\pi}\frac{h_+\dot{h}_\times - \dot{h}_+ h_\times}{h_+^2 + h_\times^2}\,. \tag{11}$$

For a simple system with an $\ell = 2, m = 2$ deformation, e.g., a compact rotating system with eccentric mass distribution like the toy model of Ref. [9] and for which $h_+(t) \propto \cos(\phi(t))$ and $h_\times(t) \propto \sin(\phi(t))$ with GW phase $\phi(t)$, one obtains the identity $\dot{E}_{\rm GW}/\dot{J}_{\rm GW} = f_{\rm GW}/(2\pi)$. Since in the long ringdown $f_{\rm GW}(t) \simeq {\rm const.} =: f_{\rm rd}$, expressions (11) explain why the radiated energy and angular momentum are linearly related.

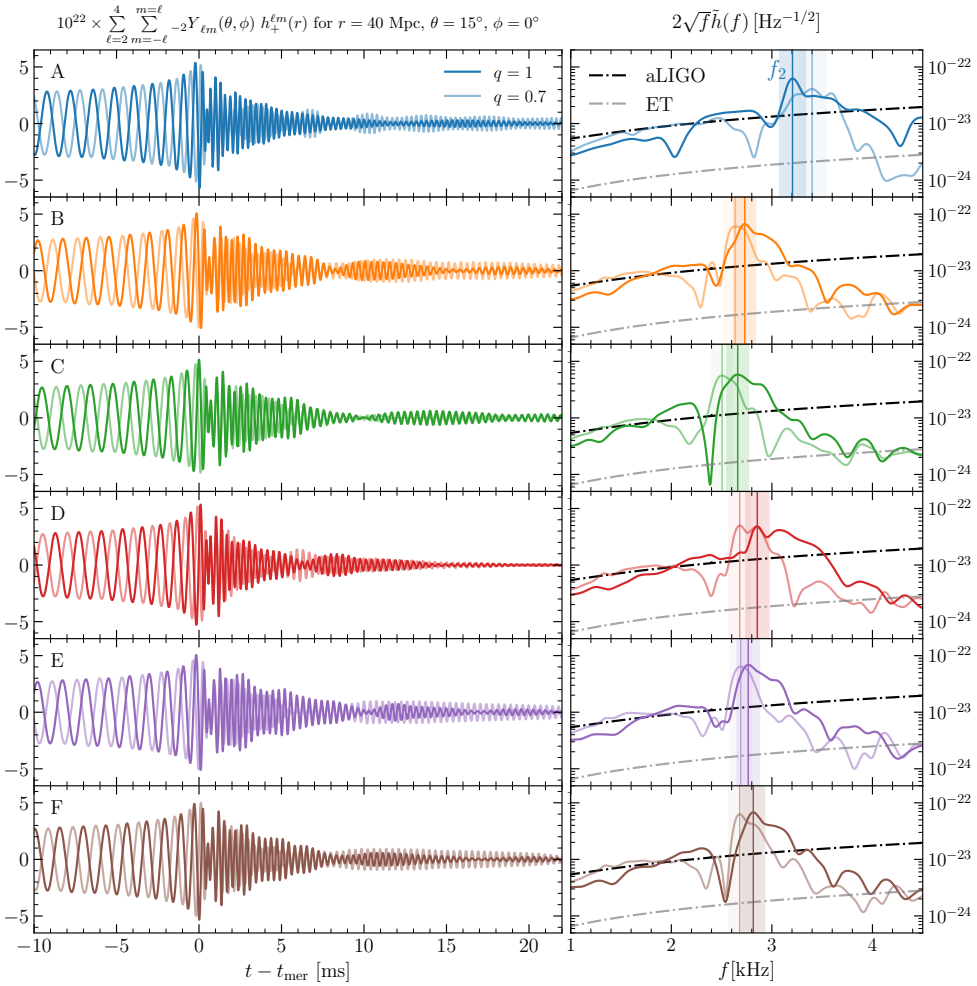

Fig. 7 Gravitational Waves GW strain (left) and post-merger power spectral density (right) at 40 Mpc detector distance and $\theta = 15°$ viewing angle for equal chirp mass $M_c = 1.18\, M_\odot$ and two different mass ratios $q = 1, 0.7$. In the right panel we mark with solid lines the frequencies estimated via $f_{\rm GW} = dE_{\rm GW}/dJ_{\rm GW}$ and by dashed lines the dominant post-merger frequency f_2 where and shaded areas indicate the 8% relative error estimate for f_2.

Finally, we analyze the spectral features of the waveforms and compute the power spectral density (PSD) of the signal as [9]

$$\tilde{h}^{\ell,m}(f) := \frac{1}{\sqrt{2}} \left(\left| \int dt\, \mathrm{e}^{-2\pi i f t} h_{+}^{\ell,m}(t) \right|^2 + \left| \int dt\, \mathrm{e}^{-2\pi i f t} h_{\times}^{\ell,m}(t) \right|^2 \right)^{1/2}, \qquad (12)$$

where the time integration is performed over the interval $t - t_{\rm mer} \in [0, 30]$ ms or up to the time at which a black hole is formed if the post-merger remnant collapses earlier.

Figure 7 summarises the GW output from a number of our simulations by reporting on the left column the GW strain and on the right column the corresponding PSD from the post-merger signal when compared with the estimated sensitivities of advanced LIGO (aLIGO) and the Einstein Telescope (ET). The data refers to BNS simulations for the EOSs A-F (top to bottom), all having the same chirp mass $\mathcal{M}_c = 1.18\,M_\odot$ and two different mass ratios $q = 1, 0.7$ (dark and light colors, respectively). Consistent with the expectations from the GW170817 event, the results shown assume a distance of $40\mathrm{Mpc}$ and a viewing angle of $\theta = 15^\circ$.

Performing the mock measurement

We perform a mock joint measurement of f_2 and the slope $d\widehat{E}_{\rm GW}/d\widehat{J}_{\rm GW}$ in the following manner. We assume a measurement whose uncertainty we model with a multivariate Gaussian distribution of f_2 and $d\widehat{E}_{\rm GW}/d\widehat{J}_{\rm GW}$ for simplicity, as well as a uniform measurement of $q \in [0.7, 1.0]$. Let us denote the joint likelihood from the measurement $P_{\rm meas}({\rm data}|f_2, d\widehat{E}_{\rm GW}/d\widehat{J}_{\rm GW}, q)$. First, we fit a two-component model to the f_2 and $d\widehat{E}_{\rm GW}/d\widehat{J}_{\rm GW}$ data, the posterior of which we denote by $P_{\rm mod}(d\widehat{E}_{\rm GW}/d\widehat{J}_{\rm GW}|{\rm EOS}, q)$ respectively. This two-component model is just the product of two models of the form (1) for f_2 and $d\widehat{E}_{\rm GW}/d\widehat{J}_{\rm GW}$. Next, we compute the likelihood that each EOS is consistent with the mock measurement by evaluating

$$\begin{aligned} P({\rm data}|{\rm EOS}, q) = \int df_2\, d\Big(d\widehat{E}_{\rm GW}/d\widehat{J}_{\rm GW}\Big) \\ \times P_{\rm meas}({\rm data}|f_2, d\widehat{E}_{\rm GW}/d\widehat{J}_{\rm GW}, q) \\ \times P_{\rm mod}(d\widehat{E}_{\rm GW}/d\widehat{J}_{\rm GW}, f_2|{\rm EOS}, q)\,, \end{aligned} \tag{13}$$

by Monte-Carlo sampling of the measurement distribution, which we then use in Bayes's theorem to generate the posteriors in Fig. 4, using a flat prior on $q \in [0.7, 1.0]$. The likelihoods when using only one of the two bilinear models is defined similarly.

On the robustness of the correlation

In order to identify potential degeneracies in the long-ringdown slope between the chirp mass and the EOS properties we simulate the equal-mass ($q = 1$) binaries with EOS A and C with three different values for the chirp mass, namely, $\mathcal{M}_{\rm chirp} = 1.13,\ 1.18,\ 1.22\,M_\odot$. Since the chirp mass represents one of the best-measured quantities in BNS mergers with a few-percent error, what we are assessing in this way is the dependence for a given EOS of the long-ringdown slope on $\mathcal{M}_{\rm chirp}$. Stated differently, we can assess how different long-ringdown slopes cluster when exploring the possible ranges in the chirp mass.

The result of this test are displayed in Fig. 8, which is similar to Fig. 2, but where we show the slope for model A in green and for model C in blue, while light to dark colors indicate small to large values of $\mathcal{M}_{\rm chirp}$, respectively. Evidently, the variations in the chirp mass lead to significantly smaller differences in the long-ringdown slope than those introduced by the EOSs. Hence, Fig. 8 highlights that the EOS represents the dominant contribution to the long-ringdown slope and that the chirp mass plays only a sub-dominant role. This is natural

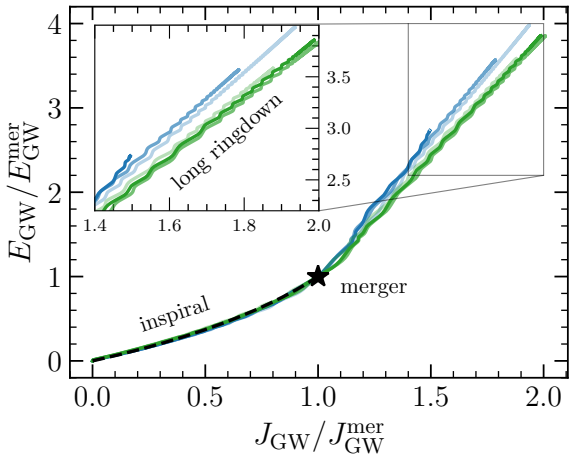

Fig. 8 Impact of chirp mass relation between normalized GW energy and angular momentum for model A (blue) and C (green) for three different values of the chirp mass $\mathcal{M}_{\rm chirp} = 1.13, 1.18, 1.22\, M_\odot$ (light to dark colors) and fixed mass ratio $q = 1$.

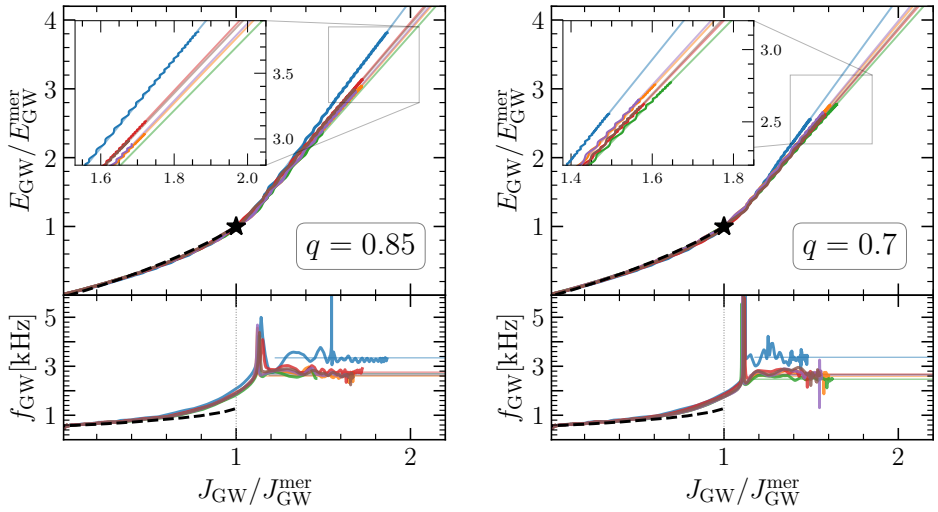

Fig. 9 Unequal-mass binaries Evolution of the normalized GW energy and GW frequency as a function of the normalized radiated angular momentum for the case of asymmetric binaries with mass ratio $q = 0.85$ (left) and $q = 0.7$ (right).

to expect since the long-ringdown slope is essentially set by the equilibrium of the HMNS, which, in turn, is predominantly determined by the EOS.

Next, we consider how the assumption of equal-mass binaries impacts the robustness of the long-ringdown slope and its correlation with the EOS. To this end, we have performed 12 additional simulations using the EOSs A–F, but with mass ratios $q = 0.85$ and $q = 0.7$; once again these values are compatible with the mass ratios inferred from the GW170817 event.

The results of this test are shown in Fig. 9, which is again analogous to Fig. 2 and complements the information shown in Fig. 3. Note that also the unequal-mass binaries show a clear linear correlation in the radiated energy and angular momentum during the long ringdown and that different EOSs lead to different slopes. At the same time, note that while the correlation for binaries with EOS A, C, and D is unchanged with respect to the behaviour for equal-mass binaries, the same is not true for the other EOSs. This is clearly shown in Fig. 3 and essentially accounts for the uncertainty in the long-ringdown slope contained in the bilinear fit (1). We should also remark that over the timescale considered here, the $\ell = 2, m = 2$ mode is still the dominant one and the contributions from the $\ell = 2, m = 1$ mode are at least two orders of magnitude smaller, although it is possible that the $\ell = 2, m = 1$ mode will dominate at later times for highly asymmetric binaries (see, e.g., [50]), the radiated energy and angular momentum will remain linearly related, albeit with a different (smaller) slope.

Another potential source of uncertainty in our results may have come from the thermal part of the EOS, which is admittedly simplified but qualitatively correct. In order to assess the impact of the thermal contributions, we study a reference EOS B with three different values that span the possible range expected for the adiabatic index, i.e., $\Gamma_{\rm th} = 1.5, 1.75, 2.0$ (see Fig. 9 of [25]). The results of this analysis are reported in Figure 10, which shows how larger values of $\Gamma_{\rm th}$ typically lead to higher thermal-pressure contributions, which help support the $\ell = 2 = m$ deformation of the merger remnant, and thus result in a more efficient GW emission in the post-merger phase. At the same time, the long-ringdown slope is essentially unaffected by the choice of $\Gamma_{\rm th}$ as can be seen from the tight overlap of the corresponding curves. As a result, we can conclude that our choice of a fiducial value of $\Gamma_{\rm th} = 1.75$ does not introduce any bias on the reported long-ringdown slopes.

Finally, in Fig. 11 we show results for two EOSs with a tabulated temperature dependence, namely the Hempel-Schaffner DD2 (HS-DD2) EOS [27] and the intermediate variant of the holographic Veneziano QCD (V-QCD) EOS [26]. While the HS-DD2 EOS models purely hadronic matter, the V-QCD EOS features a strong first-order phase transition from hadronic to quark matter that induces the HMNS to collapse to a black hole in this simulation. As shown in [24, 28], the strong phase transition of the V-QCD EOS does not allow stable quark-matter cores inside isolated stars, but a significant amount of quark matter can be formed during the metastable post-merger phase. Importantly, neither the presence of quark matter, nor the microscopic prescription for the temperature dependence in these EOSs alter the basic features of the long ringdown.

References

[1] Annala, E., Gorda, T., Hirvonen, J., Komoltsev, O., Kurkela, A., Nättilä, J., Vuorinen, A.: Strongly interacting matter exhibits deconfined behavior in massive neutron stars. Nature Communications **14**(1) (2023) https://doi.org/10.1038/s41467-023-44051-y

[2] Baiotti, L., Rezzolla, L.: Binary neutron-star mergers: a review of Einstein's richest laboratory. Rept. Prog. Phys. **80**(9), 096901 (2017) https://doi.org/10.1088/1361-6633/aa67bb arXiv:1607.03540 [gr-qc]

[3] Paschalidis, V.: General relativistic simulations of compact binary mergers as engines for short gamma-ray bursts. Classical and Quantum Gravity **34**(8), 084002 (2017) https:

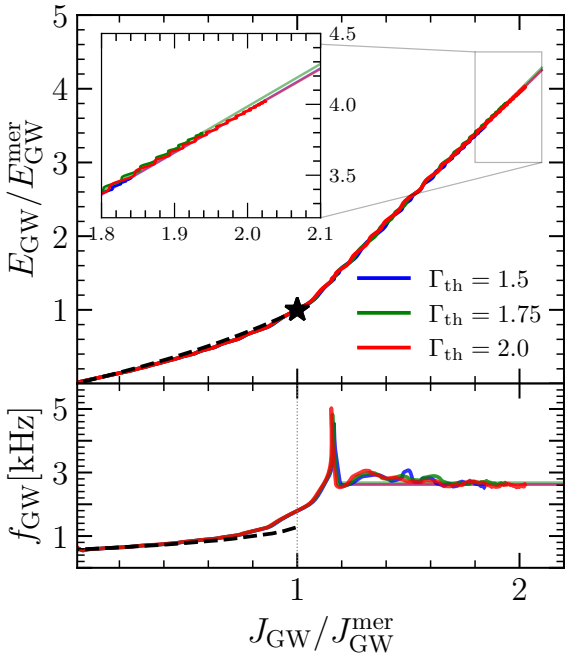

Fig. 10 Impact of $\Gamma_{\rm th}$ Same as Fig. 8 but for model B with three different values of $\Gamma_{\rm th} = 1.5, 1.75, 2.0$ and fixed binary parameters $\mathcal{M}_{\rm c} = 1.18$ and $q = 1$.

	β_0	β_1	β_2	β_3	β_4	β_5	β_6
β_0	4.16						
β_1	−6.40	10.59					
β_2	2.57	−6.32	11.27				
β_3	−3.86	6.24	−4.52	4.48			
β_4	6.15	−10.68	9.15	−7.22	12.46		
β_5	−4.39	8.85	−9.86	5.29	−10.48	10.97	
β_5	1.76	−2.08	−3.25	−0.07	−0.08	0.41	3.83

Table 2 Covariance matrix of the bilinear model The covariance matrix $\mathrm{cov}(\boldsymbol{\beta})$ of the trained bilinear model used in this work in eq. (1). The covariance matrix is symmetric. Here, the model has been trained with inputs where $p_{\rm TOV}$ is in units of $\mathrm{GeV/fm^3}$ and $n_{\rm TOV}$ is in $\mathrm{fm^{-3}}$.

//doi.org/10.1088/1361-6382/aa61ce arXiv:1611.01519 [astro-ph.HE]

[4] Radice, D., Bernuzzi, S., Perego, A.: The Dynamics of Binary Neutron Star Mergers and GW170817. Annual Review of Nuclear and Particle Science **70**, 95–119 (2020) https://doi.org/10.1146/annurev-nucl-013120-114541 arXiv:2002.03863 [astro-ph.HE]

[5] Gill, R., Nathanail, A., Rezzolla, L.: When Did the Remnant of GW170817 Collapse

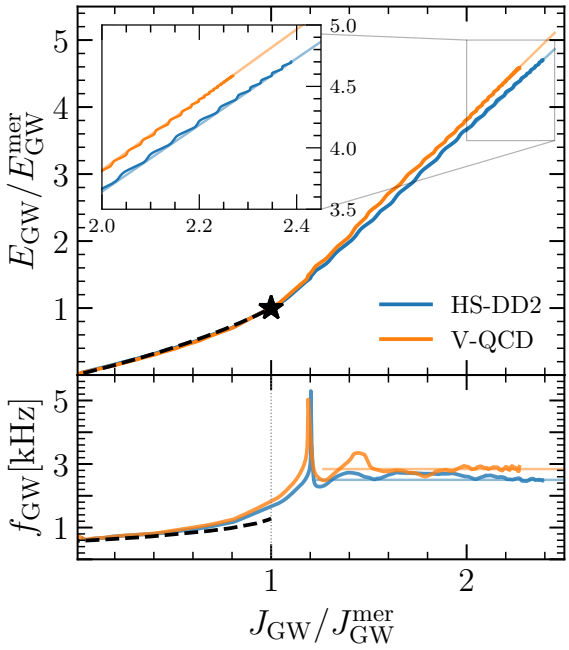

Fig. 11 Temperature dependent EOSs Same as Fig. 8, but for two models with tabulated temperature dependence, namely the HS-DD2 EOS and the intermediate variant of the holographic V-QCD EOS. Both simulations assume $q = 1$ and $\mathcal{M}_{\rm chirp} = 1.18\ M_\odot$.

to a Black Hole? Astrophys. J. **876**(2), 139 (2019) https://doi.org/10.3847/1538-4357/ab16da arXiv:1901.04138 [astro-ph.HE]

[6] Punturo, M., *et al.*: The third generation of gravitational wave observatories and their science reach. Class. Quantum Grav. **27**(8), 084007 (2010) https://doi.org/10.1088/0264-9381/27/8/084007

[7] Evans, M., Adhikari, R.X., Afle, C., Ballmer, S.W., Biscoveanu, S., Borhanian, S., Brown, D.A., Chen, Y., Eisenstein, R., Gruson, A., Gupta, A., Hall, E.D., Huxford, R., Kamai, B., Kashyap, R., Kissel, J.S., Kuns, K., Landry, P., Lenon, A., Lovelace, G., McCuller, L., Ng, K.K.Y., Nitz, A.H., Read, J., Sathyaprakash, B.S., Shoemaker, D.H., Slagmolen, B.J.J., Smith, J.R., Srivastava, V., Sun, L., Vitale, S., Weiss, R.: A Horizon Study for Cosmic Explorer: Science, Observatories, and Community. arXiv e-prints, 2109–09882 (2021) https://doi.org/10.48550/arXiv.2109.09882 arXiv:2109.09882 [astro-ph.IM]

[8] Bauswein, A., Stergioulas, N.: Unified picture of the post-merger dynamics and gravitational wave emission in neutron star mergers. Phys. Rev. D **91**(12), 124056 (2015) https://doi.org/10.1103/PhysRevD.91.124056 arXiv:1502.03176 [astro-ph.SR]

[9] Takami, K., Rezzolla, L., Baiotti, L.: Spectral properties of the post-merger

gravitational-wave signal from binary neutron stars. Phys. Rev. D **91**(6), 064001 (2015) https://doi.org/10.1103/PhysRevD.91.064001 arXiv:1412.3240 [gr-qc]

[10] Rezzolla, L., Takami, K.: Gravitational-wave signal from binary neutron stars: A systematic analysis of the spectral properties. Phys. Rev. D **93**(12), 124051 (2016) https://doi.org/10.1103/PhysRevD.93.124051 arXiv:1604.00246 [gr-qc]

[11] De Pietri, R., Feo, A., Font, J.A., Löffler, F., Pasquali, M., Stergioulas, N.: Numerical-relativity simulations of long-lived remnants of binary neutron star mergers. Phys. Rev. D **101**(6), 064052 (2020) https://doi.org/10.1103/PhysRevD.101.064052 arXiv:1910.04036 [gr-qc]

[12] Kiuchi, K., Fujibayashi, S., Hayashi, K., Kyutoku, K., Sekiguchi, Y., Shibata, M.: Self-consistent picture of the mass ejection from a one second-long binary neutron star merger leaving a short-lived remnant in general-relativistic neutrino-radiation magneto-hydrodynamic simulation. arXiv e-prints, 2211–07637 (2022) https://doi.org/10.48550/arXiv.2211.07637 arXiv:2211.07637 [astro-ph.HE]

[13] Breschi, M., Bernuzzi, S., Godzieba, D., Perego, A., Radice, D.: Constraints on the Maximum Densities of Neutron Stars from Postmerger Gravitational Waves with Third-Generation Observations. Phys. Rev. Lett. **128**(16), 161102 (2022) https://doi.org/10.1103/PhysRevLett.128.161102 arXiv:2110.06957 [gr-qc]

[14] Gorda, T., Komoltsev, O., Kurkela, A.: Ab-initio QCD calculations impact the inference of the neutron-star-matter equation of state. arXiv e-prints, 2204–11877 (2022) arXiv:2204.11877 [nucl-th]

[15] Gorda, T., Hebeler, K., Kurkela, A., Schwenk, A., Vuorinen, A.: Constraints on Strong Phase Transitions in Neutron Stars. Astrophys. J. **955**(2), 100 (2023) https://doi.org/10.3847/1538-4357/aceefb arXiv:2212.10576 [astro-ph.HE]

[16] Annala, E., Gorda, T., Kurkela, A., Nättilä, J., Vuorinen, A.: Evidence for quark-matter cores in massive neutron stars. Nature Physics **16**(9), 907–910 (2020) https://doi.org/10.1038/s41567-020-0914-9

[17] Altiparmak, S., Ecker, C., Rezzolla, L.: On the Sound Speed in Neutron Stars. Astrophys. J. Lett. **939**(2), 34 (2022) https://doi.org/10.3847/2041-8213/ac9b2a arXiv:2203.14974 [astro-ph.HE]

[18] Baiotti, L., Giacomazzo, B., Rezzolla, L.: Accurate evolutions of inspiralling neutron-star binaries: Prompt and delayed collapse to a black hole. Phys. Rev. D **78**(8), 084033 (2008) https://doi.org/10.1103/PhysRevD.78.084033 arXiv:0804.0594 [gr-qc]

[19] Bauswein, A., Janka, H., Oechslin, R.: Testing approximations of thermal effects in neutron star merger simulations. Phys. Rev. D **82**(8), 084043 (2010) https://doi.org/10.1103/PhysRevD.82.084043 arXiv:1006.3315 [astro-ph.SR]

[20] Kastaun, W., Ciolfi, R., Giacomazzo, B.: Structure of stable binary neutron star merger remnants: A case study. Phys. Rev. D **94**(4), 044060 (2016) https://doi.org/10.1103/PhysRevD.94.044060 arXiv:1607.02186 [astro-ph.HE]

[21] Hanauske, M., Takami, K., Bovard, L., Rezzolla, L., Font, J.A., Galeazzi, F., Stöcker, H.: Rotational properties of hypermassive neutron stars from binary mergers. Phys. Rev. D **96**(4), 043004 (2017) https://doi.org/10.1103/PhysRevD.96.043004 arXiv:1611.07152 [gr-qc]

[22] De Pietri, R., Feo, A., Font, J.A., Löffler, F., Maione, F., Pasquali, M., Stergioulas, N.: Convective Excitation of Inertial Modes in Binary Neutron Star Mergers. Phys. Rev. Lett. **120**(22), 221101 (2018) https://doi.org/10.1103/PhysRevLett.120.221101 arXiv:1802.03288 [gr-qc]

[23] Most, E.R., Papenfort, L.J., Dexheimer, V., Hanauske, M., Schramm, S., Stöcker, H., Rezzolla, L.: Signatures of Quark-Hadron Phase Transitions in General-Relativistic Neutron-Star Mergers. Physical Review Letters **122**(6), 061101 (2019) https://doi.org/10.1103/PhysRevLett.122.061101 arXiv:1807.03684 [astro-ph.HE]

[24] Tootle, S., Ecker, C., Topolski, K., Demircik, T., Järvinen, M., Rezzolla, L.: Quark formation and phenomenology in binary neutron-star mergers using V-QCD. SciPost Phys. **13**, 109 (2022) https://doi.org/10.21468/SciPostPhys.13.5.109 arXiv:2205.05691 [astro-ph.HE]

[25] Figura, A., Lu, J.-J., Burgio, G.F., Li, Z.H., Schulze, H.-J.: Hybrid equation of state approach in binary neutron-star merger simulations. Phys. Rev. D **102**(4), 043006 (2020) https://doi.org/10.1103/PhysRevD.102.043006 arXiv:2005.08691 [gr-qc]

[26] Demircik, T., Ecker, C., Järvinen, M.: Dense and Hot QCD at Strong Coupling. Phys. Rev. X **12**(4), 041012 (2022) https://doi.org/10.1103/PhysRevX.12.041012 arXiv:2112.12157 [hep-ph]

[27] Hempel, M., Schaffner-Bielich, J.: A statistical model for a complete supernova equation of state. Nuclear Physics A **837**, 210–254 (2010) https://doi.org/10.1016/j.nuclphysa.2010.02.010 arXiv:0911.4073 [nucl-th]

[28] Ecker, C., Topolski, K., Järvinen, M., Stehr, A.: Prompt Black Hole Formation in Binary Neutron Star Mergers. arXiv e-prints, 2402–11013 (2024) https://doi.org/10.48550/arXiv.2402.11013 arXiv:2402.11013 [astro-ph.HE]

[29] Zappa, F., Bernuzzi, S., Radice, D., Perego, A., Dietrich, T.: Gravitational-Wave Luminosity of Binary Neutron Stars Mergers. Physical Review Letters **120**(11), 111101 (2018) https://doi.org/10.1103/PhysRevLett.120.111101 arXiv:1712.04267 [gr-qc]

[30] Nathanail, A., Most, E.R., Rezzolla, L.: GW170817 and GW190814: Tension on the Maximum Mass. Astrophys. J. Lett. **908**(2), 28 (2021) https://doi.org/10.3847/2041-8213/abdfc6 arXiv:2101.01735 [astro-ph.HE]

[31] Biwer, C.M., Capano, C.D., De, S., Cabero, M., Brown, D.A., Nitz, A.H., Raymond, V.: PyCBC Inference: A Python-based parameter estimation toolkit for compact binary coalescence signals. Publ. Astron. Soc. Pac. **131**(996), 024503 (2019) https://doi.org/10.1088/1538-3873/aaef0b arXiv:1807.10312 [astro-ph.IM]

[32] Breschi, M., Bernuzzi, S., Chakravarti, K., Camilletti, A., Prakash, A., Perego, A.: Kilohertz Gravitational Waves From Binary Neutron Star Mergers: Numerical-relativity Informed Postmerger Model. arXiv e-prints, 2205–09112 (2022) https://doi.org/10.48550/arXiv.2205.09112 arXiv:2205.09112 [gr-qc]

[33] Bose, S., Chakravarti, K., Rezzolla, L., Sathyaprakash, B.S., Takami, K.: Neutron-Star Radius from a Population of Binary Neutron Star Mergers. Phys. Rev. Lett. **120**(3), 031102 (2018) https://doi.org/10.1103/PhysRevLett.120.031102 arXiv:1705.10850 [gr-qc]

[34] Baym, G., Pethick, C., Sutherland, P.: The Ground State of Matter at High Densities: Equation of State and Stellar Models. Astrophys. J. **170**, 299 (1971) https://doi.org/10.1086/151216

[35] Hebeler, K., Lattimer, J.M., Pethick, C.J., Schwenk, A.: Equation of state and neutron star properties constrained by nuclear physics and observation. Astrophys. J. **773**, 11 (2013) https://doi.org/10.1088/0004-637X/773/1/11 arXiv:1303.4662 [astro-ph.SR]

[36] Antoniadis, J., *et al.*: A Massive Pulsar in a Compact Relativistic Binary. Science **340**, 6131 (2013) https://doi.org/10.1126/science.1233232 arXiv:1304.6875 [astro-ph.HE]

[37] Fonseca, E., Pennucci, T.T., Ellis, J.A., Stairs, I.H., Nice, D.J., Ransom, S.M., Demorest, P.B., Arzoumanian, Z., Crowter, K., Dolch, T., Ferdman, R.D., Gonzalez, M.E., Jones, G., Jones, M.L., Lam, M.T., Levin, L., McLaughlin, M.A., Stovall, K., Swiggum, J.K., Zhu, W.: The NANOGrav Nine-year Data Set: Mass and Geometric Measurements of Binary Millisecond Pulsars. Astrophys. J. **832**(2), 167 (2016) https://doi.org/10.3847/0004-637X/832/2/167 arXiv:1603.00545 [astro-ph.HE]

[38] Abbott, B.P., *et al.*: Properties of the binary neutron star merger GW170817. Phys. Rev. X **9**(1), 011001 (2019) https://doi.org/10.1103/PhysRevX.9.011001 arXiv:1805.11579 [gr-qc]

[39] Miller, M.C., *et al.*: The Radius of PSR J0740+6620 from NICER and XMM-Newton Data. Astrophys. J. Lett. **918**(2), 28 (2021) https://doi.org/10.3847/2041-8213/ac089b arXiv:2105.06979 [astro-ph.HE]

[40] Komoltsev, O., Kurkela, A.: How Perturbative QCD Constrains the Equation of State at Neutron-Star Densities. Phys. Rev. Lett. **128**(20), 202701 (2022) https://doi.org/10.1103/PhysRevLett.128.202701 arXiv:2111.05350 [nucl-th]

[41] Papenfort, L.J., Tootle, S.D., Grandclément, P., Most, E.R., Rezzolla, L.: New public code for initial data of unequal-mass, spinning compact-object binaries. Phys. Rev. D

104, 024057 (2021) https://doi.org/10.1103/PhysRevD.104.024057

[42] Haas, R., *et al.*: The Einstein Toolkit. Zenodo. To find out more, visit http://einsteintoolkit.org (2020). https://doi.org/10.5281/zenodo.4298887 . https://doi.org/10.5281/zenodo.4298887

[43] Schnetter, E., Hawley, S.H., Hawke, I.: Evolutions in 3D numerical relativity using fixed mesh refinement. Class. Quantum Grav. **21**, 1465–1488 (2004) https://doi.org/10.1088/0264-9381/21/6/014 gr-qc/0310042

[44] Most, E.R., Papenfort, L.J., Rezzolla, L.: Beyond second-order convergence in simulations of magnetized binary neutron stars with realistic microphysics. Mon. Not. R. Astron. Soc. **490**(3), 3588–3600 (2019) https://doi.org/10.1093/mnras/stz2809 arXiv:1907.10328 [astro-ph.HE]

[45] Alic, D., Bona-Casas, C., Bona, C., Rezzolla, L., Palenzuela, C.: Conformal and covariant formulation of the Z4 system with constraint-violation damping. Phys. Rev. D **85**(6), 064040 (2012) https://doi.org/10.1103/PhysRevD.85.064040 arXiv:1106.2254 [gr-qc]

[46] Musolino, C., Rezzolla, L.: A practical guide to a moment approach for neutrino transport in numerical relativity. arXiv e-prints, 2304–09168 (2023) https://doi.org/10.48550/arXiv.2304.09168 arXiv:2304.09168 [gr-qc]

[47] Bishop, N.T., Rezzolla, L.: Extraction of gravitational waves in numerical relativity. Living Reviews in Relativity **19**, 2 (2016) https://doi.org/10.1007/s41114-016-0001-9 arXiv:1606.02532 [gr-qc]

[48] Abbott, B.P., *et al.*: GW170817: Observation of Gravitational Waves from a Binary Neutron Star Inspiral. Phys. Rev. Lett. **119**(16), 161101 (2017) https://doi.org/10.1103/PhysRevLett.119.161101 arXiv:1710.05832 [gr-qc]

[49] Ghirlanda, G., *et al.*: Compact radio emission indicates a structured jet was produced by a binary neutron star merger. Science **363**, 968 (2019) https://doi.org/10.1126/science.aau8815 arXiv:1808.00469 [astro-ph.HE]

[50] Topolski, K., Tootle, S.D., Rezzolla, L.: Post-merger Gravitational-wave Signal from Neutron-star Binaries: A New Look at an Old Problem. Astrophys. J. **960**(1), 86 (2024) https://doi.org/10.3847/1538-4357/ad0152 arXiv:2310.10728 [gr-qc]

Draft version March 1, 2024
Typeset using LaTeX **preprint2** style in AASTeX631

arXiv:2402.19436v1 [astro-ph.HE] 29 Feb 2024

A Model for Pair Production Limit Cycles in Pulsar Magnetospheres

Takuya Okawa[1] and Alexander Y. Chen[1]

[1] *Physics Department and McDonnell Center for the Space Sciences, Washington University in St. Louis; MO, 63130, USA*

ABSTRACT

It was recently proposed that the electric field oscillation as a result of self-consistent $e^{\pm}$ pair production may be the source of coherent radio emission from pulsars. Direct Particle-in-Cell (PIC) simulations of this process have shown that the screening of the parallel electric field by this pair cascade manifests as a limit cycle, as the parallel electric field is recurrently induced when pairs produced in the cascade escape from the gap region. In this work, we develop a simplified time-dependent kinetic model of $e^{\pm}$ pair cascades in pulsar magnetospheres that can reproduce the limit-cycle behavior of pair production and electric field screening. This model includes the effects of a magnetospheric current, the escape of $e^{\pm}$, as well as the dynamic dependence of pair production rate on the plasma density and energy. Using this simple theoretical model, we show that the power spectrum of electric field oscillations averaged over many limit cycles is compatible with the observed pulsar radio spectrum.

Keywords: Radio pulsars — Plasma Astrophysics — Neutron stars — Radio sources

1. INTRODUCTION

Pulsars are rapidly rotating, highly magnetized neutron stars that produce coherent radio emission with enormous brightness temperature (see e.g. Philippov & Kramer 2022 for a review). Very quickly after its discovery, it was realized that the magnetic field near the pulsar surface can be strong enough to ignite a QED $e^{\pm}$ pair cascade (Sturrock 1971). It was believed that pulsars can fill their surroundings with plasma through this $e^{\pm}$ pair production process, screening the electric field $E_{\parallel}$ along the magnetic field, creating a smooth force-free magnetosphere (Contopoulos et al. 1999; Spitkovsky 2006). The regions in the magnetosphere with unscreened $\mathbf{E} \cdot \mathbf{B}$ are called "gaps" and they are the main locations for pair production activity (see e.g. Ruderman & Sutherland 1975; Arons 1983; Cheng et al. 1986).

Arguably, the most important pair-producing gap is located at the pulsar polar cap, since it supplies the plasma on open field lines that is believed to be the source of coherent radio emission (Sturrock 1971). Beloborodov (2008) demonstrated theoretically that the pair production process at the polar cap must be inherently time-dependent when the magnetospheric current is spacelike, and Levinson et al. (2005) showed that this process tends to produce large-amplitude oscillations of the accelerating elec-

Corresponding author: Takuya Okawa
o.takuya@wustl.edu

tric field. Numerical simulations performed by Timokhin (2010) demonstrated such oscillations from first-principles, and showed that pair production happens in quasiperiodic bursts. Subsequent 1D and 2D Particle-in-Cell (PIC) simulations all showed the limit-cycle behavior of the pair production process (e.g. Timokhin & Arons 2013; Cruz et al. 2021), and it was proposed that this pair-production oscillation may directly source coherent radio waves (Philippov et al. 2020). A better understanding of the $e^{\pm}$ discharge physics may help us finally solve the decades-old puzzle of the origin of pulsar radio emission.

Recently, it was also realized that the intense parallel electric field in the gap region may be the strongest source of persistent oscillatory $\mathbf{E} \cdot \mathbf{B}$ in the universe. Pseudoscalar particles such as QCD axions interact with the electromagnetic sector through their coupling to $\mathbf{E}\cdot\mathbf{B}$, therefore the spark gaps in the pulsar magnetosphere may be one of the most promising regions of producing these axion-like particles (ALPs) (Prabhu 2021). The QCD axions and ALPs are physically motivated and form a popular class of dark matter candidates (Preskill et al. 1983; Abbott & Sikivie 1983; Dine & Fischler 1983). Recent work by Noordhuis et al. (2023) used the pair cascade process at pulsar polar caps to derive novel constraints on axion signals. A better understanding of the complex plasma physics behind $e^{\pm}$ pair cascade oscillations may be able to further improve the existing constraints on axion properties.

Driven by the need to explain pulsar radio emission, semi-analytic models motivated by first-principles simulations have been constructed recently (Cruz et al. 2021; Tolman et al. 2022). These models improved over the work by Levinson et al. (2005) by taking into account kinetic effects. However, no single semi-analytic model so far can properly reproduce the limit-cycle behavior of the pair cascade process, which includes the growth of the inductive electric field and its subsequent screening from pair production. Numerical simulations, on the other hand, are extremely expensive when the full QED cascade physics is taken into account, and it is impossible to simulate the parameter regime of realistic pulsars in 2D or 3D with current computational capabilities.

In this paper, we attempt to construct a minimal time-dependent theoretical model that can reproduce all salient features of the pulsar $e^{\pm}$ pair cascade process. This model takes into account the highly relativistic and nonlinear plasma physics governing the pair plasma near the pulsar polar cap, and uses a physically motivated prescription to incorporate pair production and escape. In Section 2, we outline this theoretical model and derive the differential equations governing it. In Section 3, we discuss our choice of the pair-production source term in the equations and compare a few different alternatives. In Section 4, we present numerical solutions to this model and discuss their parameter dependence. Finally, in Section 5 we discuss the observational implications and how this model can be improved in the future.

2. THEORETICAL MODEL

2.1. *Equations and Closure*

We start from the coupled Vlasov-Maxwell system in 1D, along the local magnetic field, with a source term for pair production. Using x to denote the coordinate along the field line, the system reads:

$$\frac{\partial E}{\partial t} = c(\nabla \times \mathbf{B})_{\parallel} - 4\pi j \tag{1}$$

$$\frac{\partial f_{\pm}}{\partial t} = -v\frac{\partial f_{\pm}}{\partial x} - q_{\pm}E\frac{\partial f_{\pm}}{\partial p} + S_{\pm}, \tag{2}$$

where $\pm$ denotes the electron or positron species, and $S_{\pm}$ is the source term due to $e^{\pm}$ pair production. Assuming the magnetic field is static, and does not couple to the dynamics

in the spark gap, we write $j_B = c(\nabla \times \mathbf{B})_\parallel / 4\pi$. Amperé's law becomes:

$$\frac{\partial E}{\partial t} = 4\pi(j_B - j). \tag{3}$$

The electric current density j in equation (3) can be computed directly from the distribution function:

$$j = \sum_{s=\pm} q_s \int v f_s \, \mathrm{d}p. \tag{4}$$

Taking the time-derivative of the current and using the Vlasov equation (2), we can write down the evolution equation for j:

$$\begin{aligned}\frac{\partial j}{\partial t} &= \sum_{s=\pm} q_s \int v \frac{\partial f_s}{\partial t} \, \mathrm{d}p \\ &= \sum_{s=\pm} q_s \int v \left(-v\frac{\partial f_s}{\partial x} - q_s E \frac{\partial f}{\partial p} + S_s \right) \mathrm{d}p \\ &= \sum_{s=\pm} \int \left[q_s v \left(-v\frac{\partial f_s}{\partial x} + S_s \right) + q_s^2 E f_s \frac{dv}{dp} \right] \mathrm{d}p,\end{aligned} \tag{5}$$

where we have used integration by parts to move the ∂_p onto v. Since $dv/dp = 1/m\gamma^3$, the last term can be written as:

$$\int q_s^2 E f_s \frac{dv}{dp} \, \mathrm{d}p = \frac{q_s^2 E n_s}{m} \left\langle \frac{1}{\gamma_s^3} \right\rangle, \tag{6}$$

where $n_s = \int f_s \mathrm{d}p$ is the number density of the particle species, and the angular bracket means taking the expectation value with respect to the distribution function.

Our goal is to construct a set of coupled time-dependent ODEs that can be solved numerically. Therefore, we specialize to one point in space where particle acceleration, pair production, and electric field screening are happening, similar to the approach adopted by Cruz et al. (2021) and Tolman et al. (2022). To this end, we postulate a macroscopic length scale L for the variation of plasma density and approximate the spatial derivative as $\partial_x \sim 1/L$. We further assume that pairs flow away from the point of interest at the speed of light, $v \approx c$. The Vlasov equation then becomes:

$$\frac{\partial f_\pm}{\partial t} = -\frac{c}{L} f_\pm - qE\frac{\partial f_\pm}{\partial p} + S_\pm. \tag{7}$$

This is our attempt to approximately model the plasma escape effect. Using this approximation, the time evolution equation (5) for the current becomes:

$$\frac{\partial j}{\partial t} = -\frac{c}{L} j + \sum_{s=\pm} \frac{q_s^2 E n_s}{m} \left\langle \frac{1}{\gamma_s^3} \right\rangle - q_s \int v S_s \, \mathrm{d}p. \tag{8}$$

Two extra quantities appear in equation (8): the number density of each species $n_\pm$, and the expectation value of $1/\gamma^3$ for each species. The time evolution for $n_\pm$ can be written down by simply integrating the Vlasov equation (7) over the momentum space:

$$\frac{\partial n_\pm}{\partial t} = -\frac{c}{L} n_\pm + \int S_\pm \, \mathrm{d}p. \tag{9}$$

However, the $\langle 1/\gamma^3 \rangle$ term requires an additional equation for closure, which invariably involves higher moments of the distribution function. In this paper, we make the simplest hydrodynamic approximation, $\langle 1/\gamma^3 \rangle \approx 1/\langle \gamma \rangle^3$, and use $\langle p_\pm \rangle$ for closure by computing $\langle \gamma_\pm \rangle = \sqrt{1 + \langle p_\pm \rangle^2 / m^2 c^2}$. Additional discussion about this choice is included in Appendix A, where we outline a systematic way to improve this approximation. Similar to the current equation (8), the time evolution for $\langle p_\pm \rangle$ can be obtained by substituting the Vlasov equation and equation (9), and then using integration by parts:

$$\begin{aligned}\frac{\partial \langle p_\pm \rangle}{\partial t} &= \frac{1}{n_\pm} \int p \frac{\partial f_\pm}{\partial t} \, \mathrm{d}p - \frac{\dot{n}_\pm}{n_\pm} \langle p_\pm \rangle \\ &= \frac{1}{n_\pm} \int S_\pm (p_\pm - \langle p_\pm \rangle) \, \mathrm{d}p + q_\pm E.\end{aligned} \tag{10}$$

Equations (8)–(10) involve an integral of the pair production source term S which we have

not specified. In this paper, we assume all pairs are produced at a single energy, but the pair production rate may be a general function of E, $n_\pm$, and $\langle p_\pm \rangle$, in order to take into account the feedback from electric field screening:

$$S_+ = S_- = S(E, n_\pm, \langle p_\pm \rangle)\delta(p - p_{\rm pair}). \quad (11)$$

We will be discussing our specific choices for the function S in Section 3. Since electrons and positrons are accelerated in opposite directions in the gap, the pairs produced from γ-ray photons emitted by them have opposite momenta. In addition, the pairs produced from curvature radiation emitted from primary particles have much lower energies than the accelerated electrons and positrons. Therefore we set $p_{\rm pair} = 0$ in this model, which significantly simplifies the integrals of the source term.

2.2. *Numerical Units*

In order to solve the coupled equations (3), (8), (9), and (10) together numerically, we introduce a unit system that is motivated by the physics at the pulsar polar cap. In the rest of this paper, dimensionless variables are expressed with tildes, and their units are expressed with the subscript 0, e.g. $\tilde{x} \equiv x/x_0$.

We normalize the electron and positron densities $n_\pm$ with the Goldreich-Julian density (Goldreich & Julian 1969):

$$n_{\rm GJ} = \frac{\mathbf{B}\cdot\mathbf{\Omega}_{\rm NS}}{2\pi ec} \simeq 6.9\times10^{10}\left(\frac{B}{10^{12}\ {\rm G}}\right)\left(\frac{1\ {\rm s}}{P}\right)\ {\rm cm}^{-3}, \quad (12)$$

where B is the local magnetic field strength, and Ω is the rotation angular frequency of the neutron star. The unit of length and time are determined by the plasma frequency associated with $n_{\rm GJ}$:

$$\omega_0^2 = \frac{4\pi n_{\rm GJ} e^2}{m_e}. \quad (13)$$

We then set the unit of time to be $t_0 \equiv 1/\omega_0$ and unit of length $x_0 \equiv c/\omega_0$. Using the nominal value of $n_{\rm GJ}$, our length unit is close to $x_0 \approx 2\,{\rm cm}$. Note that the real plasma frequency after pair production sets in is going to be significantly higher, and this ω_0 simply sets a lower bound for the plasma frequency.

For electron momentum, we set $p_0 \equiv m_e c$, and the dimensionless momentum is simply $\tilde{p} = \gamma\beta$. The unit of the electric field $E_0 \equiv mc/et_0$ is then determined as the strength of the electric field that increases $\tilde{p} = \gamma\beta$ by 1 in the unit time t_0. The unit electric current density $j_0 \equiv en_{GJ}c$ is equivalent to $j_0 \equiv E_0/4\pi t_0$ due to our choice of t_0. Lastly, we define the units of the electron distribution function and pair production rate as $f_0 \equiv n_{\rm GJ}/p_0$ and $S_0 \equiv f_0/t_0$, respectively. In summary, our choice of units is listed below:

$$\begin{aligned} &t_0 \equiv (4\pi e^2 n_{\rm GJ}/m_e)^{-1/2} \approx 6.7\times10^{-11}\ {\rm s} \\ &p_0 \equiv m_e c,\ n_0 \equiv n_{\rm GJ},\ E_0 \equiv mc/et_0 \\ &j_0 \equiv en_{\rm GJ}c,\ f_0 \equiv n_{\rm GJ}/p_0,\ S_0 \equiv f_0/t_0. \end{aligned} \quad (14)$$

After incorporating the source term (11) and using the unit listed above, these are the equations that we solve numerically:

$$\frac{d\tilde{E}}{d\tilde{t}} = \tilde{j}_B - \tilde{j}, \quad (15)$$

$$\frac{d\tilde{j}}{d\tilde{t}} = -\frac{\tilde{j}}{\tilde{L}} + \sum_{s=\pm}\left\langle\frac{1}{\gamma_s^3}\right\rangle\tilde{E}\tilde{n}_s, \quad (16)$$

$$\frac{d\tilde{n}_\pm}{d\tilde{t}} = -\frac{\tilde{n}_\pm}{\tilde{L}} + \tilde{S}(\tilde{E}, \tilde{n}_\pm, \langle\tilde{p}_\pm\rangle), \quad (17)$$

$$\frac{d\langle\tilde{p}_\pm\rangle}{d\tilde{t}} = -\frac{\tilde{S}(\tilde{E}, \tilde{n}_\pm, \langle\tilde{p}_\pm\rangle)}{\tilde{n}_\pm}\langle\tilde{p}_\pm\rangle + \frac{q_\pm}{e}\tilde{E}. \quad (18)$$

Apart from the pair production source function $\tilde{S}$ to be discussed in Section 3, there are two dimensionless parameters in this model, $\tilde{L}$ and $\tilde{j}_B$. The length scale $\tilde{L}$ parametrizes plasma escape, and will be taken to be approximately on the same order as the polar cap size $r_{\rm pc}$. The magnetospheric current $\tilde{j}_B$ provides a driving term for the electric field and is responsible for

its growth after the pair plasma has advected away. We typically take j_B to be a few times $en_{\rm GJ}c$, which is consistent with the magnetospheric current near the polar cap seen in global force-free and PIC simulations (see e.g. Bai & Spitkovsky 2010; Gralla et al. 2017).

Combining equations (15) and (16), the equation for $\tilde{E}$ is essentially a damped oscillator with a constant forcing term:

$$\frac{d^2\tilde{E}}{d\tilde{t}^2} + \frac{1}{\tilde{L}}\frac{d\tilde{E}}{d\tilde{t}} + \sum_{s=\pm} \tilde{n}_s \left\langle \frac{1}{\gamma_s^3} \right\rangle \tilde{E} = \frac{\tilde{j}_B}{\tilde{L}}. \quad (19)$$

We define the effective frequency of the oscillation:

$$\bar{\omega}^2 = \sum_{s=\pm} \tilde{n}_s \left\langle \frac{1}{\gamma_s^3} \right\rangle. \quad (20)$$

The growth and screening of the electric field depend on the value of this effective frequency. Initially, when $\bar{\omega}$ is very small, the particular solution to the equation is linear growth, $\tilde{E} \propto \tilde{j}_B \tilde{t}$. As the electric field increases, the plasma is accelerated and pair production sets in, which increases $\bar{\omega}$. The nature of the solution changes when $\bar{\omega}$ becomes large enough to start oscillations, which initiates the electric field screening phase.

Equation (19) also shows that the evolution of $\tilde{E}$ and $\tilde{j}$ somewhat separates from the other two equations, and the plasma properties only affect the effective frequency in the particular combination (20). This provides some robustness to the model that separates the dynamics of the electric field from the detailed microphysics model we use for pair production.

3. MODELING THE PAIR PRODUCTION SOURCE TERM

The main goal of this paper is to construct a self-contained theoretical model that can reproduce the limit-cycle behavior of $e^\pm$ pair production. To achieve this goal, we need to find a suitable function S in equation (11). The pair cascade process is a complicated (and potentially nonlocal) sequence of curvature radiation, synchrotron radiation, and magnetic pair production or photon-photon annihilation. Although numerical simulations have succeeded in describing these processes accurately, it is impossible to include their full effects in a zero-dimensional model. Therefore, we try to find a simple qualitative source function using a trial-and-error process.

Since the source function S may generally depend on $\tilde{E}$, $\tilde{n}_\pm$, and $\langle p_\pm \rangle$, we experimented with a number of different types of functional forms (in all cases g is a dimensionless parameter):

(i) Constant pair production rate: $\tilde{S} = g$;

(ii) Proportional to plasma density: $\tilde{S} = g \sum_s \tilde{n}_s$;

(iii) Proportional to average momentum: $\tilde{S} = g \sum_s |\langle \tilde{p}_s \rangle|$;

(iv) Proportional to local electric field: $\tilde{S} = g|\tilde{E}|$;

(v) Proportional to electric field and plasma density: $\tilde{S} = g|\tilde{E}| \sum_s \tilde{n}_s$;

(vi) Proportional to average momentum and plasma density: $\tilde{S} = g \sum_s \tilde{n}_s |\langle \tilde{p}_s \rangle|$.

Type (i), constant pair production rate, is similar to the pair production function used by Tolman et al. (2022). Since it does not allow for any feedback from the evolution of $\tilde{E}$ and $\langle \tilde{p} \rangle$, we expect the gap to be screened and never grow again. It is a good choice for studying the screening phase, but we do not expect it to lead to a limit cycle. Similarly, type (ii) only depends on the plasma density, and we expect the electric field will not grow again after the initial screening phase. The rest 4 types of pair production function take into feedback from the field evolution in different ways, and it is not immediately obvious which one leads to a limit-cycle behavior.

Note that we have not included a source function type that involves a pair-production threshold $\gamma_{\rm thr}$, as was done by Levinson et al. (2005) and Cruz et al. (2021). We found that since the equations (15)–(18) are already quite stiff, a threshold condition often leads to discontinuous transitions which can easily cause the solutions to run away. A more physical justification is that, since equation (18) evolves the average momentum that exponentially decreases when pair production sets in, it is not appropriate to use a threshold condition on this value directly. An additional function that tracks the energies of primary particles in the gap may be better suited for applying the threshold condition, but we will leave the experimentation of such a model to future works.

After extensive experimentation, we found that the only source function that can consistently reproduce the pair discharge limit-cycle behavior is type (vi), where $\tilde{S}$ is proportional to both the plasma density and the average particle momentum. A solution with this type of source function is plotted in Figure 1, which depicts different parts of one pair discharge cycle. We will discuss this solution and its parameter dependence in Section 4. More discussion about how other models fail is included in Appendix B.

Coincidentally, type (vi) of the source function is applicable to pairs produced by curvature photons, which may be the primary channel for pair production at pulsar polar caps. The energy loss rate of an electron of Lorentz factor γ undergoing curvature radiation is (see e.g. Jackson 1999):

$$P_{\rm CR} = \frac{2}{3}\frac{e^2 c}{\rho_c^2}\gamma^4, \tag{21}$$

where ρ_c is the field line curvature radius. The characteristic photon energy from curvature radiation is:

$$\epsilon_{\rm CR} = \frac{3}{2}\frac{\lambda\!\!\!^{-}}{\rho_c}\gamma^3 m_e c^2, \tag{22}$$

where $\lambda\!\!\!^{-}$ is the reduced electron Compton wavelength. Therefore, the number of curvature photons $n_{\rm CR} \sim P_{\rm CR}/\epsilon_{\rm CR}$ emitted by an ultra-relativistic primary electron per unit time scales as γ, and each photon converts to an $e^{\pm}$ pair. Additional synchrotron cascade may increase the total number of pairs produced by a single primary electron (**?**), but it is a reasonable first approximation to set the pair production rate to be proportional to $n_{\pm}\gamma_{\pm}$, which is our source function type (vi).

This correspondence to curvature radiation is also our way to choose the numerical parameter g in the expression of the source function. The constant g has the physical meaning of number of pairs produced per time t_0 per primary particle, divided by its Lorentz factor:

$$\begin{aligned} g &= \frac{P_{\rm CR}}{\epsilon_{\rm CR}}\frac{t_0}{\gamma} = \frac{4}{9}\frac{e^2}{\lambda\!\!\!^{-}\rho_c m_e c}t_0 \\ &\approx 6.5\times10^{-11}\left(\frac{\rho_c}{10^8\,{\rm cm}}\right)^{-1} B_{12}^{-1/2} P_1^{1/2}, \end{aligned} \tag{23}$$

where $B_{12} = B/10^{12}\,{\rm G}$ and $P_1 = P/1\,{\rm s}$. For our reference model in Section 4, we use $g = 10^{-11}$.

4. NUMERICAL SOLUTIONS AND PARAMETER DEPENDENCE

We solve the set of 6 coupled ODEs (15)–(18) using the Python library function `scipy.integrate.solve_ivp`. Anticipating a stiff set of equations, we use the library-provided "Radau" method, which is an implicit Runge-Kutta method of the Radau IIA family of order 5 (Hairer et al. 1993). Since the method is adaptive, the results are interpolated through a cubic polynomial to a dense output array of at least 500,000 points, which allows for FFT calculations to analyze the power spectrum of electric field oscillations.

There are only three numerical parameters in this model. $\tilde{j}_B$ is the magnetospheric current in units of $en_{\rm GJ}c$, which is usually order unity at pulsar polar caps. Note that although we normalize plasma density with $n_{\rm GJ}$, the system

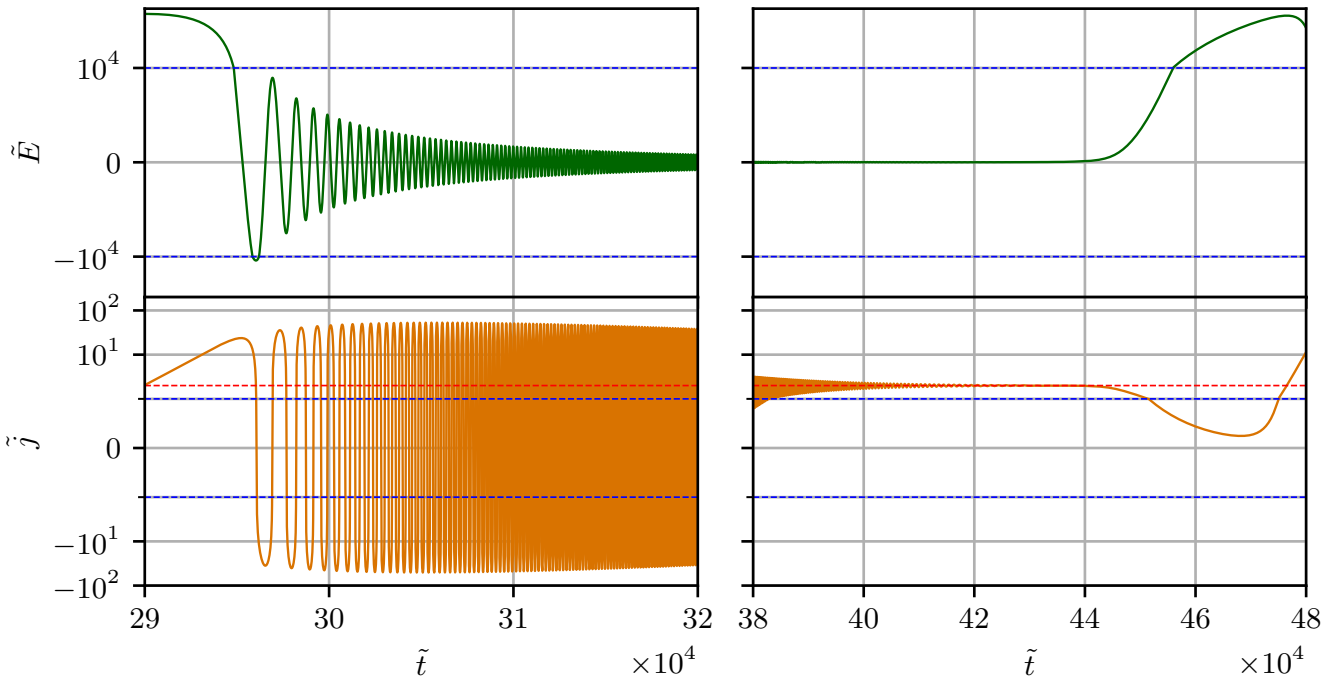

Figure 1. The zoomed-in plot of the time evolution of the electric field and the charged current in "symlog" scale, with a blue dotted line showing the threshold between linear and logarithmic scales. Left and right columns show the beginning of the screening phase and the transition to the next electric field growing phase, respectively. The escape length scale $\tilde{L}$ is set as $\tilde{L} = 10^4$, and pair production parameter is $g = 10^{-11}$. The value of $\tilde{j}_B$ is chosen to be 2 and is shown as red dotted lines.

mainly operates in the regime of $\rho \sim 0$ and the current is therefore always spacelike. $\tilde{L}$ is the dimensionless parameter that roughly characterizes the size of the pair-producing region, and controls how quickly plasma escapes from the region. We take it to be comparable or smaller than the pulsar polar cap radius. The constant g in the source function S parametrizes the pair production rate, and we use curvature radiation for typical pulsar parameters to choose its value in our reference model, as discussed in Section 3.

Figure 1 shows the evolution of electric field $\tilde{E}$ and current density $\tilde{j}$ over time for a particular set of parameters. Initially, the system is filled with $n_+ = n_- = n_{\rm GJ}$ with both species at rest. The electric field E and electric current j are initially also zero. Due to the magnetospheric current j_B, the electric field starts to grow linearly with time, accelerating both species of charges. Electron-positron pairs are continuously produced during this time, exponentially increasing the number densities $n_\pm$. Electric field screening happens when the effective frequency $\bar{\omega} = \sqrt{\sum \tilde{n}_s \langle 1/\gamma_s^3 \rangle}$ becomes large enough, $\bar{\omega} \gtrsim 1/\tilde{L}$. This is when the solution transitions to an oscillatory nature, at which point the electric field screening is well-described by a weakly damped oscillator with slowly changing frequency. The damping effect drives the electric field to 0 and the electric current to $\tilde{j}_B$. The electric field grows again when the plasma exits the region and the effective frequency drops far below $1/\tilde{L}$.

Figure 2 shows the full solution for three models with different pair production parameters g. The electric field growth and screening limit-cycle are observed in all 3 cases. However, the three models differ in their maximum electric field strength $E_{\rm max}$, the quasi-period of the limit cycle, and the maximum effective fre-

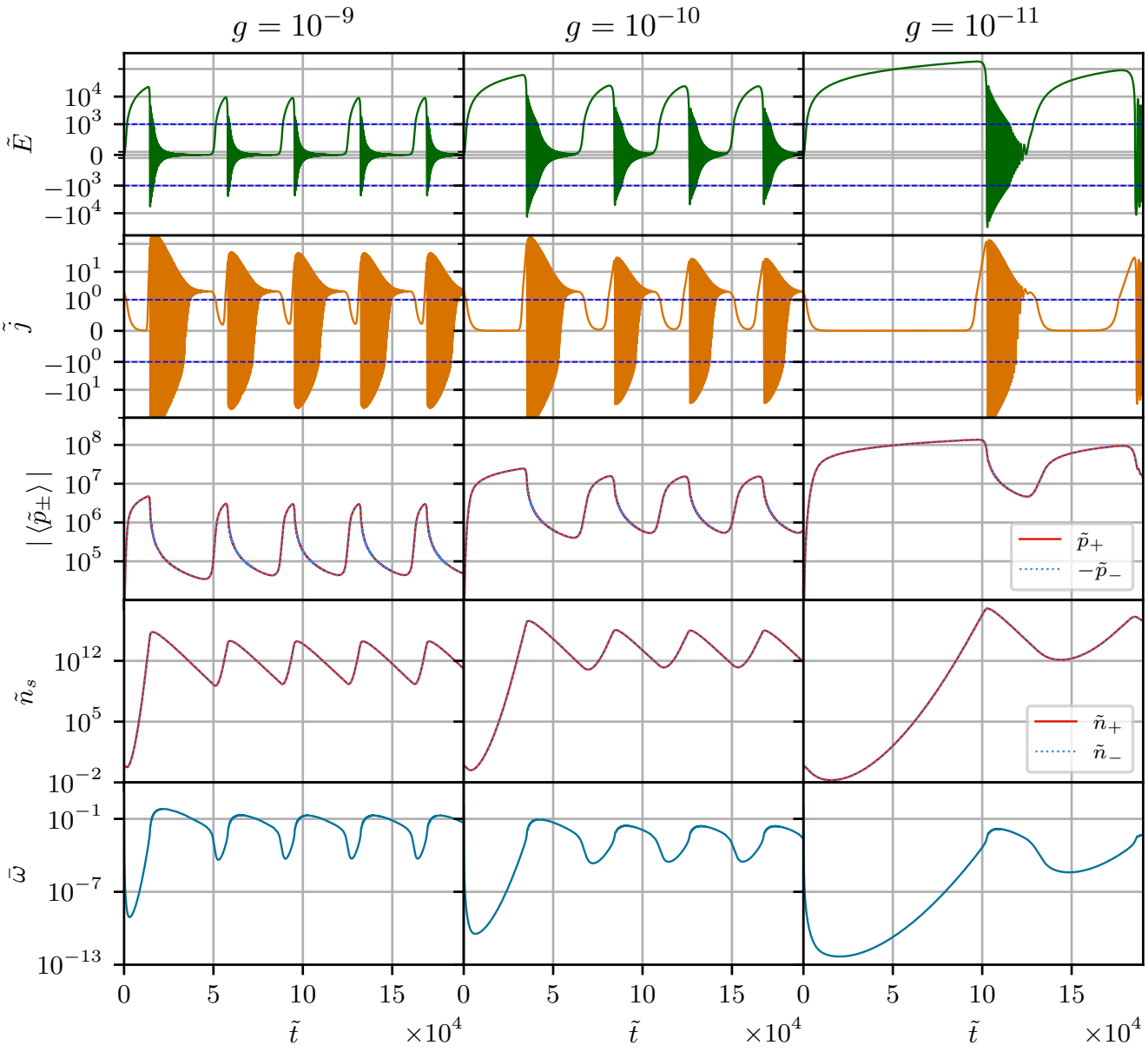

Figure 2. Full solution of equations (15)–(18) (from the top to the bottom, $\tilde{E}, \tilde{j}, |\langle\tilde{p}_\pm\rangle|$, $\tilde{n}_\pm$, and effective frequency $\bar{\omega}$) as a function of $\tilde{t}$. The first two rows are plotted in "symlog" scale and blue dashed lines denote the transition from linear to logarithmic scales. Each column assumes a different production rate of charged particles in pair cascades; $g = 10^{-9}, g = 10^{-10}$, and $g = 10^{-11}$ are chosen for the left, central, and right column, respectively. Initial conditions and model parameters are chosen as $\tilde{E}_{\rm init} = \tilde{j}_{\rm init} = \langle\tilde{p}_\pm\rangle_{\rm init} = 0$, $\tilde{n}_{\pm,{\rm init}} = 1$, $\tilde{j}_B = 2$, and $\tilde{L} = 2\times10^3$. The production rate of charged particles is set to be $\tilde{S} = g\sum_\pm \tilde{n}_\pm\,|\langle\tilde{p}_\pm\rangle|$.

quency $\bar{\omega}_{\rm max}$. We see that a lower pair production efficiency leads to a larger $E_{\rm max}$ in the gap, and the electrons and positrons are accelerated to much higher maximum energies. The maximum effective frequency for electric field oscillations $\bar{\omega}_{\rm max}$ is also lower when pair production is less efficient, due to the much higher plasma Lorentz factors.

One interesting feature of this model is that, even though $\tilde{j}$ changes sign rapidly as the electric field is screened, the mean momentum $\langle p_\pm \rangle$ just decreases but never changes sign again. We believe this is physical, as $\langle p_\pm \rangle$ can be dominated by a population of high energy particles, while these particles do not contribute as much to $\langle \beta_\pm \rangle$. As a result, the current density can become close to zero and change sign due to large amounts of pairs being produced. Note that $|\langle p_+ \rangle|$ and n_+ are completely symmetric with $|\langle p_- \rangle|$ and n_- in all solutions. This is simply a consequence of the symmetry $n_+ \leftrightarrow n_-$ and $\langle p_+ \rangle \leftrightarrow -\langle p_- \rangle$ in Equations (17) and (18).

Another feature of the model is that it predicts an extremely high pair multiplicity of $n_\pm / n_{\rm GJ} \gtrsim 10^{16}$, far greater than previous more rigorous studies (e.g. Timokhin & Harding 2019). This is a limitation of the model that stems from our choice of closure, where $\langle 1/\gamma_\pm \rangle \sim 1/\langle \gamma_\pm \rangle^3$, as well as the very simplified pair production source function discussed in Section 3. Our hydrodynamic closure may be reasonable during the electric field growing phase, where all particles are accelerated together, but it significantly underestimates this value when pair production is significant. Since electric field screening is controlled by the effective frequency $\bar{\omega}$, the system develops an unreasonably high plasma density to compensate. Experimentation with higher-order closures shows that a better estimate of $\langle 1/\gamma^3 \rangle$ does tend to reduce the number density (see Appendix A). Our source term for pair production is also quite crude, therefore we believe the model should not be used to directly study the pair multiplicities from pulsar polar cap pair cascades.

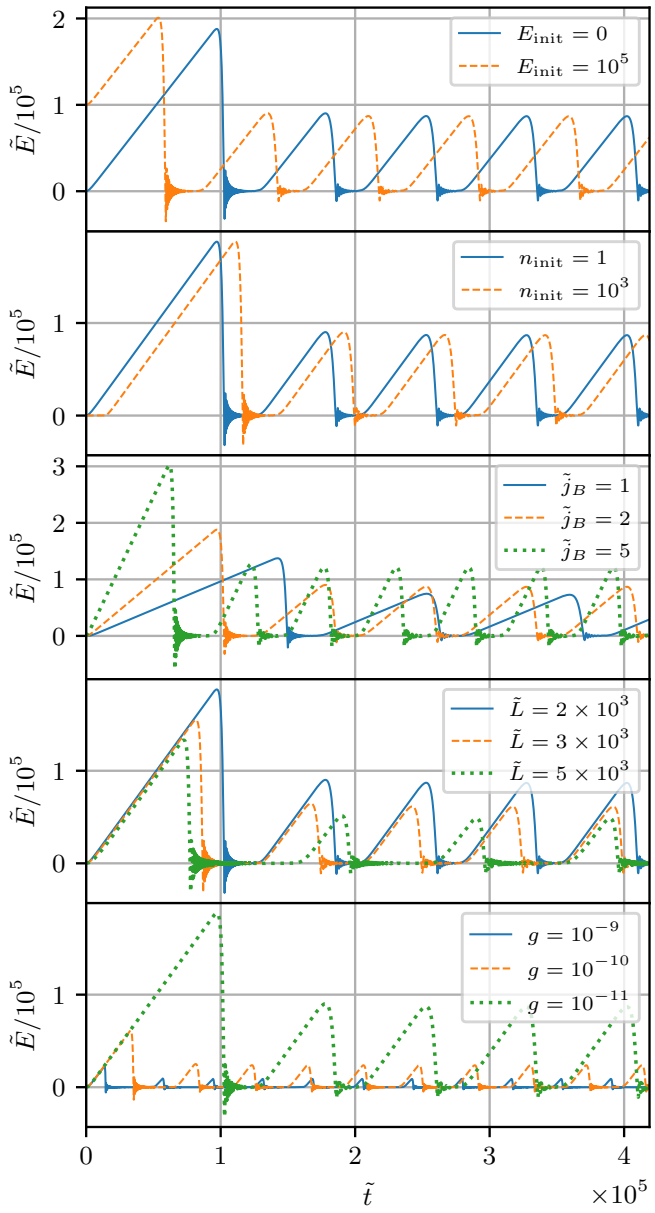

Figure 3. The plots of electric fields with different choices of one of initial conditions or parameters. From the top panel, each plot compares the behavior of electric fields with several choices of $\tilde{E}_{\rm init}$, $\tilde{n}_{\rm init}$, $\tilde{j}_B$, $\tilde{L}$, and g, respectively. The reference model used for comparison is $\tilde{j}_B = 2$, $\tilde{L} = 2 \times 10^3$, and $g = 10^{-11}$.

Figure 3 illustrates the dependence of the electric field solution on initial conditions and other

numerical parameters. Experimenting with significantly different initial conditions, we find that the initial condition doesn't affect the later recurrent behavior of the solution, as all initial conditions are attracted to the same limit cycle. Different initial electric fields and the number densities of charged particles just result in different times of onset of the electric field screening.

On the other hand, the different choices of parameters lead to the different time-evolution of the electric field. The growth rate of the electric field before its screening is only governed by $\tilde{j}_B$, as that part of the solution is described by $\tilde{E} \propto \tilde{j}_B \tilde{t}$. The systems with larger $\tilde{j}_B$ or g start screening the electric fields at the earlier time, as pair production becomes more efficient in both cases. $\tilde{L}$ describes how slowly or quickly charged particles escape from the pair-producing region, and thus a smaller $\tilde{L}$ leads to an increased duty cycle for the gap. This is because when pairs escape more quickly, the system spends less time until the electric fields start growing again.

This oscillating electric field in the polar cap has been suggested as a possible origin for pulsar coherent radio emission (Philippov et al. 2020). If this is the case, then the frequency spectrum of electric field oscillations should be directly related to the resulting radio waves. Figure 4 shows the power spectrum of the electric field energy for the three models that were shown in Figure 2. The spectrum generally follows a power law, but has a cutoff that scales with the pair production parameter g. This cutoff is located near the maximum $\bar{\omega}$, which is physically the maximum oscillation frequency of the electric field. The spectrum beyond this cutoff arises purely due to interpolation onto a dense output grid. The cutoff frequency is higher for models with more efficient pair production. For higher values of g, the frequency

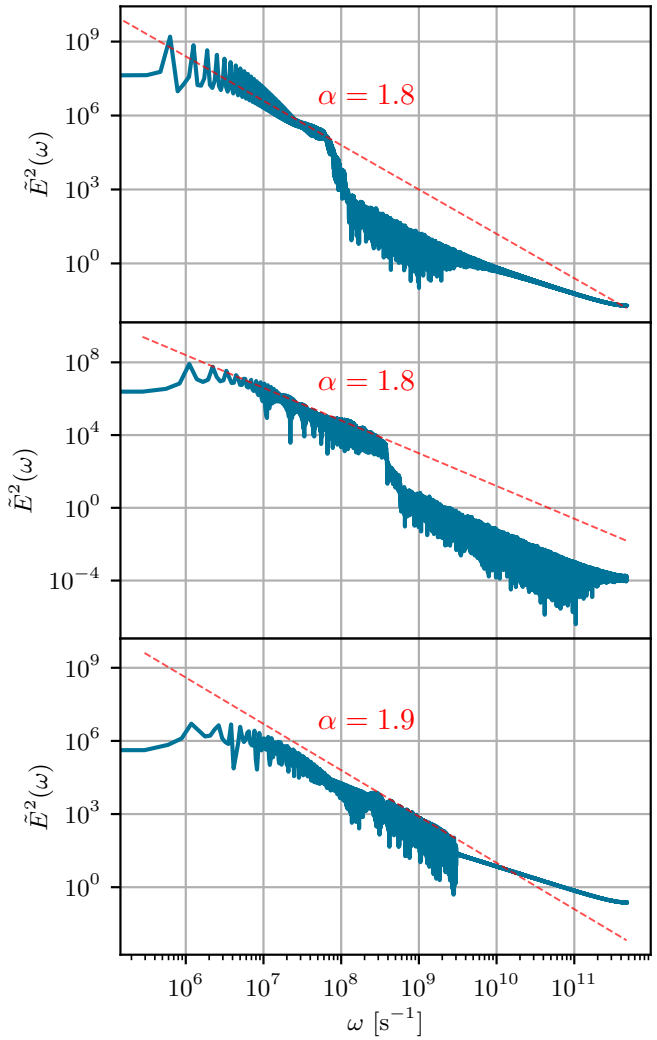

Figure 4. The power spectra of the electric field $\tilde{E}^2$ for a time interval which corresponds to four pair-production limit cycles. The different plots correspond to different values of the pair production parameter: $g = 10^{-11}$ (top), $g = 10^{-10}$ (middle), and $g = 10^{-9}$ (bottom). The dotted lines are simple estimates of the spectral indices. The spectral index is only weakly dependent on the pair production rate, but the frequency cutoff depends sensitively on the parameter g.

range contains what is typically observed in pulsar radio emission.

Compared to the frequency cutoff, we find that the power law index is only weakly dependent on the model parameters, and all lie within the 1.8–2.0 range. This is largely com-

patible with the observed pulsar radio emission spectra of $\omega^{-1.4\pm1.0}$ (Bates et al. 2013). However, even within one single model, the spectral index seems to vary over the frequency range. More detailed modeling on the escape of these oscillations as coherent electromagnetic waves is required to make definitive predictions about the radio emission spectrum.

5. SUMMARY AND DISCUSSION

We have presented a minimal time-dependent theoretical model that captures the limit-cycle behavior of the pulsar polar cap $e^{\pm}$ production process. The model has only three parameters, and reproduces correctly the complete pair discharge cycle, from the induction to the screening of $E_{\parallel}$. The solution is agnostic of initial conditions, and always settles to the same recurrent behavior under the same parameters, as characteristic of a true limit cycle. We explored the parameter dependence of the model and computed the power spectrum of the electric field oscillations. We found that the spectral index is around 1.8–2.0, weakly dependent on model parameters within the range we have experimented with. This result is largely compatible with the range of spectral indices of observed pulsar radio emission.

In addition, the frequency range of the oscillations seems to be compatible with the observed 100 MHz to several GHz range. The high-frequency cutoff of the power spectrum depends sensitively on the efficiency of pair production, and becomes lower when pair production is less efficient. This dependence may provide an alternative explanation of the pulsar death line. As a pulsar spins down, its polar cap potential drops, which decreases the pair production efficiency. This results in an overall reduction of the high-frequency cutoff of its radio spectrum, rendering it undetectable by our radio telescopes that are sensitive between the 100 MHz and a few GHz.

Although the three numerical parameters in this model have straightforward physical meanings, their values need to be fine-tuned by comparing the model with first-principles PIC simulations such as those by Timokhin & Arons (2013) and Cruz et al. (2021). Such a comparison will not only check the validity of this model, but also provide a guide for choosing the parameters, potentially allowing for extrapolation to realistic pulsars. Such a study will be the focus of a future work.

Our time-dependent pair production model not only describes $e^{\pm}$ discharge at the pulsar polar cap, but should also be applicable to other systems where a spark gap is expected, e.g. the twisted flux tubes of a magnetar (e.g. Beloborodov 2013) or black hole magnetospheres (e.g. Chen et al. 2018). For other systems, the pair production term may need to be modified accordingly, but the set of equations (15)–(18) should generally remain unchanged.

We have introduced a few simplifying assumptions to make the problem tractable. One of the most significant was replacing $\langle 1/\gamma^3 \rangle$ in equation (16) by $1/\langle\gamma\rangle^3$, which closes the equations but significantly underestimates the value of this term. As a result, the number densities $n_{\pm}$ from the model are much higher than what was generally predicted by more sophisticated theoretical models of the pair production process (e.g. Timokhin & Harding 2019). To improve the estimates of $n_{\pm}$, more moments such as $\langle p_{\pm}^2 \rangle$ can be included in the equations as discussed in Appendix A. However, more detailed modeling of the pair production term may also be needed in order to yield a more reliable prediction.

Another limitation of this model is that it assumes local feedback of pair production on the electric field, which may not be realistic due to finite photon free paths. In the case of non-local pair production, a zero-dimensional model

such as proposed in this paper is likely no longer applicable. Further comparison with direct numerical simulations should be able to measure the effect of non-local electric field screening and find the parameter regimes where local pair production is a good approximation.

Despite all its limitations, we believe this model elucidates some of the most important features of the pair cascade process. In addition, this model can potentially provide a powerful way to compute the time dependence of parallel electric field $\mathbf{E} \cdot \mathbf{B}$ in pair producing regions in the pulsar magnetosphere over a long period of time. Such a calculation can be used to estimate the production rate of ALPs and their spectra. Tracing the propagation of ALPs and their conversion back to photons can potentially give more stringent constraints on their allowable parameter space than what is currently available.

We thank Yajie Yuan for helpful discussions. AC is supported by NSF grants DMS-2235457 and AST-2308111. TO is supported by the U.S. Department of Energy under grant No. DE-SC 0017987.

REFERENCES

Abbott, L. F., & Sikivie, P. 1983, Phys. Lett. B, 120, 133, doi: 10.1016/0370-2693(83)90638-X

Arons, J. 1983, ApJ, 266, 215, doi: 10.1086/160771

Bai, X.-N., & Spitkovsky, A. 2010, ApJ, 715, 1282, doi: 10.1088/0004-637X/715/2/1282

Bates, S. D., Lorimer, D. R., & Verbiest, J. P. W. 2013, Mon. Not. Roy. Astron. Soc., 431, 1352, doi: 10.1093/mnras/stt257

Beloborodov, A. M. 2008, ApJL, 683, L41, doi: 10.1086/590079

—. 2013, ApJ, 777, 114, doi: 10.1088/0004-637X/777/2/114

Chen, A. Y., Yuan, Y., & Yang, H. 2018, ApJL, 863, L31, doi: 10.3847/2041-8213/aad8ab

Cheng, K. S., Ho, C., & Ruderman, M. 1986, ApJ, 300, 500, doi: 10.1086/163829

Contopoulos, I., Kazanas, D., & Fendt, C. 1999, ApJ, 511, 351, doi: 10.1086/306652

Cruz, F., Grismayer, T., Chen, A. Y., Spitkovsky, A., & Silva, L. O. 2021, ApJL, 919, L4, doi: 10.3847/2041-8213/ac2157

Cruz, F., Grismayer, T., & Silva, L. O. 2021, Astrophys. J., 908, 149, doi: 10.3847/1538-4357/abd2c0

Dine, M., & Fischler, W. 1983, Phys. Lett. B, 120, 137, doi: 10.1016/0370-2693(83)90639-1

Goldreich, P., & Julian, W. H. 1969, ApJ, 157, 869, doi: 10.1086/150119

Gralla, S. E., Lupsasca, A., & Philippov, A. 2017, ApJ, 851, 137, doi: 10.3847/1538-4357/aa978d

Hairer, E., Nørsett, S., & Wanner, G. 1993, Solving Ordinary Differential Equations II: Stiff and Differential-Algebraic Problems, Solving Ordinary Differential Equations II: Stiff and Differential-algebraic Problems (Springer)

Jackson, J. D. 1999, Classical electrodynamics, American Association of Physics Teachers

Levinson, A., Melrose, D., Judge, A., & Luo, Q.-h. 2005, Astrophys. J., 631, 456, doi: 10.1086/432498

Noordhuis, D., Prabhu, A., Witte, S. J., et al. 2023, Phys. Rev. Lett., 131, 111004, doi: 10.1103/PhysRevLett.131.111004

Philippov, A., & Kramer, M. 2022, Annual Review of Astronomy and Astrophysics, 60, 495, doi: 10.1146/annurev-astro-052920-112338

Philippov, A., Timokhin, A., & Spitkovsky, A. 2020, Phys. Rev. Lett., 124, 245101, doi: 10.1103/PhysRevLett.124.245101

Prabhu, A. 2021, Phys. Rev. D, 104, 055038, doi: 10.1103/PhysRevD.104.055038

Preskill, J., Wise, M. B., & Wilczek, F. 1983, Phys. Lett. B, 120, 127, doi: 10.1016/0370-2693(83)90637-8

Ruderman, M. A., & Sutherland, P. G. 1975, ApJ, 196, 51, doi: 10.1086/153393

Spitkovsky, A. 2006, ApJL, 648, L51, doi: 10.1086/507518

Sturrock, P. A. 1971, ApJ, 164, 529, doi: 10.1086/150865

Timokhin, A. N. 2010, MNRAS, 408, 2092, doi: 10.1111/j.1365-2966.2010.17286.x
Timokhin, A. N., & Arons, J. 2013, MNRAS, 429, 20, doi: 10.1093/mnras/sts298
Timokhin, A. N., & Harding, A. K. 2019, Astrophys. J., 871, 12, doi: 10.3847/1538-4357/aaf050
Tolman, E. A., Philippov, A. A., & Timokhin, A. N. 2022, Astrophys. J. Lett., 933, L37, doi: 10.3847/2041-8213/ac7c71

APPENDIX

A. COMPUTING THE EXPECTATION VALUE $\langle 1/\gamma^3 \rangle$

In the main text, we have made the bold assumption that $\langle 1/\gamma^3 \rangle \approx 1/\langle \gamma \rangle^3$ in order to close the equation set (15)–(18). In this appendix, we attempt to justify our assumption and outline a systematic way to improve this estimate. We can actually expand $1/\gamma^3$ around the expectation value $\gamma = \langle \gamma \rangle$:

$$\frac{1}{\gamma^3} = \frac{1}{\langle \gamma \rangle^3} - \frac{3}{\langle \gamma \rangle^4}(\gamma - \langle \gamma \rangle) + \frac{6}{\langle \gamma \rangle^5}(\gamma - \langle \gamma \rangle)^2 + \dots \tag{A1}$$

This is an asymptotic expansion that may not be convergent, but it still provides us with a systematic way to approximate the expectation value of $1/\gamma^3$ by truncating the series at the desired order. Taking the expectation value of equation (A1), the first order term goes to zero, we have:

$$\left\langle \frac{1}{\gamma^3} \right\rangle = \frac{1}{\langle \gamma \rangle^3} + \sum_{n=2}^{\infty} (-1)^n \frac{(n+1)(n+2)}{2\langle \gamma \rangle^{n+3}} \langle (\gamma - \langle \gamma \rangle)^n \rangle \,. \tag{A2}$$

Therefore, our assumption in the main text is equivalent to only keeping the zero-th order term in this expansion. This assumption is reasonable during the electric field growing phase, where all electrons and positrons are accelerated together and the distribution function has little spread, but it significantly underestimates $\langle 1/\gamma^3 \rangle$ when pair production has begun and the electric field is screened, as shown by Cruz et al. (2021) and Tolman et al. (2022).

We can improve the estimate by including more terms in the expansion. For example, if we truncate equation (A2) at $n = 2$, the result becomes:

$$\left\langle \frac{1}{\gamma^3} \right\rangle = \frac{1}{\langle \gamma \rangle^3} + \frac{6}{\langle \gamma \rangle^5} \left(\langle \gamma^2 \rangle - \langle \gamma \rangle^2 \right). \tag{A3}$$

At large γ, $\langle \gamma^2 \rangle \approx \langle p^2 \rangle$, for which we can write down an evolution equation:

$$\begin{aligned} \frac{\partial \langle p^2 \rangle}{\partial t} &= -\frac{\dot{n}}{n^2} \int p^2 f \, \mathrm{d}p + \frac{1}{n} \int p^2 \frac{\partial f}{\partial t} \, \mathrm{d}p \\ &= -\frac{\dot{n}}{n} \langle p^2 \rangle - \frac{c}{L} \langle p^2 \rangle + 2qE \langle p \rangle + \frac{1}{n} \int p^2 S \delta(p) \, \mathrm{d}p \\ &= -\frac{S}{n} \langle p^2 \rangle + 2qE \langle p \rangle, \end{aligned} \tag{A4}$$

where we have assumed that pairs are produced at $p = 0$, as was done in the main text. If we assume a nonzero but equal and opposite $\pm p_{\mathrm{pair}}$, then the higher moments will contain p_{pair} as a parameter. This equation shows that the time evolution of higher moments of the distribution function depends on lower moments, and we can repeat this procedure as needed up to n-th order in equation (A2).

Figure 5 shows a comparison between the solutions with the zeroth order closure used in the main text and the second order closure defined by equation (A3), with all parameters identical. The overall qualitative features of the solution remain similar, but the second order closure solution has an overall lower $\bar{\omega}$. It mainly achieves this by a lower $n_{\pm}$. We expect that including more moments in the expansion will generally lead to a more realistic number density. Such a study is out of the scope of this paper and will be deferred to future works.

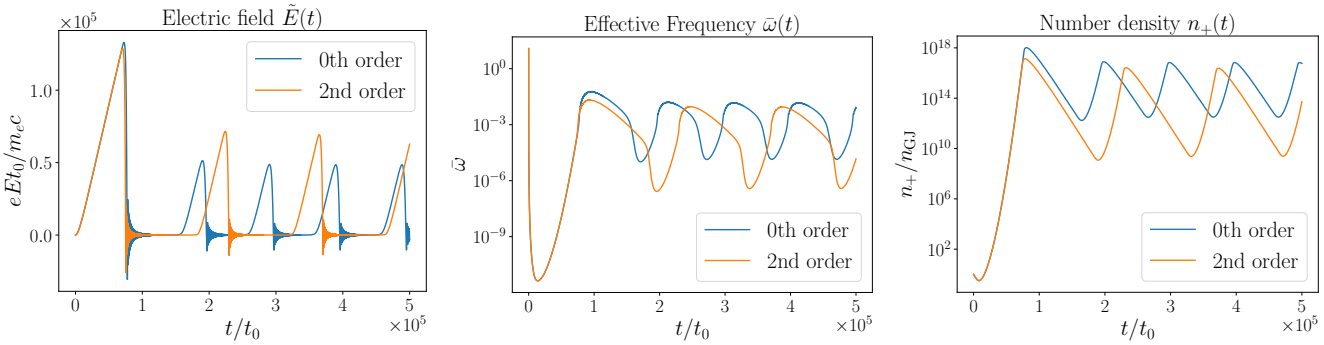

Figure 5. Comparison of the solution with different closure schemes. Blue curves show the solution with $\langle 1/\gamma^3 \rangle = 1/\langle \gamma \rangle^3$, while orange curves show the solution with the second order closure defined by equation (A3).

B. ALTERNATIVE PAIR PRODUCTION MODELS

Among six models proposed in the main text, only $\tilde{S} = g \sum_s \tilde{n}_s |\langle p_s \rangle|$ reproduces the limit-cycle behavior of electric fields. The other five models were not sufficient for yielding this behavior (see Figure 6 for some examples) with reasonable values of initial condition and parameters. Below we briefly describe where each of the other five models was unsuccessful in reproducing the limit cycle.

- $\tilde{S} = g$;

  In this case, Eq. (17) predicts that the deviation of the plasma density from its critical value $\tilde{n}_\pm = \tilde{L}g$ is exponentially suppressed as a function of time. The number density of charged particles in this model ends up being nearly constant.

- $\tilde{S} = g \sum_s \tilde{n}_s$;

  Depending on the sign of the right-hand side of Eq. (17), the plasma density endlessly either grows or drops regardless of the behaviors of the electric fields, the charged current and the averaged momentum.

- $\tilde{S} = g \sum_s |\langle \tilde{p}_s \rangle|$;

  See Figure 6, right panel. Numerical simulations have shown that the averaged momentum tends to be relaxed to a constant value. Then, the plasma density also reaches a constant value, similar to the $\tilde{S} =$ constant case. Electric field never grows appreciably.

- $\tilde{S} = g|\tilde{E}|$;

  With this form of the source term $\tilde{S}$, the averaged momentum of electrons continues to decrease. That of positrons is monotonically increased or decreased depending on the value of g.

- $\tilde{S} = g|\tilde{E}| \sum_s \tilde{n}_s$;

  See Figure 6, left panel. A limit cycle tries to form but settles to an oscillation that is different in nature. In addition, Eq. (18) has a particular solution in this model: $\langle \tilde{p}_s \rangle = q_\pm/eg$. Thus, this model cannot describe the acceleration/deceleration of charged particles due to the electric fields.

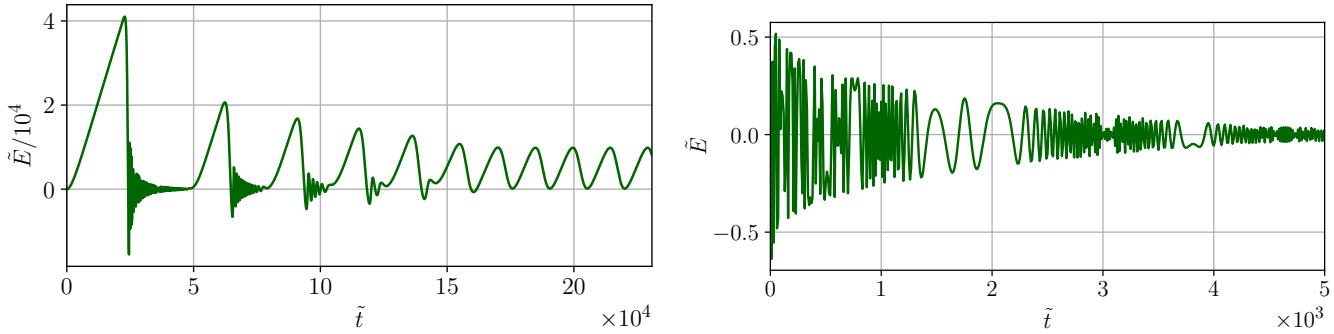

Figure 6. The plots of the electric field evolution obtained by two different models of the pair production source function. The left and right panels assume $\tilde{S} = g|\tilde{E}|\sum_s \tilde{n}_s$ and $\tilde{S} = g\sum_s |\langle \tilde{p}_s \rangle|$, respectively. All initial conditions and the value of parameters are the same as the reference model except for the efficiency of charged particle production rate g; $g = 10^{-7}$ (left) and $g = 10^{-3}$ (right).

Prepared for submission to JHEP

Complete NLO corrections to top-quark pair production with isolated photons

Daniel Stremmer and Malgorzata Worek

Institute for Theoretical Particle Physics and Cosmology, RWTH Aachen University, D-52056 Aachen, Germany

E-mail: daniel.stremmer@rwth-aachen.de, worek@physik.rwth-aachen.de

Abstract: We compute for the first time the so-called complete NLO corrections to top-quark pair production with one and two isolated photons in the di-lepton top-quark decay channel. The Narrow Width Approximation is used for the modeling of unstable top quarks and W bosons. Higher-order QCD and EW effects as well as photon bremsstrahlung are consistently included at all stages: in production and top-quark decays. We present results at the integrated and differential fiducial cross-section level for both processes for the LHC Run II center-of-mass energy of $\sqrt{s} = 13$ TeV. In addition, we investigate the scale choice in photonic observables. Finally, the individual size of each subleading contribution is discussed in detail and the origin of the main subleading corrections is scrutinised. For the latter case, alternative calculations are performed in which the subleading NLO corrections are included only in the production of $t\bar{t}\gamma$ and $t\bar{t}\gamma\gamma$.

Keywords: Higher-Order Perturbative Calculations, Top Quark, Specific QCD Phenomenology

TTK-24-06, P3H-24-005

arXiv:2403.03796v1 [hep-ph] 6 Mar 2024

Contents

1 Introduction **1**

2 Definition of the leading and subleading contributions **4**
2.1 LO contributions 4
2.2 NLO contributions 6

3 Computational framework **10**
3.1 Real corrections 11
3.2 Virtual corrections 14

4 LHC Setup for numerical predictions **16**

5 Top-quark pair production with one isolated photon **18**
5.1 Integrated fiducial cross sections 18
5.2 Differential fiducial cross sections 20

6 Top-quark pair production with two isolated photons **24**
6.1 Integrated fiducial cross sections 24
6.2 Differential fiducial cross sections 25

7 Summary **28**

1 Introduction

Of all the associated production of a top-quark pair with one electroweak gauge boson ($pp \to t\bar{t}V$, $V = Z, W^{\pm}, \gamma$) at the LHC, the $pp \to t\bar{t}\gamma$ process has the largest cross section [1, 2] and is the most interesting to model. First of all, already at the lowest order in the perturbative expansion, the $pp \to t\bar{t}\gamma$ process requires various cuts to keep the prompt photon well isolated and render the whole process infrared (IR) finite, even in the presence of stable top quarks. Secondly, due to its massless nature, the photon can be emitted from all stages of the process, i.e. in the production of $t\bar{t}$ and top-quark decays. In the latter case, prompt photons can originate not only from top quarks, but also from their decay products, including the bottom quarks, $W^{\pm}$ gauge bosons and charged leptons. In addition, they can be radiated from incoming partons. It is a well-known fact that a large fraction of isolated photons comes from radiative decays of top quarks [3, 4]. With fairly inclusive cuts applied on the finale states, that are currently used in measurements of inclusive and differential cross sections of $t\bar{t}\gamma$ production, the contribution of photons at the decay stage reaches almost 50%. Consequently, proper modeling of $pp \to t\bar{t}\gamma$ is very challenging. The $pp \to t\bar{t}\gamma$ process probes the $t - \gamma$ electroweak coupling and provides a direct way to measure the top quark electric charge [5]. The latter is known to be consistent with the Standard Model (SM), although it was measured only indirectly in the production of $t\bar{t}$ [6, 7]. Precise measurements of the $t - \gamma$ coupling at the LHC serve as an additional test of the SM. However, any deviations from the SM prediction, for example in the p_T spectrum of the photon, could point to new physics through anomalous dipole moments of the top quark [8–12]. In addition,

the $pp \to t\bar{t}\gamma$ process plays an important role in studies of the top-quark charge asymmetry (A_C^t) [13–16]. Indeed, it provides complementary information to the measured asymmetries in $t\bar{t}$ production, where A_C^t appears for the first time at next-to-leading order (NLO) only. Contrary, for the $pp \to t\bar{t}\gamma$ process this asymmetry is present already at LO in quark-induced subprocesses due to the interference effects between Feynman diagrams in which the photon is emitted from quarks in the initial state and diagrams in which it is emitted from quarks in the final state. The overall asymmetry in the $pp \to t\bar{t}\gamma$ process at the LHC with $\sqrt{s} = 13$ TeV has a negative value and is of the order of $1\% - 2\%$ depending on the fiducial phase-space regions that are scrutinised [15, 16]. However, A_C^t can be modified by beyond the SM (BSM) physics. Indeed, substantial deviations from the SM prediction can be expected in the case of BSM models with a light colour octet [17–20] or an additional Z' [21]. In both BSM cases, the absolute value of A_C^t is predicted to be much smaller [13].

In the case of the $pp \to t\bar{t}\gamma\gamma$ process, the situation is only somewhat similar to the case of $t\bar{t}\gamma$. Among all the associated production of a top-quark pair with two gauge vector bosons, i.e. $t\bar{t}W^+W^-$, $t\bar{t}ZZ$, $t\bar{t}\gamma\gamma$, $t\bar{t}W^\pm\gamma$, $t\bar{t}W^\pm Z$ and $t\bar{t}Z\gamma$, the $pp \to t\bar{t}\gamma\gamma$ process is the second largest [1]. The importance of $pp \to t\bar{t}\gamma\gamma$ stems from the fact that it is the main (irreducible) background process in SM Higgs-boson studies for the $pp \to t\bar{t}H$ signal process in the $H \to \gamma\gamma$ decay channel. However, the similarities to the production of $t\bar{t}\gamma$ are due to the distribution of photons in the $pp \to t\bar{t}\gamma\gamma$ process and the importance of the contribution, which is not entirely related to the production stage of the process. The effect of photon bremsstrahlung in the $pp \to t\bar{t}\gamma\gamma$ process has recently been studied in detail [22]. It has been shown that the so-called mixed contribution, in which two photons occur simultaneously in the production and decay of the $t\bar{t}$ pair, is the dominant contribution at the integrated and differential fiducial cross-section level.

Evidence for the production of a top-quark pair in association with an isolated photon has already been reported in $p\bar{p}$ collisions at the Tevatron collider at $\sqrt{s} = 1.96$ TeV by the CDF Collaboration [23]. The production of $t\bar{t}\gamma$ final states has been observed for the first time at the LHC at $\sqrt{s} = 7$ TeV by the ATLAS Collaboration [24]. To date, both ATLAS and CMS have observed the production of $t\bar{t}\gamma$ at the LHC at $\sqrt{s} = 8$ TeV and $\sqrt{s} = 13$ TeV [25–30], respectively. So far, no significant deviations from the SM predictions have been found, even though the measured cross sections are larger than theoretical predictions. In addition, within the current and still rather large uncertainties also, the analysed differential cross-section distributions have been fairly well described by the NLO theory predictions. The measurements in the $pp \to t\bar{t}\gamma$ process have also been interpreted in the framework of the standard model effective field theory, where rather stringent limits on the two relevant Wilson coefficients have been found. Furthermore, the measurement of the top-quark charge asymmetry in $pp \to t\bar{t}\gamma$ has recently been performed by the ATLAS collaboration [31]. Also in this case the measurement is compatible with the SM predictions within the present uncertainties. However, in all these cases, current precision is still limited, mainly due to statistical and various systematic uncertainties, leaving room for potential future improvements. Finally, the $pp \to t\bar{t}\gamma\gamma$ process has not yet been experimentally observed at the LHC.

On the theory side, NLO QCD corrections to the $pp \to t\bar{t}\gamma$ production process with stable top quarks have been calculated over ten years ago [32, 33] and calculated afresh in Ref. [1]. The results with NLO electroweak (EW) corrections have also been delivered later [34]. The results presented there have shown that for differential cross-section distributions the NLO EW corrections are significant in the high energy region due to the EW Sudakov effect. Recently, the so-called complete NLO predictions for $pp \to t\bar{t}\gamma$ have been calculated [16], again for stable top quarks only. In addition to the NLO QCD and EW corrections at $\mathcal{O}(\alpha_s^3\alpha)$ and $\mathcal{O}(\alpha_s^2\alpha^2)$ respectively, various subleading contributions, along

with their higher-order effects, have been taken into account to form the complete NLO result. In detail, the set of all the possible contributions at $\mathcal{O}(\alpha_s^2\alpha)$, $\mathcal{O}(\alpha_s\alpha^2)$ and $\mathcal{O}(\alpha_s^0\alpha^3)$ at LO, where the middle one results from the interference of the other two results at the amplitude level and from the photon initiated partonic process $g\gamma \to t\bar{t}\gamma$, as well as at $\mathcal{O}(\alpha_s^3\alpha)$, $\mathcal{O}(\alpha_s^2\alpha^2)$, $\mathcal{O}(\alpha_s\alpha^3)$ and $\mathcal{O}(\alpha_s^0\alpha^4)$ at NLO is what is denoted as the complete NLO result. Finally, the approximate NNLO cross section, with second-order soft-gluon corrections added to the NLO result including QCD and EW corrections, has been calculated in Ref. [35]. On top of the stable top-quark approximation, various predictions that take into account top-quark decays are available in the literature. First, NLO QCD theoretical predictions for $t\bar{t}\gamma$ have been matched with the PYTHIA parton shower program [36]. In this approach top-quark decays have been treated in the parton-shower approximation omitting $t\bar{t}$ spin correlations and photon emission in the parton-shower evolution. More realistic predictions at NLO in QCD have been presented in Ref. [3]. In this case, top-quark decays in the Narrow Width Approximation (NWA) have been included, maintaining $t\bar{t}$ spin correlations in the top-quark decay products. In addition, photon radiation off charged top-quark decay products has been incorporated. A complete description of the $pp \to t\bar{t}\gamma$ process in the di-lepton top-quark decay channel at NLO in QCD has also been finally provided [37]. This calculation is based on matrix elements for the $e^+\nu_e\mu^-\bar{\nu}_\mu b\bar{b}\gamma$ final state including all resonant and non-resonant Feynman diagrams, interferences and off-shell effects of the top quarks and W gauge bosons. Finally, a dedicated comparison between the full off-shell calculation and the results in the NWA has also been carried out [4]. For the $pp \to t\bar{t}\gamma\gamma$ process the situation is much more simpler. NLO QCD predictions for the process with stable top quarks have already been known for some time and have been further matched to parton shower programs [1, 38–40]. In addition to higher-order QCD effects, NLO EW corrections for $t\bar{t}\gamma\gamma$ have recently been reported [16], but again only for stable top quarks. Finally, very recently NLO QCD corrections in the NWA for the di-lepton and lepton + jet top-quark decay channels have been calculated for the $pp \to t\bar{t}\gamma\gamma$ process [22].

From the above description, we can quite clearly see a rather diverse picture for $pp \to t\bar{t}\gamma$ and $pp \to t\bar{t}\gamma\gamma$. On the one hand, we already have the complete NLO result for $t\bar{t}\gamma$, albeit only for stable top quarks. On the other hand, no such predictions exist for $t\bar{t}\gamma\gamma$. In both cases, the complete NLO result with more realistic final states is still missing. With this article, we want to mitigate the current situation and to calculate for the first time the complete NLO predictions for both $pp \to t\bar{t}\gamma$ and $pp \to t\bar{t}\gamma\gamma$ in the di-lepton top-quark decay channel.

The aim of our work is, therefore, manifold. Firstly, we perform a detailed study of the predictions with complete NLO corrections included for $pp \to t\bar{t}\gamma$ and $pp \to t\bar{t}\gamma\gamma$ in the di-lepton top-quark decay channel. Secondly, as we calculate these higher order effects within the same framework, while using the same input parameters, we want to examine whether there are common features or significant differences between the theoretical predictions for $pp \to t\bar{t}\gamma$ and $pp \to t\bar{t}\gamma\gamma$. Thirdly, we plan to analyse the impact of subleading NLO corrections on integrated and differential fiducial cross sections and systematically study the theoretical uncertainties due to missing higher orders. Finally, we are going to scrutinise the individual size of each subleading contribution and investigate the origin of the main subleading corrections. For this purpose, we perform alternative calculations for both processes in which the subleading NLO corrections are included only in the production of $t\bar{t}\gamma(\gamma)$.

The rest of the paper is organised as follows. All leading and subleading contributions at LO and NLO are carefully defined in Section 2. In Section 3 we describe the framework of the calculations and discuss various changes as well as cross-checks that have been performed. All input parameters and fiducial cuts that have been used to simulate detector response are outlined in Section 4. Numerical results for the integrated and differential cross sections for the $pp \to t\bar{t}\gamma$ process at the LHC are

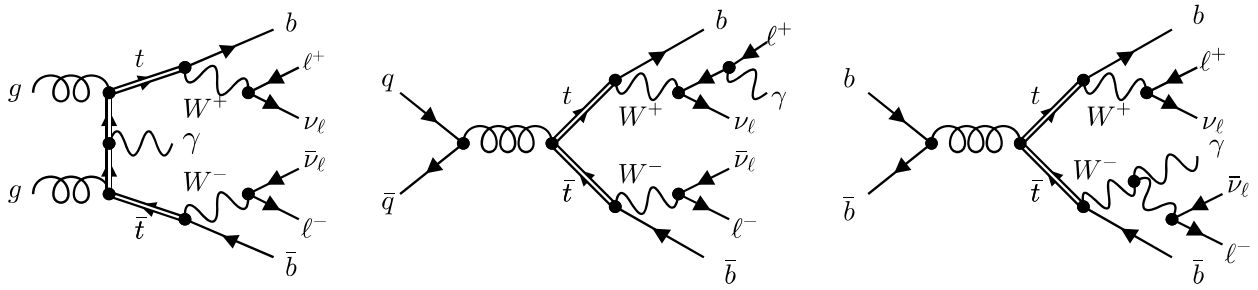

Figure 1. *Example Feynman diagrams for* $pp \to t\bar{t}\gamma$ *contributing to* LO_1. *All Feynman diagrams in this paper were produced with the help of the* FeynGame *program [48].*

presented in detail in Section 5. Our results for the $pp \to t\bar{t}\gamma\gamma$ process, on the other hand, are discussed in Section 6. We summarise our findings in Section 7.

2 Definition of the leading and subleading contributions

We calculate the full set of leading and subleading LO contributions and NLO corrections to top-quark pair production with one and two isolated photons at the LHC. We consistently include photon bremsstrahlung as well as QCD and EW corrections in both the production and decay of the top-quark pair. Decays of unstable top quarks and W gauge bosons are treated in the NWA preserving spin correlations, i.e. in the limit when $\Gamma_t/m_t \to 0$ ($\Gamma_W/m_W \to 0$). In this approximation all contributions without two resonant top quarks (and W gauge bosons) are neglected and the Breit-Wigner propagators lead to delta-functions which force the unstable particles to be on-shell, see e.g. Ref. [4, 41–47] for more details. We consider the di-lepton top-quark decay channel leading to the following decay chains

$$\begin{aligned} pp &\to t\bar{t}(\gamma) \to W^+W^-\, b\bar{b}(\gamma) \to \ell^+\nu_\ell\, \ell^-\bar{\nu}_\ell\, b\bar{b}\,\gamma + X, \\ pp &\to t\bar{t}(\gamma\gamma) \to W^+W^-\, b\bar{b}(\gamma\gamma) \to \ell^+\nu_\ell\, \ell^-\bar{\nu}_\ell\, b\bar{b}\,\gamma\gamma + X, \end{aligned} \tag{2.1}$$

with $\ell^\pm = \mu^\pm, e^\pm$ and where the brackets indicate that photon bremsstrahlung is allowed at each stage of the process. For brevity, we refer to these processes as $pp \to t\bar{t}\gamma$ and $pp \to t\bar{t}\gamma\gamma$ in the di-lepton top-quark decay channel, respectively. At LO there are in total 5 (15) possibilities or resonance histories from which the photons can be radiated off in the decay chain of $t\bar{t}\gamma(\gamma)$. At NLO, the number of resonance histories increases to 15 (35) for real radiation with an additional photon and to 15 (45) for additional QCD radiation.

2.1 LO contributions

At LO, both processes get contributions from three different orders of α_s and α. The dominant contribution is at the order $\mathcal{O}(\alpha_s^2\alpha^{4+n_\gamma})$, where n_γ is the number of photons appearing in the Born-level process, and we call it LO_1, following the notation in Ref. [49, 50]. At this order, we encounter the typical QCD production of a top-quark pair, which leads to the following partonic subprocesses

$$\begin{aligned} gg &\to \ell^+\nu_\ell\, \ell^-\bar{\nu}_\ell\, b\bar{b}\,\gamma(\gamma)\,, \\ q\bar{q}/\bar{q}q \to \ell^+\nu_\ell\, \ell^-\bar{\nu}_\ell\, b\bar{b}\,\gamma(\gamma)\,, &\qquad b\bar{b}/\bar{b}b \to \ell^+\nu_\ell\, \ell^-\bar{\nu}_\ell\, b\bar{b}\,\gamma(\gamma)\,, \end{aligned} \tag{2.2}$$

with $q = u, d, c, s$. Example Feynman diagrams for the LO_1 contribution are shown in Figure 1. We work in the five-flavour scheme and consistently include in the initial state all PDF suppressed channels

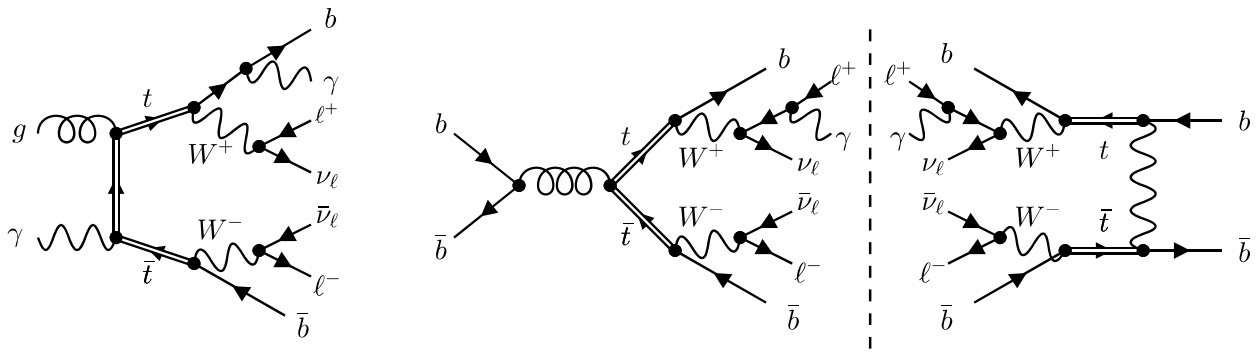

Figure 2. *Example Feynman diagrams for* $pp \to t\bar{t}\gamma$ *contributing to* LO_2.

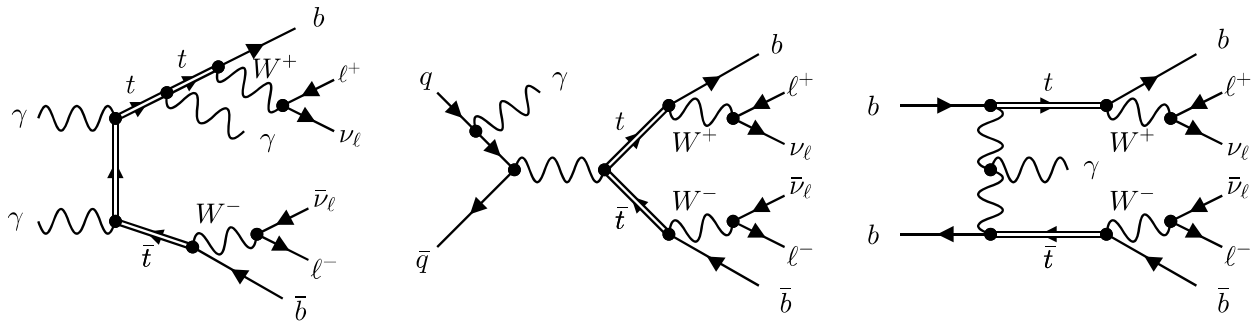

Figure 3. *Example Feynman diagrams for* $pp \to t\bar{t}\gamma$ *contributing to* LO_3.

from bottom quarks as well as photons in all subleading contributions. The LO_1 contribution can be obtained from the square of matrix elements at the order $\mathcal{O}(g_s^2 g^{4+n_\gamma})$. The $q\bar{q}$ and $b\bar{b}$ subprocesses provide additional contributions to the amplitudes at the order $\mathcal{O}(g^{6+n_\gamma})$. The interference of both types of matrix elements gives rise to the first subleading LO contribution at $\mathcal{O}(\alpha_s^1 \alpha^{5+n_\gamma})$ which we refer to as LO_2. This interference is exactly zero for the $q\bar{q}$ initial state due to color algebra, but does not vanish for the $b\bar{b}$ subprocess due to additional t-channel Feynman diagrams with an intermediate W boson, as shown on the right in Figure 2. Similar Feynman diagrams do not exist for $q\bar{q}$ because we keep the Cabibbo-Kobayashi-Maskawa (CKM) mixing matrix diagonal. In addition, at this order we encounter for the first time photon-induced channels with the $g\gamma$ initial state, as illustrated on the left in Figure 2. Thus, the partonic subprocesses of LO_2 can be summarised as

$$g\gamma/\gamma g \to \ell^+\nu_\ell\,\ell^-\bar{\nu}_\ell\,b\bar{b}\,\gamma(\gamma)\,, \qquad b\bar{b}/\bar{b}b \to \ell^+\nu_\ell\,\ell^-\bar{\nu}_\ell\,b\bar{b}\,\gamma(\gamma)\,. \tag{2.3}$$

The third and last subleading LO contribution, LO_3, is the purely EW induced production of a top-quark pair at the order $\mathcal{O}(\alpha^{6+n_\gamma})$. Example diagrams are depicted in Figure 3. Again, only the $q\bar{q}$ and $b\bar{b}$ channels are present, as well as the highly suppressed $\gamma\gamma$ channel. Therefore, the following reactions must be taken into account for LO_3

$$\begin{aligned} \gamma\gamma &\to \ell^+\nu_\ell\,\ell^-\bar{\nu}_\ell\,b\bar{b}\,\gamma(\gamma)\,, \\ q\bar{q}/\bar{q}q \to \ell^+\nu_\ell\,\ell^-\bar{\nu}_\ell\,b\bar{b}\,\gamma(\gamma)\,, &\qquad b\bar{b}/\bar{b}b \to \ell^+\nu_\ell\,\ell^-\bar{\nu}_\ell\,b\bar{b}\,\gamma(\gamma)\,. \end{aligned} \tag{2.4}$$

With respect to LO_1, this contribution is not only suppressed by the power coupling, but also the gluon PDF does not enter this contribution at all. Finally, we denote as LO the the sum of all three LO contributions

$$\mathrm{LO} = \mathrm{LO}_1 + \mathrm{LO}_2 + \mathrm{LO}_3\,. \tag{2.5}$$

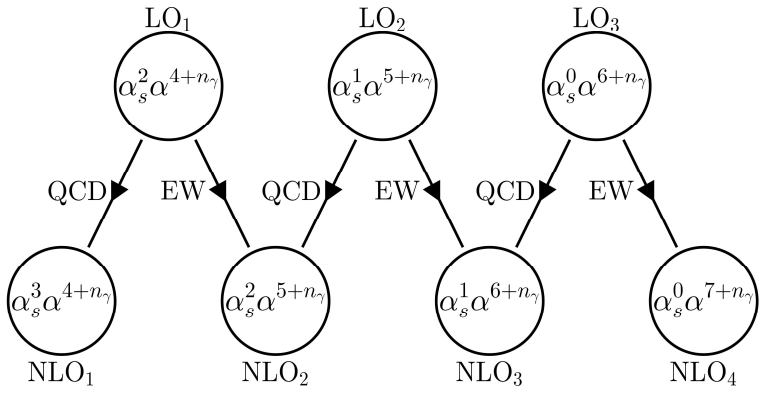

Figure 4. *LO and NLO contributions for* $pp \to t\bar{t}\gamma(\gamma)$ *with* $n_\gamma = 1(2)$.

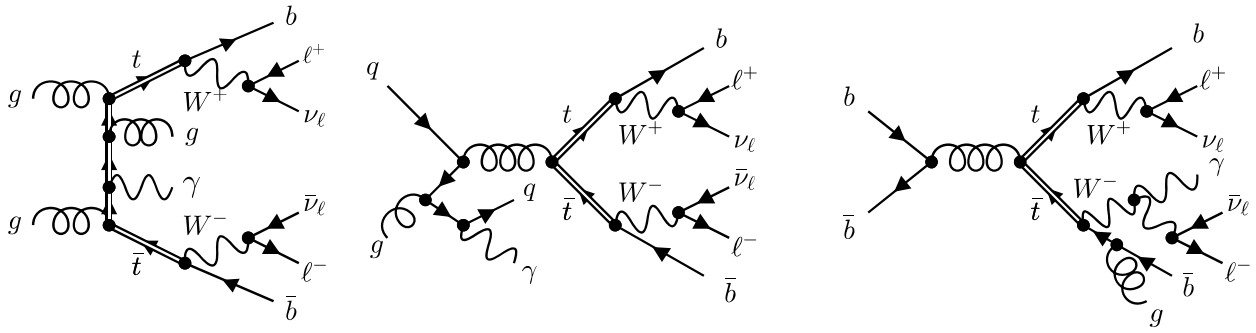

Figure 5. *Example Feynman diagrams for* $pp \to t\bar{t}\gamma$ *contributing to* NLO_1.

2.2 NLO contributions

At NLO, we obtain corrections of QCD and/or EW nature to all LO contributions, as demonstrated in Figure 4. The dominant higher-order corrections at NLO, denoted as NLO_1, arise from the QCD corrections to LO_1 at order $\mathcal{O}(\alpha_s^3\alpha^{4+n_\gamma})$. We call the sum of the two $\mathrm{NLO}_{\mathrm{QCD}}$ with

$$\mathrm{NLO}_{\mathrm{QCD}} = \mathrm{LO}_1 + \mathrm{NLO}_1\,, \tag{2.6}$$

and use it as a starting point to quantify the size of all subleading LO and NLO contributions. While the partonic subprocesses for the virtual corrections in NLO_1 are identical to those of LO_1, for the real emission part additional reactions due to extra QCD radiation have to be taken into account. In particular, all partonic subprocesses can be obtained by adding an additional gluon and all possible crossings of partons, leading to

$$\begin{aligned}
gg &\to \ell^+\nu_\ell\,\ell^-\bar{\nu}_\ell\,b\bar{b}\,\gamma(\gamma)\,g\,,\\
q\bar{q}/\bar{q}q &\to \ell^+\nu_\ell\,\ell^-\bar{\nu}_\ell\,b\bar{b}\,\gamma(\gamma)\,g\,, \qquad & b\bar{b}/\bar{b}b &\to \ell^+\nu_\ell\,\ell^-\bar{\nu}_\ell\,b\bar{b}\,\gamma(\gamma)\,g\,,\\
gq/qg &\to \ell^+\nu_\ell\,\ell^-\bar{\nu}_\ell\,b\bar{b}\,\gamma(\gamma)\,q\,, \qquad & g\bar{q}/\bar{q}g &\to \ell^+\nu_\ell\,\ell^-\bar{\nu}_\ell\,b\bar{b}\,\gamma(\gamma)\,\bar{q}\,,\\
gb/bg &\to \ell^+\nu_\ell\,\ell^-\bar{\nu}_\ell\,b\bar{b}\,\gamma(\gamma)\,b\,, \qquad & g\bar{b}/\bar{b}g &\to \ell^+\nu_\ell\,\ell^-\bar{\nu}_\ell\,b\bar{b}\,\gamma(\gamma)\,\bar{b}\,.
\end{aligned} \tag{2.7}$$

Example Feynman diagrams for the real emission part of NLO_1 are shown in Figure 5. The real corrections also consistently include additional photon and gluon radiation in all stages, i.e. in the $t\bar{t}$ production and the decays of top quarks and W gauge bosons.

The next contribution, NLO_2, at the order $\mathcal{O}(\alpha_s^2\alpha^{5+n_\gamma})$, cannot be completely separated into parts with only QCD or EW corrections. When calculating the corresponding virtual corrections we

have on the one hand, the interference of tree-level diagrams at $\mathcal{O}(g^{6+n_\gamma})$ with one-loop diagrams at $\mathcal{O}(g_s^4 g^{4+n_\gamma})$ and on the other hand, the interference between tree-level diagrams at $\mathcal{O}(g_s^2 g^{4+n_\gamma})$ and one-loop diagrams at $\mathcal{O}(g_s^2 g^{6+n_\gamma})$. The first contribution can be seen as a part of the NLO QCD corrections to LO_2. For the second contribution, no clear distinction is possible, since it can be seen as either the NLO QCD corrections to LO_2 or the NLO EW corrections to LO_1. Finally, for the $g\gamma$ channel, we have the interference of tree-level diagrams at $\mathcal{O}(g_s^1 g^{5+n_\gamma})$ with one-loop diagrams at $\mathcal{O}(g_s^3 g^{5+n_\gamma})$. Compared to NLO_1, the real corrections in NLO_2 include more partonic subprocesses, involving QCD and QED-like singularities. The first set of real corrections is obtained by additional QCD radiation to LO_2, which leads to

$$\begin{aligned}
q\bar{q}/\bar{q}q &\to \ell^+\nu_\ell\,\ell^-\bar{\nu}_\ell\,b\bar{b}\,\gamma(\gamma)\,g\,, & b\bar{b}/\bar{b}b &\to \ell^+\nu_\ell\,\ell^-\bar{\nu}_\ell\,b\bar{b}\,\gamma(\gamma)\,g\,,\\
gq/qg &\to \ell^+\nu_\ell\,\ell^-\bar{\nu}_\ell\,b\bar{b}\,\gamma(\gamma)\,q\,, & g\bar{q}/\bar{q}g &\to \ell^+\nu_\ell\,\ell^-\bar{\nu}_\ell\,b\bar{b}\,\gamma(\gamma)\,\bar{q}\,,\\
gb/bg &\to \ell^+\nu_\ell\,\ell^-\bar{\nu}_\ell\,b\bar{b}\,\gamma(\gamma)\,b\,, & g\bar{b}/\bar{b}g &\to \ell^+\nu_\ell\,\ell^-\bar{\nu}_\ell\,b\bar{b}\,\gamma(\gamma)\,\bar{b}\,.
\end{aligned} \tag{2.8}$$

In this case, we have the interference of tree-level diagrams at order $\mathcal{O}(g_s^3 g^{4+n_\gamma})$ and $\mathcal{O}(g_s^1 g^{6+n_\gamma})$. Although the $q\bar{q}$ channel is exactly zero in LO_2, its NLO QCD corrections no longer vanish, and the corresponding virtual and real corrections must be taken properly into account. In particular, the interference of initial- and final-state gluon radiation gives rise to the non-vanishing contribution, as explained in Refs. [51, 52]. The latter contribution induces singularities that are of soft nature only. Consequently, there are no collinear singularities in the $q\bar{q}$ channel and gluon radiation still vanishes in top-quark decays. It also follows that the gq and $g\bar{q}$ channels contain no collinear singularities and turn out to be IR finite. Therefore, no dipole subtraction is required for these channels and the naive usage of it can even affect the efficiency of the phase-space integration. In the Nagy-Soper [53] subtraction scheme, which is used in our calculation, the corresponding collinear subtraction terms vanish by construction if the underlying Born-level matrix element is exactly zero, since they are directly proportional to it. This is, however, not a general feature of dipole subtraction schemes. For example, in the Catani-Seymour subtraction scheme [54, 55], the corresponding subtraction term is a sum of the dipole terms $\mathcal{D}_k^{ai}$ involving color-correlated matrix elements. These dipole terms and the momentum mapping to the underlying Born-level process depend on the spectator parton k. Therefore, the sum of the dipole terms vanishes only in the exact collinear limit, where the dependence on the spectator parton k vanishes and the sum becomes proportional to the Born-level matrix element. In principle, it is possible for such initial-state singularities to choose exactly one spectator parton and to substitute the color correlator $\mathbf{T}_k \cdot \mathbf{T}_{ai} \to -\mathbf{T}_{ai}^2$ in $\mathcal{D}_k^{ai}$. In this way the corresponding subtraction term is always proportional to the Born-level matrix element and would vanish as in the Nagy-Soper case. On the other hand, collinear singularities are present in the bottom-quark induced channels. In this case, gluon radiation in top-quark decays must be consistently included. Furthermore, additional partonic subprocesses, which originate from LO_1 with additional photon radiation, have to be included, leading to

$$\begin{aligned}
gg &\to \ell^+\nu_\ell\,\ell^-\bar{\nu}_\ell\,b\bar{b}\,\gamma\gamma(\gamma)\,,\\
q\bar{q}/\bar{q}q &\to \ell^+\nu_\ell\,\ell^-\bar{\nu}_\ell\,b\bar{b}\,\gamma\gamma(\gamma)\,, & b\bar{b}/\bar{b}b &\to \ell^+\nu_\ell\,\ell^-\bar{\nu}_\ell\,b\bar{b}\,\gamma\gamma(\gamma)\,.
\end{aligned} \tag{2.9}$$

Similar to the calculation of NLO QCD corrections to the $pp \to t\bar{t}j(j)$ process in the NWA [44, 56], photons can appear simultaneously in the production and decays, as illustrated in Figure 6. Therefore, the relevant dipoles must be consistently included at each stage of the decay chain. Finally, we have new photon-induced partonic subprocesses which are constructed by gluon radiation from the $g\gamma$ channel in LO_2 and by crossing from the processes listed in Eq. (2.9), resulting in

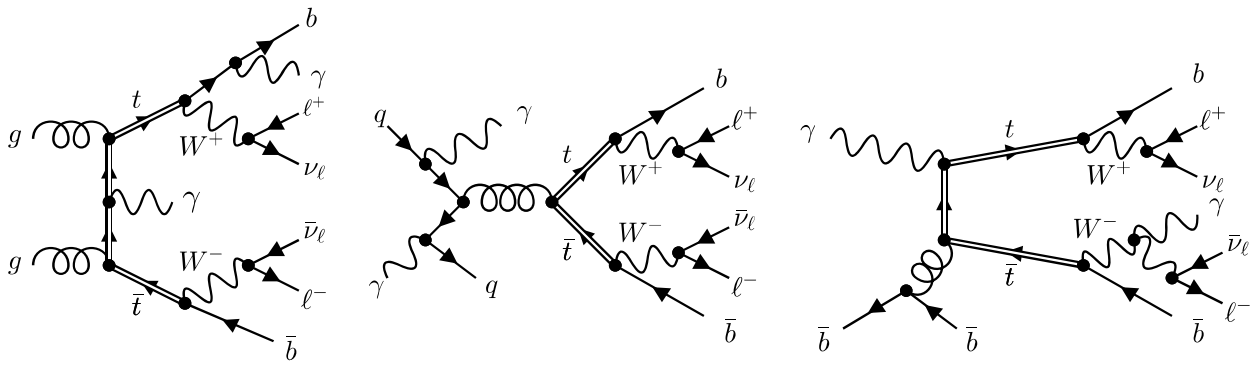

Figure 6. *Example Feynman diagrams for* $pp \to t\bar{t}\gamma$ *contributing to* NLO_2.

$$
\begin{aligned}
& g\gamma/\gamma g \to \ell^+\nu_\ell\,\ell^-\bar{\nu}_\ell\,b\bar{b}\,\gamma(\gamma)\,g\,, \\
& \gamma q/q\gamma \to \ell^+\nu_\ell\,\ell^-\bar{\nu}_\ell\,b\bar{b}\,\gamma(\gamma)\,q\,, \qquad \gamma\bar{q}/\bar{q}\gamma \to \ell^+\nu_\ell\,\ell^-\bar{\nu}_\ell\,b\bar{b}\,\gamma(\gamma)\,\bar{q}\,, \\
& \gamma b/b\gamma \to \ell^+\nu_\ell\,\ell^-\bar{\nu}_\ell\,b\bar{b}\,\gamma(\gamma)\,b\,, \qquad \gamma\bar{b}/\bar{b}\gamma \to \ell^+\nu_\ell\,\ell^-\bar{\nu}_\ell\,b\bar{b}\,\gamma(\gamma)\,\bar{b}\,.
\end{aligned}
\tag{2.10}
$$

While the $g\gamma$ channel clearly contains only QCD singularities due to gluon radiation, for the remaining partonic processes we simultaneously encounter QCD and QED initial-state singularities arising from the $\gamma \to q\bar{q}$ and $q \to gq$ splittings, as shown in Figure 6. This clearly illustrates that even real corrections cannot be divided into those of QCD or EW origin, as we have already seen in the calculation of virtual corrections.

The next subleading NLO contribution at the order $\mathcal{O}(\alpha_s^1\alpha^{6+n_\gamma})$, NLO_3, features a similarly wide range of virtual and real corrections with respect to NLO_2. This contribution is obtained from EW corrections to LO_2 and QCD corrections to LO_3. Thus, EW corrections to the $q\bar{q}$ channel in LO_2 vanish again, since with respect to the Born level the color structure remains unchanged by these corrections. The virtual corrections consist of the interference of tree-level diagrams at $\mathcal{O}(g_s^2 g^{4+n_\gamma})$ with the one-loop amplitude at $\mathcal{O}(g^{8+n_\gamma})$ and the tree-level matrix element at $\mathcal{O}(g^{6+n_\gamma})$ with one-loop diagrams at $\mathcal{O}(g_s^2 g^{6+n_\gamma})$. The first contribution can be seen as part of the NLO EW corrections to LO_2, and thus it vanishes for $q\bar{q}$ as explained before, and only has to be included for the $b\bar{b}$ initial state. In the second term again no distinction between QCD and EW corrections is possible for the $q\bar{q}$ and $b\bar{b}$ channels, while for the $\gamma\gamma$ channel this contribution consists of pure QCD corrections to LO_3. Finally, for $g\gamma$ we have the interference of tree-level diagrams at $\mathcal{O}(g_s^1 g^{5+n_\gamma})$ with one-loop diagrams at $\mathcal{O}(g_s^1 g^{7+n_\gamma})$. The real corrections can be summarised as follows. First, we have the NLO QCD corrections to LO_3, which can be obtained by additional gluon radiation, bringing about the following contributions

$$
\begin{aligned}
& \gamma\gamma \to \ell^+\nu_\ell\,\ell^-\bar{\nu}_\ell\,b\bar{b}\,\gamma(\gamma)g\,, \\
& q\bar{q}/\bar{q}q \to \ell^+\nu_\ell\,\ell^-\bar{\nu}_\ell\,b\bar{b}\,\gamma(\gamma)g\,, \qquad b\bar{b}/\bar{b}b \to \ell^+\nu_\ell\,\ell^-\bar{\nu}_\ell\,b\bar{b}\,\gamma(\gamma)\,g\,.
\end{aligned}
\tag{2.11}
$$

The crossing of initial- and final-state partons leads to the additional set of partonic subprocesses

$$
\begin{aligned}
& gq/qg \to \ell^+\nu_\ell\,\ell^-\bar{\nu}_\ell\,b\bar{b}\,\gamma(\gamma)\,q\,, \qquad g\bar{q}/\bar{q}g \to \ell^+\nu_\ell\,\ell^-\bar{\nu}_\ell\,b\bar{b}\,\gamma(\gamma)\,\bar{q}\,, \\
& gb/bg \to \ell^+\nu_\ell\,\ell^-\bar{\nu}_\ell\,b\bar{b}\,\gamma(\gamma)\,b\,, \qquad g\bar{b}/\bar{b}g \to \ell^+\nu_\ell\,\ell^-\bar{\nu}_\ell\,b\bar{b}\,\gamma(\gamma)\,\bar{b}\,,
\end{aligned}
\tag{2.12}
$$

which again contain simultaneously QCD and QED initial-state singularities, as illustrated in Figure 7. Next, we obtain additional contributions from photon radiation off the partonic subprocesses in LO_2, as exemplified in Figure 7. Together with all possible crossings of partons and photons we obtain

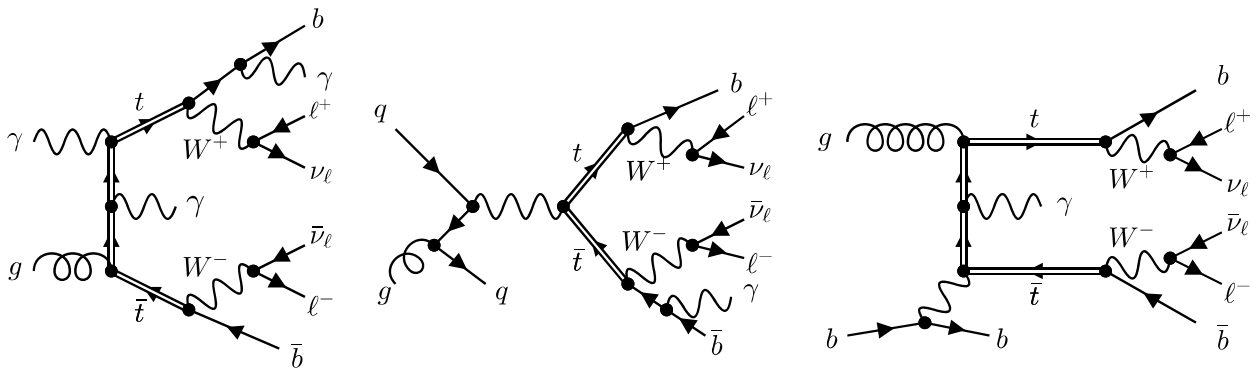

Figure 7. *Example Feynman diagrams for* $pp \to t\bar{t}\gamma$ *contributing to* NLO_3.

$$
\begin{aligned}
g\gamma/\gamma g &\to \ell^+\nu_\ell\,\ell^-\bar{\nu}_\ell\,b\bar{b}\,\gamma\gamma(\gamma) \qquad & b\bar{b}/\bar{b}b &\to \ell^+\nu_\ell\,\ell^-\bar{\nu}_\ell\,b\bar{b}\,\gamma\gamma(\gamma)\,,\\
\gamma b/b\gamma &\to \ell^+\nu_\ell\,\ell^-\bar{\nu}_\ell\,b\bar{b}\,\gamma(\gamma)\,b \qquad & \gamma\bar{b}/\bar{b}\gamma &\to \ell^+\nu_\ell\,\ell^-\bar{\nu}_\ell\,b\bar{b}\,\gamma(\gamma)\,\bar{b}\,.
\end{aligned}
\tag{2.13}
$$

In addition, $q\bar{q}$ and $\gamma q/\gamma\bar{q}$ subprocesses vanish due to color, as additional photon radiation does not change the color structure already present in LO_2.

Since in NLO_3 we find for the first time EW 1-loop corrections in photon-initiated subprocesses, in particular in the $g\gamma$ channel, we briefly mention here the choice of the renormalisation scheme for the electromagnetic coupling α, which will be explained in detail later in the article. As we are interested in the experimental signature with at least one (two) isolated photon(s), we do not consider the $\gamma \to f\bar{f}$ splitting for final state photons. Therefore, the electromagnetic coupling constant connected with final state photons has to be renormalised in the on-shell scheme to obtain IR finite results, see e.g. Refs. [16, 57]. However, the electromagnetic coupling associated with initial state photons must be renormalised in a $\overline{\mathrm{MS}}$-like scheme, because $\gamma \to f\bar{f}$ splittings are included in the evolution of the proton PDF. Thus, we use the G_μ scheme in this case and the remaining IR ϵ poles from the sum of real and virtual corrections are absorbed into a redefinition of PDFs, as for all other QCD and QED collinear initial state singularities. This leads to a collinear factorisation counterterm of the form

$$
\frac{\alpha}{2\pi}\frac{1}{\Gamma(1-\epsilon)}\frac{1}{\epsilon}\left(\frac{4\pi\mu_R^2}{\mu_F^2}\right)^{\epsilon} P_{\gamma\gamma}(x),
\tag{2.14}
$$

which has to be convoluted with the corresponding Born-level cross section. The one-loop Altarelli-Parisi QED kernel $P_{\gamma\gamma}(x)$, see e.g. Ref. [50] for more details, is given by

$$
P_{\gamma\gamma}(x) = -\frac{2}{3}\,\delta(1-x)\sum_f N_{c,f}\,Q_f^2,
\tag{2.15}
$$

where the summation runs over all massless, charged fermions, $N_{c,f}$ is a color factor, which is 3 for quarks and 1 for leptons, and Q_f is the charge of the fermion f. Unlike all other QCD and QED splitting functions, $P_{\gamma\gamma}(x)$ contains only a virtual contribution given by the delta distribution.

Finally, we have the NLO EW corrections to LO_3, called NLO_4, and all new partonic subprocesses can simply be obtained from additional photon radiation and crossing, leading to

$$
\begin{aligned}
&\gamma\gamma \to \ell^+\nu_\ell\,\ell^-\bar{\nu}_\ell\,b\bar{b}\,\gamma\gamma(\gamma)\,,\\
q\bar{q}/\bar{q}q &\to \ell^+\nu_\ell\,\ell^-\bar{\nu}_\ell\,b\bar{b}\,\gamma\gamma(\gamma)\,, \qquad & b\bar{b}/\bar{b}b &\to \ell^+\nu_\ell\,\ell^-\bar{\nu}_\ell\,b\bar{b}\,\gamma\gamma(\gamma)\,,\\
\gamma q/q\gamma &\to \ell^+\nu_\ell\,\ell^-\bar{\nu}_\ell\,b\bar{b}\,\gamma(\gamma)\,q\,, \qquad & \gamma\bar{q}/\bar{q}\gamma &\to \ell^+\nu_\ell\,\ell^-\bar{\nu}_\ell\,b\bar{b}\,\gamma(\gamma)\,\bar{q}\,,\\
\gamma b/b\gamma &\to \ell^+\nu_\ell\,\ell^-\bar{\nu}_\ell\,b\bar{b}\,\gamma(\gamma)\,b\,, \qquad & \gamma\bar{b}/\bar{b}\gamma &\to \ell^+\nu_\ell\,\ell^-\bar{\nu}_\ell\,b\bar{b}\,\gamma(\gamma)\,\bar{b}\,,
\end{aligned}
\tag{2.16}
$$

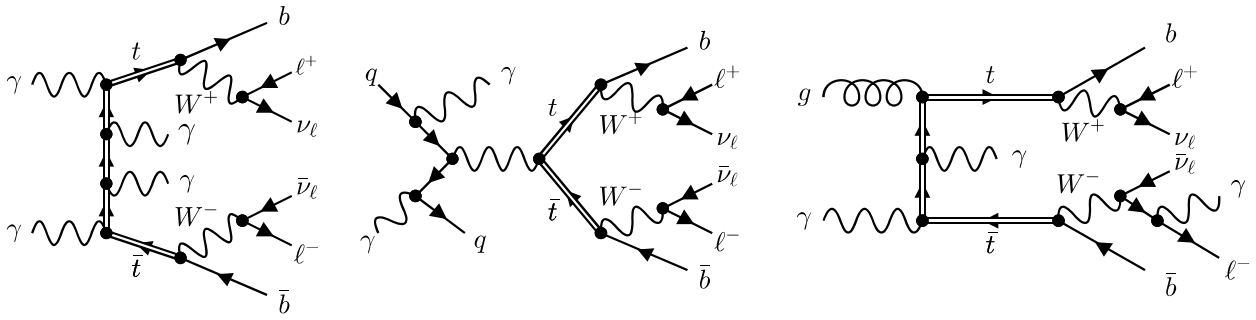

Figure 8. *Example Feynman diagrams for* $pp \to t\bar{t}\gamma$ *contributing to* NLO_4.

where example Feynman diagrams are shown in Figure 8.

We denote the complete result at NLO, including all subleading contributions, as NLO. The latter result is given by the following sum

$$\text{NLO} = \text{LO}_1 + \text{LO}_2 + \text{LO}_3 + \text{NLO}_1 + \text{NLO}_2 + \text{NLO}_3 + \text{NLO}_4. \tag{2.17}$$

We refrain from dividing our complete NLO calculation into different resonant contributions based on the origin of photon emission, as already done at NLO QCD for the $pp \to t\bar{t}\gamma$ process in Refs. [3, 4] and for $pp \to t\bar{t}\gamma\gamma$ in Ref. [22]. It is because additional photon radiation introduces further complications due to mixing of Born-level processes with different photon radiation patterns at LO. This issue has already been examined in detail in the case of the calculation of NLO QCD corrections to $pp \to t\bar{t}jj$ [56]. Instead, we perform an alternative calculation, labelled as NLO_{prd}, which we define according to

$$\text{NLO}_{\text{prd}} = \text{LO}_1 + \text{LO}_2 + \text{LO}_3 + \text{NLO}_1 + \text{NLO}_{2,\text{prd}} + \text{NLO}_{3,\text{prd}} + \text{NLO}_{4,\text{prd}}, \tag{2.18}$$

where the subscript *prd* indicates that photon bremsstrahlung and subleading NLO corrections are only included in the production stage of the $pp \to t\bar{t}\gamma(\gamma)$ process. In detail, in NLO_{prd}, all LO (LO_1, LO_2, LO_3) contributions as well as NLO_1 are fully included in both the $t\bar{t}\gamma(\gamma)$ production and decays of the top-quark pair. On the other hand, the subleading NLO corrections (NLO_2, NLO_3, NLO_4) are only included in the production stage of the $t\bar{t}\gamma(\gamma)$ process when the photon (the two photons) are also present there. In this way, we investigate the origin of the main subleading corrections. This approximation is motivated by the fact that, on the one hand, it leads to an enormous simplification of the calculations, especially for the real emission part, and ultimately in the matching to parton shower programs. On the other hand, the largest subleading NLO contributions are expected to originate from EW Sudakov logarithms in the tails of dimensionful observables. However, it is known that high p_T phase-space regions are dominated by the case where all photons are produced in the $t\bar{t}$ production [3, 4, 22], which should directly reduce the relevance of including subleading NLO corrections in other radiation patterns. With the calculation of NLO_{prd} we would like to confirm that this is the case for the $pp \to t\bar{t}\gamma(\gamma)$ process for various differential cross-section distributions. For the sake of completeness, we will also show the NLO_{prd} result for the $t\bar{t}\gamma(\gamma)$ integrated fiducial cross section.

3 Computational framework

As we have already alluded to in Section 2 the calculation of real corrections is performed with the Nagy-Soper subtraction scheme [53], which has recently been extended to NLO QCD calculations in the NWA involving internal on-shell resonances [56]. To check the validity of the results, we also use the Catani-Seymour subtraction scheme [54, 55]. Furthermore, for additional cross-checks in both

cases we utilize the phases-space restriction on the subtraction terms [58–61]. For the purposes of this study, both subtraction schemes, that are implemented in the HELAC-DIPOLES MC program [62], have been extended to deal with soft and collinear singularities of QED origin that plague the real radiation contributions of NLO EW calculations. In the following we describe both extensions in detail and discuss how the calculation of virtual corrections is organised for the purposes of our study.

3.1 Real corrections

At NLO QCD, we have to deal with contributions of different origin, on the one hand with virtual corrections due to the interference of one-loop and tree-level amplitudes, and on the other hand with real corrections arising from the emission of additional QCD partons. However, both contributions themselves are divergent, and only the sum of them is finite for IR safe observables. A standard approach nowadays is the use of a subtraction scheme, where an auxiliary cross section is introduced, which is designed to locally mimic the singular limits of the real-correction cross section. Moreover, this auxiliary cross section has to be simple enough so that the integration over the one-parton subspaces, which cause the soft and collinear divergences, is possible either analytically or numerically, leading to the so-called integrated subtration terms and/or dipoles. These can then be combined with the virtual corrections to cancel all IR divergences. In general, the subtraction term in QCD can be written as

$$\mathcal{A}^{\mathrm{D}} = \sum_{i,j,k=1}^{n+1} \mathcal{A}^{\mathrm{B}}(\{\tilde{p}\}_n^{ijk}) \otimes \mathcal{D}^{(ijk)}(\{\tilde{p}\}_n^{(ijk)}, \{p\}_{n+1}) \, (\mathbf{T}_{ij} \cdot \mathbf{T}_k) \,, \tag{3.1}$$

where $\mathcal{A}_{\mathrm{B}}$ is the tree-level matrix element of the underlying Born-level process which results from the recombination of the two partons i and j. The terms $\mathcal{D}^{(ijk)}$ are the so-called dipoles and $\{\tilde{p}\}_n^{(ijk)}$ is the new set of momenta for the underlying Born-level process, which is obtained by a momentum mapping from the initial momenta $\{p\}_{n+1}$. Spin correlations between the squared Born-level matrix element and the dipoles are indicated by the symbol $\otimes$. Finally, $\mathbf{T}_k$ are color operators according to the definitions given in Ref. [54]. The indices i, j, k indicate that in general the dipoles as well as the momentum mapping depend on the two splitting partons i, j and potentially also on the spectator parton k. The QED subtraction scheme can be obtained from the QCD one by simple substitutions. In particular, the color operators have to be replaced by charge operators according to

$$\mathbf{T}_{ij} \cdot \mathbf{T}_k \to \mathbf{Q}_{ij} \mathbf{Q}_k, \tag{3.2}$$

where $\mathbf{Q}_k$ is the charge of the particle with a relative minus sign between final- and initial-state particles, and possible further simple replacements of color factors. However, this cannot be applied to the case where the splitting pair is recombined into a photon ($Q_{ij} = 0$). Instead, in this case we perform the following substitution

$$\mathbf{T}_{ij} \cdot \mathbf{T}_k \to -w_k \mathbf{Q}_i^2 \qquad \text{with} \qquad \sum_k w_k = 1. \tag{3.3}$$

The particular choice of these weights w_k is completely arbitrary and, in our case we simply set it to δ_{k,k_0}, which implies that we choose exactly one spectator particle. In general, this spectator particle must be the same in the actual subtraction and in the calculation of the integrated dipoles, since the momentum mapping and dipoles terms depend on k. We note that in the Nagy-Soper subtraction scheme, both the momentum mapping and the collinear dipole terms are independent of the spectator particle, so that the choice of k_0 plays no role in the calculation. Finally, the structure of HELAC-DIPOLES has been modified to simultaneously keep track of different orders in α_s and α and to allow

the reweighting to different renormalisation and factorisation scale settings on the fly. To verify the new modifications, we have reproduced the results of Ref. [51] at the integrated and differential cross section level. In detail, we have calculated afresh NLO EW corrections to the $pp \to t\bar{t} + X$ process in the di-lepton top-quark decay channel for the LHC Run II center-of-mass energy of $\sqrt{s} = 13$ TeV. In this calculation all finite-width effects, resonant and non-resonant contributions of the top quark and $W^{\pm}/Z$ gauge bosons as well as interference effects have been included.

Next, we discuss the changes in the Nagy-Soper subtraction scheme for calculations involving resonant particles. These modifications are to a large extent independent of QCD or QED-like singularities. To this end, we first briefly recall the notation and main aspects of the Nagy-Soper subtraction scheme which were presented in detail in Ref. [53]. We focus on the case of final-state splittings since initial-state splittings remain unaffected. We first introduce the following definitions

$$Q = p_1 + p_2 = \sum_{l=3}^{n+1} p_l, \tag{3.4}$$

$$P_{ij} = p_i + p_j \qquad \text{and} \qquad K = Q - P_{ij}, \tag{3.5}$$

where Q is the total momentum of the process, P_{ij} is the momentum sum of the splitting partons and K is the so-called collective spectator. The momentum mapping from $\{p\}_{n+1}$ to $\{\tilde{p}\}_n^{(ij)}$ is then defined by the condition that the momentum of the splitting parton $\tilde{p}_i$ should lie in the Q-P_{ij} plane according to

$$P_{ij} = \beta \tilde{p}_i + \gamma Q, \tag{3.6}$$

where β and γ are uniquely fixed by the following two conditions

$$\tilde{Q} = Q\,, \tag{3.7}$$

$$\widetilde{K}^2 = K^2\,. \tag{3.8}$$

From Eq. (3.7) it is clear that the momentum mapping from K to $\widetilde{K}$ is given by a Lorentz transformation ($k_i^{\mu} = \Lambda(K, \widetilde{K})^{\mu}{}_{\nu}\, \tilde{k}_i^{\nu}$), which is defined as [53, 63]

$$\Lambda(K, \widetilde{K})^{\mu}{}_{\nu} = g^{\mu}{}_{\nu} - \frac{2(K + \widetilde{K})^{\mu}(K + \widetilde{K})_{\nu}}{(K + \widetilde{K})^2} + \frac{2K^{\mu}\widetilde{K}_{\nu}}{K^2}. \tag{3.9}$$

Next, the dipole terms $\mathcal{D}^{(ijk)}$ in Eq. (3.1) are decomposed into diagonal terms $W^{(ii,j)}$ containing soft and collinear singularities and interference terms $W^{(ik,j)}$ including only soft singularities according to

$$\mathcal{D}^{(ijk)}_{\tilde{s}_1\tilde{s}_2} = W^{(ii,j)}_{\tilde{s}_1\tilde{s}_2}\delta_{ik} + W^{(ik,j)}_{\tilde{s}_1\tilde{s}_2}(1 - \delta_{ik})\,, \tag{3.10}$$

where $\tilde{s}_1$ and $\tilde{s}_2$ are the helicity values of the splitting parton. The diagonal and interference terms are further split into a sum of so-called splitting functions $v^{(ij)}$ as specified by

$$W^{(ii,j)}_{\tilde{s}_1\tilde{s}_2} = \sum_{s_i,s_j} v^{(ij)}_{\tilde{s}_1 s_i s_j} \left(v^{(ij)}_{\tilde{s}_2 s_i s_j}\right)^*, \tag{3.11}$$

$$W^{(ik,j)}_{\tilde{s}_1\tilde{s}_2} = \sum_{s_i,s_j} v^{(ij),eik}_{\tilde{s}_1 s_i s_j} \left(v^{(kj),eik}_{\tilde{s}_2 s_i s_j}\right)^*, \tag{3.12}$$

where $v^{(ij),eik}$ is the eikonal approximation of these splitting functions. In QCD the $v^{(ij),eik}$ function reduces to a much simpler expression given by

$$v^{(ij),eik}_{\tilde{s}_i s_i s_j} = \sqrt{4\pi\alpha_s}\,\delta_{\tilde{s}_i s_i}\frac{\epsilon(p_j, s_j)^* \cdot p_i}{p_i \cdot p_j}. \tag{3.13}$$

The splitting functions are obtained by factorising the splitting $\tilde{p}_i \to p_i + p_j$ from the divergent matrix element in the following way $\mathcal{M}_{n+1}^{\text{div}} = \mathcal{M}_n \otimes v^{(ij)}$. The exact form for the different QCD splittings for final- and initial-state splittings can be found in Ref. [63].

The original Nagy-Soper subtraction scheme can directly be used in the case of unresolved partons in the production process. However, if an unstable particle is part of the emitter pair, then we use the spin-averaged versions of the dipole terms $\mathcal{D}^{(ijk)}$ in Eq. (3.1). In addition, we use the eikonal approximation for the splitting functions in the diagonal term $W^{(ii,j)}$ given in Eq. (3.11) when a W gauge boson is part of the emitter pair. These modifications are also applied to unstable particles in nested decay chains, such as W gauge bosons in radiative top-quark decays. Further modifications are required for the dipole subtraction in decay processes. The first change concerns the momentum mapping which is required to preserve the total momentum of the decay process, i.e. the momentum of the decaying mother particle. This is achieved by replacing the total momentum Q in the original momentum mapping with the momentum of the mother particle, which is called Q_{dec} in analogy. By definition Q_{dec} is then preserved under the momentum mapping according to the condition defined in Eq. (3.7). The dipole terms $\mathcal{D}^{(ijk)}$ also have an explicit and an additional implicit dependence on Q by the axial gauge with Q as reference vector used for the polarisation vectors of gluons and photons. Thus, to reuse all the results of the original subtraction scheme, we have to perform the replacement $Q \to Q_{\text{dec}}$ also in all the dipole terms $\mathcal{D}^{(ijk)}$ and apply a gauge transformation to the external polarisation vectors entering the splitting functions $v^{(ij)}$. The mother particle is excluded from the list of possible emitters in the dipole subtraction, but it is still included as a possible spectator particle. To properly account for all soft singularities associated with the mother particle, we replace $W^{(ik,j)}$, defined in Eq. (3.11), in the case where the mother particle is the spectator k, by $W_{\text{dec}}^{(ik,j)}$, which we define as

$$W_{\text{dec}}^{(ik,j)} = W^{(ik,j)} + W^{(ki,j)} - W^{(kk,j),eik}. \tag{3.14}$$

For the calculation of the corresponding integrated dipoles we closely follow the semi-numerical approach of Ref. [53]. In this case, the spin-averaged diagonal and interference terms are cast in the following form

$$\overline{W}^{(ii,j)} - \overline{W}_{\text{dec}}^{(ik,j)} = \underbrace{\left(\overline{W}^{(ii,j)} - \overline{W}^{(ii,j),eik}\right)}_{\mathcal{D}_{ii}} + \underbrace{\left(\overline{W}^{(ii,j),eik} - \overline{W}_{\text{dec}}^{(ik,j)}\right)}_{\mathcal{I}_{ik,\text{dec}}}, \tag{3.15}$$

where $\mathcal{D}_{ii}$ can only have collinear singularities by construction and are already known from the original formulation. The second term can have soft and collinear singularities and can be further simplified to

$$\mathcal{I}_{ik,\text{dec}} = 4\pi\alpha_s \frac{-((p_j \cdot p_k)p_i - (p_i \cdot p_j)p_k)^2}{(p_i \cdot p_j)^2(p_j \cdot p_k)^2}. \tag{3.16}$$

We have calculated and implemented this new dipole in the case of massless and massive splitting partons $\tilde{p}_i$. The latter case is required for the calculation of EW corrections to top-quark decays, i.e. for $W^\pm \to W^\pm\gamma$ splittings. In addition, it can also be used for e.g. NLO QCD corrections with massive bottom quarks inside top-quark decays. In summary, our implementation of the Nagy-Soper subtraction scheme allows us to calculate QCD and EW radiative corrections for any number of coloured, charged, massive and massless particles in nested decay chains.

We have carried out several tests to confirm the correctness of the modifications we have made. First of all, we have already used this new extension for the calculation of the NLO QCD corrections to the $pp \to t\bar{t}jj$ process in the di-lepton top-quark decay channel in the NWA [56]. These results, were

cross-checked with an alternative calculation using the Catani-Seymour subtraction scheme and its extension to the NWA case [4, 44, 64]. In addition, we have recalculated the NLO QCD corrections of the top-quark width with massive bottom quarks [65, 66] as well as the corresponding real corrections, which are presented in the appendix of Ref. [45]. Finally, we have reproduced the calculation of the NLO electroweak corrections to the top-quark decay width while treating the internal W boson in the NWA [67].

In our current calculation of the $pp \to t\bar{t}\gamma(\gamma)$ process in the NWA, we have computed the real correction part of the NLO calulations with the Nagy-Soper subtraction scheme. We have utilised two different values of the phase-space restriction on the subtraction terms and found excellent agreement for the obtained results within the corresponding MC errors. Finally, we have reproduced the results of $\text{NLO}_{i,\text{prd}}$ with $i = 1, 2, 3, 4$ using the Catani-Seymour subtraction scheme. A full comparison with the Catani-Seymour subtraction is not yet possible as our implementation is currently limited to massless emitters in decay processes.

3.2 Virtual corrections

The calculation of the virtual corrections is organized using reweighting techniques [60, 68]. In practice, partially unweighted events [69] that are generated at the Born level, are then used to calculate the one-loop corrections. The phase-space integration is performed using the programs Parni [70] and Kaleu [71]. The combined tree-level and one-loop results are then stored in modified Les Houches Event Files (LHEFs) [72, 73], which have been extended to save, for each event, the necessary information for all contributions at different orders of α_s and α. This allows us, among other things, to reweight our results to different renormalisation and factorisation scale settings. Tree-level and one-loop matrix elements are obtained with the help of the Recola matrix element generator [74, 75]. We have modified the calculation of the matrix elements in Recola to incorporate the random polarisation method [53, 76, 77] which leads to significant performance improvements in the phase-space integration. Following the notation of Ref. [74], every one-loop amplitude can be written as a linear combination of tensor integrals

$$\mathcal{A}_{1-\text{loop}} = \sum_t c^{(t)}_{\mu_1 \dots \mu_{r_t}} T^{\mu_1 \dots \mu_{r_t}}_{(t)} + \mathcal{A}_{\text{CT}} \,, \tag{3.17}$$

where $\mathcal{A}_{\text{CT}}$ include the counterterms, $c^{(t)}_{\mu_1 \dots \mu_{r_t}}$ are the tensor coefficients that do not depend on the loop momentum q, t classifies the different tensor integrals needed for the process and r_t labels the rank of the tensor integral. Furthermore, the tensor integrals are given by

$$T^{\mu_1 \dots \mu_{r_t}}_{(t)} = \frac{(2\pi\mu)^{4-D}}{i\pi^2} \int d^D q \frac{q^{\mu_1} \dots q^{\mu_{r_t}}}{D^{(t)}_0 \dots D^{(t)}_{k_t}} \,, \qquad D^{(t)}_i = (q + p^{(t)}_i)^2 - (m^{(t)}_i)^2 \,, \tag{3.18}$$

where k_t is the number of propagators. The tensor coefficients are calculated by Recola similarly to the tree-level amplitudes by recursive construction of loop off-shell currents [75, 78]. The relevant tensor integrals are computed with the Collier library [79] which implements the reduction techniques of [80, 81] and the scalar integrals of [82]. Alternatively, we have implemented the reduction to scalar integrals with CutTools [83]. The resulting scalar integrals are computed with OneLOop [84]. The CutTools program implements the OPP reduction method [85], which is based on double, triple and quadruple cuts. A similar approach has already been employed in the OpenLoops program [86]. In our case, the OPP reduction and the evaluation of the scalar integrals are performed with quadruple precision, while the tensor coefficients are calculated with double precision. Not only do we use this second reduction scheme for additional cross-checks of our framework, but also for phase-space points containing tensor integrals that have been flagged by Collier as possibly unstable.

As explained in Ref. [74] the RECOLA program offers the possibility to select the resonant parts of the amplitude, and can therefore be employed to calculate matrix elements in the pole approximation. In this approximation, only the resonant parts of the amplitude are kept, thus, the complex squared mass of the resonant particle ($\mu^2 = m^2 - i\Gamma m$) is replaced by its real part ($\Re(\mu^2) = m^2$) everywhere in the amplitude except for the denominators of resonant propagators where the width Γ of the unstable particle is still present. The NWA matrix element is then obtained by performing the usual limit $\Gamma/m \to 0$ in the Breit-Wigner propagators. Finally, we correct the symmetry factor calculated in RECOLA for processes involving identical particles in the final state but originating from different subprocesses in the decay chain, as explained in Ref. [87].

As an alternative, we have implemented a second fully automatic method for the construction of one-loop matrix elements in the NWA, which is based on the calculation of the on-shell amplitudes for the individual contributions needed in e.g. the $pp \to t\bar{t}(\gamma\gamma)$ process in the di-lepton top-quark decay channel. To this end, we compute separately the subamplitudes for $pp \to t\bar{t}(\gamma\gamma)$, $t \to W^+b(\gamma\gamma)$, $\bar{t} \to W^-\bar{b}(\gamma\gamma)$, $W^+ \to \ell^+\nu_\ell(\gamma\gamma)$ and $W^- \to \ell^-\bar{\nu}_\ell(\gamma\gamma)$ with RECOLA and then combine them appropriately in color and helicity space to obtain the full one-loop amplitude. This alternative implementation is particularly useful for cross-checking because in this case we can switch on and off one-loop corrections for specific contributions. We note here, that we have already used both approaches in Ref. [56] where NLO QCD calculations for the $pp \to t\bar{t}jj$ process in the di-lepton top-quark decay channel have been carried out.

We have performed various cross-checks between RECOLA and RECOLA2 [88] for all partonic subprocesses. Specifically, for each subprocess and for several phase-space points we checked the finite remainders as well as the coefficients of the poles in ϵ of the virtual amplitudes. For testing purposes we utilised the Background-Field-Method (BFM) as implemented in RECOLA2 [57, 89, 90]. The BFM, which is an alternative formulation for the quantisation of gauge fields that can be seen as a different gauge, can be used as a complementary method in the calculation of one-loop matrix elements besides the usual formulation.

The proper description of unstable particles like $W^\pm$ gauge bosons and top quarks in perturbation theory requires the introduction of the complex-mass scheme (CMS), which was first proposed for lowest-order calculations in Ref. [41] and then generalised to higher orders in Refs. [42, 91]. In this scheme, complex masses are introduced at the level of the Lagrangian by splitting the bare masses into complex renormalised masses and complex counterterms. This corresponds to a rearrangement of the perturbative expansion without changing the underlying theory and preserving gauge invariance. Unitarity is respected up to higher orders as long as unstable particles are excluded from the final states. Renormalisation must nevertheless be treated carefully as not to spoil these properties of the bare theory. To this end, the standard on-shell scheme has been generalised in Ref. [42] to the complex-mass case by requiring unit residues of propagators at complex poles and by taking into account the imaginary parts of the self-energies in the renormalisation constants. This necessitates, however, the calculation of the self-energies for complex squared momenta. This complication can be avoided by expanding the self-energies present in the renormalisation constants about real arguments such that one-loop accuracy is preserved. In case of the $W^\pm$ gauge boson and top-quark, extra constants must be added to the expanded self-energies in order not to spoil the one-loop accuracy of the results due to the presence of branch cuts introduced by infrared divergences. The simplified version of the complex renormalisation is described in detail in Refs. [42, 57], where all renormalisation constants are provided as well. These renormalisation constants are implemented in RECOLA and employed in our calculation of NLO QCD and EW corrections to the $pp \to t\bar{t}\gamma(\gamma)$ process in the di-lepton top-quark decay channel

without any modifications.

As already mentioned in Section 2.1, the presence of final-state photons in the Born-level process requires special care in the renormalisation of the electromagnetic coupling constant α. In particular, we split the total power of α^n into $\alpha_{G_\mu}^{n-n_\gamma}\alpha(0)^{n_\gamma}$ where $n_\gamma = 1$ ($n_\gamma = 2$) for the underlying Born-level process $pp \to t\bar{t}\gamma(\gamma)$. The powers of the electromagnetic coupling constant associated with final-state photons are renormalised in the on-shell scheme (the $\alpha(0)$ scheme) [16, 42, 57]. The remaining powers of α are renormalised in the G_μ scheme, where the renormalized electromagnetic coupling α is derived from the Fermi constant G_F, measured in muon decays, and the masses of the W and Z bosons. The renormalisation in this mixed scheme is realised by first performing the complete renormalisation of all powers of α in the G_μ scheme. The renormalisation scheme is then changed for $\alpha(0)^{n_\gamma}$ by introducing a new counterterm which is given by

$$2\,n_\gamma\,\mathrm{Re}\left(\delta Z_e\big|_{\alpha(0)} - \delta Z_e\big|_{G_\mu}\right) d\sigma^{\mathrm{LO}} = n_\gamma\,\mathrm{Re}\left(\Delta r^{(1)}\right) d\sigma^{\mathrm{LO}}, \tag{3.19}$$

where $\Delta r^{(1)}$ are the NLO EW corrections to the muon decay [92–95] and $\delta Z_e\big|_{\alpha(0)}$ as well as $\delta Z_e\big|_{G_\mu}$ are the renormalisation constants of the electric charge e in the on-shell and G_μ scheme, respectively. We note that in Eq. (3.19) and in general in the whole calculation, the electromagnetic coupling is always set to $\alpha = \alpha_{G_\mu}$ and the final result is then rescaled by $(\alpha(0)/\alpha_{G_\mu})^{n_\gamma}$. This also implies that the relative EW corrections are always calculated with $\alpha = \alpha_{G_\mu}$. In order to test the consistency of the calculation in this mixed approach we have explicitly checked the cancellation of all IR singularities in the sum of virtual corrections and integrated dipoles for a few phase-space points for all partonic subprocesses.

4 LHC Setup for numerical predictions

The calculations of complete NLO corrections for $pp \to t\bar{t}\gamma$ and $pp \to t\bar{t}\gamma\gamma$ in the di-lepton top-quark decay channel are performed for proton-proton collisions at the LHC with a center of mass energy of $\sqrt{s} = 13$ TeV. When both higher-order QCD and EW corrections as well as photon-initiated subprocesses are considered, the PDFs with QED effects and the photon content of the proton are essential. To this end, we use the NLO NNPDF3.1luxQED PDF set [96–99] with $\alpha_s(m_Z) = 0.118$, where photons are properly taken into account in the PDF evolution, at LO and NLO. The PDF set as well as the running of the strong coupling constant with two-loop accuracy is obtained using the LHAPDF interface [100]. As already explained in the last section, for α a mixed scheme is considered. In particular, α is first calculated in the G_μ-scheme according to

$$\alpha_{G_\mu} = \frac{\sqrt{2}}{\pi}\,G_\mu\,m_W^2\left(1 - \frac{m_W^2}{m_Z^2}\right), \qquad G_\mu = 1.1663787\cdot 10^{-5}\ \mathrm{GeV}^{-2}, \tag{4.1}$$

with $m_W = 80.379$ GeV and $m_Z = 91.1876$ GeV. However, α associated with Born-level final-state photons is treated in the on-shell scheme, where we use $\alpha^{-1} = \alpha^{-1}(0) = 137.035999084$ [101] as the input parameter. Additional photon radiation from the real emission part of the NLO calculation is evaluated with α_{G_μ}. We use the following input values for the masses and widths of the unstable particles

$$m_t = 172.5\ \mathrm{GeV}, \qquad \Gamma_W = 2.0972\ \mathrm{GeV},$$
$$m_H = 125\ \mathrm{GeV}, \qquad \Gamma_H = 4.07\cdot 10^{-3}\ \mathrm{GeV},$$

The width of the Z boson is set to zero to avoid artificial higher-order terms that would otherwise appear due to the complex-mass scheme, since the width of the W boson is assumed to be zero

everywhere except in the propagators, as explained in Ref. [51]. All other particles are assumed to be massless. We use the same top-quark width at LO and NLO. Taking into account NLO QCD and EW corrections, the latter width is given by

$$\Gamma_t^{\rm NLO} = 1.3735727 \text{ GeV}, \tag{4.2}$$

where we adapt the conventions given in Ref. [102], while the NLO QCD corrections are obtained from Ref. [65] for $\mu_R = m_t$. We note here that, contrary to what is usually done when calculating NLO QCD corrections, in this study we use the same PDF set as well as top-quark width for both LO and NLO predictions. This should help us to directly examine the relative magnitude of the subleading contributions, while simultaneously separating out the effects coming from the use of different settings at LO and NLO. The NLO EW corrections are computed numerically with the help of Helac-Dipoles and Recola. As already indicated in Eq. (2.18), in this scheme, the LO and NLO contributions can simply be added to give the complete result.

The event selection and scale choice are based on our previous work on NLO QCD corrections to the $pp \to t\bar{t}\gamma\gamma$ process [22]. All final-state partons with pseudo-rapidity $|\eta| < 5$ are clustered into jets with separation $R = 0.4$ in the rapidity azimuthal-angle plane via the IR-safe *anti-k_T* jet algorithm [103]. We require two oppositely charged leptons, at least two b-jets and at least one (two) photon(s) for $t\bar{t}\gamma(\gamma)$, respectively. The IR safety of the $t\bar{t}\gamma(\gamma)$ cross section involving jets and prompt photon(s) is ensured by using the smooth photon isolation prescription as described in Ref. [104]. Therefore, the event is rejected unless the following condition is fulfilled before the jet algorithm is applied

$$\sum_i E_{T\,i}\,\Theta(R - R_{\gamma i}) \leq \epsilon_\gamma\, E_{T\,\gamma} \left(\frac{1-\cos(R)}{1-\cos(R_{\gamma j})}\right)^n , \tag{4.3}$$

for all $R \leq R_{\gamma j}$ with $R_{\gamma j} = 0.4$ and $\epsilon_\gamma = n = 1$. The transverse energy of the parton i/photon is denoted by $E_{T\,i}/E_{T\,\gamma}$ and $R_{\gamma i}$ is given by

$$R_{\gamma i} = \sqrt{(y_\gamma - y_i)^2 + (\phi_\gamma - \phi_i)^2}\,. \tag{4.4}$$

In subleading NLO corrections we also encounter partonic processes with an additional photon in the final state with respect to the Born-level subprocesses. In this case, the smooth photon isolation prescription can be extended to additionally require the isolation of photons with charged leptons and photons, as suggested in Ref. [16]. In this approach, after the smooth photon isolation, charged leptons and partons are recombined with only non-isolated photons based on a jet clustering algorithm. In general, the use of the smooth photon isolation prescription is not required in this case. Alternatively, it is sufficient to perform the photon recombination directly with charged leptons and partons, where additionally the following recombination rule $\gamma + \gamma \to \gamma$ is allowed. Similar schemes have already been applied in associated photon production processes, see e.g. Refs. [105, 106]. We have used both approaches for the calculation of higher-order corrections to the $pp \to t\bar{t}\gamma$ process, where the photon recombination has also been performed with the *anti-k_T* jet algorithm with the radius parameter $R = 0.4$. We have found no phenomenologically relevant differences even at the differential cross-section level. Therefore, we remain with the second approach, not using the smooth isolation prescription in these contributions. After the jet algorithm/photon recombination, the prompt photons are defined with the following conditions

$$p_{T,\gamma} > 25 \text{ GeV}\,, \qquad |y_\gamma| < 2.5\,, \qquad \Delta R_{\gamma\gamma} > 0.4\,. \tag{4.5}$$

In order to ensure well-observable isolated b-jets and charged leptons in the central-rapidity region, we require

$$\begin{aligned} &p_{T,b} > 25 \text{ GeV}\,, \qquad &&|y_b| < 2.5\,, \qquad &&\Delta R_{bb} > 0.4\,, \\ &p_{T,\ell} > 25 \text{ GeV}\,, \qquad &&|y_\ell| < 2.5\,, \qquad &&\Delta R_{\ell\ell} > 0.4\,. \end{aligned} \tag{4.6}$$

In addition, charged leptons and photons need to be well separated from any b-jet in the rapidity-azimuthal angle plane as well as from each other

$$\Delta R_{l\gamma} > 0.4\,, \qquad \Delta R_{lb} > 0.4\,, \qquad \Delta R_{b\gamma} > 0.4\,. \tag{4.7}$$

Finally, there are no restrictions on the kinematics of the extra light jet/photon (if resolved by the jet algorithm) and the missing transverse momentum, $p_T^{miss} = |\vec{p}_{T,\nu_\ell} + \vec{p}_{T,\bar{\nu}_\ell}|$. Based on the findings in Ref. [22] we set the factorisation and renormalisation scale to a common dynamical scale setting, μ_0, given by

$$\mu_R = \mu_F = \mu_0 = \frac{E_T}{4}\,, \tag{4.8}$$

with

$$E_T = \sqrt{m_t^2 + p_{T,t}^2} + \sqrt{m_t^2 + p_{T,\bar{t}}^2} + \sum_{i=1}^{n_\gamma} p_{T,\gamma_i}\,, \tag{4.9}$$

where $p_{T,t}$ and $p_{T,\bar{t}}$ are the transverse momenta of the on-shell top quarks. In addition, for dimensionful cross-section distributions constructed from the photon kinematics, we present results for the fixed scale setting, $\mu_0 = m_t$. Theoretical uncertainties due to missing higher orders are estimated by a 7-point scale variation, where the factorisation and renormalisation scales are independently varied in the range

$$\frac{1}{2}\,\mu_0 \leq \mu_R\,, \mu_F \leq 2\,\mu_0\,, \qquad \frac{1}{2} \leq \frac{\mu_R}{\mu_F} \leq 2\,, \tag{4.10}$$

which leads to the following pairs

$$\left(\frac{\mu_R}{\mu_0}\,, \frac{\mu_F}{\mu_0}\right) = \Big\{\,(2,1)\,, (0.5,1)\,, (1,2)\,, (1,1), (1,0.5), (2,2), (0.5,0.5)\Big\}\,. \tag{4.11}$$

By searching for the minimum and maximum of the resulting cross sections we obtain the displayed uncertainty bands. We use the 7-point scale variation both at the integrated and differential cross-section level.

5 Top-quark pair production with one isolated photon

5.1 Integrated fiducial cross sections

Now we turn to the discussion of the numerical results. We begin with our findings for the $pp \to t\bar{t}\gamma$ process at the integrated fiducial cross-section level. In particular, in Table 1 we present the results for LO, NLO, NLO_{QCD} and NLO_{prd}, as defined in the last section, with the corresponding theoretical uncertainties obtained by scale variation. In addition, we display the decomposition of the LO and NLO results into the individual LO_i and NLO_i contributions calculated at the different orders in α_s and α. Finally, the relative size of all results with respect to the dominant LO contribution, LO_1, is given in the last column. We find that both subleading LO contributions, LO_2 and LO_3, are below 0.5% of LO_1. In addition, LO_3 is slightly larger than LO_2 due to cancellations in LO_2 between the $g\gamma$ and $b\bar{b}$ subprocesses. It turns out that the latter channel gives a negative result that can be attributed to the interference between the different orders in α_s and α. Although, the $b\bar{b}$ initial state is PDF suppressed

		σ_i [fb]	Ratio to LO_1
LO_1	$\mathcal{O}(\alpha_s^2\alpha^5)$	$55.604(8)^{+31.4\%}_{-22.3\%}$	1.00
LO_2	$\mathcal{O}(\alpha_s^1\alpha^6)$	$0.18775(5)^{+20.1\%}_{-15.4\%}$	+0.34%
LO_3	$\mathcal{O}(\alpha_s^0\alpha^7)$	$0.26970(4)^{+14.3\%}_{-16.9\%}$	+0.49%
NLO_1	$\mathcal{O}(\alpha_s^3\alpha^5)$	+3.44(5)	+6.19%
NLO_2	$\mathcal{O}(\alpha_s^2\alpha^6)$	−0.1553(9)	−0.28%
NLO_3	$\mathcal{O}(\alpha_s^1\alpha^7)$	+0.2339(3)	+0.42%
NLO_4	$\mathcal{O}(\alpha_s^0\alpha^8)$	+0.001595(8)	+0.003%
LO		$56.061(8)^{+31.2\%}_{-22.1\%}$	1.0082
$\mathrm{NLO}_{\mathrm{QCD}}$		$59.05(5)^{+1.6\%}_{-5.9\%}$	1.0620
$\mathrm{NLO}_{\mathrm{prd}}$		$59.08(5)^{+1.5\%}_{-5.9\%}$	1.0626
NLO		$59.59(5)^{+1.6\%}_{-5.9\%}$	1.0717

Table 1. *Integrated fiducial cross section for the $pp \to t\bar{t}\gamma + X$ process in the di-lepton top-quark decay channel at the LHC with $\sqrt{s} = 13$ TeV. Results are shown for* LO, NLO, $\mathrm{NLO}_{\mathrm{QCD}}$ *and* $\mathrm{NLO}_{\mathrm{prd}}$ *with the corresponding scale uncertainties. Additionally, all* LO_i *and* NLO_i *contributions and the ratio with respect to* LO_1 *are displayed. MC integration errors are given in parentheses. Results are provided for $\mu_0 = E_T/4$ and the NLO NNPDF3.1luxQED PDF set.*

with respect to the $q\bar{q}$ one, it provides the dominant contribution to LO_3, and is more than three times larger than the $q\bar{q}$ channel, due to the presence of additional t-channel Feynman diagrams that do not appear in the $q\bar{q}$ subprocess. The $\gamma\gamma$ initiated contribution is smaller than the MC integration error of the LO result and thus completely negligible. Consequently, at the integrated fiducial cross-section level, the subleading LO contributions are phenomenologically insignificant, especially when compared to the scale uncertainties of the complete LO result (or the dominant LO_1 contribution for that matter). The theoretical errors of both LO and LO_1 are of similar size and amount to 31%.

As expected, the dominant NLO corrections originate from the NLO QCD corrections (NLO_1) to LO_1 and lead to an increase of the integrated fiducial cross section by about 6.2%. All subleading NLO contributions are again found to be less than 0.5% of LO_1. In more detail, NLO_2 and NLO_3 are of the same order of magnitude and NLO_4 is completely negligible compared to the NLO scale uncertainties and even MC integration errors. We note that in all the contributions we used the same top-quark width ($\Gamma_t^{\mathrm{NLO,QCD+EW}} = 1.3735727$ GeV). In particular, if the LO top-quark width ($\Gamma_t^{\mathrm{LO}} = 1.4806842$ GeV) has been used instead for LO_1 and the NLO QCD one ($\Gamma_t^{\mathrm{NLO,QCD}} = 1.3535983$ GeV) for $\mathrm{NLO}_{\mathrm{QCD}}$, as it is often done in higher-order QCD calculations, we would obtain NLO QCD corrections of about 27%. Furthermore, we note that the sum of all subleading LO and NLO contributions increases the $\mathrm{NLO}_{\mathrm{QCD}}$ result by about 1% and therefore plays only a minor role at the integrated fiducial cross-section level compared to the $\mathrm{NLO}_{\mathrm{QCD}}$ scale uncertainties that are of the order of 6%. The scale uncertainties themselves remain unchanged by the inclusion of the subleading higher-order contributions, and are thus completely driven by the $\mathrm{NLO}_{\mathrm{QCD}}$ part. Finally, we can observe that $\mathrm{NLO}_{\mathrm{prd}}$ and $\mathrm{NLO}_{\mathrm{QCD}}$ agree within the MC errors, which results from the cancellation of subleading LO contributions (0.8%) and the subleading NLO corrections to the production of $pp \to t\bar{t}\gamma$ (−0.7%). In addition, the difference

between NLO and NLO_{prd}, and thus the subleading NLO corrections involving radiative top-quark decays (including photon radiation and/or QCD/EW corrections), is of similar (absolute) size as the other two effects (0.9%).

5.2 Differential fiducial cross sections

While at the integrated fiducial cross-section level the effects of the subleading LO and NLO contributions are small, it is expected that these effects might be enhanced for particular observables in certain phase-space regions. To this end, in Figure 9 we present the differential cross-section distributions for the transverse momentum of the hardest photon, p_{T,γ_1}, the invariant mass of the two hardest b-jets, $M_{b_1 b_2}$, as well as their transverse momenta, denoted as p_{T,b_1} and p_{T,b_2}, respectively. In the upper panels we provide the absolute predictions for LO, NLO, NLO_{QCD} and NLO_{prd}. The middle panels show the ratio of the three NLO results to NLO_{QCD}. In addition, both panels display the NLO_{QCD} theoretical uncertainties obtained from scale variation. Finally, the lower panels present the relative size of all subleading LO_i and NLO_i contributions with respect to LO_1.

For p_{T,γ_1} we find that the largest NLO corrections arise from NLO_1 and lead in the tail of the distribution to an increase of the LO_1 cross section by about 25%. The inclusion of all subleading LO and NLO contributions reduces the NLO_{QCD} prediction by up to 4% due to EW Sudakov logarithms induced by NLO_2. All other subleading contributions remain below 1%. The NLO_{prd} contribution, where the subleading NLO corrections are only included in the production stage of $t\bar{t}\gamma$, underestimates the full calculation by about 2%. The overall picture remains the same for the $M_{b_1 b_2}$ observable. In particular, we again find that NLO_2 is the dominant subleading contribution, leading to a reduction in the NLO_{QCD} prediction of about 5%. This reduction is about half the size of the corresponding scale uncertainties. On the other hand, NLO_{prd} recovers the full calculation correctly in the tails and only small differences up to 1.5% are found at the beginning of the spectrum. In the case of the transverse momenta of the hardest and second hardest b-jet, p_{T,b_1} and p_{T,b_2}, the relative size of NLO_2 with respect to LO_1 is increased to 10%. On the contrary, the impact of all subleading contributions on the final NLO result seems to be very different. Indeed, we find for p_{T,b_1} that NLO_3 is enhanced in the tail and amounts to $3\% - 4\%$, thus partially cancelling the EW Sudakov logarithms in NLO_2. Moreover, we find large NLO QCD corrections to LO_1 of up to 95%, which further suppress the importance of the subleading contributions. However, both effects, the enhancement of NLO_3 and the large NLO_1 contribution, have the same origin and arise from large NLO QCD real corrections to LO_1 and LO_3, induced by hard jet recoil against the $t\bar{t}$ system. This can be seen by inspecting the size of the NLO scale uncertainties, which increase continuously towards the tail of the distribution and become closer in size to those at LO. Thus, the relative size of the subleading corrections is highly dependent on the fiducial phase space and might be enhanced if a more exclusive event selection and/or jet vetos are applied. On the other hand, for p_{T,b_2} the subleading contributions have a more significant impact on its spectrum, reducing the NLO_{QCD} prediction by up to 10%. The scale uncertainties of NLO_{QCD} are about 15% and therefore comparable in size. Moreover, we find that the larger size of the subleading contributions can also affect the scale uncertainties, which in this case increase to about 20% for the complete NLO case. Finally, we can observe that, for both b-jet transverse momentum spectra the NLO_{prd} predictions fully recover the complete NLO result.

Following the findings of our previous work on the calculation of the NLO QCD corrections to the $pp \to t\bar{t}\gamma\gamma$ process in the di-lepton top-quark decay channel [22], where a traditional fixed scale setting, $\mu_0 = m_t$, led to a reduction of NLO QCD corrections and scale uncertainties for photonic observables, in the following we reexamine the p_{T,γ_1} observable also for this scale choice. To this end, in Figure 10 we present p_{T,γ_1} afresh for $\mu_0 = m_t$. We find that for this fixed scale choice the NLO_1 contribution

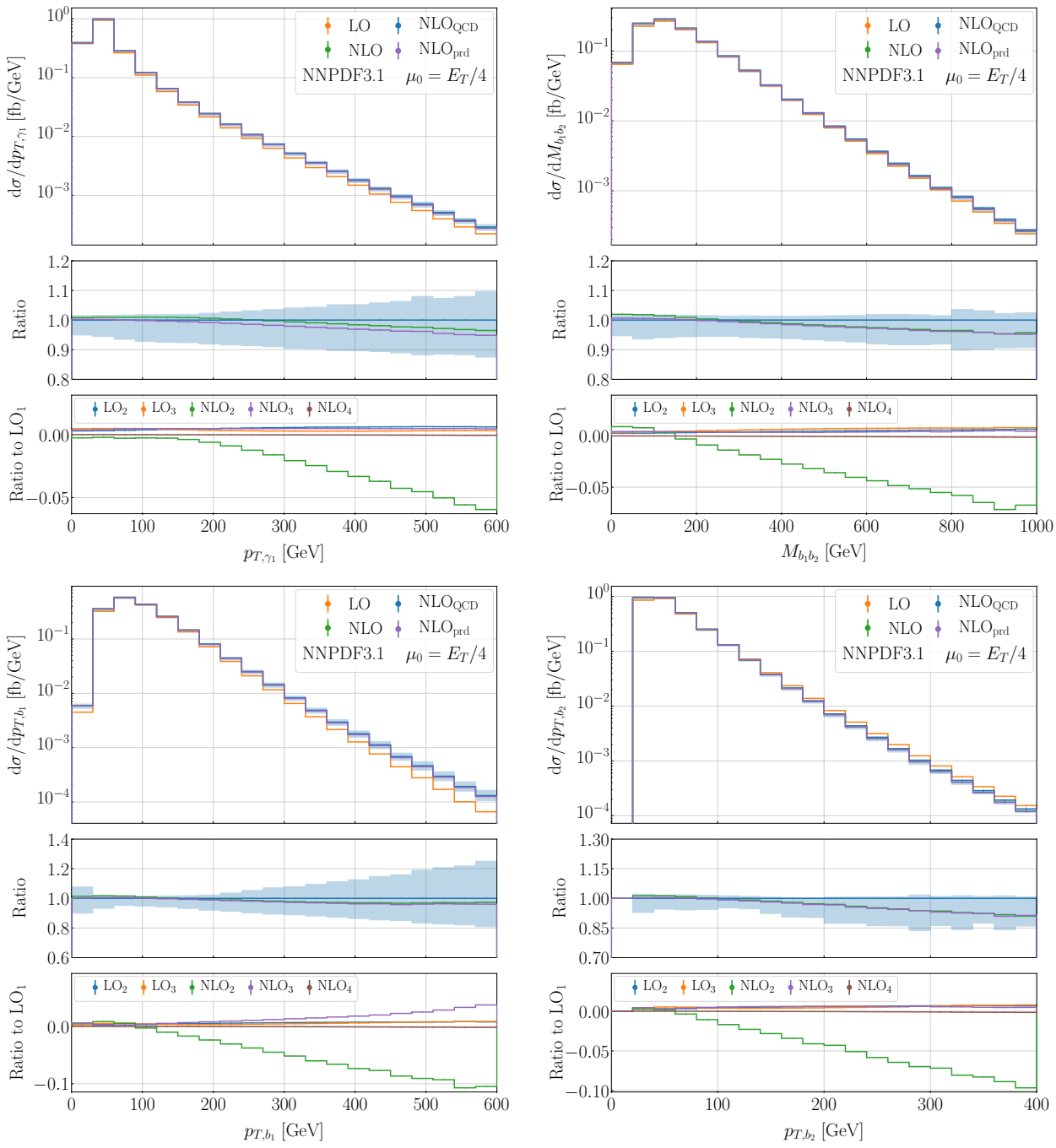

Figure 9. *Differential cross-section distributions for the observables p_{T,γ_1}, $M_{b_1b_2}$, p_{T,b_1} and p_{T,b_2} for the $pp \to t\bar{t}\gamma + X$ process in the di-lepton top-quark decay channel at the LHC with $\sqrt{s} = 13$ TeV. The upper panels present absolute predictions for* LO, NLO, NLO_{QCD} *and* NLO_{prd} *together with the* NLO_{prd} *uncertainty bands. Middle panels show the ratio of all NLO results with respect to* NLO_{QCD} *and the lower panels display the relative size of all subleading* LO_i *and* NLO_i *contributions compared to* LO_1. *Results are provided for $\mu_0 = E_T/4$ and the NLO NNPDF3.1luxQED PDF set.*

is reduced from 25% to 13%. Moreover, while for the default scale setting, $\mu_0 = E_T/4$, the largest NLO QCD corrections are present in the tail, for $\mu_0 = m_t$ the LO and NLO_{QCD} predictions coincide in this phase-space region. Furthermore, the differences of up to 13% are found at the beginning of

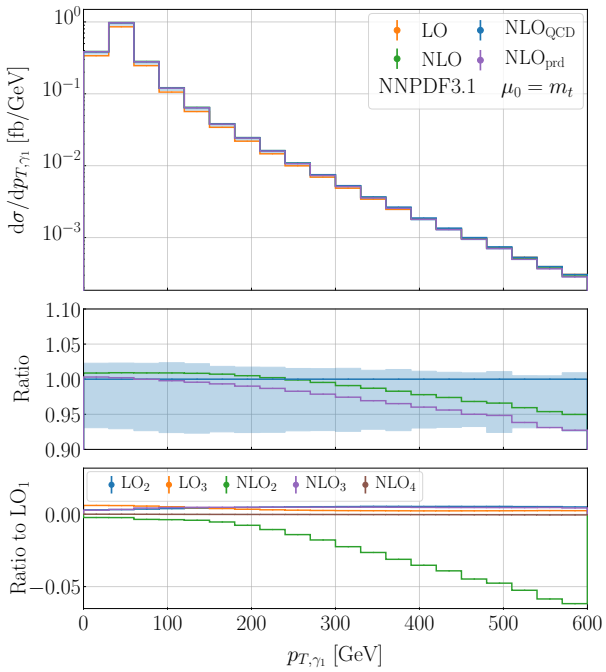

Figure 10. *Same as Figure 9 but for the observable p_{T,γ_1}. The result is shown for $\mu_0 = m_t$.*

the spectrum. The relative size of the subleading LO and NLO contributions is basically unchanged and leads to a reduction of the complete calculation of about 5% compared to 4% for $\mu_0 = E_T/4$. In addition, the scale uncertainties are slightly reduced to $7\% - 9\%$ compared to $10\% - 11\%$. Thus, for the scale setting $\mu_0 = m_t$, the subleading contributions become more important, since the subleading effects and the scale uncertainties are of similar size.

We continue the discussion and present in Figure 11 other differential cross-section distributions. In detail, we display the transverse momentum of the $b_1 b_2$ and $\ell^+\ell^-$ systems, denoted as p_{T,b_1b_2} and $p_{T,\ell^+\ell^-}$, respectively. Furthermore, we show the angular separation between γ_1 and ℓ^+ as well as γ_1 and b_1, denoted as $\Delta R_{\ell^+\gamma_1}$ and $\Delta R_{b_1\gamma_1}$, respectively. The two dimensionful observables, p_{T,b_1b_2} and $p_{T,\ell^+\ell^-}$, are affected by huge NLO QCD corrections to LO$_1$ of about 450% and 200%. These corrections arise from a kinematical suppression at LO [47, 102, 107–109]. Indeed, at the LO level the two top quarks are predominantly produced in the back-to-back configuration, so that the transverse momentum of both b-jets or leptons may separately be large, but they largely cancel each other out in the combined system. At NLO, however, this suppression is weakened due to hard jet recoil against the $t\bar{t}$ system. This leads, on the one hand, to huge NLO QCD corrections to LO$_1$, and on the other hand, also to an enhancement of the NLO QCD corrections with respect to LO$_3$ as part of NLO$_3$. In particular, for p_{T,b_1b_2} we find that NLO$_3$ is about 10% of LO$_1$. The NLO$_2$ contribution is of similar magnitude but has the opposite sign. Consequently, NLO$_3$ and NLO$_2$ cancel each other out, and the NLO$_{\rm QCD}$ and NLO predictions coincide. Since the two NLO subleading contributions are of different origins, this cancellation is too a large extend accidental and highly dependent on the event selection and for example jet vetos. Especially, vetoing undesired additional jets would drastically reduce the size of NLO$_1$ and NLO$_3$. Also for $p_{T,\ell^+\ell^-}$ we find a similar but less pronounced cancellation of NLO$_2$ (-5%) and NLO$_3$ (2%). The NLO$_{\rm prd}$ approximation is again able to fully recover the complete NLO calculation.

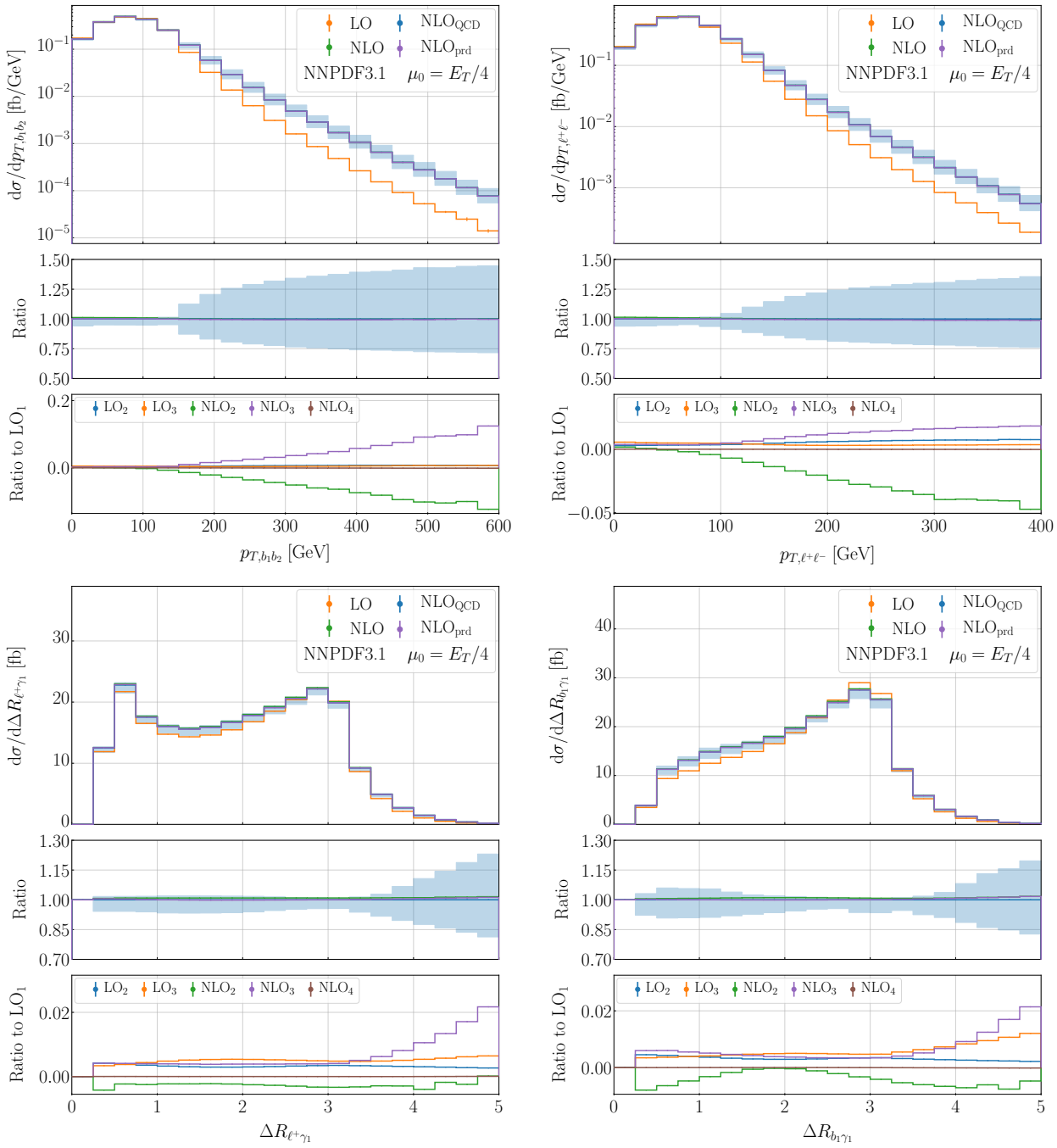

Figure 11. *Same as Figure 9 but for the observables* p_{T,b_1b_2}, $p_{T,\ell^+\ell^-}$, $\Delta R_{\ell^+\gamma_1}$ *and* $\Delta R_{b_1\gamma_1}$.

For angular distributions such as regular rapidity distributions, ΔR separations or (azimuthal) opening angles between two final states, we find no significant effects from any of the subleading LO or NLO contributions. Indeed, they are individually in the range of $0.5\% - 1.0\%$ when compared to LO_1. Only for the ΔR separation between a photon and a b-jet or charged lepton, such as $\Delta R_{\ell^+\gamma_1}$ and $\Delta R_{b_1\gamma_1}$, we find a small enhancement for the NLO_3 contribution when comparing to LO_1. This enhancement, of about 2%, is visible for large values of the ΔR separation. However, these phase-space regions are generally not only less populated but also characterized by substantial NLO scale

		σ_i [fb]	Ratio to LO_1
LO_1	$\mathcal{O}(\alpha_s^2\alpha^6)$	$0.15928(3)^{+31.3\%}_{-22.1\%}$	1.00
LO_2	$\mathcal{O}(\alpha_s^1\alpha^7)$	$0.0003798(2)^{+25.8\%}_{-19.2\%}$	+0.24%
LO_3	$\mathcal{O}(\alpha_s^0\alpha^8)$	$0.0010991(2)^{+10.6\%}_{-13.1\%}$	+0.69%
NLO_1	$\mathcal{O}(\alpha_s^3\alpha^6)$	+0.0110(2)	+6.89%
NLO_2	$\mathcal{O}(\alpha_s^2\alpha^7)$	−0.00233(2)	−1.46%
NLO_3	$\mathcal{O}(\alpha_s^1\alpha^8)$	+0.000619(1)	+0.39%
NLO_4	$\mathcal{O}(\alpha_s^0\alpha^9)$	−0.0000166(2)	−0.01%
LO		$0.16076(3)^{+30.9\%}_{-21.9\%}$	1.0093
$\mathrm{NLO}_{\mathrm{QCD}}$		$0.1703(2)^{+1.9\%}_{-6.2\%}$	1.0690
$\mathrm{NLO}_{\mathrm{prd}}$		$0.1694(2)^{+1.7\%}_{-5.9\%}$	1.0637
NLO		$0.1700(2)^{+1.8\%}_{-6.0\%}$	1.0674

Table 2. *Same as Table 1 but for the $pp \to t\bar{t}\gamma\gamma + X$ process in the di-lepton top-quark decay channel.*

uncertainties up to 15%. Such theoretical uncertainties are induced by large NLO QCD corrections to LO_1. Thus, this small enhancement of NLO_3 is still negligible.

In summary, subleading LO and NLO contributions are generally only important in the tails of dimensionful observables. In particular, the presence of EW Sudakov logarithms in NLO_2 can reduce differential predictions by up to 10%. In addition, we have found that for observables affected by large NLO QCD corrections due to real radiation, the NLO_3 contribution can be enhanced. This can lead to an accidental cancellation with NLO_2 since the origin of both contributions is vastly different. Furthermore, the cancellation might be heavily influenced by the event selection and a possible jet veto. Finally, the $\mathrm{NLO}_{\mathrm{prd}}$ prediction is able to mimic the complete NLO calculation for hadronic observables, while it underestimates the complete prediction by up to $1\% - 2\%$ for non-hadronic ones. Nevertheless, such small effects are well within the theoretical uncertainties due to scale dependence. Thus, the $\mathrm{NLO}_{\mathrm{prd}}$ theoretical prediction can be safely used to model various differential cross-section distributions in phenomenological studies at the LHC for the $pp \to t\bar{t}\gamma + X$ process in the di-lepton top-quark decay channel taking into account the current theoretical precision for this process.

6 Top-quark pair production with two isolated photons

6.1 Integrated fiducial cross sections

Next we continue with the $pp \to t\bar{t}\gamma\gamma$ process and start with the discussion of the integrated fiducial cross section, again focusing our attention on the di-lepton top-quark decay channel. In particular, we are interested in any differences between this process and $pp \to t\bar{t}\gamma$. In Table 2 we present the integrated fiducial cross section for LO, NLO, $\mathrm{NLO}_{\mathrm{QCD}}$ and $\mathrm{NLO}_{\mathrm{prd}}$ as well as the corresponding scale uncertainties. We also present the numerical results for all individual LO_i and NLO_i contributions. We find again that all subleading LO contributions amount to less than 1% of LO_1 and are therefore negligible when comparing to the LO scale uncertainties. The NLO_1 contribution is similar in size with 6.9% compared to 6.2% for $pp \to t\bar{t}\gamma$. As expected, this contribution yields the largest higher-order

corrections at the NLO level. The biggest difference between the two processes is found for NLO_2. Indeed, the NLO_2 contribution increases from -0.3% to -1.5%, which is consistent with the findings in the literature for the process at hand but with stable top quarks [16]. The NLO_3 contribution remains at the level of 0.4%. Finally, NLO_4 contributes at the level of 0.01% only. This contribution is therefore smaller than the MC integration error and phenomenologically completely irrelevant. Due to the increase in size of NLO_2, there are larger cancellations between the individual contributions, so that the difference between the NLO_{QCD} and NLO predictions decreases and both results agree within their coresponding MC errors. As for the $pp \to t\bar{t}\gamma$ process, also in this case the scale uncertainties at the integrated fiducial cross-section level are barely affected by the subleading contributions. Including all subleading LO contributions and subleading NLO corrections to the production of $pp \to t\bar{t}\gamma\gamma$ in NLO_{prd} leads to a decrease of the NLO_{QCD} result by about -0.5%. Similar to the previous process, we again have cancellations between the subleading LO contributions (0.9%) and the subleading NLO corrections (-1.4%). The differences between NLO and NLO_{prd} are reduced to 0.4% compared to 0.9% for the $pp \to t\bar{t}\gamma$ process, implying that subleading NLO corrections involving radiative top-quark decays are less important, at least at the integrated fiducial cross-section level.

6.2 Differential fiducial cross sections

Similarly to $t\bar{t}\gamma$ production, also for the $pp \to t\bar{t}\gamma\gamma + X$ process we are investigating the impact of all subleading contributions and subleading higher-order corrections on various differential cross-section distributions. In Figure 12 we show the observables $p_{T,\gamma_1\gamma_2}$, $M_{\gamma_1\gamma_2}$, p_{T,γ_1} and p_{T,b_1}. As in the case of $pp \to t\bar{t}\gamma + X$, here we again present in the upper panels the absolute predictions for LO, NLO, NLO_{QCD} and NLO_{prd}. The middle panels display the ratio with respect to NLO_{QCD}, including the scale uncertainties of NLO_{QCD}, and the lower panels show the size of the subleading contributions compared to LO_1.

First, we focus on $p_{T,\gamma_1\gamma_2}$ and $M_{\gamma_1\gamma_2}$. Their importance stems from the fact that both differential cross-section distributions can be seen as the direct and irreducible background to the kinematics of the Higgs boson in $pp \to t\bar{t}H$ production with the $H \to \gamma\gamma$ decay. For both observables we find that NLO_1 is the dominant source of NLO corrections, leading to an increase of LO_1 of up to 30% in the tails. The subleading LO and NLO contributions are dominated by NLO_2, due to EW Sudakov logarithms, which amounts to -8% for $p_{T,\gamma_1\gamma_2}$ and -5% for $M_{\gamma_1\gamma_2}$ with respect to LO_1. This results in a decrease of the full calculation by about 5% and 3%, respectively. At the same time, in these phase-space regions, the NLO scale uncertainties are larger by a factor of 2 for $p_{T,\gamma_1\gamma_2}$ and 4 for $M_{\gamma_1\gamma_2}$. The NLO_{prd} prediction fully recovers the complete calculation for $p_{T,\gamma_1\gamma_2}$ and differences of only about 1% can be found for $M_{\gamma_1\gamma_2}$. Thus, NLO_{prd} is more than sufficient to properly describe the shape of the two observables in the presence of subleading LO contributions and subleading NLO corrections.

We then turn to the p_{T,γ_1} differential cross-section distribution, where NLO QCD corrections up to $25\% - 30\%$ can be found. The subleading contributions reduce the NLO calculation by about $5\% - 6\%$ and are therefore slightly larger than those found for the $pp \to t\bar{t}\gamma$ process. Indeed, in the latter case the difference is about 4%. This small rise is due to the increase in the NLO_2 contribution that we have already observed at the integrated cross-section level. In the case of p_{T,b_1} the difference between NLO_{QCD} and NLO is somewhat enlarged in the tails from 4% for $pp \to t\bar{t}\gamma$ to 6% for the $pp \to t\bar{t}\gamma\gamma$ process. This can again be attributed to the increase of the NLO_2 corrections from -10% to -13%, while the size of NLO_3 is slight reduced to $2\% - 3\%$ from to $3\% - 4\%$ for $pp \to t\bar{t}\gamma$. In general, the presence of a second photon already at LO affects the kinematics of the $t\bar{t}$ system in such a way that the large NLO QCD corrections in NLO_1 are reduced for several observables such as p_{T,b_1} or p_{T,b_1b_2} compared to the $pp \to t\bar{t}\gamma$ process. In particular, for p_{T,b_1} we find a reduction from 95% to 55%. It

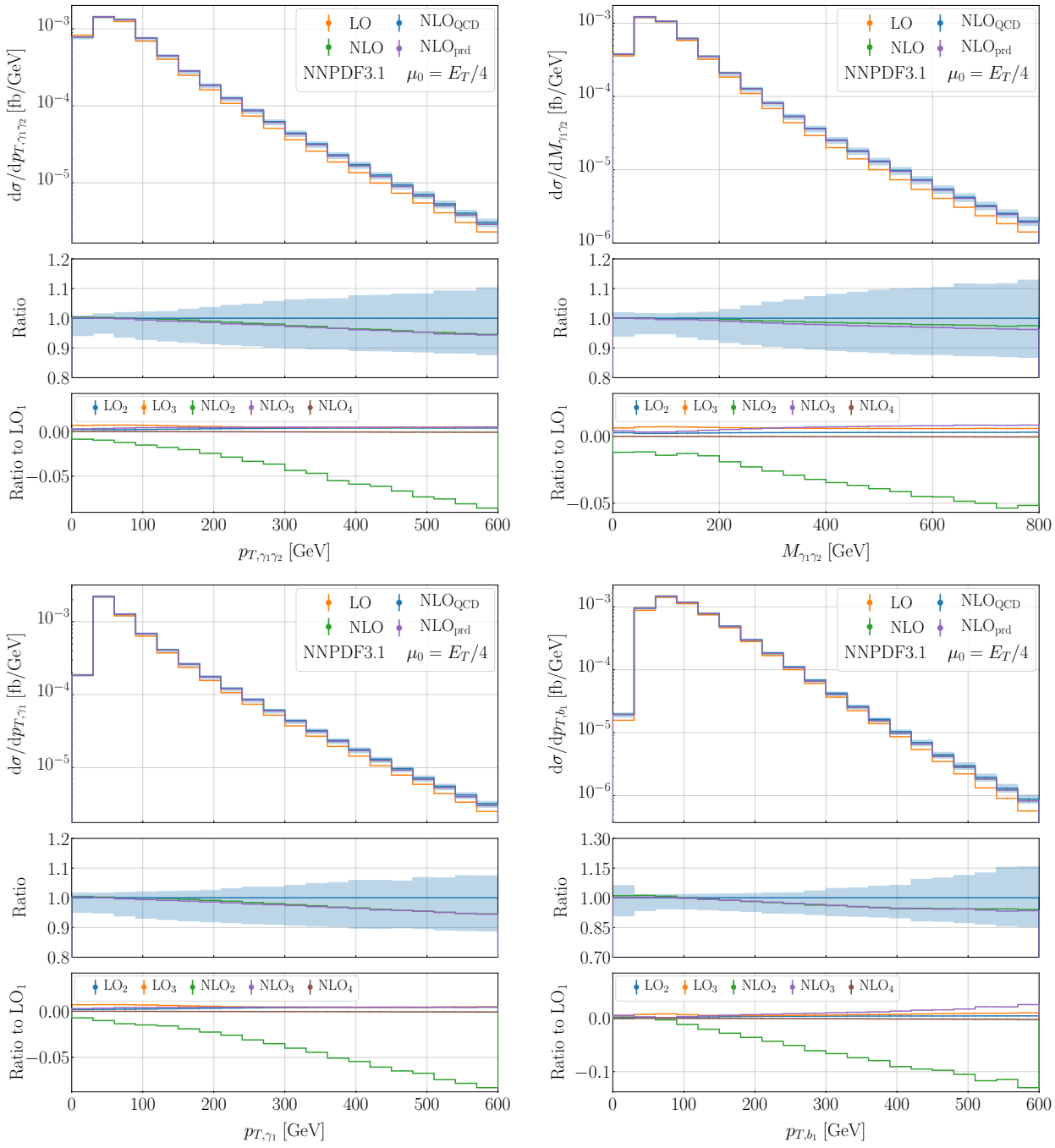

Figure 12. *Same as Figure 9 but for the $pp \to t\bar{t}\gamma\gamma + X$ process in the di-lepton top-quark decay channel and for the observables $p_{T,\gamma_1\gamma_2}$, $M_{\gamma_1\gamma_2}$, p_{T,γ_1} and p_{T,b_1}.*

follows directly that the enhancement of NLO_3 in such observables is also reduced. Therefore, the accidental cancellations between NLO_2 and NLO_3, which occurred in the $pp \to t\bar{t}\gamma$ case, although still present, are substantially reduced.

For comparison purposes and similar to what we have done for photonic observables in case of the $pp \to t\bar{t}\gamma$ process, also here we show differential cross-section distributions with the alternative scale choice. In detail, in Figure 13 we display $p_{T,\gamma_1\gamma_2}$, $M_{\gamma_1\gamma_2}$ and p_{T,γ_1} for $\mu_R = \mu_F = m_t$. For

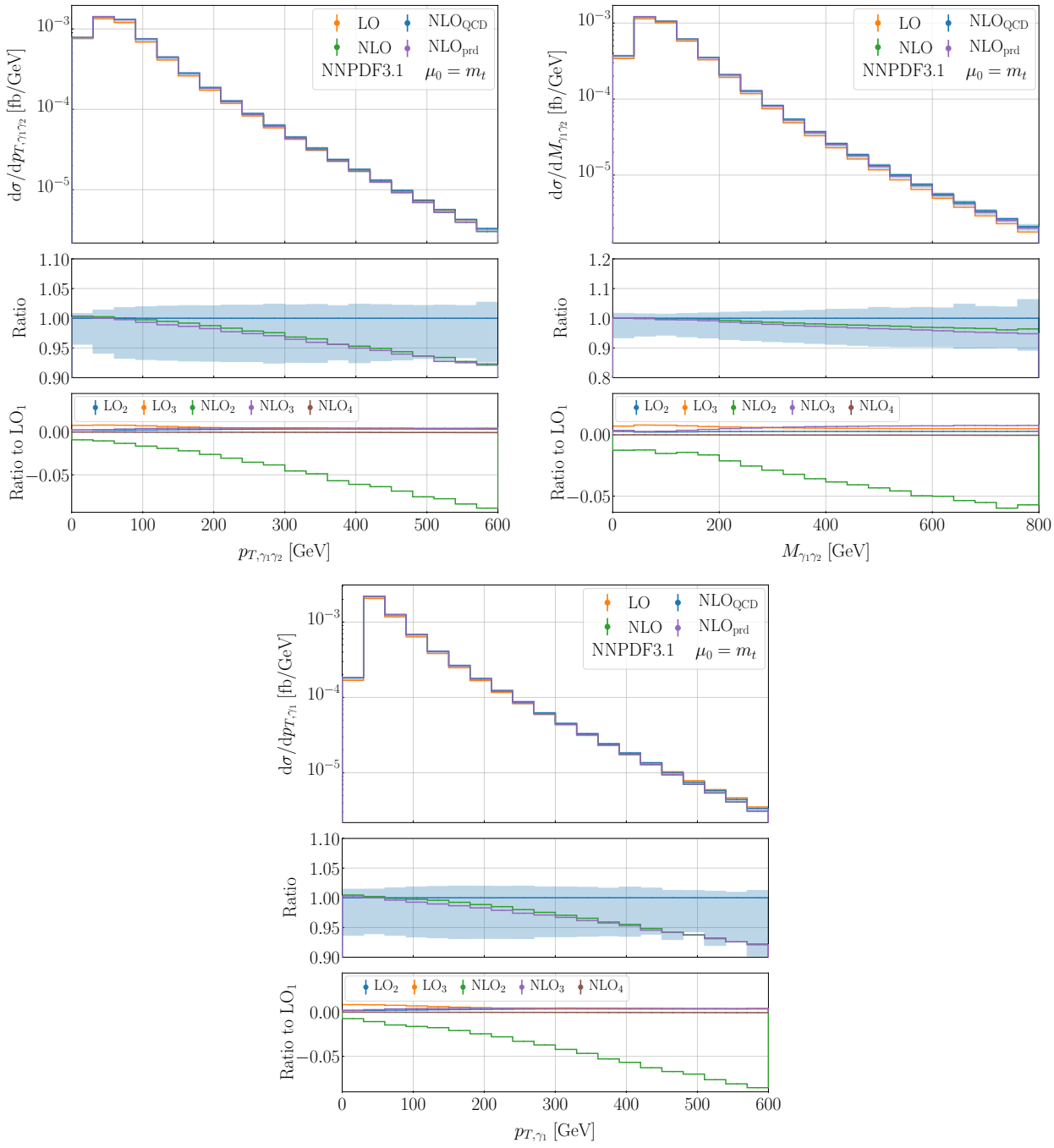

Figure 13. *Same as Figure 9 but for the* $pp \to t\bar{t}\gamma\gamma + X$ *process in the di-lepton top-quark decay channel and for the observables* $p_{T,\gamma_1\gamma_2}$, $M_{\gamma_1\gamma_2}$ *and* p_{T,γ_1}. *Results are shown for* $\mu_0 = m_t$.

$p_{T,\gamma_1\gamma_2}$ and $M_{\gamma_1\gamma_2}$, we again find that this scale choice leads to a reduction in the size of the NLO QCD corrections in NLO_1 from about 30% to $10\% - 12\%$. In addition, the scale uncertainties are changed from $12\% - 13\%$ to $8\% - 10\%$. Thus, the fixed scale setting not only decreases higher-order corrections in NLO_1, but also provides improved scale uncertainties. The reduction of higher-order effects in NLO_1 has also a direct impact on the significance of the subleading NLO corrections. In particular, because the relative size of the subleading NLO_2 corrections with respect to LO_1 does not

change for $\mu_0 = m_t$, the overall NLO_2 contribution becomes larger with respect to the complete NLO result. Indeed, we observe the rise of NLO_2 from 5% to 8% as well as from 3% to 4% for $p_{T,\gamma_1\gamma_2}$ and $M_{\gamma_1\gamma_2}$, respectively. Furthermore, for $p_{T,\gamma_1\gamma_2}$ the subleading NLO corrections become as large as the corresponding scale uncertainties of NLO_{QCD}, which are also equal in size to those of the complete NLO result. The same can be observed for the third differential cross-section distribution, namely for p_{T,γ_1}. In this case the NLO_1 contribution is reduced in the tails from 20% for $\mu_0 = E_T/4$ to 5% for $\mu_0 = m_t$. This increases the importance of the NLO_2 contribution again and leads to a reduction of the difference between NLO_2 and NLO by about 8% compared to $5\% - 6\%$ for $\mu_0 = E_T/4$. Consequently, the subleading contributions are of similar size as the scale uncertainties of the NLO_{QCD} result, and are at the level of 10%. Lastly, for all three photonic observables, the complete NLO predictions for the two scale settings differ by at most 4% in the tails and are therefore within the respective scale uncertainties.

7 Summary

We have presented the first calculation of the complete set of NLO corrections to $pp \to t\bar{t}\gamma + X$ and $pp \to t\bar{t}\gamma\gamma + X$ including top-quark decays at the LHC with $\sqrt{s} = 13$ TeV. In order to study the di-lepton top-quark decay channel we have employed the Narrow Width Approximation that works in the $\Gamma/m \to 0$ limit and preserves spin correlations. In this approximation all contributions without two resonant top quarks and W gauge bosons are simply neglected. In our calculations we have included the dominant LO contribution at $\mathcal{O}(\alpha_s^2\alpha^5)$ for $pp \to t\bar{t}\gamma + X$ and $\mathcal{O}(\alpha_s^2\alpha^6)$ for $pp \to t\bar{t}\gamma\gamma + X$ as well as the corresponding NLO QCD corrections. Furthermore, all subleading LO contributions and all remaining NLO corrections are also taken into account. In addition, NLO corrections, as well as photon radiation are consistently included in the production phase as well as in all decay stages of the process. Even if we have considerd the di-lepton decay channel of the top quark, the extension to hadronic decays of the W boson can be straightforwardly incorporated into our framework.

On the technical side, to perform these calculations, we have extended the Nagy-Soper subtraction scheme as implemented in the HELAC-DIPOLES Monte Carlo program for calculations with QED-like singularities and modified the structure of the program to allow the simultaneous calculation of all contributions at different orders in α_s and α.

The main findings of this paper apply to both processes and can be summarised as follows. At the integrated fiducial cross-section level, as well as for all the angular distributions we examined, the subleading LO contributions and subleading NLO corrections are negligibly small with respect to the NLO scale uncertainties of the complete result. On the other hand, the dominant NLO_1 contribution is essential for precise predictions, as it leads to a reduction in scale uncertainties from about 30% to 6%. Furthermore, it also introduces a change in the normalisation as well as in the shape of various differential cross-section distributions. In general, the inclusion of the subleading contributions has been found to be essential only in the tails of dimensionful observables due to one-loop EW Sudakov logarithms. Indeed, the presence of the EW Sudakov logarithms in NLO_2 leads to a reduction in the tails of up to 10% compared to the NLO_{QCD} result. Moreover, the NLO_2 contribution can be as large as the NLO_{QCD} scale uncertainties, potentially affecting the comparison between theoretical predictions and experimental measurements. In addition, for certain observables affected by large higher-order real-emission QCD corrections, e.g. for p_{T,b_1b_2}, the NLO_3 contribution can be enhanced from a few percent up to 10% with respect to LO_1. As the origins of the subleading NLO_2 and NLO_3 contributions are very different and there are random cancellations between them, they should always be considered together. We note here, that both the accidental cancellations between NLO_2 and NLO_3

as well as the size of real-emission QCD corrections depend on the exact event selection and can be substantially affected, for example, by applying a veto on an additional jet. Finally, the subleading LO contributions and the NLO_4 contribution are negligibly small at the integrated and differential fiducial cross-section level with respect to the NLO scale uncertainties.

An important finding of the paper is that the NLO_{prd} approximation models the complete NLO result very well. Indeed, differences of up to 2% only are found for some leptonic and/or photonic observables, but these are negligible compared to the NLO scale uncertainties of the complete result. We remind the readers that in NLO_{prd}, all LO contributions as well as NLO_1 are fully included in both the $t\bar{t}\gamma(\gamma)$ production and decays of the top-quark pair. However, the subleading NLO corrections (NLO_2, NLO_3, NLO_4) are only included in the production stage of the $t\bar{t}\gamma(\gamma)$ process. The same applies to photon radiation for these three NLO contributions. The NLO_{prd} approximation not only provides a great simplification of higher-order calculations, especially when it comes to the real emission corrections, but will ultimately also be of great benefit when matching NLO_{prd} predictions to parton shower programs.

Acknowledgments

We thank Ansgar Denner and Mathieu Pellen for providing us with the results for the NLO EW corrections to the $pp \to e^+\nu_e\mu^-\bar{\nu}_\mu b\bar{b} + X$ process that helped to cross check our implementation of the EW corrections in the HELAC-DIPOLES framework.

This work was supported by the Deutsche Forschungsgemeinschaft (DFG) under grant 396021762 – TRR 257: *P3H - Particle Physics Phenomenology after the Higgs Discovery*. Support by a grant of the Bundesministerium für Bildung und Forschung (BMBF) is additionally acknowledged.

The authors gratefully acknowledge the computing time provided to them at the NHR Center NHR4CES at RWTH Aachen University (project number `p0020216`). This is funded by the Federal Ministry of Education and Research, and the state governments participating on the basis of the resolutions of the GWK for national high performance computing at universities.

References

[1] F. Maltoni, D. Pagani and I. Tsinikos, *Associated production of a top-quark pair with vector bosons at NLO in QCD: impact on $t\bar{t}H$ searches at the LHC*, *JHEP* **02** (2016) 113 [1507.05640].

[2] K. Agashe et al., *Report of the Topical Group on Top quark physics and heavy flavor production for Snowmass 2021*, 2209.11267.

[3] K. Melnikov, M. Schulze and A. Scharf, *QCD corrections to top quark pair production in association with a photon at hadron colliders*, *Phys. Rev. D* **83** (2011) 074013 [1102.1967].

[4] G. Bevilacqua, H. B. Hartanto, M. Kraus, T. Weber and M. Worek, *Off-shell vs on-shell modelling of top quarks in photon associated production*, *JHEP* **03** (2020) 154 [1912.09999].

[5] U. Baur, M. Buice and L. H. Orr, *Direct measurement of the top quark charge at hadron colliders*, *Phys. Rev. D* **64** (2001) 094019 [hep-ph/0106341].

[6] D0 collaboration, *Measurement of the Electric Charge of the Top Quark in $t\bar{t}$ Events*, *Phys. Rev. D* **90** (2014) 051101 [1407.4837].

[7] ATLAS collaboration, *Measurement of the top quark charge in pp collisions at $\sqrt{s} = 7$ TeV with the ATLAS detector*, *JHEP* **11** (2013) 031 [1307.4568].

[8] U. Baur, A. Juste, L. H. Orr and D. Rainwater, *Probing electroweak top quark couplings at hadron colliders*, *Phys. Rev. D* **71** (2005) 054013 [hep-ph/0412021].

[9] A. O. Bouzas and F. Larios, *Electromagnetic dipole moments of the Top quark*, *Phys. Rev. D* **87** (2013) 074015 [1212.6575].

[10] R. Röntsch and M. Schulze, *Probing top-Z dipole moments at the LHC and ILC*, *JHEP* **08** (2015) 044 [1501.05939].

[11] M. Schulze and Y. Soreq, *Pinning down electroweak dipole operators of the top quark*, *Eur. Phys. J. C* **76** (2016) 466 [1603.08911].

[12] O. Bessidskaia Bylund, F. Maltoni, I. Tsinikos, E. Vryonidou and C. Zhang, *Probing top quark neutral couplings in the Standard Model Effective Field Theory at NLO in QCD*, *JHEP* **05** (2016) 052 [1601.08193].

[13] J. A. Aguilar-Saavedra, E. Álvarez, A. Juste and F. Rubbo, *Shedding light on the $t\bar{t}$ asymmetry: the photon handle*, *JHEP* **04** (2014) 188 [1402.3598].

[14] J. A. Aguilar-Saavedra, *Single lepton charge asymmetries in $t\bar{t}$ and $t\bar{t}\gamma$ production at the LHC*, *Eur. Phys. J. C* **78** (2018) 434 [1802.05721].

[15] J. Bergner and M. Schulze, *The top quark charge asymmetry in $t\bar{t}\gamma$ production at the LHC*, *Eur. Phys. J. C* **79** (2019) 189 [1812.10535].

[16] D. Pagani, H.-S. Shao, I. Tsinikos and M. Zaro, *Automated EW corrections with isolated photons: $t\bar{t}\gamma$, $t\bar{t}\gamma\gamma$ and $t\gamma j$ as case studies*, *JHEP* **09** (2021) 155 [2106.02059].

[17] R. Barcelo, A. Carmona, M. Masip and J. Santiago, *Stealth gluons at hadron colliders*, *Phys. Lett. B* **707** (2012) 88 [1106.4054].

[18] G. Marques Tavares and M. Schmaltz, *Explaining the $t\bar{t}$ asymmetry with a light axigluon*, *Phys. Rev. D* **84** (2011) 054008 [1107.0978].

[19] E. Alvarez, L. Da Rold, J. I. S. Vietto and A. Szynkman, *Phenomenology of a light gluon resonance in top-physics at Tevatron and LHC*, *JHEP* **09** (2011) 007 [1107.1473].

[20] J. A. Aguilar-Saavedra and M. Perez-Victoria, *Shaping the top asymmetry*, *Phys. Lett. B* **705** (2011) 228 [1107.2120].

[21] E. Alvarez, E. Coluccio Leskow, J. Drobnak and J. F. Kamenik, *Leptonic Monotops at LHC*, *Phys. Rev. D* **89** (2014) 014016 [1310.7600].

[22] D. Stremmer and M. Worek, *Associated production of a top-quark pair with two isolated photons at the LHC through NLO in QCD*, *JHEP* **08** (2023) 179 [2306.16968].

[23] CDF collaboration, *Evidence for $t\bar{t}\gamma$ Production and Measurement of $\sigma_t\bar{t}\gamma/\sigma_t\bar{t}$*, *Phys. Rev. D* **84** (2011) 031104 [1106.3970].

[24] ATLAS collaboration, *Observation of top-quark pair production in association with a photon and measurement of the $t\bar{t}\gamma$ production cross section in pp collisions at $\sqrt{s} = 7$ TeV using the ATLAS detector*, *Phys. Rev. D* **91** (2015) 072007 [1502.00586].

[25] ATLAS collaboration, *Measurement of the $t\bar{t}\gamma$ production cross section in proton-proton collisions at $\sqrt{s} = 8$ TeV with the ATLAS detector*, *JHEP* **11** (2017) 086 [1706.03046].

[26] CMS collaboration, *Measurement of the semileptonic $t\bar{t}\gamma$ production cross section in pp collisions at $\sqrt{s} = 8$ TeV*, *JHEP* **10** (2017) 006 [1706.08128].

[27] CMS collaboration, *Measurement of the inclusive and differential $t\bar{t}\gamma$ cross sections in the single-lepton channel and EFT interpretation at $\sqrt{s} = 13$ TeV*, *JHEP* **12** (2021) 180 [2107.01508].

[28] ATLAS collaboration, *Measurements of inclusive and differential fiducial cross-sections of $t\bar{t}\gamma$ production in leptonic final states at $\sqrt{s} = 13$ TeV in ATLAS*, *Eur. Phys. J. C* **79** (2019) 382 [1812.01697].

[29] ATLAS collaboration, *Measurements of inclusive and differential cross-sections of combined $t\bar{t}\gamma$ and $tW\gamma$ production in the $e\mu$ channel at 13 TeV with the ATLAS detector*, *JHEP* **09** (2020) 049 [2007.06946].

[30] CMS collaboration, *Measurement of the inclusive and differential $\mathrm{t\bar{t}}\gamma$ cross sections in the dilepton channel and effective field theory interpretation in proton-proton collisions at $\sqrt{s}$ =13 TeV*, *JHEP* **05** (2022) 091 [2201.07301].

[31] ATLAS collaboration, *Measurement of the charge asymmetry in top-quark pair production in association with a photon with the ATLAS experiment*, *Phys. Lett. B* **843** (2023) 137848 [2212.10552].

[32] P.-F. Duan, W.-G. Ma, R.-Y. Zhang, L. Han, L. Guo and S.-M. Wang, *QCD corrections to associated production of $t\bar{t}\gamma$ at hadron colliders*, *Phys. Rev. D* **80** (2009) 014022 [0907.1324].

[33] P.-F. Duan, R.-Y. Zhang, W.-G. Ma, L. Han, L. Guo and S.-M. Wang, *Next-to-leading order QCD corrections to $t\bar{t}\gamma$ production at the 7 TeV LHC*, *Chin. Phys. Lett.* **28** (2011) 111401 [1110.2315].

[34] P.-F. Duan, Y. Zhang, Y. Wang, M. Song and G. Li, *Electroweak corrections to top quark pair production in association with a hard photon at hadron colliders*, *Phys. Lett. B* **766** (2017) 102 [1612.00248].

[35] N. Kidonakis and A. Tonero, *Higher-order corrections in $tt^{-}\gamma$ cross sections*, *Phys. Rev. D* **107** (2023) 034013 [2212.00096].

[36] A. Kardos and Z. Trócsányi, *Hadroproduction of t anti-t pair in association with an isolated photon at NLO accuracy matched with parton shower*, *JHEP* **05** (2015) 090 [1406.2324].

[37] G. Bevilacqua, H. B. Hartanto, M. Kraus, T. Weber and M. Worek, *Hard Photons in Hadroproduction of Top Quarks with Realistic Final States*, *JHEP* **10** (2018) 158 [1803.09916].

[38] J. Alwall, R. Frederix, S. Frixione, V. Hirschi, F. Maltoni, O. Mattelaer et al., *The automated computation of tree-level and next-to-leading order differential cross sections, and their matching to parton shower simulations*, *JHEP* **07** (2014) 079 [1405.0301].

[39] A. Kardos and Z. Trócsányi, *Hadroproduction of $t\bar{t}$ pair with two isolated photons with PowHel*, *Nucl. Phys. B* **897** (2015) 717 [1408.0278].

[40] H. van Deurzen, R. Frederix, V. Hirschi, G. Luisoni, P. Mastrolia and G. Ossola, *Spin Polarisation of $t\bar{t}\gamma\gamma$ production at NLO+PS with GoSam interfaced to MadGraph5_aMC@NLO*, *Eur. Phys. J. C* **76** (2016) 221 [1509.02077].

[41] A. Denner, S. Dittmaier, M. Roth and D. Wackeroth, *Predictions for all processes $e^+e^- \to 4$ fermions $+ \gamma$*, *Nucl. Phys. B* **560** (1999) 33 [hep-ph/9904472].

[42] A. Denner, S. Dittmaier, M. Roth and L. H. Wieders, *Electroweak corrections to charged-current $e^+e^- \to 4$ fermion processes: Technical details and further results*, *Nucl. Phys. B* **724** (2005) 247 [hep-ph/0505042].

[43] K. Melnikov and M. Schulze, *NLO QCD corrections to top quark pair production and decay at hadron colliders*, *JHEP* **08** (2009) 049 [0907.3090].

[44] K. Melnikov, A. Scharf and M. Schulze, *Top quark pair production in association with a jet: QCD corrections and jet radiation in top quark decays*, *Phys. Rev. D* **85** (2012) 054002 [1111.4991].

[45] J. M. Campbell and R. K. Ellis, *Top-Quark Processes at NLO in Production and Decay*, *J. Phys. G* **42** (2015) 015005 [1204.1513].

[46] A. Behring, M. Czakon, A. Mitov, A. S. Papanastasiou and R. Poncelet, *Higher order corrections to spin correlations in top quark pair production at the LHC*, *Phys. Rev. Lett.* **123** (2019) 082001 [1901.05407].

[47] M. Czakon, A. Mitov and R. Poncelet, *NNLO QCD corrections to leptonic observables in top-quark pair production and decay*, *JHEP* **05** (2021) 212 [2008.11133].

[48] R. V. Harlander, S. Y. Klein and M. Lipp, *FeynGame*, *Comput. Phys. Commun.* **256** (2020) 107465 [2003.00896].

[49] R. Frederix, D. Pagani and M. Zaro, *Large NLO corrections in $t\bar{t}W^{\pm}$ and $t\bar{t}t\bar{t}$ hadroproduction from supposedly subleading EW contributions*, *JHEP* **02** (2018) 031 [1711.02116].

[50] R. Frederix, S. Frixione, V. Hirschi, D. Pagani, H. S. Shao and M. Zaro, *The automation of next-to-leading order electroweak calculations*, *JHEP* **07** (2018) 185 [1804.10017].

[51] A. Denner and M. Pellen, *NLO electroweak corrections to off-shell top-antitop production with leptonic decays at the LHC*, *JHEP* **08** (2016) 155 [1607.05571].

[52] A. Denner, D. Lombardi and G. Pelliccioli, *Complete NLO corrections to off-shell $t\bar{t}Z$ production at the LHC*, *JHEP* **09** (2023) 072 [2306.13535].

[53] G. Bevilacqua, M. Czakon, M. Kubocz and M. Worek, *Complete Nagy-Soper subtraction for next-to-leading order calculations in QCD*, *JHEP* **10** (2013) 204 [1308.5605].

[54] S. Catani and M. H. Seymour, *A General algorithm for calculating jet cross-sections in NLO QCD*, *Nucl. Phys. B* **485** (1997) 291 [hep-ph/9605323].

[55] S. Catani, S. Dittmaier, M. H. Seymour and Z. Trocsanyi, *The Dipole formalism for next-to-leading order QCD calculations with massive partons*, *Nucl. Phys. B* **627** (2002) 189 [hep-ph/0201036].

[56] G. Bevilacqua, M. Lupattelli, D. Stremmer and M. Worek, *Study of additional jet activity in top quark pair production and decay at the LHC*, *Phys. Rev. D* **107** (2023) 114027 [2212.04722].

[57] A. Denner and S. Dittmaier, *Electroweak Radiative Corrections for Collider Physics*, *Phys. Rept.* **864** (2020) 1 [1912.06823].

[58] Z. Nagy and Z. Trocsanyi, *Next-to-leading order calculation of four jet observables in electron positron annihilation*, *Phys. Rev. D* **59** (1999) 014020 [hep-ph/9806317].

[59] Z. Nagy, *Next-to-leading order calculation of three jet observables in hadron hadron collision*, *Phys. Rev. D* **68** (2003) 094002 [hep-ph/0307268].

[60] G. Bevilacqua, M. Czakon, C. G. Papadopoulos, R. Pittau and M. Worek, *Assault on the NLO Wishlist: $pp \to t\bar{t}b\bar{b}$*, *JHEP* **09** (2009) 109 [0907.4723].

[61] M. Czakon, H. B. Hartanto, M. Kraus and M. Worek, *Matching the Nagy-Soper parton shower at next-to-leading order*, *JHEP* **06** (2015) 033 [1502.00925].

[62] M. Czakon, C. G. Papadopoulos and M. Worek, *Polarizing the Dipoles*, *JHEP* **08** (2009) 085 [0905.0883].

[63] Z. Nagy and D. E. Soper, *Parton showers with quantum interference*, *JHEP* **09** (2007) 114 [0706.0017].

[64] J. M. Campbell, R. K. Ellis and F. Tramontano, *Single top production and decay at next-to-leading order*, *Phys. Rev. D* **70** (2004) 094012 [hep-ph/0408158].

[65] M. Jezabek and J. H. Kuhn, *QCD Corrections to Semileptonic Decays of Heavy Quarks*, *Nucl. Phys. B* **314** (1989) 1.

[66] A. Czarnecki, *QCD corrections to the decay $t \to Wb$ in dimensional regularization*, *Phys. Lett. B* **252** (1990) 467.

[67] L. Basso, S. Dittmaier, A. Huss and L. Oggero, *Techniques for the treatment of IR divergences in decay processes at NLO and application to the top-quark decay*, *Eur. Phys. J. C* **76** (2016) 56 [1507.04676].

[68] T. Binoth, G. Ossola, C. G. Papadopoulos and R. Pittau, *NLO QCD corrections to tri-boson production*, *JHEP* **06** (2008) 082 [0804.0350].

[69] G. Bevilacqua, H. B. Hartanto, M. Kraus and M. Worek, *Off-shell Top Quarks with One Jet at the LHC: A comprehensive analysis at NLO QCD*, *JHEP* **11** (2016) 098 [1609.01659].

[70] A. van Hameren, *PARNI for importance sampling and density estimation*, *Acta Phys. Polon. B* **40** (2009) 259 [0710.2448].

[71] A. van Hameren, *Kaleu: A General-Purpose Parton-Level Phase Space Generator*, 1003.4953.

[72] J. Alwall et al., *A Standard format for Les Houches event files*, *Comput. Phys. Commun.* **176** (2007) 300 [hep-ph/0609017].

[73] Z. Bern, L. J. Dixon, F. Febres Cordero, S. Höche, H. Ita, D. A. Kosower et al., *Ntuples for NLO Events at Hadron Colliders*, *Comput. Phys. Commun.* **185** (2014) 1443 [1310.7439].

[74] S. Actis, A. Denner, L. Hofer, J.-N. Lang, A. Scharf and S. Uccirati, *RECOLA: REcursive Computation of One-Loop Amplitudes*, *Comput. Phys. Commun.* **214** (2017) 140 [1605.01090].

[75] S. Actis, A. Denner, L. Hofer, A. Scharf and S. Uccirati, *Recursive generation of one-loop amplitudes in the Standard Model*, *JHEP* **04** (2013) 037 [1211.6316].

[76] P. Draggiotis, R. H. P. Kleiss and C. G. Papadopoulos, *On the computation of multigluon amplitudes*, *Phys. Lett. B* **439** (1998) 157 [hep-ph/9807207].

[77] P. D. Draggiotis, R. H. P. Kleiss and C. G. Papadopoulos, *Multijet production in hadron collisions*, *Eur. Phys. J. C* **24** (2002) 447 [hep-ph/0202201].

[78] A. van Hameren, *Multi-gluon one-loop amplitudes using tensor integrals*, *JHEP* **07** (2009) 088 [0905.1005].

[79] A. Denner, S. Dittmaier and L. Hofer, *Collier: a fortran-based Complex One-Loop LIbrary in Extended Regularizations*, *Comput. Phys. Commun.* **212** (2017) 220 [1604.06792].

[80] A. Denner and S. Dittmaier, *Reduction schemes for one-loop tensor integrals*, *Nucl. Phys. B* **734** (2006) 62 [hep-ph/0509141].

[81] A. Denner and S. Dittmaier, *Reduction of one loop tensor five point integrals*, *Nucl. Phys. B* **658** (2003) 175 [hep-ph/0212259].

[82] A. Denner and S. Dittmaier, *Scalar one-loop 4-point integrals*, *Nucl. Phys. B* **844** (2011) 199 [1005.2076].

[83] G. Ossola, C. G. Papadopoulos and R. Pittau, *CutTools: A Program implementing the OPP reduction method to compute one-loop amplitudes*, *JHEP* **03** (2008) 042 [0711.3596].

[84] A. van Hameren, *OneLOop: For the evaluation of one-loop scalar functions*, *Comput. Phys. Commun.* **182** (2011) 2427 [1007.4716].

[85] G. Ossola, C. G. Papadopoulos and R. Pittau, *Reducing full one-loop amplitudes to scalar integrals at the integrand level*, *Nucl. Phys. B* **763** (2007) 147 [hep-ph/0609007].

[86] F. Buccioni, S. Pozzorini and M. Zoller, *On-the-fly reduction of open loops*, *Eur. Phys. J. C* **78** (2018) 70 [1710.11452].

[87] A. Denner, J.-N. Lang and M. Pellen, *Full NLO QCD corrections to off-shell $t\bar{t}b\bar{b}$ production*, *Phys. Rev. D* **104** (2021) 056018 [2008.00918].

[88] A. Denner, J.-N. Lang and S. Uccirati, *Recola2: REcursive Computation of One-Loop Amplitudes 2*, *Comput. Phys. Commun.* **224** (2018) 346 [1711.07388].

[89] A. Denner, G. Weiglein and S. Dittmaier, *Application of the background field method to the electroweak standard model*, *Nucl. Phys. B* **440** (1995) 95 [hep-ph/9410338].

[90] A. Denner, J.-N. Lang and S. Uccirati, *NLO electroweak corrections in extended Higgs Sectors with RECOLA2*, *JHEP* **07** (2017) 087 [1705.06053].

[91] A. Denner and S. Dittmaier, *The Complex-mass scheme for perturbative calculations with unstable particles*, *Nucl. Phys. B Proc. Suppl.* **160** (2006) 22 [hep-ph/0605312].

[92] A. Sirlin, *Radiative Corrections in the SU(2)-L x U(1) Theory: A Simple Renormalization Framework*, *Phys. Rev. D* **22** (1980) 971.

[93] A. Denner, *Techniques for calculation of electroweak radiative corrections at the one loop level and results for W physics at LEP-200*, *Fortsch. Phys.* **41** (1993) 307 [0709.1075].

[94] W. F. L. Hollik, *Radiative Corrections in the Standard Model and their Role for Precision Tests of the Electroweak Theory*, *Fortsch. Phys.* **38** (1990) 165.

[95] W. J. Marciano and A. Sirlin, *Radiative Corrections to Neutrino Induced Neutral Current Phenomena in the SU(2)-L x U(1) Theory*, *Phys. Rev. D* **22** (1980) 2695.

[96] A. Manohar, P. Nason, G. P. Salam and G. Zanderighi, *How bright is the proton? A precise determination of the photon parton distribution function*, *Phys. Rev. Lett.* **117** (2016) 242002 [1607.04266].

[97] NNPDF collaboration, *Parton distributions from high-precision collider data*, *Eur. Phys. J. C* **77** (2017) 663 [1706.00428].

[98] A. V. Manohar, P. Nason, G. P. Salam and G. Zanderighi, *The Photon Content of the Proton*, *JHEP* **12** (2017) 046 [1708.01256].

[99] NNPDF collaboration, *Illuminating the photon content of the proton within a global PDF analysis*, *SciPost Phys.* **5** (2018) 008 [1712.07053].

[100] A. Buckley, J. Ferrando, S. Lloyd, K. Nordström, B. Page, M. Rüfenacht et al., *LHAPDF6: parton density access in the LHC precision era*, *Eur. Phys. J. C* **75** (2015) 132 [1412.7420].

[101] Particle Data Group collaboration, *Review of Particle Physics*, *PTEP* **2022** (2022) 083C01.

[102] A. Denner, S. Dittmaier, S. Kallweit and S. Pozzorini, *NLO QCD corrections to off-shell top-antitop production with leptonic decays at hadron colliders*, *JHEP* **10** (2012) 110 [1207.5018].

[103] M. Cacciari, G. P. Salam and G. Soyez, *The anti-k_t jet clustering algorithm*, *JHEP* **04** (2008) 063 [0802.1189].

[104] S. Frixione, *Isolated photons in perturbative QCD*, *Phys. Lett. B* **429** (1998) 369 [hep-ph/9801442].

[105] A. Denner, S. Dittmaier, M. Hecht and C. Pasold, *NLO QCD and electroweak corrections to $W + \gamma$ production with leptonic $W-$boson decays*, *JHEP* **04** (2015) 018 [1412.7421].

[106] A. Denner, S. Dittmaier, M. Hecht and C. Pasold, *NLO QCD and electroweak corrections to $Z + \gamma$ production with leptonic $Z-$boson decays*, *JHEP* **02** (2016) 057 [1510.08742].

[107] A. Denner and R. Feger, *NLO QCD corrections to off-shell top-antitop production with leptonic decays in association with a Higgs boson at the LHC*, *JHEP* **11** (2015) 209 [1506.07448].

[108] G. Bevilacqua, H. B. Hartanto, M. Kraus, T. Weber and M. Worek, *Towards constraining Dark Matter at the LHC: Higher order QCD predictions for $t\bar{t} + Z(Z \to \nu_\ell \bar{\nu}_\ell)$*, *JHEP* **11** (2019) 001 [1907.09359].

[109] D. Stremmer and M. Worek, *Production and decay of the Higgs boson in association with top quarks*, *JHEP* **02** (2022) 196 [2111.01427].

An assessment of Υ-states above $B\bar{B}$-threshold using a constituent-quark-model based meson-meson coupled-channels framework

P. G. Ortega,[1,2,*] D. R. Entem,[1,2,†] F. Fernández,[2,‡] and J. Segovia[3,§]

[1] *Departamento de Física Fundamental, Universidad de Salamanca, E-37008 Salamanca, Spain*
[2] *Instituto Universitario de Física Fundamental y Matemáticas (IUFFyM), Universidad de Salamanca, E-37008 Salamanca, Spain*
[3] *Departamento de Sistemas Físicos, Químicos y Naturales, Universidad Pablo de Olavide, E-41013 Sevilla, Spain*

(Dated: March 7, 2024)

The $\Upsilon(10753)$ state has been recently observed by the Belle and Belle II collaborations with enough global significance to motivate an assessment of the high-energy spectrum usually predicted by any reasonable *naïve* quark model. In the framework of a constituent quark model which satisfactorily describes a wide range of properties of conventional hadrons containing heavy quarks, the quark-antiquark and meson-meson degrees of freedom have been incorporated with the goal of elucidating the influence of open-bottom meson-meson thresholds into the Υ states whose masses are within the energy range of the $\Upsilon(10753)$'s mass. It is well known that such effects could be relevant enough as to generate dynamically new states and thus provide a plausible explanation of the nature of the $\Upsilon(10753)$ state. In particular, we have performed a coupled-channels calculation in which the bare states $\Upsilon(4S)$, $\Upsilon(3D)$, $\Upsilon(5S)$ and $\Upsilon(4D)$ are considered together with the threshold channels $B\bar{B}$, $B\bar{B}^*$, $B^*\bar{B}^*$, $B_s\bar{B}_s$, $B_s\bar{B}_s^*$ and $B_s^*\bar{B}_s^*$. Among the results we have described, the following conclusions are of particular interest: (i) a richer complex spectrum is gained when thresholds are present and bare bound states are sufficiently non-relativistic; (ii) those poles obtained in the complex energy plane do not have to appear as simple peaks in the relevant cross sections; and (iii) the $\Upsilon(10750)$ candidate is interpreted as a dressed hadronic resonance whose structure is an equally mixture of a conventional $b\bar{b}$ state and $B^*\bar{B}^*$ molecule.

arXiv:2403.03770v1 [hep-ph] 6 Mar 2024

I. INTRODUCTION

The so-called Υ-family, also known as bottomonia, are bound states made of a b-quark and its antiquark, $\bar{b}$, with quantum numbers $J^{PC} = 1^{--}$. They were identified for the first time by the E288 Collaboration at Fermilab in 1977 while studying proton scattering on Cu and Pb targets in an energy regime of muon-antimuon invariant mass larger than 5 GeV [1, 2]. The three observed states were called $\Upsilon(1S)$, $\Upsilon(2S)$ and $\Upsilon(3S)$; later, they were better studied at various e^+e^- storage rings and through their radiative decays into the $\chi_{bJ}(2P)$ and $\chi_{bJ}(1P)$ states, with $J = 0, 1, 2$, in a series of experiments in the 1980s [3–6]. Despite such early experimental efforts, during the next two decades there were no significant contributions to the spectrum of the Υ-family, except the presumably radial excitations of S-wave nature $\Upsilon(4S)$, $\Upsilon(10860)$ and $\Upsilon(11020)$ [7, 8]. This has been largely because the B-factories were not considered ideal facilities for the study of the bottomonium system since their beam energy was tuned to peak at the $\Upsilon(4S)$ mass, 10579 MeV, which decays in almost 100% of cases to a $B\bar{B}$ pair.

The situation has changed dramatically in the last twenty years with more than two dozens of unconventional charmonium- and bottomonium-like states, the so-called XYZ mesons, observed at B-factories (BaBar, Belle and CLEO), τ-charm facilities (CLEO-c and BESIII) and also proton–(anti-)proton colliders (CDF, D0, LHCb, ATLAS and CMS). For an extensive presentation of the status of heavy quarkonium physics, the reader is referred to several reviews [9–29].

Within the Υ-family, the Belle collaboration [30] reported in 2019 a cross section measurement of the $e^+e^- \to \pi^+\pi^-\Upsilon(nS)$, with $n = 1, 2, 3$, at energies from 10.52 to 11.02 GeV, observing a new structure, $\Upsilon(10753)$, with Breit-Wigner parameters:

$$M = \left(10752.7 \pm 5.9^{+0.7}_{-1.1}\right) \text{MeV}\,, \tag{1}$$

$$\Gamma = \left(35.5^{+17.6+3.9}_{-11.3-3.3}\right) \text{MeV}\,, \tag{2}$$

where the first error is statistical and the second is systematic. The global significance of the new resonance was 5.2 standard deviations, including systematic uncertainty. Later on, the Belle II collaboration [31] reported in 2022 the first observation of $\omega\chi_{bJ}(1P)$ ($J = 0, 1, 2$) signals at $\sqrt{s} = 10.745$ GeV. By combining Belle II data with Belle results at $\sqrt{s} = 10.867$ GeV, they find energy dependencies of the Born cross sections for $e^+e^- \to \omega\chi_{b1,b2}(1P)$ to be consistent with the shape of the $\Upsilon(10753)$ resonance; this time, the Breit-Wigner parameters were

$$M = \left(10753 \pm 6\right) \text{MeV}\,, \quad \Gamma = \left(36^{+18}_{-12}\right) \text{MeV}\,, \tag{3}$$

and the suggested quantum numbers $J^P = 1^-$.

Note also that experimentalists have been able to distinguish the $\Upsilon(1^3D_2)$ state of the triplet $\Upsilon(1^3D_J)$,

* pgortega@usal.es
† entem@usal.es
‡ fdz@usal.es
§ jsegovia@upo.es

with $J = 1, 2, 3$ [32, 33]. In Ref. [33], the $\Upsilon(1^3D_2)$ was observed through the $\Upsilon(3S) \to \gamma\gamma\Upsilon(1^3D_J) \to \gamma\gamma\pi^+\pi^-\Upsilon(1S)$ decay chain with a significance of 5.8σ, including systematic uncertainties, and a mass of $(10164.5 \pm 0.8 \pm 0.5)\,\text{MeV}$. For the other two almost-degenerate members of the $\Upsilon(1^3D_J)$ spin-triplet, $\Upsilon(1^3D_1)$ and $\Upsilon(1^3D_3)$, the significances were much lower, 1.8 and 1.6 respectively, and thus no experimental observation could be claimed.

An enormous theoretical effort has followed the experimental discoveries; in particular, focusing on the bottomonium sector, one can highlight the work done using Lattice-regularized QCD [34, 35], functional methods [36–39], QCD sum rules [40–42], effective field theories [43–46] and quark models [47–51]. Most of the mentioned references focus on the description of conventional bottomonium. This is because the first open-bottom threshold is higher in energy than the corresponding one in the charmonium sector and thus a larger number of conventional states are expected below $B\bar{B}$-threshold. Moreover, the only experimentally discovered excited states which are above the $B\bar{B}$-threshold, and so they have the ability to be strongly influenced by meson-meson thresholds, are $\Upsilon(4S)$, $\Upsilon(10860)$ and $\Upsilon(11020)$, besides the unconfirmed state $\Upsilon(10753)$.

Herein, we study the high-energy spectrum of the Υ-family in the framework of a constituent quark model [52] which satisfactorily describes a wide range of properties of conventional hadrons containing heavy quarks [53, 54]. The quark-antiquark and meson-meson degrees of freedom are incorporated with the goal of elucidating the influence of open-bottom meson-meson thresholds in the conventional states but, above all, to shed some light on the nature and structure of the $\Upsilon(10753)$ state. We should briefly mention that *charged* bottomonium-like states $Z_b(10610)^\pm$ and $Z_b(10650)^\pm$ were identified by the Belle Collaboration [55] as peaks in the invariant mass distribution of the $\pi^\pm h_b(mP)$ $(m = 1, 2)$ and $\pi^\pm\Upsilon(nS)$ $(n = 1, 2, 3)$ subsystems when the $\Upsilon(10860)$ resonance decays into two pions plus an h_b or Υ. The quantum numbers of the Z_b's were analyzed to be $I^G(J^{PC}) = 1^+(1^{+-})$ [56] and so they belong to the isospin $I = 1$ sector of bottomonium-like particles, disconnected from the conventional bottomonium states of isospin $I = 0$. In fact such exotic mesons were studied by us in Ref. [57].

A variational formalism based on a highly efficient numerical approach named the Gaussian expansion method (GEM) [58] is used to solve the bottomonium Hamiltonian. Moreover, this Gaussian expansion allows us to compute effective meson-meson interactions from the original quark–(anti-)quark potentials in a simplified way through the so-called Resonating Group Method [59, 60]. Finally, within our approach, the coupling between the quark-antiquark and meson-meson sectors requires the creation of a light quark-antiquark pair. Therefore, the associated operator should be similar to the one describing open-flavor meson strong decays and we adopt the $^3P_0$ transition operator described in, for instance, Ref. [61]. This theoretical formalism has the advantage of easily introducing the coupling with all meson-meson partial waves and the straightforward computation of the probabilities associated with the different Fock components of the physical state.

The manuscript is organized as follows. After this introduction, the theoretical framework is briefly presented in section II. Section III is mainly devoted to the analysis and discussion of our theoretical results. Finally, we summarize and draw some conclusions in Sec. IV.

II. THEORETICAL FRAMEWORK

A. CONSTITUENT QUARK MODEL

Among the wide range of chiral quark models developed in the last 50 years [62], our theoretical framework is a QCD-inspired constituent quark model (CQM) proposed in Ref. [52] and extensively reviewed in Refs. [53, 54]. Moreover, the CQM has been recently applied with success to conventional mesons containing heavy quarks, describing a wide range of physical observables that concern spectra [63–66], strong decays [67–70], hadronic transitions [71–73] as well as electromagnetic and weak reactions [74–76].

The main pieces of our CQM are spontaneous chiral symmetry breaking of the QCD Lagrangian together with perturbative one-gluon exchange (OGE) and non-perturbative color confining interactions. In the heavy quark sector, chiral symmetry is explicitly broken and Goldstone-boson exchanges do not appear. Thus, OGE and confinement are the only interactions remaining.

The OGE potential contains central, tensor and spin-orbit contributions given by

$$V_{\rm OGE}^{\rm C}(\vec{r}_{ij}) = +\frac{1}{4}\alpha_s(\vec{\lambda}_i^c\cdot\vec{\lambda}_j^c)\left[\frac{1}{r_{ij}} - \frac{1}{6m_im_j}(\vec{\sigma}_i\cdot\vec{\sigma}_j)\frac{e^{-r_{ij}/r_0(\mu)}}{r_{ij}r_0^2(\mu)}\right], \tag{4a}$$

$$V_{\rm OGE}^{\rm T}(\vec{r}_{ij}) = -\frac{1}{16}\frac{\alpha_s}{m_im_j}(\vec{\lambda}_i^c\cdot\vec{\lambda}_j^c)\left[\frac{1}{r_{ij}^3} - \frac{e^{-r_{ij}/r_g(\mu)}}{r_{ij}}\left(\frac{1}{r_{ij}^2}+\frac{1}{3r_g^2(\mu)}+\frac{1}{r_{ij}r_g(\mu)}\right)\right]S_{ij}\,, \tag{4b}$$

$$V_{\rm OGE}^{\rm SO}(\vec{r}_{ij}) = -\frac{1}{16}\frac{\alpha_s}{m_i^2m_j^2}(\vec{\lambda}_i^c\cdot\vec{\lambda}_j^c)\left[\frac{1}{r_{ij}^3} - \frac{e^{-r_{ij}/r_g(\mu)}}{r_{ij}^3}\left(1+\frac{r_{ij}}{r_g(\mu)}\right)\right]$$
$$\times\left[((m_i+m_j)^2+2m_im_j)(\vec{S}_+\cdot\vec{L}) + (m_j^2-m_i^2)(\vec{S}_-\cdot\vec{L})\right], \tag{4c}$$

where $r_0(\mu) = \hat{r}_0\frac{\mu_{nn}}{\mu_{ij}}$ and $r_g(\mu) = \hat{r}_g\frac{\mu_{nn}}{\mu_{ij}}$ are regulators which depend on μ_{ij}, the reduced mass of the $q\bar{q}$-pair; for example, $\mu_{nn} = m_n/2$ with m_n the mass of the light quark with $n = u$- or d-quark. The contact term of the central potential has been regularized as follows

$$\delta(\vec{r}_{ij}) \approx \frac{1}{4\pi r_0^2}\frac{e^{-r_{ij}/r_0}}{r_{ij}}\,. \tag{5}$$

The wide energy range needed to provide a consistent description of light, strange and heavy mesons requires an effective scale-dependent strong coupling constant. We use the frozen coupling constant of Ref. [52],

$$\alpha_s(\mu_{ij}) = \frac{\alpha_0}{\ln\left(\frac{\mu_{ij}^2+\mu_0^2}{\Lambda_0^2}\right)}\,, \tag{6}$$

in which α_0, μ_0 and Λ_0 are parameters of the model determined by a global fit to the meson spectra.

The different pieces of the color confining potential are

$$V_{\rm CON}^{\rm C}(\vec{r}_{ij}) = \left[-a_c(1-e^{-\mu_c r_{ij}})+\Delta\right](\vec{\lambda}_i^c\cdot\vec{\lambda}_j^c)\,, \tag{7a}$$

$$V_{\rm CON}^{\rm SO}(\vec{r}_{ij}) = -(\vec{\lambda}_i^c\cdot\vec{\lambda}_j^c)\frac{a_c\mu_c e^{-\mu_c r_{ij}}}{4m_i^2m_j^2r_{ij}}$$
$$\times\Big[((m_i^2+m_j^2)(1-2a_s) + 4m_im_j(1-a_s))(\vec{S}_+\cdot\vec{L}) + (m_j^2-m_i^2)(1-2a_s)(\vec{S}_-\cdot\vec{L})\Big], \tag{7b}$$

where the mixture between scalar and vector Lorentz structures of the color confinement is controlled by a_s. Besides, this potential presents at short inter-quark distances a linear behavior with an effective confinement strength given by $\sigma = -a_c\,\mu_c\,(\vec{\lambda}_i^c\cdot\vec{\lambda}_j^c)$, while it becomes constant at very large inter-quark distances showing a threshold defined by

$$V_{\rm thr} = (-a_c+\Delta)\cdot(\vec{\lambda}_i^c\cdot\vec{\lambda}_j^c)\,; \tag{8}$$

viz. there is no $q\bar{q}$ bound states with eigenenergies higher than this threshold; the system suffers a transition from a color string configuration between two static color sources into a pair of static mesons due to the breaking of the color string and the most favored decay into hadrons.

Among the different theoretical formalisms to solve the Schrödinger equation, in order to find the quark-antiquark bound states, we use the Rayleigh-Ritz variational method in which the wave function solution of the Schrödinger equation is expanded as indicated by the Gaussian Expansion Method (GEM) [58]. It has also been proven to be quite efficient on solving the bound-state problem of a few-body system [77–82], providing enough accuracy and simplifying the evaluation of matrix elements.

The radial wave function is then expressed as

$$R_\alpha(r) = \sum_{n=1}^{n_{max}} c_n^\alpha\phi_{nl}^G(r)\,, \tag{9}$$

where α refers to the channel quantum numbers. The coefficients, c_n^α, and the eigenvalue, E, are determined from the Rayleigh-Ritz variational principle:

$$\sum_{n'=1}^{n_{max}}\left[(T_{nn'}^\alpha - EN_{nn'}^\alpha)\,c_{n'}^\alpha + \sum_{\alpha'=1}^{\rm channels} V_{nn'}^{\alpha\alpha'}c_{n'}^{\alpha'} = 0\right], \tag{10}$$

where $T_{nn'}^\alpha$, $N_{nn'}^\alpha$ and $V_{nn'}^{\alpha\alpha'}$ are, respectively, the matrix elements of the kinetic energy, the normalization and the potential. $T_{nn'}^\alpha$ and $N_{nn'}^\alpha$ are diagonal, whereas the mixing between different channels is given by $V_{nn'}^{\alpha\alpha'}$.

Following Ref. [58], we employ Gaussian trial functions with ranges in geometric progression. This enables the optimization of ranges employing a small number of free parameters. Moreover, the geometric progression is dense at short distances, so that it enables the description of the dynamics mediated by short range potentials. The fast damping of the Gaussian tail does not represent an issue, since we can choose the maximal range much longer than the hadronic size.

B. COUPLED-CHANNELS CALCULATION

It is well known that conventional mesons must be influenced in a non-perturbative way by meson-meson thresholds when these are close. In order to take into account this effect within the bottomonium sector, we perform a coupled-channels calculation in which the total hadron wavefunction is described by a combination of conventional $b\bar{b}$ states and open-bottom meson-meson channels:

$$|\Psi\rangle = \sum_{\alpha} c_\alpha |\psi_\alpha\rangle + \sum_{\beta} \chi_\beta(P) |\phi_A \phi_B \beta\rangle \,, \tag{11}$$

where $|\psi_\alpha\rangle$ are $b\bar{b}$ eigenstates of the two-body Hamiltonian, ϕ_M is the wavefunction associated with meson $M = A, B$, $|\phi_A\phi_B\beta\rangle$ is the two meson state whose quantum numbers are β and $\chi_\beta(P)$ is the relative wave function between the two mesons.

Under the above assumption, two sources of interaction emerge. On one hand, the two- and four-quark sectors can be coupled via the creation of a light-quark-antiquark pair. On the other hand, there is a residual interaction, derived from the microscopic quark–(anti-)quark potential described by the CQM, among the two mesons. To derive the latter, we use the Resonating Group Method (RGM) [59, 60] (see also Refs. [26, 83] for further details).

Within RGM, the wave function of a system composed of two mesons with distinguishable quarks is given by

$$\langle \vec{p}_A \vec{p}_B \vec{P} \vec{P}_{\rm c.m.} | \phi_A \phi_B \beta \rangle = \phi_A(\vec{p}_A) \phi_B(\vec{p}_B) \chi_\beta(\vec{P}) \,, \tag{12}$$

where, *e.g.*, $\phi_A(\vec{p}_A)$ is the wave function of the meson A with $\vec{p}_A$ the relative momentum between its quark and antiquark. The wave function $\chi_\beta(\vec{P})$ takes into account the relative motion between the two mesons.

A general process $AB \to A'B'$ can be described by means of either direct or exchange potentials; the last ones appear due to the possibility of having to consider quark exchanges between clusters. In this study we do not have this case, so we only have direct potentials, which can be written as

$$\begin{aligned} {}^{\rm RGM}V_D^{\beta\beta'}(\vec{P}', \vec{P}) = \sum_{i\in A, j\in B} \int d\vec{p}_{A'} d\vec{p}_{B'} d\vec{p}_A d\vec{p}_B \\ \times \phi_A^*(\vec{p}_{A'}) \phi_B^*(\vec{p}_{B'}) V_{ij}^{\beta\beta'}(\vec{P}', \vec{P}) \phi_{A'}(\vec{p}_A) \phi_{B'}(\vec{p}_B) \,. \end{aligned} \tag{13}$$

where $\beta^{(\prime)}$ labels the set of quantum numbers needed to uniquely define a certain meson-meson partial wave, $\vec{P}^{(\prime)}$ are the initial (final) relative momentum of the meson-meson pair, and $V_{ij}^{\beta\beta'}(\vec{P}', \vec{P})$ are the microscopic quark–(anti-)quark potentials from the CQM and the sum runs over the constituent particles inside each meson cluster.

The coupling between the bottomonia and the open-bottom meson-meson thresholds requires the creation of a light quark-antiquark pair. For that purpose, we use the ${}^3P_0$ transition operator which was originally introduced in the 1970s to describe strong decays of mesons and baryons [61, 84, 85]. The associated non-relativistic operator can be written as [67, 70]:

$$\begin{aligned} T = -\sqrt{3} \sum_{\mu,\nu} \int d^3p_\mu d^3p_\nu \delta^{(3)}(\vec{p}_\mu + \vec{p}_\nu) \frac{g_s}{2m_\mu} \sqrt{2^5\pi} \\ \times \left[\mathcal{Y}_1\left(\frac{\vec{p}_\mu - \vec{p}_\nu}{2}\right) \otimes \left(\frac{1}{2}\frac{1}{2}\right) 1 \right]_0 a_\mu^\dagger(\vec{p}_\mu) b_\nu^\dagger(\vec{p}_\nu) \,. \end{aligned} \tag{14}$$

where μ (ν) are the spin, flavor and color quantum numbers of the created quark (antiquark). The orbital angular momentum and spin of the pair are both equal to one. Note that $\mathcal{Y}_{lm}(\vec{p}) = p^l Y_{lm}(\hat{p})$ is the solid harmonic defined in function of the spherical one. The unique parameter of the decay model is the strength of the quark-antiquark pair creation from the vacuum, $\gamma = g_s/2m$, where m is the mass of the created quark (antiquark).

The values of γ can be constrained through meson strong decays. A global fit to charmed, charmed-strange, hidden-charm and hidden-bottom sectors was performed in Ref. [67], finding a running of the strength parameter given by

$$\gamma(\mu) = \frac{\gamma_0}{\log\left(\frac{\mu}{\mu_0}\right)} \,, \tag{15}$$

where γ_0 and μ_0 are free parameters, whereas μ is the reduced mass of the constituent quark-antiquark pair of the decaying meson. In this work, we use the value of γ corresponding to the bottomonium sector, *i.e.* $\gamma = 0.205$.

From the operator in Eq. (14), we define the meson to meson-meson transition potential $h_{\beta\alpha}(P)$ as

$$\langle \phi_{M_1} \phi_{M_2} \beta | T | \psi_\alpha \rangle = \delta^{(3)}(\vec{P}_{\rm cm})\, P\, h_{\beta\alpha}(P), \tag{16}$$

where P is the relative momentum of the two-meson state. In order to soften the ${}^3P_0$ production vertex at high momenta, we follow the suggestion of Ref. [86] and used a Gaussian-like momentum-dependent form factor to truncate the vertex,

$$h_{\beta\alpha}(P) \to h_{\beta\alpha}(P) e^{-\frac{P^2}{2\Lambda^2}} \,, \tag{17}$$

with $\Lambda = 0.84\,\text{GeV}$. This cut-off's value is taken from similar analysis [87, 88], so no fine-tuning of parameters is employed in the present work.

Finally, within the formalism explained above, the coupled-channels equations can be written as

$$c_\alpha M_\alpha + \sum_\beta \int h_{\alpha\beta}(P) \chi_\beta(P) P^2 dP = E c_\alpha \,, \tag{18}$$

$$\begin{aligned} \sum_\beta \int H_{\beta'\beta}(P', P) \chi_\beta(P) P^2 dP + \\ + \sum_\alpha h_{\beta'\alpha}(P') c_\alpha = E \chi_{\beta'}(P') \,, \end{aligned} \tag{19}$$

where M_α are the masses of the bare $b\bar{b}$ mesons and $H_{\beta'\beta}$ is the RGM Hamiltonian for the two-meson states obtained from the naive CQM interaction. In order to explore states above and below meson-meson thresholds,

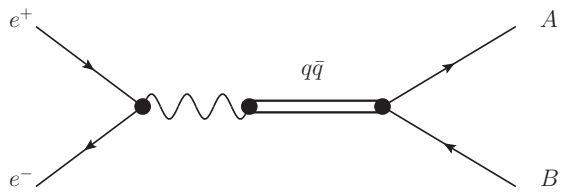

FIG. 1. Production of open-bottom mesons denoted by the AB-pair through a $q\bar{q}$ resonance with $J^{PC} = 1^{--}$. In this case a conventional state of the Υ-family is produced that decays later on in a pair of open-bottom mesons.

the former coupled-channels equations should then be written as a set of coupled Lippmann-Schwinger equations,

$$T_\beta^{\beta'}(E;p',p) = V_\beta^{\beta'}(p',p) + \sum_{\beta''}\int dp''\, p''^2\, V_{\beta''}^{\beta'}(p',p'') \times \frac{1}{E-\mathcal{E}_{\beta''}(p'')}\, T_\beta^{\beta''}(E;p'',p)\,, \tag{20}$$

where $V_\beta^{\beta'}(p',p)$ is the projected potential that contains the sum of direct potentials, Eq. (13), as well as the effective potential which encodes the coupling with the two-quark sector:

$$V_{\text{eff}}^{\beta'\beta}(P',P;E) = \sum_\alpha \frac{h_{\beta'\alpha}(P')h_{\alpha\beta}(P)}{E-M_\alpha}\,. \tag{21}$$

The $\mathcal{E}_{\beta''}(p'')$ is the energy corresponding to a momentum p'', which in the nonrelativistic case is

$$\mathcal{E}_\beta(p) = \frac{p^2}{2\mu_\beta} + \Delta M_\beta\,. \tag{22}$$

Herein, μ_β is the reduced mass of the meson-meson system corresponding to the channel β, and ΔM_β is the difference between the meson-meson threshold and the lightest one, taken as a reference.

Once the T-matrix is calculated, we determine its on-shell part which is directly related to the scattering matrix in the case of non-relativistic kinematics:

$$S_\beta^{\beta'} = 1 - 2\pi i\sqrt{\mu_\beta\mu_{\beta'}k_\beta k_{\beta'}}\, T_\beta^{\beta'}(E+i0^+;k_{\beta'},k_\beta)\,, \tag{23}$$

with k_β the on-shell momentum for channel β. All the potentials shall be analytically continued for complex momenta; this allows us to find the poles of the T-matrix in any possible Riemann sheet.

C. Production in annihilation e^+e^- through a resonance

For later convenience, our objective herein is to calculate cross section of the process $e^+e^- \to AB$ (represented in Fig. 1), with A or B denoting open-bottom mesons, through an arbitrary set of $b\bar{b}$ resonances with quantum numbers $J^{PC} = 1^{--}$. For that purpose we use the extended Van Royen-Weisskopf formalism for meson leptonic decays, considering non-zero momentum distribution for the quark (antiquark) inside the meson [89]. It should be noticed that the Feynman diagram in Fig. 1 can be used when the quark-antiquark pair acts as free particles and has a certain momentum, in this case weighted with the corresponding Υ meson's wave function, $\phi(\vec{p})$, which gives the probability amplitude of finding a quark with momentum $\vec{p}$ inside the $b\bar{b}$ meson.

The process to be studied is $\langle e^+e^-|AB\rangle_\beta$ through one or few $|q\bar{q}\rangle_\alpha$ resonances. This process can be factorized as,

$$\langle e^+e^-|AB\rangle_\beta = \sum_\alpha \langle e^+e^-|q\bar{q}\rangle_{\alpha\,\alpha}\langle q\bar{q}|AB\rangle_\beta\,. \tag{24}$$

In the center-of-mass reference system, the S-matrix of the process $\langle e^+e^-|q\bar{q}\rangle_\alpha$ can be written as

$$S = -ie^2e_q(2\pi)^4\int d^3p \frac{\delta^{(4)}(P_i-P_f)m_l m_q}{(2\pi)^3E_p(2\pi)^3E_q} \times \sum_{M_1M_2\mu_L\mu_S}\langle L\mu_L S\mu_S|J\mu_J\rangle\,\langle\frac{1}{2}M_1\frac{1}{2}M_2|S\mu_S\rangle\phi(\vec{p})\frac{g_{\mu\nu}}{s} \times [\bar{u}_l(q,\xi_1)\gamma^\mu v_l(-q,\xi_2)]\,[\bar{v}_q(-p,M_2)\gamma^\nu u_q(p,M_1)]\,, \tag{25}$$

where $\{m_l, e, E_q, \vec{q}, \xi\}$ represents the mass, charge, energy, momentum and spin projection of the incoming electron (positron); $\{m_q, e_q, E_p, \vec{p}, M\}$ the same for the created quark (antiquark), bound in a $J^{PC} = 1^{--}$ state with quantum numbers $\{J, L, S\}$ and $\{\mu_J, \mu_L, \mu_S\}$ projections. We express the Clebsch-Gordan coefficients as $\langle j_1m_1\, j_2m_2|j_3m_3\rangle$. The virtual photon's four-momentum verifies $k_\gamma^2 = s$.

The above S-matrix expression can be simplified and written in terms of the invariant amplitude $\mathcal{M}$,

$$S = -2\pi i\delta^{(4)}(\sum p_f - \sum p_i)\mathcal{M}\,, \tag{26}$$

so we arrive at

$$\mathcal{M} = e^2e_q\frac{1}{(2\pi)^{3/2}}\frac{m_l}{E_q}\frac{2}{3s}\overline{\Psi(0)}(-1)^{1/2+\xi_2}\frac{E_q+m_l}{2m_l} \left[\left(1+\frac{q^2}{(E_q+m_l)^2}\right)\langle\frac{1}{2}\xi_1\frac{1}{2}\xi_2|1\mu_J\rangle - \frac{2}{(E_q+m_l)^2}\sum_n(-1)^n\langle\frac{1}{2}\xi_1\frac{1}{2}\xi_2|1n\rangle q_{-n}q_{\mu_J}\right], \tag{27}$$

where we have defined

$$\overline{\Psi(0)} = \left[\Psi(0)\delta_{L,0} - \frac{\sqrt{2}}{6\pi}\sqrt{2L+1}\langle L010|10\rangle I_4\right]. \tag{28}$$

Here, $\Psi(0)$ is the Υ meson wave function at the origin. The second term encodes the contribution of $L = 2$ states, where

$$I_4 \equiv \int \frac{p^4 dp R_r(p)}{E_p(E_p + m_q)} \,. \tag{29}$$

It is worth noticing that this definition of $\overline{\Psi(0)}$ allows the contribution of both $\Upsilon\ ^3S_1$ and $\Upsilon\ ^3D_1$ states due to the non-zero quark momentum distribution inside the meson.

Concerning the decay of the Υ meson into two mesons, we can extract the ${}_\alpha\langle q\bar{q}|AB\rangle_\beta$ amplitude from the coupled channels formalism [83], and it is given by

$${}_\alpha\langle q\bar{q}|AB\rangle_\beta = \sum_{\alpha'} \bar{h}_{\alpha'\beta}(\sqrt{s}; k)\Delta_{\alpha'\alpha}(\sqrt{s})^{-1} \,, \tag{30}$$

with k the relative on-shell momentum of the two mesons and $\Delta_{\alpha'\alpha}$ the full resonance propagator, given by

$$\Delta_{\alpha'\alpha}(E) = (E - M_\alpha)\delta_{\alpha'\alpha} + \mathcal{G}_{\alpha'\alpha}(E) \tag{31}$$

with $\mathcal{G}_{\alpha'\alpha}$ the mass-shift function

$$\mathcal{G}_{\alpha'\alpha}(E) = \sum_\beta \int \frac{\bar{h}_{\alpha\beta}(E; q)h_{\beta\alpha'}(q)}{q^2/2\mu + m_A + m_B - E} q^2 dq \,. \tag{32}$$

The function $\bar{h}^{\beta\alpha}$ can be interpreted as the $^3P_0$ vertex dressed by the meson-meson interaction

$$\bar{h}_{\beta\alpha}(E; P) = h_{\beta\alpha}(P) - \sum_{\beta'} \int \frac{T_V^{\beta\beta'}(P, q; E)h_{\beta'\alpha}(q)}{q^2/2\mu + m_A + m_B - E} \, q^2 dq \,, \tag{33}$$

where $T_V^{\beta'\beta}(P', P; E)$ is the T matrix of the RGM potential excluding the coupling to the $q\bar{q}$ pairs.

The expression for the total cross section $e^+e^- \to b\bar{b} \to AB$ in the center-of-mass reference system is given by

$$d\sigma_\beta = (2\pi)^4 \frac{E_A E_B}{\sqrt{s}k_0} \delta(k - k_0) \frac{E_q}{2|q|} |\mathcal{M}_\beta|^2 d^3k \,, \tag{34}$$

where the on-shell momentum is

$$k_o = \frac{\sqrt{[s - (m_A + m_B)^2]\,[s - (m_A - m_B)^2]}}{2\sqrt{s}} \,. \tag{35}$$

Averaging $\mathcal{M}$ over the polarizations of the initial states and sum over final states, we arrive at

$$\sigma_\beta = \frac{4\pi^2}{3} e^4 e_q^2 \frac{\sqrt{k_o^2 + m_A^2}\sqrt{k_o^2 + m_B^2}k_o}{s^{5/2}} \times \left| \sum_{\nu,\nu'} \phi_{\nu'\beta}(k_o; \sqrt{s})\Delta_{\nu'\nu}(\sqrt{s})^{-1}\overline{\Psi_\nu(0)} \right|^2 , \tag{36}$$

which only depends on the on-shell momentum of the mesons in the final state.

TABLE I. Quark model parameters.

Quark masses	m_n (MeV)	313
	m_s (MeV)	555
	m_b (MeV)	5110
OGE	$\hat{r}_0$ (fm)	0.181
	$\hat{r}_g$ (fm)	0.259
	α_0	2.118
	Λ_0 (fm^{-1})	0.113
	μ_0 (MeV)	36.976
Confinement	a_c (MeV)	507.4
	μ_c (fm^{-1})	0.576
	Δ (MeV)	184.432
	a_s	0.81

TABLE II. Masses, in MeV, of the bottomonium states with quantum numbers $J^{PC} = 1^{--}$ (the so-called Υ-family) predicted by our constituent quark model. nL identifies the radial excitation, being $n = 1$ the ground state, and the dominant orbital angular momentum component in each wave function.

State	J^{PC}	nL	The. (MeV)	Exp. (MeV) [90]
Υ	1^{--}	$1S$	9502	9460.40 ± 0.10
		$2S$	10015	10023.4 ± 0.5
		$1D$	10117	-
		$3S$	10349	10355.1 ± 0.5
		$2D$	10414	-
		$4S$	10607	10579.4 ± 1.2
		$3D$	10653	-
		$5S$	10818	10885.2 ± 3.1
		$4D$	10853	-
		$6S$	10995	11000 ± 4
		$5D$	11023	-

III. RESULTS

The relevant parameters of our *naïve* CQM are shown in Table I, and they are the same used in, *e.g.*, Ref. [54]. Table II shows the predicted bottomonium states with quantum numbers $J^{PC} = 1^{--}$ as well as the world average masses reported in the Review of Particle Physics (RPP) [90] provided by the Particle Data Group. It is inferred from Table II that a global description of the Υ-family is obtained by our CQM.

It is also evident that the model does not provide a conventional state compatible with the experimentally observed $\Upsilon(10753)$ state. One would be tempted to assert that our CQM has some major deficiency; however, it is well known that any reasonable quark model describes well the bottomonium sector, providing a comparable spectrum and having very similar characteristics. This fact may imply that the $\Upsilon(10753)$ cannot be explained

TABLE III. Masses, in MeV, of the isospin-averaged $B\bar{B}$, $B\bar{B}^*$, $B^*\bar{B}^*$, $B_s\bar{B}_s$, $B_s\bar{B}_s^*$ and $B_s^*\bar{B}_s^*$ thresholds, from PDG [90].

Channel	$B\bar{B}$	$B\bar{B}^*$	$B^*\bar{B}^*$	$B_s\bar{B}_s$	$B_s\bar{B}_s^*$	$B_s^*\bar{B}_s^*$
Mass	10558.8	10604.1	10649.4	10733.8	10782.7	10831.6

TABLE IV. Masses and widths, in MeV, of the poles predicted by our constituent-quark-model-based meson-meson coupled-channels calculation. Theoretical uncertainties have been estimated by modifying the most relevant model parameters within a range of 10%.

State	$M_{\rm pole}$	$\Gamma_{\rm pole}$
1	10562 ± 1	29 ± 5
2	10601 ± 5	3 ± 2
3	10645 ± 1	23 ± 1
4	10694 ± 1	8 ± 1
5	10712 ± 5	41 ± 4
6	10835 ± 2	52 ± 7
7	10859 ± 2	13 ± 3
8	10888 ± 1	3 ± 1

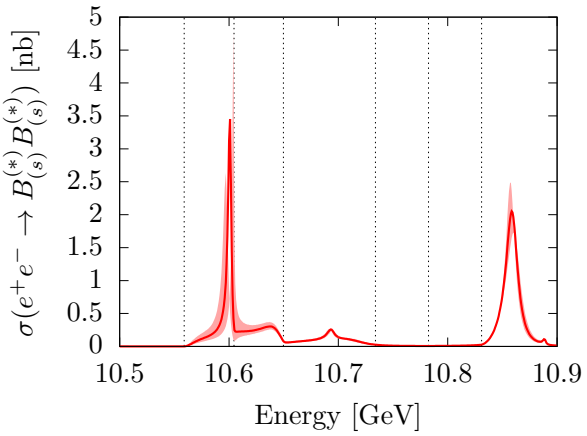

FIG. 2. Production cross section, in nb, of the Υ states when annihilating a pair of electron-positron and measuring in the final state one of the $B_{(s)}^{(*)}\bar{B}_{(s)}^{(*)}$ channels. The vertical black dashed lines indicate the open-bottom meson-meson thresholds which, from left to right, are $B\bar{B}$, $B\bar{B}^*$, $B^*\bar{B}^*$, $B_s\bar{B}_s$, $B_s\bar{B}_s^*$ and $B_s^*\bar{B}_s^*$. Theoretical uncertainties have been estimated by modifying the most relevant model parameters within a range of 10%.

as a conventional bottomonium system and thus it has an exotic origin. In other words, there should be another important mechanism in the dynamics of the $\Upsilon(10753)$ that is not implemented in our, even any, *naïve* CQM.

The lowest open-bottom meson-meson threshold is $B\bar{B}$, with a non-interacting mass of about 10.56 GeV. Moreover, the dominant open-bottom meson-meson strong decay channels of the Υ-family are considered to be $B\bar{B}$, $B\bar{B}^*$, $B^*\bar{B}^*$, $B_s\bar{B}_s$, $B_s\bar{B}_s^*$ and $B_s^*\bar{B}_s^*$ [1]. Their non-interacting mass thresholds are shown in Table III and they belong to an energy range between 10.56 to 10.83 GeV. In order to assess agreement between theory and experiment, we should include those coupled-channels effects that may play an important role in our description of the Υ-family, at least, for the $\Upsilon(4S)$ up to the $\Upsilon(4D)$ which fall within the range of energies of the most important open-flavor meson-meson thresholds.

The coupling of bare $b\bar{b}$ states with open-bottom meson-meson channels depends on the relative position of the $b\bar{b}$ mass and the non-interacting meson-meson energy threshold. One may infer from Sec. II that when the value of threshold energy, E, is far from the $b\bar{b}$ mass, M, the coupling effects are small. Moreover, when $M < E$ the effective potential is repulsive and it is unlikely that the coupling can generate relevant non-perturbative emergent phenomena; in fact, one usually obtains the same but dressed state due to the influence of near thresholds, moving to lower masses. However, if $M > E$ the effective potential becomes negative and a variety of emergent phenomena such as dynamically generated states with a dominant molecular structure may appear.

We perform a coupled-channels calculation in which the bare states $\Upsilon(4S)$, $\Upsilon(3D)$, $\Upsilon(5S)$ and $\Upsilon(4D)$ are considered together with the threshold channels $B\bar{B}$, $B\bar{B}^*$, $B^*\bar{B}^*$, $B_s\bar{B}_s$, $B_s\bar{B}_s^*$ and $B_s^*\bar{B}_s^*$. In order to compensate for the large mass-shifts that higher thresholds add to the bare states, which are already coded in the screened confinement potential, we move up the masses of the bare states 35 MeV. Our results are shown in Tables IV, V and VI. First mentioned table shows the pole position in complex energy plane characterized by mass and width ($E = M - i\,\Gamma/2$), the second one gives the probability of each channel that compose the wave function of the dressed hadron and the third table provides hadron's decay branching fractions to the different open-bottom meson-meson channels considered herein.

Concerning Table IV, eight poles in the complex energy plane are predicted; all of them are resonances, *i.e.* they are singularities that appear in the physical sheet. It may seem like there are many, al least more than observed experimentally. However, as shown in Fig. 2, only three peaks are present in the most common production process of Υ states: $e^+e^- \to B_{(s)}^{(*)}\bar{B}_{(s)}^{(*)}$. The two dominant peaks appear at around the masses of well-established $\Upsilon(4S)$ and $\Upsilon(10860)$ states, the small bump at approximately 10.7 GeV is our assignment of the $\Upsilon(10750)$ signal observed in $e^+e^- \to \pi^+\pi^-\Upsilon(nS)$. If our interpretation is correct, we have learned from Table IV and Fig 2 that (i) a richer complex spectrum is gained when thresholds are present and bare bound states are sufficiently non-relativistic; (ii) those poles obtained in the complex energy plane do not have to appear as simple peaks in the

[1] For now on, we denote $B_{(s)}\bar{B}_{(s)}^* \equiv B_{(s)}\bar{B}_{(s)}^*$+h.c.

TABLE V. Probability, in %, of each channel that compose the wave function of the poles predicted by our constituent-quark-model-based meson-meson coupled-channels calculation. Theoretical uncertainties have been estimated by modifying the most relevant model parameters within a range of 10%.

State	$\mathcal{P}_{\Upsilon(4S)}$	$\mathcal{P}_{\Upsilon(3D)}$	$\mathcal{P}_{\Upsilon(5S)}$	$\mathcal{P}_{\Upsilon(4D)}$	$\mathcal{P}_{B\bar{B}}$	$\mathcal{P}_{B\bar{B}^*}$	$\mathcal{P}_{B^*\bar{B}^*}$	$\mathcal{P}_{B_s\bar{B}_s}$	$\mathcal{P}_{B_s\bar{B}_s^*}$	$\mathcal{P}_{B_s^*\bar{B}_s^*}$
1	40^{+3}_{-4}	16 ± 5	$1.5^{+0.4}_{-0.3}$	$1.5^{+0.6}_{-0.5}$	33 ± 8	$1.9^{+0.6}_{-0.5}$	$5.2^{+0.4}_{-0.6}$	$0.141^{+0.002}_{-0.006}$	0.05 ± 0.01	$0.24^{+0.01}_{-0.03}$
2	19^{+3}_{-5}	1.1 ± 0.4	$0.13^{+0.02}_{-0.04}$	0.04 ± 0.01	48^{+1}_{-2}	28^{+6}_{-2}	4 ± 1	$0.017^{+0.005}_{-0.007}$	0.11 ± 0.04	0.10 ± 0.04
3	22^{+5}_{-4}	9 ± 1	0.07 ± 0.01	$0.14^{+0.01}_{-0.02}$	6 ± 1	$34.1^{+0.4}_{-0.6}$	28^{+1}_{-2}	0.14 ± 0.02	$0.102^{+0.004}_{-0.006}$	$0.193^{+0.008}_{-0.009}$
4	$1.7^{+0.1}_{-0.2}$	40 ± 2	$0.027^{+0.001}_{-0.004}$	$0.007^{+0.002}_{-0.001}$	$12.0^{+0.8}_{-0.7}$	16 ± 1	29.6 ± 0.1	$0.32^{+0.05}_{-0.04}$	$0.32^{+0.07}_{-0.06}$	$0.029^{+0.005}_{-0.004}$
5	36 ± 5	$8.8^{+0.8}_{-1.0}$	3.3 ± 0.2	0.166 ± 0.003	$4.5^{+1.0}_{-0.9}$	$2.74^{+0.09}_{-0.04}$	43^{+4}_{-5}	0.9 ± 0.2	$0.22^{+0.03}_{-0.02}$	$0.55^{+0.06}_{-0.07}$
6	4 ± 1	$0.71^{+0.06}_{-0.04}$	80^{+2}_{-3}	1.4 ± 0.1	$1.3^{+0.4}_{-0.3}$	$2.1^{+0.5}_{-0.4}$	6 ± 1	0.4 ± 0.1	$1.2^{+0.4}_{-0.3}$	3 ± 1
7	$0.4^{+0.3}_{-0.2}$	0.03 ± 0.01	$53.7^{+0.0}_{-0.9}$	$0.2^{+0.2}_{-0.1}$	1.9 ± 0.1	$4.4^{+0.2}_{-0.1}$	5.7 ± 0.8	$1.33^{+0.06}_{-0.04}$	2.1 ± 0.4	30 ± 1
8	0.004 ± 0.002	0.005 ± 0.002	$0.05^{+0.03}_{-0.02}$	$50.23^{+0.00}_{-0.02}$	16.6 ± 0.1	$16.1^{+0.2}_{-0.3}$	$2.80^{+0.05}_{-0.04}$	4.9 ± 0.1	8.5 ± 0.2	$0.8^{+0.2}_{-0.1}$

TABLE VI. Decay branching fractions, in %, to the different open-bottom meson-meson channels of the poles predicted by our constituent-quark-model-based meson-meson coupled-channels calculation. Theoretical uncertainties have been estimated by modifying the most relevant model parameters within a range of 10%.

State	$\mathcal{BR}_{B\bar{B}}$	$\mathcal{BR}_{B\bar{B}^*}$	$\mathcal{BR}_{B^*\bar{B}^*}$	$\mathcal{BR}_{B_s\bar{B}_s}$	$\mathcal{BR}_{B_s\bar{B}_s^*}$	$\mathcal{BR}_{B_s^*\bar{B}_s^*}$
1	100 ± 0	0 ± 0	0 ± 0	0 ± 0	0 ± 0	0 ± 0
2	100 ± 0	0 ± 0	0 ± 0	0 ± 0	0 ± 0	0 ± 0
3	6 ± 1	94 ± 1	0 ± 0	0 ± 0	0 ± 0	0 ± 0
4	23 ± 1	14^{+1}_{-2}	$63.2^{+0.1}_{-0.2}$	0 ± 0	0 ± 0	0 ± 0
5	8^{+2}_{-1}	$3.0^{+0.4}_{-0.2}$	90 ± 1	0 ± 0	0 ± 0	0 ± 0
6	$7.4^{+0.1}_{-0.3}$	$4.3^{+0.3}_{-0.1}$	$5.5^{+0.6}_{-0.1}$	2 ± 0	4 ± 1	77^{+0}_{-2}
7	$4.1^{+0.3}_{-0.4}$	8 ± 0	$2.2^{+0.1}_{-0.2}$	3.0 ± 0.1	$1.8^{+0.6}_{-0.4}$	$81.4^{+0.1}_{-0.2}$
8	$33.9^{+0.4}_{-0.3}$	$32.9^{+0.3}_{-0.5}$	5 ± 0	$9.8^{+0.3}_{-0.2}$	17.3 ± 0.3	0.8 ± 0.1

relevant cross sections due to many reasons such as their distance from the energy real-axis, coupling with the corresponding final channel, etc; and (iii) when comparing with experiment, the so-called $\Upsilon(4S)$ and $\Upsilon(10860)$ signals are clearly identified but there should be another small one, corresponding to the $\Upsilon(10750)$ case, whose origin cannot be traced back to any bare quark-antiquark bound state.

It is convenient to analyze Tables V and VI together. The first pole has a mass, 10562 MeV, and a total decay width, 29 MeV, compatible with those values collected in the PDG for the $\Upsilon(4S)$ state. Moreover, its wave function has as the dominant channel the $\Upsilon(4S)$, *i.e.* a canonical bottom-antibottom 4S bound state; followed by $B\bar{B}$ and $\Upsilon(3D)$ components; moreover, its decay branching fraction of $B\bar{B}$ is 100%. Therefore, the natural assignment to this dressed state is the experimentally observed $\Upsilon(4S)$ state.

The following two poles seems to be singularities produced dynamically in the complex energy plane due to the coupling between conventional bottomonium states and meson-meson thresholds. In fact this coupling makes them mostly $B\bar{B} - B\bar{B}^*$ and $B\bar{B}^* - B^*\bar{B}^*$ molecules, respectively; having also measurable traces of $\Upsilon(4S)$ and $\Upsilon(3D)$ components in their wave functions. Nevertheless, as one can see in Fig. 2, these structures do not materialize in the production cross section.

We assign the fourth pole to the so-called $\Upsilon(3D)$ state. Our predictions for the mass and total decay width are 10645 MeV and 23 MeV. Its wave function exhibit a dominant $3D\ b\bar{b}$ constituent, followed by important $B\bar{B}$, $B\bar{B}^*$ and $B^*\bar{B}^*$ components. Table VI shows that the decay branching fractions of this state into the $B\bar{B}$, $B\bar{B}^*$ and $B^*\bar{B}^*$ final channels are 23%, 14% and 63%, respectively. As one can see in Fig. 2, this state takes part on the second bump observed in production cross section; however, its contribution is small because it depends on the value of I_4 in Eq. (29), which is small compared to the contribution of S-wave Υ states.

The last observation is connected with our interpretation of the fifth pole as the $\Upsilon(10750)$ candidate because, as one can see in Table V, its corresponding wave function shows a large $\Upsilon(4S)$ component which provides the leverage for its production. Note also that the wavefunction's $B^*\bar{B}^*$ channel is of the same order of magnitude than the former, encouraging us to conclude that this dressed hadronic state is in fact a resonance whose structure is an equally mixture of a conventional $b\bar{b}\ 4S$ state and $B^*\bar{B}^*$ molecule. Looking at Table IV, its theoretical mass and width are 10712 MeV and 41 MeV, respectively, which are in reasonable agreement with the experimental data, Eq. (3). Finally, Table VI shows that this state decays 90% of the time into $B^*\bar{B}^*$ followed by the $B\bar{B}$ final state with a branching fraction of 8%.

Concerning the bump that can be seen in the production cross section (Fig. 2) at around 10.85 GeV, it is mostly produced by the sixth pole because, as shown in Table V, its wave function exhibits a very dominant $5S$ $b\bar{b}$ component, with a probability of 80%; being the rest channels an order of magnitude less probable. Without changing our attention from Table V, the other two poles are constituted by an equally mixture of canonical bottomonium structure and open-bottom meson-meson molecule. Table VI shows the branching fractions of these three dressed states to $B_{(s)}^{(*)}\bar{B}_{(s)}^{(*)}$ channels. For our tentative assignment of the $\Upsilon(5S)$ state as $\Upsilon(10860)$, the theoretical mass and width are in fair agreement with experiment; our mass value is a bit lower than the experimental one, 10885 MeV, whereas our width is higher than the PDG's figure, 37 MeV. This may be explained by the projection in real-axis of the singularities shown in the complex energy plane at the relevant energy, which is the only measurable feature. It is also worth to note that we provide correct orders of magnitude for the branching fractions of the $B^{(*)}\bar{B}^{(*)}$ state whereas unfortunately the one corresponding to the $B_s^*\bar{B}_s^*$ channel is far larger than experiment.

IV. SUMMARY

The $\Upsilon(10753)$ signal seems to be a potential candidate of the Υ-family. It was firstly observed by the Belle collaboration in 2019 and, later on, by the Belle II collaboration in 2022. The joint significance is 5.2 standard deviations; moreover, its mass, total decay width and quantum numbers are also determined: $M = 10753$ MeV, $\Gamma = 36^{+18}_{-12}$ MeV and $J^P = 1^-$. Since this new state does not fit into the spectrum predicted by any reasonable constituent quark model, everything points that it may be an exotic state whose nature is explained by some mechanism that goes beyond the simple quark-antiquark interaction. The most logical extension to the naive quark model is the coupling of bare bottomonia with their closest open-bottom thresholds in order to assess if emergent non-perturbative dynamical states could be produced.

We have analyzed the predicted spectrum of the Υ-family, within an energy range around the $\Upsilon(10753)$'s mass, in the framework of a constituent quark model [52] which satisfactorily describes a wide range of properties of conventional hadrons containing heavy quarks [53, 54]. The quark-antiquark and meson-meson degrees of freedom have been incorporated with the goal of elucidating the influence of open-bottom meson-meson thresholds into the concerning bare states and to shed some light on the nature and structure of the $\Upsilon(10753)$ state. In particular, we have performed a coupled-channels calculation in which the bare states $\Upsilon(4S)$, $\Upsilon(3D)$, $\Upsilon(5S)$ and $\Upsilon(4D)$ are considered together with the threshold channels $B\bar{B}$, $B\bar{B}^*$, $B^*\bar{B}^*$, $B_s\bar{B}_s$, $B_s\bar{B}_s^*$ and $B_s^*\bar{B}_s^*$.

Among the results we have described, the following conclusions are of particular interest: (i) a richer complex spectrum is gained when thresholds are present and bare bound states are sufficiently non-relativistic; (ii) those poles obtained in the complex energy plane do not have to appear as simple peaks in the relevant cross sections; and (iii) the $\Upsilon(10750)$ candidate is interpreted as a dressed hadronic resonance whose structure is an equally mixture of a conventional $b\bar{b}$ state and B^*B^* molecule.

ACKNOWLEDGMENTS

Work partially financed by EU Horizon 2020 research and innovation program, STRONG-2020 project, under grant agreement no. 824093; Ministerio Español de Ciencia e Innovación under grant Nos. PID2019-105439GB-C22, PID2019-107844GB-C22 and PID2022-140440NB-C22;Junta de Andalucía under contract Nos. Operativo FEDER Andalucía 2014-2020 UHU-1264517, P18-FR-5057 and also PAIDI FQM-370.

[1] S. W. Herb *et al.* (E288), Phys. Rev. Lett. **39**, 252 (1977).
[2] W. R. Innes *et al.* (E288), Phys. Rev. Lett. **39**, 1240 (1977), [Erratum: Phys.Rev.Lett. 39, 1640 (1977)].
[3] K. Han *et al.*, Phys. Rev. Lett. **49**, 1612 (1982).
[4] G. Eigen *et al.*, Phys. Rev. Lett. **49**, 1616 (1982).
[5] C. Klopfenstein *et al.*, Phys. Rev. Lett. **51**, 160 (1983).
[6] F. Pauss *et al.*, Phys. Lett. B **130**, 439 (1983).
[7] D. Besson *et al.* (CLEO), Phys. Rev. Lett. **54**, 381 (1985).
[8] D. M. J. Lovelock *et al.*, Phys. Rev. Lett. **54**, 377 (1985).
[9] R. F. Lebed, R. E. Mitchell, and E. S. Swanson, Prog. Part. Nucl. Phys. **93**, 143 (2017), arXiv:1610.04528 [hep-ph].
[10] H.-X. Chen, W. Chen, X. Liu, and S.-L. Zhu, Phys. Rept. **639**, 1 (2016), arXiv:1601.02092 [hep-ph].
[11] H.-X. Chen, W. Chen, X. Liu, Y.-R. Liu, and S.-L. Zhu, Rept. Prog. Phys. **80**, 076201 (2017), arXiv:1609.08928 [hep-ph].
[12] A. Ali, J. S. Lange, and S. Stone, Prog. Part. Nucl. Phys. **97**, 123 (2017), arXiv:1706.00610 [hep-ph].
[13] F.-K. Guo, C. Hanhart, U.-G. Meißner, Q. Wang, Q. Zhao, and B.-S. Zou, Rev. Mod. Phys. **90**, 015004 (2018), [Erratum: Rev.Mod.Phys. 94, 029901 (2022)], arXiv:1705.00141 [hep-ph].
[14] S. L. Olsen, T. Skwarnicki, and D. Zieminska, Rev. Mod. Phys. **90**, 015003 (2018), arXiv:1708.04012 [hep-ph].
[15] Y.-R. Liu, H.-X. Chen, W. Chen, X. Liu, and S.-L. Zhu, Prog. Part. Nucl. Phys. **107**, 237 (2019), arXiv:1903.11976 [hep-ph].
[16] N. Brambilla, S. Eidelman, C. Hanhart, A. Nefediev, C.-P. Shen, C. E. Thomas, A. Vairo, and C.-Z. Yuan, Phys. Rept. **873**, 1 (2020), arXiv:1907.07583 [hep-ex].
[17] G. Yang, J. Ping, and J. Segovia, Symmetry **12**, 1869 (2020), arXiv:2009.00238 [hep-ph].
[18] X.-K. Dong, F.-K. Guo, and B.-S. Zou, Phys. Rev. Lett.

126, 152001 (2021), arXiv:2011.14517 [hep-ph].
[19] X.-K. Dong, F.-K. Guo, and B.-S. Zou, Commun. Theor. Phys. **73**, 125201 (2021), arXiv:2108.02673 [hep-ph].
[20] H.-X. Chen, Phys. Rev. D **105**, 094003 (2022), arXiv:2103.08586 [hep-ph].
[21] X. Cao, Front. Phys. (Beijing) **18**, 44600 (2023), arXiv:2301.11253 [hep-ph].
[22] M. Mai, U.-G. Meißner, and C. Urbach, Phys. Rept. **1001**, 1 (2023), arXiv:2206.01477 [hep-ph].
[23] L. Meng, B. Wang, G.-J. Wang, and S.-L. Zhu, Phys. Rept. **1019**, 1 (2023), arXiv:2204.08716 [hep-ph].
[24] H.-X. Chen, W. Chen, X. Liu, Y.-R. Liu, and S.-L. Zhu, Rept. Prog. Phys. **86**, 026201 (2023), arXiv:2204.02649 [hep-ph].
[25] F.-K. Guo, H. Peng, J.-J. Xie, and X. Zhou, (2022), arXiv:2203.07141 [hep-ph].
[26] P. G. Ortega and D. R. Entem, Symmetry **13**, 279 (2021), arXiv:2012.10105 [hep-ph].
[27] H. Huang, C. Deng, X. Liu, Y. Tan, and J. Ping, Symmetry **15**, 1298 (2023).
[28] R. F. Lebed, PoS **FPCP2023**, 028 (2023), arXiv:2308.00781 [hep-ph].
[29] B.-S. Zou, Sci. Bull. **66**, 1258 (2021), arXiv:2103.15273 [hep-ph].
[30] R. Mizuk *et al.* (Belle), JHEP **10**, 220 (2019), arXiv:1905.05521 [hep-ex].
[31] I. Adachi *et al.* (Belle-II), Phys. Rev. Lett. **130**, 091902 (2023), arXiv:2208.13189 [hep-ex].
[32] G. Bonvicini *et al.* (CLEO), Phys. Rev. D **70**, 032001 (2004), arXiv:hep-ex/0404021.
[33] P. del Amo Sanchez *et al.* (BaBar), Phys. Rev. D **82**, 111102 (2010), arXiv:1004.0175 [hep-ex].
[34] S. M. Ryan and D. J. Wilson (Hadron Spectrum), JHEP **02**, 214 (2021), arXiv:2008.02656 [hep-lat].
[35] J. Bulava *et al.*, in *Snowmass 2021* (2022) arXiv:2203.03230 [hep-lat].
[36] T. Hilger, C. Popovici, M. Gomez-Rocha, and A. Krassnigg, Phys. Rev. D **91**, 034013 (2015), arXiv:1409.3205 [hep-ph].
[37] C. S. Fischer, S. Kubrak, and R. Williams, Eur. Phys. J. A **51**, 10 (2015), arXiv:1409.5076 [hep-ph].
[38] P.-L. Yin, C. Chen, G. a. Krein, C. D. Roberts, J. Segovia, and S.-S. Xu, Phys. Rev. D **100**, 034008 (2019), arXiv:1903.00160 [nucl-th].
[39] P.-L. Yin, Z.-F. Cui, C. D. Roberts, and J. Segovia, Eur. Phys. J. C **81**, 327 (2021), arXiv:2102.12568 [hep-ph].
[40] P. Parui, S. De, A. Kumar, and A. Mishra, (2021), arXiv:2104.05471 [hep-ph].
[41] W. Chen, R. T. Kleiv, T. G. Steele, B. Bulthuis, D. Harnett, J. Ho, T. Richards, and S.-L. Zhu, in *Meeting of the APS Division of Particles and Fields* (2013) arXiv:1310.0431 [hep-ph].
[42] R. Kleiv, *QCD sum rule studies of heavy quarkonium-like states*, Ph.D. thesis, Saskatchewan U. (2013), arXiv:1407.2292 [hep-ph].
[43] N. Brambilla, A. Pineda, J. Soto, and A. Vairo, Rev. Mod. Phys. **77**, 1423 (2005), arXiv:hep-ph/0410047.
[44] N. Brambilla, A. Pineda, J. Soto, and A. Vairo, Nucl. Phys. B **566**, 275 (2000), arXiv:hep-ph/9907240.
[45] J. Segovia, S. Steinbeißer, and A. Vairo, Phys. Rev. D **99**, 074011 (2019), arXiv:1811.07590 [hep-ph].
[46] C. Peset, A. Pineda, and J. Segovia, Phys. Rev. D **98**, 094003 (2018), arXiv:1809.09124 [hep-ph].
[47] T. Barnes, F. E. Close, P. R. Page, and E. S. Swanson, Phys. Rev. D **55**, 4157 (1997), arXiv:hep-ph/9609339.
[48] D. Ebert, R. N. Faustov, and V. O. Galkin, Phys. Rev. D **67**, 014027 (2003), arXiv:hep-ph/0210381.
[49] E. Eichten, S. Godfrey, H. Mahlke, and J. L. Rosner, Rev. Mod. Phys. **80**, 1161 (2008), arXiv:hep-ph/0701208.
[50] J. Ferretti and E. Santopinto, Phys. Rev. D **90**, 094022 (2014), arXiv:1306.2874 [hep-ph].
[51] S. Godfrey and K. Moats, Phys. Rev. D **92**, 054034 (2015), arXiv:1507.00024 [hep-ph].
[52] J. Vijande, F. Fernandez, and A. Valcarce, J. Phys. G **31**, 481 (2005), arXiv:hep-ph/0411299.
[53] J. Segovia, D. R. Entem, F. Fernandez, and E. Hernandez, Int. J. Mod. Phys. E **22**, 1330026 (2013), arXiv:1309.6926 [hep-ph].
[54] J. Segovia, P. G. Ortega, D. R. Entem, and F. Fernández, Phys. Rev. D **93**, 074027 (2016), arXiv:1601.05093 [hep-ph].
[55] A. Bondar *et al.* (Belle), Phys. Rev. Lett. **108**, 122001 (2012), arXiv:1110.2251 [hep-ex].
[56] I. Adachi (Belle), in *9th Conference on Flavor Physics and CP Violation* (2011) arXiv:1105.4583 [hep-ex].
[57] P. G. Ortega, J. Segovia, and F. Fernandez, Phys. Rev. D **104**, 094004 (2021), arXiv:2107.02544 [hep-ph].
[58] E. Hiyama, Y. Kino, and M. Kamimura, Prog. Part. Nucl. Phys. **51**, 223 (2003).
[59] J. A. Wheeler, Phys. Rev. **52**, 1083 (1937).
[60] Y. C. Tang, M. Lemere, and D. R. Thompson, Phys. Rept. **47**, 167 (1978).
[61] L. Micu, Nucl. Phys. B **10**, 521 (1969).
[62] F. Fernández and J. Segovia, Symmetry **13**, 252 (2021).
[63] J. Segovia, A. M. Yasser, D. R. Entem, and F. Fernandez, Phys. Rev. D **78**, 114033 (2008).
[64] J. Segovia, D. R. Entem, and F. Fernandez, Phys. Rev. D **91**, 094020 (2015), arXiv:1502.03827 [hep-ph].
[65] P. G. Ortega, J. Segovia, D. R. Entem, and F. Fernández, Phys. Rev. D **94**, 114018 (2016), arXiv:1608.01325 [hep-ph].
[66] P. G. Ortega, J. Segovia, D. R. Entem, and F. Fernandez, Eur. Phys. J. C **80**, 223 (2020), arXiv:2001.08093 [hep-ph].
[67] J. Segovia, D. R. Entem, and F. Fernández, Phys. Lett. B **715**, 322 (2012), arXiv:1205.2215 [hep-ph].
[68] J. Segovia, A. M. Yasser, D. R. Entem, and F. Fernandez, Phys. Rev. D **80**, 054017 (2009).
[69] J. Segovia, D. R. Entem, and F. Fernandez, Phys. Rev. D **83**, 114018 (2011).
[70] J. Segovia, D. R. Entem, and F. Fernandez, Nucl. Phys. A **915**, 125 (2013), arXiv:1301.2592 [hep-ph].
[71] J. Segovia, D. R. Entem, and F. Fernández, Phys. Rev. D **91**, 014002 (2015), arXiv:1409.7079 [hep-ph].
[72] J. Segovia, F. Fernandez, and D. R. Entem, Few Body Syst. **57**, 275 (2016), arXiv:1507.01607 [hep-ph].
[73] B. Martín-González, P. G. Ortega, D. R. Entem, F. Fernández, and J. Segovia, Phys. Rev. D **106**, 054009 (2022), arXiv:2205.05950 [hep-ph].
[74] J. Segovia, C. Albertus, D. R. Entem, F. Fernandez, E. Hernandez, and M. A. Perez-Garcia, Phys. Rev. D **84**, 094029 (2011), arXiv:1107.4248 [hep-ph].
[75] J. Segovia, C. Albertus, E. Hernandez, F. Fernandez, and D. R. Entem, Phys. Rev. D **86**, 014010 (2012), arXiv:1203.4362 [hep-ph].
[76] J. Segovia, E. Hernández, F. Fernández, and D. R. Entem, Phys. Rev. D **87**, 114009 (2013), arXiv:1304.4970 [hep-ph].

[77] G. Yang, J. Ping, and J. Segovia, Few Body Syst. **59**, 113 (2018), arXiv:1709.09315 [hep-ph].

[78] G. Yang, J. Ping, P. G. Ortega, and J. Segovia, Chin. Phys. C **44**, 023102 (2020), arXiv:1904.10166 [hep-ph].

[79] G. Yang, J. Ping, and J. Segovia, Phys. Rev. D **102**, 054023 (2020), arXiv:2007.05190 [hep-ph].

[80] G. Yang, J. Ping, and J. Segovia, Phys. Rev. D **104**, 094035 (2021), arXiv:2109.04311 [hep-ph].

[81] G. Yang, J. Ping, and J. Segovia, Phys. Rev. D **101**, 074030 (2020), arXiv:2003.05253 [hep-ph].

[82] G. Yang, J. Ping, and J. Segovia, Phys. Rev. D **99**, 014035 (2019), arXiv:1809.06193 [hep-ph].

[83] P. G. Ortega, D. R. Entem, and F. Fernandez, J. Phys. G **40**, 065107 (2013), arXiv:1205.1699 [hep-ph].

[84] A. Le Yaouanc, L. Oliver, O. Pene, and J. C. Raynal, Phys. Rev. D **8**, 2223 (1973).

[85] A. Le Yaouanc, L. Oliver, O. Pene, and J. C. Raynal, Phys. Rev. D **9**, 1415 (1974).

[86] D. Morel and S. Capstick, (2002), arXiv:nucl-th/0204014.

[87] P. G. Ortega, J. Segovia, D. R. Entem, and F. Fernandez, Phys. Rev. D **94**, 074037 (2016), arXiv:1603.07000 [hep-ph].

[88] P. G. Ortega, J. Segovia, D. R. Entem, and F. Fernández, Phys. Rev. D **95**, 034010 (2017), arXiv:1612.04826 [hep-ph].

[89] L. A. Blanco, R. Bonnaz, B. Silvestre-Brac, F. Fernandez, and A. Valcarce, Nucl. Phys. A **699**, 690 (2002), arXiv:nucl-th/0109080.

[90] R. L. Workman *et al.* (Particle Data Group), PTEP **2022**, 083C01 (2022).

Impact of theoretical uncertainties on model parameter reconstruction from GW signals sourced by cosmological phase transitions

Marek Lewicki [1,*] Marco Merchand [2,3,†] Laura Sagunski [4,‡] Philipp Schicho [4,§] and Daniel Schmitt [4,¶]

[1] *Faculty of Physics, University of Warsaw ul. Pasteura 5, 02-093 Warsaw, Poland*
[2] *KTH Royal Institute of Technology, Department of Physics, SE-10691 Stockholm, Sweden*
[3] *The Oskar Klein Centre for Cosmoparticle Physics, AlbaNova University Centre, SE-10691 Stockholm, Sweden*
[4] *Institute for Theoretical Physics, Goethe Universität Frankfurt, 60438 Frankfurt, Germany*

Different computational techniques for cosmological phase transition parameters can impact the Gravitational Wave (GW) spectra predicted in a given particle physics model. To scrutinize the importance of this effect, we perform large-scale parameter scans of the dynamical real-singlet extended Standard Model using three perturbative approximations for the effective potential: the $\overline{\text{MS}}$ and on-shell schemes at leading order, and three-dimensional thermal effective theory (3D EFT) at next-to-leading order. While predictions of GW amplitudes are typically unreliable in the absence of higher-order corrections, we show that the reconstructed model parameter spaces are robust up to a few percent in uncertainty. While 3D EFT is accurate from one loop order, theoretical uncertainties of reconstructed model parameters, using four-dimensional standard techniques, remain dominant over the experimental ones even for signals merely strong enough to claim a detection by LISA.

arXiv:2403.03769v1 [hep-ph] 6 Mar 2024

I. INTRODUCTION

Recent strong indication for a stochastic gravitational wave (GW) background by pulsar timing array collaborations [1–7] is a milestone in deciphering the history of the early universe. One of the prominent early universe scenarios that produce a stochastic GW background and remains a viable source behind the recent observations is a first-order phase transition (PT) [8–10]. The main motivation for such a signal, however, is associated with (electroweak) symmetry breaking which proceeds by a first-order PT in numerous extensions beyond the Standard Model (SM) and would lead to the production of a GW background in the mHz regime accessible to future experiments such as the upcoming LISA [11–13].

Reliable descriptions of first-order PTs including the nucleating bubbles, hydro- and thermodynamics require non-perturbative analyses [14–17]. Such computations are expensive and scans of multi-dimensional parameter spaces untenable, which motivates using perturbation theory when possible. Concerning thermodynamics, recent progress involving high-temperature effective field theory (EFT) [18, 19] allows us to fully describe PTs that exhibit a scale hierarchy [20]. While this description is by now state of the art, practical applications still rely on four-dimensional (4D), incomplete thermally resummed effective potentials [21–23]. In this *article*, we quantify the theoretical uncertainties remaining in perturbative computations of the PT equilibrium thermodynamics.

Inverting a measured GW spectrum to determine the underlying quantum theory Lagrangian is known as the GW *inverse problem* [11, 12, 24–28]. Its theoretical challenge during the GW signal reconstruction is to discern the most reliable approach to PT thermodynamics since predictions from different levels of computational diligence can be ambiguous in the reconstructed parameter space [29, 30]. In fact, some approaches can even predict inconsistent parameter spaces [31]. Ensuring theoretical robustness affects all phenomenological analyses that investigate the impact of new states beyond the SM (BSM) during the electroweak PT on GW signals through a perturbative effective potential. For such BSM theories to predict a GW signal detectable by upcoming experiments, their new states need to be dynamical in the infrared (IR) to modify the low-energy behavior of the SM [32, 33].

This *article* addresses the problem of such ambiguous predictions by performing a large-scale scan of a minimal BSM scalar extension with more than one light scalar in the IR; this scan is the first to use the 3D EFT of [34, 35]. In a proof-of-principle analysis, we employ different perturbative approaches to the effective potential, to demonstrate that the theoretical uncertainties still dominate over the experimental ones by contrasting reconstructed parameter spaces from the different approaches. We show that in three-dimensional (3D) thermal EFT, the perturbative series converges quickly and already at next-to-leading order (NLO), predictions are unambiguous and robust. Common but perturbatively inconsistent 4D approaches at incomplete leading order (LO) [36] yield errors in the reconstructed parameters of $\mathcal{O}(1\%)$. However, such errors would still dominate over the experimental uncertainties on the parameters if the signal was detected with a signal-to-noise ratio (SNR) of SNR $\simeq 10$ by LISA.

Section II reviews the resummation methods used in our analysis. Sec. III introduces the thermal parameters that are used in sec. IV to determine GW signals. After comparing the impact of different resummation methods on model parameter predictions and estimating sources of theoretical uncertainty, we conclude in sec. V.

* marek.lewicki@fuw.edu.pl
† marcomm@kth.se
‡ sagunski@itp.uni-frankfurt.de
§ schicho@itp.uni-frankfurt.de
¶ dschmitt@itp.uni-frankfurt.de

II. COMPARING RESUMMATION METHODS

By minimally extending the SM with one neutral scalar (xSM) [32, 34–40], we discuss different levels of diligence in computing the corresponding thermal potentials and their influence on phenomenological predictions.

We study the Z_2-symmetric potential for the xSM

$$V_0(\Phi,S) = \mu_h^2\Phi^\dagger\Phi + \lambda(\Phi^\dagger\Phi)^2 + \frac{1}{2}\mu_s^2 S^2 + \frac{\lambda_s}{4}S^4 + \frac{\lambda_{hs}}{2}S^2\Phi^\dagger\Phi\,, \tag{1}$$

where the tree-level scalar mass matrix is diagonal and $\mu_h^2 < 0$ at zero temperature. The field $\Phi = \big(G^+, \frac{1}{\sqrt{2}}(v + h + iG^0)\big)^{\mathrm{T}}$ is the $\mathrm{SU(2)_L}$ SM Higgs doublet with vacuum expectation value (VEV) $v_0 \simeq 246$ GeV, $S = (x + s)$ is the gauge singlet, odd under a parity Z_2-symmetry, and $G^\pm$, G are the would-be Goldstones fields. The tree-level potential

$$V_0(\boldsymbol{\phi}) = \frac{1}{2}\mu_h^2 v^2 + \frac{1}{4}\lambda v^4 + \frac{1}{2}\mu_s^2 x^2 + \frac{1}{4}\lambda_s x^4 + \frac{1}{4}\lambda_{hs}v^2x^2\,, \tag{2}$$

with $\boldsymbol{\phi} = (v, x)$ depends on the homogeneous background fields v and x. The $\mathrm{SU(2)_L}$ and $\mathrm{U(1)_Y}$ gauge field, would-be Goldstone, and physical scalar eigenstate masses read

$$m_h^2 = \mu_h^2 + 3\lambda v^2 + \frac{1}{2}\lambda_{hs}x^2\,, \quad m_G^2 = m_h^2 - 2\lambda v^2\,, \tag{3}$$

$$m_s^2 = \mu_s^2 + 3\lambda_s x^2 + \frac{1}{2}\lambda_{hs}v^2\,, \quad m_W^2 = \frac{1}{4}g^2v^2\,, \tag{4}$$

$$m_Z^2 = \frac{1}{4}\left(g^2 + g'^2\right)v^2\,. \tag{5}$$

All approaches employ Landau gauge ($\xi = 0$) motivated by the arguments in [35]. In this gauge, ghosts and scalars decouple as well as kinetic mixing between scalar and vector fields is removed [41]. The xSM gives rise to two-step PTs from symmetric to singlet to vacuum Higgs minimum *viz.*

$$(0,0) \xrightarrow{\texttt{step1}} (0,x) \xrightarrow{\texttt{step2}} (v_0,0)\,. \tag{6}$$

This *article* focuses on `step2` as the source of GWs.

For our GW signal analysis, we list the different approaches to construct the effective potential, $V_{\rm eff}(\boldsymbol{\phi},T)$, at finite temperature. This potential is prone to collective IR sensitivities [42] that render perturbation theory slowly convergent and can be treated by various forms of resummation. This *article* compares different forms of resummation bearing in mind, that a significant mismatch among them is related to the failure of perturbation theory when misidentifying corrections as higher order in the underlying strict EFT power counting [20, 43]. As an example, at finite temperature the complete LO requires two-loop thermal mass effects [36].

Such collective IR effects modify the vacuum masses by thermal corrections. At one-loop level, the effective masses are

$$\mu_{h,3}^2 = \mu_h^2 + T^2\Big[\frac{3g^2}{16} + \frac{g'^2}{16} + \frac{\lambda}{2} + \frac{y_t^2}{4} + \frac{\lambda_{hs}}{24}\Big]\,, \tag{7}$$

$$\mu_{s,3}^2 = \mu_s^2 + T^2\Big[\frac{1}{4}\lambda_s + \frac{1}{6}\lambda_{hs}\Big]\,, \tag{8}$$

$$m_{\rm D}^2 = \frac{g^2T^2}{3}\Big[\frac{5}{2} + \frac{N_{\rm c}+1}{4}n_{\rm f}\Big]\,, \tag{9}$$

where $n_{\rm f} = 3$ is the number of fermion families, $N_{\rm c} = 3$ the number of colors, and y_t the SM top Yukawa coupling. Subscripts indicate that thermal corrections are an inherently soft 3D effect, and $m_{\rm D}$ is the $\mathrm{SU(2)_L}$ Debye mass – the thermal mass of longitudinal gauge bosons. Two-loop corrections are obtained via [34, 35, 44].

A. Four dimensions: $\overline{\rm MS}$ scheme

This scheme uses dimensional regularization with $\bar{\mu}$ being a $\overline{\rm MS}$ renormalization-group (RG) scale. After renormalization, physical quantities should be $\bar{\mu}$-independent order by order. In the imaginary time formalism and at one-loop level, the effective potential, V_1, consists of corrections from the vacuum and thermal medium [22],

$$V_1(\boldsymbol{\phi},T) = \sum_i n_i\, J_4(m_i^2(\boldsymbol{\phi},T),T)\,, \tag{10}$$

$$J_4(m^2,T) = \frac{1}{2}\sum\!\!\!\!\!\!\int_P \ln\left(P^2 + m^2\right) = J_{\rm CW}(m^2) + J_{T,\mathrm{B(F)}}(m^2)\,. \tag{11}$$

Here, $J_{\rm CW}$ is the Coleman-Weinberg contribution [45, 46] and $J_{T,\mathrm{B(F)}}$ the thermal bosonic (fermionic) contribution. The sum-integral $\sum\!\!\!\!\!\!\int_P = T\sum_{p_n}\int_{\mathbf{p}}$ contains a sum over p_n Matsubara modes, $\int_{\mathbf{p}} = \mu^{2\epsilon}\int\frac{\mathrm{d}^dp}{(2\pi)^d}$, and $d = 3 - 2\epsilon$. The numbers of degrees of freedom, n_i, are d-dependent and positive (negative) for bosons (fermions). Since the thermal integrals $J_{T,\mathrm{B(F)}}$ are finite in the ultraviolet (UV), they are evaluated directly.

Relevant parameters of the theory are RG-evolved to the 4D RG-scale $\bar{\mu} = v_0$ at one-loop level. In this scheme, vacuum renormalization is achieved by the renormalization condition

$$\partial_v V_0 = 0\,, \qquad \partial_v^2 V_0 = M_h^2\,, \tag{12}$$

where capital masses indicate pole masses, e.g. M_h is the Higgs pole mass. For the Z_2-symmetric xSM $m_h = M_h$ and $m_s = M_s$. At the electroweak (EW) scale with a minimum at the field values $\boldsymbol{\phi} = (v_0, 0)$, the zero-temperature Higgs mass is reproduced at $\bar{\mu} = v_0$. Higher corrections are included by introducing an additional set of counterterms that tune model parameters such that the tree-level vacuum structure of eq. (12) of the potential is preserved when $V_0 \to V_{\rm eff}$. See appendix B 1

for details. This scheme is conventionally dubbed $\overline{\text{MS}}$ scheme [21] but not to be confused with the original $\overline{\text{MS}}$ scheme where counterterms only remove UV divergences; cf. II C.

Without RG improvement, the PT parameters depend on $\bar{\mu}$ through higher-order effects. In practice, this dependence appears to be small for the fixed $\bar{\mu} = v_0$ but becomes relevant when considering a thermal scale $\bar{\mu} \sim T$; see sec. IV for details. The remaining scale dependence is related to the implicit running of the model parameters in the thermal, effective, parameters, e.g. eqs. (7)–(9). The corresponding $\bar{\mu}$-dependent logarithms are counterfeit by RG improvement contained in the two-loop thermal masses of the 3D EFT [36]; cf. sec. II C.

In all our comparisons, we report the model parameters at the input scale, the Z-boson mass, M_Z, such that in all plots below e.g. $\lambda_{hs} = \lambda_{hs}(\bar{\mu} = M_Z)$.

B. Four dimensions: On-shell scheme

The on-shell scheme [47, 48] computes the one-loop vacuum correction of the effective potential (10) by installing a cutoff regularization for the radial integration with a UV cutoff, Λ. The potential then directly depends on Λ via [49]

$$J_{\text{CW}}(m^2, \Lambda) = \frac{1}{2} \int_P^\Lambda \ln\left(P^2 + m^2\right), \tag{13}$$

where $\int_P = \int \frac{\mathrm{d}^4 P}{(2\pi)^4}$ and UV divergences are regulated via counterterms. The tree-level VEV and mass eigenstates from eq. (12) are preserved at one-loop level by imposing for scalar masses to not change with respect to their tree-level values. This is achieved by relating $\Lambda^2 \to m_{0i}^2$, where m_{0i} is the mass of particle i at the EW vacuum. As typically done in this simple approximation, we ignore the running of all coupling constants.

In both the on-shell and $\overline{\text{MS}}$ scheme (cf. sec. II A), we implement IR resummation by the truncated full dressing approach [50, 51]. This procedure replaces the vacuum by one-loop thermally corrected masses in the tree-level field-dependent masses as $m_i^2 \to m_{i,3}^2 = m_i^2\big|_{\mu_i \to \mu_{i,3}}$.

C. Dimensional reduction and 3D EFT expansion

The finite-temperature scale hierarchy separates *hard*, *soft*, and *ultrasoft* scales, *viz.*

$$\pi T \gg g T \gg g^2 T\,, \tag{14}$$

and the dynamics of the PTs is driven by IR effects. By recasting theories in the EFT picture of dimensional reduction [18, 19, 52], it becomes evident that for modes that are deeper in the IR, the perturbative series converges increasingly slowly [42]. This is the case for transitioning Lorentz scalars, such as the Higgs or the light singlet scalar of the xSM. The validity of perturbation theory can then be extended by integrating out heavy degrees of freedom which eliminates hierarchy-induced large logarithms via RG equations. The final theory is the 3D bosonic IR sector of the parent theory.

This theory, the *softer* 3D EFT, is structurally identical to the conventional ultrasoft EFT [52] but is valid for transitions between the soft and ultrasoft scale, $gT \gg |p| \gg g^2 T$, where $m_{\text{D}} \gg m_A \sim m_\phi$. Here, m_A are the spatial gauge boson and m_{D} the Debye masses. After dimensional reduction, we utilize the effective potential up to two-loop order with NLO matching of the 3D EFT. This EFT construction is obtained by in-house `FORM` [53] software, by `DRalgo` [44, 54], and by previous calculations of the EFT [34, 35].[1] All barred and subscripted quantities are understood in the 3D EFT (e.g., $\mu_h \to \bar{\mu}_{h,3}$) with $\bar{\boldsymbol{\phi}} \sim \boldsymbol{\phi} T^{-\frac{1}{2}}$.

Up to two-loop order, the 3D effective potential is

$$V_{\text{eff},3} = V_{0,3} + V_{1,3} + V_{2,3}\,, \tag{15}$$

$$V_{1,3} = \sum_i n_i\, J_3 \bar{m}_i^2(\boldsymbol{\phi}, T))\,, \tag{16}$$

where $d = 3 - 2\epsilon$, $V_{0,3}(\boldsymbol{\phi}, T)$ is the three-dimensional version of the tree-level potential (2) [35], and the degrees of freedom, n_i, are d-dependent. The corresponding mass eigenvalues $\bar{m}_i$ of the dynamical fields $i \in \{W, Z, G, h, s\}$ in the 3D EFT take the same structure as for eqs. (3)–(5). At one-loop level, in $V_{1,3}$, the integrals are UV-finite and three-dimensional

$$J_3(m^2) = \frac{T}{2} \int_{\mathbf{p}} \ln(p^2 + m^2) \overset{d=3-2\epsilon}{=} -\frac{T}{12\pi} [m^2]^{\frac{3}{2}}\,. \tag{17}$$

The two-loop contributions, $V_{2,3}$, to the potential (15), as well as the two-loop 3D EFT matching relations are adopted from [35, 44].

Due to the Z_2-symmetry of the potential (1) in the xSM, a tree-level barrier appears to be absent even at the softer scale in general. If this potential gives rise to a first-order transition, then the perturbative expansion is expected to converge slower since the expansion around the minimum receives radiative corrections already at LO. As a result, the effective potential exhibits known pathologies such as imaginary parts [55], IR divergences related to Goldstone modes [20, 29, 56], as well as gauge dependence [57].[2] In perturbation theory, such pathologies can be consistently treated in a strict EFT expansion [20, 58, 59].

In a practical approach to the problem, we focus on a direct minimization at the softer scale [29],[3] and on

[1] The updated [35], installs the correct scaling $x_3 \sim x_3' \sim \sqrt{T}$.

[2] For the potential, we verified that gauge dependence is a minor effect compared to incomplete resummation.

[3] Taking the absolute magnitude of the squared masses or omitting the imaginary part of the potential differs numerically. In practice, we discard the imaginary part if numerically $\text{Im}\, V_{\text{eff}} < \text{Re}\, V_{\text{eff}}$ at the minima [21].

two-step transitions of the form eq. (6); see [60, 61] for non-perturbative analyses. For light singlet scalar masses and since perturbatively the barrier vanishes in singlet-direction, we assume for `step1` in eq. (6) to be of second order [60]. Then the second transition step, `step2` in eq. (6), again features a tree-level barrier through a spontaneously broken Z_2-symmetry [35, 36] where $\langle S\rangle \neq 0$. Consequently, the transition is rendered strong with the advantage of avoiding difficulties related to radiatively induced transitions at the softer scale [36].

Since the 3D EFT is constructed in the high-temperature expansion $m/T \ll 1$, we inspect only temperature regions where the high-temperature assumption holds and effects of the scalar masses are small compared to the temperature. Especially, by retaining explicit terms of $J_3(m^2_{X_0})$ in a soft-scale EFT for (adjoint) temporal scalars $X_0 \in \{A_0, B_0, C_0\}$, we confirm that $m^2_{\rm D} \gg h_3 v^2$ effects are small for our analysis at the softer-scale EFT. Here, h_3 is the coupling between Lorentz and temporal scalars X_0 [20, 52, 62]. Given the maximal ratio $\phi/T \sim \mathcal{O}(1)$ we encountered, and after both expanding and explicitly keeping J_3-functions, we identify soft effects to modify the predicted parameter space of sec. IV by $\mathcal{O}(0.1\%)$. This analysis is reported in a second xSM scan in appendix D.

For the 3D EFT, we relate $\overline{\rm MS}$- with physical parameters using the one-loop improved vacuum renormalization of appendix B 2 and [35]. This procedure has the advantage, that the minimization condition (12) is only needed at tree-level and momentum corrections are consistently included. Corrections to the tree-level relations are then contained in vacuum pole mass renormalization at higher orders.

III. FIRST-ORDER PHASE TRANSITIONS

Cosmological first-order PTs occur via nucleating true-vacuum bubbles which expand in a space filled with false vacuum. At finite temperature, the probability per unit time and volume of jumping from a metastable to a state of lower energy, has the semi-classical approximation [63–67]

$$\Gamma(T) = A_{\rm dyn} \times A_{\rm stat}\, e^{-S_3/T}\,, \tag{18}$$

where the prefactor factorizes into $A_{\rm dyn}$, a dynamical and $A_{\rm stat}$, a statistical contribution at all orders [68]. Focusing only on equilibrium thermodynamic contributions, we use the standard approximation [65, 66]

$$A_{\rm stat} \approx T^3\Big(\frac{S_3}{2\pi T}\Big)^{\frac{3}{2}}\,, \qquad A_{\rm dyn} \approx T\,, \tag{19}$$

which suppresses effects of inhomogeneous contributions to the functional determinant of the fluctuation operator of $A_{\rm stat}$. Such effects are formally of higher order but can dominate the exponent [29, 69, 70] in extreme cases. We justify the choice in eq. (19) since the absence of both higher-order effects and a self-consistent bounce solution [71] are systematic errors to all schemes of sec. II. The Euclidean action, S_3, of the critical bubble or bounce for $O(3)$-symmetric thermal systems, is then computed at $\mathcal{O}(\hbar^1)$ for the one-loop and $\mathcal{O}(\hbar^2)$ for the two-loop softer EFT, bearing in mind that this systematically discards real-time physics encoded in $A_{\rm dyn}$ and field-dependent gradient terms in the effective action; see [72] for out-of-equilibrium effects and [70, 73, 74] for approaches using nucleation EFT.

From the rate (18), we compute the temperature scales of the transition. At the nucleation temperature, $T_{\rm n}$, the tunneling rate per horizon volume becomes relevant[4]

$$\int_{t_{\rm c}}^{t_{\rm n}} {\rm d}t \frac{\Gamma(t)}{H(t)^3} = \int_{T_{\rm n}}^{T_{\rm c}} {\rm d}T \frac{\Gamma(T)}{H(t)^4 T} = 1\,. \tag{20}$$

The integration is bounded by the critical temperature, $T_{\rm c}$, where the two-phase minima become degenerate. Conversely, $t_{\rm c}$ and $t_{\rm n}$ are the times related to $T_{\rm c}$ and $T_{\rm n}$, respectively. The Hubble rate is defined as

$$H^2(T) = \frac{\rho_{\rm tot}}{3M^2_{\rm Pl}}\,, \qquad \rho_{\rm tot} = \rho_r + \Delta V_{\rm eff}(T)\,, \tag{21}$$

with $M_{\rm Pl} = 2.4 \times 10^{18}$ GeV the reduced Planck mass, $\rho_r = \frac{\pi^2}{30} g_*(T) T^4$ the radiation energy density of relativistic species, and $g_*(T)$ the number of radiative degrees of freedom [75]. Differences between the meta-stable $(+)$ and stable $(-)$ phase are henceforth denoted as $\Delta X = X^{(+)} - X^{(-)}$ for e.g. $X = V_{\rm eff}$.

To estimate the time of bubble collisions, we employ the percolation temperature T_p. It is defined by requiring the probability, that a point in space remains in the false vacuum, to be $P(T_p) = e^{-I(T_p)} \simeq 71\%$ [76]:

$$I(T_p) = \frac{4\pi}{3} \int_{T_p}^{T_{\rm c}} {\rm d}T' \frac{\Gamma(T')}{H(T')} \frac{r(T,T')^3}{T'^4} = 0.34\,. \tag{22}$$

The comoving radius of a bubble nucleated at time t' and propagated until t with velocity v_w is $r(t,t') = \int_{t'}^{t} {\rm d}\tilde{t} \frac{v_w(\tilde{t})}{a(\tilde{t})}$, and we require a shrinking volume in the false vacuum, *viz.* $\frac{{\rm d}I(T)}{{\rm d}\ln T} < -3$. After the PT, the false vacuum energy is re-transferred to the thermal bath that is reheated to $T_* = T_p[1+\alpha(T_p)]^{1/4}$ [76]. The strength of a cosmological PT [12, 77] and its inverse time duration are approximated as

$$\alpha \equiv \frac{1}{\rho_r}\Big(\Delta V_{\rm eff} - \frac{1}{4}\frac{{\rm d}\Delta V_{\rm eff}}{{\rm d}\ln T}\Big)\Big|_{T=T_p}\,, \tag{23}$$

$$\frac{\beta}{H} \equiv \frac{\rm d}{{\rm d}\ln T}\Big(\frac{S_3}{T}\Big)\Big|_{T=T_p}\,. \tag{24}$$

The trace of the energy-momentum tensor for α is taken in the relativistic plasma limit and in practice receives

[4] To convert temporal to temperature integration $a(T) = 1/T$, ${\rm d}t = -a(T)/H(T){\rm d}T$, and $a(t)$ is the FLRW metric scale factor.

further corrections if the speed of sound differs from $c_s^2 = 1/3$ [78, 79].

The thermodynamic parameters required to compute the GW spectra are T_*, $\alpha(T_p)$, $\beta(T_p)$, the speed of sound c_s and the bubble wall velocity v_w. The latter is particularly challenging to compute as it requires an out-of-equilibrium computation [80–94]. It has been shown [89, 95] that whenever the properties of the wall can be extracted with the semi-classical approximation [83, 84], the associated GW signals are too weak to be observed by the future experiments. For very strong transitions with $\alpha \approx 0.1$, the semi-classical approximation fails and the bubbles are expected to run away with ultra-relativistic velocities. Since we are interested in strong transitions that allow for a reasonable reconstruction, we henceforth assume $v_w = 1$; see [92] for a more careful evaluation of v_w in the xSM.

To obtain the thermodynamic parameters, we use a modified version of `CosmoTransitions` [96] that takes as an input the effective potential $V_{\rm eff}(\phi, T)$ for the different schemes.[5]

IV. IMPACT ON THE GW SIGNALS

By focussing on two-step transitions (6), from symmetric to singlet to vacuum Higgs minimum, we inspect GWs sourced by sound waves in the plasma [11, 12]. Transitions in the xSM are never significantly supercooled [76] and we can refrain from including GWs sourced by relativistic fluid motion or bubble collisions [98–102]. For them to be relevant much stronger transitions are required. We neglect possible contributions from turbulence [12] since despite significant progress to understand that source [103–105], its overall amplitude remains uncertain. The spectrum produced by sound waves in the plasma also evolved in recent years [106–111], predicting a modified spectral shape depending on the wall velocity. In the xSM, sound wave modifications are less important since mostly transitions with $v_w \approx 1$ predict observable signals [89, 95, 112]. Thus, we can use the results of lattice simulations for the shape of the signal [77, 113, 114].

The sound wave spectrum, its shape, and peak frequency can be expressed as

$$\Omega_{\rm GW}(f)h^2 = 4.13\times10^{-7}\,(R_*H_*)\left(1-\frac{1}{\sqrt{1+2\tau_{\rm sw}H_*}}\right) \times\left(\frac{\kappa_{\rm sw}\,\alpha}{1+\alpha}\right)^2\left(\frac{100}{g_*}\right)^{\frac{1}{3}} S_{\rm sw}(f)\,, \tag{25}$$

$$S_{\rm sw}(f) = \left(\frac{f}{f_{\rm p}}\right)^3\left[\frac{4}{7}+\frac{3}{7}\left(\frac{f}{f_{\rm p}}\right)^2\right]^{-\frac{7}{2}}, \tag{26}$$

[5] Our `python` software `DRansitions` [97] implements a generic potential in the softer 3D EFT of the xSM using `DRalgo` [44, 54].

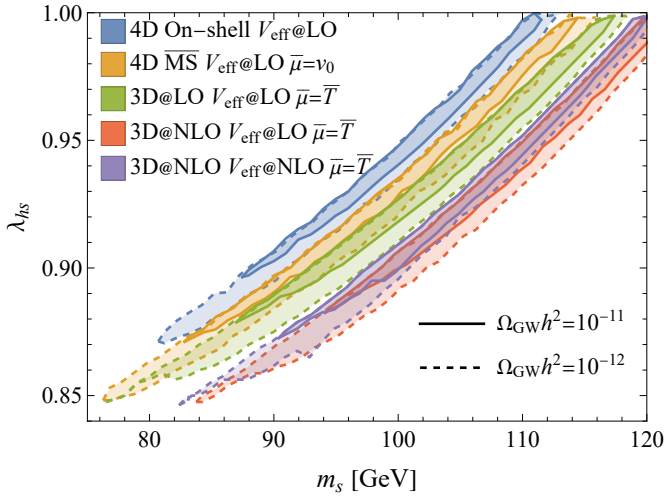

FIG. 1. Regions in the xSM parameter space predicting GW abundances above $\Omega_{\rm GW}h^2 = 10^{-11}$ (solid) and $\Omega_{\rm GW}h^2 = 10^{-12}$ (dashed) for two-step transitions where only the second step sources a strong first-order PT. Results are displayed as functions of the physical broken phase mass m_s and portal coupling λ_{hs} at fixed scalar self coupling $\lambda_s = 1$. The input scale $\bar{\mu} = M_Z$. The effective potential was computed in the on-shell (orange), and $\overline{\rm MS}$ (blue) schemes at one-loop, and the 3D EFT at LO using one-loop potential (green) and NLO using both one- (red) and two-loop (purple) effective potentials with 4D RG-scales $\bar{\mu} = v_0$ for $\overline{\rm MS}$- and $\bar{\mu} = \overline{T} = 4\pi e^{-\gamma}T$ for 3D approaches. In regions above each respective area, the EW minimum and the initial one become degenerate and percolation fails. For even larger λ_{hs}, the EW minimum is not global at zero temperature. Such models are excluded.

$$f_{\rm p} = f_{\rm sw} = 2.6\times10^{-5}\ {\rm Hz}\,(R_*H_*)^{-1} \times\left(\frac{T_*}{100\ {\rm GeV}}\right)\left(\frac{g_*}{100}\right)^{\frac{1}{6}}, \tag{27}$$

with efficiency factor $\kappa_{\rm sw}$. The average bubble radius normalized to the horizon size reads [12]

$$H_*R_* \approx (8\pi)^{\frac{1}{3}}\ \max\{v_w, c_s\}\left(\frac{\beta}{H}\right)^{-1}, \tag{28}$$

where for strong transitions $v_w > c_s$. The sound wave period normalized to the Hubble rate is approximated as [33, 76, 77, 98, 115]

$$\tau_{\rm sw}H_* = \frac{H_*R_*}{\bar{U}_f}\,, \qquad \bar{U}_f \approx \sqrt{\frac{3}{4}\frac{\alpha}{1+\alpha}\kappa_{\rm sw}}\,, \tag{29}$$

with the root-mean-square of the fluid velocity $\bar{U}_f$.

To predict the experimental accessibility of the xSM, we scan a large section of its parameter space by varying[6] $\lambda_{hs} \in [0.1, 1.2]$, $\frac{m_h}{2} < m_s < 130$ GeV, and $\lambda_s \in \{0.1, 1.0\}$. We restrict the physical masses m_h and m_s

[6] In the simplest Z_2-symmetric incarnation of the xSM, direct de-

EFT matching	1-loop $V_{\rm eff}$	2-loop $V_{\rm eff}$
LO	3D@LO $V_{\rm eff}$@LO	3D@LO $V_{\rm eff}$@NLO
NLO	–	3D@NLO $V_{\rm eff}$@NLO

TABLE I. Different levels of diligence in the 3D EFT approach for different orders of EFT matching using high-temperature dimensional reduction and loop orders of the effective potential $V_{\rm eff}$. The $\overline{\rm MS}$-approach is identical to (3D@LO $V_{\rm eff}$@LO) at high temperatures.

from eq. (4) for both scalars to be dynamical in the IR. Figure 1 shows the predicted GW abundance as a function of the scalar mass and Higgs-scalar coupling for fixed scalar self-coupling $\lambda_s = 1$.[7] The different regions are obtained by computing the xSM effective potential in the $\overline{\rm MS}$ scheme, the on-shell scheme and the 3D EFT.

For the 3D EFT approach, the EFT is constructed via dimensional reduction at LO (3D@LO) and NLO (3D@NLO) while the 3D effective potential is computed at one- ($V_{\rm eff}$@LO) and two-loop ($V_{\rm eff}$@NLO) levels; see tab I for nomenclature. The minimal approach using (3D@NLO $V_{\rm eff}$@LO) was proposed in [120]. The RG-scale is fixed to $\bar{\mu} = v_0$ for the $\overline{\rm MS}$ scheme and $\bar{\mu} = \overline{T}$ for the 3D EFT where $\overline{T} = 4\pi e^{-\gamma} T$ and γ is the Euler-Mascheroni constant.

The (3D@NLO) methods are the most stable and their predictions change little when using NLO corrections to the effective potential. Since the $\overline{\rm MS}$ scheme and the (3D@LO) results are identical in the high-temperature limit, their results are naturally closest with the difference rooted in using the conventional scale $\bar{\mu} = v_0$ in the $\overline{\rm MS}$ scheme instead of a scale more natural to a thermal transition $\bar{\mu} = \overline{T}$. Finally, the relatively large differences in signal amplitudes, $\Omega_{\rm GW}h^2$, between the various methods convert to relatively small differences of the corresponding model parameters. Predictions of (m_s, λ_{hs}) amount to uncertainties of at most 10% in extreme cases. However, the parameter space predicting a strong two-step transition is often narrow and shifts of a few percent can become qualitatively important. They can even change the nature of the transition entirely.

To inspect the impact of resummation methods of the potential on reconstructing sources behind future observed signals with LISA [109, 121–123], we perform Fisher matrix analyses [124]. The matrix elements for the two spectral parameters, the peak amplitude and frequency, $\theta_i \in \{\Omega_{\rm sw}, f_{\rm sw}\}$, read

$$\Gamma_{ij} = \mathcal{T} \int \frac{{\rm d}f}{\Omega_{\rm tot}(f)^2} \frac{\partial \Omega_{\rm tot}(f)}{\partial \theta_i} \frac{\partial \Omega_{\rm tot}(f)}{\partial \theta_j} \,, \qquad (30)$$

where the mission operation time $\mathcal{T} = 4\,{\rm yr}$ and the variance of parameters $\sigma_i^2 = \Gamma_{ii}^{-1}$. By including only the instrumental noise (see e.g. [121])

$$\Omega_{\rm tot}(f) = \Omega_{\rm GW}(f) + \Omega_{\rm instr}(f) \,, \qquad (31)$$

we neglect astrophysical noise sources of binary white dwarfs [125, 126] and the black hole population currently probed by LIGO-Virgo-KAGRA [127]. Including the latter would effectively reduce the sensitivity of the experiment such that a stronger spectrum would be necessary to reproduce benchmarks with the same relative uncertainty on the parameters of the spectrum. Our results would otherwise remain unchanged. The Fisher matrix approach we follow, is a simplification and a more accurate reconstruction would require a Markov Chain Monte Carlo fit. However, the methods will agree provided the errors on the reconstruction are smaller than about 10% which is exactly the accuracy we find in our benchmark. For details on the state-of-the-art reconstruction of phase transition parameters with LISA see [23], which also provides a comparison of the two methods and a discussion of the exact impact of the inclusion of foregrounds.[8]

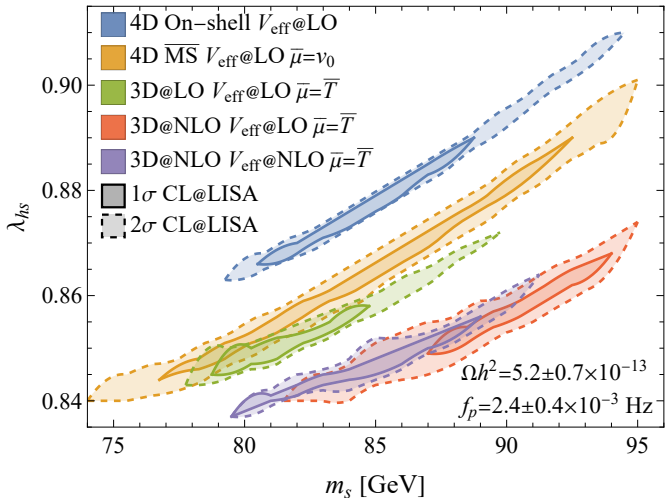

FIG. 2. Parameter reconstruction with LISA of the benchmark point spectrum defined by abundance $\Omega_{\rm GW}h^2 = 5.2 \times 10^{-13}$ and peak frequency $f_{\rm p} = 2.4 \times 10^{-3}$ Hz. Using Fisher analysis, we estimate the error associated with the reconstruction and indicate uncertainties with central values at 1σ (68%, solid) and 2σ (95%, dashed) confidence levels (CL). As in fig. 1, the colored regions indicate the method of resummation. With SNR = 10, the chosen benchmark corresponds to a barely detectable signal.

tection experiments exclude most of the parameter space due to an overabundance of the scalar dark matter (DM) [116] while the transition parameters might be modified due to the presence of domain walls [117]. To evade these issues, we assume minimal modifications: new particles in the dark sector destabilize the scalar DM [118] and a small Z_2-breaking term erases the domain walls [119]. Neither of these would impact our main results.

[7] Varying λ_s shifts the observable parameter space, since for different λ_s, the hyperplane in the $(m_s, \lambda_{hs}, \lambda_{s,\rm fixed})$-space changes (cf. appendix V). The main results remain unchanged.

[8] The reconstruction also proves robust under a more general noise model for LISA [128].

As a representative benchmark point, we chose a spectrum with the abundance $\Omega_{\rm GW}h^2 = 5.2 \pm 0.7 \times 10^{-13}$ and peak frequency $f_{\rm p} = 2.4 \pm 0.4 \times 10^{-3}$ Hz. The signal-to-noise ratio observed by LISA would be SNR = 10 and render it one of the weakest signals where one can claim a detection. Figure 2 shows the reconstructed parameter space based on the various methods used for computing the transition parameters. While (3D@NLO) predictions converge at 2σ confidence level (CL), the differences between 4D and (3D@NLO) predictions do not overlap at 2σ CL. Such a discrepancy indicates that theoretical uncertainties in the computation of the potential are at least of the same order as those stemming from the reconstruction of the GW spectrum with LISA. For all stronger and more easily observable spectra, the error from the experimental reconstruction would be smaller indicating that theoretical errors in thermodynamic computations of the potential would be the main source of uncertainty in all observable spectra. Hence, state-of-the-art methods (cf. e.g. [20, 29, 44, 72]) need to be used to improve our determination of the parameter space of the underlying model any further in the future.

Another factor in carefully estimating theoretical uncertainty is renormalization scale dependence. Since perturbative approximations of the effective potential generally depend on the employed 4D RG-scale, its variation can impact the predicted parameter space of GW signals detectable by LISA [29, 36]. Such RG-scale variation serves a proxy for quantifying the importance of absent higher-order corrections. At finite temperature, the potential is scale-dependent at $\mathcal{O}(g^4T^2)$ through the implicit running of the thermal parameters eqs. (7)–(9) [36].

Both 4D methods, the on-shell scheme and the $\overline{\rm MS}$ scheme at $\bar{\mu} \sim v_0$, effectively fix the scale and therefore lack an estimate of their theoretical uncertainty. Their nearly scale-invariant reconstructed parameter spaces should not be mistaken for theoretical robustness. First, the on-shell scheme does not exhibit an explicit RG-scale dependence since divergent integrals are regulated by a UV cutoff. Since the cutoff is fixed at the pole masses of the respective particles, phenomenological predictions are manifestly $\bar{\mu}$-independent. This does not indicate the inclusion of higher-order corrections that are theoretically relevant. At the same time dimensional regularization has the advantage of being manifestly Lorentz invariant which is absent in cutoff regularization. Second, the $\overline{\rm MS}$ scheme at $\bar{\mu} \sim v_0$, uses a non-thermal RG scale which renders it almost insensitive to RG-scale variation. We explicitly verified, that the remaining $\bar{\mu}$-variation via $\bar{\mu} \in \{1/2, 1, 2\} \times v_0$ results in a $\mathcal{O}(0.1\%)$ shift of the parameter space.

To estimate the relevance of higher-order contributions, however, we focus on the 3D EFT since it also contains the $\overline{\rm MS}$ scheme via (3D@LO $V_{\rm eff}$@LO), and impose two different values of the 4D RG-scale

$$\text{3D EFT:} \qquad \bar{\mu} = \{1/2, 4e^{-\gamma}\} \times \pi T\,, \qquad (32)$$

where $\overline{T} = 4\pi e^{-\gamma} T$ is the weighted sum of a nonzero bosonic Matsubara frequency that arise within logarithms at one-loop order. Using the 3D EFT approach, we restrict ourselves to a comparison between (3D@LO $V_{\rm eff}$@LO) and (3D@NLO $V_{\rm eff}$@LO), i.e. the one-loop effective potential with LO (NLO) dimensional reduction. The reconstructed parameter space predicting the GW abundance $\Omega_{\rm GW} > 10^{-12}$ is shown in fig. 3. For the parts of the parameter space where these regions coincide, we show the ratio between the predicted GW amplitudes

$$\Delta\Omega_{\rm GW} = \frac{\Omega_{\rm GW}(\bar{\mu} = \frac{1}{2}\pi T)}{\Omega_{\rm GW}(\bar{\mu} = \overline{T})}\,. \qquad (33)$$

The observable parameter space for the (3D@LO $V_{\rm eff}$@LO) potential in the 3D EFT, is shifted by $\mathcal{O}(1\%)$ depending on the singlet mass m_s and exhibits deviations up to $\Delta\Omega_{\rm GW} \sim \mathcal{O}(10^3)$ as previously predicted [29, 36]. This is identical for the $\overline{\rm MS}$ scheme at high temperatures. The observed scale-dependence also increases logarithmically with m_s through the implicit running of the thermal parameters. Predictions from the (3D@NLO $V_{\rm eff}$@LO) potential, remain mostly insensitive under the RG-scale variation. They are more robust and the $\bar{\mu}$-variation of eq. (32) changes the amplitude by at most $\Delta\Omega_{\rm GW} \lesssim \mathcal{O}(10^2)$. As expected, utilizing two-loop thermal masses, shifts the $\bar{\mu}$-dependence to higher orders [36] due to parametric scale cancellation. This is true already at the one-loop level for $V_{\rm eff}$ [120].

Notably, large variations of the predicted signal correspond to shifts at the $\mathcal{O}(1\%)$ level in the reconstructed values of the parameters. We summarize our findings as follows:

(i) in the $\overline{\rm MS}$ scheme (3D@LO $V_{\rm eff}$@LO), the parameter space is displaced by $\mathcal{O}(1\%)$ when varying the RG-scale $\bar{\mu}$,

(ii) the on-shell scheme does not involve running of couplings such that parameter spaces are fixed and implicitly affected by missing higher-order corrections,

(iii) in the 3D EFT, (3D@NLO $V_{\rm eff}$@LO), the parameter space is displaced by $\mathcal{O}(0.1\%)$ when varying four-dimensional RG-scale $\bar{\mu}$.

Theoretical uncertainty is also intrinsically linked with residual gauge dependence [29]. In all approaches of sec. II, gauge dependence would only affect the effective potential since the matching relations up to (3D@NLO) are gauge-invariant. Studying the dependence of our results on different gauges [41] other than Landau gauge is deferred to future work; cf. [31] for such a study for the thermodynamics in 4D approaches. Focusing on $\xi = 0$ is justifiable, since gauge dependence affects all stages of our computation in a similar manner and can therefore be treated as a systematic error of our analysis. Additionally, we expect that strong transitions in the xSM are dominated by the residual RG-scale dependence [129].

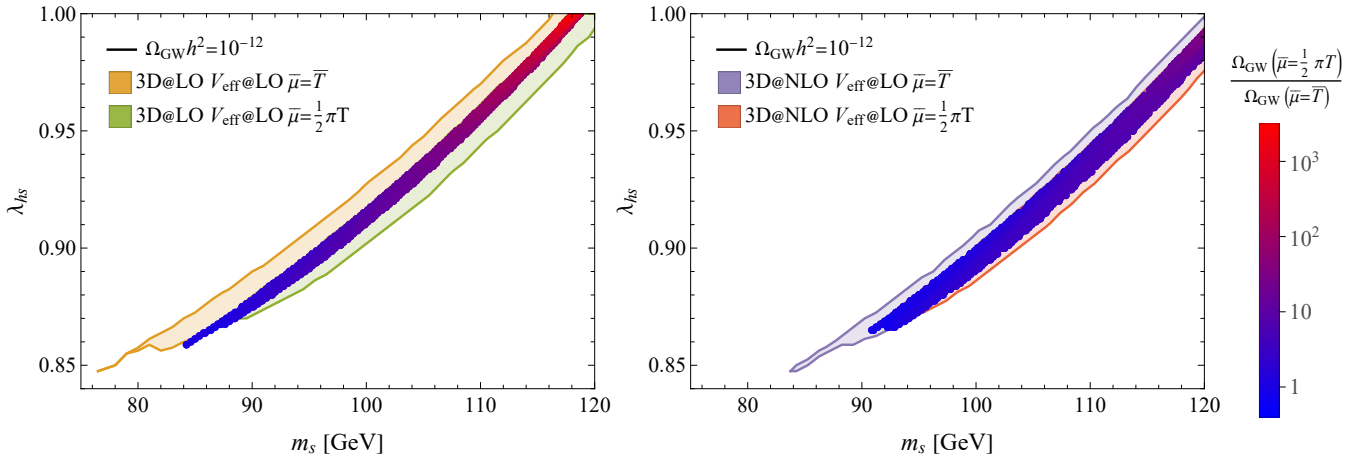

FIG. 3. Regions in the xSM parameter space predicting GW abundances $\Omega_{\rm GW} > 10^{-12}$ computed at LO (left) and NLO (right) in dimensional reduction. To quantify the scale dependence of each method in both panels, we show results at the 4D RG-scales $\bar{\mu} = \{\frac{1}{2}\pi T, \overline{T}\}$. The ratio (33) of the resulting GW amplitudes at these scales is indicated by the heatmap with ratios up to $\Delta\Omega_{\rm GW} \sim \mathcal{O}(10^3)$.

V. CONCLUSIONS

This *article* compares methods of thermal resummation between the state-of-the-art 3D EFT and the 4D daisy resummed potentials in cosmological PTs realized in the simplest SM extension featuring a neutral scalar, the xSM. We confirm that the amplitude of the predicted GW signal can change between the methods by many orders of magnitude. Conversely, we report that this theoretical uncertainty corresponds to a small shift of $\mathcal{O}(1\%)$ for the model parameters needed to realize the signal. Despite the relatively small shifts, we find that for any signal visible to LISA, these theoretical uncertainties would exceed the experimental ones assuming a SNR $\simeq 10$ threshold corresponding to an observation. For stronger signals, where experimental uncertainties would be significantly reduced, a further theoretical effort is inevitable to obtain more information on the underlying model Lagrangian.

The perturbative expansion of state-of-the-art high-precision 3D EFT approaches quickly converges with the loop order. We show that once two-loop thermal resummation (3D@NLO) is included, the predicted parameter spaces become robust. Higher orders in Matsubara zero-mode loops are compatible with leading orders – thus forming the most promising route towards robust predictions. For radiatively-induced transitions, higher orders of the 3D effective potential become relevant again [35].

The differences between the perturbative approaches can be traced back to missing higher-order corrections to the effective potential in a strict EFT expansion [20]. The most severe deficiency is therefore imprinted on the 4D on-shell and $\overline{\rm MS}$ approaches, which lack higher-order contributions in thermal resummation. A similar analysis concerning residual gauge dependence is kept for future work.

However, all approaches suffer from IR sensitivities from the soft scale if the true transition is radiatively induced at the softer scale. Then further degrees of freedom such as spatial gauge fields need to be integrated out to ensure a tree-level barrier at the softer-scale EFT. This leads to a much more pronounced uncertainty in classically scale-invariant models where the symmetry is broken radiatively [62]. Since we focus on transitions that are barrier-inducing at the softer scale, the impact of thermal resummation can be analyzed without further resummation in the 3D EFT [20]. Otherwise, there would be a systematic error present from soft scale resummation in the proof-of-principle analysis of this *article*. While recent advancements in the bubble nucleation rate [68, 70] warrant to investigate the impact of these improvements, multi-field tunneling at the nucleation scale EFT [72] and higher-order corrections to the nucleation rate [69] remain theoretical and practical challenges.

ACKNOWLEDGMENTS

We acknowledge enlightening discussions with Andreas Ekstedt, Oliver Gould, Maciej Kierkla, Lauri Niemi, Bogumiła Świeżewska, Tuomas V. I. Tenkanen, and Jorinde van de Vis. This work was supported by the Polish National Science Center grant 2018/31/D/ST2/02048. ML was also supported by the Polish National Agency for Academic Exchange within Polish Returns Programme under agreement PPN/PPO/2020/1/00013/U/00001. MM acknowledges support from Norwegian Financial Mechanism for years 2014–2021, grant no. DEC-2019/34/H/ST2/00707 and from the Swedish Research Council (Vetenskapsrådet) through contract no. 2017-03934. LS, PS, and DS acknowledge support by the Deutsche Forschungsgemeinschaft (DFG, German Research Foundation) through the

CRC-TR 211 'Strong-interaction matter under extreme conditions' – project no. 315477589 – TRR 211. PS and DS acknowledge the hospitality of the University of Warsaw during the final stages of this work.

APPENDIX

This section discusses the technical details for vacuum renormalization and further determining the robustness of the thermal effective potential for the various approaches discussed in sec. II.

Appendix A: Renormalization group evolution

Following [35, 39, 130] after proper rescaling of our parameters and with $t = \log \bar{\mu}^2$, the one-loop RG equations are given by

$$\partial_t g_1^2 = \frac{g_1^4}{(4\pi)^2}\Big(\frac{1}{6} + \frac{20}{9} n_{\rm f}\Big)\,, \tag{A1}$$

$$\partial_t g_2^2 = \frac{g_2^4}{(4\pi)^2}\Big(-\frac{43}{6} + \frac{4}{3} n_{\rm f}\Big)\,, \tag{A2}$$

$$\partial_t g_3^2 = \frac{g_3^4}{(4\pi)^2}\Big(-\frac{11 N_{\rm c}}{3} + \frac{4 n_{\rm f}}{3}\Big)\,, \tag{A3}$$

$$\partial_t y_t^2 = \frac{y_t^2}{(4\pi)^2}\Big(\frac{2N_{\rm c}+3}{2} y_t^2 - 6 C_{\rm F} g_3^2 - \frac{9}{4} g_2^2 - \frac{17}{12} g_1^2\Big)\,, \tag{A4}$$

$$\begin{aligned}\partial_t \lambda = \frac{1}{(4\pi)^2}\Big(&12\lambda^2 + \frac{\lambda_{hs}^2}{4} - \lambda\frac{3}{2}(3g_2^2 + g_1^2) \\ &+ \frac{3}{16} g_1^4 + \frac{3}{8} g_2^2 g_1^2 + \frac{9}{16} g_2^4 \\ &- N_{\rm c} y_t^4 + 2 N_{\rm c} y_t^2 \lambda\Big)\,,\end{aligned} \tag{A5}$$

$$\begin{aligned}\partial_t \lambda_{hs} = \frac{\lambda_{hs}}{(4\pi)^2}\Big(&2\lambda_{hs} + 3\lambda_s - \frac{3}{4}(3g_2^2 + g_1^2) \\ &+ N_{\rm c} y_t^2 + 6\lambda\Big)\,,\end{aligned} \tag{A6}$$

$$\partial_t \lambda_s = \frac{1}{(4\pi)^2}\Big(\lambda_{hs}^2 + 9\lambda_s^2\Big)\,, \tag{A7}$$

$$\begin{aligned}\partial_t \mu_h^2 = \frac{1}{(4\pi)^2}\Big(&\mu_h^2\Big(6\lambda + N_{\rm c} y_t^2 - \frac{9}{4} g_2^2 - \frac{3}{4} g_1^2\Big) \\ &+ \frac{1}{2}\lambda_{hs}\mu_s^2\Big)\,,\end{aligned} \tag{A8}$$

$$\partial_t \mu_s^2 = \frac{1}{(4\pi)^2}\Big(2\mu_h^2\lambda_{hs} + 3\mu_s^2\lambda_s\Big)\,, \tag{A9}$$

$$\partial_t v = \frac{1}{(4\pi)^2}\frac{1}{2}\Big(N_{\rm c} y_t^2 - \frac{9}{4} g_2^2 - \frac{3}{4} g_1^2\Big)\,, \tag{A10}$$

$$\partial_t x = 0\,, \tag{A11}$$

where g_i for $i = 1, \ldots, 3$ are the $\mathrm{U(1)_Y}$, $\mathrm{SU(2)_L}$, $\mathrm{SU(3)_c}$ gauge couplings, respectively. Here, y_t is the top Yukawa coupling, $\mu_h^2 < 0$, $n_{\rm f} = 3$ the number of fermion families, $N_{\rm c} = 3$ the number of colors, and $\gamma_v = \partial_t v$ the Higgs and $\gamma_x = \partial_t x$ singlet anomalous dimension.

In all our analyses, the input scale is $\bar{\mu} = M_Z$ and as initial conditions, we impose

$$\begin{aligned} g_1(M_Z) &= 0.344\,, & g_2(M_Z) &= 0.64\,, \\ g_3(M_Z) &= 1.22\,, & y_t(M_Z) &= 1\,, \end{aligned} \tag{A12}$$

using the physically observed masses, the pole masses, at their numerical values [131]

$$\begin{aligned}&(M_t, M_W, M_Z, M_h) \\ &\quad = (172.69, 80.377, 91.1876, 125.25)\ \text{GeV}\,.\end{aligned} \tag{A13}$$

Appendix B: Relating $\overline{\rm MS}$ parameters to physical observables

During our analysis, we employed two different procedures for vacuum renormalization:

1. Vacuum renormalization through counterterms

For the vacuum renormalization in the 4D $\overline{\rm MS}$ scheme, the initial conditions for the parameters λ, μ_h^2, and μ_s^2 are obtained by requiring the tree-level potential, V_0, to have a minimum at the electroweak vacuum $\boldsymbol{\phi} = (v_0, 0)$ and to yield the correct mass eigenvalues. These requirements, give rise to the conditions

$$\frac{\partial V_0}{\partial \phi_i}\Big|_{\substack{\boldsymbol{\phi} = (v_0\xi(v_0), 0) \\ \bar{\mu} = v_0}} = 0\,, \tag{B1}$$

$$\frac{\partial^2 V_0}{\partial \phi_i^2}\Big|_{\substack{\boldsymbol{\phi} = (v_0\xi(v_0), 0) \\ \bar{\mu} = v_0}} = M_i^2\,, \tag{B2}$$

where M_i are the pole masses with $\phi_i = v, x$, and the off-diagonal Hessian derivative vanishes trivially when the Z_2-symmetry remains unbroken. The minimization conditions thus read

$$\mu_h^2(v_0) = -\frac{1}{2}\frac{M_h^2}{\xi(v_0)^2}\,, \tag{B3}$$

$$\mu_s^2(v_0) = M_s^2 - \frac{1}{2}\lambda_{hs}(v_0) v_0^2 \xi(v_0)^2\,, \tag{B4}$$

$$\lambda(v_0) = \frac{1}{2}\frac{M_h^2}{v_0^2 \xi(v_0)^4}\,, \tag{B5}$$

where

$$\xi(\bar{\mu}) = \exp\left[\int_{\log(\bar{\mu}^2)}^{\log(M_Z^2)} \mathrm{d}t\, \gamma_v(t)\right], \tag{B6}$$

encodes the solution of the Higgs field RG equation, $v(\bar{\mu}) = \xi(\bar{\mu}) v$. Since we fix $M_h = 125.25$ GeV and $v_0 \simeq 246$ GeV, the only free parameters are the singlet mass m_s, its quartic self-interaction λ_s and the Higgs portal coupling λ_{hs} which we fix at the input scale M_Z.

At one-loop level, this procedure ensures that the minimization conditions of eqs. (B1) and (B2) are fulfilled for $V_0 \to V_{\rm eff}$. By introducing counterterms [21], the model parameters μ_h^2, μ_s^2, and λ are tuned accordingly and yield one-loop improvements to the relations (B3)–(B5). The counterterm potential has the following form:

$$V_{\rm CT} = \frac{\delta\mu_h^2}{2}v^2 + \frac{\delta\mu_s^2}{2}x^2 + \frac{\delta\lambda}{4}v^4\,, \tag{B7}$$

where

$$\begin{aligned}
\delta\mu_h^2 &= -\Big(\frac{3}{2}\frac{1}{v_0\xi(v_0)}\partial_v - \frac{1}{2}\partial_v^2\Big)V_{\rm CW}\Big|_{\substack{\phi\,=\,(v_0\xi(v_0),\,0)\\ \bar\mu\,=\,v_0}}\,,\\
\delta\lambda &= \frac{1}{2v_0^3\xi(v_0)^3}\Big(\partial_v - v_0\xi(v_0)\partial_v^2\Big)V_{\rm CW}\Big|_{\substack{\phi\,=\,(v_0\xi(v_0),\,0)\\ \bar\mu\,=\,v_0}}\,,\\
\delta\mu_s^2 &= -\partial_x^2 V_{\rm CW}\Big|_{\substack{\phi\,=\,(v_0\xi(v_0),\,0)\\ \bar\mu\,=\,v_0}}\,,
\end{aligned} \tag{B8}$$

are obtained by the renormalization conditions and $V_{\rm CW}(\boldsymbol{\phi}) = \sum_i n_i J_{\rm CW}(m_i^2(\boldsymbol{\phi}))$ is the vacuum contribution in eq. (10) or the Coleman-Weinberg potential.

2. One-loop corrected vacuum renormalization

In the 3D EFT, we use one-loop corrected vacuum values for the above couplings, as described in appendix A of [35] and [52]. The xSM model parameters are fixed by the following physical scheme:

In: Parameters $M_s, \lambda_s, \lambda_{hs}$, and pole masses at numerical values eq. (A13).

(i) minimize the scalar potential at tree level (cf. eq. (B1)), with $\langle S\rangle = 0$ to determine the Higgs VEV,

(ii) solve the renormalized parameters at $\overline{\rm MS}$-scale $\bar\mu = M_Z$ from the one-loop corrected relations [52]; see [35] for the xSM, [29] for the SM, and [132] for the Two Higgs Doublet model,

(iii) run the parameters to the matching scale $\bar\mu = X\overline{T}$ using one-loop β-functions (A1)–(A9). Here, X is a constant typically varied to quantify the importance of higher-order corrections.

Out: $\overline{\rm MS}$-parameters as function of physical parameters and $\overline{T}$.

By relating pole masses to physical two-point functions, this scheme ensures that higher order corrections in the renormalization conditions are included and the momentum dependence of the pole masses is respected.

The effective potential is not a physical quantity and is independent of momentum. Momentum dependence is necessary to physically fix the pole mass. Since we evaluate the vacuum renormalization at M_Z, appendix B 1 (cf. [29]) is a naive approximation of the prescription in appendix B 2 and reproduces the renormalization condition of the Higgs sector. To also relate parameters beyond μ_h and λ to physical observables, the full one-loop corrected vacuum renormalization of appendix B 2 is required [35].

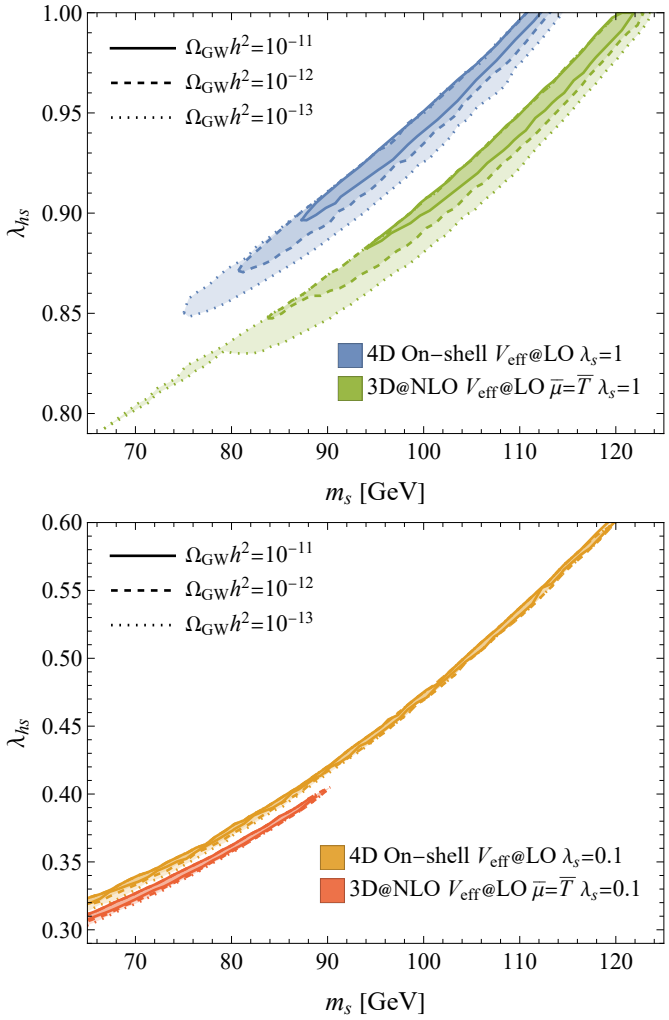

FIG. 4. Comparison of the parameter space upon varying the quartic singlet scalar self-coupling, $\lambda_s \in \{0.1, 1.0\}$, for the on-shell scheme and the 3D EFT approach at 4D RG scale $\bar\mu = \overline{T}$ using (3D@NLO $V_{\rm eff}$@LO) in the EFT.

Appendix C: Impact of the scalar self-coupling λ_s

The main body discusses parameter space scans in the $(m_s, \lambda_{hs}, \lambda_s)$-hyperplane. The singlet quartic self-coupling is fixed at $\lambda_s = 1$. To demonstrate that these results are qualitatively λ_s-independent, we display in fig. 4 the parameter spaces at fixed $\lambda_s = 0.1$ in the on-shell scheme and the 3D EFT. For the 3D EFT analysis, we again employ (3D@NLO $V_{\rm eff}$@LO), namely a one-loop effective potential with NLO dimensional reduction.

For both approximations, the detectable parameter

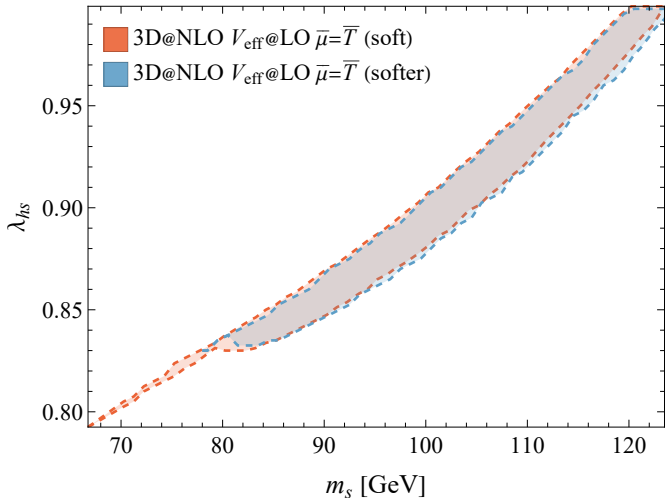

FIG. 5. Comparison of the parameter spaces with $\Omega_{\rm GW}h^2 \geq 10^{-13}$ predicted from the (3D@NLO $V_{\rm eff}$@LO) potential using NLO dimensional reduction and LO effective potential either in the soft or the softer EFT. The soft EFT retains explicit terms of $J_3(m^2_{X_0})$ for (adjoint) temporal scalars $X_0 \in \{A_0, B_0, C_0\}$.

space moves towards smaller values of λ_{hs}. Due to the decreasing mass range that produces observable GW signals, the overall relevant parameter space shrinks. By contrasting both approaches, a similar $\mathcal{O}(1\%)$ uncertainty in the signal reconstruction is expected – similar to the $\lambda_s = 1$ case. Hence, we conclude that our results are robust including variations of the quartic self-coupling of the singlet scalar.

Appendix D: Impact of soft-scale effects on 3D EFT

This section investigates the effects of missing higher-order terms in the v/T and x/T expansions at the softer scale by retaining the full soft dynamics of the 3D EFT at one-loop level.

To this end, we use the soft potential at one-loop level from [35] now also in the background of the (adjoint) temporal gauge fields $X_0 \in \{A_0, B_0, C_0\}$. Due to an effective explicit center symmetry breaking during the EFT construction, in the 3D EFT the only minimum that can be resolved is $\langle X_0 \rangle \sim 0$ such that X_0-backgrounds vanish identically at the corresponding minimum [133].

By expanding the functions $J_3(m^2_{X_0})$ for (adjoint) temporal scalars X_0 in terms of their mass eigenvalues, we see that the ultrasoft matching relations contain merely the first few terms in a $\frac{h_3 v^2}{m_{\rm D}}$ expansion [52]. Here, h_3 is the coupling between Lorentz and temporal scalars X_0 [20, 52, 62]. To include also effects of large field values which is the case in strong transitions as studied in this *article* one needs to monitor the effect of these soft corrections. Here, we report that they are subdominant to the two-loop contributions in resummation as seen in fig. 5.

[1] G. Agazie *et al.* (NANOGrav), Astrophys. J. Lett. **951**, L8 (2023), arXiv:2306.16213 [astro-ph.HE].
[2] G. Agazie *et al.* (NANOGrav), Astrophys. J. Lett. **951**, L9 (2023), arXiv:2306.16217 [astro-ph.HE].
[3] J. Antoniadis *et al.* (EPTA), Astron. Astrophys. **678**, A48 (2023), arXiv:2306.16224 [astro-ph.HE].
[4] J. Antoniadis *et al.* (EPTA, InPTA:), Astron. Astrophys. **678**, A50 (2023), arXiv:2306.16214 [astro-ph.HE].
[5] A. Zic *et al.*, Publ. Astron. Soc. Austral. **40**, e049 (2023), arXiv:2306.16230 [astro-ph.HE].
[6] D. J. Reardon *et al.*, Astrophys. J. Lett. **951**, L6 (2023), arXiv:2306.16215 [astro-ph.HE].
[7] H. Xu *et al.*, Res. Astron. Astrophys. **23**, 075024 (2023), arXiv:2306.16216 [astro-ph.HE].
[8] A. Afzal *et al.* (NANOGrav), Astrophys. J. Lett. **951**, L11 (2023), arXiv:2306.16219 [astro-ph.HE].
[9] D. G. Figueroa, M. Pieroni, A. Ricciardone, and P. Simakachorn, (2023), arXiv:2307.02399 [astro-ph.CO].
[10] J. Ellis, M. Fairbairn, G. Franciolini, G. Hütsi, A. Iovino, M. Lewicki, M. Raidal, J. Urrutia, V. Vaskonen, and H. Veermäe, Phys. Rev. D **109**, 023522 (2024), arXiv:2308.08546 [astro-ph.CO].
[11] C. Caprini *et al.*, JCAP **04**, 001 (2016), arXiv:1512.06239 [astro-ph.CO].
[12] C. Caprini *et al.*, JCAP **03**, 024 (2020), arXiv:1910.13125 [astro-ph.CO].
[13] P. Auclair *et al.* (LISA Cosmology Working Group), Living Rev. Rel. **26**, 5 (2023), arXiv:2204.05434 [astro-ph.CO].
[14] K. Farakos, K. Kajantie, K. Rummukainen, and M. E. Shaposhnikov, Nucl. Phys. B **442**, 317 (1995), arXiv:hep-lat/9412091.
[15] K. Kajantie, M. Laine, K. Rummukainen, and M. E. Shaposhnikov, Nucl. Phys. B **466**, 189 (1996), arXiv:hep-lat/9510020.
[16] G. D. Moore and K. Rummukainen, Phys. Rev. **D63**, 045002 (2001), arXiv:hep-ph/0009132 [hep-ph].
[17] O. Gould, S. Güyer, and K. Rummukainen, Phys. Rev. D **106**, 114507 (2022), arXiv:2205.07238 [hep-lat].
[18] P. H. Ginsparg, Nucl. Phys. **B170**, 388 (1980).
[19] T. Appelquist and R. D. Pisarski, Phys. Rev. **D23**, 2305 (1981).
[20] O. Gould and T. V. I. Tenkanen, JHEP **01**, 048 (2024), arXiv:2309.01672 [hep-ph].
[21] C. Delaunay, C. Grojean, and J. D. Wells, JHEP **04**, 029 (2008), arXiv:0711.2511 [hep-ph].
[22] H. H. Patel and M. J. Ramsey-Musolf, JHEP **07**, 029 (2011), arXiv:1101.4665 [hep-ph].
[23] C. Caprini, R. Jinno, M. Lewicki, E. Madge, M. Merchand, G. Nardini, M. Pieroni, A. Roper Pol, and V. Vaskonen (LISA Cosmology Working Group),

arXiv:to appear [astro-ph.CO].
[24] C. Grojean and G. Servant, Phys. Rev. D **75**, 043507 (2007), arXiv:hep-ph/0607107.
[25] Z. Kang, P. Ko, and T. Matsui, JHEP **02**, 115 (2018), arXiv:1706.09721 [hep-ph].
[26] K. Hashino, M. Kakizaki, S. Kanemura, P. Ko, and T. Matsui, Phys. Lett. B **766**, 49 (2017), arXiv:1609.00297 [hep-ph].
[27] L. Bian, H.-K. Guo, Y. Wu, and R. Zhou, Phys. Rev. D **101**, 035011 (2020), arXiv:1906.11664 [hep-ph].
[28] L. S. Friedrich, M. J. Ramsey-Musolf, T. V. I. Tenkanen, and V. Q. Tran, (2022), arXiv:2203.05889 [hep-ph].
[29] D. Croon, O. Gould, P. Schicho, T. V. I. Tenkanen, and G. White, JHEP **04**, 055 (2021), arXiv:2009.10080 [hep-ph].
[30] O. Gould and C. Xie, JHEP **12**, 049 (2023), arXiv:2310.02308 [hep-ph].
[31] P. Athron, C. Balazs, A. Fowlie, L. Morris, G. White, and Y. Zhang, JHEP **01**, 050 (2023), arXiv:2208.01319 [hep-ph].
[32] O. Gould, J. Kozaczuk, L. Niemi, M. J. Ramsey-Musolf, T. V. I. Tenkanen, and D. J. Weir, Phys. Rev. D **100**, 115024 (2019), arXiv:1903.11604 [hep-ph].
[33] J. Ellis, M. Lewicki, and J. M. No, JCAP **07**, 050 (2020), arXiv:2003.07360 [hep-ph].
[34] P. M. Schicho, T. V. I. Tenkanen, and J. Österman, JHEP **06**, 130 (2021), arXiv:2102.11145 [hep-ph].
[35] L. Niemi, P. Schicho, and T. V. I. Tenkanen, Phys. Rev. D **103**, 115035 (2021), [Erratum: Phys.Rev.D 109, 039902 (2024)], arXiv:2103.07467 [hep-ph].
[36] O. Gould and T. V. I. Tenkanen, JHEP **06**, 069 (2021), arXiv:2104.04399 [hep-ph].
[37] J. R. Espinosa, T. Konstandin, and F. Riva, Nucl. Phys. B **854**, 592 (2012), arXiv:1107.5441 [hep-ph].
[38] S. Profumo, M. J. Ramsey-Musolf, C. L. Wainwright, and P. Winslow, Phys. Rev. D **91**, 035018 (2015), arXiv:1407.5342 [hep-ph].
[39] T. Brauner, T. V. I. Tenkanen, A. Tranberg, A. Vuorinen, and D. J. Weir, JHEP **03**, 007 (2017), arXiv:1609.06230 [hep-ph].
[40] L. Sagunski, P. Schicho, and D. Schmitt, Phys. Rev. D **107**, 123512 (2023), arXiv:2303.02450 [hep-ph].
[41] S. P. Martin and H. H. Patel, Phys. Rev. D **98**, 076008 (2018), arXiv:1808.07615 [hep-ph].
[42] A. D. Linde, Phys. Lett. B **96**, 289 (1980).
[43] J. Löfgren, J. Phys. G **50**, 125008 (2023), arXiv:2301.05197 [hep-ph].
[44] A. Ekstedt, P. Schicho, and T. V. I. Tenkanen, Comput. Phys. Commun. **288**, 108725 (2023), arXiv:2205.08815 [hep-ph].
[45] S. R. Coleman and E. J. Weinberg, Phys. Rev. D **7**, 1888 (1973).
[46] R. Jackiw, Phys. Rev. D **9**, 1686 (1974).
[47] G. W. Anderson and L. J. Hall, Phys. Rev. D **45**, 2685 (1992).
[48] D. Curtin, P. Meade, and C.-T. Yu, JHEP **11**, 127 (2014), arXiv:1409.0005 [hep-ph].
[49] M. Quiros, in *ICTP Summer School in High-Energy Physics and Cosmology* (1999) pp. 187–259, arXiv:hep-ph/9901312.
[50] R. R. Parwani, Phys. Rev. D **45**, 4695 (1992), [Erratum: Phys.Rev.D 48, 5965 (1993)], arXiv:hep-ph/9204216.
[51] D. Curtin, P. Meade, and H. Ramani, Eur. Phys. J. C **78**, 787 (2018), arXiv:1612.00466 [hep-ph].
[52] K. Kajantie, M. Laine, K. Rummukainen, and M. E. Shaposhnikov, Nucl. Phys. B **458**, 90 (1996), arXiv:hep-ph/9508379.
[53] B. Ruijl, T. Ueda, and J. Vermaseren, (2017), arXiv:1707.06453 [hep-ph].
[54] R. M. Fonseca, Comput. Phys. Commun. **267**, 108085 (2021), arXiv:2011.01764 [hep-th].
[55] E. J. Weinberg and A.-q. Wu, Phys. Rev. D **36**, 2474 (1987).
[56] M. Laine, Phys. Rev. D **51**, 4525 (1995), arXiv:hep-ph/9411252.
[57] C. L. Wainwright, S. Profumo, and M. J. Ramsey-Musolf, Phys. Rev. D **86**, 083537 (2012), arXiv:1204.5464 [hep-ph].
[58] R. Fukuda and T. Kugo, Phys. Rev. D **13**, 3469 (1976).
[59] A. Ekstedt, O. Gould, and J. Löfgren, Phys. Rev. D **106**, 036012 (2022), arXiv:2205.07241 [hep-ph].
[60] L. Niemi, M. J. Ramsey-Musolf, T. V. I. Tenkanen, and D. J. Weir, Phys. Rev. Lett. **126**, 171802 (2021), arXiv:2005.11332 [hep-ph].
[61] L. Niemi, H. H. Patel, M. J. Ramsey-Musolf, T. V. I. Tenkanen, and D. J. Weir, Phys. Rev. D **100**, 035002 (2019), arXiv:1802.10500 [hep-ph].
[62] M. Kierkla, B. Swiezewska, T. V. I. Tenkanen, and J. van de Vis, (2023), arXiv:2312.12413 [hep-ph].
[63] J. S. Langer, Annals Phys. **54**, 258 (1969).
[64] S. R. Coleman, Phys. Rev. D **15**, 2929 (1977), [Erratum: Phys.Rev.D 16, 1248 (1977)].
[65] A. D. Linde, Phys. Lett. B **100**, 37 (1981).
[66] A. D. Linde, Nucl. Phys. B **216**, 421 (1983), [Erratum: Nucl.Phys.B 223, 544 (1983)].
[67] I. Affleck, Phys. Rev. Lett. **46**, 388 (1981).
[68] A. Ekstedt, JHEP **08**, 115 (2022), arXiv:2201.07331 [hep-ph].
[69] A. Ekstedt, Eur. Phys. J. C **82**, 173 (2022), arXiv:2104.11804 [hep-ph].
[70] O. Gould and J. Hirvonen, Phys. Rev. D **104**, 096015 (2021), arXiv:2108.04377 [hep-ph].
[71] W.-Y. Ai, J. Alexandre, and S. Sarkar, Phys. Rev. D **109**, 045010 (2024), arXiv:2312.04482 [hep-ph].
[72] A. Ekstedt, O. Gould, and J. Hirvonen, JHEP **12**, 056 (2023), arXiv:2308.15652 [hep-ph].
[73] J. Löfgren, M. J. Ramsey-Musolf, P. Schicho, and T. V. I. Tenkanen, Phys. Rev. Lett. **130**, 251801 (2023), arXiv:2112.05472 [hep-ph].
[74] J. Hirvonen, J. Löfgren, M. J. Ramsey-Musolf, P. Schicho, and T. V. I. Tenkanen, JHEP **07**, 135 (2022), arXiv:2112.08912 [hep-ph].
[75] K. Saikawa and S. Shirai, JCAP **05**, 035 (2018), arXiv:1803.01038 [hep-ph].
[76] J. Ellis, M. Lewicki, and J. M. No, JCAP **04**, 003 (2019), arXiv:1809.08242 [hep-ph].
[77] M. Hindmarsh, S. J. Huber, K. Rummukainen, and D. J. Weir, Phys. Rev. D **96**, 103520 (2017), [Erratum: Phys.Rev.D 101, 089902 (2020)], arXiv:1704.05871 [astro-ph.CO].
[78] F. Giese, T. Konstandin, and J. van de Vis, JCAP **07**, 057 (2020), arXiv:2004.06995 [astro-ph.CO].
[79] T. V. I. Tenkanen and J. van de Vis, JHEP **08**, 302 (2022), arXiv:2206.01130 [hep-ph].
[80] T. Konstandin, G. Nardini, and I. Rues, JCAP **09**, 028 (2014), arXiv:1407.3132 [hep-ph].
[81] J. Kozaczuk, JHEP **10**, 135 (2015), arXiv:1506.04741

[hep-ph].
[82] A. Friedlander, I. Banta, J. M. Cline, and D. Tucker-Smith, Phys. Rev. D **103**, 055020 (2021), arXiv:2009.14295 [hep-ph].
[83] G. D. Moore and T. Prokopec, Phys. Rev. Lett. **75**, 777 (1995), arXiv:hep-ph/9503296.
[84] G. D. Moore and T. Prokopec, Phys. Rev. D **52**, 7182 (1995), arXiv:hep-ph/9506475.
[85] S. De Curtis, L. D. Rose, A. Guiggiani, A. G. Muyor, and G. Panico, JHEP **03**, 163 (2022), arXiv:2201.08220 [hep-ph].
[86] G. C. Dorsch, S. J. Huber, and T. Konstandin, JCAP **04**, 010 (2022), arXiv:2112.12548 [hep-ph].
[87] D. Bodeker and G. D. Moore, JCAP **05**, 025 (2017), arXiv:1703.08215 [hep-ph].
[88] B.-H. Liu, L. D. McLerran, and N. Turok, Phys. Rev. D **46**, 2668 (1992).
[89] J. M. Cline, A. Friedlander, D.-M. He, K. Kainulainen, B. Laurent, and D. Tucker-Smith, Phys. Rev. D **103**, 123529 (2021), arXiv:2102.12490 [hep-ph].
[90] M. Dine, R. G. Leigh, P. Y. Huet, A. D. Linde, and D. A. Linde, Phys. Rev. D **46**, 550 (1992), arXiv:hep-ph/9203203.
[91] B. Laurent and J. M. Cline, Phys. Rev. D **102**, 063516 (2020), arXiv:2007.10935 [hep-ph].
[92] B. Laurent and J. M. Cline, Phys. Rev. D **106**, 023501 (2022), arXiv:2204.13120 [hep-ph].
[93] W.-Y. Ai, B. Laurent, and J. van de Vis, JCAP **07**, 002 (2023), arXiv:2303.10171 [astro-ph.CO].
[94] T. Krajewski, M. Lewicki, and M. Zych, (2024), arXiv:2402.15408 [astro-ph.CO].
[95] M. Lewicki, M. Merchand, and M. Zych, JHEP **02**, 017 (2022), arXiv:2111.02393 [astro-ph.CO].
[96] C. L. Wainwright, Comput. Phys. Commun. **183**, 2006 (2012), arXiv:1109.4189 [hep-ph].
[97] P. Schicho and D. Schmitt, `https://github.com/DMGW-Goethe/DRansitions` (2024).
[98] J. Ellis, M. Lewicki, J. M. No, and V. Vaskonen, JCAP **06**, 024 (2019), arXiv:1903.09642 [hep-ph].
[99] M. Lewicki and V. Vaskonen, Phys. Dark Univ. **30**, 100672 (2020), arXiv:1912.00997 [astro-ph.CO].
[100] M. Lewicki and V. Vaskonen, Eur. Phys. J. C **80**, 1003 (2020), arXiv:2007.04967 [astro-ph.CO].
[101] M. Lewicki and V. Vaskonen, Eur. Phys. J. C **81**, 437 (2021), arXiv:2012.07826 [astro-ph.CO].
[102] M. Lewicki and V. Vaskonen, Eur. Phys. J. C **83**, 109 (2023), arXiv:2208.11697 [astro-ph.CO].
[103] A. Roper Pol, S. Mandal, A. Brandenburg, T. Kahniashvili, and A. Kosowsky, Phys. Rev. D **102**, 083512 (2020), arXiv:1903.08585 [astro-ph.CO].
[104] T. Kahniashvili, A. Brandenburg, G. Gogoberidze, S. Mandal, and A. Roper Pol, Phys. Rev. Res. **3**, 013193 (2021), arXiv:2011.05556 [astro-ph.CO].
[105] A. Roper Pol, S. Mandal, A. Brandenburg, and T. Kahniashvili, JCAP **04**, 019 (2022), arXiv:2107.05356 [gr-qc].
[106] M. Hindmarsh, Phys. Rev. Lett. **120**, 071301 (2018), arXiv:1608.04735 [astro-ph.CO].
[107] M. Hindmarsh and M. Hijazi, JCAP **12**, 062 (2019), arXiv:1909.10040 [astro-ph.CO].
[108] R. Jinno, T. Konstandin, and H. Rubira, JCAP **04**, 014 (2021), arXiv:2010.00971 [astro-ph.CO].
[109] C. Gowling and M. Hindmarsh, JCAP **10**, 039 (2021), arXiv:2106.05984 [astro-ph.CO].
[110] A. Roper Pol, S. Procacci, and C. Caprini, (2023), arXiv:2308.12943 [gr-qc].
[111] R. Sharma, J. Dahl, A. Brandenburg, and M. Hindmarsh, JCAP **12**, 042 (2023), arXiv:2308.12916 [gr-qc].
[112] J. Ellis, M. Lewicki, M. Merchand, J. M. No, and M. Zych, JHEP **01**, 093 (2023), arXiv:2210.16305 [hep-ph].
[113] M. Hindmarsh, S. J. Huber, K. Rummukainen, and D. J. Weir, Phys. Rev. Lett. **112**, 041301 (2014), arXiv:1304.2433 [hep-ph].
[114] M. Hindmarsh, S. J. Huber, K. Rummukainen, and D. J. Weir, Phys. Rev. D **92**, 123009 (2015), arXiv:1504.03291 [astro-ph.CO].
[115] H.-K. Guo, K. Sinha, D. Vagie, and G. White, JCAP **01**, 001 (2021), arXiv:2007.08537 [hep-ph].
[116] A. Beniwal, M. Lewicki, J. D. Wells, M. White, and A. G. Williams, JHEP **08**, 108 (2017), arXiv:1702.06124 [hep-ph].
[117] S. Blasi and A. Mariotti, Phys. Rev. Lett. **129**, 261303 (2022), arXiv:2203.16450 [hep-ph].
[118] A. Beniwal, M. Lewicki, M. White, and A. G. Williams, JHEP **02**, 183 (2019), arXiv:1810.02380 [hep-ph].
[119] A. Azatov, G. Barni, S. Chakraborty, M. Vanvlasselaer, and W. Yin, JHEP **10**, 017 (2022), arXiv:2207.02230 [hep-ph].
[120] P. Schicho, T. V. I. Tenkanen, and G. White, JHEP **11**, 047 (2022), arXiv:2203.04284 [hep-ph].
[121] T. L. Smith, T. L. Smith, R. R. Caldwell, and R. Caldwell, Phys. Rev. D **100**, 104055 (2019), [Erratum: Phys.Rev.D 105, 029902 (2022)], arXiv:1908.00546 [astro-ph.CO].
[122] M. Pieroni and E. Barausse, JCAP **07**, 021 (2020), [Erratum: JCAP 09, E01 (2020)], arXiv:2004.01135 [astro-ph.CO].
[123] R. Flauger, N. Karnesis, G. Nardini, M. Pieroni, A. Ricciardone, and J. Torrado, JCAP **01**, 059 (2021), arXiv:2009.11845 [astro-ph.CO].
[124] R. A. Fisher, Phil. Trans. Roy. Soc. Lond. A **222**, 309 (1922).
[125] N. Cornish and T. Robson, J. Phys. Conf. Ser. **840**, 012024 (2017), arXiv:1703.09858 [astro-ph.IM].
[126] T. Robson, N. J. Cornish, and C. Liu, Class. Quant. Grav. **36**, 105011 (2019), arXiv:1803.01944 [astro-ph.HE].
[127] M. Lewicki and V. Vaskonen, Eur. Phys. J. C **83**, 168 (2023), arXiv:2111.05847 [astro-ph.CO].
[128] O. Hartwig, M. Lilley, M. Muratore, and M. Pieroni, Phys. Rev. D **107**, 123531 (2023), arXiv:2303.15929 [gr-qc].
[129] C.-W. Chiang, Y.-T. Li, and E. Senaha, Phys. Lett. B **789**, 154 (2019), arXiv:1808.01098 [hep-ph].
[130] M. Gonderinger, Y. Li, H. Patel, and M. J. Ramsey-Musolf, JHEP **01**, 053 (2010), arXiv:0910.3167 [hep-ph].
[131] R. L. Workman and Others (Particle Data Group), PTEP **2022**, 083C01 (2022).
[132] K. Kainulainen, V. Keus, L. Niemi, K. Rummukainen, T. V. I. Tenkanen, and V. Vaskonen, JHEP **06**, 075 (2019), arXiv:1904.01329 [hep-ph].
[133] K. Kajantie, M. Laine, A. Rajantie, K. Rummukainen, and M. Tsypin, JHEP **11**, 011 (1998), arXiv:hep-lat/9811004.

How these characterized higher charmonia shape the puzzling data of the $e^+e^- \to \eta J/\psi$ cross section

Tian-Cai Peng,[1,2,3,4,*] Zi-Yue Bai,[1,2,3,4,†] Jun-Zhang Wang,[5,1,‡] and Xiang Liu[1,2,3,4,6,§]

[1]School of Physical Science and Technology, Lanzhou University, Lanzhou 730000, China
[2]Lanzhou Center for Theoretical Physics, Key Laboratory of Theoretical Physics of Gansu Province, Lanzhou University, Lanzhou 730000, China
[3]Key Laboratory of Quantum Theory and Applications of MoE, Lanzhou University, Lanzhou 730000, China
[4]Research Center for Hadron and CSR Physics, Lanzhou University and Institute of Modern Physics of CAS, Lanzhou 730000, China
[5]School of Physics and Center of High Energy Physics, Peking University, Beijing 100871, China
[6]MoE Frontiers Science Center for Rare Isotopes, Lanzhou University, Lanzhou 730000, China

(Dated: March 7, 2024)

Recently, the BESIII Collaboration performed a precise measurement of the $e^+e^- \to \eta J/\psi$ cross section. It is puzzling that the resonance parameters of the reported $Y(4230)$ show a substantial divergence from the previously measured results in both the open-charmed and hidden-charmed decay channels, and the line shape asymmetry of the data approaching 4.2 GeV also suggests that it might be difficult to characterize the details of the structure around 4.2 GeV by a single resonance. This has motivated our great curiosity about how the charmonium states are distributed in the measured energy range and how they shape the puzzling data of the $e^+e^- \to \eta J/\psi$ cross section. In this work, we use five theoretically constructed charmonia in the range of $4.0 \sim 4.5$ GeV, i.e. $\psi(4040)$, $\psi(4160)$, $\psi(4220)$, $\psi(4380)$, and $\psi(4415)$, to apply a combined fit to the data, in which their calculated decay ratios into $\eta J/\psi$ via hadronic loop mechanism are taken as input. The fit results can reproduce the measured cross section data well, especially for the subtle line shape around 4.2 GeV, showing that the structure around 4.2 GeV is possible from the contribution of both $\psi(4160)$ and $\psi(4220)$.

arXiv:2403.03705v1 [hep-ph] 6 Mar 2024

I. INTRODUCTION

With the continuous accumulation of data, an increasing number of charmoniumlike XYZ states have been documented in various experimental endeavors, such as Belle, BESIII, LHCb, and CMS. This surge in reported states has invigorated the field of hadron spectroscopy, giving it a remarkable level of activity and importance (see review articles [1–9] for more details). This research landscape has led to significant advances in our construction of hadron spectroscopy. In particular, it has advanced our understanding of the intricate nonperturbative dynamics associated with the strong interactions, which is a central frontier of contemporary physics research.

Recently, the BESIII Collaboration made a remarkable discovery by measuring the $e^+e^- \to \eta J/\psi$ cross section over a center-of-mass energy range of $\sqrt{s} = 3.808 - 4.951$ GeV [10]. This measurement was made by analyzing a data sample with an integrated luminosity of 22.42 fb^{-1} [10]. To depict this data, BESIII introduced three resonant structures, i.e., the charmonium state $\psi(4040)$ and two charmoniumlike states, namely $Y(4230)$ and $Y(4360)$. The resonance parameters of these introduced states were determined. For the $Y(4230)$ state, the resonance mass was found to be $m_{Y(4230)} = 4219.7 \pm 2.5 \pm 4.5$ MeV, and the corresponding width was measured to be $\Gamma_{Y(4230)} = 80.7 \pm 4.4 \pm 1.4$ MeV. Similarly, the $Y(4360)$ state showed a mass of $m_{Y(4360)} = 4386 \pm 13 \pm 17$ MeV, accompanied by a width of $\Gamma_{Y(4360)} = 177 \pm 32 \pm 13$ MeV [10]. It is worth noting that the observed width of the $Y(4230)$ state, as reported, exceeds those found in other hidden-charm and open-charm decay channels. These include processes such as $e^+e^- \to \pi^+\pi^- J/\psi$ [11, 12], $\pi^0\pi^0 J/\psi$ [13], $\psi(2S)\pi^+\pi^-$ [14], $\pi^+\pi^-\psi(3686)$ [15], $h_c\pi^+\pi^-$ [16], $\chi_{c0}\omega$ [17], $K^+K^- J/\psi$[18], and $D^0D^{*-}\pi^+$[19]. This difference in width hints at some distinct nature of this reported $Y(4230)$ structure in $e^+e^- \to \eta J/\psi$ [10].

As collected by the Particle Data Group (PDG) [20], the family of charmonium encompasses two well-established entities, namely $\psi(4160)$ and $\psi(4415)$, in addition to $\psi(4040)$. However, upon meticulous examination of the experimental data reported by BESIII, a conspicuous absence is observed within the cross section distribution of $e^+e^- \to \eta J/\psi$, pertaining specifically to the aforementioned charmonium states, $\psi(4160)$ and $\psi(4415)$. Remarkably, the established charmonium $\psi(4160)$ possess sizable decay fractions into $\eta J/\psi$ channel according to the theoretical calculation [21]. Moreover, if carefully checking the BESIII's data, we may find an asymmetric line shape, associated with the resonance structure denoted as $Y(4230)$. Confronted by this puzzling phenomenon existing in the cross section data of $e^+e^- \to \eta J/\psi$ [10], a pressing need arises for the formulation of a cogent resolution to address this perplexing issue. We should mention the distinct characterized energy level structure of higher charmonia within the framework of the unquenched picture, a contribution credited to the diligent efforts of the Lanzhou group [22–24]. In the newly constructed J/ψ family, there are six vector charmonium states in the energy range of $4 \sim 4.5$ GeV, i.e., $\psi(4040)$, $\psi(4160)$, $\psi(4220)$, $\psi(4380)$, $\psi(4415)$, and $\psi(4500)$ [22]. In this work, we reveal how these characterized higher charmonia shape the puzzling data of the $e^+e^- \to \eta J/\psi$ cross section.

This paper is organized as follows. After the introduction, we briefly review the status of these higher charmonia in the range of $4.0 \sim 4.5$ GeV, which are used to solve the puzzles

*Electronic address: pengtc20@lzu.edu.cn
†Electronic address: baizy15@lzu.edu.cn
‡Electronic address: wangjzh2022@pku.edu.cn
§Electronic address: xiangliu@lzu.edu.cn

appearing in the cross section data of the $e^+e^- \to J/\psi\eta$ in Sec. II. We then illustrate the calculation details of these charmonium decays into $\eta J/\psi$ via the hadronic loop mechanism in Sec. II A. Based on these results, we perform a combined fit to show how these characterized higher charmonia shape the puzzling data of the $e^+e^- \to \eta J/\psi$ cross section in Sec. II B. The paper ends with a short summary in Sec. III.

II. AN ANALYSIS TO THE CROSS SECTION OF $e^+e^- \to \eta J/\psi$

The continued accumulation of the experimental data in the range of 4.0 ~ 4.5 GeV has deepened our understanding of the spectrum of higher vector charmonium above 4.0 GeV. Recently, the BESIII Collaboration performed a precise measurement of the $e^+e^- \to \eta J/\psi$ cross section over a center-of-mass energy range of $\sqrt{s}$ = 3.808 – 4.951 GeV, and obtained the charmonium state $\psi(4040)$ and the other two charmoniumlike states named $Y(4230)$ and $Y(4360)$ from a Breit-Wigner fit, but the extracted resonance parameters of the observed $Y(4230)$ state against other measurements of the open-charmed and hidden-charmed decay channels [11–19]. And the line shape of the observed $Y(4230)$ looks asymmetric and irregular, and could not be formed by the contribution of just one resonance. It seems that the structure around 4.2 GeV from the measured cross section data of $e^+e^- \to \eta J/\psi$ may have some substructures.

In order to fully understand these puzzling data, the theoretical inputs of the vector charmonia located in the range of 4.0 ~ 4.5 GeV are crucial. Besides the well constructed charmonia, i.e., $\psi(4040)$, $\psi(4160)$ and $\psi(4415)$ in the range of 4.0 ~ 4.5 GeV, the Lanzhou group indicated that there should exist a narrow charmonium $\psi(4220)$ corresponding to $Y(4220)$ reported in the processes of $e^+e^- \to J/\psi\pi^+\pi^-$, $e^+e^- \to h_c\pi^+\pi^-$, $e^+e^- \to \chi_{c0}\omega$ and $e^+e^- \to \psi(3686)\pi^+\pi^-$ [25–28]. In Ref. [22], the Lanzhou group used an unquenched potential model with $\psi(4220)$ as the scaling point and predicted another two more charmonium states named $\psi(4380)$ and $\psi(4500)$. The information of these charmonia is summarized in Table I. It is worth mentioning that the BESIII experiment recently indeed found a new structure around 4.5 GeV in the measurement of $e^+e^- \to K^+K^-J/\psi$ [18], which just can relate to our predicted charmonium $\psi(4500)$. With these six vector charmonia, theoretically established in the range of 4.0 ~ 4.5, they have shown that the experimental cross section measurements of $e^+e^- \to \psi(2S)\pi^+\pi^-$ [22], $e^+e^- \to K^+K^-J/\psi$ [23] and $e^+e^- \to \pi^+D^0D^{*-}$ [24] can be explained in a unified framework. In this work, we aim to show that the newly measured $e^+e^- \to \eta J/\psi$ cross section data can also be understood by the contributions of the same characterized energy level structures, and how they shape the puzzling $e^+e^- \to \eta J/\psi$ cross section data.

The contribution of genuine intermediate charmonium to $e^+e^- \to \eta J/\psi$ can be described by a phase space corrected Breit-Wigner function, i.e.,

$$\mathcal{M}_\psi(s) = \frac{\sqrt{12\pi\Gamma_\psi^{e^+e^-}\mathcal{B}(\psi \to \eta J/\psi)\Gamma_\psi}}{s - m_\psi^2 + im_\psi\Gamma_\psi} \times \sqrt{\frac{\Phi_{2\to2}(s)}{\Phi_{2\to2}(m_\psi^2)}}, \quad (1)$$

where m_ψ, Γ_ψ and $\Gamma_\psi^{e^+e^-}$ are the mass, total width and the di-electron width of the intermediate charmonium, respectively. $\Phi_{2\to2}$ is the phase space and s donates the center-of-mass energy. The only remaining unknown term $\mathcal{BR}(\psi \to \eta J/\psi)$ is the branching ratio of the associated charmonium decay into $\eta J/\psi$, we will present the details of the calculation for the $\psi \to \eta J/\psi$ decay next.

TABLE I: The theoretical mixing angles, assignments, masses, total widths, and dielectron widths of higher charmonia in the range of 4.0 ~ 4.5 GeV, which are obtained from the theoretical predictions [22–24] and some experimental values which are close to the theoretical predictions.

States	θ	Assignment	Mass (MeV)	Γ (MeV)	$\Gamma_\psi^{e^+e^-}$ (keV)
$\psi(4040)$	20°	ψ'_{3S-2D}	4039 ± 1 [20]	80 ± 10 [20]	0.830 [29]
$\psi(4160)$	20°	ψ''_{3S-2D}	4159 ± 20 [30]	78 ± 20 [30]	0.480 [29]
$\psi(4220)$	34°	ψ'_{4S-3D}	4222	44	0.290
$\psi(4380)$	34°	ψ''_{4S-3D}	4389	80	0.257
$\psi(4415)$	30°	ψ'_{5S-4D}	4414	33	0.230
$\psi(4500)$	30°	ψ''_{5S-4D}	4509	50	0.113

A. Calculating the branching ratios of higher charmonium decays into $\eta J/\psi$

In Ref. [22], an S-D mixing scheme was proposed to construct the energy level structure of vector charmonia in the range of 4.0 ~ 4.5 GeV, as shown below,

$$\begin{pmatrix} |\psi'\rangle \\ |\psi''\rangle \end{pmatrix} = \begin{pmatrix} \cos\theta & \sin\theta \\ -\sin\theta & \cos\theta \end{pmatrix} \begin{pmatrix} |\psi(nS)\rangle \\ |\psi((n-1)D)\rangle \end{pmatrix}, \quad (2)$$

where θ denotes the mixing angle.

In this scheme, $\psi(4220)$ was assigned to a $4S$-$3D$ mixing state while its partner $\psi(4380)$ was predicted. The well-established $\psi(4415)$ was assigned into a $5S$-$4D$ mixing state while its partner $\psi(4500)$ was predicted and was found to exist in the BESIII measurement of $e^+e^- \to K^+K^-J/\psi$ [23]. The assignment of $\psi(4040)$ and $\psi(4160)$ with a $3S$-$2D$ mixing scheme has also been proposed in Ref. [23] to match the experimental di-electron width of $\psi(4160)$ [29]. The mixing angles are listed in Table I. Next, we will utilize the hadronic loop mechanism to calculate the branching ratios of the hidden-charm decays of $\psi \to \eta J/\psi$ for the above charmonia.

The hadronic loop mechanism has been widely used to study the hidden-flavor decays of heavy quarkonia above the

open-flavor thresholds [31–52] and the calculated branching ratios are usually comparable to the experimental measurements. In the framework of the hadronic loop mechanism, the higher charmonium ψ'/ψ'' within an S-D mixture first decay into a pair of charmed mesons $D^{(*)}\bar{D}^{(*)}$, and reach the $\eta J/\psi$ final states by exchanging a D or D^* meson as shown in Fig. 1. The general expression for the amplitude mediated by the charmed meson loop is

$$\mathcal{M} = \int \frac{d^4q}{(2\pi)^4} \frac{\mathcal{V}_1\mathcal{V}_2\mathcal{V}_3}{\mathcal{P}_1\mathcal{P}_2\mathcal{P}_E} \mathcal{F}^2(q^2, m_E^2), \tag{3}$$

where $\mathcal{V}_i (i = 1, 2, 3)$ are interaction vertices, and $\mathcal{P}_i (i = 1, 2, E)$ denote the corresponding propagators of intermediate charmed mesons. The form factor $\mathcal{F}(q^2, m_E^2)$ is introduced to compensate for the off-shell effect of the exchanged $D^{(*)}$ meson and to depict the structure effect of the interaction vertices. In our calculation, the monopole form factor is taken as

$$\mathcal{F}(q^2, m_E^2) = \frac{\Lambda^2 - m_E^2}{\Lambda^2 - q^2}, \tag{4}$$

where m_E and q are the mass and four momentum of the exchanged intermediate meson, respectively. The cutoff Λ can be parameterized as $\Lambda = m_E + \alpha\Lambda_{QCD}$, with $\Lambda_{QCD} = 220$ MeV [31–33], α is usually of order of 1 and depends on the specific processes [52].

The effective Lagrangian approach is used to give the concrete expressions for the decay amplitudes defined in Eq. (3). The Lagrangians of the concrete interactions involved in Fig. 1 are listed below [48],

$$\begin{aligned}\mathcal{L}_{\psi_{(S)}\mathcal{D}^{(*)}\mathcal{D}^{(*)}} =& ig_{\psi_{(S)}\mathcal{D}\mathcal{D}}\psi^\mu(\partial_\mu\mathcal{D}^\dagger\mathcal{D} - \mathcal{D}^\dagger\partial_\mu\mathcal{D}) \\ &+ g_{\psi_{(S)}\mathcal{D}\mathcal{D}^*}\varepsilon_{\mu\nu\alpha\beta}\partial^\mu\psi^\nu(\mathcal{D}^{*\alpha\dagger}\partial^\nu\mathcal{D} - \mathcal{D}^\dagger\partial^{\vec{\beta}}\mathcal{D}^{*\alpha}) \\ &+ ig_{\psi_{(S)}\mathcal{D}^*\mathcal{D}^*}\psi^\mu(\partial_\nu\mathcal{D}^{*\dagger}_\mu\mathcal{D}^{*\nu} - \mathcal{D}^{*\nu\dagger}\partial_\nu\mathcal{D}^*_\mu \\ &+ \mathcal{D}^{*\nu\dagger}\partial_\mu\mathcal{D}^*_\nu),\end{aligned} \tag{5}$$

$$\begin{aligned}\mathcal{L}_{\psi_{(D)}\mathcal{D}^{(*)}\mathcal{D}^{(*)}} =& ig_{\psi_{(D)}\mathcal{D}\mathcal{D}}\psi^\mu(\partial_\mu\mathcal{D}^\dagger\mathcal{D} - \mathcal{D}^\dagger\partial_\mu\mathcal{D}) \\ &+ g_{\psi_{(D)}\mathcal{D}\mathcal{D}^*}\varepsilon_{\mu\nu\alpha\beta}\partial^\mu\psi^\nu(\mathcal{D}^{*\alpha\dagger}\partial^\nu\mathcal{D} - \mathcal{D}^\dagger\partial^{\vec{\beta}}\mathcal{D}^{*\alpha}) \\ &+ ig_{\psi_{(D)}\mathcal{D}^*\mathcal{D}^*}\psi^\mu(\partial_\nu\mathcal{D}^{*\dagger}_\mu\mathcal{D}^{*\nu} - \mathcal{D}^{*\nu\dagger}\partial_\nu\mathcal{D}^*_\mu \\ &+ 4\mathcal{D}^{*\nu\dagger}\partial_\mu\mathcal{D}^*_\nu),\end{aligned} \tag{6}$$

$$\begin{aligned}\mathcal{L}_{\mathcal{D}^{(*)}\mathcal{D}^*\eta} =& ig_{\mathcal{D}\mathcal{D}^*\eta}(\mathcal{D}^{*\dagger}_\mu\mathcal{D} - \mathcal{D}^\dagger\mathcal{D}^*_\mu)\partial^\mu\eta \\ &- g_{\mathcal{D}^*\mathcal{D}^*\eta}\varepsilon_{\mu\nu\alpha\beta}\partial^\mu\mathcal{D}^{*\dagger\nu}\partial^\alpha\mathcal{D}^{*\beta}\eta\end{aligned} \tag{7}$$

with $\mathcal{D}^{(*)\dagger} = (D^{(*)0}, D^{(*)+})$ and $\mathcal{D}^{(*)} = (\bar{D}^{(*)0}, \bar{D}^{(*)-})^T$.

With the above preparations, we can write down the amplitudes of $\psi(4040)$ and $\psi(4160)$ decays into $\eta J/\psi$ within the $3S$-$2D$ mixing scheme defined in Eq. (2), as shown in Fig. 1,

$$\mathcal{M}^{\text{Total}}_{\psi(4040)} = 4\sum_{i=1}^{6}\mathcal{M}^{(i)}_{\psi(4040)}, \tag{8}$$

$$\mathcal{M}^{\text{Total}}_{\psi(4160)} = 4\sum_{i=1}^{6}\mathcal{M}^{(i)}_{\psi(4160)}, \tag{9}$$

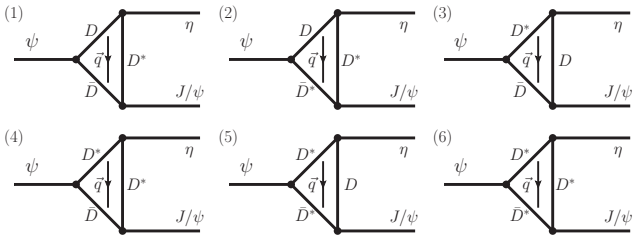

FIG. 1: The schematic diagrams illustrate the decay of higher charmonium into $\eta J/\psi$ via the hadronic loop mechanism.

where the fourfold factor comes from the charge conjugation transformation ($D^{(*)} \leftrightarrow \bar{D}^{(*)}$) and the isospin transformations ($D^{(*)0} \leftrightarrow D^{(*)+}$ and $\bar{D}^{(*)0} \leftrightarrow D^{(*)-}$) of the bridged $D^{(*)}$ mesons. The concrete expressions of $\mathcal{M}^{(i)}_{\psi(4040)}$ and $\mathcal{M}^{(i)}_{\psi(4160)}$ are given in Appendix A, the amplitudes of the others are similar to the group of $\psi(4040)$ and $\psi(4160)$ with different coupling constants and mixing angles.

TABLE II: The coupling constants of the $g_{\psi D^{(*)}D^{(*)}}$ and $\mathcal{S}$ values recommended in Table III of Ref. [23], where $g_{\psi(4040)D^{(*)}D^{(*)}}$ and $g_{\psi(4160)D^{(*)}D^{(*)}}$ are determined by the theoretical partial widths of $\psi(4040)/\psi(4160) \to D^{(*)}\bar{D}^{(*)}$ listed in Table III.

Charmonia	θ	$g_{\psi DD}$	$g_{\psi DD^*}$ (GeV^{-1})	$g_{\psi D^*D^*}$	$\mathcal{S}$
$\psi(4040)$	20°	0.378	0.462	8.607	1.140
$\psi(4160)$	20°	−2.730	−0.070	−1.881	−0.762
$\psi(4220)$	34°	0.760	0.054	1.220	1.471
$\psi(4380)$	34°	0.570	−0.150	−0.410	−1.077
$\psi(4415)$	30°	0.680	0.003	0.430	1.705
$\psi(4500)$	30°	0.440	−0.076	−0.015	−33.989

TABLE III: The partial width of $\psi(4040)/\psi(4160) \to D^{(*)}\bar{D}^{(*)}$ calculated by the quark pair creation (QPC) model, the parameters are in agreement with Ref. [22].

Charmonia	$D\bar{D}$ (MeV)	$D\bar{D}^* + c.c.$ (MeV)	$D^*\bar{D}^*$ (MeV)
$\psi(4040)$	0.433	17.187	40.893
$\psi(4160)$	35.620	0.919	51.223

Finally, the branching ratio of the charmonium decay into $\eta J/\psi$ can be obtained by

$$\mathcal{BR}[\psi \to J/\psi\eta] = \frac{1}{3}\frac{|\vec{p}_1|}{8\pi m_\psi^2}\sum_{spin}\left|\mathcal{M}_\psi{}^{\text{Total}}\right|^2/\Gamma_\psi, \tag{10}$$

where m_ψ and Γ_ψ are the mass and total width of the initial charmonium listed in Table I, $\vec{p}_1$ is the three-momentum of the η meson in the rest frame of the initial state. The coefficient 1/3 and the sum $\sum_{spin}$ come from the averaging over the polarizations of the initial state and summing up the polarizations of the final state.

TABLE IV: The fitting parameters in Scheme I, and the solutions A, B and C in Scheme II. The g and a are parameters for the background, and $\mathcal{BR}_i$ and ϕ_i (rad) are decay branching ratios into $J/\psi\eta$ and phases for five ψ states (successively $\psi(4040)$, $\psi(4160)$, $\psi(4220)$, $\psi(4380)$ and $\psi(4415)$), respectively.

Parameters	Scheme I	Scheme II		
	Fit I	Solution A	Solution B	Solution C
$\mathcal{BR}_1$	5.086×10^{-3}	$(2.627\pm0.305)\times10^{-3}$	$(6.708\pm0.344)\times10^{-3}$	$(3.256\pm0.232)\times10^{-3}$
$\mathcal{BR}_2$	1.516×10^{-3}	$(2.598\pm0.626)\times10^{-3}$	$(6.853\pm0.259)\times10^{-3}$	$(9.461\pm0.361)\times10^{-3}$
$\mathcal{BR}_3$	1.970×10^{-3}	$(4.332\pm0.359)\times10^{-3}$	$(5.343\pm0.226)\times10^{-3}$	$(2.299\pm0.052)\times10^{-2}$
$\mathcal{BR}_4$	4.063×10^{-4}	$(1.370\pm0.129)\times10^{-3}$	$(1.663\pm0.152)\times10^{-3}$	$(2.145\pm0.182)\times10^{-3}$
$\mathcal{BR}_5$	1.746×10^{-3}	$(2.971\pm0.570)\times10^{-4}$	$(3.047\pm0.621)\times10^{-4}$	$(3.147\pm0.681)\times10^{-4}$
ϕ_1 (rad)	2.347 ± 0.294	3.075 ± 0.179	3.841 ± 0.031	3.440 ± 0.045
ϕ_2 (rad)	0.665 ± 0.199	2.698 ± 0.049	1.647 ± 0.029	3.746 ± 0.020
ϕ_3 (rad)	2.413 ± 0.094	4.391 ± 0.086	3.646 ± 0.053	1.311 ± 0.017
ϕ_4 (rad)	5.107 ± 0.128	0.279 ± 0.116	0.070 ± 0.055	6.035 ± 0.051
ϕ_5 (rad)	4.264 ± 0.196	0.217 ± 0.207	0.047 ± 0.237	6.049 ± 0.223
$\chi^2/d.o.f.$	1.653	0.817	0.811	0.806

Below is a brief description of the method for determining the relevant coupling constants, as they appear in the concrete amplitudes outlined in Appendix A.

The coupling constants of $g_{D^{(*)}D^*\eta}$ are given in Ref. [48],

$$\frac{g_{D^*D\eta}}{\sqrt{m_D m_{D^*}}} = g_{D^*D^*\eta} = \frac{2g_H}{f_\pi}\alpha, \tag{11}$$

with $\alpha = \frac{1}{\sqrt{6}}\cos(-19.1^\circ)$ and $f_\pi = 131\,\text{MeV}$, and $g_H = 0.569$ is determined by the measured decay width of $D^{*+} \to D^0\pi^+$ [43]. $g_{J/\psi DD} = 7.44$, $g_{J/\psi DD^*} = 3.84\,\text{GeV}^{-1}$ and $g_{J/\psi D^*D^*} = 8.00$ are obtained by the vector meson dominance model [53, 54].

Taking the $3S-2D$ mixing charmonia $\psi(4040)$ and $\psi(4160)$ as examples, the coupling constants of $g_{\psi(4040)D^{(*)}D^{(*)}}$ and $g_{\psi(4160)D^{(*)}D^{(*)}}$ are defined by

$$\begin{cases} g_{\psi(4040)D^{(*)}D^{(*)}} = g_{\psi(3S)D^{(*)}D^{(*)}}\cos\theta + g_{\psi(2D)D^{(*)}D^{(*)}}\sin\theta \\ g_{\psi(4160)D^{(*)}D^{(*)}} = -g_{\psi(3S)D^{(*)}D^{(*)}}\sin\theta + g_{\psi(2D)D^{(*)}D^{(*)}}\cos\theta \end{cases}, \tag{12}$$

The values are determined by the theoretical partial widths of $\psi(4040)/\psi(4160) \to D^{(*)}D^{(*)}$ calculated by the QPC model [55–57], in which the mixing angle $\theta = 20^\circ$ is considered [23]. The other parameters required by the model are in agreement with Ref. [22], and the calculated partial widths associated with $\psi(4040)$ and $\psi(4160)$ are listed in Table III. Other coupling constants of $g_{\psi(4220)D^{(*)}D^{(*)}}$, $g_{\psi(4380)D^{(*)}D^{(*)}}$, $g_{\psi(4415)D^{(*)}D^{(*)}}$ and $g_{\psi(4500)D^{(*)}D^{(*)}}$ have been calculated in Table III of Ref. [23], which were determined by the corresponding experimental or theoretical partial widths of $\psi \to D^{(*)}D^{(*)}$. Both of them are listed in Table II. In addition, for convenience, the $\mathcal{S}$ factors in the decay amplitudes of Appendix A are defined as

$$\begin{cases} \mathcal{S}_{\psi(4040)} = \dfrac{g_{\psi(3S)D^*D^*}\cos\theta + 4g_{\psi(2D)D^*D^*}\sin\theta}{g_{\psi(3S)D^*D^*}\cos\theta + g_{\psi(2D)D^*D^*}\sin\theta} \\ \mathcal{S}_{\psi(4160)} = \dfrac{-g_{\psi(3S)D^*D^*}\sin\theta + 4g_{\psi(2D)D^*D^*}\cos\theta}{-g_{\psi(3S)D^*D^*}\sin\theta + g_{\psi(2D)D^*D^*}\cos\theta} \end{cases}. \tag{13}$$

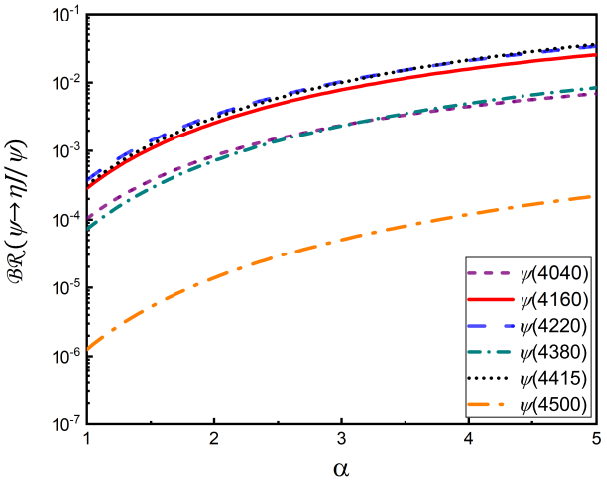

FIG. 2: The α parameter dependence of the predicted branching ratios, including $\mathcal{BR}(\psi(4040) \to \eta J/\psi)$, $\mathcal{BR}(\psi(4160) \to \eta J/\psi)$, $\mathcal{BR}(\psi(4220) \to \eta J/\psi)$, $\mathcal{BR}(\psi(4380) \to \eta J/\psi)$, $\mathcal{BR}(\psi(4415) \to \eta J/\psi)$, and $\mathcal{BR}(\psi(4500) \to \eta J/\psi)$.

With the determined coupling constants discussed above, we calculate the branching ratios of the six theoretically constructed charmonia, i.e., $\psi(4040)$, $\psi(4160)$, $\psi(4220)$, $\psi(4380)$, $\psi(4415)$ and $\psi(4500)$ decays into $\eta J/\psi$, which depend on the cutoff parameter α introduced by the form factor of Eq. (4) in

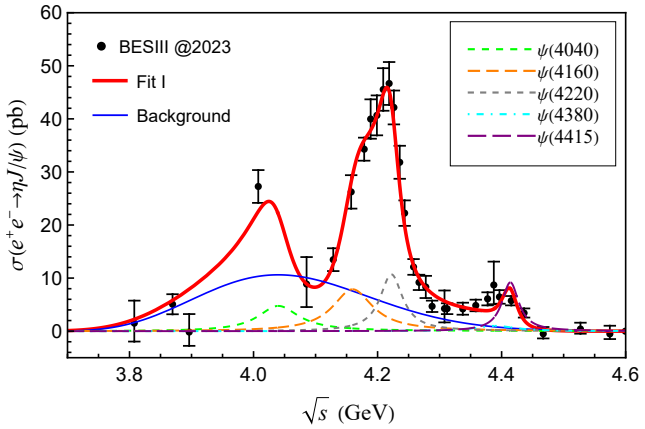

FIG. 3: Our fit to the higher vector charmonium contribution in the cross section distribution of $e^+e^- \to \eta J/\psi$ within scheme I. Here, the data points are from BESIII measurement [10], the five dashed lines represent the contributions of the higher charmonium states, the blue line represents the background, and the red line represents the total contribution.

the range of $[1, 5]$, as shown in Fig. 2. It can be seen that the branching ratios associated with $\psi(4040)$, $\psi(4160)$, $\psi(4220)$ and $\psi(4380)$, $\psi(4415)$ can reach the order of $10^{-4} \sim 10^{-2}$ and $10^{-4} \sim 10^{-3}$, respectively, while $\mathcal{BR}(\psi(4500) \to \eta J/\psi)$ is only of order of $10^{-6} \sim 10^{-5}$.

B. A combined fit to the cross section data of $e^+e^- \to \eta J/\psi$

With the input of the branching ratios $\mathcal{BR}(\psi \to \eta J/\psi)$ predicted by the hadronic loop mechanism as shown in Fig. 2, we can now obtain the contribution of each vector charmonium to the cross section of $e^+e^- \to \eta J/\psi$ from Eq. (1), and apply a combined fit to the experimental data.

Since the branching ratio of $\psi(4500) \to \eta J/\psi$ is at least two orders of magnitude smaller than the others, and there is indeed no signal of structures around 4.5 GeV in the measured data of $e^+e^- \to \eta J/\psi$, we believe that the contribution of $\psi(4500)$ to the cross section of $e^+e^- \to \eta J/\psi$ can be safely dropped. In the following, we will use the left five theoretically constructed charmonia, i.e. $\psi(4040)$, $\psi(4160)$, $\psi(4220)$, $\psi(4380)$, $\psi(4415)$, as well as their theoretical branching ratios of decays into $\eta J/\psi$, dependent on the α parameter, to perform a combined fit to the cross section data of $e^+e^- \to \eta J/\psi$.

The total amplitude of $e^+e^- \to \eta J/\psi$ can be written as

$$\mathcal{M}_{\rm Total}(s) = \mathcal{M}_0(s) + \sum_i e^{i\phi_i}\mathcal{M}_{\psi_i}(s), \tag{14}$$

with an exponentially parameterized background formulated as

$$\mathcal{M}_0(s) = g(\sqrt{s} - m_\eta - m_{J/\psi})^2 e^{-a(\sqrt{s}-m_\eta-m_{J/\psi})^2}, \tag{15}$$

where ϕ_i is the phase angle between the resonance amplitude $\mathcal{M}_{\psi_i}(s)$ and the background $\mathcal{M}_0(s)$, g and a are two free parameters.

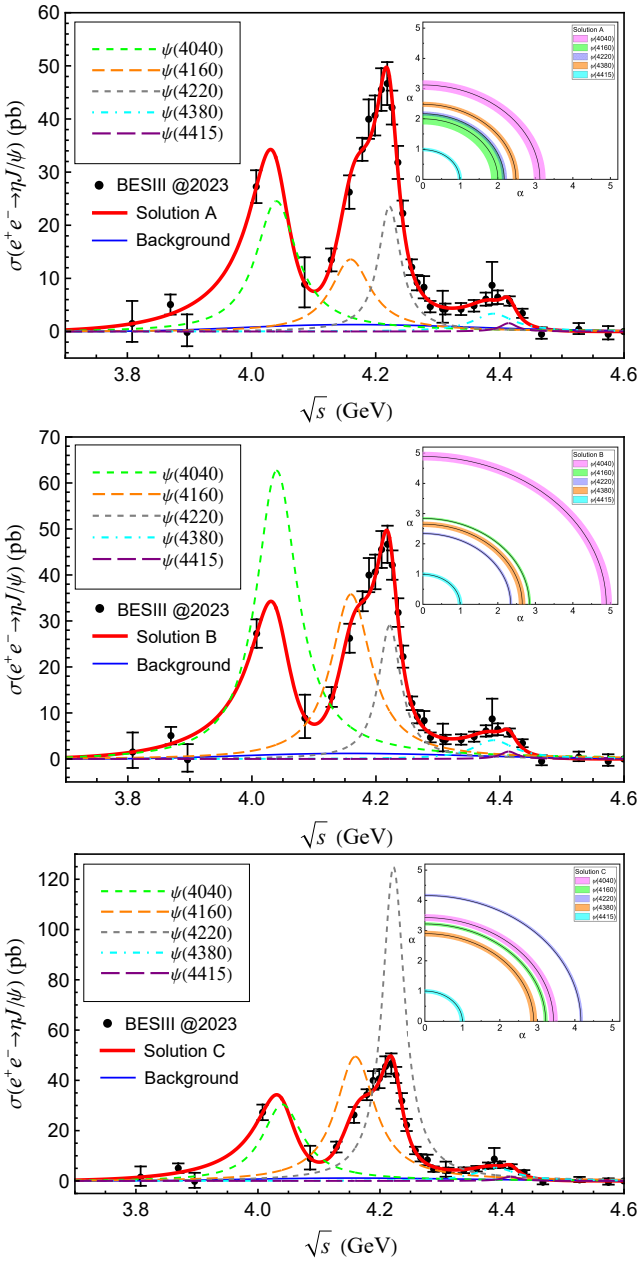

FIG. 4: Our fit to the cross section of the $e^+e^- \to \eta J/\psi$ process between E_{cm}=3.808 to 4.600 GeV by Scheme II. Here, the five dashed lines represent the contributions of the higher charmonium states, the blue line represents the background, and the red line represents the total contribution. The inset plots represent the α values corresponding to the fitted branching ratios in Table IV by the results of the hadronic loop predictions in Fig. 2, where the central values and the errors are represented by the solid black lines and the coloured bands, respectively.

The total cross section can be represented by

$$\sigma(s) = |\mathcal{M}_{\rm Total}(s)|^2. \tag{16}$$

Here, we employ two fitting schemes. In the first scheme, we assume a same α parameter for all charmonium states. The best fitting result in Scheme I, represented by a red curve, is

shown in Fig. 3, with $\chi^2/d.o.f = 1.65$. The relevant fitting parameters in Scheme I are listed in Table IV.

A direct observation in Fig. 3 shows that the line shape around 4.0 GeV is not well reproduced in Scheme I. This is mainly due to the scarcity of cross section data points around 4.0 GeV, which puzzles us in determining the contribution of the resonance state $\psi(4040)$. Our analysis suggests two resonance contributions from $\psi(4160)$ and $\psi(4220)$ around 4.2 GeV, and also reveals a significant resonance signal from $\psi(4415)$ in $e^+e^- \to \eta J/\psi$, which should be a focus of future BESIII and Belle II experiments. In particular, we found that the interference effect plays a crucial role in broadening the distribution of the resonance signal associated with $Y(4230)$, explaining its large width of $80.4 \pm 4.4 \pm 1.4$ MeV in the experimental fit and the line shape puzzle around 4.2 GeV in the $e^+e^- \to \eta J/\psi$ cross section.

In Scheme II, we consider a range of α parameters $[1, 5]$ for the five charmonium states without extra limit. The three solutions A, B and C in scheme II, represented by red curve, are shown in Fig. 4 with $\chi^2/d.o.f$ around 0.81, which is obviously improved compared to that of scheme I. The relevant fitting parameters in Scheme II are listed in Table IV.

Similar to Scheme I, our analysis in Scheme II shows the significant role of the interference effects in broadening the distribution of the resonance signal associated with $\psi(4160)$ and $\psi(4220)$, which naturally explains the asymmetric line shape associated with the resonance structure denoted as $Y(4230)$. Of the three solutions, $\psi(4040)$ gives different contributions to the cross section, and we hope that the experiment will complement the data points around in this part and clarify the contribution of $\psi(4040)$. And around 4.4 GeV, each solution in Scheme II shows an unremarkable resonance signal of $\psi(4415)$ in $e^+e^- \to \eta J/\psi$. Further investigation in future BESIII and Belle II experiments is indeed necessary to solve the broad width puzzle associated with the resonance structure denoted as $Y(4360)$.

III. SUMMARY

Recently, the BESIII Collaboration measured the Born cross section of $e^+e^- \to \eta J/\psi$ from 3.808 to 4.951 GeV, and reported three structures, the charmonium $\psi(4040)$ and two other charmoniumlike states, named $Y(4230)$ and $Y(4360)$ [10]. It is curious that the measured width of $Y(4230)$ is so large and has a large difference from the other open-charm and hidden-charm measurements, and the more subtle details of the line shape around 4.2 GeV with asymmetry suggest that the structure of the observed $Y(4230)$ may not be formed by a single resonance.

In order to understand the puzzles arising in the measured data, the energy levels structures of the charmonia from theoretical inputs are crucial. In this work, we focus on the six charmonia constructed by an unquenched potential model in the range of $4.0 \sim 4.5$ GeV, i.e., $\psi(4040)$, $\psi(4160)$, $\psi(4220)$, $\psi(4380)$, $\psi(4415)$, $\psi(4500)$. Using the hadronic loop mechanism, we are able to quantitatively calculate the branching ratios of the higher charmonium state decays into $\eta J/\psi$. The results indicate that the contribution of $\psi(4500)$ to the cross section of $e^+e^- \to \eta J/\psi$ is negligible, which is in agreement with the measured data, while others have sizable contributions. We then perform a combined fit with the left five charmonia to the newly measured cross section data of $e^+e^- \to \eta J/\psi$, the corresponding branching ratios of these charmonia decaying into $\eta J/\psi$ are constrained within a reasonable range, suggested by the hadronic loop mechanism. We have made two attempts with different cut-off parameter constraint schemes. Both fitting results show that the newly measured cross section of $e^+e^- \to \eta J/\psi$ can be reproduced by the five charmonia from the theoretical inputs, the puzzling large width and asymmetric line shape of the 4.2 GeV structure can be naturally explained by the contributions of the neighbouring charmonia $\psi(4160)$ and $\psi(4220)$. Moreover, the introduction of $\psi(4380)$ predicted by the theory in the combined fit is compatible with the experimental data, which together with $\psi(4415)$ can reproduce the third broad enhancement structure around 4.4 GeV reported by BESIII. More importantly, the results support the characterized energy level construction of higher vector charmonia in the range of $4.0 \sim 4.5$ GeV.

With the increasing accumulation of experimental data on the varieties of final states in this particular charmonium energy range, as well as the continuing attention of experimentalists and theorists, our understanding of the inner nature of higher charmonium states is becoming more mature and profound.

IV. ACKNOWLEDGMENTS

This work is supported by the National Natural Science Foundation of China under Grant Nos. 12335001 and 12247101, the China National Funds for Distinguished Young Scientists under Grant No. 11825503, National Key Research and Development Program of China under Contract No. 2020YFA0406400, the 111 Project under Grant No. B20063, the fundamental Research Funds for the Central Universities, and the project for top-notch innovative talents of Gansu province. J.Z.W. is also supported by the National Postdoctoral Program for Innovative Talent.

Appendix A: The decay amplitudes of hadronic loop mechanism

$$\mathcal{M}^{(1)}_{\psi(4040)} = \int \frac{d^4q}{(2\pi)^4} g_{\psi(4040)DD} \times \epsilon^{\mu}_{\psi}(q_{2\mu} - q_{1\mu})(-g_{DD^*\eta}) p_1^{\alpha} g_{J/\psi DD^*} \varepsilon_{\lambda\gamma\beta\rho} p_2^{\lambda} \varepsilon^{\gamma}_{J/\psi}(q_2^{\rho} - q^{\rho}) \tag{A1}$$
$$\times (-g^{\beta}_{\alpha} + q_{\alpha}q^{\beta}/m^2_{D^*}) \frac{\mathcal{F}^2(q^2, m^2_{B^*})}{q^2 - m^2_{D^*}},$$

$$\mathcal{M}^{(2)}_{\psi(4040)} = \int \frac{d^4q}{(2\pi)^4} g_{\psi(4040)DD^*} \varepsilon_{\nu\mu\alpha\beta} \epsilon^{\mu}_{\psi}(q_2^{\beta} - q_1^{\beta})(-g_{D^*D^*\eta}) \varepsilon_{\rho\eta\lambda\theta} q^{\rho} q_1^{\lambda} (g_{J/\psi DD^*}) \varepsilon_{\delta\theta\tau\gamma} \epsilon^{\theta}_{J/\psi} p_2^{\delta}(q^{\gamma} - q_2^{\gamma}) \tag{A2}$$
$$\times (-g^{\alpha\eta} + q_1^{\alpha}q_1^{\eta}/m^2_{D^*})(-g^{\tau\sigma} + q^{\tau}q^{\sigma}/m^2_{D^*}) \frac{\mathcal{F}^2(q^2, m^2_{B^*})}{q^2 - m^2_{D^*}},$$

$$\mathcal{M}^{(3)}_{\psi(4040)} = \int \frac{d^4q}{(2\pi)^4} g_{\psi(4040)DD^*} \varepsilon_{\nu\mu\alpha\beta} \epsilon^{\mu}_{\psi} p^{\nu}(q_2^{\beta} - q_1^{\beta})(g_{D^*D\eta}) p_1^{\gamma}(g_{J/\psi DD}) \epsilon^{\rho}_{J/\psi}(q_{\rho} - q_{2\rho}) \tag{A3}$$
$$\times (-g^{\alpha}_{\gamma} + q_1^{\alpha}q_1^{\gamma}/m^2_{D^*}) \frac{\mathcal{F}^2(q^2, m^2_{B^*})}{q^2 - m^2_{D}},$$

$$\mathcal{M}^{(4)}_{\psi(4040)} = \int \frac{d^4q}{(2\pi)^4} g_{\psi(4040)DD^*} \varepsilon_{\nu\mu\alpha\beta} \epsilon^{\mu}_{\psi}(q_2^{\beta} - q_1^{\beta})(g_{D^*D\eta}) p_1^{\gamma}(g_{J/\psi D^*D}) \epsilon^{\rho}_{J/\psi}[g_{\sigma\rho}q_{2\eta} - g_{\eta\rho}q_{1\sigma} + g_{\theta\eta}(q_{\rho} - q_{2\rho})] \tag{A4}$$
$$\times (-g^{\alpha\sigma} + q_2^{\alpha}q_2^{\sigma}/m^2_{D^*})(-g^{\eta}_{\gamma} + q_{\gamma}q^{\eta}/m^2_{D^*}) \frac{\mathcal{F}^2(q^2, m^2_{B^*})}{q^2 - m^2_{D^*}},$$

$$\mathcal{M}^{(5)}_{\psi(4040)} = \int \frac{d^4q}{(2\pi)^4} g_{\psi(4040)D^*D^*} \epsilon^{\mu}_{\psi}[g_{\beta\mu}q_{2\alpha} - g_{\alpha\mu}q_{1\beta} + \mathcal{S} \cdot g_{\alpha\beta}(q_{1\mu} - q_{2\mu})](-g_{D^*D^*\eta}) \varepsilon_{\rho\sigma\lambda\eta} q_1^{\lambda} q^{\rho} (g_{J/\psi DD^*}) \tag{A5}$$
$$\times \epsilon^{\gamma}_{J/\psi}[g_{\tau\gamma}q_{2\theta} - g_{\theta\gamma}q_{1\tau} + g_{\tau\theta}(q_{\gamma} - q_{2\gamma})]$$
$$\times (-g^{\alpha\eta} + q_1^{\alpha}q_1^{\eta}/m^2_{D^*})(-g^{\tau\beta} + q_2^{\tau}q_2^{\beta}/m^2_{D^*})(-g^{\sigma\theta} + q^{\sigma}q^{\theta}/m^2_{D^*}) \frac{\mathcal{F}^2(q^2, m^2_{B^*})}{q^2 - m^2_{D^*}},$$

$$\mathcal{M}^{(6)}_{\psi(4040)} = \int \frac{d^4q}{(2\pi)^4} g_{\psi(4040)D^*D^*} \epsilon^{\mu}_{\psi}[g_{\beta\mu}q_{2\alpha} - g_{\alpha\mu}q_{1\beta} + \mathcal{S} \cdot g_{\alpha\beta}(q_{1\mu} - q_{2\mu})](g_{D^*D\eta}) p_1^{\gamma}(g_{J/\psi DD^*}) \varepsilon_{\lambda\eta\sigma\rho} \epsilon^{\eta}_{J/\psi} p_2^{\lambda}(q^{\rho} - q_2^{\rho}) \tag{A6}$$
$$\times (-g^{\alpha}_{\gamma} + q_1^{\alpha}q_{1\gamma}/m^2_{D^*})(-g^{\beta\sigma} + q^{\beta}q^{\sigma}/m^2_{D^*}) \frac{\mathcal{F}^2(q^2, m^2_{B^*})}{q^2 - m^2_{D^*}},$$

$$\mathcal{M}^{(1)}_{\psi(4160)} = \int \frac{d^4q}{(2\pi)^4} g_{\psi(4160)DD} \times \epsilon^{\mu}_{\psi}(q_{2\mu} - q_{1\mu})(-g_{DD^*\eta}) p_1^{\alpha} g_{J/\psi DD^*} \varepsilon_{\lambda\gamma\beta\rho} p_2^{\lambda} \varepsilon^{\gamma}_{J/\psi}(q_2^{\rho} - q^{\rho}) \tag{A7}$$
$$\times (-g^{\beta}_{\alpha} + q_{\alpha}q^{\beta}/m^2_{D^*}) \frac{\mathcal{F}^2(q^2, m^2_{B^*})}{q^2 - m^2_{D^*}},$$

$$\mathcal{M}^{(2)}_{\psi(4160)} = \int \frac{d^4q}{(2\pi)^4} g_{\psi(4160))DD^*} \varepsilon_{\nu\mu\alpha\beta} \epsilon^{\mu}_{\psi}(q_2^{\beta} - q_1^{\beta})(-g_{D^*D^*\eta}) \varepsilon_{\rho\eta\lambda\theta} q^{\rho} q_1^{\lambda} (g_{J/\psi DD^*}) \varepsilon_{\delta\theta\tau\gamma} \epsilon^{\theta}_{J/\psi} p_2^{\delta}(q^{\gamma} - q_2^{\gamma}) \tag{A8}$$
$$\times (-g^{\alpha\eta} + q_1^{\alpha}q_1^{\eta}/m^2_{D^*})(-g^{\tau\sigma} + q^{\tau}q^{\sigma}/m^2_{D^*}) \frac{\mathcal{F}^2(q^2, m^2_{B^*})}{q^2 - m^2_{D^*}},$$

$$\mathcal{M}^{(3)}_{\psi(4160)} = \int \frac{d^4q}{(2\pi)^4} g_{\psi(4160)DD^*} \varepsilon_{\nu\mu\alpha\beta} \epsilon^{\mu}_{\psi} p^{\nu}(q_2^{\beta} - q_1^{\beta})(g_{D^*D\eta}) p_1^{\gamma}(g_{J/\psi DD}) \epsilon^{\rho}_{J/\psi}(q_{\rho} - q_{2\rho}) \tag{A9}$$
$$\times (-g^{\alpha}_{\gamma} + q_1^{\alpha}q_1^{\gamma}/m^2_{D^*}) \frac{\mathcal{F}^2(q^2, m^2_{B^*})}{q^2 - m^2_{D}},$$

$$\mathcal{M}^{(4)}_{\psi(4160)} = \int \frac{d^4q}{(2\pi)^4} g_{\psi(4160)DD^*} \varepsilon_{\nu\mu\alpha\beta} \epsilon^{\mu}_{\psi}(q_2^{\beta} - q_1^{\beta})(g_{D^*D\eta}) p_1^{\gamma}(g_{J/\psi D^*D^*}) \epsilon^{\rho}_{J/\psi}[g_{\sigma\rho}q_{2\eta} - g_{\eta\rho}q_{1\sigma} + g_{\theta\eta}(q_{\rho} - q_{2\rho})] \tag{A10}$$
$$\times (-g^{\alpha\sigma} + q_2^{\alpha}q_2^{\sigma}/m^2_{D^*})(-g^{\eta}_{\gamma} + q_{\gamma}q^{\eta}/m^2_{D^*}) \frac{\mathcal{F}^2(q^2, m^2_{B^*})}{q^2 - m^2_{D^*}},$$

$$\mathcal{M}^{(5)}_{\psi(4160)} = \int \frac{d^4q}{(2\pi)^4} g_{\psi(4160)D^*D^*}\epsilon^{\mu}_{\psi}[g_{\beta\mu}q_{2\alpha} - g_{\alpha\mu}q_{1\beta} + \mathcal{S}\cdot g_{\alpha\beta}(q_{1\mu} - q_{2\mu})](-g_{D^*D^*\eta})\varepsilon_{\rho\sigma\lambda\eta}q_1^{\lambda}q^{\rho}(g_{J/\psi D^*D^*}) \tag{A11}$$
$$\times \epsilon^{\gamma}_{J/\psi}[g_{\tau\gamma}q_{2\theta} - g_{\theta\gamma}q_{1\tau} + g_{\tau\theta}(q_{\gamma} - q_{2\gamma})]$$
$$\times (-g^{\alpha\eta} + q_1^{\alpha}q_1^{\eta}/m^2_{D^*})(-g^{\tau\beta} + q_2^{\tau}q_2^{\beta}/m^2_{D^*})(-g^{\sigma\theta} + q^{\sigma}q^{\theta}/m^2_{D^*})\frac{\mathcal{F}^2(q^2, m^2_{B^*})}{q^2 - m^2_{D^*}},$$

$$\mathcal{M}^{(6)}_{\psi(4160)} = \int \frac{d^4q}{(2\pi)^4} g_{\psi(4160)D^*D^*}\epsilon^{\mu}_{\psi}[g_{\beta\mu}q_{2\alpha} - g_{\alpha\mu}q_{1\beta} + \mathcal{S}\cdot g_{\alpha\beta}(q_{1\mu} - q_{2\mu})](g_{D^*D\eta})p_1^{\gamma}(g_{J/\psi DD^*})\varepsilon_{\lambda\eta\sigma\rho}\epsilon^{\eta}_{J/\psi}p_2^{\lambda}(q^{\rho} - q_2^{\rho}) \tag{A12}$$
$$\times (-g_{\gamma}^{\alpha} + q_1^{\alpha}q_{1\gamma}/m^2_{D^*})(-g^{\beta\sigma} + q^{\beta}q^{\sigma}/m^2_{D^*})\frac{\mathcal{F}^2(q^2, m^2_{B^*})}{q^2 - m^2_{D^*}}.$$

[1] X. Liu, An overview of *XYZ* new particles, Chin. Sci. Bull. **59**, 3815 (2014).
[2] H. X. Chen, W. Chen, X. Liu, and S. L. Zhu, The hidden-charm pentaquark and tetraquark states, Phys. Rept. **639** (2016), 1.
[3] A. Esposito, A. Pilloni, and A. D. Polosa, Multiquark Resonances, Phys. Rept. **668**, 1 (2017).
[4] H. X. Chen, W. Chen, X. Liu, Y. R. Liu, and S. L. Zhu, A review of the open charm and open bottom systems, Rept. Prog. Phys. **80**, 076201 (2017).
[5] F. K. Guo, C. Hanhart, U. G. Meißner, Q. Wang, Q. Zhao, and B. S. Zou, Hadronic molecules, Rev. Mod. Phys. **90**, 015004 (2018); **94**, 029901 (E) (2022).
[6] S. L. Olsen, T. Skwarnicki, and D. Zieminska, Nonstandard heavy mesons and baryons: Experimental evidence, Rev. Mod. Phys. **90**, 015003 (2018).
[7] Y. R. Liu, H. X. Chen, W. Chen, X. Liu, and S. L. Zhu, Pentaquark and Tetraquark states, Prog. Part. Nucl. Phys. **107**, 237 (2019).
[8] N. Brambilla, S. Eidelman, C. Hanhart, A. Nefediev, C. P. Shen, C. E. Thomas, A. Vairo, and C. Z. Yuan, The *XYZ* states: experimental and theoretical status and perspectives, Phys. Rept. **873**, 1 (2020).
[9] H. X. Chen, W. Chen, X. Liu, Y. R. Liu, and S. L. Zhu, An updated review of the new hadron states, Rept. Prog. Phys. **86**, 026201 (2023).
[10] M. Ablikim *et al.* [BESIII], Measurement of $e^+e^- \to \eta J/\psi$ Cross Section from $\sqrt{s}$ = 3.808 GeV to 4.951 GeV, arXiv:2310.03361.
[11] B. Aubert *et al.* [BaBar], Observation of a broad structure in the $\pi^+\pi^- J/\psi$ mass spectrum around 4.26 GeV/c^2, Phys. Rev. Lett. **95**, 142001 (2005).
[12] M. Ablikim *et al.* [BESIII], Precise measurement of the $e^+e^- \to \pi^+\pi^- J/\psi$ cross section at center-of-mass energies from 3.77 to 4.60 GeV, Phys. Rev. Lett. **118**, 092001 (2017).
[13] M. Ablikim *et al.* [BESIII], Study of the process $e^+e^- \to \pi^0\pi^0 J/\psi$ and neutral charmonium-like state $Z_c(3900)^0$, Phys. Rev. D **102**, 012009 (2020).
[14] B. Aubert *et al.* [BaBar] Evidence of a broad structure at an invariant mass of 4.32 GeV/c^2 in the reaction $e^+e^- \to \pi^+\pi^-\psi(2S)$ measured at BaBar, Phys. Rev. Lett. **98**, 212001 (2007).
[15] M. Ablikim *et al.* [BESIII], Measurement of $e^+e^- \to \pi^+\pi^-\psi(3686)$ from 4.008 to 4.600 GeV and observation of a charged structure in the $\pi^+\psi(3686)$ mass spectrum, Phys. Rev. D **96**, 032004 (2017).
[16] M. Ablikim *et al.* [BESIII], Evidence of Two Resonant Structures in $e^+e^- \to \pi^+\pi^- h_c$, Phys. Rev. Lett. **118**, 092002 (2017).
[17] M. Ablikim *et al.* [BESIII], Cross section measurements of $e^+e^- \to \omega\chi_{c0}$ form $\sqrt{s}$ = 4.178 to 4.278 GeV, Phys. Rev. D **99**, 091103 (2019).
[18] M. Ablikim *et al.* [(BESIII), and BESIII], Observation of the Y(4230) and a new structure in $e^+e^- \to K^+K^- J/\psi$, Chin. Phys. C **46**, 111002 (2022).
[19] M. Ablikim *et al.* [BESIII], Evidence of a resonant structure in the $e^+e^- \to \pi^+ D^0 D^{*-}$ cross section between 4.05 and 4.60 GeV, Phys. Rev. Lett. **122**, 102002 (2019).
[20] R. L. Workman *et al.* [Particle Data Group], Review of Particle Physics, PTEP **2022**, 083C01 (2022).
[21] D. Y. Chen, X. Liu and T. Matsuki, η transitions between charmonia with meson loop contributions, Phys. Rev. D **87**, 054006 (2013).
[22] J. Z. Wang, D. Y. Chen, X. Liu and T. Matsuki, Constructing J/ψ family with updated data of charmoniumlike *Y* states, Phys. Rev. D **99**, 114003 (2019).
[23] J. Z. Wang, and X. Liu, Confirming the existence of a new higher charmonium $\psi(4500)$ by the newly released data of $e^+e^- \to K^+K^- J/\psi$, Phys. Rev. D **107**, 054016 (2023).
[24] J. Z. Wang, and X. Liu, Identifying a characterized energy level structure of higher charmonium well matched to the peak structures in $e^+e^- \to \pi^+ D^0 D^{*-}$, Phys. Lett. B **849**, 138456 (2024).
[25] L. P. He, D. Y. Chen, X. Liu, and T. Matsuki, Prediction of a missing higher charmonium around 4.26 GeV in J/ψ family, Eur. Phys. J. C **74**, 3208 (2014).
[26] D. Y. Chen, X. Liu, and T. Matsuki, Observation of $e^+e^- \to \chi_{c0}\omega$ and missing higher charmonium $\psi(4S)$, Phys. Rev. D **91**, 094023 (2015).
[27] D. Y. Chen, X. Liu, and T. Matsuki, Search for missing $\psi(4S)$ in the $e^+e^- \to \pi^+\pi^-\psi(2S)$ process, Phys. Rev. D **93**, 034028 (2016).
[28] D. Y. Chen, X. Liu, and T. Matsuki, Interference effect as resonance killer of newly observed charmoniumlike states *Y*(4320) and *Y*(4390), Eur. Phys. J. C **78**, 136 (2018).
[29] M. Ablikim *et al.* [BES], Determination of the $\psi(3770)$, $\psi(4040)$, $\psi(4160)$ and $\psi(4415)$ resonance parameters, Phys. Lett. B **660**, 315 (2008).
[30] R. Brandelik *et al.* [DASP], Total cross section for Hadron Production by e^+e^- Annihilation at Center-of-mass Energies Between 3.6 GeV and 5.2 GeV, Phys. Lett. B **76**, 361 (1978).
[31] X. Liu, X. Q. Zeng, and X. Q. Li, Study on contributions of hadronic loops to decays of $J/\psi \to$ vector + pseudoscalar mesons, Phys. Rev. D **74**, 074003 (2006).

[32] X. Liu, B. Zhang, and X. Q. Li, The puzzle of excessive non-$D\bar{D}$ component of the inclusive $\psi(3770)$ decay and the long-distant contribution,Phys. Lett. B **675**, 441 (2009).

[33] G. Li, X. h. Liu, Q. Wang, and Q. Zhao, Further understanding of the non-$D\bar{D}$ decays of $\psi(3770)$, Phys. Rev. D **88**, 014010 (2013).

[34] C. Meng, and K. T. Chao, Scalar resonance contributions to the dipion transition rates of $\Upsilon(4S, 5S)$ in the re-scattering model, Phys. Rev. D **77**, 074003 (2008).

[35] C. Mengs, and K. T. Chao, Peak shifts due to $B^{(*)} - \bar{B}^{(*)}$ rescattering in $\Upsilon(5S)$ dipion transitions, Phys. Rev. D **78**, 034022 (2008).

[36] C. Meng, and K. T. Chao, $\Upsilon(4S, 5S) \to \Upsilon(1S)\eta$ transitions in the rescattering model, and the new *BABAR* measurement, Phys. Rev. D **78**, 074001 (2008).

[37] D. Y. Chen, J. He, X. Q. Li, and X. Liu, Dipion invariant mass distribution of the anomalous $\Upsilon(1S)\pi^+\pi^-$ and $\Upsilon(2S)\pi^+\pi^-$ production near the peak of $\Upsilon(10860)$, Phys. Rev. D **84**, 074006 (2011).

[38] D. Y. Chen, X. Liu, and S. L. Zhu, Charged bottomonium-like states $Z_b(10610)$ and $Z_b(10650)$ and the $\Upsilon(5S) \to \Upsilon(2S)\pi^+\pi^-$ decay, Phys. Rev. D **84**, 074016 (2011).

[39] D. Y. Chen, and X. Liu, $Z_b(10610)$ and $Z_b(10650)$ structures produced by the initial single pion emission in the $\Upsilon(5S)$ decays, Phys. Rev. D **84**, 094003 (2011).

[40] D. Y. Chen, X. Liu, and X. Q. Li, Anomalous dipion invariant mass distribution of the $\Upsilon(4S)$ decays into $\Upsilon(1S)\pi^+\pi^-$ and $\Upsilon(2S)\pi^+\pi^-$, Eur. Phys. J. C **71**, 1808 (2011).

[41] D. Y. Chen, X. Liu, and T. Matsuki, Explaining the anomalous $\Upsilon(5S) \to \chi_{bJ}\omega$ decays through the hadronic loop effect, Phys. Rev. D **90**, 034019 (2014).

[42] B. Wang, H. Xu, X. Liu, D. Y. Chen, S. Coito, and E. Eichten, Using $X(3823) \to J/\psi\pi^+\pi^-$ to identify coupled-channel effects, Front. Phys. (Beijing) **11**, 111402 (2016).

[43] B. Wang, X. Liu, and D. Y. Chen, Prediction of anomalous $\Upsilon(5S) \to \Upsilon(1^3D_J)\eta$ transitions, Phys. Rev. D **94**, 094039 (2016).

[44] Q. Huang, B. Wang, X. Liu, D. Y. Chen, and T. Matsuki, Exploring the $\Upsilon(6S) \to \chi_{bJ}\phi$ and $\Upsilon(6S) \to \chi_{bJ}\omega$ hidden-bottom hadronic transitions, Eur. Phys. J. C **77**, 165 (2017).

[45] Y. Zhang, and G. Li, Exploring the $\Upsilon(4S, 5S, 6S) \to h_b(1P)\eta$ hidden-bottom hadronic transitions, Phys. Rev. D **97**, 014018 (2018).

[46] Q. Huang, H. Xu, X. Liu, and T. Matsuki, Potential observation of the $\Upsilon(6S) \to \Upsilon(1^3D_J)\eta$ transitions at Belle II, Phys. Rev. D **97**, 094018 (2018).

[47] Q. Huang, X. Liu, and T. Matsuki, Proposal of searching for the $\Upsilon(6S)$ hadronic decays into $\Upsilon(nS)$ plus $\eta^{(\prime)}$, Phys. Rev. D **98**, 054008 (2018).

[48] Y. S. Li, Z. Y. Bai, Q. Huang, and X. Liu, Hidden-bottom hadronic decays of $\Upsilon(10753)$ with a $\eta^{(\prime)}$ or ω emission, Phys. Rev. D **104**, 034036 (2021).

[49] Z. Y. Bai, Y. S. Li, Q. Huang, X. Liu, and T. Matsuki, $\Upsilon(10753) \to \Upsilon(nS)\pi^+\pi^-$decays induced by hadronic loop mechanism, Phys. Rev. D **105**, 074007 (2022).

[50] Y. S. Li, Z. Y. Bai, and X. Liu, Investigating the $\Upsilon(10753) \to \Upsilon(1^3D_J)\eta$ transitions, Phys. Rev. D **105**, 114041 (2022).

[51] Z. Y. Bai, Q. S. Zhou, and X. Liu, Higher strangeonium decays into light flavor baryon pairs like $\Lambda\bar{\Lambda}$, $\Sigma\bar{\Sigma}$, and $\Xi\bar{\Xi}$, Phys. Rev. D **108**, 094036 (2023).

[52] H. Y. Cheng, C. K. Chua, and A. Soni, Final state interactions in hadronic B decays, Phys. Rev. D **71**, 014030 (2005).

[53] N. N. Achasov, and A. A. Kozhevnikov, Dynamical violation of the OZI rule and G parity in the decays of heavy quarkonia,Phys. Rev. D **49**, 275 (1994).

[54] A. Deandrea, G. Nardulli, and A. D. Polosa, J/ψ couplings to charmed resonances and to π, Phys. Rev. D **68** (2003), 034002.

[55] L. Micu, Decay rates of meson resonances in a quark model, Nucl. Phys. B **10**, 521 (1969).

[56] A. Le Yaouanc, L. Oliver, O. Pene, and J. C. Raynal, Why is $\psi(4.414)$ so narrow?, Phys. Lett. B **72**, 57 (1977).

[57] M. Jacob, and G. C. Wick, On the General Theory of Collisions for Particles with Spin, Annals Phys. **7**, 404 (1959); **281**, 774 (2020).

Mass and decay width of T_{ccs} from symmetries

Mitsuru Tanaka,[1,*] Yasuhiro Yamaguchi,[1,2,3,†] and Masayasu Harada[2,1,4,‡]

[1] *Department of Physics, Nagoya University, Nagoya 464-8602, Japan*
[2] *Kobayashi-Maskawa Institute for the Origin of Particles and the Universe, Nagoya University, Nagoya, 464-8602, Japan*
[3] *Meson Science Laboratory, Cluster for Pioneering Research, RIKEN, Hirosawa, Wako, Saitama 351-0198, Japan*
[4] *Advanced Science Research Center, Japan Atomic Energy Agency, Tokai 319-1195, Japan*

(Dated: March 7, 2024)

We analyze the mass and width of the doubly heavy tetraquark T_{ccs} composed of a heavy diquark and a light quark cloud with strangeness with assuming that a color anti-triplet heavy diquark is a dominant component of the doubly charmed tetraquarks T_{cc} and T_{ccs}. We construct an effective Lagrangian for masses of heavy hadrons based on the superflavor symmetry between the doubly heavy tetraquarks and the singly heavy baryons with including the terms which simultaneously break the heavy-quark and light flavor symmetries, and predict the mass of T_{ccs} as $M(T_{ccs}) = 4057 \pm 40\,\mathrm{MeV}$. The comparison of this prediction with future experimental observation will give a clue to understand the color structure of the heavy diquark. We also predict the spin-averaged mass of Ω_{cc} ($J^P = 1/2^+, 3/2^+$) as $M(\Omega_{cc}) = 3760 \pm 18\,\mathrm{MeV}$. We next calculate the decay width of T_{ccs}, based on solely the light flavor symmetry, as $\Gamma(T_{ccs}) = 1.2 \pm 0.3\,\mathrm{MeV}$.

Keywords: superflavor symmetry, heavy quark symmetry, flavor symmetry, diquark, doubly heavy tetraquark

arXiv:2403.03548v1 [hep-ph] 6 Mar 2024

I. INTRODUCTION

The discovery of $X(3872)$ [1] marked the beginning of numerous exotic hadron discoveries in the heavy quark sectors, yet their structure remains poorly understood. Hadrons with exotic structures beyond ordinary baryons (qqq) and mesons ($q\bar{q}$) were already indicated by Gell-Mann and Zweig in the 1960s [2–6]. Possible structures of the multiquark state being a color singlet have been discussed in many literatures (See, for a reviews, e.g. Refs. [7, 8]). The compact multiquark has been investigated as a color singlet state of few-body multiquark systems by the constituent quark model etc (See e.g. Refs. [9–16]). The emergence of the hadronic molecules as a deuteron-like state, discussed as a deuson in Ref. [17], is expected near the thresholds. In fact many candidates of a hadronic molecule have been reported in the experimental studies as the XYZ tetraquarks being a meson-meson state and the P_c pentaquarks being a meson-baryon one. Investigating the exotic structures would lead to an understanding of the QCD phenomena such as color confinement.

The doubly charmed tetraquark T_{cc}^+ was reported in the LHCb experiment in 2021 [18, 19]. The reported state is consistent with a genuine exotic hadron having a flavor structure $cc\bar{u}\bar{d}$. The spin and parity of T_{cc}^+ are determined to be $J^P = 1^+$, and the LHCb considers T_{cc}^+ as an isoscalar. The mass of T_{cc}^+ is 3874.817 MeV close to the D^0D^{*+} threshold. The decay to $D^0D^0\pi^+$ has been confirmed, with a decay width of 48 keV [18] or 410 keV [19]. Furthermore, the LHCb analysis supports that T_{cc}^+ decays to $D^0D^0\pi^+$ via the intermediate state D^{*+}.

Since the discovery of T_{cc}^+, research on the doubly heavy tetraquarks (DHTs) has been actively conducted [7]. However at present, no clear answer has been obtained regarding the structure of DHTs. For example, analyses based on the hadronic molecular model, which assumes that T_{cc}^+ is a loosely bound state with D and D^*, have been conducted [20, 21]. This is due to the fact that the mass of T_{cc}^+ resides in the vicinity of the DD^* threshold. On the other hand, a compact tetraquark structure of DHT is considered [22], based on the diquark picture proposed by Jaffe [23].

Symmetries such as flavor symmetry and chiral symmetry play a crucial role in the classification of hadronic states. For exotic hadrons including heavy quarks, symmetries that emerge in the heavy quark limit, such as heavy quark symmetry (HQS) (see e.g. Ref. [24]) and superflavor symmetry (SFS) [25–27], are considered potentially useful for understanding the structures of exotics. The superflavor symmetry emerges in an exchange of an anti-heavy quark and a heavy diquark with the same color configuration $\bar{3}$ in the heavy quark limit. Due to the sufficiently large mass of the heavy diquark, the spin–dependent color magnetic force is negligible, and does not contribute in the heavy quark limit. In this context, the heavy diquark and an anti-heavy quark behave as the static color $\bar{3}$ source and are equivalent in terms of color interaction. The property of hadrons remains invariant under the interchange of the heavy diquark and anti heavy quark. We will refer to hadrons related under this superflavor symmetry as superflavor partners. For instance, an anti-heavy meson(HM) $\bar{Q}q$ and a doubly heavy baryon(DHB) QQq are superflavor partners. Another color representation for diquarks, 6, is also allowed in DHTs but not in ordinary hadrons. If diquarks take color 6 representation, the superflavor sym-

* tanaka@hken.phys.nagoya-u.ac.jp
† yamaguchi@hken.phys.nagoya-u.ac.jp
‡ harada@hken.phys.nagoya-u.ac.jp

metry does not arise. Hence, superflavor symmetry might shed light on the color configuration of exotic hadrons. We think that understanding the color configuration of the diquark in DHTs is important because the interaction changes according to the color representation.

In order to analyze the mass spectrum of DHTs in terms of superflavor symmetry, this study assumes that DHTs consist of a color heavy diquark, treated as a spatially compact object, and a light quark cloud surrounding it. Although it may exist in a mixed state within a DHT, we also assume that the color anti-triplet state is the dominant state of the diquark because the color $\bar{3}$ diquark is likely realized in the ground state [7, 28, 29]. Here, "being spatially compact" means that the heavy diquark can be approximated as a point-like particle, with no radial excitation occurring between two heavy quarks. The analyses of T_{bb}, being the bottom counterpart of T_{cc}, based on the quark model [29–31] suggest that the distance between the two bottom quarks is shorter compared to other quark distances. This observation appears to support the notion that T_{bb} is composed of a heavy diquark and a light quark cloud. In the present analysis, we assume that T_{cc} also holds such heavy diquark structure. For simplicity, this analysis focuses solely on diquarks where both heavy quarks are of the same flavor. Under these conditions, a color $\bar{3}$ diquark possesses spin one ($S_{QQ} = 1$), whereas a color 6 diquark has spin zero ($S_{QQ} = 0$).

If T_{cc}^+ is the superflavor partner of Λ_c^+, we can naturally expect the existence of T_{ccs} as the superflavor partner of Ξ_c, which belongs to the same flavor multiplet as Λ_c^+. We consider that investigation of T_{ccs} is useful to understand the nature not only of T_{ccs} itself but also of T_{cc}^+. We analyze T_{ccs} by using experimental result of T_{cc}^+ as an input. Thus if the results obtained in this paper are eventually consistent with results in future experiments, it can be interpreted that the color anti-triplet state is dominant in DHTs T_{cc}^+ and T_{ccs}. In the following, we first derive simple mass relations assuming that the heavy diquark is spatially compact and color anti-triplet state together with superflavor symmetry. We note that the relations agree with the ones derived in Ref. [32]. However, we find a discrepancy between the prediction by the simple mass relation and the recent experimental data of T_{cc}^+. Thus we invent the improved mass relations with correction terms violating the symmetries and a mixing term of color $\bar{3}$ and 6 states of the cc diquark. Then, we obtain new relations among HMs, DHBs, SHBs and DHTs, and predict the mass of T_{ccs}. Furthermore, we also predict the decay width of T_{ccs} from the SU(3) flavor symmetry.

This paper is organized as follows. In Sec, II, we derive the simple mass relations among singly heavy and doubly heavy hadrons based on the heavy quark and superflavor symmetries. We point out the existence of discrepancy between the theoretical formulas and the experimental results. In Sec. III, we construct the effective Lagrangians including corrections and obtain the improved mass relations. The mass of T_{ccs} and in addition, the one of Ω_{cc} are predicted. In Sec. IV, the decay width of T_{ccs} is predicted by using the effective Lagrangian approach respecting the flavor symmetry. Finally, Sec. V is devoted to the summary.

II. SIMPLE MASS RELATIONS FROM SUPERFLAVOR AND LIGHT-FLAVOR SYMMETRIES

In this section, we first introduce simple mass relations among superflavor partners, primarily derived from superflavor, heavy quark, and light-flavor symmetries. Then, we demonstrate that these mass relations are somewhat broken among real hadrons, indicating the need for improvements to the mass relations. Under the superflavor symmetry, a DHT is related to an anti-SHB, and a DHB to an anti-HM. Considering that T_{cc}^+ has isospin $I = 0$, the superflavor partners of T_{cc}^+, T_{ccs}^+, and T_{ccs}^{++} are respectively the anti-baryons of Λ_c^+, Ξ_c^+, and Ξ_c^0. Similarly, the superflavor partners of DHBs like Ξ_{cc} and Ω_{cc} are the heavy mesons (HMs), $\bar{D}$ and $\bar{D}_s$, respectively.

We first study the relation between the masses of the DHBs and HMs in terms of the superflavor symmetry, and then extend the analysis to the DHTs and SHBs. Based on the HQS, we divide a heavy hadron into a heavy object and light-quark cloud which includes the interaction between them. Therefore, the dynamics of these hadrons are determined by the properties of the light quark cloud. As a result, the masses of heavy hadrons treated in the present analysis are expressed as a sum of the mass of heavy objects and the energy of light quark cloud in the heavy quark limit. Let us first estimate the masses of HMs. Here, we consider the spin average of the doublet under the HQS. We note that due to the spin average, the first-order term in $1/m_Q$ expansion that breaks only the heavy quark spin symmetry does not appear in the mass formulas. As a result, the spin-averaged mass can be expressed as

$$M_{\rm ave}\left(\bar{Q}q\right) = M\left(\bar{Q}\right) + E\left(q\right), \tag{1}$$

where $M(\bar{Q})$ ($\bar{Q} = \bar{c}, \bar{b}$) is the mass of anti-heavy quark, and $E(q)$ ($q = u, d, s$) denotes the contribution from the light-quark cloud. From Eq. (1), we obtain the meson mass difference between flavor partners as

$$M_{\rm ave}(\bar{Q}s) - M_{\rm ave}(\bar{Q}n) = E(s) - E(n)\ , \tag{2}$$

where $n = u, d$.

In the DHBs, the heavy diquark QQ takes the color $\bar{3}$ representation, so that the anti-HMs and the DHBs include common light-quark cloud in the heavy quark limit. Thus, the spin-averaged mass of the doublet members of DHBs is expressed in a similar formula as for the HMs:

$$M_{\rm ave}\left(QQq\right) = M\left(QQ\right) + E\left(q\right)\ . \tag{3}$$

We stress that the term $E\left(q\right)$ is common in Eqs. (1) and (3). The mass difference between flavor partners is

$E(\bar{q}_1) - E(\bar{q}_2)$, where $q_1, q_2 = u, d, s$. This leads to the following mass relation [33]:

$$M_{\rm ave}\left(QQq_1\right) - M_{\rm ave}\left(QQq_2\right) = M_{\rm ave}\left(\bar{Q}q_1\right) - M_{\rm ave}\left(\bar{Q}q_2\right) \ . \quad (4)$$

This implies that the mass differences between flavor partners are the same in the superflavor partners.

Next, we consider the masses of anti-SHBs and DHTs. By a similar argument as above, the mass of an anti-SHB $(\bar{Q}\bar{q}\bar{q})$ is expressed as

$$M_{\rm ave}\left(\bar{Q}\bar{q}_1\bar{q}_2\right) = M\left(\bar{Q}\right) + E\left(\bar{q}_1\bar{q}_2\right) \ . \quad (5)$$

We note that we generally employ the notation $M_{\rm ave}$ even though the anti-SHB considered here belongs to a HQS singlet.

As we stated above, we assume that two charm quarks inside T_{cc} form a compact diquark and that the diquark belonging to the color $\bar{3}$ representation is dominated. Therefore, in the heavy quark limit, the DHT shares a common light-quark cloud with the anti-SHB according to the superflavor symmetry. Consequently, the mass of DHT is expressed as

$$M_{\rm ave}\left(QQ\bar{q}_1\bar{q}_2\right) = M\left(QQ\right) + E\left(\bar{q}_1\bar{q}_2\right) \ . \quad (6)$$

From the mass formulas in Eqs. (5) and (6), we obtain the following mass relation corresponding to the mass reletion (4):

$$M_{\rm ave}\left(QQ\bar{q}_1\bar{q}_2\right) - M_{\rm ave}\left(QQ\bar{q}_3\bar{q}_4\right) = M_{\rm ave}\left(\bar{Q}\bar{q}_1\bar{q}_2\right) - M_{\rm ave}\left(\bar{Q}\bar{q}_3\bar{q}_4\right) \ . \quad (7)$$

where $\bar{q}_i = \bar{u}, \bar{d}, \bar{s}$ $(i = 1, 2, 3, 4)$.

We further combine Eqs. (1), (3), (5) and (6) to derive the following simple mass relation:

$$M_{\rm ave}\left(QQ\bar{q}_1\bar{q}_2\right) - M_{\rm ave}\left(\bar{Q}\bar{q}_1\bar{q}_2\right) = M_{\rm ave}\left(QQq\right) - M_{\rm ave}\left(\bar{Q}q\right) \ , \quad (8)$$

Now, we compare the obtained simple mass relations with existing experimental data. We first note that the relation (2) implies that the mass difference between D and D_s is equal to that between B and B_s, namely

$$M_{\rm ave}(D_s) - M_{\rm ave}(D) = M_{\rm ave}(B_s) - M_{\rm ave}(B)\,, \quad (9)$$

because the energy difference between light clouds, $E(s) - E(n)$, is independent of the heavy flavor. However, from the experimental values of masses shown in Table I, the mass differences are obtained as

$$M_{\rm ave}\left(D_s\right) - M_{\rm ave}\left(D\right) = 103\,{\rm MeV}, \quad (10)$$

$$M_{\rm ave}\left(B_s\right) - M_{\rm ave}\left(B\right) = 78\,{\rm MeV}. \quad (11)$$

This discrepancy implies the necessity of considering correction terms that break both the heavy quark flavor symmetry and the light flavor symmetry.

Hadrons	Mass (MeV)	Input Value (MeV)
T_{cc}^+	3874.74	3875
Ξ_{cc}^+	3623.0	3622
Ξ_{cc}^{++}	3621.55	3622
D^0	1864.84	1867
$D^\pm$	1869.66	1867
D^{*0}	2006.85	2009
$D^{*\pm}$	2010.26	2009
$D_s^\pm$	1968.35	1968
$D_s^{*\pm}$	2112.2	2112
Λ_c^+	2286.46	2286
Ξ_c^+	2467.71	2469
Ξ_c^0	2470.44	2469
$D^{*0}D_s^\pm$	3975.20	3979
$D^{*\pm}D_s^\pm$	3978.61	3979
$D^0D_s^{*\pm}$	3977.0	3980
$D^\pm D_s^{*\pm}$	3981.9	3980
$B^\pm$	5279.34	5280
B^0	5279.66	5280
B^*	5324.71	5325
B_s^0	5366.92	5367
B_s^*	5415.4	5415

TABLE I. Experimental values [18, 19, 34] and input values in this study.

Similarly, applying the mass relation (8) to T_{cc}, we obtain the following mass relation:

$$M_{\rm ave}\left(T_{cc}^+\right) - M_{\rm ave}\left(\Lambda_c^+\right) = M_{\rm ave}\left(\Xi_{cc}\right) - M_{\rm ave}\left(D\right) \ . \quad (12)$$

Since Ξ_{cc}^* has not experimentally confirmed yet, we estimate its mass using the following mass relation obtained from the superflavor symmetry [27, 35]:

$$M_{\Xi_{cc}^*} - M_{\Xi_{cc}} = \frac{3}{4}\left(M_{D^*} - M_D\right) \ , \quad (13)$$

leading to $M_{\Xi_{cc}^*} = 3728\,{\rm MeV}$, and thus $M_{\rm ave}(\Xi_{cc}) = 3693\,{\rm MeV}$. Substituting this value into Eq. (12), we get $M\left(T_{cc}^+\right) = 3970\,{\rm MeV}$. This value is clearly different from experimental value, 3875MeV, which motivates us to consider the mixing between a state with a heavy diquark in the color 3 representation and one in the color 6 representation.

III. IMPROVED MASS RELATIONS

In this section, we construct effective Lagrangian terms for solving the problems raised in the previous section for heavy mesons and the T_{cc}. As we stated in the previous section, we need to include the terms which simultaneously break the heavy quark flavor symmetry and SU(3)-flavor symmetry for light quarks to cure the problem of masses of heavy mesons. For the problem of the mass of T_{cc}, we include a term leading to the mixing between the states constructed from the heavy-diquark in the color $\bar{3}$ representation and the one in the color 6 representation.

At first, we define the effective DHB(QQq) fields with quantum numbers $J^P = \frac{1}{2}^+$ and $J^P = \frac{3}{2}^+$ in the heavy quark limit by combining the heavy diquark with $J^P_{\rm heavy} = 1^+$ to light quark cloud with $J^P_{\rm light} = \frac{1}{2}^+$. This doubly-heavy baryon field $\mathcal{B}$ is expressed as

$$[\mathcal{B}]_{hh'l} = \left[P_+\gamma_\mu C P_+^T\right]_{hh'} \psi_l^\mu \ , \tag{14}$$

where h and h' are spinor indices for heavy quarks and l is the spinor index for the light quark cloud, and ψ^μ is the field for the heavy-quark spin doublet with $J^P = (1/2^+, 3/2^+)$. We should note that the field $\mathcal{B}$ carries the index to specify the heavy quark flavor Q. But here and henceforce, we omit the index to avoid too many indices for one field. The projection operator for heavy quark P_+ is defined as $P_+ = (1 + v^\mu\gamma_\mu)/2$, where v^μ is the velocity of the heavy-diquark. The ψ^μ field is further decomposed into $J^P = 1/2^+$ field $\psi_{1/2}$ and $J^P = 3/2^+$ field $\psi^\mu_{3/2}$ field as

$$\psi^\mu = \frac{1}{\sqrt{3}}\sigma^{\mu\nu}v_\nu\,\psi_{1/2} + \psi^\mu_{3/2} \ , \tag{15}$$

where

$$\sigma^{\mu\nu} = \frac{i}{2}\left[\gamma^\mu\,,\,\gamma^\nu\right] \ , \tag{16}$$

and the spin-3/2 Rarita-Schwinger field $\psi^\mu_{3/2}$ satisfies

$$\begin{aligned} &v^\mu\gamma_\mu\,\psi^\mu_{3/2} = \psi^\mu_{3/2} \ , \\ &v_\mu\psi^\mu_{3/2} = \gamma_\mu\psi^\mu_{3/2} = 0 \ . \end{aligned} \tag{17}$$

For later use, we define the conjugate field $\bar{\mathcal{B}}$ for DHB as

$$\left[\bar{\mathcal{B}}\right]_{hh'l} = [\gamma_0]_{hh_1}\left[\mathcal{B}^\dagger\right]_{h_1h_2l_1}[\gamma_0]_{h_2h'}[\gamma_0]_{l_1l} \ . \tag{18}$$

For realizing the superflavor symmetry, we take the effective DHB field $\mathcal{B}$ and the effective anti-HM field $\bar{H}(\sim\bar{Q}q)$ into a unified field $\bar{\Psi}$ as

$$\bar{\Psi} = \begin{pmatrix}\bar{H}\\ B\end{pmatrix} \ . \tag{19}$$

The parity transformations are given by

$$\bar{H} \to \gamma_0\bar{H}\gamma_0, \tag{20}$$

$$[B]_{hh'l} \to [\gamma_0]_{ll_1}[\gamma_0]_{hh_1}[B]_{h_1h_2l_1}[\gamma_0]_{h_2h'}, \tag{21}$$

where h, h', h_1, h_2 are heavy quark spinor index and l, l_1 are spinor indices for light cloud. Since the field $\bar{\Psi}$ belongs to 3 representation of $\mathrm{SU(3)_f}$ light flavor, the $\mathrm{SU(3)_f}$ transformation is given by

$$\bar{\Psi}^i \to U^i_{\ j}\bar{\Psi}^j \ , \tag{22}$$

where i, j are the light flavor indices and $U \in \mathrm{SU(3)_f}$.

Next, we define the effective DHT($\sim\bar{Q}\bar{Q}qq$) fields. As we stated in the previous section, we include two DHT fields: One is constructed from the heavy diquark with color $\bar{3}$ representation carrying $J^P_{\rm heavy} = 1^+$, which is combined with the light-quark cloud with $J^P_{\rm light} = 0^+$ to make the DHT with $J^P = 1^+$. Another one is constructed from the heavy diquark carrying color 6 representation and $J^P_{\rm heavy} = 0^+$ combined with $J^P_{\rm light} = 1^+$ to make the one with $J^P = 1^+$. The former one is denoted as $T^{(\bar{3})}_\mu$ and the latter as $T^{(6)}_\mu$. These fields are defined as

$$\left[T^{(\bar{3})}_\mu\right]_{hh'} = \left[P_+\gamma_\mu C P_+^T\right]_{hh'}\,\phi \ , \tag{23}$$

$$\left[T^{(6)}_\mu\right]_{hh'} = \left[P_+\gamma_5 C P_+^T\right]_{hh'}\,\varphi_\mu \ , \tag{24}$$

where h and h' are spinor-indices for heavy quarks, and the upper indices of T, $(\bar{3})$ and (6), represent the color representation of heavy diquark in DHTs. We note that ϕ and φ_μ stand for the annihilation operators and the same applies to T. We also note that these fields have the index of light quark flavor. As we said in the introduction, we consider heavy diquarks made from two heavy quarks with the same flavor. The light quark cloud is made from two anti light quarks in the flavor anti-symmetric representation. Then, the fields T belong to 3 representation of $\mathrm{SU(3)_f}$ light flavor symmetry.

Based on the superflavor symmetry, the field $T^{(3)}_\mu$ and the effective anti-SHB field $\bar{S}(\sim\bar{Q}\bar{q}\bar{q})$ are arranged into a unified field Φ as

$$\bar{\Phi} = \begin{pmatrix}\bar{S}\\ T^{(\bar{3})}_\mu\end{pmatrix} \ . \tag{25}$$

The parity transformations are given by

$$\bar{S} \to \bar{S}\gamma_0 \ , \tag{26}$$

$$[T]_{hh'} \to [\gamma_0]_{hh_1}[T]_{h_1h_2}[\gamma_0]_{h_2h'} \ . \tag{27}$$

The conjugate fields are defined as

$$S = \gamma_0\bar{S}^\dagger, \tag{28}$$

$$[\bar{T}]_{hh'} = [\gamma_0]_{hh_1}[T^\dagger]_{h_1h_2}[\gamma_0]_{h_2h'} \ . \tag{29}$$

The $\mathrm{SU(3)_f}$ transformation is given by

$$\bar{\Phi}_{ij} \to (U^*)_i^{\ k}\,\bar{\Phi}_{kl}\left(U^\dagger\right)^l_{\ j} \tag{30}$$

Let us construct the effective Lagrangian for the DHT, SHB, DHB and HM. As we said in the previous section, we need to include the terms which break simultaneously the heavy-quark flavor symmetry and the light flavor symmetry. We first note that the terms which break the heavy quark flavor symmetry are inversely proportional to the heavy quark mass, i.e. $\propto 1/m_Q$. We also include the term for generating the mixing between $\bar{T}^{(3)}_\mu$ and $\bar{T}^{(\bar{6})}_\mu$, which must include $1/m_Q$ since the mixing vanishes at the heavy quark limit. For the light-flavor symmetry breaking, we use the spurion field corresponding to the

light quark mass matrix $\mathcal{M}_q$ as

$$\mathcal{M}_q = \begin{pmatrix} m_u & & \\ & m_d & \\ & & m_s \end{pmatrix} , \tag{31}$$

where m_u, m_d and m_s are the current quark masses of u, d and s quarks, respectively. This $\mathcal{M}_q$ transforms as

$$(\mathcal{M}_q)^i{}_j \to (U)^i{}_k \, (\mathcal{M}_q)^k{}_\ell \, \left(U^\dagger\right)^\ell{}_j . \tag{32}$$

Now, the kinetic and mass terms invariant under the heavy quark symmetry and SU(3) light flavor symmetry are given by

$$\begin{aligned} \mathcal{L}_0 =& - \mathrm{Tr}\left[\bar{\Psi} iv\cdot\partial\, \Psi + \bar{\Phi} iv\cdot\partial\, \Phi\right] \\ & - \Lambda_\Psi \,\mathrm{Tr}\left[\bar{\Psi}\Psi\right] - \Lambda_\Phi \,\mathrm{Tr}\left[\bar{\Phi}\Phi\right] , \end{aligned} \tag{33}$$

where Λ_Ψ and Λ_Φ are constants with mass dimension one, and Tr implies that the traces in the light-flavor space in addition to the spinor space and heavy-spin space are taken. In the following, we explicitly write the indices for light flavor while we omit the indices for heavy quark spin and flavor.

A possible term which breaks the SU(3) light flavor symmetry for Ψ field is written as

$$\mathcal{L}_{\Psi-\mathrm{br}} = - c_\Psi \,\mathrm{tr}\left[\bar{\Psi}^i \Psi_j\right] (\mathcal{M}_q)^j{}_i , \tag{34}$$

where c_Ψ is a constant with mass dimension zero and tr indicates that the traces in spinor space and heavy-spin space are taken.

By noting that two light quarks in the Φ field are anti-symmetric in flavor, the light flavor breaking term is expressed as

$$\mathcal{L}_{\Phi-\mathrm{br}} = - c_\Phi \,\mathrm{tr}\left[\bar{\Phi}_{ij} \, (\mathcal{M}_q)^j{}_k \Phi^{ki}\right] , \tag{35}$$

where c_Φ is a constant with mass dimension zero.

We next construct possible terms which break both SU(3) light flavor symmetry and the heavy quark flavor symmetry. We note that the terms also break the superflavor symmetry, so that the terms should be written separately for superflavor partners. The terms for $\bar{H}$ (anti-HM) and B (DHB) included in Ψ are expressed as

$$\begin{aligned} \mathcal{L}_{\mathrm{HB}-\mathrm{br}} =& - \frac{\Lambda_q}{m_Q} \mathrm{tr}\left[\bar{H}^i \, H_j \, (\mathcal{M}_q)^j{}_i\right] \\ & - \frac{\Lambda'_q}{2m_Q} \mathrm{tr}\left[B^i \, \bar{B}_j \, (\mathcal{M}_q)^j{}_i\right] , \end{aligned} \tag{36}$$

where Λ_q and Λ'_q are constants with mass dimension one. We put an extra factor 1/2 in the second line since the DHB includes two heavy quarks. Similarly, possible breaking terms for $\bar{S}$ (anti-SHB) and T (DHT) in Φ field are expressed as

$$\begin{aligned} \mathcal{L}_{\mathrm{ST}-\mathrm{br}} =& - \frac{\Lambda_{qq}}{m_Q} \,\mathrm{tr}\left[\bar{S}_{ij} \, (\mathcal{M}_q)^j{}_k S^{ki}\right] \\ & - \frac{\Lambda'_{qq}}{2m_Q} \,\mathrm{tr}\left[\left(T^{(\bar{3})}_\mu\right)_{ij} (\mathcal{M}_q)^j{}_k \left(\bar{T}^{(\bar{3})\mu}\right)^{ki}\right] , \end{aligned} \tag{37}$$

where Λ_{qq} and Λ'_{qq} are constants with mass dimension one.

Finally, we consider a DHT field $T^{(6)}_\mu$ constructed from the heavy diquark with color 6 representation. The kinetic and mass terms are written as

$$\mathcal{L}_{T^{(6)}} = -\mathrm{Tr}\left[\bar{T}^{(6)}_\mu \left(iv\cdot\partial + \Lambda_6\right) T^{(6)\mu}\right] , \tag{38}$$

where Λ_6 is a constant with mass dimension one. The term for the mixing between two DHT fields $T^{(3)}_\mu$ and $T^{(6)}_\mu$ is expressed as

$$\mathcal{L}_{\mathrm{mix}} = - \frac{\Lambda^2_{\mathrm{mix}}}{2m_Q} \mathrm{Tr}\left[\left(\bar{T}^{(6)\mu}\right)\left(T^{(\bar{3})}_\mu\right) + \left(\bar{T}^{(\bar{3})\mu}\right)\left(T^{(6)}_\mu\right)\right] . \tag{39}$$

From the above Lagrangian terms, the masses of HM, DHB and SHB are modified from Eqs. (1), (3) and (5) as

$$M_{\mathrm{ave}}\left(\bar{Q}q\right) = M\left(\bar{Q}\right) + E\left(q\right) + \frac{m_q}{m_Q}\Lambda_q, \tag{40}$$

$$M_{\mathrm{ave}}\left(QQq\right) = M\left(QQ\right) + E\left(q\right) + \frac{m_q}{2m_Q}\Lambda'_q, \tag{41}$$

$$M_{\mathrm{ave}}\left(\bar{Q}\bar{q}_1\bar{q}_2\right) = M\left(\bar{Q}\right) + E\left(\bar{q}_1\bar{q}_2\right) + \frac{m_{q_1}+m_{q_2}}{m_Q}\Lambda_{qq}, \tag{42}$$

where

$$\begin{aligned} E(q) &= \Lambda_\Psi + c_\Psi m_q , \\ E(\bar{q}_1\bar{q}_2) &= \Lambda_\Phi + c_\Phi \left(m_{q_1} + m_{q_2}\right) . \end{aligned} \tag{43}$$

The square mass matrix for two DHT fields is expressed as

$$\begin{pmatrix} M_3^2 & \frac{\Lambda^2_{\mathrm{mix}}}{2m_Q}\sqrt{M_6 M_3} \\ \frac{\Lambda^2_{\mathrm{mix}}}{2m_Q}\sqrt{M_6 M_3} & M_6^2 \end{pmatrix} , \tag{44}$$

where

$$M_3 = M\left(QQ\right) + E\left(\bar{q}_1\bar{q}_2\right) + \frac{m_{q_1}+m_{q_2}}{2m_Q}\Lambda'_{qq} , \tag{45}$$

and M_6 is the mass of $T^{(6)}_\mu$ field before mixing. By diagonalizing this matrix up to $1/m_Q$ order, the mass of lightest DHT is obtained as

$$\begin{aligned} M_{\mathrm{ave}}\left(QQ\bar{q}_1\bar{q}_2\right) =& \, M\left(QQ\right) + E\left(\bar{q}_1\bar{q}_2\right) \\ & + \frac{m_{q_1}+m_{q_2}}{2m_Q}\Lambda'_{qq} - \frac{M_6}{2(M_6^2 - M_3^2)}\left(\frac{\Lambda^2_{\mathrm{mix}}}{2m_Q}\right)^2 . \end{aligned} \tag{46}$$

Combining the above mass formulas, we obtain the

Quarks	Mass (MeV)
u, d	3.415
s	93.40
c	1270
b	4180

TABLE II. Mass of quarks [34] used as inputs.

following modified mass relations:

$$M_{\rm ave}\left(QQs\right) - M_{\rm ave}\left(QQn\right) - \frac{m_s - m_n}{2m_Q}\Lambda_q' = M_{\rm ave}\left(\bar{Q}s\right) - M_{\rm ave}\left(\bar{Q}n\right) - \frac{m_s - m_n}{m_Q}\Lambda_q, \tag{47}$$

$$M_{\rm ave}\left(QQ\bar{s}\bar{n}\right) - M_{\rm ave}\left(QQ\bar{u}\bar{d}\right) - \frac{m_s - m_n}{2m_Q}\Lambda_{qq}' = M_{\rm ave}\left(\bar{Q}\bar{s}\bar{n}\right) - M_{\rm ave}\left(\bar{Q}\bar{u}\bar{d}\right) - \frac{m_s - m_n}{m_Q}\Lambda_{qq}, \tag{48}$$

$$M_{\rm ave}\left(QQ\bar{u}\bar{d}\right) - M_{\rm ave}\left(\bar{Q}\bar{u}\bar{d}\right) + \frac{M_6}{2\left(M_6^2 - M_3^2\right)}\left(\frac{\Lambda_{\rm mix}^2}{2m_Q}\right)^2 - \frac{m_n}{2m_Q}\left(\Lambda_{qq}' - 2\Lambda_{qq}\right) = M_{\rm ave}\left(QQn\right) - M_{\rm ave}\left(\bar{Q}n\right) - \frac{m_n}{2m_Q}\left(\Lambda_q' - 2\Lambda_q\right)\ , \tag{49}$$

where $n = u, d$ and $m_n = (m_u + m_d)/2$ is the isospin averaged mass of up and down quarks. Furthermore, from Eq. (40), we obtain the following mass relation:

$$\left[M_{\rm ave}(D_s) - M_{\rm ave}(D)\right] - \left[M_{\rm ave}(B_s) - M_{\rm ave}(B)\right] = \left(m_s - m_n\right)\left(\frac{1}{m_c} - \frac{1}{m_b}\right)\Lambda_q\ , \tag{50}$$

where $n = u, d$. Using the mass differences in Eqs. (10) and (11) together with the current quark masses shown in Table II, we determine the value of Λ_q as

$$\Lambda_q = 506\,{\rm MeV}\ . \tag{51}$$

The other parameters Λ_q', Λ_{qq} and Λ_{qq}' cannot be determined due to lack of input hadron masses. We therefore assume that they are of the same order as Λ_q. Specifically, we set their median values as 0 and assign an error margin of $\pm 506\,{\rm MeV}$, resulting in $\Lambda_q' = \Lambda_{qq} = \Lambda_{qq}' = 0 \pm 506\,{\rm MeV}$.

By applying the improved mass relation corresponding to Eq. (7) to T_{cc}^+, we derive

$$M_{\rm ave}\left(T_{ccs}\right) - M_{\rm ave}\left(T_{cc}^+\right) + \frac{m_s - m_n}{2m_c}\Lambda_{qq}' = M_{\rm ave}\left(\Xi_c\right) - M_{\rm ave}\left(\Lambda_c^+\right) + \frac{m_s - m_n}{m_c}\Lambda_{qq}\ , \tag{52}$$

and we obtain the mass of T_{ccs} as

$$M_{\rm ave}\left(T_{ccs}\right) = 4057 \pm 40\,{\rm MeV}, \tag{53}$$

Hadrons	Mass (MeV)	
T_{ccs}	4057 ± 40	Our result
	4106	NQM [36]
T_{ccs}^+	3969 ± 8	Lattice QCD [37]

TABLE III. Theoretical predictions for the masses of T_{ccs}. NQM imply non-relativistic quark model.

Hadrons	Mass (MeV)	
Ω_{cc}	3760 ± 18	Our result
	3811	NQM [38]
	3753	RQM [39]
	3841	RQM [40]
	3657	NQM [41]
	3856	NQM [42]
	3773	Lattice QCD [43]
	3754	Lattice QCD [44]

TABLE IV. Theoretical predictions of the mass of Ω_{cc}. NQM and RQM imply non-relativistic and relativistic quark models, respctively.

where $M_{\rm ave}(T_{ccs})$ denotes the isospin averaged mass of T_{ccs}^+ and T_{ccs}^{++}. If this result agrees with future experimental data, it means that the color anti-triplet state of the heavy diquark is dominant in T_{cc}^+ and T_{ccs}. We compare our result with other results in Table III.

From the mass relation in Eq. (47), we further obtain

$$M_{\rm ave}\left(\Omega_{cc}\right) - M_{\rm ave}\left(\Xi_{cc}\right) + \frac{m_s - m_n}{2m_c}\Lambda_q' = M_{\rm ave}\left(D_s\right) - M_{\rm ave}\left(D\right) + \frac{m_s - m_n}{m_c}\Lambda_q. \tag{54}$$

From this relation, the mass of Ω_{cc} which has not been experimentally reported so far is also predicted as

$$M_{\rm ave}\left(\Omega_{cc}\right) = 3760 \pm 18\,{\rm MeV}. \tag{55}$$

This result serves as another indicator for assessing whether our mass relations are correct. If this result does not match future experimental results, one possible reason might be that Λ_q' is larger than Λ_q. Additionally, the second-order effects of $1/m_Q$ might also contribute. We show comparison with other results in Table IV.

IV. WIDTH OF T_{ccs}^+

In this section, we construct the Lagrangian solely from the SU(3) light flavor symmetry and predict the decay width of T_{ccs} using the decay width of T_{cc}^+ as an input. Our approach hinges on the fact that both T_{ccs} and T_{cc}^+ belong to the same light flavor representation. Notably, this method is independent of both superflavor symmetry and color representation.

Since T_{cc}^+ locates just below the DD^* threshold, we consider the decay process of $T_{cc}^+ \to D^0 D^0 \pi^+$ and $T_{cc}^+ \to$

$D^0D^+\pi^0$ with D^* as an intermediate state, as depicted in Fig. 1. While the decay $T_{cc}^+ \to D^0D^+\pi^0$ has not been observed in experiments [18, 19], it is not prohibited kinematically. Hence, in this study, we also incorporate Fig. 1(b),(c). For T_{ccs}, we consider the decay processes $T_{ccs} \to DD_s^*$ and $T_{ccs} \to D^*D_s$ as shown in Fig. 2, because the mass of T_{ccs} predicted in the previous section is above the DD_s^* and D^*D_s thresholds.

Let us construct an effective Lagrangian for the interaction among the tetraquarks and charmed mesons based on just light flavor symmetry. In the following we use relativistic field T^μ for the mass eigenstates of flavor triplet tetraquarks:

$$T^\mu = \begin{pmatrix} 0 & T_{cc}^+ & T_{ccs}^{++} \\ -T_{cc}^+ & 0 & T_{ccs}^+ \\ -T_{ccs}^{++} & -T_{ccs}^+ & 0 \end{pmatrix} , \tag{56}$$

While the fields for charmed mesons with $J^P = (0^-, 1^-)$ are represented by relativistic fields $(D, D^{*\mu})$:

$$D = \begin{pmatrix} D^0 \\ D^+ \\ D_s \end{pmatrix} , \quad D^* = \begin{pmatrix} D^{*0} \\ D^{*+} \\ D_s^* \end{pmatrix} . \tag{57}$$

From Eqs. (22) and (30), the SU(3) light flavor transformations of these fields are given as

$$\begin{aligned} &T_{ij}^\mu \to (U^*)_i^{\ k}\, T_{kl}^\mu \left(U^\dagger\right)^l_{\ j} , \\ &D_i \to D_j \left(U^\dagger\right)^j_{\ i} , \; D_i^{*\mu} \to D_j^{*\mu} \left(U^\dagger\right)^j_{\ i} . \end{aligned} \tag{58}$$

The Lagrangian for $T_{cc(s)}$ and heavy mesons invariant under this transformation is given by

$$\mathcal{L} = g_{TDD} \bar{D}_\mu^{*i} T_{ij}^\mu \bar{D}^j . \tag{59}$$

As we said above, we determine the value of g_{TDD} from the decay width of T_{cc} assuming that decay is dominated by the process shown in Fig. 1. By using the value of $D^*D\pi$ coupling constant determined from the decay of D^* meson (see e.g. Ref [24]), the value of g_{TDD} is calculated as

$$g_{TDD} = 0.68 \times 10^3 \text{ MeV} . \tag{60}$$

We note that this value is natural when nondimensionalized by the mass of the charm quark.

Now, based on the processes shown in Fig. 2. the formula of the decay width of T_{ccs} is calculated as

$$\Gamma\left(T_{ccs}\right) = g_{TDD}^2 \frac{|P_1| + |P_2|}{6\pi M\left(T_{ccs}\right)^2} , \tag{61}$$

where P_1 and P_2 and the momenta for $D_s^\pm$ and D^0, respectively. By using the mass of T_{ccs} predicted in Eq. (53) together with the value of g_{TDD} in Eq. (60), the decay width is predicted as

$$\Gamma\left(T_{ccs}\right) = 1.2 \pm 0.3 \text{ MeV} . \tag{62}$$

We consider this decay width to be sufficiently small as to be an experimentally observable.

V. SUMMARY

In this study, we investigated the mass and decay width of the doubly heavy tetraquark T_{ccs} from the superflavor and SU(3) light flavor symmetries. We assumed that doubly charmed tetraquarks are constructed from a color anti-triplet cc diquark and thus they are the superflavor partners of the singly heavy baryons. First, we derived the simple mass relations under heavy quark and superflavor symmetries. However, we found discrepancy between predictions of the obtained mass relations and the experimental data. Then, we constructed an effective Lagrangian based on these symmetries with including correction terms violating simultaneously the heavy quark symmetry and the light flavor symmetry. From the Lagrangian, we obtained the improved mass relations among heavy mesons (HMs), doubly heavy baryons (DHBs), singly heavy baryons (SHBs) and doubly heavy tetraquarks (DHTs). Based on the relations, we predicted the mass of unobserved tetraquark T_{ccs} as $M\left(T_{ccs}\right) = 4057 \pm 40\,\text{MeV}$. We also predicted the mass of unobserved Ω_{cc} as $M(\Omega_{cc}) = 3760 \pm 18\,\text{MeV}$.

We then constructed an effective Lagrangian term for the decay of T_{ccs} based on SU(3) light flavor symmetry. The unknown coupling constant was determined by using the T_{cc} decay data. Incorporating the predicted mass, we derived the decay width of T_{ccs} as $\Gamma\left(T_{ccs}\right) = 1.2 \pm 0.3\,\text{MeV}$.

The obtained masses and widths will be useful to understand the color configuration of DHTs. If these results agree with future experimental data, it means that the color anti-triplet state in T_{cc}^+ and T_{ccs} is dominant.

In this study, we have primarily focused on the charm sector. This is because hadrons containing two b quarks have not yet been experimentally discovered, and we cannot determine the value of $M(bb) - M(b)$. However, our results are immediately applicable to the bottom sector once hadrons such as Ξ_{bb}, Ω_{bb}, T_{bb}, and T_{bbs} are found.

This work was supported in part by JSPS KAKENHI Grant Nos. JP20K03927, JP23H05439 (MH) and JP20K14478 (YY).

[1] S. K. Choi et al. (Belle), Observation of a narrow charmonium-like state in exclusive $B^\pm \to K^\pm\pi^+\pi^- J/\psi$ decays, Phys. Rev. Lett. **91**, 262001 (2003), arXiv:hep-ex/0309032.

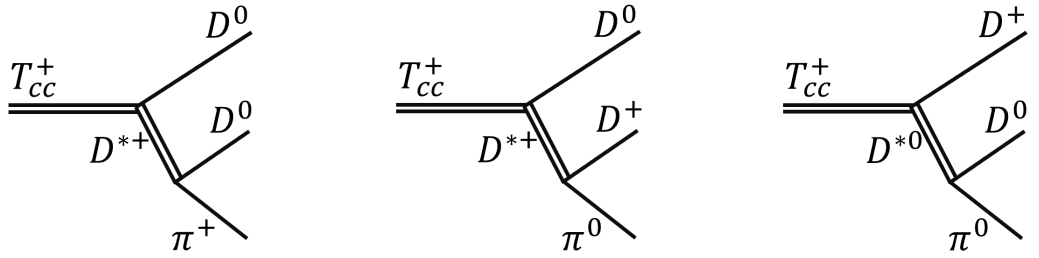

(a) (b) (c)

FIG. 1. Feynmann diagrams of the $T_{cc}^+ \to DD\pi$ decays.

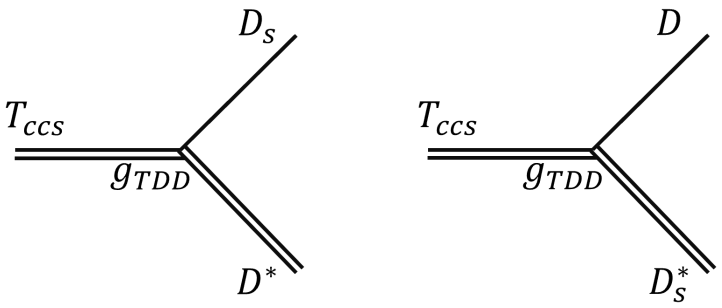

(a) (b)

FIG. 2. Feynmann diagrams of the $T_{ccs} \to DD_s^*$ and D^*D_s decays.

[2] M. Gell-Mann, A Schematic Model of Baryons and Mesons, Phys. Lett. **8**, 214 (1964).

[3] G. Zweig, An SU(3) model for strong interaction symmetry and its breaking. Version 1, (1964).

[4] G. Zweig, An SU(3) model for strong interaction symmetry and its breaking. Version 2 (1964) pp. 22–101.

[5] E. S. Swanson, The New heavy mesons: A Status report, Phys. Rept. **429**, 243 (2006), arXiv:hep-ph/0601110.

[6] Y. Yamaguchi, A. Hosaka, S. Takeuchi, and M. Takizawa, Heavy hadronic molecules with pion exchange and quark core couplings: a guide for practitioners, J. Phys. G **47**, 053001 (2020), arXiv:1908.08790 [hep-ph].

[7] H.-X. Chen, W. Chen, X. Liu, Y.-R. Liu, and S.-L. Zhu, An updated review of the new hadron states, Rept. Prog. Phys. **86**, 026201 (2023), arXiv:2204.02649 [hep-ph].

[8] L. Meng, B. Wang, G.-J. Wang, and S.-L. Zhu, Chiral perturbation theory for heavy hadrons and chiral effective field theory for heavy hadronic molecules, Phys. Rept. **1019**, 1 (2023), arXiv:2204.08716 [hep-ph].

[9] J. Vijande, F. Fernandez, A. Valcarce, and B. Silvestre-Brac, Tetraquarks in a chiral constituent quark model, Eur. Phys. J. A **19**, 383 (2004), arXiv:hep-ph/0310007.

[10] G. Yang, J. Ping, and F. Wang, Structure of pentaquarks P_c^+ in the chiral quark model, Phys. Rev. D **95**, 014010 (2017).

[11] E. Hiyama, A. Hosaka, M. Oka, and J.-M. Richard, Quark model estimate of hidden-charm pentaquark resonances, Phys. Rev. C **98**, 045208 (2018), arXiv:1803.11369 [nucl-th].

[12] Q. Meng, E. Hiyama, K. U. Can, P. Gubler, M. Oka, A. Hosaka, and H. Zong, Compact $ssscar{c}$ pentaquark states predicted by a quark model, Phys. Lett. B **798**, 135028 (2019), arXiv:1907.00144 [nucl-th].

[13] Q. Zhang, B.-R. He, and J.-L. Ping, Pentaquarks with the $qqsar{Q}Q$ configuration in the Chiral Quark Model, (2020), arXiv:2006.01042 [hep-ph].

[14] G.-J. Wang, Q. Meng, and M. Oka, S-wave fully charmed tetraquark resonant states, Phys. Rev. D **106**, 096005 (2022), arXiv:2208.07292 [hep-ph].

[15] G. Yang, J. Ping, and J. Segovia, Hidden-charm pentaquarks with strangeness in a chiral quark model, (2023), arXiv:2311.01044 [hep-ph].

[16] H. Huang, C. Deng, X. Liu, Y. Tan, and J. Ping, Tetraquarks and Pentaquarks from Quark Model Perspective, Symmetry **15**, 1298 (2023).

[17] N. A. Tornqvist, From the deuteron to deusons, an analysis of deuteron - like meson meson bound states, Z. Phys. C **61**, 525 (1994), arXiv:hep-ph/9310247.

[18] R. Aaij et al. (LHCb), Observation of an exotic narrow doubly charmed tetraquark, Nature Phys. **18**, 751 (2022), arXiv:2109.01038 [hep-ex].

[19] R. Aaij et al. (LHCb), Study of the doubly charmed tetraquark T_{cc}^+, Nature Commun. **13**, 3351 (2022), arXiv:2109.01056 [hep-ex].

[20] A. V. Manohar and M. B. Wise, Exotic Q Q anti-q anti-q states in QCD, Nucl. Phys. B **399**, 17 (1993), arXiv:hep-ph/9212236.

[21] D. Janc and M. Rosina, The $T_{cc} = DD^*$ molecular state, Few Body Syst. **35**, 175 (2004), arXiv:hep-ph/0405208.

[22] Y. Kim, M. Oka, and K. Suzuki, Doubly heavy tetraquarks in a chiral-diquark picture, Phys. Rev. D **105**, 074021 (2022), arXiv:2202.06520 [hep-ph].

[23] R. L. Jaffe, Multi-Quark Hadrons. 1. The Phenomenology of (2 Quark 2 anti-Quark) Mesons, Phys. Rev. D **15**, 267

(1977).
[24] A. V. Manohar and M. B. Wise, Heavy quark physics, Vol. 10 (2000).
[25] H. Georgi and M. B. Wise, Superflavor Symmetry for Heavy Particles, Phys. Lett. B **243**, 279 (1990).
[26] M. J. Savage and M. B. Wise, Spectrum of baryons with two heavy quarks, Phys. Lett. B **248**, 177 (1990).
[27] S. Fleming and T. Mehen, Doubly heavy baryons, heavy quark-diquark symmetry and NRQCD, Phys. Rev. D **73**, 034502 (2006), arXiv:hep-ph/0509313.
[28] J. Carlson, L. Heller, and J. A. Tjon, Stability of Dimesons, Phys. Rev. D **37**, 744 (1988).
[29] Q. Meng, E. Hiyama, A. Hosaka, M. Oka, P. Gubler, K. U. Can, T. T. Takahashi, and H. S. Zong, Stable double-heavy tetraquarks: spectrum and structure, Phys. Lett. B **814**, 136095 (2021), arXiv:2009.14493 [nucl-th].
[30] Q. Meng, M. Harada, E. Hiyama, A. Hosaka, and M. Oka, Doubly heavy tetraquark resonant states, Phys. Lett. B **824**, 136800 (2022), arXiv:2106.11868 [hep-ph].
[31] B.-R. He, M. Harada, and B.-S. Zou, Quark model with hidden local symmetry and its application to Tcc, Phys. Rev. D **108**, 054025 (2023), arXiv:2306.03526 [hep-ph].
[32] E. J. Eichten and C. Quigg, Heavy-quark symmetry implies stable heavy tetraquark mesons $Q_iQ_j\bar{q}_k\bar{q}_l$, Phys. Rev. Lett. **119**, 202002 (2017).
[33] Y.-L. Ma and M. Harada, Chiral partner structure of doubly heavy baryons with heavy quark spin-flavor symmetry, J. Phys. G **45**, 075006 (2018), arXiv:1709.09746 [hep-ph].
[34] Particle Data Group, Review of Particle Physics, Prog. Theor. Exp. Phys. **2023**, 083C01 (2023).
[35] N. Brambilla, A. Vairo, and T. Rosch, Effective field theory Lagrangians for baryons with two and three heavy quarks, Phys. Rev. D **72**, 034021 (2005), arXiv:hep-ph/0506065.
[36] M. Karliner and J. L. Rosner, Doubly charmed strange tetraquark, Phys. Rev. D **105**, 034020 (2022), arXiv:2110.12054 [hep-ph].
[37] P. Junnarkar, N. Mathur, and M. Padmanath, Study of doubly heavy tetraquarks in Lattice QCD, Phys. Rev. D **99**, 034507 (2019), arXiv:1810.12285 [hep-lat].
[38] E. Ortiz-Pacheco and R. Bijker, Masses and radiative decay widths of S- and P-wave singly, doubly, and triply heavy charm and bottom baryons, Phys. Rev. D **108**, 054014 (2023), arXiv:2307.04939 [hep-ph].
[39] Q.-F. Lü, K.-L. Wang, L.-Y. Xiao, and X.-H. Zhong, Mass spectra and radiative transitions of doubly heavy baryons in a relativized quark model, Phys. Rev. D **96**, 114006 (2017), arXiv:1708.04468 [hep-ph].
[40] D. Ebert, R. N. Faustov, V. O. Galkin, and A. P. Martynenko, Mass spectra of doubly heavy baryons in the relativistic quark model, Phys. Rev. D **66**, 014008 (2002), arXiv:hep-ph/0201217.
[41] S. S. Gershtein, V. V. Kiselev, A. K. Likhoded, and A. I. Onishchenko, Spectroscopy of doubly heavy baryons, Phys. Rev. D **62**, 054021 (2000).
[42] W. Roberts and M. Pervin, Heavy baryons in a quark model, Int. J. Mod. Phys. A **23**, 2817 (2008), arXiv:0711.2492 [nucl-th].
[43] H. Bahtiyar, K. U. Can, G. Erkol, P. Gubler, M. Oka, and T. T. Takahashi (TRJQCD Collaboration), Charmed baryon spectrum from lattice qcd near the physical point, Phys. Rev. D **102**, 054513 (2020).
[44] Y. Namekawa et al. (PACS-CS), Charmed baryons at the physical point in 2+1 flavor lattice QCD, Phys. Rev. D **87**, 094512 (2013), arXiv:1301.4743 [hep-lat].
[45] J. Hu and T. Mehen, Chiral Lagrangian with heavy quark-diquark symmetry, Phys. Rev. D **73**, 054003 (2006), arXiv:hep-ph/0511321.
[46] Q. Meng, E. Hiyama, A. Hosaka, M. Oka, P. Gubler, K. U. Can, T. T. Takahashi, and H. Zong, Prediction of Double-heavy Tetraquarks Bound States in Quark Model, Few Body Syst. **62**, 79 (2021).
[47] H. Ren, F. Wu, and R. Zhu, Hadronic Molecule Interpretation of Tcc+ and Its Beauty Partners, Adv. High Energy Phys. **2022**, 9103031 (2022), arXiv:2109.02531 [hep-ph].
[48] R. Aaij et al. (LHCb), Observation of a narrow pentaquark state, $P_c(4312)^+$, and of two-peak structure of the $P_c(4450)^+$, Phys. Rev. Lett. **122**, 222001 (2019), arXiv:1904.03947 [hep-ex].
[49] Z.-M. Ding, H.-Y. Jiang, D. Song, and J. He, Hidden and doubly heavy molecular states from interactions $D^{(*)}_{(s)}\bar{D}^{(*)}_s/B^{(*)}_{(s)}\bar{B}^{(*)}_s$ and $D^{(*)}_{(s)}D^{(*)}_s/B^{(*)}_{(s)}B^{(*)}_s$, Eur. Phys. J. C **81**, 732 (2021), arXiv:2107.00855 [hep-ph].
[50] Y. Li, Y.-B. He, X.-H. Liu, B. Chen, and H.-W. Ke, Searching for doubly charmed tetraquark candidates T_{cc} and $T_{cc\bar{s}}$ in B_c decays, Eur. Phys. J. C **83**, 258 (2023), arXiv:2302.02518 [hep-ph].
[51] X. Chen, F.-L. Wang, Y. Tan, and Y. Yang, Double-heavy tetraquarks with strangeness in the chiral quark model*, Chin. Phys. C **47**, 023102 (2023), arXiv:2206.10917 [hep-ph].
[52] R. L. Workman et al. (Particle Data Group), Review of Particle Physics, PTEP **2022**, 083C01 (2022).
[53] A. Francis, R. J. Hudspith, R. Lewis, and K. Maltman, Lattice prediction for deeply bound doubly heavy tetraquarks, Phys. Rev. Lett. **118**, 142001 (2017).
[54] R. Lewis and R. M. Woloshyn, Bottom baryons from a dynamical lattice qcd simulation, Phys. Rev. D **79**, 014502 (2009).
[55] S. S. Agaev, K. Azizi, and H. Sundu, Strange partners of the doubly charmed tetraquark T_{cc}^+, Eur. Phys. J. Plus **138**, 621 (2023), arXiv:2210.14499 [hep-ph].
[56] X. Liu, D. Chen, H. Huang, and J. Ping, Predictions of the Strange partner of T_{cc} in the quark delocalization color screening model, (2023), arXiv:2309.07728 [hep-ph].
[57] P. Junnarkar, N. Mathur, and M. Padmanath, Study of doubly heavy tetraquarks in lattice qcd, Phys. Rev. D **99**, 034507 (2019).
[58] M. Harada, Y.-R. Liu, M. Oka, and K. Suzuki, Chiral effective theory of diquarks and the $U_A(1)$ anomaly, Phys. Rev. D **101**, 054038 (2020), arXiv:1912.09659 [hep-ph].
[59] H. Takada, D. Suenaga, M. Harada, A. Hosaka, and M. Oka, Axial anomaly effect on three-quark and five-quark singly heavy baryons, Phys. Rev. D **108**, 054033 (2023), arXiv:2307.15304 [hep-ph].
[60] Y. Kawakami, M. Harada, M. Oka, and K. Suzuki, Suppression of decay widths in singly heavy baryons induced by the $U_A(1)$ anomaly, Phys. Rev. D **102**, 114004 (2020), arXiv:2009.06243 [hep-ph].
[61] T. Yoshida, E. Hiyama, A. Hosaka, M. Oka, and K. Sadato, Spectrum of heavy baryons in the quark model, Phys. Rev. D **92**, 114029 (2015), arXiv:1510.01067 [hep-ph].

Quark Counting, Drell-Yan West, and the Pion Wave Function

Mary Alberg[1,2] and Gerald A. Miller[2]

[1] *Department of Physics, Seattle University, Seattle, Washington 98122,USA*
[2] *Department of Physics, University of Washington, Seattle, WA 98195-1560, USA*

(Dated: March 7, 2024 - 2:9)

The relation between the pion's quark distribution function, $q(x)$, its light-front wave function, and the elastic charge form factor, $F(\Delta^2)$ is explored. The square of the leading-twist pion wave function at a special probe scale, ζ_H, is determined using models and Poincare covariance from realistic results for $q(x)$. This wave function is then used to compute form factors with the result that the Drell-Yan-West and quark counting relationships are not satisfied. A new relationship between $q(x)$ and $F(\Delta^2)$ is proposed.

arXiv:2403.03356v1 [hep-ph] 5 Mar 2024

INTRODUCTION

The structure of the pion continues to be of interest to many physicists. There are plans to measure the pion electromagnetic form factor at JLab and at the planned EIC [1]. There are also plans to re-measure the quark distribution of the pion, $q(x)$ via a new Drell-Yan measurement [2]. Much recent and old theoretical attention has been devoted to determining and understanding the behavior of the valence pion quark distribution function, $q_v(x)$, at high values of Bjorken x, see *e.g.* the review [3].

Much of the recent interest stems from efforts to understand the behavior at high x. While many use the parameterization $q_v(x) \sim x^\alpha (1-x)^\beta$ there is a controversy over the value of β and its dependence on the variables x and the resolution scale, Q^2. See, for example, the differing approaches of [4],[5] and [6, 7]. Ref. [4] finds that $\beta = 1$ at low resolution scales, rising to 1.5 at $Q^2 = 27$ GeV^2, while [7] finds that $\beta = 2 + \gamma(Q^2)$ with γ positive and increasing at Q^2 rises. Both sets of authors claim agreement with the available data set. The small values of β result from perturbative QCD and the larger values from non-perturbative techniques. Indeed, [5] finds that the value of β can lie between 1 and 2.5 depending on the technique used to resum the contributions of large logarithms in computing the relationship between $q(x)$ and the measured Drell-Yan cross section data. It would be beneficial to find the relation (if any) between the behavior at large values of x and the underlying dynamics.

The wide interest in the form factor and distribution function originates in the early hypotheses of the connection between the two observable quantities. Drell & Yan [8] and West [9] suggested a relation between $q(x)$ for large values of x and the elastic proton's Dirac form factor $F_1(\Delta^2)$, where Δ^2 is the negative of the square of the four-momentum transfer to the target hadron, at large values of Δ^2. Different aspects of the wave function are used to compute distribution functions and form factors, so the following relation is very surprising, namely

$$\lim_{x\to 1} q(x) = (1-x)^{n_H} \tag{1}$$

leads to the result

$$\lim_{\Delta^2\to\infty} F_1(\Delta^2) \propto \frac{1}{(\Delta^2)^{(n_H+1)/2}}, \tag{2}$$

with n_H the number of partons in the hadron. The F_1 form factor is the matrix element of the plus-component of the electromagnetic current operator between proton states of the same spin. So the proof would provide the same relations for the pion. The original papers are heavily quoted now despite the ancient nature of these relations.

Another relationship between structure functions and form factors is obtained from the use of perturbative QCD and leads to quark counting rules for the proton and pion obtained in [10–13] and reviewed in [14]. These are

$$\lim_{x\to 1} q(x, Q^2) \propto (1-x)^{2n_H - 3 + 2|\Delta_s| + \Delta\gamma}, \tag{3}$$

$$\lim_{\Delta^2\to\infty} F_H(\Delta^2) \propto \frac{1}{(\Delta^2)^{n_H-1}}, \tag{4}$$

with $\Delta\gamma$ a correction accounting for evolution that vanishes at a starting scale ζ_H^2, n_H is the minimum number of elementary constituents of the hadron, and we have taken the number of spectators to be $n_H - 1$. The quantity Δ_s is the difference between the z-components of the quark and hadron spin. Thus for a proton the dominant term at high x has $|\Delta S_z| = 0$ and for a pion $|\Delta S_z| = 1/2$. The two sets of relations (Eq. (1), Eq. (2)) and (Eq. (3), Eq. (4)) are approximately the same for the proton at ζ_H^2: namely, $q(x) \sim (1-x)^3$ and $F_1 \sim 1/\Delta^4$ with $n_H = 3$. There are two sets of predictions for the pion $q(x) \sim (1-x)^2, F(\Delta^2) \sim 1/\Delta^3$ for Drell-Yan West, and $q(x) = (1-x)^2, F(\Delta^2) \sim 1/\Delta^2$ for the quark counting rules. We now focus on the pion.

The current literature tells us that the relation between the high-x behavior of $q(x)$ and the pion form factor is interesting. In other words, what can the value of β be used for? We aim to study the connection between $q(x)$ and the square of the pion valence light-front wave function.

LIGHT-FRONT ANALYSIS

Hadronic wave functions depend on a factorization scale, ζ at which the hadron is probed. It has been widely argued that [7, 15, 16] there is a scale at which the hadron consists of only valence quarks linked to quarks of the quark-parton model as an object dressed by quark-gluon QCD interactions as obtained from the quark gap equation. Gluon emission from valence quarks begins at ζ_H [17]. Thus, at ζ_H the dressed valence u and $\bar{d}$ quarks carry all of the momentum of the π^+ and each constituent (of equal mass) carries 1/2 of the pion momentum. The result of every calculation of pionic properties that respects Poincare covariance, and the Ward-Green-Takahashi identities along with the consequences of dynamical symmetry breaking inherent in the quark gap-equation has these features. See *e.g.* Ref. [18].

The relation between the light-front wave function, evaluated at the hadron scale ζ_H^2. is given by

$$q(x) = \frac{1}{\pi}\int \frac{d^2k_\perp}{x(1-x)}|\Phi(x,k_\perp)|^2 \tag{5}$$

where $\Phi(x,k_\perp)$ is the wave function of the $q\bar{q}$ component. The function Φ represents the leading-twist component of the pion wave function, in which the quark and antiquark spins combine to 0. This component dominates computations of the high-momentum transfer form factor and the high x behavior of $q(x)$. The normalization is $\int_0^1 dx\, q(x) = 1$. We drop the explicit dependence on ζ_H^2 to simplify the equations.

There is a special feature of the wave function at ζ_H. Rotational invariance requires that $\Phi(x,k_\perp)$ is a function of a single variable, $\Phi(M_0^2)$, with $M_0^2 \equiv \frac{k_\perp^2+M^2}{x(1-x)}$, and M is the constituent quark mass [19, 20]. The key point is that in the two-body sector one may construct a self-consistent representation of the Poincare generators. Both $k_\perp^2$ and M^2 are dimensionless variables measured in terms of an appropriate intrinsic momentum scale, Λ^2. Then changing variables to $z = M_0^2$ leads to the exact result,

$$q(x) = \int_{\frac{M^2}{x(1-x)}}^{\infty} dz|\Phi(z)|^2. \tag{6}$$

A curious feature is that if $M = 0$, $q(x) = 1$ in disagreement with realistic extractions of $q(x)$ at the hadronic scale [7]. Moreover, the idea that there is a scale ζ_H goes along with the feature that spontaneous symmetry breaking causes M to be significantly larger than its current quark value. Thus we do not expect that $q(x)$ is constant when evaluated at ζ_H.

The next step is to take x to be near unity so that

$$q_{x\to 1}(x) \approx \int_{\frac{M^2}{1-x}}^{\infty} dz|\Phi(z)|^2. \tag{7}$$

The lower limit is large $M^2/(1-x) \gg 1$. This shows immediately the connection between the large x behavior and the high-momentum part of the light front wave function. An interesting relation can be obtained by differentiating Eq. (7) with respect to x:

$$q'_{x\to 1}(x) = -\frac{M^2}{(1-x)^2}|\Phi(\frac{M^2}{1-x})|^2. \tag{8}$$

Given a model wave function one can obtain the high x behavior of $q'(x)$ and thus also that of $q(x)$ at ζ_H^2. Then DGLAP evolution can be used to obtain the structure functions at larger values of probe scales.
Moreover, the finite nature of $q'(x)$ at $x \to 1$ immediately gives information about the high momentum behavior of the pion wave function. Namely,

$$\lim_{x\to 1}|\Phi(\frac{M^2}{1-x})|^2 = c(1-x)^2 f(1-x), \tag{9}$$

where c is a finite number and $f(1-x)$ is finite as $x \to 1$. Thus the high x behavior of $q(x)$ tells us about specific features of the pion wave function. Can one say more?

Form factors are matrix elements of a conserved current and so are independent of the factorization scale [21] so that one may evaluate the form factor using the constraint at ζ_H. Then the form factor is given by the expression

$$F(\Delta^2) = \frac{1}{\pi}\int_0^1 dx \int \frac{d^2k_\perp}{x(1-x)}\Phi(\frac{k_\perp^2+M^2}{x(1-x)})\Phi(\frac{(\mathbf{k}_\perp+(1-x)\mathbf{\Delta})^2+M^2}{x(1-x)}), \tag{10}$$

where the plus-component of the space-like momentum transfer to the proton is taken as zero, so that the momentum transfer, $(\mathbf{\Delta})$ is in a transverse $(\perp)$direction.

To see if there is a connection between $F(\Delta^2)$ and $q(x)$ we use model wave functions to compute both quantities. The connection between wave functions and $q(x)$ is given by Eq. (6).

It is convenient to use a flexible power law (PL) form:

$$|\Phi^{\rm PL}(z)|^2 \to \frac{K}{(z)^{n+1}}, q^{\rm PL} \sim (1-x)^n \tag{11}$$

with $n \geq 1$. This form does not build in the asymptotic behavior predicted by using perturbative QCD. However, the applicability of perturbative QCD to exclusive processes at non-asymptotic, experimentally realizable values of the momentum transfer has been questioned [22–26] for a variety of reasons including lack of knowledge of the non-perturbative part of the wave function, convergence issues, higher twist effects and those of Sudakov supression. Radyushkin [23] wrote, "for accessible energies and momentum transfers the soft (nonperturbative) contributions dominate over those due to the hard quark rescattering subprocesses". Much of the problems are related to the importance of the high-x region in computing the form factors that Feynman argued [27] was dominant. Despite progress in understanding nonperturbative aspects using lattice QCD (see *e.g.* [28], and Dyson-Schwinger techniques (see *e.g.* [7, 29], we believe that it is worthwhile to examine models of nonperturbative wave functions.

With $n = 1$, $F(\Delta^2) \sim 1/\Delta^3$ with Drell-Yan-West and $F \sim 1/\Delta^2$ with quark counting. These predictions can be checked by doing the exact model calculation. We thus expect the asymptotic form factor to behave as $\sim 1/\Delta^2$, Eq. (4), if quark counting is correct. We now check to see if the quark counting relations are respected if Eq. (11) describes the wave function.

Note that in the non-relativistic limit that the integral appearing in Eq. (10) is dominated by values of x near 1/2, and if $\Delta^2 \gg (M^2)$ then $F_{\rm NR}(\Delta^2) \sim \Phi(1/2\Delta^2) \sim (1/\Delta^2)^{(n+1)/2}$ in accord with Eq. (2). This result is similar to the non-relativistic arguments presented by Brodsky & Lepage [30]. However, the region of x near unity is very important because the effects of a large value of Δ are mitigated.

To understand this, let's compute the form factor using Eq. (11) in Eq. (10) with $m \equiv (n+1)/2$. Combining denominators using the Feynman parametrization and integrating over the transverse momentum variable leads to the result

$$F_m(\Delta^2) = CK_m \int_0^1 dx \int_0^1 du \frac{(x(1-x))^{2m-1}(u(1-u))^{m-1}}{(1+\Delta^2(1-x)^2u(1-u))^{2m-1}}, \tag{12}$$

with Δ^2 expressed in units of M^2, and $CK_m = \frac{\Gamma(4m)\Gamma(m+1)}{\Gamma(m)^2\Gamma(2m)}$. A brief look at the integrand of Eq. (12) shows why it is difficult to determine the asymptotic behavior of $F(\Delta^2)$. The value of Δ^2 can be taken to be large, but the multiplying factor, $(1-x)^2u(1-u)$ can be very small. One must do the integral first and then take Δ^2 to be large. Closed form expressions for F_m can be obtained for values of m between 1 and 3, and the asymptotic forms of F_m for $n = 1, 2, 3$ are shown in Table I.

n	$\lim_{\Delta^2\to\infty} F_m(\Delta^2)$
1	$6\left(\frac{\log^2(\Delta^2)-4\log(\Delta^2)+8}{2\Delta^2} - \frac{2(\log(\Delta^2)+2)}{\Delta^4}\right)$
2	$180\sqrt{\pi}\left(\frac{(\Delta^2-6)\log\left(\sqrt{\Delta^2}+\sqrt{\frac{\Delta^2}{4}+1}\right)}{(\Delta^2)^{5/2}} + \frac{16-5\sqrt{\Delta^2+4}}{2\Delta^4}\right)$
3	$840\left(\frac{3(\log^2(\Delta^2)-3\log(\Delta^2)+7)}{\Delta^6} + \frac{3\log(\Delta^2)-14}{6\Delta^4}\right)$

TABLE I. Asymptotic behavior of F_m. The two leading terms are kept, and $n = 2m-1$.

The results in Table I and Eq. (11) show that the Drell-Yan-West relations Eq. (1) and Eq. (2) are violated by the logarithms, which are not related to those of perturbative QCD that involve the strong coupling constant α_S. If one uses the quark counting relations Eq. (3), Eq. (4) with $\Delta\gamma = 0$ from using the hadronic scale, and $n = 2n_s, n_H = n_s + 1 = n/2 + 1$ the powers of Δ^2 do not match. In particular, if $n = 2$ quark counting rules would say $F \sim 1/\Delta^2$ instead we observe that $F \sim \log\Delta/\Delta^3$. Moreover, the appearance of logarithms in Table 1 shows that the approach to asymptotic limit is extremely slow. Power law wave functions are not consistent with quark counting rules, but nevertheless are relevant. This is because terms like $\Delta^2(1-x)^2u(1-u)$ appear in the integrals resulting from the evaluation of Feynman diagrams and the values of x and u approach unity when evaluating integrals.

REALISTIC FORM FACTORS

The next step is to see if the power law form has any phenomenological relevance. To this end, we note that $q(x)$ at ζ_H^2 is described as a parameter-free prediction of the pion valence-quark distribution function in Ref. [7, 29]:

$$\begin{aligned} q(x) &= 375.32x^2(1-x)^2 \\ &[1 - 2.5088\sqrt{x(1-x)} + 2.0250x(1-x)]^2, \\ &\equiv \textstyle\sum_{N=4}^{8} C_N(x(1-x))^{N/2}. \end{aligned} \tag{13}$$

This distribution is defined as Model 1. The corresponding pion wave function can then be written in a more general form than Eq. (11) as

$$\Phi(z) = \frac{1}{\sqrt{\pi}} \sum_{n=3}^{5} \frac{A_n}{z^{n/2}}. \tag{14}$$

Then, using Eq. (5)

$$q(x) = \; = \sum_{n=3}^{5}\sum_{N=4}^{8} \frac{2}{N} A_n A_{N+2-n}(x(1-x))^{N/2}. \tag{15}$$

Then A_n is determined by equating Eq. (15) with Eq. (13). The result is

$$q(x) = \sum_{n=3}^{5}\sum_{N=4}^{8} \widetilde{C}(n, N+2-n)(x(1-x))^{N/2}, \tag{16}$$

with $\widetilde{C}(3,3) = C_4$, $\widetilde{C}(3,4) = C_5$, $\widetilde{C}(3,5) = 3C_6 - (7/4)^2 C_7^2/C_8$, $\widetilde{C}(4,4) = (7/4)^2 C_7^2/C_8$, $\widetilde{C}(4,5) = 7/4 C_7$, $\widetilde{C}(5,5) = 4C_8$, and $\widetilde{C}(n,m) = \widetilde{C}(m,n)$.

The form factor is obtained from Eq. (10) and is given by

$$F(\Delta^2) = \sum_{m,n=3}^{5} \widetilde{C}(n,m) I_{nm}(\Delta^2) \quad (17)$$

$$I_{nm} \equiv \frac{\delta_{n+m,N+2}}{B(n/2,m/2)} \int_0^1 dx (x(1-x))^{N/2-1} \int_0^1 du \frac{u^{n/2-1}(1-u)^{m/2-1}}{(1-\Delta^2(1-x)^2 u(1-u))} \quad (18)$$

with B the beta function. The results are shown in Fig. 1. The units of Δ^2 are converted to GeV^2 by introducing a mass scale. We use $M = 134$ MeV to reproduce measured data.

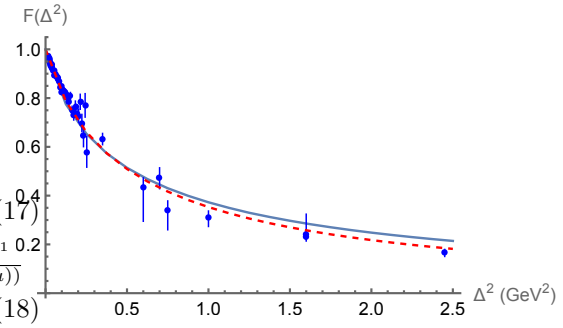

FIG. 1. $F(\Delta^2)$ Solid - Model 1, $F(\Delta^2)$ of Eq. (10). Dashed - Model 2, $\tilde{F}(\Delta^2)$ of Eq. (22). The data for $\Delta^2 \leq 0.253$GeV^2 are from CERN Ref. [31]. The data for higher values are from JLab [32].

An alternative model, Model 2 is presented in Ref. [18]:

$$\tilde{q}(x) = 213.32(x(1-x))^2 \times (1 - 2.9342\sqrt{x(1-x)} + 2.2911 x(1-x)). \quad (19)$$

This quark distribution can be rewritten in a form consistent with $\Phi^2(M^2/x(1-x))$:

$$\tilde{q}(x) = \frac{C}{(\Lambda^2 + \frac{M^2}{x(1-x)})^\alpha}. \quad (20)$$

The constants are given by $\frac{M^2}{\Lambda^2} = 0.0550309$ and $\alpha = 3.26654703$. and C is for normalization. Note that the end-point behavior of the two expressions Eq. (19) and Eq. (20) are very different with latter $\sim (1-x)^{3.27}$ instead of an exponent of 2. Nevertheless, the first 11 moments are reproduced to better than 1%. The next 5 to better than 2%. The two distributions are experimentally indistinguishable, showing the elusive behavior of the end-point behavior of $q(x)$.

Using Eq. (6) yields the square of the wave function to be

$$\Phi^2(z) = \frac{\alpha C}{\Lambda^{2\alpha}(1+z)^{1+\alpha}}. \quad (21)$$

Then using Eq. (10) the form factor is found to be

$$\tilde{F}(\Delta^2) = K \int_0^1 dx \int_0^1 du \frac{(x(1-x))^\alpha (u(1-u))^{\frac{1}{2}(\alpha-1)}}{[x(1-x) + M^2 + \Delta^2(1-x)^2 u(1-u)]^\alpha} \quad (22)$$

Integration over u leads to the generalized parton distribution $H(x,\Delta^2)$:

$$H(x,\Delta^2) \propto \frac{((1-x)x)^{2\beta-1}\, {}_2F_1\left(\frac{1}{2}, 2\beta-1; \beta+\frac{1}{2}; \frac{(1-x)^2\Delta^2}{(1-x)^2\Delta^2 + 4(M^2+(1-x)x)}\right)}{(4(M^2+(1-x)x) + \Delta^2(1-x)^2)^{1-2\beta}} \quad (23)$$

where $\beta = (1+\alpha)/2$ and ${}_2F_1$ is the hypergeometric function and $H(x,0) = \tilde{q}(x)$. Both M^2 and Δ^2 are given in units of Λ^2. We choose $\Lambda^2 = 0.36$ GeV^2 to reproduce data. The corresponds to $M = 140$ MeV.

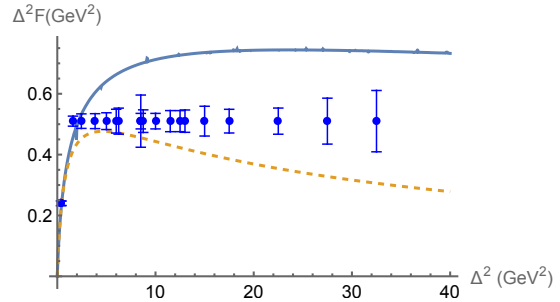

FIG. 2. $\Delta^2 F(\Delta^2)$ in units of GeV^2. Solid - Model 1, $F(\Delta^2)$ of Eq. (10). Dashed - Model 2, $\tilde{F}(\Delta^2)$ of Eq. (22). The projected error bars for the data points between $\Delta^2 = 0.375$ and 6 Ge V^2 are from [33] and G. M. Huber (private communication). The projected error bars for the data points between $\Delta^2 = 8.50$ and 15 GeV2. are from [34] and show what might be possible at a 22 GeV facility at JLab. The projected error bars for higher values of Δ^2 are from G. M. Huber (private communication) and [35]. In each case the values of $F(\Delta^2)$ are arbitrary.

The result for both form factors are shown in Fig. 2. There are significant differences in the region that is not yet experimentally explored.

CONCLUSIONS

If the non-perturbative pion wave function can be modeled as a power-law form, or if the high-x behavior is important for computing the form factor, both the Drell-Yan & West relations and quark counting rules for the pion are not correct. Based on our calculations we propose that the Drell-Yan-West relations should be modified to

$$\lim_{x\to 1} q(x) = (1-x)^{n_H} \to F_1(\Delta^2) \sim \frac{\log(\Delta^2)}{(\Delta^2)^{(n_H+1)/2}}, \quad (24)$$

with $q(x)$ evaluated at the hadron scale ζ_H^2, and with the log not accompanied by a factor involving the strong coupling constant, α_S.

ACKNOWLEDGEMENTS

The work of M.A. is partially supported by the Research in Undergraduate Institutions Program of the US National Science Foundation under Grant No. 2012982. The work of G.A.M. is partially supported by the DOE Office of Science, Office of Nuclear Physics under Grant DE-FG02-97ER-41014. We thank Garth Huber for providing the data in Figs. 1 & 2. We thank Craig Roberts for many useful discussions. This work is inspired by the QGT Topical Collaboration.

[1] Arlene C. Aguilar *et al.*, "Pion and Kaon Structure at the Electron-Ion Collider," Eur. Phys. J. A **55**, 190 (2019), arXiv:1907.08218 [nucl-ex].

[2] B. Adams *et al.*, "Letter of Intent: A New QCD facility at the M2 beam line of the CERN SPS (COMPASS++/AMBER)," (2018), arXiv:1808.00848 [hep-ex].

[3] Roy J. Holt and Craig D. Roberts, "Distribution Functions of the Nucleon and Pion in the Valence Region," Rev. Mod. Phys. **82**, 2991–3044 (2010), arXiv:1002.4666 [nucl-th].

[4] Guy F. de Teramond, Tianbo Liu, Raza Sabbir Sufian, Hans Günter Dosch, Stanley J. Brodsky, and Alexandre Deur (HLFHS), "Universality of Generalized Parton Distributions in Light-Front Holographic QCD," Phys. Rev. Lett. **120**, 182001 (2018), arXiv:1801.09154 [hep-ph].

[5] P. C. Barry, Chueng-Ryong Ji, N. Sato, and W. Melnitchouk (Jefferson Lab Angular Momentum (JAM)), "Global QCD Analysis of Pion Parton Distributions with Threshold Resummation," Phys. Rev. Lett. **127**, 232001 (2021), arXiv:2108.05822 [hep-ph].

[6] Z. F. Cui, Minghui Ding, J. M. Morgado, K. Raya, D. Binosi, L. Chang, F. De Soto, C. D. Roberts, J. Rodríguez-Quintero, and S. M. Schmidt, "Emergence of pion parton distributions," Phys. Rev. D **105**, L091502 (2022), arXiv:2201.00884 [hep-ph].

[7] Z. F. Cui, Minghui Ding, J. M. Morgado, K. Raya, D. Binosi, L. Chang, J. Papavassiliou, C. D. Roberts, J. Rodríguez-Quintero, and S. M. Schmidt, "Concerning pion parton distributions," Eur. Phys. J. A **58**, 10 (2022), arXiv:2112.09210 [hep-ph].

[8] S. D. Drell and Tung-Mow Yan, "Connection of Elastic Electromagnetic Nucleon Form-Factors at Large Q**2 and Deep Inelastic Structure Functions Near Threshold," Phys. Rev. Lett. **24**, 181–185 (1970).

[9] Geoffrey B. West, "Phenomenological model for the electromagnetic structure of the proton," Phys. Rev. Lett. **24**, 1206–1209 (1970).

[10] Stanley J. Brodsky and Glennys R. Farrar, "Scaling Laws at Large Transverse Momentum," Phys. Rev. Lett. **31**, 1153–1156 (1973).

[11] Stanley J. Brodsky and Glennys R. Farrar, "Scaling Laws for Large Momentum Transfer Processes," Phys. Rev. D **11**, 1309 (1975).

[12] Glennys R. Farrar and Darrell R. Jackson, "Pion and Nucleon Structure Functions Near x=1," Phys. Rev. Lett. **35**, 1416 (1975).

[13] Glennys R. Farrar and Darrell R. Jackson, "The Pion Form-Factor," Phys. Rev. Lett. **43**, 246 (1979).

[14] Dennis W. Sivers, "WHAT CAN WE COUNT ON?" Ann. Rev. Nucl. Part. Sci. **32**, 149–175 (1982).

[15] R. L. Jaffe and Graham G. Ross, "Normalizing the Renormalization Group Analysis of Deep Inelastic Leptoproduction," Phys. Lett. B **93**, 313–317 (1980).

[16] A. De Rújula and Fran çois Martin, "Structure of hadron structure functions," Phys. Rev. D **22**, 1787–1808 (1980).

[17] Stanley J. Brodsky and G. Peter Lepage, "Perturbative Quantum Chromodynamics," Prog. Math. Phys. **4**, 255–422 (1979).

[18] Minghui Ding, Khépani Raya, Daniele Binosi, Lei Chang, Craig D Roberts, and Sebastian M. Schmidt, "Symmetry, symmetry breaking, and pion parton distributions," Phys. Rev. D **101**, 054014 (2020), arXiv:1905.05208 [nucl-th].

[19] M V Terent'ev, "On the structure of the wave functions of mesons considered as bound states of relativistic quarks," Sov. J. Nucl. Phys. (Engl. Transl.); (United States) **24**, 1 (1976).

[20] L. L. Frankfurt and M. I. Strikman, "High-Energy Phenomena, Short Range Nuclear Structure and QCD," Phys. Rept. **76**, 215–347 (1981).

[21] M. Diehl, "Generalized parton distributions," Phys. Rept. **388**, 41–277 (2003), arXiv:hep-ph/0307382.

[22] Nathan Isgur and C. H. Llewellyn Smith, "The Applicability of Perturbative QCD to Exclusive Processes," Nucl. Phys. B **317**, 526–572 (1989).

[23] A.V. Radyushkin, "Hadronic form factors: Perturbative qcd vs qcd sum rules," Nuclear Physics A **532**, 141–154 (1991).

[24] Adam Szczepaniak, Anatoly Radyushkin, and Chueng-Ryong Ji, "Consistent analysis of O (alpha-s) corrections to pion elastic form-factor," Phys. Rev. D **57**, 2813–2822 (1998), arXiv:hep-ph/9708237.

[25] G. A. Miller and J. Pasupathy, "Higher twist and higher order contributions to the pion electromagnetic form-factor," Z. Phys. A **348**, 123–127 (1994).

[26] Hsiang-nan Li and George F. Sterman, "The Perturbative pion form-factor with Sudakov suppression," Nucl. Phys. B **381**, 129–140 (1992).

[27] Richard P. Feynman, *Photon-Hadron Interactions* (W. A. Benjamin, Inc., Reading, 1972).

[28] A. Abdel-Rehim *et al.*, "Nucleon and pion structure with lattice QCD simulations at physical value of the pion mass," Phys. Rev. D **92**, 114513 (2015), [Erratum: Phys.Rev.D 93, 039904 (2016)], arXiv:1507.04936 [hep-lat].

[29] Zhu-Fang Cui, Minghui Ding, Fei Gao, Khépani Raya, Daniele Binosi, Lei Chang, Craig D Roberts, Jose Rodríguez-Quintero, and Sebastian M Schmidt, "Kaon and pion parton distributions," Eur. Phys. J. C **80**, 1064 (2020).

[30] Stanley J. Brodsky and G. Peter Lepage, "Exclusive Processes in Quantum Chromodynamics," Adv. Ser. Direct. High Energy Phys. **5**, 93–240 (1989).

[31] S. R. Amendolia *et al.* (NA7), "A Measurement of the Space - Like Pion Electromagnetic Form-Factor," Nucl. Phys. B **277**, 168 (1986).

[32] G. M. Huber *et al.* (Jefferson Lab), "Charged pion form-factor between Q**2 = 0.60-GeV**2 and 2.45-GeV**2. II. Determination of, and results for, the pion form-factor," Phys. Rev. C **78**, 045203 (2008), arXiv:0809.3052

[nucl-ex].
[33] "Measurement of the Charged Pion Form Factor to High Q^2 ," https://www.jlab.org/exp_prog/proposals/06/PR12-06-101.pdf.
[34] A. Accardi *et al.*, "Strong Interaction Physics at the Luminosity Frontier with 22 GeV Electrons at Jefferson Lab," (2023), arXiv:2306.09360 [nucl-ex].
[35] A. Bylinkin *et al.*, "Detector requirements and simulation results for the EIC exclusive, diffractive and tagging physics program using the ECCE detector concept," Nucl. Instrum. Meth. A **1052**, 168238 (2023), arXiv:2208.14575 [physics.ins-det].

CERN-TH-2024-031, DESY-24-031

Nonthermal Heavy Dark Matter from a First-Order Phase Transition

Gian F. Giudice [1], **Hyun Min Lee** [2], **Alex Pomarol** [3,4], **Bibhushan Shakya** [5]

[1] *CERN, Theory Department, 1211 Geneva 23, Switzerland.*
[2] *Department of Physics, Chung-Ang University, Seoul 06974, Korea.*
[3] *IFAE and BIST, Universitat Aut'onoma de Barcelona, 08193 Bellaterra, Barcelona*
[4] *Departament de Fisica, Universitat Autonoma de Barcelona, 08193 Bellaterra, Barcelona*
[5] *Deutsches Elektronen-Synchrotron DESY, Notkestr. 85, 22607 Hamburg, Germany*

arXiv:2403.03252v1 [hep-ph] 5 Mar 2024

Abstract

We study nonthermal production of heavy dark matter from the dynamics of the background scalar field during a first-order phase transition, predominantly from bubble collisions. In scenarios where bubble walls achieve runaway behavior and get boosted to very high energies, we find that it is possible to produce dark matter with mass several orders of magnitude above the symmetry breaking scale or the highest temperature ever reached by the thermal plasma. We also demonstrate that the existing formalism for calculating particle production from bubble dynamics in a first-order phase transition is not gauge invariant, and can lead to spurious results. While a rigorous and complete resolution of this problem is still lacking, we provide a practical prescription for the computation that avoids unphysical contributions and should provide reliable order-of-magnitude estimates of this effect. Furthermore, we point out the importance of three-body decays of the background field excitations into scalars and gauge bosons, which provide the dominant contributions at energy scales above the scale of symmetry breaking. Using our improved results, we find that scalar, fermion, and vector dark matter are all viable across a large range of mass scales, from $\mathcal{O}(10)$ TeV to a few orders of magnitude below the Planck scale, and the corresponding phase transitions can be probed with current and future gravitational wave experiments.

Contents

1 Motivation **2**

2 Framework **3**

2.1 Phase Transition Parameters 4

2.2 (Runaway) Phase Transition Configurations 5

2.3 Particle Content 7

3 Formalism: Particle Production Calculation **9**

3.1 Bubble Nucleation 9

3.2 Bubble Expansion 9

3.3 Bubble Collision 10

3.4 Particle Physics Aspects 12

4 Gauge Dependence and Production of Gauge Bosons **13**

4.1 Gauge Dependence 13

4.2 High Energy Behavior 15

4.3 Other Processes 16

4.4 Backreaction Effects 17

5 Dark Matter Production **18**

5.1 Pre-Transition Contributions 18

5.2 Other Contributions during the Transition 19

5.3 Post-Transition Contributions 20

5.4 Subsequent Evolution 22

6 Dark Matter Parameter Space **22**

6.1 Gravitational Waves 24

6.2 Scalar Dark Matter 24

6.3 Fermion Dark Matter 30

6.4 Vector Dark Matter 31

7 Summary and Discussions **32**

References **34**

1 Motivation

The topic of first-order phase transitions (FOPTs) [1–7] – where the metastable (false, unbroken) vacuum of the early Universe decays into its stable (true, broken) configuration through the nucleation, expansion, and percolation of bubbles of true vacuum – has received intense scrutiny in the community in recent years. Studied extensively in the context of inflation [8, 9] several decades ago, this phenomenon has become the subject of renewed interest due to its promise as a viable cosmological source of gravitational waves (GWs) [10–14] that can be detected with current and upcoming gravitational wave experiments. Although the Standard Model (SM) of particle physics in its current form does not feature any FOPTs, such transitions can be readily realized in many realistic beyond the Standard Model (BSM) scenarios [15–30] and therefore are of great interest.

In this paper, we will be interested in FOPT processes that also address one of the most glaring shortcomings of the SM of particle physics: the identity of dark matter (DM). We will focus, in particular, on scenarios where the dynamics of the background field during the FOPT process is also responsible for DM production. Several papers in the literature have explored various qualitatively different realizations of this prospect. Refs. [31, 32] examined configurations where a pre-existing thermal DM abundance in the unbroken phase can be filtered into the broken phase by slow-moving bubble walls to realize the correct exponentially suppressed relic abundance. Ref. [33, 34] studied cases where particles crossing across relativistic bubble walls can upscatter into heavy states that are, or can produce, DM. Ref. [35–37] studied frameworks where the dynamcis associated with supercooled transitions in a confining sector produce the correct DM abundance. Ref. [38] explored the prospects of producing heavy DM from bubble collisions in an electroweak phase transition, finding that scalar DM cannot be produced with the desired abundance but the production of heavy vector or fermion DM is possible; Ref. [39] extended this idea to DM in a dark sector. Ref. [40] considered DM production from the collisions of shells of boosted particles around the bubble walls.

Note that all of the above ideas (except [38, 39]) rely on interactions between bubble walls and particles in the ambient thermal bath. In this paper, we focus on DM production from the spacetime dynamics of the background scalar field itself as it undergoes various stages of the phase transition. This is a fundamental, unavoidable contribution that is present in *any* FOPT (including all of the above cases), irrespective of the existence or nature of a thermal bath of particles. Particle production from a changing background field is a well-known physical phenomenon familiar from various contexts, such as gravitational particle production [41–44] (for some specific applications to dark matter production, see e.g. [45, 46]), Schwinger effect [47], and Hawking radiation from black holes [48,49]. The calculation of particle production from background field dynamics during various stages of a FOPT, in particular from bubble collisions, is complicated due to the inhomogeneous nature of the process, but can be calculated in a manner analogous to the production of gravitational waves. The formalism to study this process was first developed in [50] in the context of reheating after first-order inflation. This formalism was then explored by [51] for cold baryogenesis, and further developed in [38] with semi-analytic results for some idealized bubble collision cases and applications for nonthermal DM production. More recently, the results were refined with numerical studies for more realistic bubble collisions in [52], and various aspects of the underlying physics clarified in [53]. In this paper, we use the improved results from [52, 53] to calculate the production of DM from the background field dynamics in a dark phase transition.

While the DM production mechanism we discuss here is very general, it is particularly well-suited for the production of heavy DM with mass far above the scale of symmetry breaking or the temperature of the plasma following the phase transition. Ultraheavy DM, with mass ranging from $\mathcal{O}(100)$ TeV to the Planck scale, is of broad interest to the community for several theoretical as well

as experimental reasons [54], but generally suffers from the lack of viable production mechanisms that realize the correct relic density. Recall that if the Universe reheats to temperatures comparable to the DM mass (in particular, above the freezeout temperature of DM), DM will rethermalize with the bath, erasing the effects of earlier cosmological events (such as bubble dynamics), and will undergo conventional freezeout, which cannot produce the correct relic abundance for DM masses above the unitarity bound of $\mathcal{O}(100)$ TeV. Hence nonthermal production mechanisms are required for the production of ultraheavy DM. Nonthermal freeze-in requires extremely small ($\sim 10^{-10}$) couplings [55, 56], whereas production at temperatures lower than the DM mass suffers from exponential (Boltzmann) suppression. In this context, FOPTs provide a unique configuration not found in other cosmological setups that can nonthermally produce extremely heavy particles with masses significantly larger than any other energy scale achieved in the early Universe: since the bubble walls can accelerate to relativistic speeds in the absence of friction from the plasma, they can reach energies far above the energy scale of the phase transition or the temperature of the ambient plasma. The possibility of producing particles with masses far greater than the scale of phase transition from the collisions of such bubbles was recognized in [50], and subsequently employed for heavy DM production in [38, 39]; we will extend these studies, clarifying and improving on several important aspects. We will discuss scalar, fermion, and vector DM, highlighting qualitatively distinct features and novel developments relative to the existing literature in each case. Furthermore, since FOPTs from dark sectors can give rise to large gravitational wave signals, such configurations provide an opportunity to detect this production mechanism for DM in dark sectors (otherwise inaccessible with other experimental probes) with gravitational waves, providing added motivation for this study.

This paper also contains two important developments on the formalism to calculate particle production. First, we demonstrate that the existing formalism is gauge-dependent and leads to spurious results in certain cases if not treated carefully. While we are unable to provide a complete resolution of this problem, we provide a practical prescription for the computation that extracts physical contributions and can be reliably used for order-of-magnitude estimates of this effect. Second, we point out that for the production of gauge bosons and scalars, three-body decays of the background field excitations (rather than two-body decays, which is the only contribution currently considered in the literature) provide the dominant contribution for heavy DM. Both results are crucial and substantially change the conclusions regarding the viability and parameter space for DM derived in previous works.

This paper is organized as follows. In Sec. 2, we describe the framework for the study, discussing the relevant phase transition configurations, parameters, and particle content. The formalism for the calculation of particle production from various stages of a FOPT is described in Sec. 3. Sec. 4 discusses issues related to the gauge dependence of the formalism, and provides a practical solution to the problem that enables the calculation of scalar and gauge boson production, including the three-body configurations that provide the dominant contributions. In Sec. 5, we discuss dark matter production contributions from other processes before, during, and after the phase transition, as well as subsequent evolution of the DM population. The parameter space where DM can be produced with the correct relic abundance from FOPTs is presented in Sec. 6. Sec. 7 contains a summary of the main results of this paper and a discussion of various related ideas.

2 Framework

The dark matter production from FOPT background field dynamics that we calculate in this paper is very generic: it occurs unavoidably at any FOPT if the DM particles couples directly or indirectly

to the background field undergoing the phase transition, independently of the details of the FOPT or the thermal plasma. We therefore present our analysis and results in a "model independent" manner, in terms of phenomenologically relevant parameters characterizing the phase transition and for simplified minimal DM setups, so that the results can be applied in a straightforward manner to specific dark sector and DM models.

2.1 Phase Transition Parameters

Here, we list the phenomenological parameters that are relevant for the calculation. Consider a FOPT in a dark/hidden sector where a background field ϕ transitions from a metastable, false vacuum, where it has a vanishing vacuum expectation value (vev) $\langle\phi\rangle = 0$, to a stable, true vacuum configuration with non-vanishing vev $\langle\phi\rangle = v_\phi$. The latent energy released in the phase transition is given by the difference in the potential energies of the two vacua, and we parameterize it as

$$\Delta V \equiv V_{\langle\phi\rangle=0} - V_{\langle\phi\rangle=v_\phi} = c_V\, v_\phi^4\,. \tag{1}$$

The phase transition parameters relevant to our calculation of DM production and abundance are:

- T_n: temperature of the thermal bath at which the FOPT is triggered, i.e. when bubbles of true vacuum begin to nucleate at a rate greater than the Hubble scale.
- R_0: critical radius of nucleated bubble that can grow. This is typically $\mathcal{O}(T_n^{-1})$.
- α: strength of the phase transition, defined as $\alpha \equiv \frac{\rho(\text{vacuum})}{\rho(\text{radiation})}$, where $\rho(\text{vacuum}) = \Delta V$ and $\rho(\text{radiation})$ represents the energy density in the radiation bath (SM and dark sectors combined) at T_n.
- β: (inverse) duration of phase transition. This is generally parametrized relative to the Hubble scale as β/H, which is a dimensionless parameter.
- v_w: velocity of the bubble wall. This quantity is time-dependent: as the bubbles expand, vacuum energy gets transferred to the wall, accelerating it. Hence v_w tends to grow, but can asymptote to a constant value in the presence of significant frictional forces.
- γ_w: Lorentz boost factor of the bubble wall, determined from v_w via the relation $\gamma_w = 1/\sqrt{1-v_w^2}$. In this paper we are interested in the relativistic regime $v_w \approx 1,\ \gamma_w \gg 1$.
- l_w: thickness of the bubble wall. This quantity is also time dependent: while the wall thickness at bubble nucleation is $l_{w_0} \sim \mathcal{O}(v_\phi^{-1})$, the *apparent* wall thickness in the plasma frame gets Lorentz contracted as the bubble accelerates to greater velocities, hence $l_w = l_{w_0}/\gamma_w$ tends to decrease with time.
- R_*: typical size of vacuum bubbles at collision; this is determined from the timescale over which the transition completes, $R_* \approx v_w\,(8\pi)^{1/3}\beta^{-1}$.
- T_*: temperature of the thermal bath at which bubbles of true vacuum percolate and the phase transition ends. Since phase transitions complete within a fraction of Hubble time, $T_* \approx T_n$ if the Universe remains radiation dominated throughout. If the Universe instead becomes vacuum dominated, then T_* is determined through energy conservation conditions at the end of the transition.

In a specific model, these quantities can be calculated from the parameters in the underlying theory, as described in detail in several extensive reviews of phase transitions (see e.g. [10–14]). For our purposes, we will treat them as independent parameters (except for the relations described above), so that it should be straightforward to map our results to any given model by calculating the corresponding parameters in the model.

2.2 (Runaway) Phase Transition Configurations

We now discuss the phase transition setups that are relevant for ultraheavy DM production. As stated earlier, we are particularly interested in scenarios where the DM mass is higher than the scale of the phase transition as well as the temperature of the thermal bath. This requires the bubble walls to gain sufficient energy to produce the heavy DM particles. We are thus interested in configurations where the bubble walls achieve so-called "runaway" behavior, i.e. are not slowed down by friction effects but continue to accelerate as they gain the latent energy in the false vacuum released in the transition. As we discuss here, whether this occurs depends on the details of the contents of the thermal bath as well as the nature of the transition.

If the dark sector is in thermal equilibrium with the SM bath at some point in the early Universe, the two sectors share the same temperature, which remains true after the two sectors decouple (up to small corrections). However, this is not necessary, and the dark sector may be cold, i.e. has a temperature substantially smaller than that of the SM bath (this occurs, for instance, if the inflaton or the lightest moduli fields preferentially reheat the visible (SM) sector), or hotter (in the opposite scenario). Requiring the two sectors to remain decoupled in this manner enforces an upper limit on possible portal couplings between the two sectors. This condition can be approximately quantified as $\lambda_{\rm portal} \lesssim \sqrt{T/M_{Pl}}$ for any temperature T higher than the mass of the corresponding dark sector particle. Here M_{Pl} is the Planck mass, and the portal coupling could be e.g. a quartic coupling between the scalar ϕ and the SM Higgs boson, or a kinetic mixing between a dark gauge boson and the SM hypercharge.

In general, a FOPT can occur either due to thermal effects (temperature dependent corrections to the scalar potential causes the true vacuum to become energetically favoured) or via quantum tunneling (the age of the Universe approaches the lifetime for the scalar field to tunnel into the true vacuum even with the zero temperature potential) – see e.g. [27] for detailed discussions. The former requires a thermal bath of hidden sector particles (which may or may not be in equilibrium with the SM bath), and a large coupling between the scalar field and some other particle in the bath; in this case, with $\mathcal{O}(1)$ couplings, the phase transition generally occurs at a temperature $T_* \sim v_\phi$ (if the dark and visible sectors have different temperatures, then it is the dark sector temperature that is relevant here), and is completed within a small fraction of Hubble time, $\beta/H_* \sim 100 - 1000$ (where H_* is the Hubble scale at temperature T_* when the phase transition completes), as the bubble nucleation rate becomes extremely rapid once thermal corrections make the true vacuum energetically favorable. Transitions via quantum tunneling, on the other hand, do not require a thermal bath of hidden sector particles (i.e. the hidden sector can be extremely cold before the transition, and the hidden sector energy density exists primarily in the form of vacuum energy), although it might be present; the time of transition is determined by the shape of the potential. In such instances, T_* can be several orders of magnitude smaller than v_ϕ. Such transitions tend to last longer, completing in an $\mathcal{O}(1)$ fraction of Hubble time, so that $\beta/H_* \sim 10$.

In either case, bubbles of true vacuum nucleate with critical radii R_0 and expand, accelerating as the latent energy released from the false vacuum is converted to kinetic and gradient energies in the bubble walls. Expanding bubbles encounter friction due to particles in the thermal bath

crossing the wall and becoming massive in the broken phase. A full thermal distribution of a particle species crossing into the bubble is known to produces a pressure [57] (see also [58, 59]):

$$\mathcal{P}_{\rm LO} \approx \frac{1}{24} m^2 T^2 \,, \tag{2}$$

where m is the mass of the particle in the broken phase and T is the temperature of the bath. If the sum of such effects from all particles exceeds the energy available from the transition, ΔV, the walls achieve a terminal velocity corresponding to some steady state configuration; if not, the walls continue to accelerate. As the walls become relativistic, friction due to splitting or transition radiation, corresponding to radiation of gauge bosons from particles crossing into the bubbles, becomes increasingly important [60–62], producing pressure that scales as

$$\mathcal{P}_{\rm NLO} \sim g^2 \, \gamma_w \, m_V \, T^3 \,, \tag{3}$$

where g is the gauge coupling and m_V is now the mass of the gauge boson, and we have dropped some $\mathcal{O}(1)$ factors. This implies that the bubble walls reach a terminal velocity corresponding to $\gamma_w \sim \Delta V/(g^3 T^3 v_\phi)$ (where we have used $m_V = g v_\phi$) if they have not collided with other bubbles before this value is reached.

If the frictional energy loss remains subdominant to ΔV, energy conservation dictates that the boost factor of the wall grows with the growing bubble radius R as $\gamma \approx \frac{2R}{3R_0}$ [63]. In such configurations, the boost factor can reach extremely large values; parametrically,

$$\gamma_{\rm max} \sim \frac{1}{\beta/H} \frac{M_{Pl}}{v_\phi} \,, \tag{4}$$

where we have used the relations in Sec. 2.1 and assumed $T \sim v_\phi$. The energy density in the bubble wall at collision is then $E_{\rm wall} = \gamma_{\rm max}/l_{w0} \sim M_{Pl}/(\beta/H)$, making it possible to produce heavy particles up to this scale. Remarkably, note that $E_{\rm wall}$ is independent of v_ϕ: a transition at a lower scale v_ϕ, where the bubble walls have lower energy, is compensated by a lower Hubble scale, which allows the bubbles to expand for longer before collisions occur, and thus the bubble walls can get boosted for a longer period.

Viable scenarios that can realize such $\gamma \gg 1$ runaway behavior needed for producing ultraheavy DM can broadly be classified into four distinct categories:

Scenario I: Thermal transition without a gauge boson

This corresponds to scenarios where the FOPT is thermally triggered, i.e. a thermal bath that interacts with the bubble walls is present, but $\Delta V > \mathcal{P}_{\rm LO}$, so that the friction from particles crossing into the bubbles and becoming massive is not sufficient to slow the walls down, and in the absence of a gauge boson there is no $\mathcal{P}_{\rm NLO}$ contribution.

Scenario II: Thermal transition with a light gauge boson

Even if the broken symmetry is gauged, runaway behavior can be realized if the corresponding gauge boson is light ($m_V \ll v_\phi$), i.e. the gauge coupling is small ($g \ll 1$). Recall that friction due to splitting radiation (Eq. 3), which grows linearly with γ_w, eventually saturates the released latent energy, resulting in a terminal value $\gamma_w \sim \Delta V/(g^3 T^3 v_\phi)$ for the wall boost factor. Assuming $T \sim v_\phi$, we have $\gamma_w \sim c_V/g^3$, hence $\gamma_w \gg 1$ is possible if $g \ll 1$. In such cases, the boost factor at collision is

$$\gamma_w \sim \min\left[\frac{c_V}{g^3}, \; \frac{2R_*}{3R_0}\right] \,, \tag{5}$$

i.e. either the terminal behavior described above is reached, or the bubble walls collide before this occurs.

Scenario III: Supercooled phase transition

Alternately, one could have a supercooled FOPT [15, 36, 64–74]. In such transitions, $\Delta V > \rho_{\rm radiation}$, leading to a period of vacuum domination and inflation that causes significant dilution of the pre-existing thermal bath before the phase transition completes. The bubble walls therefore effectively expand in vacuum, encountering negligible friction, and can reach runaway behavior. In this case, note that reheating after the completion of the phase transition creates a thermal bath with $\rho_{\rm radiation} \approx \Delta V$.

Scenario IV: Quantum tunneling in a cold dark sector

Even if a dark thermal bath is effectively absent, the transition could occur via quantum tunneling; in this case, there are essentially no particles that interact with the bubble walls, and the walls continue to accelerate as the bubbles expand. The SM bath could be present or absent; if it is absent or its energy density is lower than the latent energy ΔV in the false vacuum, this leads to a vacuum dominated epoch, corresponding to the supercooled regime discussed above. For transitions that occur via quantum tunneling, the bubbles generally cannot percolate in a vacuum dominated inflating regime (this is essentially the graceful exit problem in first-order inflation models); to avoid this, we can assume for simplicity that the SM bath is present with energy density equal to or greater than the latent energy in the false vacuum, so that the Universe remains radiation dominated throughout and does not enter an inflationary phase during the phase transition. To draw the distinction with Scenario III above, by quantum tunneling we will therefore mean a transition that occurs in the absence of a dark sector bath, but without a supercooled (i.e. vacuum-dominated) phase due to the dominance of the SM bath.

2.3 Particle Content

As stated earlier, we will perform our analysis and calculations for DM production in simplified frameworks. We will assume the FOPT is characterized by a scalar field ϕ with vevs $\langle\phi\rangle = 0, v_\phi$ and masses $m_\phi = m_f, m_t$ in the false (unbroken) and true (broken) vacua, with a self-interaction term $\frac{\lambda_\phi}{4!}\phi^4$. The broken symmetry might be global or local; this implies the existence of either a massless Goldstone or massive gauge boson, respectively, in the broken theory. In the latter case, the mass of the gauge boson Z' is $m_{Z'} = g\, v_\phi$, where g is the dark gauge coupling. We will assume that all of these dark sector particles (with the exception of the DM particle) can decay into the SM through small portal couplings, so that the energy in the dark sector eventually gets transferred to the SM bath. Such decays could be necessary to avoid overclosing the Universe or producing dark radiation that leads to excessively large contributions to the effective number of relativistic degrees of freedom $N_{\rm eff}$ in the late Universe if the energy density in the dark sector is substantial. Such decays into the SM might not exist for the Goldstone, which can obtain a small mass due to quantum-gravity effects but might not have any SM decay channels kinematically accessible. In this case, one must ensure that the Goldstone accounts for less than roughly one percent of the total energy density in the Universe for consistency with $N_{\rm eff}$.

For the DM particle χ, we will examine scalar, fermion, as well as vector candidates, which we denote as χ_s, χ_f, and χ_v, respectively. If the DM mass is at or below the scale of symmetry breaking, $m_\chi \lesssim v_\phi$, DM could have obtained its mass during the FOPT from the ϕ vev. For ultraheavy masses $m_\chi \gg v_\phi$, which is the primary regime of interest to us, DM mass is generated at some heavy scale, and the dynamics of symmetry breaking associated with the FOPT has negligible effect on the DM mass.

We will consider the following simplified interactions between the DM candidates and the back-

ground field:

- **Scalar DM** χ_s, with mass m_{χ_s} and interaction $\frac{\lambda_s}{4}\phi^2\chi_s^2$.

  Note that this is a renormalizable operator that can be valid to arbitrarily high scales. Since the above interaction term produces a mass contribution $\sqrt{\lambda_s/2}\,v_\phi$ once ϕ obtains a nonzero vev, we will focus on the regime $m_{\chi_s}^2 > \frac{1}{2}\lambda_s v_\phi^2$, and treat m_{χ_s} and λ_s as independent quantities for simplicity.

- **Fermion DM** χ_f, with mass m_{χ_f} and effective interaction $y_f\phi\chi_f\bar{\chi}_f$.

  Here the $\phi\chi_f\bar{\chi}_f$ interaction implies that the $\chi_f\bar{\chi}_f$ combination is charged under the symmetry that is broken by the ϕ vev. Here χ_f could be a chiral fermion, obtaining its mass from the ϕ vev after the symmetry is broken, analogous to the fermions interacting with the Higgs field in the SM; however, in this case $m_{\chi_f} = y_f v_\phi \lesssim v_\phi$. Alternately, the effective $y_f\phi\chi_f\bar{\chi}_f$ interaction could have been derived from a higher dimensional operator of the form $\frac{y'_f}{\Lambda_f}|\phi|^2\chi_f\bar{\chi}_f$, where Λ_f is some ultraviolet (UV)-cutoff scale. In this case, χ_f does not have to carry any charge associated with ϕ, and its mass can be significantly larger than the symmetry breaking scale of interest, $m_{\chi_f} \gg v_\phi$, and the effective coupling is $y_f = 2y'_f\,v_\phi/\Lambda_f$. A specific realization of this (see [38]) involves ϕ mixing with some singlet scalar S that couples to the fermion χ_f. Here we remain agnostic about such underlying details and simply work with the effective interaction term $y_f\phi\chi_f\bar{\chi}_f$. As with the scalar case, we will focus on masses larger than that obtained from the symmetry breaking, $m_{\chi_f} > y_f\,v_\phi$, and consider m_{χ_f} and y_f as independent parameters.

- **Vector DM** χ_v, with mass m_{χ_v} and an interaction of the form $\frac{1}{2}\lambda_V|\phi|^2\chi_v^\mu\chi_{v\,\mu}$.

  Again, this interaction does not necessitate that the gauge boson χ_v corresponds to the gauge symmetry broken by ϕ, as it could arise from integrating out intermediate particles (e.g. a singlet mediator field, see [38] for more detailed discussions). For a vector boson, additional subtleties arise from the interplay between its transverse and longitudinal modes; these aspects will be discussed in Sec. 6.4. As in the previous two cases, we will treat the mass and coupling as independent quantities.

In all scenarios, we will restrict ourselves to cases where DM is heavier than the scalar and the gauge/Goldstone boson, i.e. $m_\chi > m_f, m_t, m_{Z'}, m_G$, so that DM cannot be produced from decays of other particles in the dark sector, otherwise it can be produced from the oscillations of the scalar field long after the bubble collisions, effectively reaching a thermal abundance, in which case it either re-establishes thermal equilibrium with the bath or tends to be overproduced and overclose the Universe.

Note that the coupling of the scalar field ϕ to particles far heavier than its mass can produce radiative contributions that can lift its mass to the heavy scale, hence the hierarchy $m_\phi, v_\phi \ll m_\chi$ could involve significant fine-tuning. Such concerns are best addressed in complete particle physics models, and we ignore such considerations in our simplified framework treatment in this paper.

Finally, additional dark sector particles beyond the ones discussed above might exist, but their existence is irrelevant as long as they do not couple more strongly to DM than the scalar ϕ and do not produce significant effects on bubble wall dynamics; we will assume this to be the case for the purposes of this paper.

3 Formalism: Particle Production Calculation

In this section, we describe the formalism for calculating particle production from the dynamics of the background field during a FOPT. The transition consists of three stages: bubble nucleation, expansion, and collision, all of which contribute to particle production, see [53] for detailed discussions. Although the contributions from the former two stages are subdominant for the production of heavy particles, we will discuss them here briefly for completion.

3.1 Bubble Nucleation

In the thin-wall limit (where the thickness of bubble walls separating the true and false vacua is significantly smaller than the size of the nucleated bubble, $l_{w0} \ll R_0$), the dynamics of the background field within the bubble can be assumed to be homogeneous, and the number density of a particle species Y produced within the bubble during the nucleation process can be estimated as [53]

$$n_Y \approx \frac{g_Y}{4\pi^5}\, l_w^{-3} \left(\frac{R_0}{R_*}\right)^3 \mathcal{I}\left(l_{w0}\, m_Y\right) e^{-m_Y/(\lambda_Y v_\phi)}\,, \tag{6}$$

where g_Y is the number of degrees of freedom in field Y, λ_Y is the coupling between the background field and Y, and the dimensionless integral factor $\mathcal{I}(a)$ is

$$\begin{aligned}
\mathcal{I}(a) &\equiv \int_0^\infty dx\, x^2 \times \frac{\sinh^2\left[\frac{1}{4}\left(\sqrt{a^2+x^2}-x\right)\right]}{\sinh\left(\frac{1}{2}\sqrt{a^2+x^2}\right)\sinh\left(\frac{1}{2}x\right)} \qquad \text{(bosons)} \\
\mathcal{I}(a) &\equiv \int_0^\infty dx\, x^2 \times \frac{\cosh\left(\frac{1}{2}a\right)-\cosh\left[\frac{1}{2}\left(\sqrt{a^2+x^2}-x\right)\right]}{2\sinh\left(\frac{1}{2}\sqrt{a^2+x^2}\right)\sinh\left(\frac{1}{2}x\right)} \qquad \text{(fermions)}
\end{aligned} \tag{7}$$

The dilution factor $\left(\frac{R_0}{R_*}\right)^3$ in Eq. 6 accounts for the fact that the particles produced within the nucleated bubbles eventually diffuse out over the entire volume of the expanded bubble. Since $R_0 \gg R_*$ (recall that $R_0 \sim v_\phi^{-1}$ whereas $R_* \sim H^{-1}$), this contribution from bubble nucleation is generally negligible compared to the contribution from subsequent bubble evolution calculated below. Furthermore, note the exponential suppression factor $e^{-m_Y/(\lambda_Y v_\phi)}$: particle Y obtains a contribution to its mass $\Delta m_Y = \lambda_Y v_\phi$ from the phase transition; if this is smaller than the bare mass m_Y, the field Y is effectively insensitive to the changing background, hence particle production gets shut off exponentially. Thus, the production of ultraheavy DM $m_\chi \gg \lambda_\chi v_\phi$ during bubble nucleation will be exponentially suppressed.

For a thick-walled bubble, spatial inhomogeneities within the bubble are expected to further suppress particle production compared to the thin-wall case.

3.2 Bubble Expansion

A bubble wall propagating at constant velocity does not produce any particles (for a rigorous derivation, see [53]): one can simply boost to its rest frame, where the configuration is static, hence no particle production can take place. However, in the configurations of interest to us for ultraheavy DM production, bubble walls achieve runaway behavior: they gain the latent energy released from the phase transition and accelerate to larger boost factors as they propagate outwards. Particle

production from such accelerating bubble walls can be estimated by making use of the equivalence principle: a nonuniformly accelerating bubble wall is equivalent to a wall at rest in a changing gravitational field, and the familiar calculation of gravitational particle production yields a number density of produced particles $\sim y_\chi^2 R_*^{-3}$ [53]. This will also be subdominant to the contribution from bubble collisions discussed in the next subsection.

For thick-wall bubbles, the scalar field might not be at its true minimum anywhere in the bubble when the bubble nucleates, and instead evolves towards the true minimum and performs oscillations around it as the bubble expands. This can also be responsible for some particle production (for related discussions, see [63, 75]). Since we are focusing on DM particles that are more massive than the background scalar field, such oscillations cannot produce any DM particles.

3.3 Bubble Collision

Particle production from the collision of bubble walls and the subsequent evolution of the background field is a complicated phenomenon due to the highly inhomogeneous nature of the process. The collision of bubbles was first considered in [76], and particle production from such collisions was first studied in detail in [50]. Based on the formalism in [50], analytic results were derived in simplified ideal limits in [38], and recently refined with numerical studies of more realistic setups in [52] and analytic treatment in [53]. Here we provide a brief outline of the formalism; the interested reader is referred to [38, 50, 52, 53] for greater details.

The probability of particle production from the dynamics of the field ϕ is given by the imaginary part of its effective action,

$$\mathcal{P} = 2\,\mathrm{Im}\,(\,\Gamma[\phi\,]\,), \tag{8}$$

where $\Gamma[\phi\,]$, the effective action, is the generating functional of one-particle irreducible (1PI) Green functions

$$\Gamma[\phi\,] = \sum_{n=2}^{\infty} \frac{1}{n!} \int d^4x_1 ... d^4x_n \Gamma^{(n)}(x_1, ..., x_n)\phi(x_1)...\phi(x_n). \tag{9}$$

The leading ($n = 2$) term suffices for our purposes (we will briefly discuss higher order terms in the next section)

$$\mathrm{Im}\,(\Gamma[\phi]) = \frac{1}{2} \int d^4x_1 d^4x_2 \phi(x_1)\phi(x_2) \int \frac{d^4p}{(2\pi)^4} e^{ip(x_1-x_2)} \mathrm{Im}(\tilde{\Gamma}^{(2)}(p^2))\,, \tag{10}$$

where $\tilde{\Gamma}^{(2)}$ is the Fourier transform of $\Gamma^{(2)}$.

The Fourier transform of the background field is $\tilde{\phi}(p) = \int d^4x \phi(x) e^{ipx}$. We assume that the bubble walls are planar and collisions occur in the $z-$direction, so that $\tilde{\phi}(p) = (2\pi)^2 \delta(p_x)\delta(p_y)\tilde{\phi}(p_z, \omega)$. Using these and the above expressions, the number of particles produced per unit area of colliding bubble walls can be written as [38, 50]

$$\frac{N}{A} = 2 \int \frac{dp_z\, d\omega}{(2\pi)^2} \,|\tilde{\phi}(p_z, \omega)|^2\, \mathrm{Im}[\tilde{\Gamma}^{(2)}(\omega^2 - p_z^2)]\,. \tag{11}$$

This formula invites the following interpretation. The classical background field configuration can be decomposed via a Fourier transform into its momentum modes. Modes of definite four-momentum $p^2 = \omega^2 - p_z^2 > 0$ are to be interpreted as (off-shell) propagating field quanta of the background field with mass $m^2 = p^2$ — we will henceforth denote these as ϕ_p^* — and the probability for each such mode to decay is given by the imaginary part of its Green function.

Following a change of variables, the above formula can be simplified and expressed in terms of the four-momentum of the background field excitations as [38]

$$\frac{N}{A} = \frac{1}{2\pi^2} \int_{p^2_{\rm min}}^{p^2_{\rm max}} dp^2 \, f(p^2) \, {\rm Im}[\tilde{\Gamma}^{(2)}(p^2)]. \tag{12}$$

Here $f(p^2)$ encapsulates the details and nature of the collisions as contained in the Fourier decomposition of the background field configuration, representing the *efficiency factor* for particle production at a given energy scale p. The integral has a lower limit $p_{min} = 2\,m$ (for pair production), set by the mass of the particle species being produced, or the inverse size of the bubble, $(2R_*)^{-1}$ (at lower momenta, the existence of multiple bubbles needs to be taken into account), whichever is greater. The upper cutoff is provided by $p_{max} = 2/l_w = 2\gamma_w/l_{w0}$, the energy in the two colliding bubble walls, which represents the maximum energy available in the process. The particles produced on the bubble wall collision surface (Eq. 12) will diffuse out over the volume occupied by the bubble, so that the final number density of particles per unit volume is

$$n = \frac{3}{4\pi^2 R_*} \int_{p^2_{\rm min}}^{p^2_{\rm max}} dp^2 \, f(p^2) \, {\rm Im}[\tilde{\Gamma}^{(2)}(p^2)]. \tag{13}$$

Similarly, the energy density in particles per unit area is

$$\frac{E}{A} = \frac{1}{2\pi^2} \int_{p^2_{\rm min}}^{p^2_{\rm max}} dp^2 \, p \, f(p^2) \, {\rm Im}[\tilde{\Gamma}^{(2)}(p^2)]. \tag{14}$$

The wall collisions can be broadly classified as elastic (where the bubble walls bounce back after collision, restoring the false vacuum in between) or inelastic (where the walls completely dissipate their energy into scalar oscillations, and the true vacuum is established everywhere immediately following the collision). From numerical studies of realistic bubble collision processes, the efficiency factor in the two cases can be parametrized as [52]

$$f_{\rm elastic}(p^2) = f_{\rm PE}(p^2) + \frac{v_\phi^2 L_p^2}{15 m_{\rm t}^2} \exp\left(\frac{-(p^2 - m_{\rm t}^2 + 12 m_{\rm t}/L_p)^2}{440\, m_{\rm t}^2/L_p^2} \right) \qquad \text{(elastic collisions)} \tag{15}$$

$$f_{\rm inelastic}(p^2) = f_{\rm PE}(p^2) + \frac{v_\phi^2 L_p^2}{4 m_{\rm f}^2} \exp\left(\frac{-(p^2 - m_{\rm f}^2 + 31 m_{\rm f}/L_p)^2}{650\, m_{\rm f}^2/L_p^2} \right) \qquad \text{(inelastic collisions)} \tag{16}$$

Here m_t, m_f are the scalar masses in the true and false vacua respectively. $L_p = \min(R_*, \Gamma_\phi^{-1})$, where Γ_ϕ is the decay rate of the scalar as it performs oscillations around its true or false minimum and R_* is the typical bubble size at collision, provides a measure of the extent to which scalar oscillations propagate in spacetime. Finally, $f_{\rm PE}$ is the efficiency factor for a perfectly elastic collision, derived analytically in [38]

$$f_{\rm PE}(p^2) = \frac{16 v_\phi^2}{p^4} \, {\rm Log}\left[\frac{2(1/l_w)^2 - p^2 + 2(1/l_w)\sqrt{(1/l_w)^2 - p^2}}{p^2} \right]. \tag{17}$$

Recall that $l_w = l_{w0}/\gamma_w$ is the Lorentz-contracted bubble wall thickness.

Note that Eq. 15 and 16 contain two distinct contributions: an approximately power law component $f_{\rm PE} \sim p^{-4}$, originating from the nontrivial dynamics of the background field when the

bubbles collide, and an approximately Gaussian peak centered around the mass of the scalar in the relevant vacuum, coming from the oscillation of the scalar field around its relevant minimum after the collision. Since we assume that the DM particle is heavier than the scalar, $m_\chi > m_t, m_f$, the oscillations do not contribute to DM production, and we can ignore the latter component. DM is thus produced solely via $f(p^2) = f_{\rm PE}$ for both elastic and inelastic collisions.

3.4 Particle Physics Aspects

In the formalism above, in Eqs. 13, 14, the efficiency factor $f(p^2)$ encodes information about the spacetime dynamics of the background field. The particle physics information is encoded in the 2-point 1PI Green function $\Gamma^{(2)}$, to which we now turn our attention.

Using the Optical Theorem, the imaginary part of the 2-point 1PI Green function is given by the sum [38, 50]

$$\mathrm{Im}[\tilde{\Gamma}^{(2)}(p^2)] = \frac{1}{2}\sum_k \int d\Pi_k |\bar{\mathcal{M}}(\phi_p^* \to k)|^2 \tag{18}$$

Here the sum runs over all possible final states k that can be produced from the background field excitations ϕ_p^*, $|\bar{\mathcal{M}}(\phi_p^* \to k)|^2$ is the spin-averaged squared amplitude for the decay of ϕ_p^* into the given final state k, and $d\Pi_k$ denotes the relativistically invariant n-body phase space element.

Note that the imaginary part of the 2PI Green function is an inclusive quantity that necessitates summing over all possible states k that can contribute. To calculate the overall decay probability of the background field, we therefore need to calculate $|\bar{\mathcal{M}}(\phi_p^* \to k)|^2$ for all particle combinations that are allowed in the setup. However, to calculate the decay probability into a given final state (such as the DM particle), it is sufficient to perform the calculation solely for this channel, and the full sum is not required provided the full decay probability remains smaller than 1, i.e. that there are no channels that are so strong that particle production backreacts on the system.

The scalar ϕ particles themselves can be produced through the background field excitations, via the quartic term $\frac{\lambda_\phi}{4!}\phi^4$ in the scalar potential; this gives rise to $\phi_p^* \to \phi\phi$ (with a single vev insertion) and $\phi_p^* \to 3\phi$ decay processes. These lead to

$$\mathrm{Im}[\tilde{\Gamma}^{(2)}(p^2)]_{\phi_p^* \to \phi\phi} = \frac{\lambda_\phi^2\, v_\phi^2}{8\pi}(1 - 4m_\phi^2/p^2)\,\Theta(p - 2m_\phi) \tag{19}$$

and

$$\mathrm{Im}[\tilde{\Gamma}^{(2)}(p^2)]_{\phi_p^* \to 3\phi} = \frac{\lambda_\phi^2\, p^2}{3072\,\pi^3}(1 - 9m_\phi^2/p^2)\,\Theta(p - 3m_\phi) \tag{20}$$

Note that the three-body process is suppressed relative to the two-body process by a loop factor due to an additional particle in the final state, but is proportional to p^2 rather than v_ϕ^2, hence can become more important at higher p^2 as it can be realized even in the $v_\phi \to 0$ limit where the symmetry is unbroken.

For scalar DM, which couples as $\frac{\lambda_s}{4}\phi^2\chi_s^2$, the formulae for two- and three-body decays $\phi_p^* \to \chi_s\chi_s$ and $\phi_p^* \to \phi\chi_s\chi_s$ are analogous to Eqs. 19, 20, with $\lambda_\phi \to \lambda_s$, $3072 \to 1024$ due to modified symmetry factors, and appropriate modifications of the final state masses in the phase space factors and step functions.

For fermion DM, the relevant expression is

$$\mathrm{Im}[\tilde{\Gamma}^{(2)}(p^2)]_{\phi_p^* \to \chi_f\bar{\chi}_f} = \frac{y_f^2}{8\pi}p^2(1 - 4m_{\chi_f}^2/p^2)^{3/2}\,\Theta(p^2 - 4m_{\chi_f}^2)\,. \tag{21}$$

Note that this quantity is proportional to p^2 and can occur in the $v_\phi \to 0$ limit of unbroken symmetry, similar to the three-body scalar decay channel above.

The calculation for vector DM, and final states involving gauge bosons in general, is more subtle and requires a discussion of the gauge dependence of the formalism. This will be the subject of the next section.

4 Gauge Dependence and Production of Gauge Bosons

Here, we consider the case where the scalar vev breaks a local symmetry, and discuss the production of the massive gauge boson V associated with the broken symmetry. The results can be extended in a straightforward manner to other vector bosons, in particular the vector DM candidate we are interested in.

4.1 Gauge Dependence

To understand the subtleties regarding the gauge dependence of the formalism, let us consider the decay of a background field excitation into two gauge bosons, $\phi_p^* \to VV$, which occurs via the interaction term $g v_\phi \phi V_\mu V^\mu$. The calculation of the squared amplitude of this process requires a sum over the gauge boson polarizations. Its general form, in R_ξ gauge, is

$$\sum \epsilon^\mu \epsilon^\nu \to -g^{\mu\nu} + (1-\xi)\frac{p^\mu p^\nu}{p^2 - \xi m_V^2}\,. \tag{22}$$

Recall that in R_ξ gauge, one must also add the contributions from the Goldstone and ghost fields, which have mass $m^2 = \xi m_V^2$. For a physical process, the choice of ξ and the separation of the degrees of freedom into gauge, Goldstone, and ghost fields is simply a matter of bookkeeping, and the final result should be gauge-invariant, i.e. $\xi-$independent. As we will see below, this will not be the case for the above configuration and formalism describing bubble collisions, hence greater care is needed to avoid spurious results.

Generally, a convenient choice is unitary gauge ($\xi \to \infty$), where the Goldstone and ghost fields decouple, and one simply needs to consider the gauge degrees of freedom, for which the above sum over polarization reduces to the familiar expression $\sum \epsilon^\mu \epsilon^\nu \to -g^{\mu\nu} + \frac{p^\mu p^\nu}{m_V^2}$. Using this, the squared amplitude for the $\phi_p^* \to VV$ process can be calculated to be

$$|\bar{\mathcal{M}}(\phi_p^* \to VV)|^2 = g^2 m_V^2 \left(3 - \frac{p^2}{m_V^2} + \frac{p^4}{4m_V^4}\right) \qquad \text{(Unitary gauge)}. \tag{23}$$

One can, instead, perform this calculation in Feynman-'t Hooft gauge ($\xi = 1$). With this choice, the polarization sum yields $\sum \epsilon^\mu \epsilon^\nu \to -g^{\mu\nu}$, and one has to add the Goldstone and ghost contributions separately. Adding these contributions together results in the following expression for the squared amplitude

$$|\bar{\mathcal{M}}(\phi_p^* \to VV)|^2 = g^2 m_V^2 \left(3 - \frac{p^2}{m_V^2} + \frac{\lambda_\phi^2}{g^4}\right) \qquad \text{(Feynman-'t Hooft gauge)}. \tag{24}$$

For a physical process, both results should match and give the correct (physical) result. When the decaying mode corresponds to an on-shell ϕ particle, i.e. $p^2 = m_\phi^2$, this is indeed seen to be true: in this case $p^4/(4m_V^4) = m_\phi^4/(4m_V^4) = \lambda_\phi^2/g^4$, hence the final expressions in the parentheses

in the two equations are identical. The problem arises when the excitation ϕ_p^* is taken off-shell, i.e. $p^2 \neq m_\phi^2$. In this case, the two expressions clearly disagree: in particular, at large $p^2 \gg m_\phi^2, m_V^2$, the unitary gauge result scales as $\sim g^2\, p^4/m_V^2$, whereas the Feynman-'t Hooft gauge result scales as $\sim -g^2\, p^2$. Clearly, this discrepancy persists even after the sum over modes (Eq. 12) is performed; hence the final result for the number density of gauge bosons produced from a bubble collision appears to be gauge-dependent.

Both results above, Eq. 23 and Eq. 24, are however unphysical. The Feynman-'t Hooft gauge result gives a negative decay probability at large p^2, which is clearly unphysical. The problem with the unitary gauge result can be seen most clearly by considering the analogous contribution from the higher multiplicity process $\phi_p^* \to 4V$. Compared to the $\phi_p^* \to 2V$ process, the $4V$ process has an additional scalar propagator, whose contribution to the amplitude squared scales approximately as $\sim \frac{1}{p^4}$; two additional vector bosons in the final state, which give additional phase space factors $(\frac{d^3k}{(2\pi)^3 2p})^2 \sim (\frac{p^2}{4\pi^2})^2$; and a sum over the two additional gauge boson polarization vectors, which yields another factor of $\left(3 - \frac{p^2}{m_V^2} + \frac{p^4}{4m_V^4}\right)$. Thus, we can estimate the leading order contributions at large p from the $\phi_p^* \to 4V$ and $\phi_p^* \to 2V$ processes to the imaginary part of the two point 1PI Green function in unitary gauge to be

$$\mathrm{Im}[\tilde{\Gamma}^{(2)}(p^2)]_{\phi_p^* \to 4V} \sim \frac{g^6 m_V^2}{8\pi(4\pi^2)^2}\left(\frac{p^4}{4m_V^4}\right)^2, \qquad \mathrm{Im}[\tilde{\Gamma}^{(2)}(p^2)]_{\phi_p^* \to 2V} \sim \frac{g^2 m_V^2}{8\pi}\left(\frac{p^4}{4m_V^4}\right). \tag{25}$$

Therefore, the $\phi_p^* \to 4V$ contribution appears to grow faster than the $\phi_p^* \to 2V$ contribution at large p^2. By similar arguments, processes with higher vector boson multiplicity in the final state should grow even faster with p^2. If true, this would preclude the calculation of Eq. 18, which is an inclusive quantity that requires the addition of all of these higher order processes. More worryingly, this unabated growth suggests a breakdown of perturbativity despite the absence of any strong coupling in the theory. This is a clear indication that the growth of the squared amplitude with energy in Eq. 23 is spurious.

A general form of the squared amplitude in R_ξ gauge can be written down but is too cumbersome to be useful, since the gauge, Goldstone, and ghost fields have unequal masses, leading to unequal phase space weights for any finite p, so that their contributions cannot be expressed as a simple sum as in Eqs. 23 and 24. Note that the above two cases are the only exceptions to this: in Feynman-'t Hooft gauge their masses are equal, so that the phase space factor is the same for all contributions and can be factored out, whereas in unitary gauge the Goldstone and ghost fields decouple, and only the gauge component contributes to the amplitude. Nevertheless, one can write the following asymptotic expansions:

$$|\bar{\mathcal{M}}(\phi_p^* \to VV)|^2 = g^2 m_V^2 \times \begin{cases} \frac{(\xi-3)p^2}{2m_V^2} + \frac{\lambda_\phi^2}{g^4} + 3 & \text{for } \frac{p^2}{m_V^2} \gg \xi, 1 \\ \frac{p^4}{4m_V^4} - \frac{p^2}{m_V^2} + 3 & \text{for } \xi \gg \frac{p^2}{m_V^2}, 1 \end{cases} \quad (R_\xi \text{ gauge}). \tag{26}$$

This further illustrates that the high-energy behavior of the off-shell ϕ_p^* decay squared amplitude is gauge-dependent and can become $\mathcal{O}(g^2p^4/m_V^2)$, $\mathcal{O}(g^2p^2)$, or $\mathcal{O}(g^2m_V^2)$, depending on the value of ξ. In particular, in the Fried-Yennie gauge ($\xi = 3$), both the p^4 and p^2 terms are absent in the large-p^2 expansion.

In any gauge-specific calculation, the problem arises due to the inclusion of unphysical contributions that do not get cancelled. For the unitary gauge result, note that the problematic final term in Eq. 23 comes from the prescription of taking $\epsilon_L \to p_i/m_V$ for the production of two longitudinal modes. However, in the large p_i limit, we know that the emission of the longitudinal component

of the gauge boson should be equivalent to the emission of the corresponding Goldstone boson "eaten" by the gauge boson, as prescribed by the Goldstone Equivalence Theorem (GET). Since the Goldstone is a component of the scalar field, this contribution to the matrix element should therefore scale as $\sim \lambda_\phi^2 v_\phi^2$ at high energies, and this $\sim p^4/m_V^2$ growth is unphysical. The Feynman-'t Hooft gauge result rectifies this problem: in Eq. 24, the final term, which comes from adding the emission of two Goldstone bosons, indeed scales as $\sim \lambda_\phi^2 v_\phi^2$ rather than $\sim p^4/m_V^2$, hence the spurious growth with energy encountered in the unitarty gauge calculation is eliminated and the behavior anticipated from the GET is recovered. [1] However, the polarization sum $\sum \epsilon^\mu \epsilon^\nu \to -g^{\mu\nu}$, which includes physical as well as unphysical contributions, now gives rise to the negative (second) term in Eq. 24, resulting in unphysical (negative) probabilities, suggesting that unphysical contributions to the polarization sum have not been cancelled in the final result.

Fully restoring the gauge independence of the calculation requires choosing an initial configuration that is physical, which should result in the cancellation of all unphysical contributions and guarantee gauge independence of the final result. The gauge dependence of the formalism we are considering here can be traced to the assumption that the Fourier transform of the classical field configuration can be interpreted as a collection of off-shell field quanta of different effective masses corresponding to different four-momenta (see Eq. 11 and the paragraph below it). Since an ensemble of off-shell quanta is not a physical configuration, there is no guarantee that the ensuing calculation is gauge invariant.

The issue at hand can be understood in analogy with the familiar example of gauge boson scattering, $VV \to VV$, at center of mass energy E. If one only considers the process $VV \to \phi^* \to VV$ mediated by an s-channel scalar particle, the leading contribution grows as $\sim E^4$. As is well known, this term is cancelled when adding all other diagrams that contribute to $VV \to VV$ scattering; however, to obtain this physical result, it is necessary to sum over all contributions that are relevant. Similarly, the spurious pieces in Eq. 23 and Eq. 24 should also be similarly cancelled if all contributions relevant to the physical process at hand are appropriately included. However, our starting point for the calculation is not a physical process (as in VV scattering) but a collection of off-shell massive excitations ϕ_p^* (akin to only picking out the $VV \to \phi^* \to VV$ contribution for vector boson scattering, which is incomplete), which cannot ensure gauge invariance.

This suggests that the decomposition of the classical scalar field configuration at bubble collision into a collection of Fourier modes of off-shell field quanta in the above formalism misses contributions that are relevant. Without knowing these contributions, a fully gauge invariant calculation cannot be performed. Nevertheless, as we will see below, it is still possible to extract meaningful physical, gauge independent results from the known contributions by making use of the Goldstone Equivalence Theorem, which provides a practical path to performing the necessary calculation.

4.2 High Energy Behavior

Practically speaking, the spurious results above arise from unphysical terms in the sum over gauge boson polarizations. In unitary gauge ($\xi \to \infty$) (Eq. 23), the third term contributes the p^4/m_V^2 term that is unphysical and should have been cancelled by contributions from other relevant diagrams. On the other hand, in Feynman-'t Hooft gauge, $\sum \epsilon^\mu \epsilon^\nu \to -g^{\mu\nu}$ sums over all polarizations, *including* unphysical ones; these, again, should be cancelled by contributions from other relevant diagrams, but remain in their absence and contribute the unphysical $-p^2$ piece in Eq. 24. Therefore, a practical solution would be to only pick out physical contributions from physically allowed

[1] For a related discussion of an equivalent gauge that makes the Goldstone equivalence manifest at high energies, see [77, 78].

polarization states explicitly when performing the sum.

Instead of using Eq. 22 to perform the sum over polarizations, we can instead explicitly pick the polarization states. For a gauge boson moving in the $z-$direction, the transverse (T) polarization states are $\epsilon_T^\mu = (0,1,0,0),\ (0,0,1,0)$, whereas the longitudinal (L) polarization vector is $\epsilon_L^\mu = (p/m_V, 0, 0, E_V/m_V)$. The latter has the problematic p/m_V growth at large p; however, this can be tamed with the Goldstone Equivalence Theorem (GET), which states that at high energies the amplitude for the emission of a longitudinally polarized massive gauge boson becomes equal to the amplitude for emission of the Goldstone mode ϕ_G "eaten" by the gauge boson, up to corrections of order $\mathcal{O}(m_V^2/p^2)$. Thus, even in the absence of all contributing diagrams, the GET provides a prescription for extracting the physical behavior of the longitudinal mode at high energies that is free of unphysical contributions and does not require choosing a specific gauge for the calculation.

We can apply this strategy to the $\phi_p^* \to VV$ process discussed above to extract its high energy behavior. Three polarization combinations contribute to the calculation of $|\mathcal{M}|^2$:

- TT: The emission of transverse modes is well behaved, and gives $2m_V^2$.
- LL: Using the GET, this is equivalent to the emission of two Goldstones $\phi_p^* \to \phi_G\phi_G$, and gives $\lambda_\phi^2 v_\phi^2$, or equivalently $(\lambda_\phi^2/g^2)m_V^2$.
- TL: Invoking the GET, we need to calculate $\phi_p^* \to V_T(p_1)\phi_G(p_2)$ to obtain the high energy behavior of this contribution. This diagram comes from the kinetic term of the scalar, and has a vertex factor $ig(p^\mu + p_2^\mu)$ that contracts with the gauge boson polarization ϵ_T^μ. In the rest frame of ϕ_p^*, the two emitted particles are back to back, these vectors are othogonal, and this contraction vanishes, hence this combination does not contribute at high energies. [2]

Adding these contributions, we obtain the following form of the squared amplitude at high energies:

$$|\bar{\mathcal{M}}(\phi_p^* \to VV)|^2 \xrightarrow{p^2 > m_V^2} (2g^2 + \frac{\lambda_\phi^2}{g^2})\, m_V^2\, (1 + \mathcal{O}(m_V^2/p^2)) \qquad \text{(Goldstone Equivalence Theorem).} \tag{27}$$

Note that this result is well-behaved and contains neither the spurious $\propto p^4$ growing term from the unitary gauge calculation nor the $-p^2$ term from the calculation in Feynman-'t Hooft gauge; the above prescription has eliminated all unphysical ingredients and picked out the relevant physical contributions from the process at hand, without requiring any explicit computation in a specific gauge. This will continue to be the case for all other relevant diagrams, as we discuss below. Therefore, we can interpolate between the low energy behavior (Eq. 23) and the high energy behavior (Eq. 27) to obtain an approximate result for the production of gauge bosons; this method introduces inaccuracies in the intermediate regime ($p^2 \sim m_V \sim v_\phi$), but the final result for the total number of particles is expected to be correct within an $\mathcal{O}(1)$ factor.

4.3 Other Processes

In addition to $\phi_p^* \to VV$, there also exists the three-body decay process $\phi_p^* \to \phi VV$. Naive gauge-specific calculations also give unphysical results for this decay channel for the reasons described

[2] Strictly speaking, the collection of background field excitation modes has a distribution of p_z, and there is no frame where they are all collectively at rest. Nevertheless, we have assumed that for the decay of each excitation, the calculation can be performed in its rest frame, as is conventionally done for a collection of particles with a distribution of momenta, otherwise the result is not Lorentz invariant.

above, but one can similarly use the prescription above to estimate its high energy behavior:

$$\phi_p^* \to \phi VV: \qquad |\bar{\mathcal{M}}|^2_{p<v_\phi} \sim g^4\left(3-\frac{p^2}{m_V^2}+\frac{p^4}{4m_V^4}\right), \qquad |\bar{\mathcal{M}}|^2_{p>v_\phi} \sim \lambda_\phi^2+2g^4\,. \tag{28}$$

Note that this three-body decay will be phase-space suppressed relative to the two-body decay by a factor $\sim(16\pi^2)^{-1}$ due to an additional particle in the final state but can nevertheless dominate at large p, analogously to the two and three-body scalar decay processes in Eqs.19, 20.

Similarly, particles can also be produced due to interactions between multiple Fourier modes, e.g. $\phi^*_{p1}\phi^*_{p2} \to \phi\phi, VV, \chi\chi$. These correspond to higher order terms in the expansion in Eq. 9. The Fourier transform of the additional $\phi^*_{p_i}$ excitation in the initial state scales as $\sim(v_\phi/p^2)^2$, hence the higher order $\phi^*_{p1}\phi^*_{p2} \to \phi\phi, VV, \chi\chi$ processes are subdominant for very heavy DM but can introduce $O(1)$ corrections for DM whose mass arises from its coupling to ϕ.

However, further higher order terms corresponding to additional ϕ^* in the initial configuration, or additional vev insertions, can be important in processes involving particles with mass lighter than the scale of symmetry breaking. For concreteness, consider the scalar DM candidate with χ_s with mass m_{χ_s} that couples to ϕ via the interaction $\frac{\lambda_s}{4}\phi^2\chi_s^2$. A double ϕ^* insertion on the DM state introduces a factor $\sim\left(\frac{v_\phi}{p^2}\right)^4$ from the Fourier transform of the additional ϕ excitations, vertex factor λ_s^2, an additional DM propagator, which gives a $\frac{1}{p^4}$ contribution, and phase space factors that scale with some appropriate power of p, resulting in an overall contribution that is a factor $\sim\lambda_s^2\left(\frac{v_\phi}{p}\right)^4$ larger than the original diagram. Therefore, one cannot truncate the expansion in Eq. 9 at the leading term if $p^2 \lesssim \lambda_s\, v_\phi^2$. However, as mentioned in Sec. 2.3, we restrict ourselves to $m_{\chi_s}^2 > \frac{1}{2}\lambda_s v_\phi^2$, hence it is consistent to ignore such higher order corrections in this region of parameter space.

4.4 Backreaction Effects

In the previous subsections, we have highlighted two important aspects of particle production from bubble dynamics: (i) the calculation for gauge boson production is gauge dependent, and the correct scaling at high energies can be obtained by making use of the Goldstone equivalence theorem; (ii) at high energies, the emission of three (scalar or gauge) bosons is enhanced compared to the emission of two bosons despite the phase space suppression, as the squared matrix element scales as $\sim p^2$ in the former case and as $\sim v_\phi^2$ in the latter. Here we briefly discuss the relevance of these results for backreaction effects on bubble dynamics and DM abundance; for more detailed discussions on backreaction effects, see [53].

If the energy density in the produced particles is a significant fraction of the latent energy released in the phase transition, this creates a backreaction effect on the bubble dynamics, which should be appropriately taken into account for phenomenological applications such as the calculation of gravitational waves from the scalar field at and after bubble collision, and for calculating the relic abundance of DM. From the formula for the energy density in the produced particles (Eq. 14), we see that the energy density depends critically on the form of $\mathrm{Im}[\tilde{\Gamma}^{(2)}]$, or equivalently the matrix element $|\mathcal{M}|^2$. Since $f(p^2) \sim p^{-4}$ (Eq. 17), if $\mathrm{Im}[\tilde{\Gamma}^{(2)}] \sim p^x$ with $x > 1$, the energy density in particles grows as a positive power of p^2, hence backreaction can become significant for large values of p.

Previous works [38, 50] concluded that the production of scalars (for which the matrix element for pair production scales as $|\mathcal{M}|^2 \propto p^0$) is not strong enough, but pair production of fermions

($|\mathcal{M}|^2 \propto p^2$) and gauge bosons ($|\mathcal{M}|^2 \propto p^4$) can be efficient enough to backreact on bubble dynamics; in particular, the production of gauge bosons is so efficient at high energies (as can be seen from inserting $|\mathcal{M}|^2 \propto p^4$ in Eq. 14) that it significantly reduces the energy available for other states, so that it precludes the possibility for scalar DM in a first-order electroweak phase transition (and other gauged transitions in general), whereas fermion DM remains marginally possible, and vector DM can be realized across a large range of masses from $\sim 1 - 10^8$ TeV.

Our results disagree with these conclusions. As discussed in Sec 4.1 above, the $|\mathcal{M}|^2 \propto p^4$ scaling for gauge boson pair production at large p^2 is a spurious gauge artifact, and the correct scaling at energies above the scale of symmetry breaking is in fact $|\mathcal{M}|^2 \propto p^0$ (Eq. 27). However, we noted that the three-body decay processes involving scalars and gauge bosons $\phi_p^* \to 3\phi,\ \phi VV$, Eq. 20, 28 (which were not considered in [38, 50], but discussed in [53]), do scale as $\mathrm{Im}[\tilde{\Gamma}^{(2)}] \propto p^2$ (albeit with additional phase space suppression). As a result, there is no process with $\mathrm{Im}[\tilde{\Gamma}^{(2)}] \propto p^4$ that can backreact severely on the bubble dynamics, but the processes with $\mathrm{Im}[\tilde{\Gamma}^{(2)}] \propto p^2$ can backreact if the associated coupling is sufficiently large; see [53] for a more detailed and qualitative treatment. As we will see below, these modified results open up significant parameter space for scalar, fermion, and vector DM.

5 Dark Matter Production

Before exploring the parameter space where the above mechanism yields the correct dark matter relic abundance, we first discuss other DM production mechanisms that might be active at various stages of the phase transition in different cases. Here we will use the general interaction form $\frac{1}{4}\lambda_\chi \phi^2 \chi^2$, using the general notation χ for DM and λ_χ for its coupling to the background field, as the discussion is broadly applicable to DM of arbitrary spin. We will revert to spin-specific notations as introduced in Sec. 2.3 where this is not the case. Here we are simply interested in obtaining order-of-magnitude estimates, hence we will make use of several approximations without worrying about $\mathcal{O}(1)$ factors.

The relic abundance of DM can be written as

$$\Omega_\chi h^2 = 6.3 \times 10^8 \frac{m_\chi}{\mathrm{GeV}} \frac{n_\chi}{g_*(T_*) T_*^3}\,, \tag{29}$$

where n_χ is the DM number density at the time of production (in our case, given by Eq. 13), when the temperature of the thermal bath after the FOPT is T_*, and g_* is the number of degrees of freedom in the bath at this time. Recall that the observed abundance of DM corresponds to $\Omega_{DM} h^2 = 0.12$.

5.1 Pre-Transition Contributions

The early Universe before the phase transition could already contain some DM abundance. If DM is in thermal equilibrium with the bath, it obtains an equilibrium number density $n_\chi \sim T^3$ before undergoing thermal freezeout, during which its abundance can drop exponentially for $T < m_\chi$. For DM masses beyond the unitarity bound $\mathcal{O}(100)$ TeV, the frozen-out relic abundance is too large and not viable; in this case, the abundance can be suppressed below $\Omega_{DM} h^2 = 0.12$ if there is a large amount of entropy injection that dilutes the DM yield by several orders of magnitude. This can occur if the transition is supercooled, or through late decays of some heavy particles, or if the dark sector is decoupled from the visible (SM) sector and colder.

Freeze-in:

Another viable possibility for masses beyond the unitarity bound involves DM never reaching equilibrium with the dark or SM bath, but only realizing smaller, nonthermal abundances via the freeze-in mechanism [55, 56]. This can occur if the reheat temperature of the Universe T_R, defined as the maximum temperature of the thermal bath after the onset of radiation domination following inflation, is below the freezeout temperature for DM.[3] Alternately, non-equilibrium is maintained at higher temperatures above the DM mass if the associated coupling is sufficiently small; this is achieved for $\lambda_\chi \lesssim \sqrt{v_\phi/M_{Pl}}$. In both cases, DM is produced gradually via freeze-in processes such as $\phi\phi \to \chi\chi$.

If ϕ is in thermal equilibrium with the SM bath and the $\phi\phi \to \chi\chi$ process originates from a renormalizable coupling $\frac{\lambda_\chi}{4}\phi^2\chi^2$, as would be the case if DM is a scalar or a vector, the DM relic abundance from this contribution is [56]

$$\Omega_\chi h^2 \sim 10^{20}\, \lambda_\chi^2 e^{-2m_\chi/T_R} \left(\frac{T_n}{T_*}\right)^3, \tag{30}$$

where the exponential factor has been added to account for the Boltzmann suppression that exists if $m_\chi > T_R$, and the $\left(\frac{T_n}{T_*}\right)^3$ factor accounts for entropy dilution from the energy injection from the FOPT. Recall that we have assumed that none of the dark sector particles can decay into DM, so that there is no contribution from $\phi \to \chi\chi$ or other dark sector decays.

If, instead, this annihilation occurs through a higher dimensional operator of the form $\frac{1}{\Lambda}\phi\phi\chi\chi$, as could be the case for fermion DM, or for DM in the presence of a heavy mediator (in this case additional considerations might be relevant, see [81]), the abundance is UV-dominated [82, 83], i.e. receives dominant contributions at the largest temperatures. If ϕ is in equilibrium with the SM bath, the UV freeze-in abundance of fermion DM produced from this operator is [83]

$$\Omega_\chi h^2 \sim 0.1 \left(\frac{m_\chi}{\text{GeV}}\right) \left(\frac{1000\, T_R\, M_{Pl}}{\Lambda^2}\right) e^{-2m_\chi/T_R} \left(\frac{T_n}{T_*}\right)^3. \tag{31}$$

If ϕ is out of equilibrium with the SM bath, then ϕ itself gets produced via freeze-in processes, and its subsequent annihilations produce DM. The DM abundance in this case can be calculated analogously using appropriately modified versions of the above formulae.

Note that the above contributions only exist in the presence of a dark sector bath (Scenarios I, II in Section 2.2), but are irrelevant in scenarios where a dark sector bath is essentially absent (Scenarios III, IV).

5.2 Other Contributions during the Transition

Wall-plasma interactions:

In the presence of a dark sector bath, additional DM production can occur when ϕ particles present in the bath interact with relativistic bubble walls as they cross into true vacuum bubbles [4] [33, 34, 85, 86]. For a renormalizable interaction of the form $\frac{\lambda_\chi}{4}\phi^2\chi^2$, the probability for a ϕ particle

[3] The Universe could have reached temperatures higher than T_R during the thermalization phase between the end of inflation and the onset of radiation domination [79], which can also enable the production of massive particles [80].

[4] It is also worth noting here that for properly calculating the effects of particles transitioning across the bubble wall in a gauged theory, the fields need to be appropriately quantized across the bubble wall, and the quantization of the longitudinal mode of the gauge boson in particular is subtle [84].

to up-scatter into $\chi\chi$ as it transitions across a bubble wall is [33]

$$P(\phi \to \chi\chi) = \frac{\lambda_\chi^2\, v_\phi^2}{96\pi^2 m_\chi^2}\,. \tag{32}$$

Here, $\lambda_\chi^2 v_\phi^2/m_\chi^2$ can be thought of as an effective mixing angle between ϕ and the $\chi\chi$ state. This transition requires the crossing of the ϕ particle across the bubble wall to be non-adiabatic, i.e. the evolution occurs sufficiently rapidly that the ϕ particle cannot adiabatically track the massive ϕ eigenstate across the wall but instead upscatters into the $\chi\chi$ combination. This non-adiabaticity condition is given by [33, 34, 85]

$$\gamma_w > \frac{l_{w0}\, m_\chi^2}{T_*} \sim \frac{m_\chi^2}{v_\phi^2}\,, \tag{33}$$

where in the second step we have assumed $l_{w0}^{-1} \sim T_* \sim v_\phi$. Thus we see that merely being above the kinematic threshold for DM production, $\gamma_w T_* > m_\chi$, is not sufficient; the non-adiabaticity condition requires γ_w to be larger than this by an additional factor of m_χ/v_ϕ. Provided Eq. 33 is satisfied, the DM contribution from the above particle-bubble interaction process is [33]

$$\Omega_\chi h^2 \approx \frac{1.35\times 10^5 \lambda_\chi^2}{g_*} \frac{v_\phi^2}{m_\chi^2} \frac{m_\chi}{\mathrm{GeV}} \left(\frac{T_n}{T_*}\right)^3\,. \tag{34}$$

Bubbletron:

Particle-bubble interactions can also produce DM via another mechanism. Particles gaining mass from bubble crossing can produce shells of accelerated particles with large boost factors that get dragged along with the bubble walls, and when the bubble walls collide, these particle shells also collide with high energies, an event dubbed a "bubbletron" [40]. The realization of this configuration requires the particles to retain their energies over the course of the expansion phase (i.e. not interact with other particles in their vicinity). In this case, since the accelerated particles gain boost factors comparable to the boost factor of the wall $\sim \gamma_w$, their collisions can also produce very heavy DM. The modeling of such particles shells and their phase space distributions and collisions is complicated and the subject of ongoing work in the literature (see [40]). Here, using the simple estimates from [40], we approximate the DM contribution from this process to be

$$\Omega_\chi h^2 \sim 10^{-15}\, \lambda_\chi^2\, \frac{\beta}{H} \left(\frac{T_n}{T_*}\right)^4 \frac{m_\chi\, v_\phi}{\mathrm{GeV}^2}\,. \tag{35}$$

We have checked that this is consistent with the DM abundance estimated by (optimistically) assuming that a collection of particles with a thermal abundance $\sim T_n^3$ undergoes collisions with energy $\sim \gamma_w/l_{w0}$ for a duration $\sim R_*^{-1}$.

5.3 Post-Transition Contributions

The phase transition completes when the bubbles of true vacuum collide, and the energy carried by the bubble walls dissipates into dark sector particles and scalar waves. Recall that the bubble collisions produce particles with very high energies, up to $\sim 1/l_w = \gamma_w/l_{w0} \sim \gamma_w v_\phi$. Therefore, these particles are energetic enough to produce DM through their collisions even when the DM mass is significantly higher than the temperature of the bath T_* or the scale of symmetry breaking v_ϕ (or even the reheat temperature T_R). Note that this post-transition contribution exists for all

FOPTs (Scenarios I-IV in Sec. 2.2), including the ones that are devoid of a dark sector bath before the phase transition, since the bubble collisions populate dark sector particles in all cases.

We can make some simple qualitative observations to estimate the importance of this effect. From the previous sections, we know that the leading order diagram for the production of a particle of any spin scales as $|\mathcal{M}|^2 \propto p^2$ at high energies through either two- or three-body decays; therefore, the abundances of dark sector particles at a given energy are approximately proportional to their couplings to the background field. From this, it is straightforward to deduce that any dark sector particle with a coupling to the background field smaller than that of the DM particle is produced with lower abundance than DM (beyond the kinematic threshold where DM can be produced), and cannot affect its abundance. It is only possible to substantially alter the DM abundance in the presence of a dark sector particle that has a larger coupling to the background field than the DM particle.

Scalar Annihilation:

The existence of such particles is a model-dependent question; nevertheless, in the minimal model we can consider the contribution from the production and subsequent annihilations of the scalar field ϕ itself. In the presence of a large self coupling ($\lambda_\phi > \lambda_\chi$), ϕ particles are produced at high energies with a greater abundance than χ particles through the $\phi_p^* \to 3\phi$ process (Eq. 20). These high energy ϕ particles decay with a finite lifetime into the SM bath, but before they decay, they can self-scatter and thermalize through the quartic coupling, approaching a thermal distribution. During this thermalization process, they can also (with a lower probability) annihilate into DM states. Since we are interested in $m_\phi \ll m_\chi$, we can only consider the fraction of the ϕ population with energies greater than the DM mass. For this population, a simple estimate for the number density of DM particles from ϕ annihilation in a Hubble time after the completion of the phase transition is

$$n_{\chi\,(\phi\phi\to\chi\chi)} \approx n_{\phi\,(E_\phi > 2m_\chi)} n_\phi\, \sigma_{\phi\phi\to\chi\chi}/H \approx \frac{\lambda_\chi^2}{32\pi\sqrt{g_*}} \frac{n_{\phi\,(E_\phi>2m_\chi)} n_\phi\, M_{Pl}}{m_\chi^2\, T_*^2}\,, \tag{36}$$

where n_ϕ, the abundance of scalar particles produced from bubble collisions, can be calculated using the formalism described in the previous sections. We will calculate this contribution numerically in the next section, but it is possible to provide some qualitative arguments that the above can at most be an $\mathcal{O}(1)$ correction to DM abundance, as follows: The ratio of the abundances is given approximately by the ratio of the squares of the corresponding couplings, $n_\chi/n_{\phi\,(E_\phi>2m_\chi)} \sim y_\chi^2/\lambda_\phi^2$. The fraction of high energy ϕ states that annihilate into DM states rather than losing their energy through scattering can be roughly estimated to be $\sim y_\chi^2/\lambda_\phi^2$. Therefore, the ϕ particles with sufficient energy to produce DM through annihilations are $\sim \lambda_\phi^2/y_\chi^2$ times as abundant as DM, but only a $\sim y_\chi^2/\lambda_\phi^2$ fraction annihilate into DM, hence this contribution to the DM relic abundance is expected to be an $\mathcal{O}(1)$ effect. Once the ϕ particles attain a thermal distribution, or decay into a thermal SM bath, this thermal population does not contain sufficient energy to produce DM. The above estimates hold if all ϕ particles participate in annihilations or scatterings; in practice, the number density n_ϕ can be sufficiently low that these interactions do not occur frequently as the Universe expands, in which case the DM contribution is correspondingly smaller.

In addition to the scalar ϕ, there exists at least one other dark sector particle in the physical spectrum: either a (pseudo) Goldstone boson (if the broken symmetry is global) or a gauge boson (if the broken symmetry is gauged). Goldstone annihilations are expected to give a contribution comparable to that from the scalar, since annihilations that produce heavy DM occur at energies above the scale of symmetry breaking, where Goldstone interactions are expected to be similar to scalar interactions. Gauge bosons can only annihilate directly to DM provided the DM particle is

charged under the symmetry that the gauge boson corresponds to; in this case, the contribution from this process can be calculated in the same way. In the absence of a direct (gauge) coupling, gauge boson annihilation to DM can occur through diagrams mediated by the scalar, but this contribution is expected to be subdominant compared to the abundance produced directly from scalar annihilations.

In a specific model, the DM abundance from such ϕ as well as other dark sector particle annihilations can be obtained by numerically solving the Boltzmann equations with the appropriate injection of the dark sector particle spectra from bubble collisions; however, this is beyond the scope of the present work.

5.4 Subsequent Evolution

At production, the DM particles are localized around sites of bubble collisions, but since they are highly boosted, with energies $E_\chi \sim \gamma_w v_\phi$, they quickly propagate over all space and reach a homogeneous distribution. For consistency with observations, the DM population is required to become cold (i.e. nonrelativistic) by the time of matter-radiation equality, which should occur when the temperature of the radiation bath drops down to the keV scale. If $E_\chi/m_\chi > T_*/\text{keV}$, the redshift of momenta due to the expansion of the Universe is not sufficient to achieve this, and DM particles need to scatter multiple times with other dark sector particles to become sufficiently cold. To this end, one can check if a DM particle scatters with a ϕ particle within a Hubble time after the completion of the phase transition, weighed by the fractional momentum loss from each collision; the condition for this to occur is [34]

$$n_\phi \, \sigma_{\phi\chi\to\phi\chi} v \frac{\delta p_{\rm DM}}{p_{\rm DM}} > H \quad \Rightarrow \quad n_\phi \, \frac{\lambda_\chi^2}{64\, m_\chi^2} \frac{T_n}{T_*} > 1.66\sqrt{g_*}\frac{T_*^2}{M_{Pl}} \,, \tag{37}$$

where in the second step we have used various relations given in [34]. It can be challenging to satisfy the above condition if DM only has a small coupling λ_χ to the scalar field, or if the ϕ number density n_ϕ is significantly smaller than a thermal abundance $\sim T^3$. In such cases, DM cannot dissipate its energy and might be too hot at late times to be consistent with observations.

If DM does cool sufficiently through a combination of redshift due to the expansion of the Universe and scattering with other dark sector particles, such DM particles can nevertheless feature long free-streaming lengths that can leave observable imprints. Ref. [34] explored various observational effects of heavy DM produced with large boosts, and found that such long free-streaming lengths for DM can result in a suppressed matter power spectrum that could provide measurable effects for future cosmological observations; see Ref. [34] for further details. It is also interesting to note that a small fraction of DM, if sufficiently boosted, might also contribute to dark radiation at Big Bang Nucleosynthesis (BBN) (see e.g. [87]). Finally, it is worth noting that ultraheavy DM close to the Planck scale could potentially also be detected purely through its gravitational interactions with experimental efforts such as the Windchime project [88].

6 Dark Matter Parameter Space

In this section, we explore the parameter space where dark matter can be produced with the desired abundance using the formalism described in the previous sections. We will provide an extensive discussion for the case of scalar DM, and discuss fermion and vector DM, which involve more subtleties (see discussion in Sec. 2.3), more briefly.

First, it is useful to rewrite various relevant expressions and conditions discussed above in terms of the phase transition parameters defined in Sec. 2.1. We assume that the energy released in the phase transition gets converted to a thermal bath of SM and dark sector particles. Eventually all dark sector particles (other than DM) decay into the SM. Using energy conservation, the temperature T_* of this SM bath can be calculated via

$$\frac{\pi^2}{30} g_* T_*^4 = \rho_{\rm radiation} + \Delta V = \frac{\Delta V}{\alpha} + \Delta V = \frac{1+\alpha}{\alpha}\, c_V\, v_\phi^4 \,, \tag{38}$$

where $\rho_{\rm radiation}$ is the energy density in the radiation bath prior to the phase transition, T_* is the temperature of the thermalized bath, g_* is the number of degrees of freedom (d.o.f.) in the final thermal bath (for which we will use $g_* = 100$, which approximates the SM d.o.f. above the QCD phase transition), and we have used various definitions and relations provided in Sec. 2.1. Thus we have

$$T_* = \left(\frac{30(1+\alpha)}{g_* \pi^2 \alpha} c_V\right)^{1/4} v_\phi \,. \tag{39}$$

For the temperature T_n at which the phase transition commences, we can similarly use

$$\frac{\pi^2}{30} g_{*i} T_n^4 = \frac{\Delta V}{\alpha} \quad \Rightarrow \quad T_n = \left(\frac{30}{g_{*i} \pi^2 \alpha} c_V\right)^{1/4} v_\phi \,, \tag{40}$$

where g_{*i} is now the number of degrees of freedom in the plasma when the phase transition occurs. For simplicity, we will assume that the initial bath is made up of both SM and dark sector particles, and use $g_{*i} \approx g_* = 100$; if the bath only contains the SM or dark sector, this only introduces $\mathcal{O}(1)$ corrections to our final results. Thus we have $T_n/T_* = (1+\alpha)^{-1/4}$.

We can also rewrite the formula for the DM abundance, Eq. 29, in terms of the phase transition parameters from Sec. 2.1 and the formula for the number density produced from background field dynamics, Eq. 13, as

$$\Omega_\chi h^2 \approx 5 \times 10^{-12} \frac{\beta}{H} \left(\frac{\alpha}{(1+\alpha) g_* c_V}\right)^{1/4} \frac{m_\chi}{v_\phi} \frac{1}{\rm GeV^2} \int_{p^2_{\rm min}}^{p^2_{\rm max}} dp^2\, f(p^2)\, {\rm Im}[\tilde{\Gamma}^{(2)}(p^2)] \,. \tag{41}$$

As stated earlier, we can use the functional form $f(p^2) = f_{\rm PE}(p^2)$ from Eq. 17 for both elastic and inelastic collisions, as we assume that DM is heavier than the scalar field ϕ, hence the second terms in Eqs.15, 16, corresponding to scalar field oscillations after wall collision, cannot produce DM particles and can be neglected. The logarithmic factor in the expression for $f_{\rm PE}(p^2)$ requires a numerical evaluation of the integral in Eq. 41, which is cumbersome and time-consuming; a simplification can be made by observing that this logarithmic factor evaluates to a number between 6 and 60 across the range of parameter values of interest to us, hence we can reasonably approximate ${\rm Log}\left[\frac{2(\gamma_w/l_w)^2 - p^2 + 2(\gamma_w/l_w)\sqrt{(\gamma_w/l_w)^2 - p^2}}{p^2}\right] \approx 20$ for all cases to simplify our calculations. This enables us to further simplify the above formula as

$$\Omega_\chi h^2 \approx 0.1 \left(\frac{\beta/H}{10}\right) \left(\frac{\alpha}{(1+\alpha) g_* c_V}\right)^{1/4} \frac{m_\chi\, v_\phi}{(2.5\ {\rm TeV})^2} \int_{p^2_{\rm min}}^{p^2_{\rm max}} \frac{dp^2}{p^4}\, {\rm Im}[\tilde{\Gamma}^{(2)}(p^2)] \,. \tag{42}$$

For a given form of the function ${\rm Im}[\tilde{\Gamma}^{(2)}(p^2)]$, it is then possible to solve this integral analytically, thereby obtaining a fully analytic expression for the DM relic abundance. We will do this for various cases in the following subsections.

Experiment	$f_{optimal}$/**Hz**	v_ϕ/**GeV**	$m_{\rm DM}$/GeV
Pulsar Timing Arrays (PTAs) [107]	10^{-8}	0.1	$10^{13} - 10^{16}$
LISA [108]	0.001	10^4	$10^6 - 10^{15}$
BBO [109], DECIGO [110]	0.1	10^6	$10^5 - 10^{13}$
Einstein Telescope (ET) [111], Cosmic Explorer (CE) [112]	10	10^8	$10^6 - 10^{10}$

Table 1: Peak gravitational wave frequencies, corresponding scales of phase transition, and ranges of viable (scalar) dark matter masses (with couplings in the range 10^{-4} to 1) for various existing and planned gravitational wave experiments.

6.1 Gravitational Waves

Before delving into the details of DM production, it is worth discussing the connection with gravitational waves. One of the main attractive features of FOPTs in contemporary research is that they can give rise to stochastic GW signals that can be observed with a variety of existing and upcoming GW detectors. It is therefore judicious to examine whether the FOPTs that can produce the correct DM relic abundance can also give sizable GW signals, which would provide a unique observational probe of this DM production mechanism.

FOPTs can produce gravitational waves in several ways: through the scalar field energy densities in the bubble walls after collision [4–7, 57, 75, 89–95], the production of sound waves [96–101] and turbulence [7, 99, 102–106] in the surrounding plasma, or through energy transfer to nontrivial spatial configurations of feebly-interacting particles [30]. In this paper, we are primarily interested in runaway bubble configurations, where the bubble walls carry most of the energy released in the transition, hence the GWs are primarily sourced by bubble wall collisions, i.e. the scalar field. For such GWs, we use the peak frequency of the signal today as obtained from the results of [75], which can be expressed as [34]

$$f_{\rm peak(GW)} = 15\ \mu{\rm Hz}\ \frac{\beta}{H}\, g_*^{1/6} \left(\frac{T_*}{10^3\,{\rm GeV}}\right) = 20\ \mu{\rm Hz}\ \frac{\beta/H}{g_*^{1/12}} \left(\frac{(1+\alpha)}{\alpha} c_V\right)^{1/4} \left(\frac{v_\phi}{10^3\,{\rm GeV}}\right). \tag{43}$$

Using this relation, we can map the scale of the phase transition v_ϕ to the optimal frequencies of various gravitational wave detectors, as shown in Table 1. The table shows the corresponding scales of FOPTs that provide GW signals that peak at the optimal frequencies of various detectors as determined by the above formula for some reasonable choices of parameters ($\beta/H = 10$, $g_* = 100$, $\alpha = 1, c_V = 0.1$). For these parameter choices, we also list the viable window of DM masses that can be produced from bubble collisions for reasonable couplings between DM and the background field (in the range 10^{-4} to 1) in each case, as derived from our calculations below (see Sec. 6.2, Fig. 2; these numbers correspond to the case of scalar DM, but the numbers for fermion or vector DM should be comparable).

Here, it is worth mentioning that if particle production (including DM production) from bubble collisions is a strong effect, it can affect the subsequent production of GWs, modifying the amplitude as well as shape of the GW signal.

6.2 Scalar Dark Matter

Consider scalar DM χ_s that couples to the background field ϕ via $\frac{1}{4}\lambda_s\phi^2\chi_s^2$, and can be produced via $\phi_p^* \to \chi_s^2,\ \phi\chi_s^2$. Substituting the expressions from Eqs. 19, 20 into Eq. 42, and dropping the

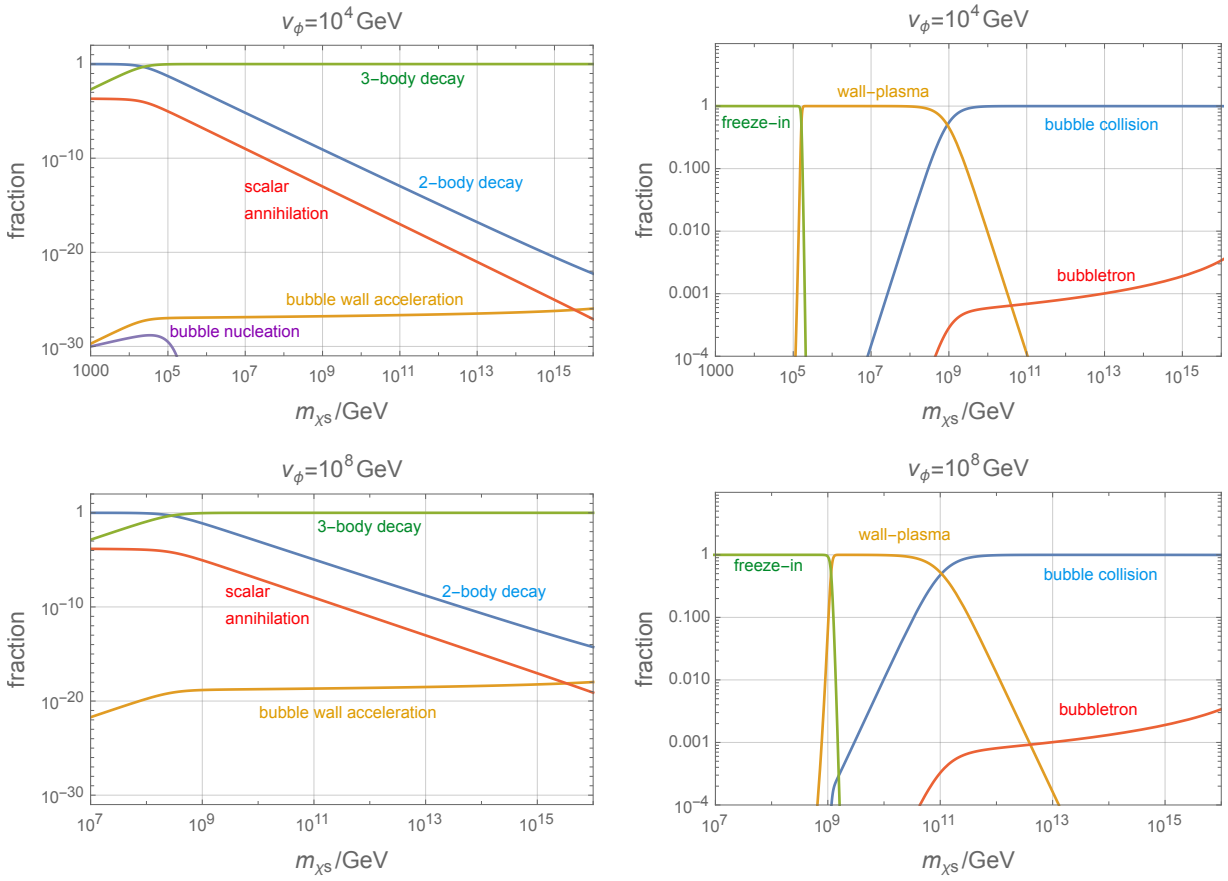

Figure 1: Relative contributions to scalar dark matter relic abundance from various processes as a function of dark matter mass, for $v_\phi = 10^4$ GeV (top row) and $v_\phi = 10^8$ GeV (bottom row), in the absence (left panels) or presence (right panels) of a thermal bath. See text for details.

phase space factors in these equations to enable the integral to be performed analytically, we derive the following expression for the scalar DM relic abundance

$$\Omega_\chi h^2 \approx 0.1 \frac{\beta/H}{10} \left(\frac{\alpha}{(1+\alpha) g_* c_V}\right)^{1/4} \frac{\lambda_s^2 \, m_{\chi_s} \, v_\phi}{(24 \text{ TeV})^2} \left[\frac{v_\phi^2}{m_{\chi_s}^2} + \frac{1}{16\pi^2} \ln\left(\frac{2\,\gamma_w/l_{w0}}{(2m_{\chi_s} + m_\phi)}\right)\right] . \tag{44}$$

The two terms in the square parenthesis correspond to contributions from the two- and three-body decays, respectively. We can see that the latter contribution dominates for $m_{\chi_s} \gtrsim 4\pi \, v_\phi$, clearly demonstrating the importance of the three-body decay channel for heavy scalar DM. We have numerically checked that the above analytic result matches the full numerical result (obtained from evaluating Eqs. 17, 19, 20 numerically without dropping any factors) up to an $\mathcal{O}(1)$ factor over the parameter space we are interested in.

As discussed in the previous sections, several processes contribute to DM production in FOPTs in addition to the background field dynamics at bubble collision: bubble nucleation, bubble expansion (bubble wall acceleration), and annihilations of dark sector particles produced from bubble collisions in all cases (with or without a thermal bath), as well as freeze-in from the thermal bath, wall-plasma interactions, and collisions of accelerated particle shells in the presence of a thermal bath of particles. In Fig. 1, we plot the relative weights of these contributions in the final DM relic density as a function of DM mass for various parameters choices in the absence (left column) or

presence (right column) of a thermal bath of particles. We have chosen $v_\phi = 10^4$ GeV in the top panel (the relevant scale for a GW signal observable by LISA) and $v_\phi = 10^8$ GeV in the bottom panel (the appropriate scale for Einstein Telescope / Cosmic Explorer). In all cases, the coupling λ_s has been chosen such that the sum of all contributions produces the correct DM relic density. For these plots, we have chosen the following values for the various parameters:

$$c_V = 0.1,\ \beta/H = 10,\ \alpha = 1,\ R_0 = 10/v_\phi,\ l_{w0} = 1/v_\phi\,. \tag{45}$$

We have assumed that the bubble walls are in the runaway regime throughout the bubble expansion phase, and with the parameters of Eq. 45 the wall boost factor at the time of collision is

$$\gamma_w = \frac{2R_*}{3\,R_0} \approx \frac{0.15}{\beta/H}\frac{M_{Pl}}{v_\phi}\,, \tag{46}$$

where we have used the relations and parameters listed above. Recall that in the presence of a light gauge boson, the boost factor can reach a terminal value smaller than the above expression (see Eq. 5); however, we do not consider this possibility in this paper.

In the left panels, we plot the two- and three-body decay contributions from $\phi^* \to \chi^2,\ \phi\chi^2$ separately, in blue and green respectively. It can be seen that the former dominates for $m_\chi \lesssim 4\pi v_\phi$, whereas the latter takes prominence for higher DM masses, as anticipated from earlier discussions. The contribution from the annihilation of ϕ particles produced from bubble collisions into DM (assuming the scalar quartic coupling $\lambda_\phi = 1$), corresponding to Eq. 36, is shown in red; this contribution is always found to be a few orders of magnitude smaller than the two-body contribution, and therefore subdominant. Likewise, we also plot the contributions from the bubble nucleation and bubble wall acceleration phases (Sec. 3), in purple and gold respectively. These contributions are seen to be several orders of magnitude smaller than that from bubble collision due to the reasons discussed in Sec. 3 and therefore completely negligible. These patterns continue to hold as v_ϕ is increased from 10^4 to 10^8 GeV (top to bottom left panel). The wall acceleration contribution increases by a few orders of magnitude since it scales as $R_*^{-3} \sim H^3$ and the Hubble scale is higher for higher v_ϕ, but remains negligible. Meanwhile, the bubble nucleation contribution gets further suppressed as it does not rise as rapidly as the other contributions with v_ϕ. Therefore, in the absence of a thermal bath, we find that bubble collisions are the dominant DM production mechanism for any choice of parameters.

In the right panels, we show the relative contributions from various processes in the presence of a thermal bath. We now combine the two- and three-body decays into a single contribution, denoted by the blue curves labelled "bubble collision". As discussed in the previous section, the presence of a thermal bath introduces several new DM production mechanisms: freeze-in from the annihilation of the scalar particles present in the thermal bath $\phi\phi \to \chi_s\chi_s$ (Eq. 30), denoted by the green curves labelled "freeze-in"; non-adiabatic transition of ϕ to $\chi_s\chi_s$ when ϕ particles from the plasma interact with the bubble walls (Eq. 34), denoted by the gold curves labelled "wall-plasma"; and the collisions of boosted ϕ particle shells (Eq, 35), denoted by the red curves labelled "bubbletron". We see that the freeze-in contribution from annihilations of ϕ particles in the thermal bath can dominate for $m_{\chi_s} \lesssim v_\phi$, but rapidly becomes ineffective for $m_{\chi_s} \gtrsim v_\phi$ as the exponential suppression in (Eq. 30) becomes significant (here we chose $T_R \approx v_\phi$; for larger T_R, the freeze-in contribution is expected to dominate for $m_{\chi_s} \lesssim T_R$). The non-adiabatic wall-plasma interaction contribution dominates in the intermediate DM mass regime, as long as

$$\frac{1}{\beta/H}\left(\frac{m_{\chi_s}/v_\phi}{10^5}\right)^2 \frac{v_\phi}{10^4\ \text{GeV}} \lesssim 1\,. \tag{47}$$

Raising m_{χ_s}/v_ϕ results in the suppression of the effective mixing angle between ϕ and $\chi_s\chi_s$ (see discussion surrounding Eq. 33), which eventually makes this contribution subdominant to the abundance produced from three-body decays of the background field excitations. For higher m_{χ_s} values, bubble collision therefore becomes the dominant DM production process. The bubbletron contribution is seen to grow in importance with increasing m_{χ_s} but does not dominate in any part of the parameter space, only contributing at percent level at best; however, annihilation cross-sections at high energies scale as $\sim E^{-2} \sim (\gamma_w v_\phi)^{-2}$ (using γ_w from Eq. 46), so it is possible that a configuration with smaller γ_w could enhance the bubbletron contribution and make it relevant in some parts of parameter space. Note that the above contributions exist in the presence of a plasma, but can be suppressed in a supercooled phase transition, where a brief inflationary phase due to vacuum domination can lead to significant dilution of the pre-existing thermal bath, thereby suppressing these contributions.

Here it is worth emphasizing that previous studies only considered the two-body decay channel $\phi_p^* \to \chi_s\chi_s$ and hence underestimated particle production from bubble collisions, finding it to be subdominant to the wall-plasma or bubbletron contribtutions. When the three-body decay process $\phi_p^* \to \phi\chi_s\chi_s$ is taken into account, we find that this can constitute the dominant contribution for heavy DM even in the presence of a thermal bath and the above processes.

Having examined the relative importance of various processes, we next plot, in Fig. 2, contours of the magnitude of the coupling λ_s required to produce the correct DM relic abundance from bubble collisions as a function of v_ϕ and m_{χ_s}, together with various constraints. This figure shows that bubble collisions can account for the correct DM relic density across a vast range of scales spanning several orders of magnitude. In this plot, we have restricted v_ϕ to values above 100 MeV (below this, an FOPT is likely to disrupt BBN) and m_{χ_s} to values above 100 GeV (lower values are possible, but there are no qualitatively new features beyond what is already seen in the figure). On both axes, we implement an upper cutoff of 10^{16} GeV; beyond this, the value approaches the UV-cutoff of the system (given by the bubble wall thickness at collision γ_w/l_{w0}), and details of the bubble wall profile, which we have not taken into account, become important. The dashed vertical lines denote the FOPT symmetry breaking scales corresponding to the peak sensitivities of various gravitational wave experiments, as described in Sec. 6.1 (see Table 1). We see that ultraheavy DM several orders of magnitude heavier than the symmetry breaking scale v_ϕ can be produced for reasonable values of the coupling λ_s across a large range of FOPT scales of interest for various current and planned GW experiments. It should be emphasized that the DM mass could also be significantly larger than the highest temperature ever reached in our cosmic history.

In the figure, we see that all the contours feature sharp kinks at $m_{\chi_s} \sim 4\pi v_\phi$. This corresponds to the transition between regions of parameter space where two- or three-body decays of the background field excitations dominate the DM production process. For $m_{\chi_s} \lesssim 4\pi v_\phi$, the two-body process dominates; from Eq. 44, $\Omega_\chi h^2 \propto 1/m_{\chi_s}$ when the first term in the parenthesis dominates, hence as m_{χ_s} is increased for fixed v_ϕ, the required coupling increases. In the opposite regime $m_{\chi_s} \gtrsim 4\pi v_\phi$, the three-body process dominates, and the relic density scaling from Eq. 44 when the second term in the parenthesis dominates is instead $\Omega_\chi h^2 \propto m_{\chi_s}$, and now the required coupling decreases as m_{χ_s} is increased for fixed v_ϕ. This explains the reversal of the contour shapes across the two regions in the plot.

The shaded regions denote various constraints, as follows:

- The red region in the bottom left denotes parameter space where the backreaction from particle production becomes important, given approximately by the condition $\lambda_s > 10$; note that this also corresponds to a regime where the coupling becomes nonperturbative.

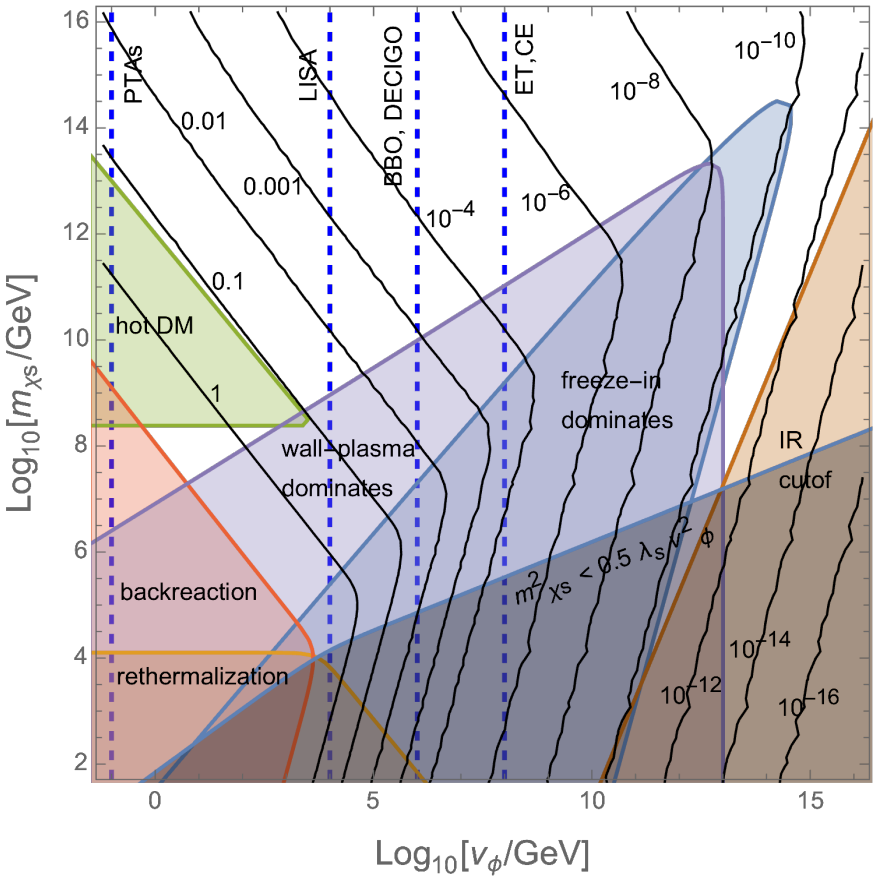

Figure 2: Contours of the value of the coupling λ_s for which the correct scalar dark matter relic density is achieved, as a function of the dark matter mass and the scale of symmetry breaking. The vertical dashed blue lines denote the transition scales that produce gravitational waves at peak sensitivity frequencies for various GW detectors (see Sec. 6.1). The shaded regions represent various constraints, see text for detailed discussions. Note that the blue ("freeze-in dominates") and purple ("wall-plasma dominates") regions are only applicable if a thermal dark sector bath is present before the phase transition, whereas the other regions are applicable for all FOPTs, with or without a bath.

- The green triangular region denotes parameter space where DM is too hot to account for the structures observed today. The constraint disappears for higher m_{χ_s} because heavier DM is not as boosted and can redshift to become cold by the time of matter-radiation equality. Similarly, the constraint also disappears below $m_{\chi_s} \approx 10^{8.5}$ GeV because the value of λ_s required to produce the correct relic density increases, enabling more efficient $\chi_s - \phi$ scattering, which disperses the energy carried by DM particles, allowing them to cool.

- The orange region in the bottom left represents parameter space where the produced DM population re-enters chemical equilibrium with the dark sector bath (i.e. the rate for $\chi_s\chi_s \to \phi\phi$ scattering is faster than Hubble), in which case imprints of the bubble collision process are washed out and DM subsequently undergoes thermal freezeout. Note that this region disappears to the right even though $m_{\chi_s} \ll v_\phi$ since the associated coupling λ_s also becomes very small.

- The brown region in the bottom right corresponds to configurations where $m_{\chi_s} < R_*^{-1}$, i.e. the formalism used to calculate particle production from bubble collisions falls below its IR

cutoff and is no longer valid, since the existence of multiple bubbles should be taken into account in the Fourier transform of the background field.

- The blue region corresponds to parameter space where freeze-in from the annihilation of the scalar particles $\phi\phi \to \chi_s\chi_s$ (Eq. 30) from the pre-existing thermal bath, if present, dominates over production from bubble collision. Note that its upper boundary occurs at roughly $m_{\chi_s} \sim v_\phi$; for heavier DM masses, the exponential suppression in Eq. 30 rapidly suppresses this contribution (recall that we chose $T_R \sim v_\phi$; for larger T_R this region is expected to get bigger). Likewise, the lower boundary of this region coincides approximately with the $\lambda_s \sim 10^{-10}$ contour; as we can see from Eq. 30, even in the absence of the exponential, freeze-in cannot provide the correct relic density for smaller values of λ_s.

- The purple region represents parameter space where the non-adiabatic transition of ϕ to $\chi_s\chi_s$ due to ϕ particles from the plasma (if it exists) interacting with the bubble walls (Eq. 34) dominates over the bubble collision contribution. Beyond the upper boundary and to the right of this region, the non-adiabaticity condition from Eq. 33 continues to hold, but production becomes less efficient than that from bubble collisions. Where blue and purple regions overlap, the blue (freeze-in) contribution generally tends to be larger (see Fig. 1).

- As discussed earlier, we grey out the region $m_{\chi_s}^2 < \frac{1}{2}\lambda_s v_\phi^2$, where the mass contribution expected from the phase transition exceeds the DM mass. In this part of the parameter space, higher order insertions beyond the leading contribution considered in this paper can also become important, as discussed in Sec. 4.3. Furthermore, in this region DM is likely lighter than ϕ as well as other dark sector states, hence the assumption that decays of dark sector particles do not produce DM also possibly breaks down.

Note that Eq. 44 can be further simplified by approximating the second parenthesis as 1 when $\alpha \geq 1$ and the log factor as 10 over the region of parameter space shown in Fig. 2. In the regime where three-body decays dominate (generally the case for $m_{\chi_s} \gtrsim 4\pi v_\phi$), this yields the following simple relation among the parameters to achieve the correct DM relic density

$$\frac{\lambda_s^2\,\beta/H}{10}\,\frac{m_{\chi_s}\,v_\phi}{(100\text{ TeV})^2} \approx 1. \tag{48}$$

This is found to be in excellent agreement with the results shown in Fig. 2.

Finally, we provide an intuitive discussion of the number density of heavy DM particles produced from bubble collisions, based on the results derived above (in particular Eqs. 13, 29, 41, 44). Parametrically, we see that the number of particles produced per unit area of colliding bubble walls scales as $\sim \lambda_s^2\, v_\phi^2$ (times a logarithmic factor), with no other parametric suppression. This diffuses over the size of the bubble to yield a number density $n \sim \lambda_s^2\, v_\phi^2/R_*$; since $l_{w0} \sim v_\phi^{-1}$ and $T_* \sim v_\phi$, this can be rewritten as $n \sim \lambda_s^2\, T_*^3 (l_{w0}/R_*)$. This invites the interpretation that for $\mathcal{O}(1)$ couplings, bubble collisions are efficient at producing essentially a thermal abundance $\sim T_*^3$ of particles within the extent of the bubble wall l_{w0} (as seen in its rest frame), which then diffuses out throughout the bubble. One can also understand the above parametric scaling through a different argument: the energy released in the phase transition is $\Delta V \sim v_\phi^4$, whereas bubble collisions produce particles with typical energy $\gamma_w v_\phi$. Hence efficient particle production from bubble collisions should lead to a number density $n \sim v_\phi^3/\gamma_w$. Recalling that $\gamma_w \sim R_*/R_0 \sim R_*/l_{w0}$, this is the same number density as above for $\mathcal{O}(1)$ couplings.

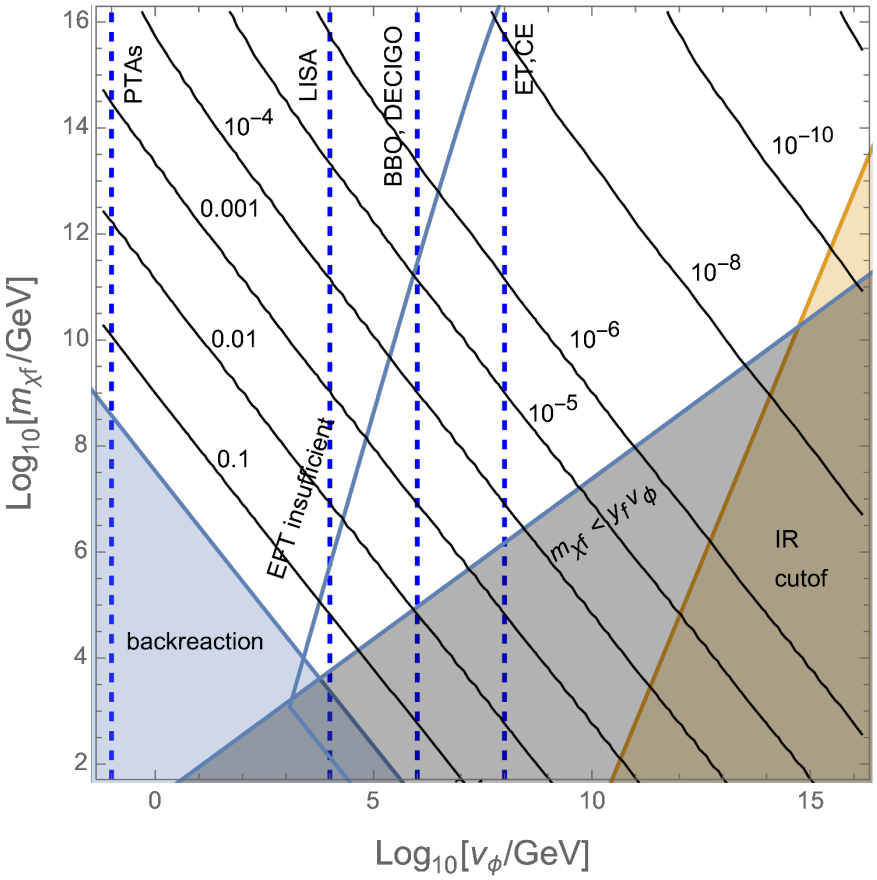

Figure 3: Contours of the value of the coupling y_f for which the correct fermion DM relic density is achieved, as a function of the scale of symmetry breaking and the DM mass. The vertical dashed blue lines denote the transition scales that produce gravitational waves at peak sensitivity frequencies for various detectors (see Sec. 6.1). Details of the constraints in the various regions are discussed in the text.

6.3 Fermion Dark Matter

We now consider the case of fermion DM. Many of the qualitative details and discussions are similar to the case of scalar DM, and we will not repeat them here but instead focus on the differences.

The fermion DM relic abundance from $\phi_p^* \to \chi_f \bar{\chi}_f$ decays arising from the interaction term $y_f \phi \chi_f \bar{\chi}_f$ can be expressed as

$$\Omega_\chi h^2 \approx 0.1 \frac{\beta/H}{10} \left(\frac{\alpha}{(1+\alpha) g_* c_V} \right)^{1/4} \frac{m_{\chi_f} v_\phi}{(8.6 \text{ TeV})^2} y_f^2 \ln \left(\frac{\gamma_w / l_{w0}}{m_{\chi_f}} \right) . \tag{49}$$

In Fig. 3, we plot contours of the magnitude of the coupling y_f required to produce the correct fermion DM relic abundance as a function of v_ϕ and m_{χ_f}, analogous to the scalar DM case in Fig. 2. We choose the same parameters as for scalar DM (Eq. 45), with the boost factor given by Eq. 46. As in Fig. 2, we denote the exclusion region (shaded golden) where the DM mass falls beyond the IR cutoff and the Fourier transform of a single bubble collision is no longer sufficient, and the region (shaded blue) where backreaction from particle production becomes important, i.e. the energy density in the DM particles (calculated using Eq. 14) exceeds the latent energy released in the phase transition, ΔV. The latter region is found to correspond to $y_f > 1.5$. Note that this

backreaction region for fermion DM is larger than the corresponding region for the scalar DM case in Fig. 2 (corresponding approximately to $\lambda_s > 10$) since the fermion is produced via the two-body decay channel $\phi_p^* \to \chi_f \bar{\chi}_f$, whereas the leading contribution for scalar DM at high energies is the phase-space suppressed three-body decay $\phi_p^* \to \phi \chi_s^2$. Also note that the contours of constant y_f in Fig. 3 are straight lines, as two-body decay is the only relevant process for fermion DM, and do not feature the kinks observed in Fig. 2 due to two- and three- body decays being important in different parts of parameter space for scalar DM. Similarly, we show the boundary $m_{\chi_f} = y_f v_\phi$ below which higher order corrections become important and need to be included to get the correct result (see Sec. 4.3).

Unlike Fig. 2, here we do not plot any constraints arising from interactions, such as hot DM, rethermalization, or freeze-in constraints, since these involve $2 \to 2$ interactions, whose nature depends on the UV-completion of the $y_f \phi \chi_f \bar{\chi}_f$ term. As discussed in Sec. 2.3, if χ_f is not charged under the symmetry broken by ϕ, the above interaction is an effective field theory (EFT) interaction derived from some higher dimensional operator of the form $\frac{1}{\Lambda_f}\phi^2 \chi_f \bar{\chi}_f$, obtained by integrating out some UV physics at the scale Λ_f to give the low energy effective coupling $y_f = v_\phi/\Lambda_f$. In the plot, we denote the region (labelled "EFT insufficient") where $\Lambda_f < \min(m_{\chi_f}, v_\phi)$, which corresponds to the breakdown of this EFT, where the new degrees of freedom are no longer heavy and cannot be integrated out. This does not mean that fermion DM with such masses cannot be produced with FOPTs at these scales, but simply that additional physics beyond the minimal EFT interaction considered above would be relevant and could provide the leading effect, hence the EFT calculation can no longer be trusted to give the correct result. Note that these new d.o.f. at the scale Λ_f also affect the result in the remainder of parameter space where $\Lambda_f > m_{\chi_f}, v_\phi$: the particle production calculation involves evaluating the integral in Eq. 42, which runs up to $p_{\max} \approx E_w$. Since the EFT interaction term is only valid up to $p = \Lambda_f$, the new d.o.f. would modify the integrand at larger p values; however, since the integral evaluates to a logarithm (see Eq. 49), we expect this to modify the result only by an $\mathcal{O}(1)$ factor.

Finally, we can also obtain a very simple approximate relation among the parameters that achieves the correct fermion DM relic density, analogous to Eq. 48 and obtained by making the same approximations:

$$\frac{y_f^2\, \beta/H}{10} \frac{m_{\chi_f}\, v_\phi}{(2.7\ \text{TeV})^2} \approx 1. \tag{50}$$

6.4 Vector Dark Matter

Next, we briefly discuss the case of a vector DM particle χ_v, which gets produced via the effective operator $\frac{1}{2}\lambda_V \phi^2 \chi_v^\mu \chi_{v\,\mu}$ introduced in Sec. 2.3. The production of vector DM is similar to the case of scalar DM discussed in Sec. 6.2 and Fig. 2 (since it gets produced through two- and three-body decays $\phi_p^* \to \chi_v \chi_v$, $\phi \chi_v \chi_v$ similar to the scalar case), with the same UV-completion caveats as for fermion DM (Sec. 6.3). We therefore do not make a separate plot for vector DM or repeat similar discussions, but simply mention the additional aspects relevant for the vector case.

If χ_v is the gauge boson corresponding to the symmetry broken by the ϕ vev (in which case $m_{\chi_v} = g\, v_\phi \lesssim v_\phi$, , where g is the gauge coupling), the details of production of transverse and longitudinal modes map directly to the discussion in Sec. 4, with $\lambda_V \to g^2$. In this case, for the two-body decay $\phi_p^* \to \chi_v \chi_v$ one can interpolate between the low energy ($p^2 < m_{\chi_v}^2$) behavior given by Eq. 23 and the high energy ($p^2 > m_{\chi_v}^2$) behavior obtained from the Goldstone Equivalence Theorem, Eq. 27, to construct an approximate solution valid across all energy scales. For the three-body decay $\phi_p^* \to \phi \chi_v \chi_v$, one can similarly interpolate between the two expressions in Eq. 28 to

construct an approximate solution across all energies. Note that the production rate now depends not only on the gauge coupling g but also the scalar quartic coupling λ_ϕ, as the longitudinal component of the gauge boson behaves as the Goldstone field at high energies, as anticipated from the GET.

For $m_{\chi_v} \gg g v_\phi$, χ_v cannot be the gauge boson of the broken symmetry and hence does not couple directly to ϕ, and the effective operator $\frac{1}{2}\lambda_V \phi^2 \chi_v^\mu \chi_{v\,\mu}$ must arise from integrating out some mediator fields at some scale Λ_v. As discussed for the case of fermion DM, the new d.o.f. can modify the results obtained from the EFT operator, and even invalidate the EFT approach in some regions of parameter space. For vector DM, this also introduces an additional consideration: as discussed in Sec. 4, a practical approach to obtain physical, pathology-free results for the production of vectors, which might otherwise be gauge-dependent, is to use the Goldstone Equivalence Theorem to obtain the high energy behavior of longitudinal mode production. This requires appropriately replacing the longitudinal mode with the corresponding Goldstone mode at high energies in the UV theory.

Overall, we expect the production of vector DM to be as general and efficient as the production of scalar DM (from Fig. 2), but any model-specific study of vector DM production from bubble collisions must properly address the various aspects discussed above.

7 Summary and Discussions

Here, we summarize the main points of our paper:

- We have studied nonthermal production of ultraheavy dark matter (DM) from background field dynamics during a first-order phase transition (FOPT), dominated by bubble collisions, where the bubble walls achieve runaway behavior. This constitutes an unavoidable contribution to DM abundance that exists in any FOPT, irrespective of the nature of the transition or the plasma, when DM couples directly or indirectly to the background field undergoing the transition. The contribution studied in this paper can constitute the dominant production mechanism for heavy DM even in the presence of a thermal plasma and the existence of other well-known DM production mechanisms.

- This mechanism is very general and can produce the correct relic density of scalar, fermion, or vector DM across a large range of masses, from $\mathcal{O}(10)$ TeV to a few orders of magnitude below the Planck scale. This broad regime of validity is the result of the DM number density from bubble collisions being only logarithmically sensitive to the DM mass, resulting in a milder DM mass dependence for the DM relic density (see e.g. Eq. 44, Eq. 49) compared to other traditional production mechanisms.

- Such setups provide a natural configuration to produce ultraheavy DM with masses many orders of magnitude greater than the scale of the phase transition as well as the temperature of the thermal bath at any point in cosmological history – for instance, a phase transition at the GeV scale can produce DM as heavy as $\sim 10^{16}$ GeV (see e.g. Fig. 2).

- We have demonstrated that the existing formalism for the calculation of particle production in a gauge theory is not gauge invariant, and can lead to spurious results if not treated carefully (see Sec. 4). We offer a practical prescription to avoid these complications that makes use of explicit polarization vectors and the Goldstone Equivalence Theorem to extricate physically relevant contributions while avoiding spurious unphysical components.

- We have pointed out the importance of three-body decays of the background field excitations, generally ignored in the literature, for the production of scalar and vector particles, which dominate over two-body decays at large energies and provide the dominant contributions for heavy scalar and vector DM. Such three-body decays can also be relevant for fermion DM if the interaction between the background field and fermion DM is mediated by scalar or vector states.

- Although DM from bubble collisions does not require any significant couplings to Standard Model particles, which hampers the detection prospects from traditional direct and indirect DM searches, three phenomenological aspects are noteworthy. (i) FOPTs that produce the correct DM relic abundance can also produce observable gravitational wave signals across a large range of frequencies relevant for current and planned gravitational wave experiments (see Fig. 2, Fig. 3). (ii) DM produced from bubble collisions is highly boosted, which gives rise to a modified matter power spectrum that could be detectable with future cosmological observations. (iii) Ultraheavy DM with mass close to the Planck scale, which can readily be produced via the mechanism discussed in this paper, could be detectable purely through its gravitational couplings.

We conclude by discussing the broader implications of our work and highlighting several specific directions that could benefit from further study. We have provided model-independent results for heavy DM production from a FOPT with runaway bubbles, which was found to be viable over a large region of parameter space spanning several orders of magnitude. These results have broad applicability and can be implemented in a straightforward manner in specific models of FOPTs, hence it will be interesting to check whether various well-motivated BSM scenarios that give rise to FOPTs with runaway bubbles can be extended to include heavy DM candidates. At the same time, the gauge dependence of the formalism suggests that it is not on rigorous footing, and awaits additional theoretical developments towards a proper completion. It would also be interesting to study the effects of particle production from bubble collisions on the subsequent generation of gravitational wave signals. Various cosmological and astrophysical aspects of ultraheavy boosted DM from bubble collisions, in particular the observational aspects of a modified matter power spectrum, are also worth exploring in greater detail. Beyond DM, the formalism for particle production from bubble collisions developed here could also find applications in other open questions in particle physics, such as baryogenesis or leptogenesis [113]. We leave the pursuit of such questions for future work.

Acknowledgments

We are grateful to Thomas Konstandin, Geraldine Servant, Ville Vaskonen, and Andrea Wulzer for insightful discussions. The work of H.M.L is supported in part by Basic Science Research Program through the National Research Foundation of Korea (NRF) funded by the Ministry of Education, Science and Technology (NRF-2022R1A2C2003567 and NRF-2021R1A4A2001897). A.P. has been partly supported by the Departament de Recerca i Universitats from Generalitat de Catalunya to the Grup de Recerca "Grup de Física Teòrica UAB/IFAE" (Codi: 2021 SGR 00649) and the research grant PID2020-115845GB-I00/AEI/10.13039/501100011033. B.S. is supported by the Deutsche Forschungsgemeinschaft under Germany's Excellence Strategy - EXC 2121 Quantum Universe - 390833306. B.S. also thanks the CERN Theory Department and the Lawrence Berkeley National Laboratory for hospitality during multiple visits over the duration of completion of this project.

References

[1] C. J. Hogan, "NUCLEATION OF COSMOLOGICAL PHASE TRANSITIONS," *Phys. Lett. B* **133** (1983) 172–176.

[2] E. Witten, "Cosmic Separation of Phases," *Phys. Rev. D* **30** (1984) 272–285.

[3] C. J. Hogan, "Gravitational radiation from cosmological phase transitions," *Mon. Not. Roy. Astron. Soc.* **218** (1986) 629–636.

[4] A. Kosowsky, M. S. Turner, and R. Watkins, "Gravitational radiation from colliding vacuum bubbles," *Phys. Rev. D* **45** (1992) 4514–4535.

[5] A. Kosowsky, M. S. Turner, and R. Watkins, "Gravitational waves from first order cosmological phase transitions," *Phys. Rev. Lett.* **69** (1992) 2026–2029.

[6] A. Kosowsky and M. S. Turner, "Gravitational radiation from colliding vacuum bubbles: envelope approximation to many bubble collisions," *Phys. Rev. D* **47** (1993) 4372–4391, arXiv:astro-ph/9211004.

[7] M. Kamionkowski, A. Kosowsky, and M. S. Turner, "Gravitational radiation from first order phase transitions," *Phys. Rev. D* **49** (1994) 2837–2851, arXiv:astro-ph/9310044.

[8] A. H. Guth, "Inflationary universe: A possible solution to the horizon and flatness problems," *Phys. Rev. D* **23** (Jan, 1981) 347–356. https://link.aps.org/doi/10.1103/PhysRevD.23.347.

[9] D. La and P. J. Steinhardt, "Extended inflationary cosmology," *Phys. Rev. Lett.* **62** (Jan, 1989) 376–378. https://link.aps.org/doi/10.1103/PhysRevLett.62.376.

[10] C. Grojean and G. Servant, "Gravitational Waves from Phase Transitions at the Electroweak Scale and Beyond," *Phys. Rev.* **D75** (2007) 043507, arXiv:hep-ph/0607107 [hep-ph].

[11] C. Caprini *et al.*, "Science with the space-based interferometer eLISA. II: Gravitational waves from cosmological phase transitions," *JCAP* **1604** (2016) 001, arXiv:1512.06239 [astro-ph.CO].

[12] C. Caprini and D. G. Figueroa, "Cosmological Backgrounds of Gravitational Waves," *Class. Quant. Grav.* **35** no. 16, (2018) 163001, arXiv:1801.04268 [astro-ph.CO].

[13] C. Caprini *et al.*, "Detecting gravitational waves from cosmological phase transitions with LISA: an update," *JCAP* **2003** (2020) 024, arXiv:1910.13125 [astro-ph.CO].

[14] P. Athron, C. Balázs, A. Fowlie, L. Morris, and L. Wu, "Cosmological phase transitions: from perturbative particle physics to gravitational waves," arXiv:2305.02357 [hep-ph].

[15] L. Randall and G. Servant, "Gravitational waves from warped spacetime," *JHEP* **05** (2007) 054, arXiv:hep-ph/0607158.

[16] P. Schwaller, "Gravitational Waves from a Dark Phase Transition," *Phys. Rev. Lett.* **115** no. 18, (2015) 181101, arXiv:1504.07263 [hep-ph].

[17] J. Jaeckel, V. V. Khoze, and M. Spannowsky, "Hearing the signal of dark sectors with gravitational wave detectors," *Phys. Rev. D* **94** no. 10, (2016) 103519, arXiv:1602.03901 [hep-ph].

[18] P. S. B. Dev and A. Mazumdar, "Probing the Scale of New Physics by Advanced LIGO/VIRGO," *Phys. Rev. D* **93** no. 10, (2016) 104001, arXiv:1602.04203 [hep-ph].

[19] I. Baldes, "Gravitational waves from the asymmetric-dark-matter generating phase transition," *JCAP* **05** (2017) 028, arXiv:1702.02117 [hep-ph].

[20] K. Tsumura, M. Yamada, and Y. Yamaguchi, "Gravitational wave from dark sector with dark pion," *JCAP* **07** (2017) 044, arXiv:1704.00219 [hep-ph].

[21] N. Okada and O. Seto, "Probing the seesaw scale with gravitational waves," *Phys. Rev. D* **98** no. 6, (2018) 063532, arXiv:1807.00336 [hep-ph].

[22] D. Croon, V. Sanz, and G. White, "Model Discrimination in Gravitational Wave spectra from Dark Phase Transitions," *JHEP* **08** (2018) 203, arXiv:1806.02332 [hep-ph].

[23] I. Baldes and C. Garcia-Cely, "Strong gravitational radiation from a simple dark matter model," *JHEP* **05** (2019) 190, arXiv:1809.01198 [hep-ph].

[24] T. Prokopec, J. Rezacek, and B. Świeżewska, "Gravitational waves from conformal symmetry breaking," *JCAP* **02** (2019) 009, arXiv:1809.11129 [hep-ph].

[25] Y. Bai, A. J. Long, and S. Lu, "Dark Quark Nuggets," *Phys. Rev. D* **99** no. 5, (2019) 055047, arXiv:1810.04360 [hep-ph].

[26] M. Breitbach, J. Kopp, E. Madge, T. Opferkuch, and P. Schwaller, "Dark, Cold, and Noisy: Constraining Secluded Hidden Sectors with Gravitational Waves," *JCAP* **07** (2019) 007, arXiv:1811.11175 [hep-ph].

[27] M. Fairbairn, E. Hardy, and A. Wickens, "Hearing without seeing: gravitational waves from hot and cold hidden sectors," *JHEP* **07** (2019) 044, arXiv:1901.11038 [hep-ph].

[28] A. J. Helmboldt, J. Kubo, and S. van der Woude, "Observational prospects for gravitational waves from hidden or dark chiral phase transitions," *Phys. Rev. D* **100** no. 5, (2019) 055025, arXiv:1904.07891 [hep-ph].

[29] F. Ertas, F. Kahlhoefer, and C. Tasillo, "Turn up the volume: listening to phase transitions in hot dark sectors," *JCAP* **02** no. 02, (2022) 014, arXiv:2109.06208 [astro-ph.CO].

[30] R. Jinno, B. Shakya, and J. van de Vis, "Gravitational Waves from Feebly Interacting Particles in a First Order Phase Transition," (11, 2022) , arXiv:2211.06405 [gr-qc].

[31] M. J. Baker, J. Kopp, and A. J. Long, "Filtered Dark Matter at a First Order Phase Transition," arXiv:1912.02830 [hep-ph].

[32] D. Chway, T. H. Jung, and C. S. Shin, "Dark matter filtering-out effect during a first-order phase transition," arXiv:1912.04238 [hep-ph].

[33] A. Azatov, M. Vanvlasselaer, and W. Yin, "Dark Matter production from relativistic bubble walls," *JHEP* **03** (2021) 288, arXiv:2101.05721 [hep-ph].

[34] I. Baldes, Y. Gouttenoire, and F. Sala, "Hot and heavy dark matter from a weak scale phase transition," *SciPost Phys.* **14** no. 3, (2023) 033, arXiv:2207.05096 [hep-ph].

[35] T. Hambye, A. Strumia, and D. Teresi, "Super-cool Dark Matter," *JHEP* **08** (2018) 188, arXiv:1805.01473 [hep-ph].

[36] P. Baratella, A. Pomarol, and F. Rompineve, "The Supercooled Universe," *JHEP* **03** (2019) 100, arXiv:1812.06996 [hep-ph].

[37] I. Baldes, Y. Gouttenoire, F. Sala, and G. Servant, "Supercool composite Dark Matter beyond 100 TeV," *JHEP* **07** (2022) 084, arXiv:2110.13926 [hep-ph].

[38] A. Falkowski and J. M. No, "Non-thermal Dark Matter Production from the Electroweak Phase Transition: Multi-TeV WIMPs and 'Baby-Zillas'," *JHEP* **02** (2013) 034, arXiv:1211.5615 [hep-ph].

[39] K. Freese and M. W. Winkler, "Dark matter and gravitational waves from a dark big bang," *Phys. Rev. D* **107** no. 8, (2023) 083522, arXiv:2302.11579 [astro-ph.CO].

[40] I. Baldes, M. Dichtl, Y. Gouttenoire, and F. Sala, "Bubbletrons," arXiv:2306.15555 [hep-ph].

[41] L. Parker, "Quantized fields and particle creation in expanding universes. 1.," *Phys. Rev.* **183** (1969) 1057–1068.

[42] A. A. Grib and S. G. Mamaev, "On field theory in the friedman space," *Yad. Fiz.* **10** (1969) 1276–1281.

[43] Y. B. Zeldovich and A. A. Starobinsky, "Particle production and vacuum polarization in an anisotropic gravitational field," *Zh. Eksp. Teor. Fiz.* **61** (1971) 2161–2175.

[44] E. W. Kolb and A. J. Long, "Cosmological gravitational particle production and its implications for cosmological relics," arXiv:2312.09042 [astro-ph.CO].

[45] S. Aoki, H. M. Lee, A. G. Menkara, and K. Yamashita, "Reheating and dark matter freeze-in in the Higgs-R^2 inflation model," *JHEP* **05** (2022) 121, arXiv:2202.13063 [hep-ph].

[46] H. M. Lee and A. G. Menkara, "Graceful exit from inflation and reheating with twin waterfall scalar fields," *Phys. Rev. D* **107** no. 11, (2023) 115019, arXiv:2304.08686 [hep-ph].

[47] J. S. Schwinger, "On gauge invariance and vacuum polarization," *Phys. Rev.* **82** (1951) 664–679.

[48] S. W. Hawking, "Black hole explosions," *Nature* **248** (1974) 30–31.

[49] S. W. Hawking, "Particle Creation by Black Holes," *Commun. Math. Phys.* **43** (1975) 199–220. [Erratum: Commun.Math.Phys. 46, 206 (1976)].

[50] R. Watkins and L. M. Widrow, "Aspects of reheating in first order inflation," *Nucl. Phys.* **B374** (1992) 446–468.

[51] T. Konstandin and G. Servant, "Natural Cold Baryogenesis from Strongly Interacting Electroweak Symmetry Breaking," *JCAP* **07** (2011) 024, arXiv:1104.4793 [hep-ph].

[52] H. Mansour and B. Shakya, "On Particle Production from Phase Transition Bubbles," arXiv:2308.13070 [hep-ph].

[53] B. Shakya, "Aspects of Particle Production from Bubble Dynamics at a First Order Phase Transition," arXiv:2308.16224 [hep-ph].

[54] D. Carney *et al.*, "Snowmass2021 Cosmic Frontier White Paper: Ultraheavy particle dark matter," arXiv:2203.06508 [hep-ph].

[55] J. McDonald, "Thermally generated gauge singlet scalars as selfinteracting dark matter," *Phys. Rev. Lett.* **88** (2002) 091304, arXiv:hep-ph/0106249.

[56] L. J. Hall, K. Jedamzik, J. March-Russell, and S. M. West, "Freeze-In Production of FIMP Dark Matter," *JHEP* **03** (2010) 080, arXiv:0911.1120 [hep-ph].

[57] D. Bodeker and G. D. Moore, "Can electroweak bubble walls run away?," *JCAP* **05** (2009) 009, arXiv:0903.4099 [hep-ph].

[58] G. C. Dorsch, S. J. Huber, and T. Konstandin, "Bubble wall velocities in the Standard Model and beyond," *JCAP* **12** (2018) 034, arXiv:1809.04907 [hep-ph].

[59] J. R. Espinosa, T. Konstandin, J. M. No, and G. Servant, "Energy Budget of Cosmological First-order Phase Transitions," *JCAP* **06** (2010) 028, arXiv:1004.4187 [hep-ph].

[60] D. Bodeker and G. D. Moore, "Electroweak Bubble Wall Speed Limit," *JCAP* **05** (2017) 025, arXiv:1703.08215 [hep-ph].

[61] S. Höche, J. Kozaczuk, A. J. Long, J. Turner, and Y. Wang, "Towards an all-orders calculation of the electroweak bubble wall velocity," *JCAP* **03** (2021) 009, arXiv:2007.10343 [hep-ph].

[62] Y. Gouttenoire, R. Jinno, and F. Sala, "Friction pressure on relativistic bubble walls," (12, 2021) , arXiv:2112.07686 [hep-ph].

[63] J. Ellis, M. Lewicki, and V. Vaskonen, "Updated predictions for gravitational waves produced in a strongly supercooled phase transition," arXiv:2007.15586 [astro-ph.CO].

[64] T. Konstandin and G. Servant, "Cosmological Consequences of Nearly Conformal Dynamics at the TeV scale," *JCAP* **12** (2011) 009, arXiv:1104.4791 [hep-ph].

[65] B. von Harling and G. Servant, "QCD-induced Electroweak Phase Transition," *JHEP* **01** (2018) 159, arXiv:1711.11554 [hep-ph].

[66] J. Ellis, M. Lewicki, and J. M. No, "On the Maximal Strength of a First-Order Electroweak Phase Transition and its Gravitational Wave Signal," *JCAP* **04** (2019) 003, arXiv:1809.08242 [hep-ph].

[67] S. Bruggisser, B. Von Harling, O. Matsedonskyi, and G. Servant, "Electroweak Phase Transition and Baryogenesis in Composite Higgs Models," *JHEP* **12** (2018) 099, arXiv:1804.07314 [hep-ph].

[68] L. Delle Rose, G. Panico, M. Redi, and A. Tesi, "Gravitational Waves from Supercool Axions," *JHEP* **04** (2020) 025, arXiv:1912.06139 [hep-ph].

[69] B. Von Harling, A. Pomarol, O. Pujolàs, and F. Rompineve, "Peccei-Quinn Phase Transition at LIGO," *JHEP* **04** (2020) 195, arXiv:1912.07587 [hep-ph].

[70] K. Fujikura, Y. Nakai, and M. Yamada, "A more attractive scheme for radion stabilization and supercooled phase transition," *JHEP* **02** (2020) 111, arXiv:1910.07546 [hep-ph].

[71] J. Ellis, M. Lewicki, J. M. No, and V. Vaskonen, "Gravitational wave energy budget in strongly supercooled phase transitions," *JCAP* **06** (2019) 024, arXiv:1903.09642 [hep-ph].

[72] V. Brdar, A. J. Helmboldt, and M. Lindner, "Strong Supercooling as a Consequence of Renormalization Group Consistency," *JHEP* **12** (2019) 158, arXiv:1910.13460 [hep-ph].

[73] I. Baldes, Y. Gouttenoire, and F. Sala, "String Fragmentation in Supercooled Confinement and Implications for Dark Matter," *JHEP* **04** (2021) 278, arXiv:2007.08440 [hep-ph].

[74] S. Bruggisser, B. von Harling, O. Matsedonskyi, and G. Servant, "Status of electroweak baryogenesis in minimal composite Higgs," *JHEP* **08** (2023) 012, arXiv:2212.11953 [hep-ph].

[75] D. Cutting, E. G. Escartin, M. Hindmarsh, and D. J. Weir, "Gravitational waves from vacuum first order phase transitions II: from thin to thick walls," *Phys. Rev. D* **103** no. 2, (2021) 023531, arXiv:2005.13537 [astro-ph.CO].

[76] S. W. Hawking, I. G. Moss, and J. M. Stewart, "Bubble Collisions in the Very Early Universe," *Phys. Rev. D* **26** (1982) 2681.

[77] G. Cuomo, L. Vecchi, and A. Wulzer, "Goldstone Equivalence and High Energy Electroweak Physics," *SciPost Phys.* **8** no. 5, (2020) 078, arXiv:1911.12366 [hep-ph].

[78] A. Wulzer, "An Equivalent Gauge and the Equivalence Theorem," *Nucl. Phys. B* **885** (2014) 97–126, arXiv:1309.6055 [hep-ph].

[79] G. F. Giudice, E. W. Kolb, and A. Riotto, "Largest temperature of the radiation era and its cosmological implications," *Phys. Rev. D* **64** (2001) 023508, arXiv:hep-ph/0005123.

[80] D. J. H. Chung, E. W. Kolb, and A. Riotto, "Production of massive particles during reheating," *Phys. Rev. D* **60** (1999) 063504, arXiv:hep-ph/9809453.

[81] E. Frangipane, S. Gori, and B. Shakya, "Dark matter freeze-in with a heavy mediator: beyond the EFT approach," *JHEP* **09** (2022) 083, arXiv:2110.10711 [hep-ph].

[82] F. Elahi, C. Kolda, and J. Unwin, "UltraViolet Freeze-in," *JHEP* **03** (2015) 048, arXiv:1410.6157 [hep-ph].

[83] S. B. Roland and B. Shakya, "Cosmological Imprints of Frozen-In Light Sterile Neutrinos," *JCAP* **05** (2017) 027, arXiv:1609.06739 [hep-ph].

[84] A. Azatov, G. Barni, R. Petrossian-Byrne, and M. Vanvlasselaer, "Quantisation Across Bubble Walls and Friction," arXiv:2310.06972 [hep-ph].

[85] A. Azatov and M. Vanvlasselaer, "Bubble wall velocity: heavy physics effects," *JCAP* **01** (2021) 058, arXiv:2010.02590 [hep-ph].

[86] A. Azatov, G. Barni, S. Chakraborty, M. Vanvlasselaer, and W. Yin, "Ultra-relativistic bubbles from the simplest Higgs portal and their cosmological consequences," *JHEP* **10** (2022) 017, arXiv:2207.02230 [hep-ph].

[87] B. Shakya and J. D. Wells, "Sterile Neutrino Dark Matter with Supersymmetry," *Phys. Rev. D* **96** no. 3, (2017) 031702, arXiv:1611.01517 [hep-ph].

[88] **Windchime** Collaboration, A. Attanasio *et al.*, "Snowmass 2021 White Paper: The Windchime Project," in *Snowmass 2021*. 3, 2022. arXiv:2203.07242 [hep-ex].

[89] C. Caprini, R. Durrer, and G. Servant, "Gravitational wave generation from bubble collisions in first-order phase transitions: An analytic approach," *Phys. Rev. D* **77** (2008) 124015, arXiv:0711.2593 [astro-ph].

[90] S. J. Huber and T. Konstandin, "Gravitational Wave Production by Collisions: More Bubbles," *JCAP* **09** (2008) 022, arXiv:0806.1828 [hep-ph].

[91] R. Jinno and M. Takimoto, "Gravitational waves from bubble collisions: An analytic derivation," *Phys. Rev. D* **95** no. 2, (2017) 024009, arXiv:1605.01403 [astro-ph.CO].

[92] R. Jinno and M. Takimoto, "Gravitational waves from bubble dynamics: Beyond the Envelope," *JCAP* **01** (2019) 060, arXiv:1707.03111 [hep-ph].

[93] T. Konstandin, "Gravitational radiation from a bulk flow model," *JCAP* **03** (2018) 047, arXiv:1712.06869 [astro-ph.CO].

[94] D. Cutting, M. Hindmarsh, and D. J. Weir, "Gravitational waves from vacuum first-order phase transitions: from the envelope to the lattice," *Phys. Rev. D* **97** no. 12, (2018) 123513, arXiv:1802.05712 [astro-ph.CO].

[95] M. Lewicki and V. Vaskonen, "Gravitational waves from colliding vacuum bubbles in gauge theories," *Eur. Phys. J. C* **81** no. 5, (2021) 437, arXiv:2012.07826 [astro-ph.CO]. [Erratum: Eur.Phys.J.C 81, 1077 (2021)].

[96] M. Hindmarsh, S. J. Huber, K. Rummukainen, and D. J. Weir, "Gravitational waves from the sound of a first order phase transition," *Phys. Rev. Lett.* **112** (2014) 041301, arXiv:1304.2433 [hep-ph].

[97] M. Hindmarsh, S. J. Huber, K. Rummukainen, and D. J. Weir, "Numerical simulations of acoustically generated gravitational waves at a first order phase transition," *Phys. Rev. D* **92** no. 12, (2015) 123009, arXiv:1504.03291 [astro-ph.CO].

[98] M. Hindmarsh, S. J. Huber, K. Rummukainen, and D. J. Weir, "Shape of the acoustic gravitational wave power spectrum from a first order phase transition," *Phys. Rev. D* **96** no. 10, (2017) 103520, arXiv:1704.05871 [astro-ph.CO]. [Erratum: Phys.Rev.D 101, 089902 (2020)].

[99] D. Cutting, M. Hindmarsh, and D. J. Weir, "Vorticity, kinetic energy, and suppressed gravitational wave production in strong first order phase transitions," *Phys. Rev. Lett.* **125** no. 2, (2020) 021302, arXiv:1906.00480 [hep-ph].

[100] M. Hindmarsh, "Sound shell model for acoustic gravitational wave production at a first-order phase transition in the early Universe," *Phys. Rev. Lett.* **120** no. 7, (2018) 071301, arXiv:1608.04735 [astro-ph.CO].

[101] M. Hindmarsh and M. Hijazi, "Gravitational waves from first order cosmological phase transitions in the Sound Shell Model," *JCAP* **12** (2019) 062, arXiv:1909.10040 [astro-ph.CO].

[102] C. Caprini, R. Durrer, and G. Servant, "The stochastic gravitational wave background from turbulence and magnetic fields generated by a first-order phase transition," *JCAP* **12** (2009) 024, arXiv:0909.0622 [astro-ph.CO].

[103] A. Brandenburg, T. Kahniashvili, S. Mandal, A. Roper Pol, A. G. Tevzadze, and T. Vachaspati, "Evolution of hydromagnetic turbulence from the electroweak phase transition," *Phys. Rev. D* **96** no. 12, (2017) 123528, arXiv:1711.03804 [astro-ph.CO].

[104] A. Roper Pol, S. Mandal, A. Brandenburg, T. Kahniashvili, and A. Kosowsky, "Numerical simulations of gravitational waves from early-universe turbulence," *Phys. Rev. D* **102** no. 8, (2020) 083512, arXiv:1903.08585 [astro-ph.CO].

[105] J. Dahl, M. Hindmarsh, K. Rummukainen, and D. Weir, "Decay of acoustic turbulence in two dimensions and implications for cosmological gravitational waves," (12, 2021) , arXiv:2112.12013 [gr-qc].

[106] P. Auclair, C. Caprini, D. Cutting, M. Hindmarsh, K. Rummukainen, D. A. Steer, and D. J. Weir, "Generation of gravitational waves from freely decaying turbulence," *JCAP* **09** (2022) 029, arXiv:2205.02588 [astro-ph.CO].

[107] T. Bringmann, P. F. Depta, T. Konstandin, K. Schmidt-Hoberg, and C. Tasillo, "Does NANOGrav observe a dark sector phase transition?," *JCAP* **11** (2023) 053, arXiv:2306.09411 [astro-ph.CO].

[108] **LISA** Collaboration, P. Amaro-Seoane *et al.*, "Laser Interferometer Space Antenna," arXiv:1702.00786 [astro-ph.IM].

[109] G. M. Harry, P. Fritschel, D. A. Shaddock, W. Folkner, and E. S. Phinney, "Laser interferometry for the big bang observer," *Class. Quant. Grav.* **23** (2006) 4887–4894. [Erratum: Class.Quant.Grav. 23, 7361 (2006)].

[110] S. Kawamura *et al.*, "The Japanese space gravitational wave antenna DECIGO," *Class. Quant. Grav.* **23** (2006) S125–S132.

[111] M. Punturo *et al.*, "The Einstein Telescope: A third-generation gravitational wave observatory," *Class. Quant. Grav.* **27** (2010) 194002.

[112] D. Reitze *et al.*, "Cosmic Explorer: The U.S. Contribution to Gravitational-Wave Astronomy beyond LIGO," *Bull. Am. Astron. Soc.* **51** no. 7, (2019) 035, arXiv:1907.04833 [astro-ph.IM].

[113] M. Cataldi and B. Shakya [in preparation].